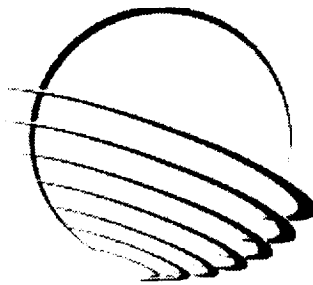




35th Aerospace Mechanisms Symposium

Compiled by: Edward A. Boesiger



Proceedings of a symposium held at
The Four Points Hotel, Sunnyvale, CA
Hosted by the Ames Research Center and
Lockheed Martin Space Systems Company
Organized by the Mechanisms Education Association

May 9–11, 2001

May 2001

Available from:

NASA Center for AeroSpace Information
7121 Standard Drive
Hanover, MD 21076-1320
(301) 621-0390

National Technical Information Service
5285 Port Royal Road
Springfield, VA 22161
(703) 487-4650

PREFACE

The Aerospace Mechanisms Symposium (AMS) provides a unique forum for those active in the design, production and use of aerospace mechanisms. A major focus is the reporting of problems and solutions associated with the development and flight certification of new mechanisms. Organized by the Mechanisms Education Association, the National Aeronautics and Space Administration and Lockheed Martin Space Systems Company (LMSSC) share the responsibility for hosting the AMS. Now in its 35th year, the AMS continues to be well attended, attracting participants from both the U.S. and abroad.

The 35th AMS, hosted by the Ames Research Center (ARC) in Mountain View, California, was held May 9, 10 and 11, 2001. During these three days, 25 papers were presented. Topics included deployment mechanisms, bearings, actuators, pointing and optical mechanisms, Space Station mechanisms, release mechanisms, and test equipment. Hardware displays during the supplier fair gave attendees an opportunity to meet with developers of current and future mechanism components.

The high quality of this symposium is a result of the work of many people, and their efforts are gratefully acknowledged. This extends to the voluntary members of the symposium organizing committee representing the eight NASA field centers, LMSSC, and the European Space Agency. Appreciation is also extended to the session chairs, the authors, and particularly the personnel at ARC responsible for the symposium arrangements and the publication of these proceedings. A sincere thank you also goes to the symposium executive committee who is responsible for the year-to-year management of the AMS, including paper processing and preparation of the program.

The use of trade names of manufacturers in this publication does not constitute an official endorsement of such products or manufacturers, either expressed or implied, by the National Aeronautics and Space Administration.

SYMPOSIUM SCHEDULE

TUESDAY, 8 MAY 2001

6:30-8:30 CHECK-IN
Four Points – Pinot Noir Room

WEDNESDAY, 9 MAY 2001

8:00 Wednesday Presenters' Breakfast – Petit Sirah Room

8:00 **CHECK-IN AND REFRESHMENTS** – Grand Ball Room

9:00 **INTRODUCTORY REMARKS**

Ron Mancini, Host Chairman
NASA Ames Research Center, Mountain View, CA
Stuart H. Loewenthal, General Chairman
Lockheed Martin Space Systems Company, Sunnyvale, CA

CENTER WELCOME

Dr. Henry McDonald, Center Director
NASA Ames Research Center, Mountain View, CA

9:30 **SESSION I – BEARINGS & TRIBOLOGY**

Michael Eiden, Session Chair
ESA/ESTeC, Noordwijk, The Netherlands

- The Role of Bearing and Scan Mechanism Life Testing in Flight Qualification of the MODIS Instrument
Steven VanDyk, Raytheon Systems Company, Santa Barbara, CA; Brian Dietz, Moog, Inc., Chatsworth, CA; Kenneth Street, William Jones & Mark Jansen, NASA Glenn Research Center, Cleveland, OH; Michael Dube, Nye Lubricants, Inc., New Bedford, MA; Rajeev Sharma & Roamer Predmore, NASA Goddard Space Flight Center, Greenbelt, MD
- Dry Lubrication of Space-Related Tribocomponents with Diamond-Like Carbon Coatings
Gabriel Pont, CNES, Toulouse, France; C. Donnet, J. Fontaine, M. Belin & T. Le Mogne, LTDS, Ecully, France; Y. Berthier & S. Descartes, LMC, Villeurbanne, France; C. Heau, HEF, Andrezieux-Boutheon, France
- Effect of Alternate Solvent Diluents on PFPE Performance
Christopher Dayton & Robert Warden, Ball Aerospace & Technologies Corporation, Boulder, CO
- Improving the Robustness to Vibration and Temperature Effects for a Scanner Duplex Ball Bearing Assembly
Merritt Webb, Thomas Brewer & Benjamin Joffe, ITT Defense Aerospace/Communications Division, Fort Wayne, IN

11:30 **LUNCH BREAK**

1:00 **SESSION II – DEPLOY/RETRACT**

Andy Tao, Session Chair
TRW Space & Technology Division, Redondo Beach, CA

- Retractable Trunnion Pin Mechanism
Wayne Jermstad & Mark Landeck, NASA Johnson Space Center, Houston, TX
- Design of the X34 Speedbrake Mechanism Under Volume, Stiffness, Cost and Schedule Constraints
William Kim, Orbital Sciences Corporation, Dulles, VA
- Dust Cover for a Mars Lander Solar Cell Experiment
Scott Christiansen & Kurt Lankford, Starsys Research Corporation, Boulder, CO

- SRTM Mast Damping Subsystem Design and Failure Investigation
Jeffrey Umland, Jet Propulsion Laboratory, Pasadena, CA
- Fly Cast Maneuver for Shuttle Radar Topography Mission
Thomas Trautt, AEC-Able Engineering Company, Goleta, CA

3:30 **BREAK**

3:45 **SESSION III – POSTER PREVIEW**

Dave Putnam, Session Chair

Lockheed Martin Space Systems Company, Sunnyvale, CA

- Development of “Super-Flat” Strain Wave Gearing
Yoshihide Kiyosawa, Yoshihiro Tanioka & Keiji Ueura, Harmonic Drive Systems, Nagano, Japan
- Zero Play Hinge Latch

Mike Cabiran, Lockheed Martin Space Operations, Houston, TX

- Non-Metallic Hold Down and Release for an RF Antenna

David Hernandez, NEA Electronics, Inc., Chatsworth, CA

- Fault tolerant Magnetic Bearing for Turbomachinery

Benjamin Choi & Andrew Provenza, NASA Glenn Research Center, Cleveland, OH

- Methods for Improving Yield of Liquid Salt Bath Nitrocarburized 13-8PH Steel Components

Irwin Hochler, Aeroflex Laboratories, Farmingdale, NY

- Wear and Corrosion Resistant PM Tool Steels for Advanced Bearing Applications

Brian Hann, P. Kilonsky & M. Sperber, Crucible Compaction Metals Division, Oakdale, PA; Dennis Smith, Honeywell Aerospace Electronic Systems, Glendale, AZ

- A Low-Shock Stage Separation Mechanism

S. Vara Prasad Rao & Deepak Agrawal, Defense Research & Development Laboratory, Hyderabad, India

6:30-9:30 **RECEPTION & DISPLAYS AT THE FOUR POINTS** – Champagne Room

Invited component and software suppliers display current products and provide tutorials.

THURSDAY, 10 MAY 2001

8:00 Thursday Presenters' Breakfast - Petit Sirah Room

9:00 **SESSION IV - ACTUATORS & LATCHES**

Bob Neff, Session Chair

Space Systems/Loral, Palo Alto, CA

- Design of a High Resolution Hexapod Positioning Mechanism
Jamie Britt, NASA Goddard Space Flight Center, Greenbelt, MD
- Lessons Learned from the Design and Implementation of a Potentiometer Assembly for an Antenna Pointing Mechanism Application

Bradley Arkwright & Pietro DiLeonardo, Honeywell Aerospace Electronic Systems, Glendale, AZ;

Colin Francis & Richard Gahart, Space Systems/Loral, Palo Alto, CA

- MIRO Calibration Switch Mechanism

Jason Suchman, Yuki Salinas & Holly Kubo, Jet Propulsion Laboratory, Pasadena, CA

- A Robotic Rover-Based Deep Driller for Mars Exploration

Tomi Ylikorpi, Technical Research Center, Helsinki, Finland; G. Visentin, ESA, Noordwijk, The Netherlands; J. Suomela, Helsinki University of Technology, Helsinki, Finland

- Design and Verification of Space Station EVA-Operated Truss Attachment System

Gabriel Katell, The Boeing Company, Canoga Park, CA

11:30 **LUNCH BREAK**

1:00 **SESSION V – SOLAR ARRAYS**

Jason Wakugawa

Boeing Satellite Systems Inc., El Segundo, CA

- A Four Panel, Rotating Solar Array Wing for the TIMED Spacecraft Mechanism Design, Development and Test Results

Steven Vernon & David Persons, Johns Hopkins University Applied Physics Laboratory, Laurel, MD

- Validation of TSX-5 Solar Array Deployment by Correlated Simulation and Test

Brian Gore, The Aerospace Corporation, El Segundo, CA

- Milstar Solar Array Boom Deployment

Thomas Pace & Steven Honodel, Lockheed Martin Space Systems Company, Sunnyvale, CA

- The "Curwin" Design: A Novel Solar Array Concept for Constellations

Henk Cruijssen & Gerard Kester, Fokker Space BV, Leiden, The Netherlands

3:00 **BREAK**

3:15 **ANNOUNCEMENTS**

DR. CHARLES COALE AWARD ANNOUNCEMENT

EUROPEAN SPACE MECHANISMS & TRIBOLOGY SYMPOSIUM PREVIEW

3:30 **SPECIAL PRESENTATION**

SOFIA – Stratospheric Observatory For Infrared Astronomy – A Project Overview

Nans Kunz, SOFIA Project Engineering Manager, NASA Ames Research Center

5:30-10:30 **SYMPOSIUM BANQUET ON SAN FRANCISCO BAY**

5:30 Buses leave hotel parking lot

7:00 Bay Cruise / Dinner

10:00 Disembark cruise, board buses, and return to the hotel

FRIDAY, 11 MAY 2001

8:00 Friday Presenters' Breakfast – Petit Sirah Room

9:00 **SESSION VI – RELEASE MECHANISMS**

Brian Gore, Session Chair

The Aerospace Corporation, El Segundo, CA

- Hitchhiker Marman Band Interconnect Linkage

Gary Slebzak & Gene Barrett, Swales Aerospace, Inc., Beltsville, MD

- Taking Commercial Spacecraft Practices Too Far

Chuck Lazansky & Scott Christiansen, Starsys Research Corporation, Boulder, CO

- Design and Development of a Miniature Mechanisms Toolkit for Micro Spacecraft

Cliff Willey & Stuart Hill, Johns Hopkins University Applied Physics Laboratory, Laurel, MD; Brett

Huettl, Starsys Research Corporation, Boulder, CO

- Design, Development and Testing of a T-0 Environmental Control System Ground Disconnect

Paul Schwindt & Bruce Hardman, NASA Kennedy Space Center, FL

11:00 **BREAK**

11:15 **PRESENTATION: An Overview of ARC**

William E. Berry, Deputy Center Director

NASA Ames Research Center

11:45 **TECHNICAL SESSIONS CONCLUSION**

1:00-3:00 **AMES RESEARCH CENTER FACILITY TOUR**

SYMPOSIUM ORGANIZING COMMITTEE

Ronald E. Mancini, Host Chairman, NASA ARC

Stuart H. Loewenthal, General Chairman, Lockheed Martin
Edward A. Boesiger, Operations Chairman, Lockheed Martin

Obie H. Bradley, Jr., NASA LRC
Michael J. Eiden, ESA/ESTeC
Carlton L. Foster, NASA MSFC
Robert L. Fusaro, NASA GRC
Claef F. Hakun, NASA GSFC
Christopher P. Hansen, NASA JSC
Alan C. Littlefield, NASA KSC
Edward C. Litty, JPL
Fred G. Martwick, NASA ARC
Stewart C. Meyers, NASA GSFC
Martha E. Milton, NASA MSFC
Fred B. Oswald, NASA GRC
Minh Phan, NASA GSFC
John F. Rogers, NASA LRC
Donald R. Sevilla, JPL
Mark F. Turner, NASA ARC
James J. Zakrajsek, NASA GRC

SYMPOSIUM ADVISORY COMMITTEE

H. Mervyn Briscoe, ESA/ESTeC (ret)
David F. Engelbert, NASA ARC (ret)
Otto H. Fedor, Lockheed Martin (ret)
John W. Redmon, Sr., NASA MSFC (ret)
Alfred L. Rinaldo, Lockheed Martin (ret)
William C. Schneider, NASA JSC (ret)
Bowden W. Ward, Jr., NASA GSFC (ret)

CONTENTS

Symposium Schedule	vii
Symposium Organizing and Advisory Committees	x
The Role of Bearing and Scan Mechanism Life Testing in Flight Qualification of the MODIS Instrument.....	1
Steven VanDyk, Brian Dietz, Kenneth Street, William Jones, Mark Jansen, Michael Dube; Rajeev Sharma & Roamer Predmore	
Dry Lubrication of Space-Related Tribocomponents with Diamond-Like Carbon Coatings	15
Gabriel Pont, C. Donnet, J. Fontaine, M. Belin, T. Le Mogne; Y. Berthier S. Descartes; C. Heau	
Effect of Alternate Solvent Diluents on PFPE Performance	25
Christopher Dayton & Robert Warden	
Improving the Robustness to Vibration and Temperature Effects for a Scanner Duplex Ball Bearing Assembly.....	35
Merritt Webb, Thomas Brewer & Benjamin Joffe	
Retractable Trunnion Pin Mechanism	47
Wayne Jermstad & Mark Landeck	
Design of the X34 Speedbrake Mechanism Under Volume, Stiffness, Cost and Schedule Constraints.....	57
William Kim	
Dust Cover for a Mars Lander Solar Cell Experiment	71
Scott Christiansen & Kurt Lankford	
SRTM Mast Damping Subsystem Design and Failure Investigation	83
Jeffrey Umland	
Fly Cast Maneuver for Shuttle Radar Topography Mission	95
Thomas Trautt	
Development of "Super-Flat" Strain Wave Gearing.....	109
Yoshihide Kiyosawa, Yoshihiro Tanioka & Keiji Ueura	
Zero Play Hinge Latch	115
Mike Cabiran	
Non-Metallic Hold Down and Release for an RF Antenna.....	121
David Hernandez, Jr	
Fault tolerant Magnetic Bearing for Turbomachinery	127
Benjamin Choi & Andrew Provenza	

Methods for Improving Yield of Liquid Salt Bath Nitrocarburized 13-8PH Steel Components	133
Irwin Hochler	
Wear and Corrosion Resistant PM Tool Steels for Advanced Bearing Applications.....	139
Brian Hann, P. Kilonsky, Dennis Smith & M. Sperber	
A Low-Shock Stage Separation Mechanism	145
S. Vara Prasad Rao & Deepak Agrawal	
Design of a High Resolution Hexapod Positioning Mechanism.....	149
Jamie Britt	
Lessons Learned from the Design and Implementation of a Potentiometer Assembly for an Antenna Pointing Mechanism Application	163
Bradley Arkwright, Pietro DiLeonardo, Colin Francis & Richard Gahart	
MIRO Calibration Switch Mechanism	179
Jason Suchman, Yuki Salinas & Holly Kubo	
A Robotic Rover-Based Deep Driller for Mars Exploration.....	185
Tomi Ylikorpi, G. Visentin; & J. Suomela	
Design and Verification of Space Station EVA-Operated Truss Attachment System	199
Gabriel Katell	
A Four Panel, Rotating Solar Array Wing for the TIMED Spacecraft Mechanism Design, Development and Test Results	213
Steven Vernon & David Persons	
Validation of TSX-5 Solar Array Deployment by Correlated Simulation and Test	227
Brian Gore	
Milstar Solar Array Boom Deployment.....	237
Thomas Pace & Steven Honodel	
The "Curwin" Design: A Novel Solar Array Concept for Constellations	251
Henk Cruijssen & Gerard Kester	
Hitchhiker Marman Band Interconnect Linkage	265
Gary Slebzak & Gene Barrett	
Taking Commercial Spacecraft Practices Too Far.....	275
Chuck Lazansky & Scott Christiansen	
Design and Development of a Miniature Mechanisms Toolkit for Micro Spacecraft.....	287
Cliff Willey, Brett Huettl & Stuart Hill	
Design, Development and Testing of a T-0 Environmental Control System Ground Disconnect	301
Paul Schwindt & Bruce Hardman	

5, /19

The Role of Bearing and Scan Mechanism Life Testing in Flight Qualification of the MODIS Instrument

Steven G. VanDyk^{*}, Brian J. Dietz^{**}, Kenneth W. Street⁺, William R. Jones⁺, Jr., Mark J. Jansen⁺, Michael Dube^{**}, Rajeev Sharma^{***}, Roamer E. Predmore^{***}

Abstract

The Moderate Resolution Imaging Spectroradiometer (MODIS) is an instrument aboard the Terra (EOS AM-1) satellite and has been operating successfully since December 1999. MODIS has been viewing the entire Earth's surface and gathering data to better understand the global dynamics and processes occurring on land, in the oceans, and in the lower atmosphere. All observations are made through an extremely high resolution, optically and mechanically precise, scan mirror motor/encoder assembly. The reliable performance of this assembly depends on two duplex bearing pairs lubricated with Pennzane, a synthetic hydrocarbon, formulated with lead naphthanate. This paper describes the results of accelerated and operational life tests. It also describes the post-test analyses of the disassembled bearings. Analyses were performed using micro-Raman, micro-FTIR, X-ray Photoelectron Spectroscopy (XPS), Scanning Electron Microscopy (SEM), and Size Exclusion Chromatography (SEC). In general, the three sets of bearings in each of the test stations were in very good condition after accumulating 68, 144, and 209 million revolutions, respectively. Some of the bearings exhibited lubricant degradation, indicated by viscous lubricant deposits on the cage and raceways.

Introduction

At the onset of the MODIS development, Pennzane had not been flown on Goddard long-life lubricated space mechanisms. Accelerated and real-time life tests were conducted on MODIS scan bearings to demonstrate that Pennzane would successfully lubricate the mechanism for the 5-year (53.4 million cycles) life. Three sets of duplex MODIS bearings were tested at 23°C & 20.3 RPM for 68 million revolutions (Station IV); at 37°C & 50 RPM for 144 million revolutions (Station III); and at 45°C & 72 RPM for 209 million revolutions (Station II). Six months before launch, the 37°C accelerated life test was disassembled and two of the three bearing sets were severely worn (Ref. 1). These results raised doubts about flightworthiness of the MODIS instrument. Fortunately, a flight quality scan mechanism had also been tested for 4.7 years at that time. Measurements of torque margins and operating parameters of the engineering model scan mechanism with only a few months of operating time and the life test mechanism showed no torque variation or operating parameter variation. From these measurements, it was concluded that no measurable bearing wear or lubricant degradation occurred during the 4.7-year life test. After almost 5 years of damage free scan mechanism life testing, it was concluded that the TERRA/MODIS instrument was safe to fly. The wisdom of Goddard's requirement for an expensive scan mechanism life test rather than less expensive bearing life testing was demonstrated.

This paper describes the bearing wear and lubricant degradation and distribution after the accelerated bearing life test at 45°C and the real time life test at 23°C. After 68 million cycles (1.3 lives) in the boundary lubrication regime at 23°C, part of the oil had crept into the support structure. The oil color was dark amber, but in many cases the viscosity was unchanged, all balls, retainers and races were wetted and contained oil meniscuses, and little wear was observed on the balls or races. After 209 million revolutions (3.9 lives) at 45°C, more oil crept into the support cups, the oil was black and viscous, all balls, retainers and races were wetted, small meniscuses of oil were at the ball race junctions, and very

-
- ^{*} Raytheon Systems Company, Santa Barbara Remote Sensing, Santa Barbara, CA
 - ^{**} Moog, Inc., Schaeffer Magnetics Division, Chatsworth, CA
 - ⁺ NASA Glenn Research Center, Cleveland, OH
 - ^{**} Nye Lubricants, Inc., New Bedford, MA
 - ^{***} NASA Goddard Space Flight Center, Greenbelt, MD

limited wear was observed on the balls and races. Dark deposits of lead or lead naphthanate were not visible, indicating the lead naphthanate remained dissolved in Pennzane after 209 million revolutions at 45°C. This formulation of Pennzane performed very well at high temperature and in the boundary lubrication regime. The lubricant and bearing surfaces have been analyzed using micro-Raman, micro-FTIR, XPS, SEM and SEC and the results summarized.

Comparison of the bearing wear and the lubricant degradation after life testing at 23°C and 45°C, clearly demonstrated that the severe bearing damage found in the 37°C accelerated life test originated from a thermal control failure. This drove the bearing test temperature well above 90°C, as suggested in the Reference 1.

As with most long-life lubricated mechanisms, lubrication life, bearing precision, and dynamic performance are the critical factors in the operation of the scan motor/encoder. As a first phase of lubricant selection for MODIS, bearings were lubricated with several candidate lubricants, accelerated life tests performed, and results evaluated. A synthetic hydrocarbon, Pennzane SHF-X-2000 with 2.5% lead naphthanate and 0.6% antioxidant additives, was selected. The second phase of lubricant selection consisted of three lubricant life tests. These results were reported in Ref. 1 and in this paper. The third phase was the successful qualification life test of the scan motor/encoder mechanism.

Three bearing test stations were constructed to evaluate the life of Pennzane lubricant for the MODIS optical scan mechanism. Five-flight quality scan motor/encoder mechanisms were fabricated, assembled and tested. The engineering model was used to develop the optical scanning control system. The second mechanism was used for qualification life testing and has successfully completed that testing. The third mechanism was flown in the MODIS instrument on the TERRA satellite. The fourth mechanism will be flown in the MODIS instrument on the AQUA satellite later this year. The fifth mechanism remains as a spare.

Each scan motor/encoder mechanism contains two duplex bearing pairs driven by a brushless dc-motor. Pennzane SHF-X-2000 is a synthetic hydrocarbon lubricant and was chosen for the bearings and mechanism. To mitigate instrument risk, both accelerated and operational speed life testing were conducted in parallel with the mechanism design and fabrication in order to verify the lubricant life early enough in the program to switch lubricants for MODIS if accelerated testing revealed early anomalies.

Accelerated and Real-Time Pennzane Life Test Method

In each test station, three flight quality, 440C steel, 66.675-mm (2.625-inch) outer diameter, 50.800-mm (2-inch) inner diameter, DF duplex pair bearings with a 165-N (37-pound) preload were used. The bearings, phenolic laminate retainers, and sintered nylon reservoirs were lubricated in accordance with flight requirements. The test station is illustrated as Figure 1. Each bearing pair was contained in its own clamp/housing. The housings also contained lubricant reservoirs. Station II and III housings were fitted with inner and outer race heaters. A strain gauge was mounted on a cantilever beam supporting each bearing enclosure to measure the torque. The inner races of three duplex pairs were driven by a common drive shaft. Instantaneous torque readings were recorded every 15 minutes. The monthly average of these readings was plotted over the life of the test (see Figure 2). One telemetry platinum resistance thermometer (PRT) was mounted to each bearing outer race housing. Two control PRTs (Stations II and III only) were also mounted to each bearing housing (one on the outer race and one for the inner race). All testing was performed under vacuum. Although all the Pennzane lubricant was tested in the boundary lubrication regime, the acceleration factor was established as similar calculated specific film thickness (λ) in all three-test stations. This method was used as an arbitrary way of creating an accelerated lubrication life test. Three duplex pairs of bearings were tested in Station II at 72 RPM and 45°C, in Station III at 50 RPM and 37°C and 22°C and in Station IV at 20.3 RPM and 23°C.

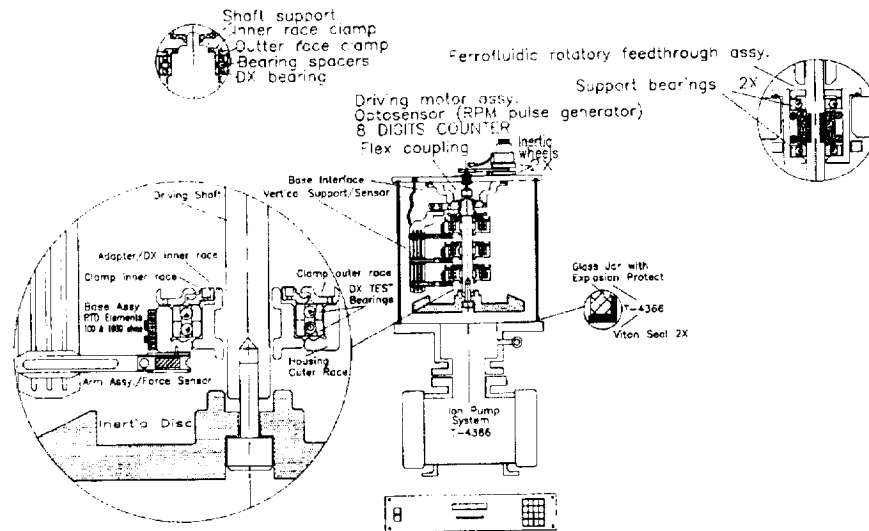


Figure 1. Test Station

Performance Evaluation of the Qualification Life Test Scan Mechanism

Evaluation of the life test bearings from Station III (37°C and 50 RPM) had shown severe degradation (Ref. 1). To regain confidence in the MODIS scan mechanism before the launch of TERRA/MODIS, a performance evaluation was conducted on the like-new engineering model (EM) and the qualification life test mechanism after 4.7 years of testing.

The performance of the two test units was measured by evaluating the motor drag torque and phase error signals. At that time (11-1999), the EM scanner had accumulated a few hundred thousand cycles whereas the LTU had completed close to one mission lifetime, about 45.8 million cycles, in vacuum testing.

Both scanners tested had their spin axis vertical with an equivalent inertia disk attached to represent the scanner mirror at the top end of the drive system shaft. The hardware used to record the drag torque and phase error signals was a portable data acquisition system running LabVIEW™ software and all data was recorded at 250 samples per second.

The steady state drag torques measured on the MODIS EM and LTU scanner units were about 67 mN-m (9.4 oz-in) and 87 mN-m (12.2 oz-in) respectively, indicating a beginning-of-life and a end-of-life torque margin of greater than 20. The more important parameter of margin on phase lock for both units is a healthy 200 percent. Because of the design similarities between the EM and LTU scanner units and the PFM and FM-1 MODIS scanners, it was concluded that the PFM and FM-1 unit MODIS scanners had sufficient margin for a five-year mission life on the Terra and EOS-PM programs.

Test Results From Station III — 50 RPM at 37°C

Bearing life test Station III results were reported at the 34th Aerospace Mechanisms Symposium (Ref. 1). Bearings in this station indicated consistent operation well past 57 million revolutions until a suspected heater malfunction occurred at 88 million cycles (Figure 2). The test continued until 144 million revolutions were achieved, then it was switched off, and disassembled.

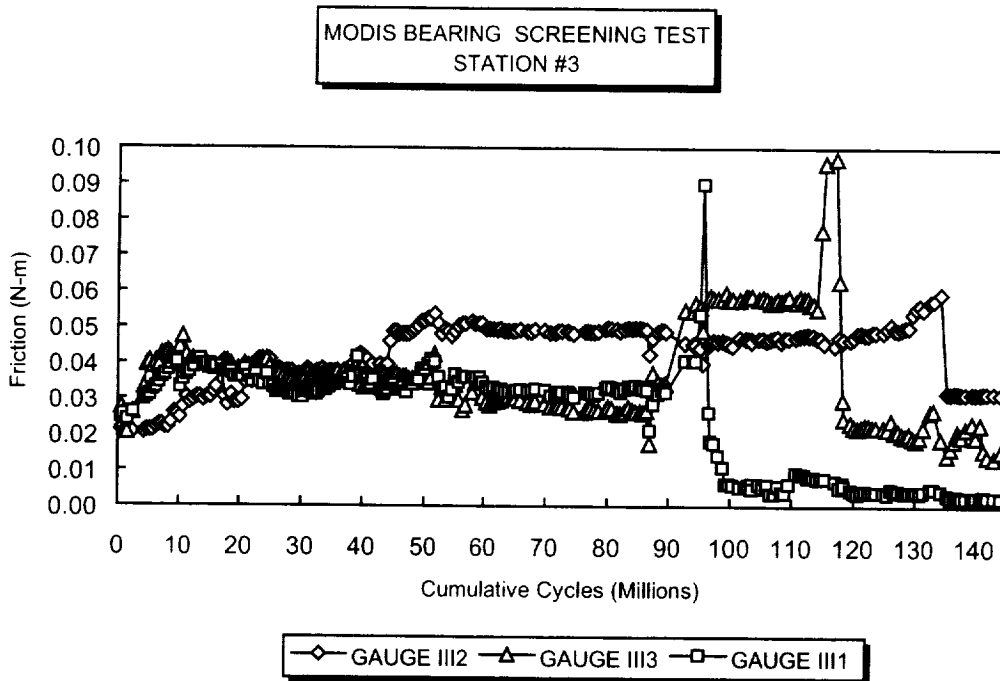


Figure 2. Torque vs. revolutions for upper pair bearings (III1), middle bearings (III2), and lower bearings (III3)

Performance Evaluation of the Station II And IV Scan Mechanisms

These test stations were an accelerated life test running at 72 RPM (Sta. II), and an operational speed station running at approximately 20 RPM (Sta. IV). In order to compensate for the higher speed, heaters were added to the accelerated station to decrease the viscosity of the lubricant. The original plan specified a life test duration of 57 million revolutions. After the bearing life tests successfully achieved the required 57 million revolutions, the test torque data was reviewed and it was concluded that there was no indication of failure so the tests were allowed to continue.

The decision to disassemble these two test stations was finally made after the operational test station surpassed 57 million cycles. At the time of disassembly, the 72 RPM station had accumulated 209 million cycles while the operational speed station had achieved 68 million cycles. Upon disassembly some lubricant discoloration was observed but no visible damage. The bottom bearings of each pair had more lubricant and a stickier feel than the upper bearings. Bearing torque remained well below the operational requirements of the system ≤ 13 N-m (18 oz-in) drag torque throughout the life test.

Average torque data is shown in Figure 3 for Station II. Intermittent jittering of the upper bearing pair housing was observed toward the end of testing. Torque characterization with and without visible vibration is shown in Figures 4 and 5.

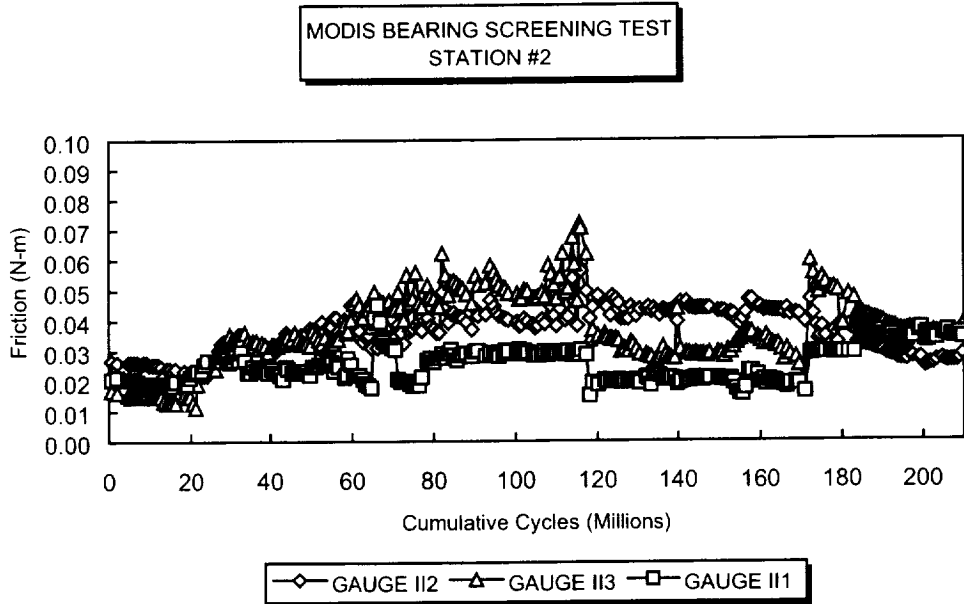


Figure 3. Torque vs. revolutions for upper pair bearings (II1), middle bearings (II2), and lower bearings (II3)

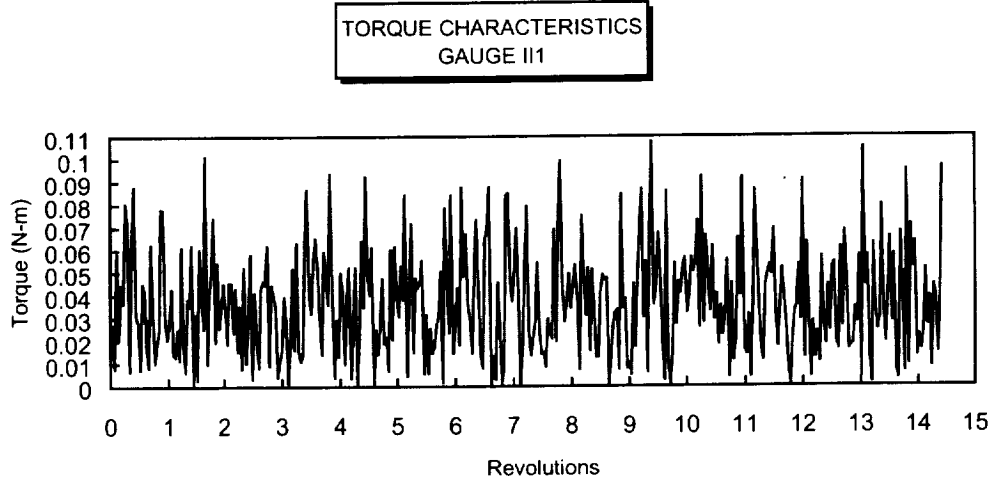


Figure 4. Torque characterization for Station II upper bearing pair with visible vibration

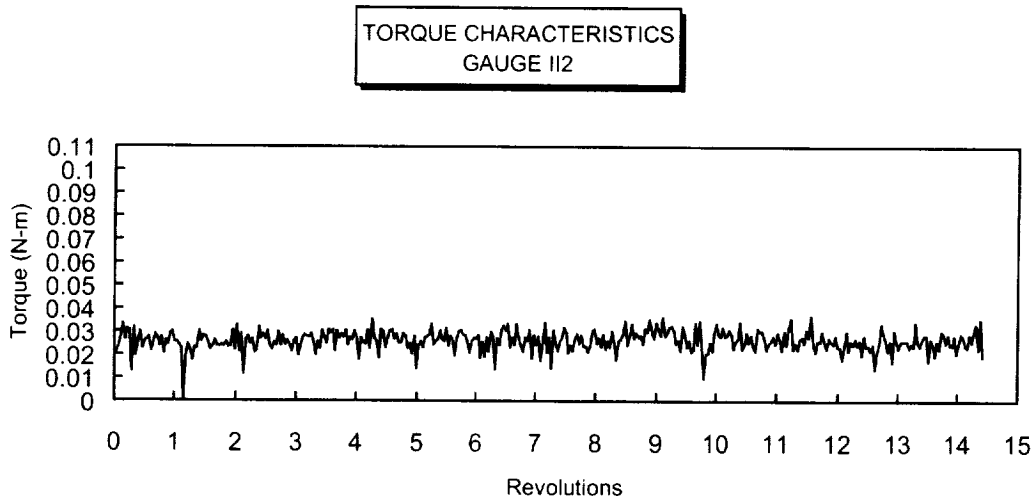


Figure 5. Torque Characterization for Station II Middle Bearings without Vibration

Station IV operated for 68 million cycles at 20.3 RPM or operational speed. This station operated at room temperature and exhibited vibration that randomly affected the bearings at different times. The vibration was visible and varied with intensity. At times there was no vibration noted on any of the bearings. Torque history for all bearing pairs appears in Figure 6.

Upon completion of 209 and 68 million cycles for Stations II and IV, respectively, the stations were disassembled. Photographs were taken throughout the disassembly and inspection process. A test station

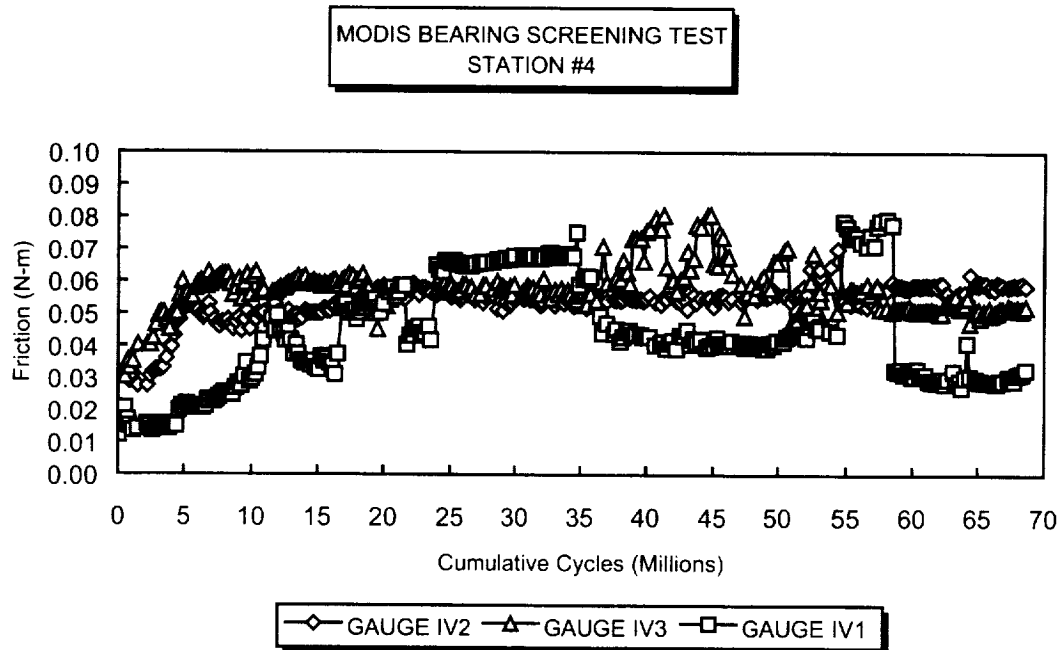


Figure 6. Torque vs. revolutions for station IV upper pair bearings (IV1), middle bearings (IV2), and lower bearings (IV3)

prior to disassembly is shown in Figure 7. The complete shaft and all bearing components were removed from the test station and transported to a class 100 flow bench in a class 100,000 clean room for further inspection.

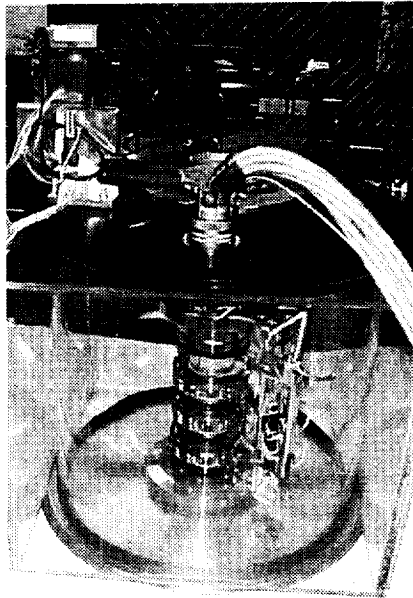


Figure 7. Test station prior to disassembly

One of the disassembled bearings (4-012) is shown in Figure 8. Although not easily seen in the macro photograph (Figure 8), dark viscous deposits are seen on the cage and raceways. A higher magnification photograph (Figure 9) shows an example of these deposits in a raceway. Two other photographs showing the variation and distribution of lubricant within the raceways appear in Figures 10 (greater amount of lubricant) and Figure 11 (lesser amount of lubricant).

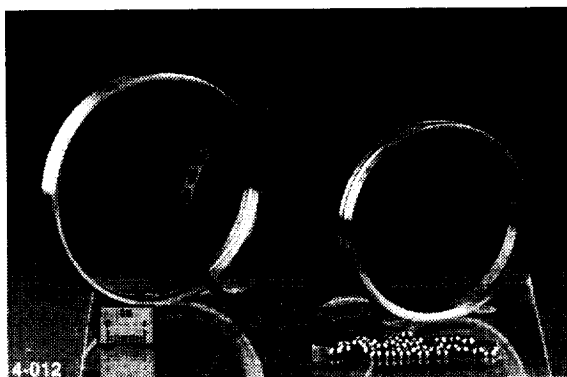


Figure 8. Disassembled MODIS 4-012 bearing



Figure 9. Darkened lubricant deposit

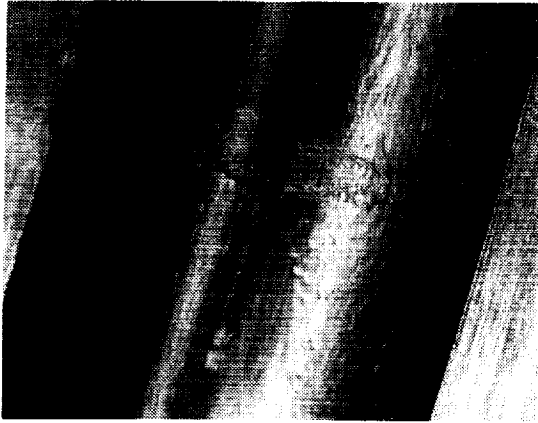


Figure 10. One bearing from Station II with a greater amount of lubricant



Figure 11. One bearing from Station II with a lesser amount of lubricant

Analytical Results

In general, the results showed the balls, retainers, and races were still lubricated and in good condition at the end of test. The top bearing assemblies had less lubricant in both stations II and IV and bottom bearing assemblies had a thicker grease-type residue. There was no sign of dry debris in any of the bearing assemblies. The oil had darkened significantly and was more viscous, almost like honey. Wear paths were seen in the races and on some of the balls. There was no sign of elongation in the retainer pockets. However, some slight metallic debris was observed on some of the retainers. The metallic debris was noticed only on station IV.

Raman and Infrared analyses of the lubricant indicated the standard signature for non-degraded Pennzane. XPS, SEM, and EDAX showed the normal elemental composition for 440C steel. The most striking demonstration of lubricant degradation was observed in some bearings as a thickened lubricant deposit with almost grease like in consistency. These deposits occurred on both races and on the cage. For the SEC analysis, the cages were all weighted and then extracted using tetrahydrofuran (THF). The solution was then concentrated and injected into a size exclusion chromatograph. An example from bearing 4-012 appears in Figure 12. The detector signal is plotted as a function of molecular weight (MW). Several peaks are evident. The negative peaks at low MW are injection peaks. The peak at 195, which occurs in all samples, is an artifact from a preservative in the mobile phase (THF). The next peak represents the degraded Pennzane compound. The higher MW peak at about 1300 represents the primary Pennzane material as well as a contribution from the lead naphthanate. The broad high MW peak centered about 18,000 represents polymerized lubricant. This high MW peak does not occur in unused samples.

The weight of extracted lubricant varied from bearing to bearing with the smallest amount being about 9 mg from cage 4-015 and 49 mg from cage 4-002A. This compares to the nominal amount of 75 mg impregnated at build up. In addition, dark residues were observed on cages 4-002A, 4-005A, 4-006A and 4-015A. Photographs for these two cages after THF extraction appear in Figures 13a and 13b.

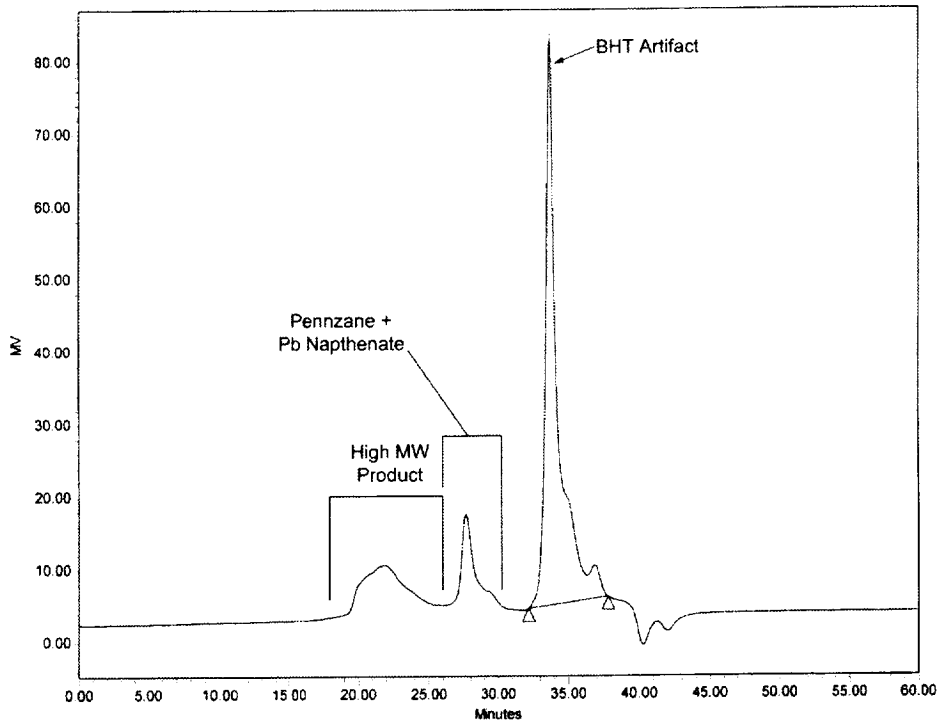


Figure 12. Size exclusion chromatogram from extracted lubricant from cage 4-012

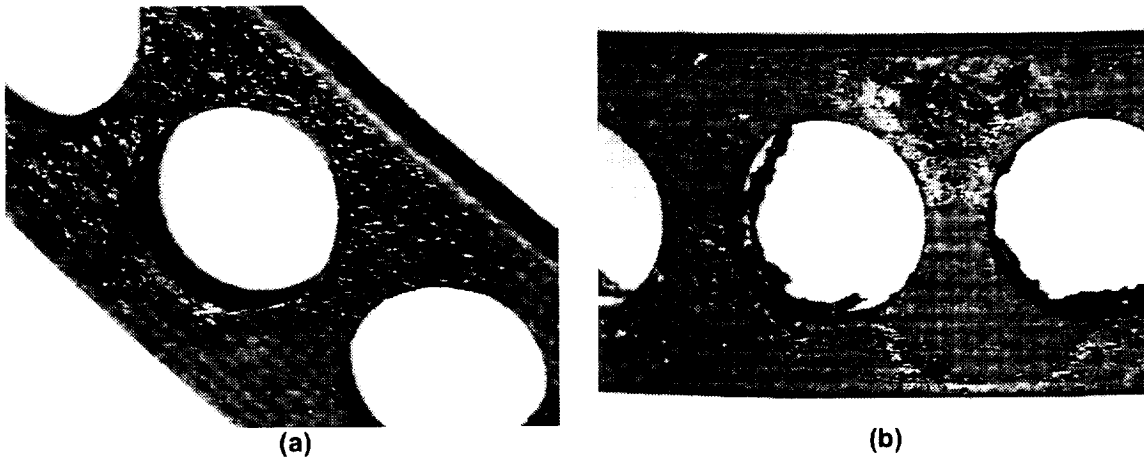


Figure 13. Photograph of extracted cage from 4-002A (a) and 4-015A (b)

Performance Measurement Test

Performance tests on the MODIS engineering model (EM) and life test unit (LTU) scanners were made to determine the changes in performance over the expected on-orbit life of the flight unit. The EM and LTU scanners tested were equivalent units to the PFM (in service) and FM-1 scanner, which is scheduled to fly shortly on the EOS-PM (Aqua) program. As a minimum, the scanner drive systems must operate continuously for five years in a constant velocity mode for Earth scanning. The scanner drive system utilized a phase-lock loop control system for maintaining scan rate at the desired value during operation.

Scan motor drag torque and phase error signal performance from both test units was measured, recorded and evaluated. The EM scanner had seen a few hundred thousand rotation cycles whereas the LTU had completed more than one mission lifetime and about 58 million cycles in vacuum testing.

Both scanners tested had their spin axis vertical with an equivalent inertia disk attached to represent the scanner mirror at the top end of the drive system shaft. The hardware used to record the drag torque and phase error signals was a data acquisition system running LabVIEW™ software and all data was recorded at 250 samples per second. Figures 14 through 19 document results obtained from the tests performed and are discussed below.

Figure 14 documented the running or steady state drag torque of the EM scanner, which had an average value of 67 mN-m (9.4 oz-in). During this test, the EM unit maintained the required rotation rate of 20.3 rpm with phase-lock control. The beginning-of-life requirement for this value was 110 mN-m (15 oz-in), which was met. The current limit on the PFM and FM-1 MODIS units was about one amp for the flight condition which indicated that the beginning of life torque margin for the scanner was greater than 20.

Figure 15 documented the measured phase error signal of the EM scanner under turn ON and steady state conditions. When the scanner was initially turned on, there was a large error signal generated between the commanded rate and the actual rate, shown by the indicated spike shortly after turn-on. The phase-lock circuitry was designed to reduce the error between the commanded rate and the actual rate over a given time, therefore the error signal reduced shortly after turn-on to a value of about 1 volt peak-to-peak. This was equivalent to a phase error of about 20 micro-radians under steady state scanner rotation.

In Figures 16 and 17 eight attempts to bring the EM scanner out of phase lock by increasing the external drag torque on the drive system were shown. Due to the limitation of the test setup, the external drag was increased manually and the LED on the EM scanner electrical control box was observed to go out indicating the scanner was out of phase lock. The two figures also showed maximum drag torque where the scanner went out of phase lock. This drag torque compared to the maximum available torque of the scanner motor established the margin that existed for being in phase lock for the EM scanner unit. When the transient drag torque events on Figures 16 and 17, were omitted, retrieving and averaging the maximum drag from the eight attempts indicated that the drag at which point the scanner phase lock was lost occurred at about 710 mN-m (100 oz-in). The PFM and FM-1 units had a scanner actuator current limit of about one amp from their power supplies, which indicated a margin on phase lock of about 200% at the beginning-of-life. This meant that the PFM and FM-1 unit scanners had about three times the available torque capacity in their scanner drive systems to maintain scanner phase lock.

Figure 18 documented the running or steady state drag torque of the LTU scanner which had an average value measured of about 86 mN-m (12.2 oz-in) after running more than one mission lifetime of 58 million cycles in vacuum. During this test, the LTU unit maintained the required rotation rate of 20.3 rpm with phase-lock control. The measurement indicated that at the end of (one mission) life, the torque margin for the scanner was greater than 20.

Figure 19 documented the measured phase error signal of the LTU scanner under turn ON and steady state conditions. Similarly as with the EM unit system, when the LTU scanner was initially turned on, there was a large error signal generated between the commanded rate and the actual rate, shown by the indicated spike shortly after turn-on. The phase-lock circuitry was designed to reduce the error between the commanded rate and the actual rate over a given time, therefore there was a reduction in error signal shortly after turn-on to a value of about 0.5 volt peak-to-peak. This was equivalent to a phase error of about 10 micro-radians under LTU scanner steady state rotation.

Due to the LTU scanner test vacuum apparatus, it was not possible to perform the phase lock tests for comparison to the EM data. Nonetheless, based on phase error and drag torque measurements there was good confidence that the life test unit, after greater than one mission life, had no significant difference in measurable parameters and therefore has good correlation in margin for phase lock equivalent to the EM unit measured data.

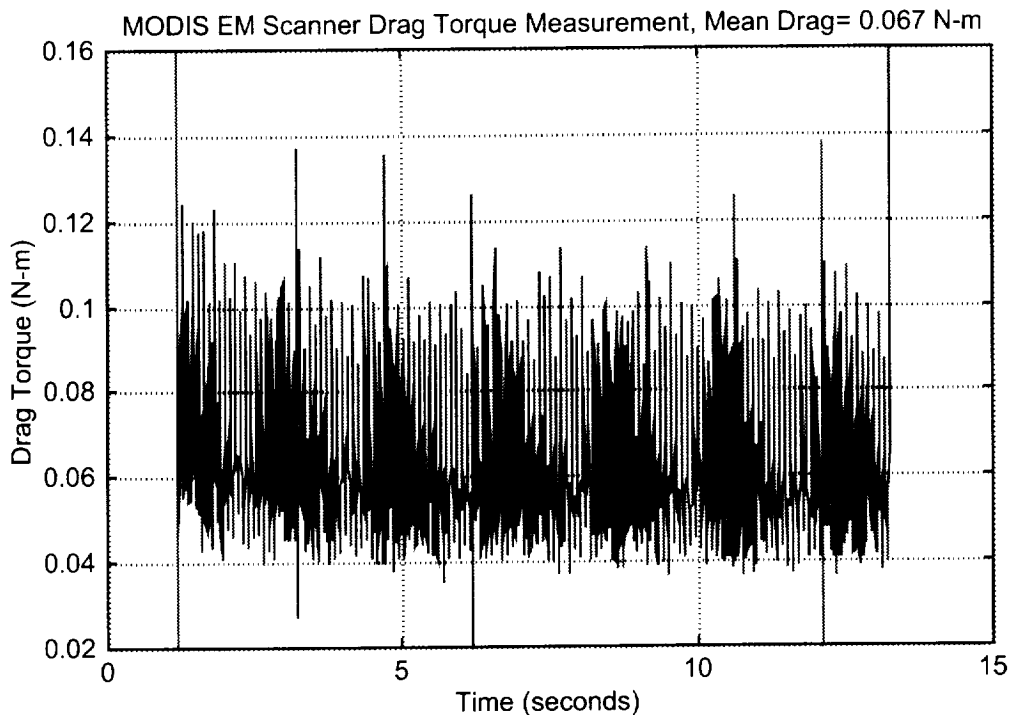


Figure 14. MODIS EM Scanner Steady State Drag Torque

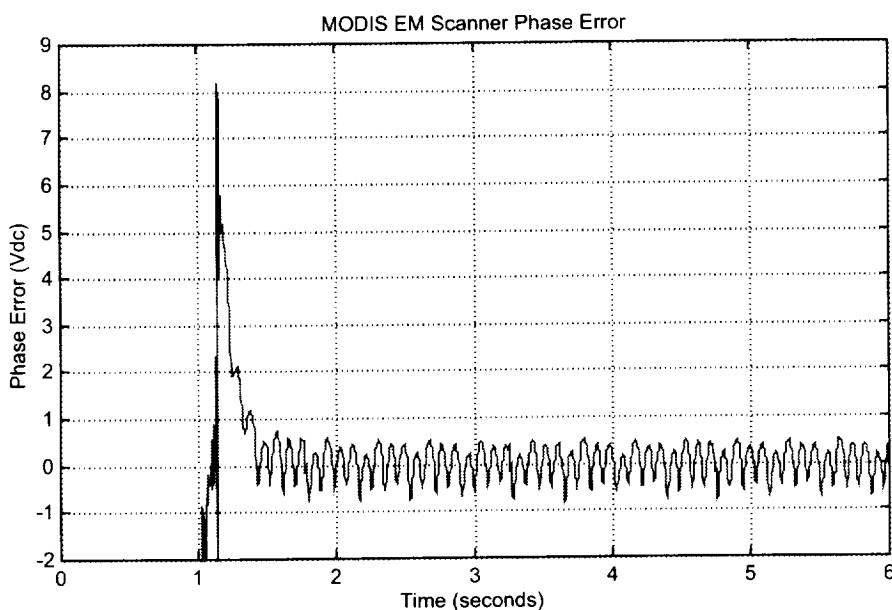


Figure 15. MODIS EM Scanner Phase Error

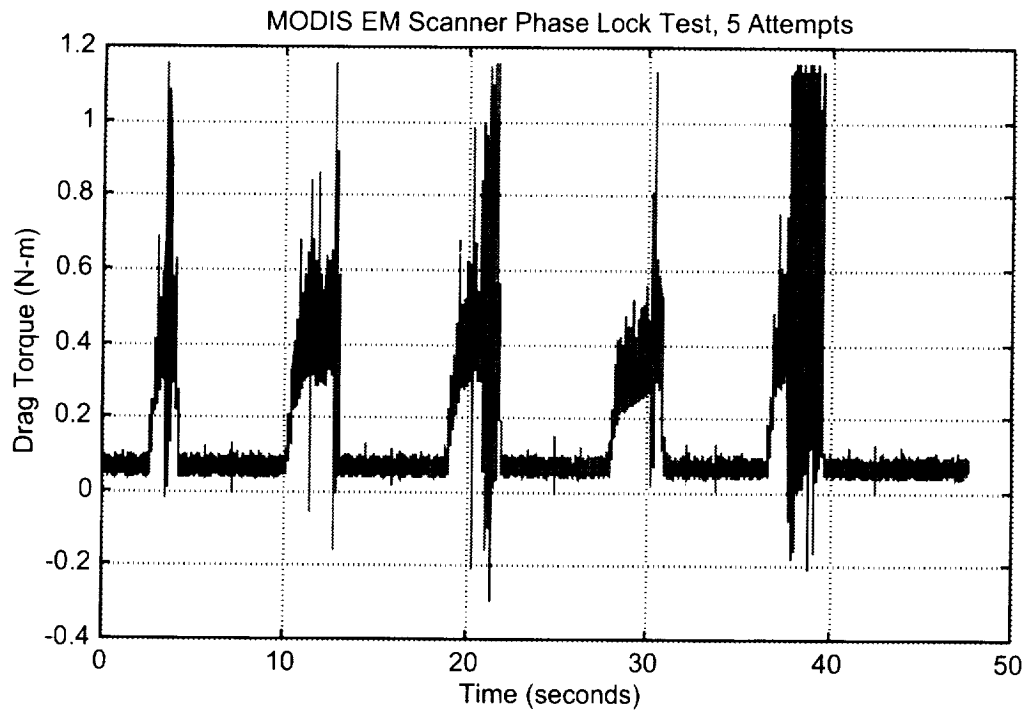


Figure 16. MODIS EM Scanner Phase Lock Test 1

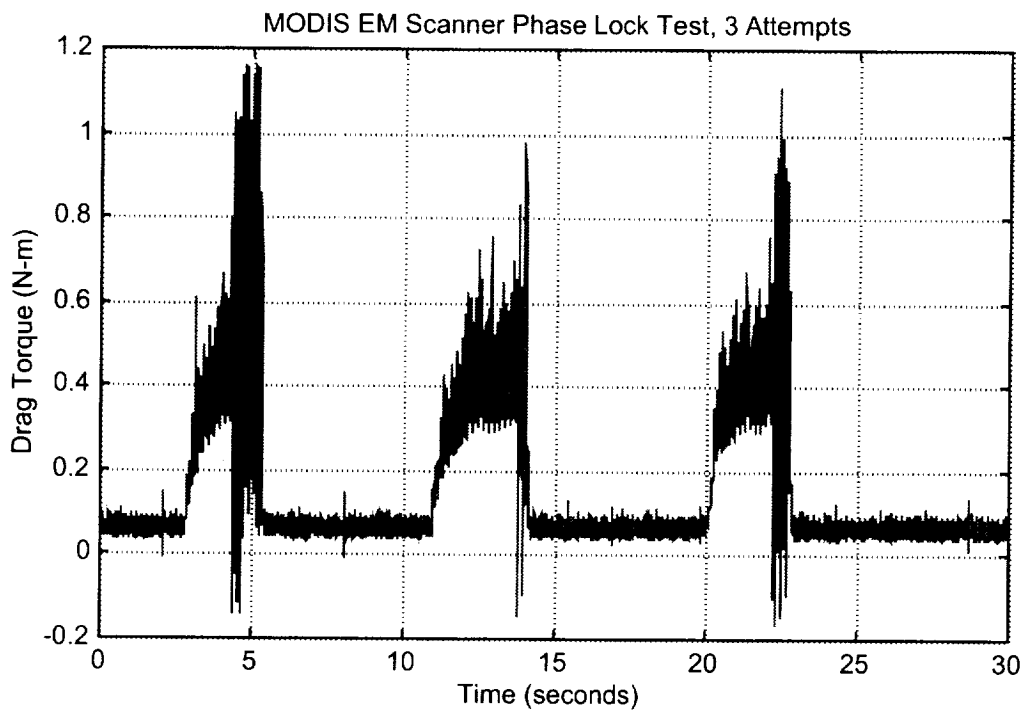


Figure 17. MODIS EM Scanner Phase Lock Test 2

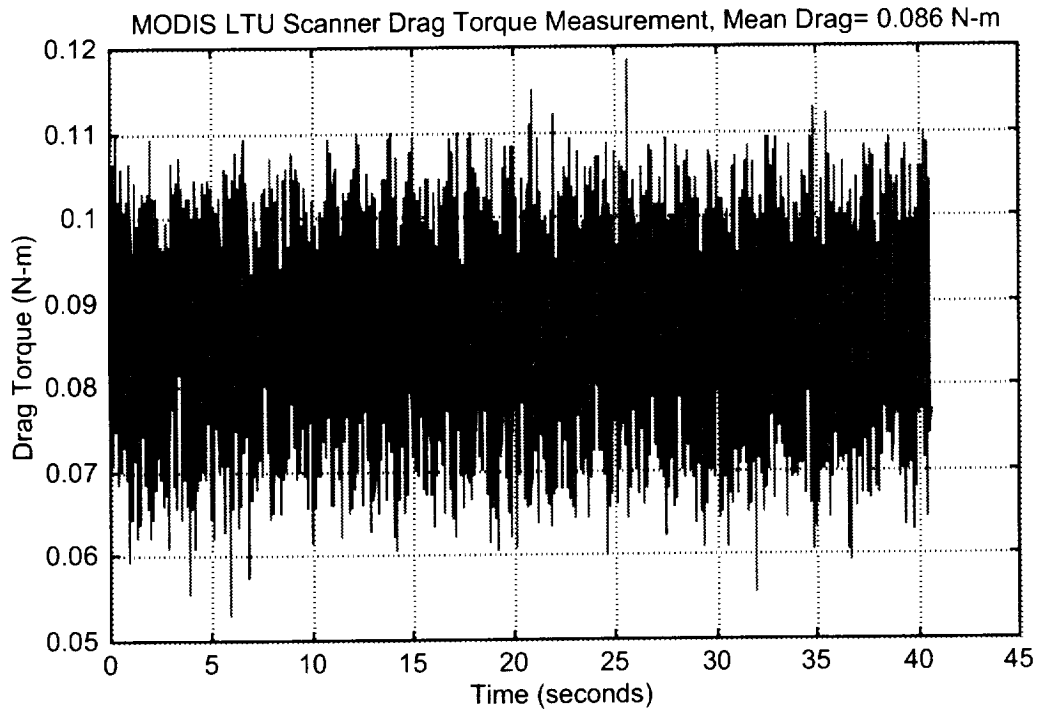


Figure 18. MODIS LTU Scanner Steady State Drag Torque

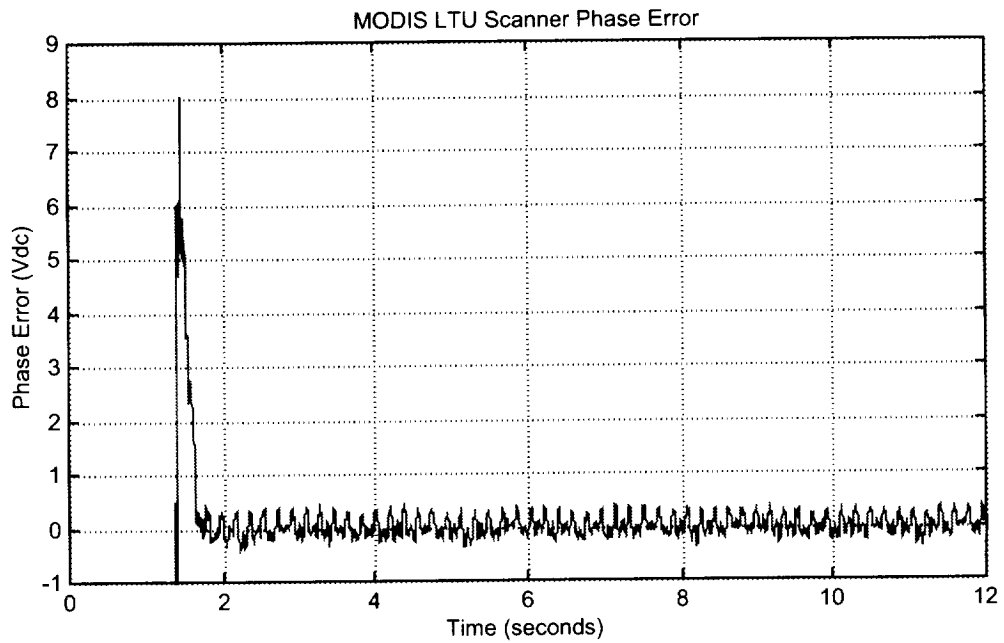


Figure 19. MODIS LTU Scanner Phase Error

Conclusions

The steady state drag torques measured on the MODIS EM and LTU scanner units were about 67 mN-m (9.4 oz-in) and 87 mN-m (12.2 oz-in) respectively indicating a beginning-of-life and a end-of-life torque margin of greater than 20. The more important parameter of phase lock margin for both units was a healthy 200 percent. Because of the design similarities between the EM and LTU scanner units and the PFM and FM-1 MODIS scanners, it was concluded that the PFM and FM-1 unit MODIS scanners had sufficient margin for a five-year mission life on the EOS-AM (Terra) and EOS-PM (Aqua) programs respectively.

Lessons Learned

As a worn slip ring was the cause of heater loss in the accelerated test station, it was shown that the test equipment must be more robust than the hardware being tested. Also, in the presence of gravity, considerations for the orientation of test samples should be given. Where feasible, rotation of the samples should be performed to counter the effects of gravity. The labyrinth seal should match that of the flight configuration. And lastly, when testing mechanical systems consider the frequency of the test apparatus. In this test it was noted that jitter, seen during life testing, was likely due to the cantilevered test arm resonating or coupling with the rotational speed of the bearings.

Acknowledgements

J. Uber, S. Cicchelli, and M. Roberto, NASA Goddard Space Flight Center.
A. DeForrest, Raytheon Systems Company, Santa Barbara Remote Sensing.
L. Alegre, S. Natvipada, D. Owens, T. Phan, P. Tokeshi and H. Tsui, Moog SMD.
N. St. Pierre and M. LaRochelle, Nye Lubricants

References

1. Brian J. Dietz, Steven G. VanDyk and Roamer E. Predmore, "Earth Scanner Bearing Accelerated Life Test", 34th Aerospace Mechanisms Symposium, May 2000, pp 303-316.

23/27

Dry Lubrication of Space-Rated Tribocomponents with Diamond-Like Carbon Coatings

G. Pont^{*}, C. Donnet^{**}, J. Fontaine^{**}, M. Belin^{**}, T. Le Mogne^{**}, Y. Berthier^{***}, S. Descartes^{***}, C Heau^{****}

Abstract

This paper details a four year effort in the development of Diamond-Like Carbon (DLC) coatings for space related tribocomponents. After a brief presentation of the coating deposition technique, flat-on-disc tribometer results are shown. These results, coupled with analytical characterizations, show that the coatings tribological behavior strongly depends on deposition parameters. The deposited films may be divided into two categories: the high-friction ones and the ultralow-friction ones. Tribological tests have been performed on bearings in high vacuum conditions after optimizing the adhesion underlayers. The results show that the DLC tested could be very satisfactory for some applications. Some others DLC coated components (gears, screw-nut) will be tested in a very near future.

Introduction

DLC coatings as dry lubricants are being studied all over the world because they are very promising when used under certain conditions. For example, friction coefficient under Ultra-High-Vacuum (UHV) can be very low. Today, some industries already use DLC as a dry lubricant (hard disks drives in computer manufacturing for example).

A few years ago, CNES (French Space Agency) and LTDS, studied various commercial DLC coatings in order to assess the film composition parameters that led to effective coatings for space mechanisms dry lubrication. During this phase, strong contacts were established with the IBM Research Division (Watson, NY), who provided DLC samples showing ultralow friction under UHV [1]. Then, CNES, LTDS, LMC and HEF (a surface treatments specialized French company) decided to go further in the development of DLC coatings that could be used in the space industry [2]. The goal of this paper is to present the main results of this study as some DLC coated space mechanisms components (bearings, gears, screw-nut) are being tested.

What is DLC?

A DLC is an amorphous metastable material deposited by PVD or PECVD techniques on a few micrometers. It consists of a disordered covalent network of carbon atoms, containing several carbon hybridization (mainly sp^2 and sp^3), in which different elements, mainly hydrogen, sometimes impurities or doping elements (nitrogen, fluorine...) can be incorporated. The main parameters describing the structure are thus the sp^2/sp^3 ratio and the hydrogen content [3], which in turn strongly depend on the deposition process.

Many kinds of DLC, with various properties, have been developed all over the world. In fact, the 'DLC' terminology describes more a family of materials than a single material. Depending on the elaboration process, DLC with a wide range of hydrogen content (a-C or a-C:H) may be deposited, showing high (up to 0.7) or very low (down to 0.007) friction coefficient [4]. The DLC we have been interested in during this study are hydrogenated DLC (a-C:H), produced without doping agents.

^{*} CNES Mechanisms Department, Toulouse, France

^{**} Laboratoire de Tribologie et de Dynamique des Systèmes (LTDS), Ecully, France

^{***} Laboratoire de Mécanique des Contacts (LMC), Villeurbanne, France

^{****} HEF, Andrézieux-Bouthéon, France

Experimental setup

Deposition Process

The deposition method, selected at the beginning of the project, is a hybrid technique of Magnetron Sputtering and Plasma Assisted Chemical Vapor Deposition (PACVD).

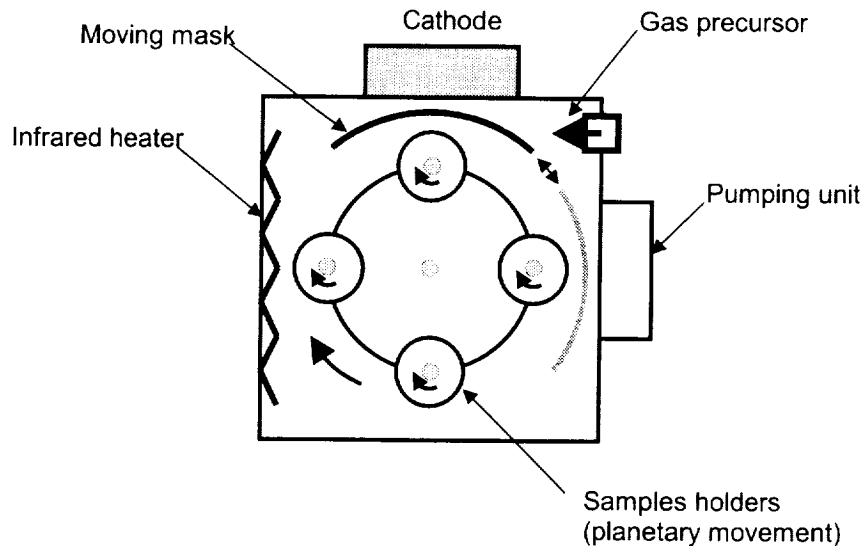


Figure 1. HEF Industrial Reactor [2]

Samples are placed on holders having a planetary movement in the reactor so that DLC thickness should be constant all around cylindrical-shaped samples, which is the case for most of the tribology components used in space. All the coatings consist in a gradient, from titanium as underlayer, to DLC, in order to reach a strong adhesion on the substrate. This gradient is obtained by increasing C/Ti ratios from the substrate to the DLC itself, by adjusting the deposition conditions during the deposition (nature and flow of gaseous precursors, bias voltage).

Optimization of the functionally gradient films for UHV low friction and wear

In order to optimize the coatings, friction tests have been performed with AISI 440 C samples while analytical characterizations have been performed with silicon ones. Friction tests have consisted in a reciprocating pin-on-flat configuration, a sliding speed of 1 mm/s and a maximum Hertzian contact pressure of 1 GPa. A limited number of 500 cycles has been performed to discriminate the set of films, depending on their deposition conditions. The coatings have been systematically deposited on the plane counterface, whatever the bias conditions. The films have also been deposited on the steel pin counterface at different deposition parameters to check if the tribological behavior depends or not on the deposition of the films on both counterfaces, in comparison to the deposition on the plane only. Each test has been performed several times in the same conditions to check the measurements reproducibility. All the tests were performed at room temperature either in ambient air at relative humidity RH = 40 – 60 %, or in ultrahigh vacuum (UHV) at 10^{-8} Pa.

The films have been characterized by Rutherford Backscattering Spectroscopy (RBS) and Forward Recoil Elastic Scattering (FRES) to determine the composition, and by Fourier-Transform InfraRed spectroscopy to determine the nature of the CH bonds. The film thicknesses have been measured by cross sectional micrographs. The film density values have been estimated by combining the previous thickness values with the thickness deduced from RBS measurements (in $\text{g}\cdot\text{cm}^{-2}$). The residual stress has been determined from the curvature induced in the silicon wafer by the deposited film [5].

Experimental results

Links have been established between the coatings tribological behavior and their compositions. For example, the link between the friction coefficient and the hydrogen content (measured with FRES) has been highlighted (Figure 2). There really is a threshold between the high friction DLC (up to 0.7 friction coefficient for up to 47 at.% hydrogen content) and the low friction DLC (down to less than 0.01 friction coefficient for hydrogen content greater than 47 at.%). This hydrogen content may be regulated by many parameters of the deposition reactor, as for example the bias voltage.

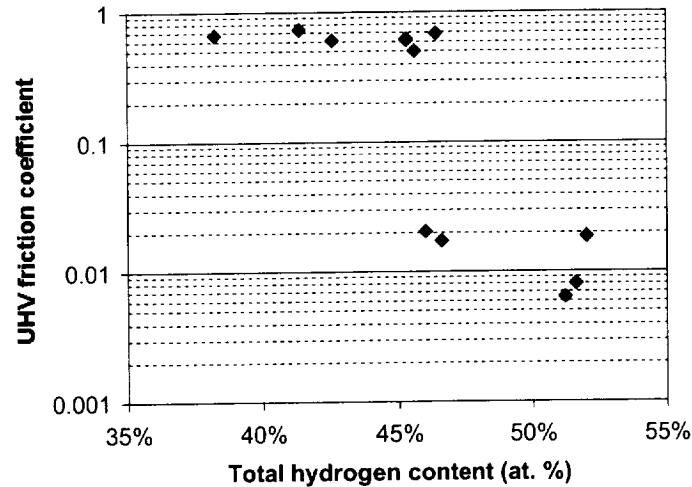


Figure 2. Steady-state friction in UHV versus hydrogen content of the films [6]

On Figure 3, one can observe the difference between low and high friction DLC coatings. The -60 V bias voltage DLC exhibits a very low friction coefficient and a very small wear while the -120 V bias voltage DLC exhibits a relatively high friction coefficient and a higher wear. The -60 V bias voltage DLC corresponds to 51 at.% hydrogen content and the -120 V bias voltage DLC corresponds to 45 at.% hydrogen content. So, the tribological behavior of the DLC strongly depends on the deposition conditions.

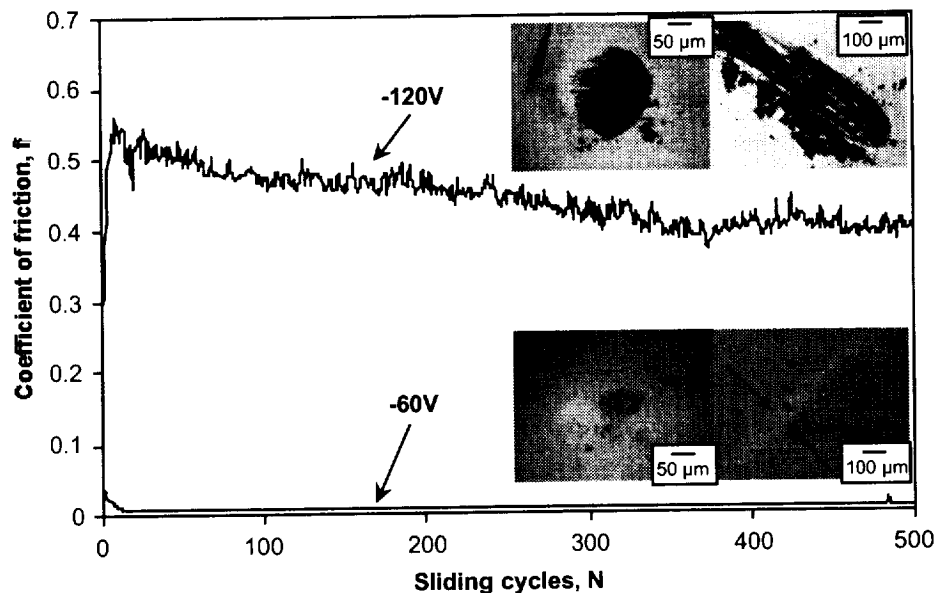


Figure 3. Friction coefficient evolution in UHV, versus number of reciprocating sliding cycles, for the films deposited at -60 V and -120 V. Optical micrographs of the wear tracks of the pins (left) and on the planes (right) after 500 cycles are shown inset [6].

Optimized DLC characteristics

After the optimization process, coatings were selected in order to be tested while coated on real mechanisms parts. The main characteristics of these coatings are summarized Table 1.

Table 1. Optimized DLC characteristics [5]

Friction coefficient under UHV	0.01
Friction coefficient under ambient air	0.2
Typical thickness (including underlayer) (μm)	4
Top layer hydrogen content (at%)	51
Density ($\text{g}\cdot\text{cm}^{-3}$)	1.5
Residual stress (GPa)	-0.6

Environment sensitivity

Some tests have been performed in order to check environment DLC sensitivity, with IBM DLC coated samples [1][7]. The hydrogen content of the coating was 42 at.% and the tests conditions were the same than those described before. While these IBM films should not be directly compared to the TiCH films presented in this paper, they have been considered as model DLC films for the study of the environmental effects on the friction. Both belong to the hydrogenated DLC film category, deposited by the same basic technique (PACVD). Since the IBM reactor is however different than the HEF one, the films do not exhibit exactly the same properties for the same composition. This result is paramount for the study of DLC films, whose properties and tribological behavior are always related to their optimization on a given deposition reactor only.

It was found that the value of the friction coefficient doesn't depend on the oxygen partial pressure. This is not the same regarding water vapor pressure. Figure 4 presents the friction coefficient variations and the water vapor partial pressure as functions of the number of cycles.

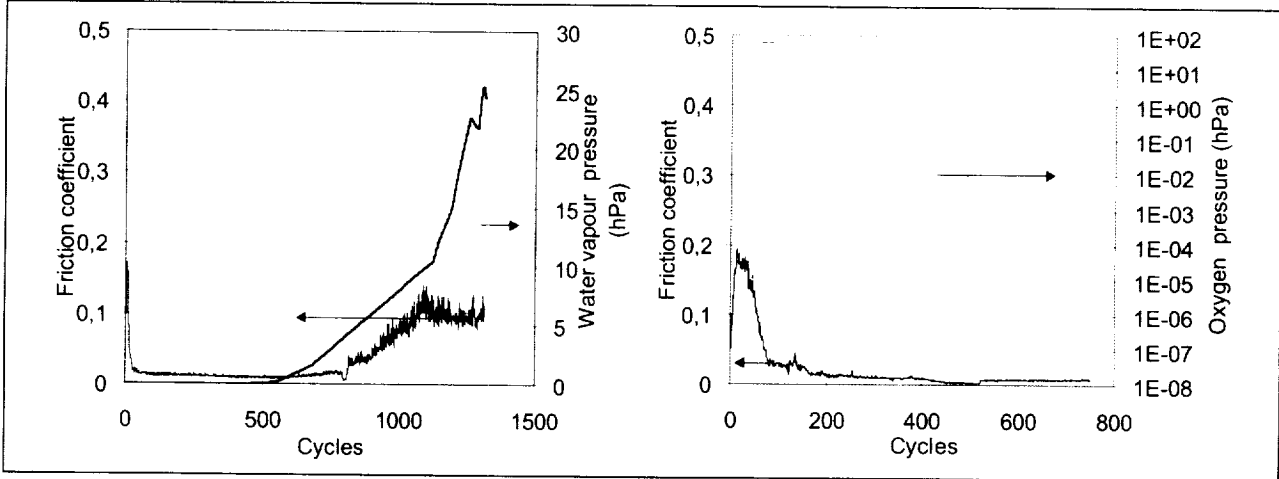


Figure 4. DLC water pressure sensitivity [7]

The friction coefficient really seems to be water vapor sensitive : it ranges from some hundredths under UHV to some tenths when the pressure is high. There is a step in the friction increase when the water vapor partial pressure reaches 0.5 hPa (Rh=2%). The effect of this water vapor seems to be reversible : when the pressure is reduced until UHV, the friction coefficient returns to its initial value under UHV. The proposed explanation of this phenomenon is that the water vapor could inhibit the transfer mechanisms and thus increase friction [7]. This has to be confirmed with some additional tests, and especially with HEF DLCs. But, in the case of space mechanisms lubrication, when tests have to be performed under air before running under UHV in space, this really is an interesting result, when one compares this behavior with the irreversible dramatic tribo-oxidation of MoS₂ films when exposed to water vapor.

DLC coated mechanisms components testing

Ball Bearings

The first tests of the optimized DLC coatings were performed on angular contact ball bearings from ADR Company. The DLC tested has been deposited at a bias of $-60V$ and a current intensity of $2 A$. Their characteristics are summarized Table 2.

Table 2. Tested bearings characteristics

Outside diameter (mm)	55
Inside diameter (mm)	35
Ball diameter (mm)	3.969
Number of balls	26
Contact angle (°)	15
Preload (N)	100 ± 10
Induced Contact Stress (MPa)	1130
Material	AISI 440C
Parts coated	Rings (tracks) and cages

After the first bearing pair was coated, the external rings appeared to be very deformed. This was due to the joint effect of the temperature and the rings support. We proceeded to a test that measured the highest temperature during the process. It appeared to be higher locally than the stainless steel tempering temperature. This maximum temperature was reached during the etching of the substrate, prior to deposition. So, we decided to adjust the etching temperature and, also, to change the ring support geometry in order not to radially stress the rings.

A second pair of bearings was coated and tested. First, the torque was measured under air in order to verify that no major changes had occurred with the coating. Then, the bearing pair was placed in a Ultra-High-Vacuum chamber and a 'life test' began. This test consisted in a continuous rotation movement (30 rpm), during which the torque, the temperature inside the torquemeter and near one of the motionless rings were measured. Figure 5 is a picture of the test bench and Table 3 shows the evolution of the torque during the test.

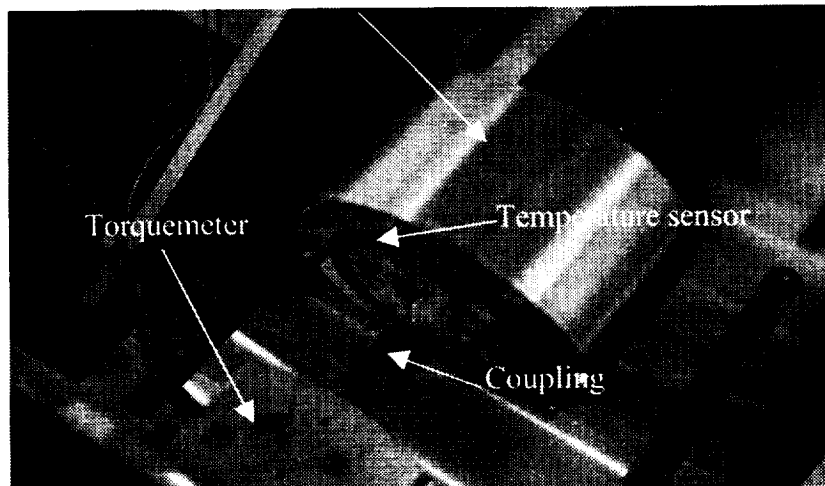


Figure 5. Test Bench

Table 3. Torque Measurements During Bearings Tests

	Atmosphere	Mean Torque (cN-cm)	Torque Noise (cN-cm)
Before deposition*	Air	50	110
Just after deposition	Air	55	100
Nitrogen test	Nitrogen	80	30
Life test start	UHV	75	60
Stabilized torque	UHV	12	15
End of test	UHV	15	>200

*This test is done with a few liquid lubricant in order to avoid bearings damages

After a running-in period (10000 revs), the torque appeared to be stable and noiseless for more than 400000 revs. Then, the torque noise began to increase and it was decided to stop the test at 500000 cycles and to inspect the bearings in order to try to find out what caused the noise increase. Bearing inspection shows that third body flows take place in the bearing. One can observe the phenomenon on Figure 6.

The races show different kinds of wear with a third body flow going outside the race while the balls show that some DLC has been transferred from the race to the balls. The wear of the cages is very significant and could have led to the torque noise increase at the end of the test. Also, this wear should be reduced with a better quality surface inside the cage pockets. Some machining marks can be easily observed and we know that DLC don't like rough surfaces. So, a new test is going to be performed with improved cages.

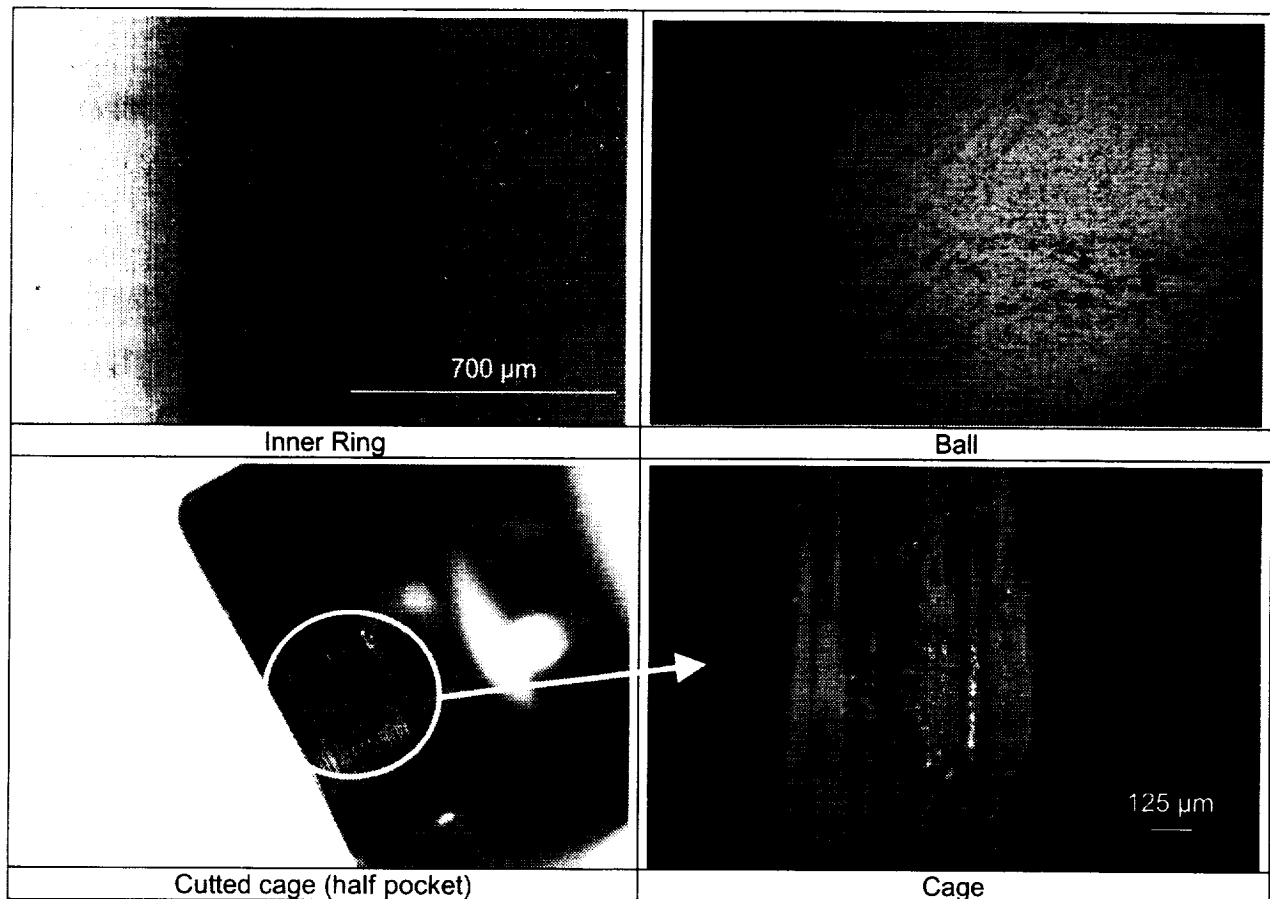


Figure 6. Some Pictures from Tested Bearings

RF Switch Bearing

RADIALL Company uses a small bearing from RMB company in T-type coaxial switches. This bearing is submitted to quick oscillating movements (60° amplitude in about 20 ms in each direction). An axial load of about 15 N is applied to this bearing via the actuator magnet. The main characteristics of the bearing are summarized Table 4.

Table 4. RF switch bearing characteristics

Outside diameter (mm)	8
Inside diameter (mm)	5
Balls diameter (mm)	1
Number of balls	11
Axial load at rest (N)	15
Switching axial load (N)	23
Material	AISI 440C
Parts coated	Rings (tracks) and cages

Two kinds of tests, relative to the bearing lubrication, have been performed at RADIALL. First, the existing MoS₂ lubrication under ambient atmosphere (50% RH) led to switching problems at about 50000 commutations. The need is 300000 commutations under space vacuum condition, but the product can be operated by customers before launch under variable and indefinite conditions (humidity, pressure, number of commutations...) due to storage, ground operations, transportation. So ideally RADIALL wishes the product to be able to withstand the complete life (300000 commutations) including a period in ground condition as well as the period in orbit condition. The recommendation for the use of the MoS₂ lubrication might be difficult to achieve for ground operations, storage and transportation. There is a need for a new dry lubricant.

RADIALL decided to lubricate the bearing with the same DLC that was deposited on the ADR bearings presented above. With the present DLC, there was no problem to perform the whole number of commutations under atmosphere. At the beginning of 2001, RADIALL is going to perform a qualification tests sequence (including commutations under UHV) with a DLC lubricated bearings switch. This really is the first commercial application of our DLC.

Since the qualification test deals with the whole commutator, it is not possible to have direct information on the bearing behavior. Incorporating bearing dedicated sensors would significantly modify the commutator. It has thus been decided to perform bearing tests in order to compare DLC to MoS₂ using torque measurements on a specific test bench.

Gears

A set of four gears (two AISI 440C gears and two 35NCD16 gears) has been coated with the same DLC used hereand will be tested on a specific test bench in 2001. Figure 7 is a picture of a gear, showing the good visual quality of the coating.



Figure 7. DLC coated gear (teeth height 2 mm)

Screw-nut

For the Mars Netlander mission, the 'Institut de Physique du Globe de Paris' (IPGP), SODERN company and CNES are developing a Very Broad Band seismometer in order to better understand the Martian internal structure [8]. This seismometer consists in a pendulum (spring and mass) rotating around an elastic pivot. This pendulum being very sensitive, it has to be balanced via a mass displacement system, driven by a motor and a screw-nut device.

The screw-nut device has to be designed taking into account the fact that the seismometer is placed in a vacuum chamber in order to obtain a good quality pendulum. The screw is made of titanium, its diameter is 3 mm and its step is 0.25 mm. Backlash is removed from the system by using a pair of half-nuts separated by a spring which induces a 0.2 N radial preload. Half-nuts are usually made of brass. Tests with this last configuration showed limited life, so it has been decided to test DLC-coated nuts made of titanium.

Tests have been performed with and without DLC lubrication on the half-nuts in order to assess DLC effectiveness. Motor current was measured in each direction, under air or vacuum ($<10^{-3}$ Torr). All the results shown below represent the current in stabilized phase, after the running-in period. Figure 8 shows the values (averages over the whole test sequence) of the motor current for each direction, with or without DLC lubrication, under air (6 hours test) or vacuum (1 hour test) at ambient temperature. The number of cycles induced by the tests duration is quite representative of the mission needs.

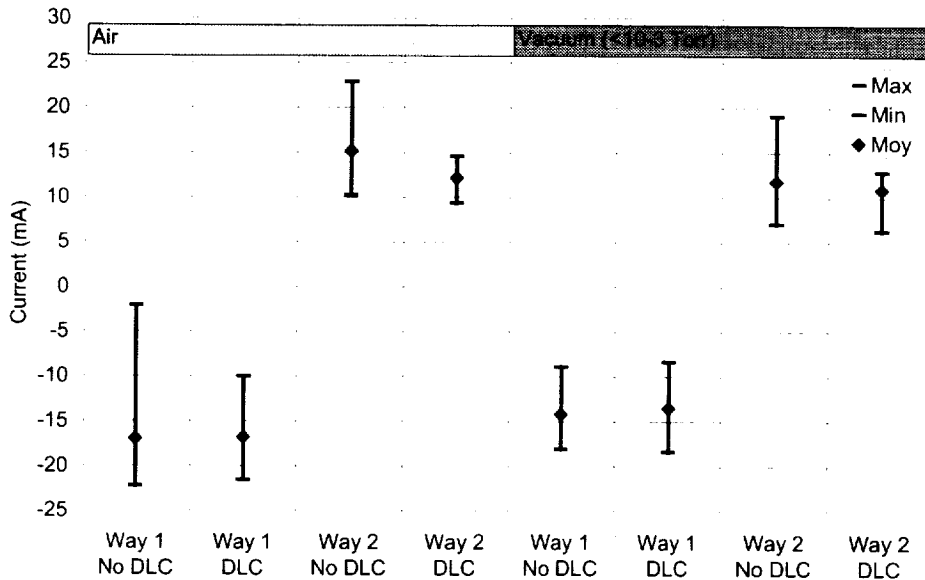


Figure 8. Comparison between non-lubricated and DLC-lubricated nut

Table 5 shows the influence (percentage) of DLC on the motor mean current and on the current noise, defined as the difference between the maximum current and the minimum current. Except for the current noise under vacuum in the first direction (way 1), DLC reduces significantly the values of the mean current and the current noise. Inspection of the screw-nut didn't show any problem of wear, and long-life tests will be performed. As it was shown with flat-on-disc tests, DLC seems to be a good lubricant when pure sliding occurs, which is the case in a plain screw-nut system.

Table 5. DLC influence on motor current (%)

		Mean Current	Current Noise
Air	Way 1	-1	-43
	Way 2	-20	-59
Vacuum	Way 1	-5	+9
	Way 2	-7	-45

Conclusion

Diamond-Like Carbon (DLC) coatings, deposited by a hybrid technique of magnetron sputtering and plasma-assisted chemical vapor deposition, have been studied. Friction tests, coupled with analytical characterizations, show that the coatings exhibit a wide range of friction behavior, depending on the coating composition and, thus, on the deposition conditions. An underlayer optimization study has also been performed in order to obtain a strong adhesion on the substrate. The selected solution is a gradient from titanium to DLC, from the steel substrate to the surface.

Promising tribological results have been obtained with DLC deposited ball bearings even though a lot of additional work still remains. For example, the cage/ball contacts will be optimized in order to decrease the significant wear observed. Nevertheless, a small DLC coated RF switch bearing showed better behavior than MoS₂ coated bearing and could lead to the first space commercial application of the DLC coatings if the qualification tests succeed. Some other components are going to be tested in the next months (screw-nut device, gears, other bearings...) The work presented here is very innovative because it could lead to the qualification of a new space mechanisms lubrication solution. It is consistent with the current development of diamond-like carbon films for various applications, including low friction and wear in extreme conditions.

Acknowledgments

We are grateful to the Région Rhône-Alpes for supporting the present study. We thank N. Striebig, S. Cacho, O. Pot and B. Brient from IPGP for the screw-nut tests, which have been performed in IPGP laboratories.

References

- [1] Donnet Ch, Le Mogne Th, Belin M, Sicre J, Pont G, Grill A, Patel V, Jahnes C; "Diamond-Like Carbon Coatings for Vacuum and Space Tribology"; 7th European Space Mechanisms and Tribology Symposium; Noordwijk (Ned); October 1997
- [2] Fontaine J.; "Elaboration, Caractérisation et Tribologie de Couches Minces DLC (Diamond-Like Carbon) pour la Lubrification des Mécanismes Spatiaux"; Thèse de Doctorat; 2000.
- [3] Donnet Ch, Fontaine J., Le Mogne Th, Belin M, Terrat J.P., Heau Ch., Pont G; "Tribologie de Couches Minces de Carbone pour Mécanismes Spatiaux"; Journée Technique CETIM; December 1998.
- [4] Grill A., Diamond and Related Materials, 8 (1999) 428.
- [5] Fontaine J., Donnet Ch, Le Mogne Th, Belin M, Berthier Y, Terrat J.P., Heau Ch., Pont G; "Towards the Solid Lubrication of Space Mechanisms by Diamond-Like Carbon Coatings"; 8th European Space Mechanisms and Tribology Symposium; Toulouse (France); Sept 1999.
- [6] Donnet Ch, Fontaine J., Le Mogne Th, Belin M, Terrat J.P., Heau Ch., Vaux F., Pont G; "Diamondlike Carbon-Based Functionally Gradient Coatings for Space Tribology"; ICMCTF'99; 1999.
- [7] Donnet Ch., Le Mogne Th, Ponsonnet L., Belin M, Grill A., Patel V., Jahnes C.; "The Respective Role of Oxygen and Water Vapor on the Tribology of Hydrogenated Diamond-Like carbon Coatings"; Tribology Letters 4; 1998.
- [8] Cacho S., Lognonné P., Karczewski J.F., Pont G., Coste G.; "A Very Broad Band 3 Axis Seismometer to Study Internal Structure of Mars"; 8th European Space Mechanisms and Tribology Symposium; Toulouse (Fra); September 1999.

3/27

Effect of Alternate Solvent Diluents on PFPE Performance

Christopher J. Dayton and Robert M. Warden*

Abstract

A lubrication study has been completed which tested the effect of various CFC (Freon) substitutes on the performance of perfluoroalkylpolyether (PFPE) lubricants applied to rolling element bearings. Three bearing pairs were tested concurrently, differing only in the diluent used for the final step in the processing of the bearings. The objectives of the bearing tests were to: 1) quantify in terms of stress-cycles the approximate point at which the onset of lubricant polymerization occurs and 2) determine what effect the use of different solvents have on the period of time prior to the onset of polymerization. This paper provides a detailed description of the processing of the ball bearings, the test articles, the test fixture, the data logging philosophy, and the results of the study.

Introduction

The long-term reliable performance of bearings operating in a space environment requires careful selection of the appropriate liquid or dry lubricant. PFPE is one class of liquid lubricant with extensive space flight history. Relative to hydrocarbon lubricants, PFPE's generally have lower vapor pressures, which reduces the evaporative loss from critical interfaces. They also have higher viscosity index values, which translates into lower bearing torques at low operating temperatures. This type of lubricant, however, does not possess good miscibility for traditional, space-proven additives that readily dissolve in hydrocarbon lubricants. Also, PFPE's have a tendency to polymerize, especially when employed in interfaces where metal-to-metal contact is prevalent (the boundary lubrication regime). Unfortunately, this is the typical operating regime for many components within space-borne instruments.

Over the past fifteen years, the propensity of PFPE's to undergo an autocatalytic polymerization when subjected to stress in the presence of certain metals has been the subject of extensive study.^{1,2} Furthermore, several articles have been written documenting the varying response of this class of lubricant relative to its propensity to polymerize with respect to both the cleaning methods and the type of contacting materials employed.^{3,4,5} These latter studies were largely prompted by the Montreal Protocol, which prohibits the production of certain ozone depleting chemicals (ODC's), such as CFC-113 (Freon TF), that had been widely used as cleaning agents and PFPE diluents.

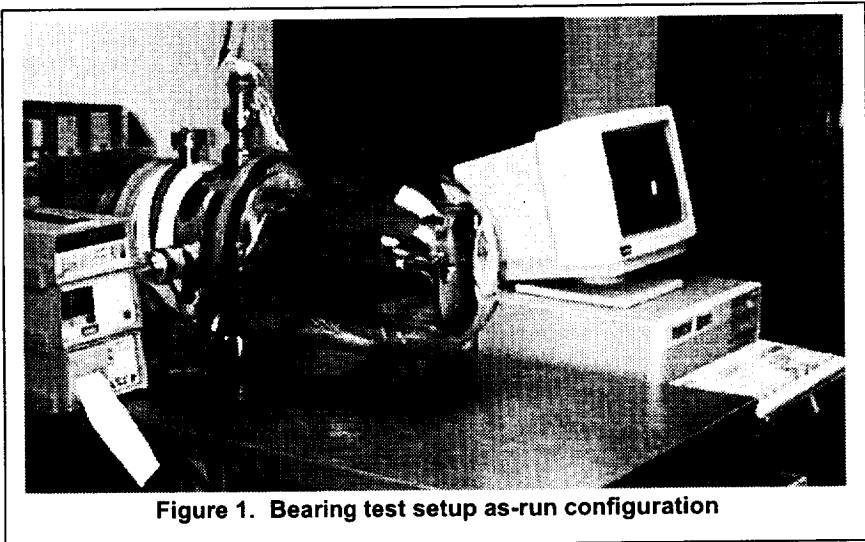


Figure 1. Bearing test setup as-run configuration

The linear PFPE oil Brayco 815Z, and the grease analogue Braycote 601, have been used for many years in space flight instruments. For example, when the last of the Hubble Space Telescope (HST) science

* Ball Aerospace & Technologies Corporation, Boulder, CO

instruments are installed by the year 2004, these lubricants will be present in at least one mechanism per science instrument. Although prone to polymerization, there are applications where the use of this lubricant is justified; usually due to a relatively low total number of revolutions in combination with low to moderate bearing stresses. To verify suitability, comparison to similar life-tested engineering models may be performed. Another approach, defined below, is to quantify the cumulative combined effect of duty cycles and contact stresses. This first-order technique for establishing performance margins is narrowly defined by the expected operating parameters, such as lubricant operating regime, Hertzian contact stress, and duty cycles, established by the hardware to be simulated.

This objective was accomplished through the simultaneous testing of three bearing pairs operating at low contact stress, with the only variable distinguishing one set from another being limited to the oil diluent. The diluent was used in the preparation of an oil solution, which in turn was used to rinse off excess oil, and to perform particle counts. As explained below, this process was subsequent to all cleaning and lubrication steps. It was anticipated that this test would therefore not only provide the time period prior the onset of lubricant polymerization, but also yield information regarding the effect of the diluent, if any, with respect to the performance of the lubricated bearings.

Test Approach

The solvents studied were: Du Pont's Freon TF (CFC-113), Du Pont's Vertrel[®] XF, and 3M's Novec[™] HFE-7100. Vertrel XF is a hydrofluorocarbon, or HFC solvent, whereas HFE-7100 is a hydrofluoroether. Like Vertrel XF, HFE-7100 has zero Ozone Depletion Potential, but lower values for Global Warming Potential and Atmospheric Lifetimes than Freon TF or Vertrel XF. Neither replacement solvent is considered to be a volatile organic compound by the EPA. The Freon TF served as the control.

Three back-to-back bearing pairs, SBB part number 3HAR007P5A, were procured for this test. These non-separable 440C angular contact bearings were obtained with one-piece machined phenolic cages, and were selected based on availability. Since the reliability of the test could therefore not be increased by duplicating bearing pairs, great care was exercised during the processing of the bearings to minimize variables. All bearing pairs were maintained as sets throughout processing by serial numbers positioned on the large face of each outer race. To avoid potential preload problems, balls were segregated and maintained with the appropriate inner and outer race.⁶

The bearing lubrication was performed at Ball Aerospace & Technologies Corp., and was typical of the processing performed for the lubrication of flight bearings. The processing consisted of disassembly using a fixture used to heat the outer race, and cool the inner race. All components were inspected at high magnification after an initial hydrocarbon solvent cleaning. Following further hydrocarbon solvent cleaning and extensive baking, all phenolic cages were simultaneously impregnated for several hundred hours at elevated temperature with the same lot of specially processed Brayco 815Z. The special process is a proprietary vacuum baking procedure that reduces the volatility of the oil. The vapor pressure measured at Ball Aerospace using a thermally controlled quartz crystal microbalance measurement technique was found to be less than $1 \cdot 10^{-14}$ torr at room temperature.

Following the impregnation of the cages and reassembly, each bearing was cleaned until the particle levels were in accordance with MIL-STD-1246 Level 100 for metals, and less than Level 200 for all particles. This process used a five-percent by weight solution of the oil in the appropriate solvent: either Freon TF, Vertrel XF, or HFE-7100. This solvent substitution was the only difference that each bearing pair was subjected to during processing. The rinse resulted in a deposition of approximately 20 mg of oil on the ball and raceway surfaces; enough to produce a slight oil meniscus between the ball and raceway, but slightly less than what would normally be required for flight bearings. If these had been flight bearings, additional oil would have been added.

Using a Ball Aerospace-developed lubricant film thickness program that corrects for side leakage from the contact ellipse, and the bearing parameters summarized in Table I, the lambda ratio (elastohydrodynamic film thickness to composite ball and raceway surface roughness) was determined to be approximately 0.6 when the bearings were operated at room temperature and 50 rpm. This calculated lambda ratio is probably greater than what actually existed since flooded conditions were assumed. The surface roughness term was calculated from an average of measurements of the bearing inner raceways, performed by the bearing manufacturer and summarized later in the paper in Table II.

Table I. Test Bearing Properties

Property	Value
Part Number	SBB 3HAR007P5A
Number of Grade 10 Balls, Diameter	18, 6.35 mm (0.25 inch)
Pitch Diameter	45 mm (1.771 inch)
Initial Contact Angle	12.80
Outer and Inner Race Conformities	0.524 and 0.520
Thrust Load	approximately 62 N (14.0 lb)
Mean Inner Raceway Hertzian Compression Stress	approximately 450,000 kPa (65,000 psi)

The test was performed in a vacuum chamber at less than 1×10^{-5} torr, at room temperature, with one three day excursion to +13 deg C and another short excursion to +30 deg C. Each set of test bearings was continuously monitored for torque (method defined in the Test Apparatus section).

Each of the sets of angular contact bearings were housed in separate stainless steel bearing cartridges with a compliant axial preload of about 62 N (14 lb). This load resulted in a nominal ball-to-inner-raceway Hertzian contact stress of approximately 450 MPa (65 ksi). The objective was to operate the processed bearings under boundary lubrication conditions. The intention of using a light preload was twofold: it was representative of several bearing pairs operating in the HST, and it was thought that this would allow for a longer test duration prior to the onset of polymerization.

Labyrinth seals with a length-to-gap ratio of approximately 30 to 1 enclosed both sides of the duplex pair. This resulted in reducing the apparent exit area by approximately 88 percent, thus reducing evaporative loss. The labyrinths, coupled with the low vapor pressure of the vacuum-stripped lubricant resulted in a negligible evaporative loss.

Low surface energy barrier film was applied to surfaces adjacent to the bearings to limit loss due to creep.

Prior to commencement of the test, the preloaded bearings were run-in under the same thermal vacuum conditions that would be present during the test. The run-in period was 16 days. This was followed by removal of the

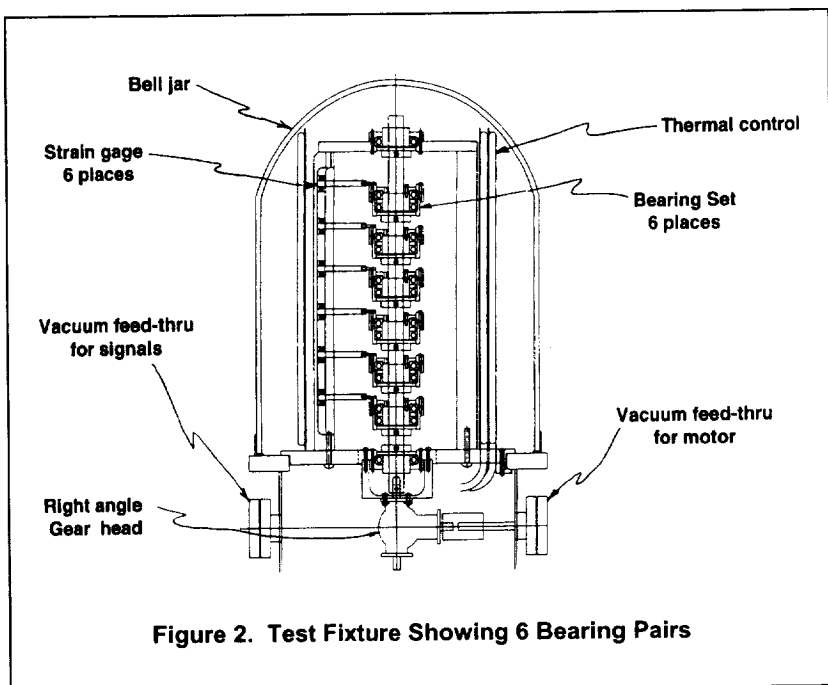


Figure 2. Test Fixture Showing 6 Bearing Pairs

bearings from the cartridges, and recleaning to the particle levels stated above, followed by barrier film application to the bearing faces. Care was taken during reassembly to duplicate, as close as possible, the orientation of the bearings within the cartridges present during run-in.

Test Apparatus

The bearing test assembly, depicted in the as-run configuration in Figure 1, and a cross-sectional view in Figure 2, was designed and built to simultaneously test several pairs of bearings under identical environmental conditions. The speed and temperature can be varied but the changes apply to all the bearings.

In order for the bearings to be tested under load, two bearings were mounted in a cartridge and compliantly preloaded back-to-back (Figure 3). In this way, each bearing pair is preloaded within the pair, independent of the test fixture.

The preload was set by compressing the wave washer a predetermined amount. Each wave washer had been characterized through the generation of force versus displacement curves. A tang extends from the outer part of the cartridge so that when the inner subassembly is rotated, the force on the tang keeps the outer subassembly from rotating. By measuring the force on this tang over long periods of bearing rotation, the effectiveness of the bearing cleaning and lubrication can be measured.

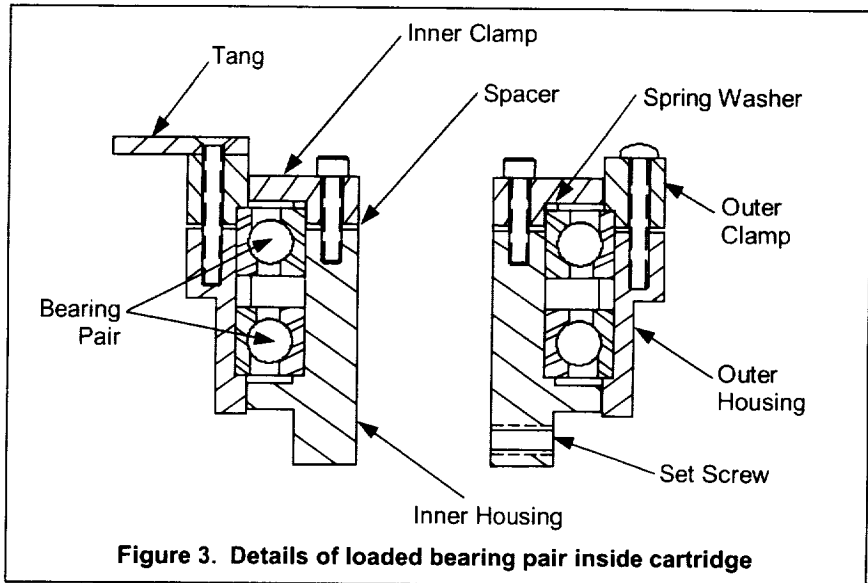


Figure 3. Details of loaded bearing pair inside cartridge

A common shaft drives the inner subassembly of each bearing pair at the same speed. The tang on the outer ring is restrained by a cantilevered beam, which is attached to an offset column. The distance from the center of rotation to the point of contact with the beam is 66 mm (2.6 inches) as shown in Figure 4. These beams act as small leaf springs, which are instrumented with strain gages to indicate force. The force gages are calibrated before being assembled into the vacuum chamber. The zero value can be verified at any time by simply stopping the drive shaft and backing it off the tang.

The vacuum chamber was a simple bell jar over a multi-port access collar. One access port was used for the rotary feed-through which drove the drive shaft by means of a right angle gearhead. A flex coupling was used between the rotary feed-through and the right-angle gearhead to accommodate alignment errors.

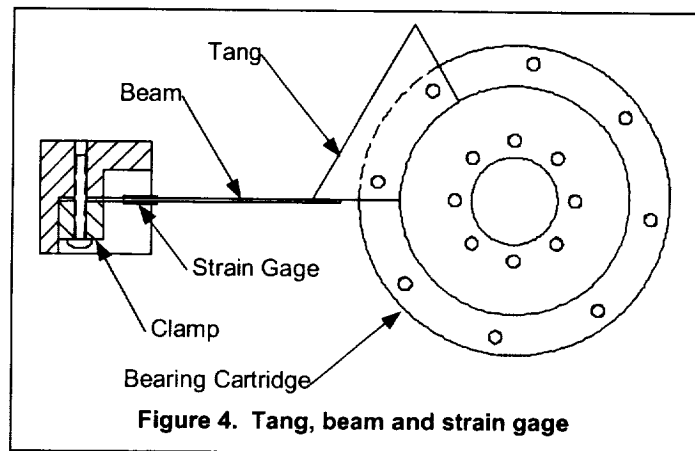


Figure 4. Tang, beam and strain gage

One of the early concerns was cross-contamination between the bearing cartridges. Although this threat was slight, it was considered since the exit areas associated with the labyrinth gaps were line-of-sight between adjacent cartridges. To reduce this effect, large disks were placed between the cartridges. To

further reduce particulate contamination, the entire vacuum chamber was oriented on its side, so that any errant particles would be pulled by gravity to the side of the chamber instead of landing on the adjacent cartridge. Barrier film was used to prevent lubricant losses due to creeping.

To heat and cool the bearings evenly, a thermal shroud was placed between the bearing test fixture and the inside of the bell jar. The thermal shroud was simply a large sheet of copper with copper tubing soldered on to the exterior surface in an "S" pattern. To increase the emissivity of the interior surface of the shroud, a Ball Aerospace-developed black polyimide paint was applied. This assembly was then rolled into a cylinder. The ends of the tubing were run through liquid feed-throughs in the access ring. Hot or cold liquid could then be pumped through the shroud, which could then radiatively heat or cool the bearings. In order to offset the heat sinking caused by the vacuum chamber flange and housing, the housing was wrapped with thermal tape. By balancing the shroud and housing temperatures, a fairly uniform end-to-end temperature was achieved.

The process of collecting data for a long-term test presented some interesting challenges to the design of the data logging system. Although the measurement of the data needed to be accurate, the process only needed to occur about once every hour. A typical printout is shown in Figure 5. Reliability and flexibility became more important than bandwidth. An "elegant" solution was found by using a data logger system manufactured by Validyne Engineering Corp. This system consisted of an interface board on to which the signal wires were connected and a processing card, which plugs into a spare slot in a personal computer. For this test, a surplus 386-50 was used with DOS 5.0 as the operating system.

Date	Time	1	2	3	4	T1	T2
05/27/98	14:49:15	0.000	0.1706	0.1679	0.1293	29.36	29.54
05/27/98	14:59:15	0.000	0.1835	0.1478	0.1203	29.12	29.18
05/27/98	15:09:15	0.000	0.1801	0.1573	0.1116	28.88	29.03
05/27/98	15:19:15	0.000	0.1974	0.1329	0.1231	29.13	29.30

Key: 1 = empty bay; 2 = Freon TF processed bearing pair retention force (pounds); 3 = Vertrel XF processed bearing pair; 4 = HFE-7100 processed bearing pair; T1 = Base Temperature (C); T2 = Top Temperature (C)

Figure 5. Typical printout

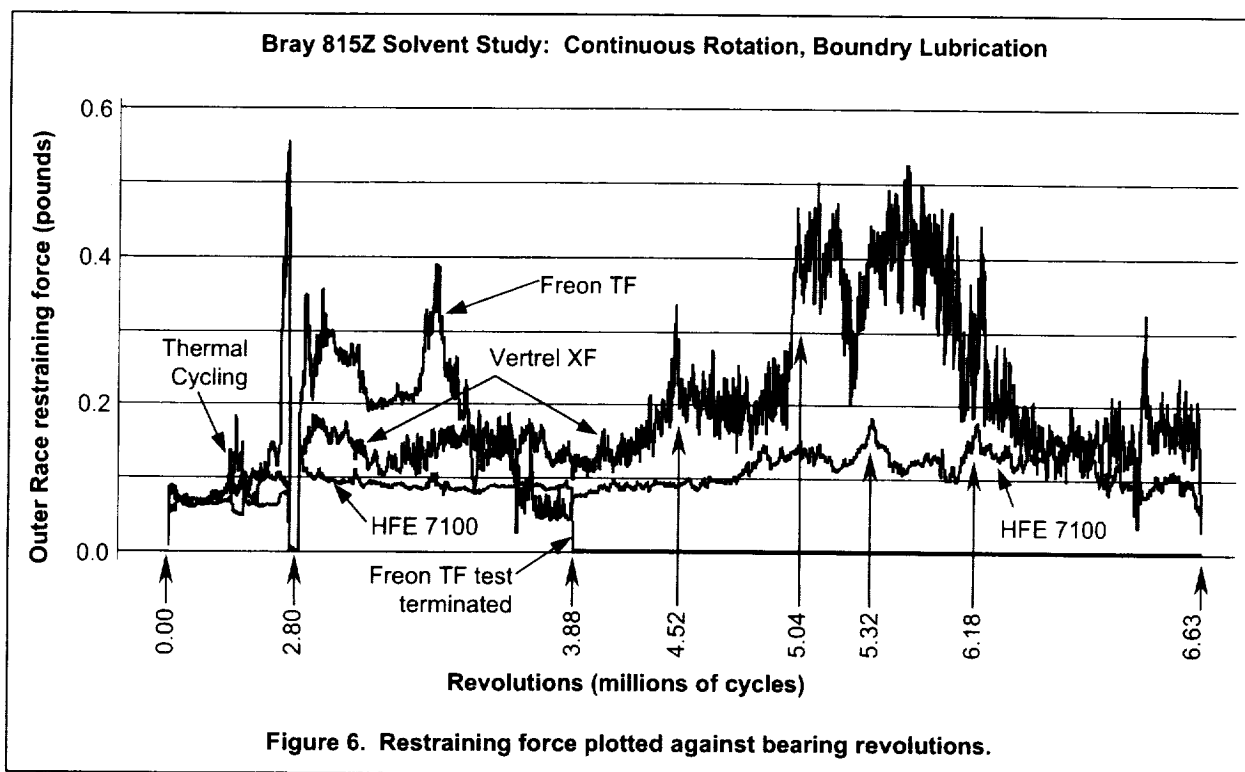
The outputs from the strain gages as well as thermocouple leads were passed through electrical feed-throughs in the access collar of the vacuum chamber. These wires were then attached to the interface board, which also converted the signal from analog to digital. The interface board can be configured many ways so that each of the eight channels can be hooked up to monitor voltage, current or temperature. This board is connected to the computer by a 50-wire ribbon cable.

The display is meant to be toggled between two modes. The set-up mode allows data acquisition properties such as report frequency and averaging to be set. Also in this mode, channel titles and number of decimal places are selected. In the logging mode, data is being gathered and displayed on the screen. Up to 32 different channels can be monitored and viewed at the same time.

The Validyne processor can process information much faster than what was needed for this test, but it also allows long periods of time between cycles. For this test, the time period between readings was initially set at 3600 seconds, but increased to six times per hour after $2.85 \cdot 10^6$ revolutions. At the appropriate time, the data logger would read the strain gage values as well as the temperature values. The reported values were actually an average of 50 instantaneous values. The date, time and eight data values were then printed in a single row on the printer, and also appended to files on a both the hard disk, and a 3.5-inch floppy. For hard copy backup, a wide-carriage, tractor-feed, dot-matrix printer allowed printing of all relevant data on a single line. A box of fan-fold paper would last many months without interruption.

Test Results

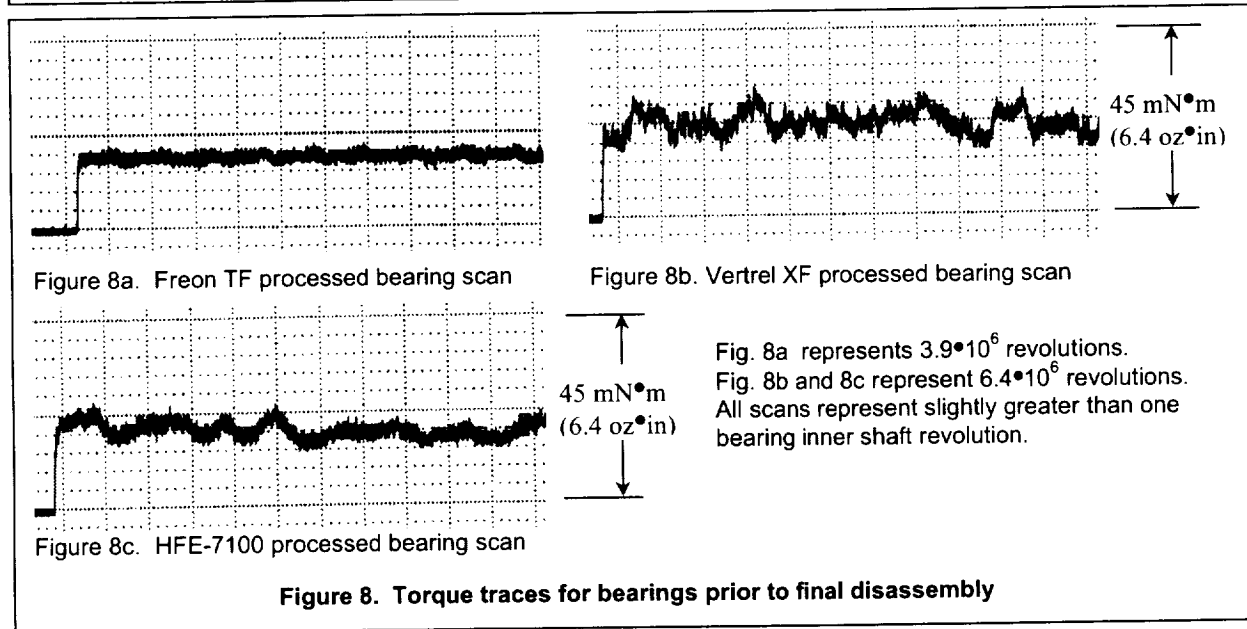
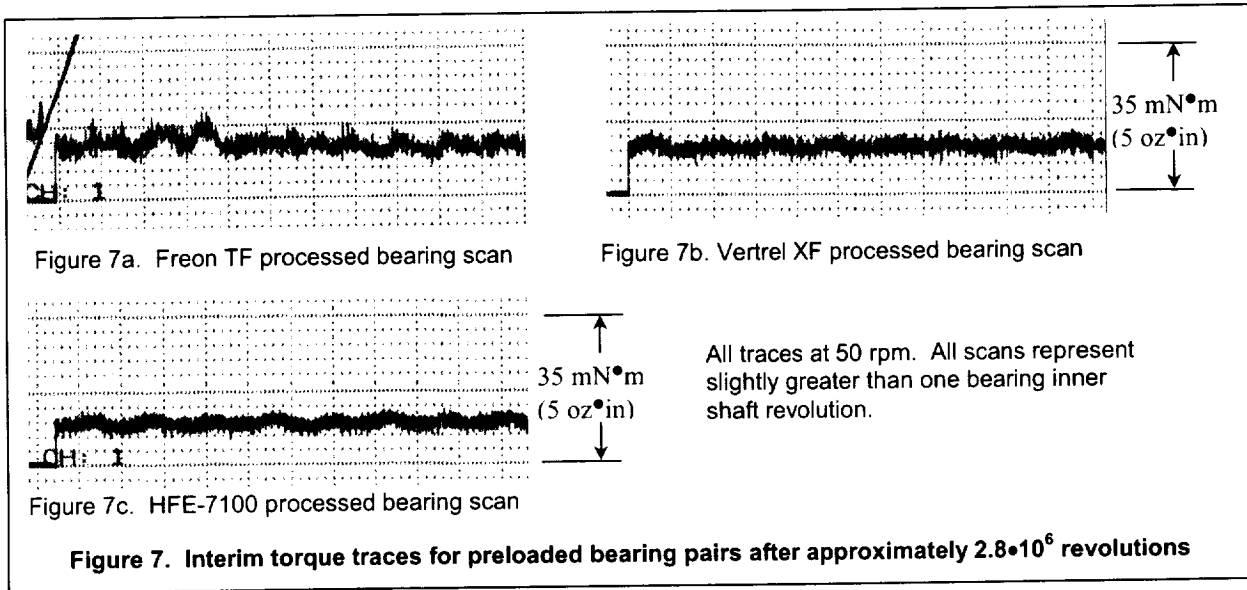
A test endpoint based on achieving a predetermined torque relative to the initial steady-state value was not established. Instead, the bearings were allowed to run until it was obvious from in-situ retention force measurements that the lubricant had failed, or was nearing the end of its useful life. For the Freon TF, and to a lesser extent, the Vertrel XF treated bearings, the onset of lubricant polymerization was characterized by a sudden increase in torque, followed by a gradual decline. The HFE-7100 processed bearing pair, however, also followed this pattern, but with average slopes more shallow relative to the other bearing pairs (Figure 6).



The point at which the Freon TF processed pair exceeded two, and essentially, four times the initial steady-state restraining force of approximately 0.35 N (0.08 lb) was at $2.73 \cdot 10^6$ revolutions. Using the summation for the product of the number of times a given spot on the inner raceway is compressed times the mean Hertzian inner raceway contact stress of 450 MPa (65 ksi), and accounting for the differential speeds of the inner race versus the pitch diameter, this number of revolutions corresponded to approximately $1.37 \cdot 10^{12}$ psi-crossings.

Interim torque traces (clockwise and counterclockwise) were taken using a strip chart recorder shortly after this event. Following the resumption of the test, this bearing pair continued to operate at greater than two times the initial restraining force until essentially all the oil had polymerized, and was pushed out of the wear track. This event is represented in Figure 6 by a gradual decline in torque until test termination at $3.88 \cdot 10^6$ revolutions, or $1.95 \cdot 10^{12}$ psi-crossings.

The point at which a twofold increase in the restraining force for the Vertrel XF processed bearing pair was achieved was at $4.52 \cdot 10^6$ revolutions ($2.27 \cdot 10^{12}$ psi-crossings), and $5.04 \cdot 10^6$ revolutions ($2.54 \cdot 10^{12}$ psi-crossings) for a fourfold increase. The outer race restraining force for the HFE-7100 processed bearing pair doubled at $5.32 \cdot 10^6$ revolutions ($2.68 \cdot 10^{12}$ psi-crossings). The restraining force increased only slightly between this point and test termination at $6.63 \cdot 10^6$, or $3.33 \cdot 10^{12}$ psi-crossings. Torque traces (strip charts) were performed at $2.80 \cdot 10^6$ revolutions for the three pairs (Figure 7), and after the test end points for each respective bearing pair, but prior to disassembly (Figure 8). Note that the peak-to-peak bearing torque noise for the Freon TF diluted oil decreased from $8.5 \text{ mN}\cdot\text{m}$ ($1.2 \text{ oz}\cdot\text{in}$) in Figure 7a to $5.0 \text{ mN}\cdot\text{m}$ ($0.7 \text{ oz}\cdot\text{in}$) in Figure 8a due to the formation, then subsequent displacement of polymerized lubricant. In contrast, the amplitude of the torque noise for the Vertrel and HFE-7100 processed bearings roughly doubled from the interim traces to the final traces. This indicated a lag in the noticeable effect of polymer formation relative to the performance of the Freon TF processed bearings.



The bearings were disassembled as shown in Figure 9. A visual examination at 7 to 30X magnification of the disassembled bearing components, as well as SEM imaging of inner raceways, was then performed. For all three bearing pairs, polymerized product was evident in the ball pockets (at a minimum) of each bearing separator. Also in all three bearing pairs, wear marks in the raceways of the outer races were difficult to see at 30-power magnification. No oil had crept past the barrier film treated bearing faces in any of the bearings.

On the inner raceways of the Freon TF processed bearings, there was essentially no free oil apparent. There was no oil in evidence, and very little polymer left in the bearing wear tracks (Figure 9a). The inner raceway wear tracks had a frosted appearance, typical of inadequate lubrication. The raceways exhibited a great deal more wear relative to the other bearing pairs. There was also a faint blue tint to the inner raceway wear tracks, indicating the possibility that surface damage due to heat had occurred. The balls were a uniform dark gray, similar in appearance to a black oxide coating.

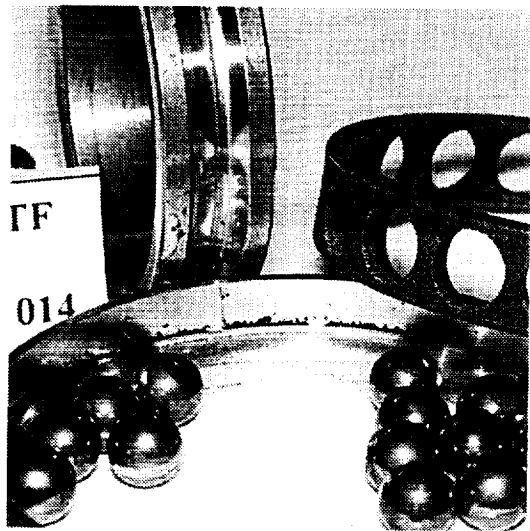


Figure 9a. Brayco 815Z and Freon TF

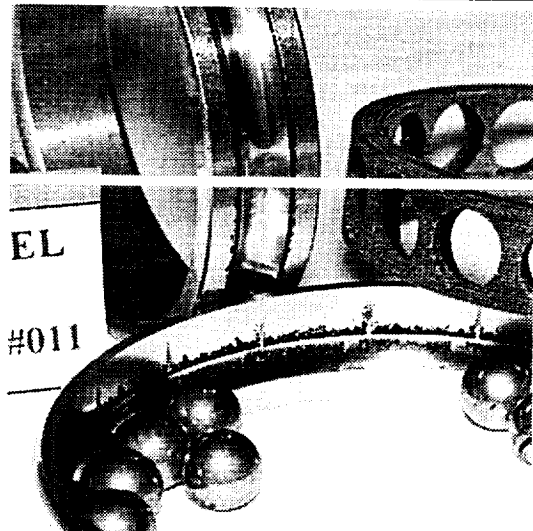


Figure 9b. Brayco 815Z and Vertrel XF

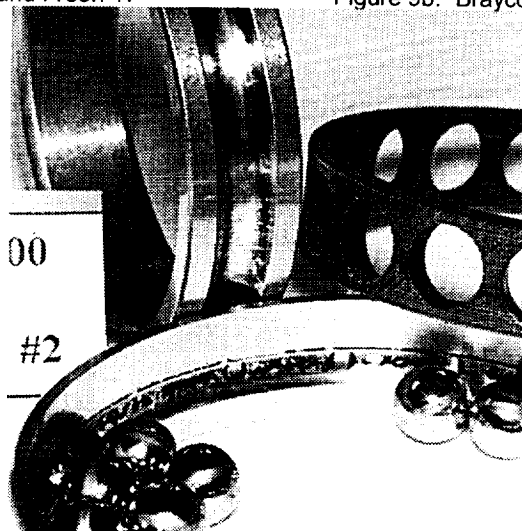


Figure 9c. Brayco 815Z and HFE 7100

Figure 9. Post-test images of representative bearings

The Vertrel XF treated bearing had a slight amount of oil mixed in with the polymer present in the (predominantly inner) raceways. While wear marks were present on the inner raceways, the grinding grooves introduced during the bearing manufacturing process were still readily apparent. The balls were a lighter shade of gray relative to those associated with the Freon TF processed bearings.

A surprising amount of oil was present and intermixed with the polymer located within the inner raceway of the HFE-7100 processed bearings. Other than the great circle wear marks, the balls looked almost new. The races were only lightly worn.

Axial profilometer measurements were taken for the inner races of each bearing before and after testing (Table II). The post-test roughness values are a composite average of measurements of the wear track plus approximately an equal axial distance outside the wear track. Note that only in one instance did the surface roughness increase, and not surprisingly, it is associated with one of the Freon TF processed bearings. It is surprising, however, that the other half of the pair was not as rough. This observation was supported by SEM imaging.

Table II. Inner Raceway Axial Surface Roughness

Diluent & Bearing Serial No.	Surface Finish (rms)	
	Before Test*	After Test**
Freon TF; #13	3.77	6.14
Freon TF; #14	4.83	2.92
Vertrel XF; #11	5.98	2.64
Vertrel XF; #12	6.92	2.27
HFE-7100; #01	3.99	3.67
HFE-7100; #02	3.73	2.47

*Performed by Split Ballbearing, Div. MPB Corp.

**Performed by FALEX Corp.

Discussion and Future Work

The stress-cycle values obtained from bearing tests are of benefit only when the test and actual hardware parameters (materials, stress levels, cleaning techniques, etc.) are similar. For example, it has been demonstrated that an exponential correlation exists between stress and useful lubricant life;⁵ therefore, linear extrapolations for projected bearing performance from bearing tests operated at reduced stress levels should be approached with caution. The bearing parameters evaluated in this test, however, were similar to the parameters that exist in certain HST bearings (recently processed with Vertrel XF diluted Brayco 815Z), with the exception that the HST bearings contained varying ball counts. The psi-crossing allowables generated in this test provided a means to calculate "ballpark" performance margins, with respect to lubricant polymerization, for these bearings.

From the results of this limited study, there is an indication of potential benefit obtained from the use of the HFE-7100 to process Brayco 815Z lubricated 440C bearings relative to the diluents Freon TF, or Vertrel XF. No attempt was made to determine the quantity or chemical nature of any possible impurities associated with the solvents tested. The construction of further bearing tests would consider the inclusion of a greater number of bearing pairs to increase the reliability of the test, and the use of different lots of HFE-7100. The use of HFE-7100DL (hard disk lubricant grade with low ionics, and less than 1 ppm nonvolatile residue) may be included to further investigate the role that impurity quantity may play.

Conclusion

The use of non-CFC solvents and diluents compare favorably with the traditional CFC-113 (Freon) solvent and diluent and in this test resulted in improved ball bearing performance. These results support previous findings for Vertrel XF, and indicate possible further benefits through the use of a hydrofluoroether diluent rather than Freon TF in the processing bearings.

Acknowledgements

The authors wish to thank Mr. Kent Roller for his expertise in the post-test inspection of the bearing surfaces, as well as Mr. Brad Scott and Mr. Harry Poehlmann for their comments in reviewing this paper. The authors also want to recognize the contributions of all the machinists and technicians who helped to put this test together and keep it running.

References

1. Mori, S., Morales, W., "Reaction of Perfluoroalkylpolyethers (PFPE) With 440C Stainless Steel in Vacuum Under Sliding Conditions at Room Temperature," NASA Technical Paper 2883, 1989
2. Carré, D, "The Performance of Perfluoropolyalkylether Oils Under Boundary Lubrication Conditions," Tribology Transactions, Volume 31, 4, pp. 437-441
3. Loewenthal, S.H., Jones, Jr., W.R., and Predmore, R.E., "Life of Pennzane and 815Z Lubricated Instrument Bearings Cleaned With Non-CFC Solvents," NASA Technical Note NASA/TM 1999-209392, September, 1999
4. Didziulis, S.V., Childs, J.L., and Carré, "Effects of Varying Ball Bearing Cleaning Processes on Lubricant Life," Aerospace Report Number ATR-98(2126)-1, The Aerospace Corporation, El Segundo, CA
5. Jones, Jr., W.R., Pepper, S.V., Jansen, M.J., Nguyen, Q.N., Kingsbury, E.P., Loewenthal, S.H., Predmore, R.E., "A New Apparatus to Evaluate Lubricants for Space Applications - The Spiral Orbit Tribometer (SOT)," NASA Technical Report Number NASA/TM 2000-209935, March, 2000
6. Phinney, D.D., Pollard, C.L., and Hinricks, J.T., "Experience with Duplex Bearings in Narrow Angle Oscillating Applications," 22nd Aerospace Mechanisms Symposium, NASA Langley, May 4-6, 1988

4/37

Improving the Robustness to Vibration and Temperature Effects for a Scanner Duplex Ball Bearing Assembly

Merritt Webb*, Thomas Brewer* & Benjamin Joffe*

Abstract

Precision mechanisms such as scanners require precise bearing preloads coupled with preload stability over temperature and vibration. The bearing retaining system is critical to achieving the required preload and maintaining it. A scanning motor bearing retaining system was recently redesigned to achieve bearing preload stability. A new retaining system design, coupled with material changes, resulted in a precise and tailorable design. When the motor was subjected to vibration and thermal variation, the modal properties did not shift indicating the bearing preload had not changed. This was a significant improvement over the previous design which often showed modal shifts of vibration of 25 Hz or more.

Introduction

The National Oceanic and Atmospheric Administration and the National Aeronautics and Space Administration have developed and operated a series of polar orbiting meteorological satellites since 1978. There were originally known as the Television Infrared Observation Satellites and are now known as Polar Orbiting Environmental Satellites (POES). The POES satellite operates in an 870 km circular near polar orbit. The orbit is sun synchronous. The primary imaging instrument on the POES is the Advanced Very High Resolution Radiometer (AVHRR).

The AVHRR is a six channel imaging radiometer. The six channels cover the spectrum from the visible and near infrared to 12 microns. The channels are co-registered to provide multispectral data. The instrument has an instantaneous field of view of 1.3 milliradians, providing a nominal spatial resolution of 1.1 km at nadir.

The first AVHRR, a /1 series, was launched in 1978. Improvements were implemented and the first /2 series was launched in 1981. Improvements to the scan motor were implemented to provide more torque and longer life resulting in the /3 series. The first /3 AVHRR was launched in 1995.

The AVHRR images are produced by a rotating scanner sweeping across the earth. The collected energy is focused on discrete co-registered detectors. The detectors are sampled, as a group, by an analog to digital converter at discrete time intervals. For an image to be assembled from this data, a very precise rotation rate is required of the scanner.

The AVHRR scanner uses an 80-pole hysteresis synchronous motor. The motor is a 2-phase motor driven by 240-Hz square waves in quadrature. The scanner is shown in Figure 1. This motor produces a rotational rate of 37.699 radians/second (360 RPM). The motor is inherently synchronized to the drive wave, producing very low jitter. The cardinal requirements for the scanner are listed in Table 1.

The two square waves in quadrature alternately energize the motor windings. The square wave drive signal is derived from a high precision clock, in order to provide a low jitter drive source. The motor rotor accelerates during start-up until it becomes synchronous with the rotating field. It then follows the field with a phase delay. This phase delay is referred to as the "slip angle". The slip angle will vary if the load varies.

In order to minimize the torque hash variations the motor uses MPB S1724 ball bearings (1.0625-inch bore) in a duplex pair. The bearings are Class 7T+, produced to an ITT-generated source control drawing.

* ITT Defense, Aerospace/Communications Division, Fort Wayne, Indiana.

The motor is driven open loop with 2 square waves in quadrature. This makes the drive electronics, simple, inexpensive and very reliable. The actual life, on-orbit of the AVHRR scanner has averaged 5 years. Failure of the spacecraft has been the most common cause for the end of scanner life.

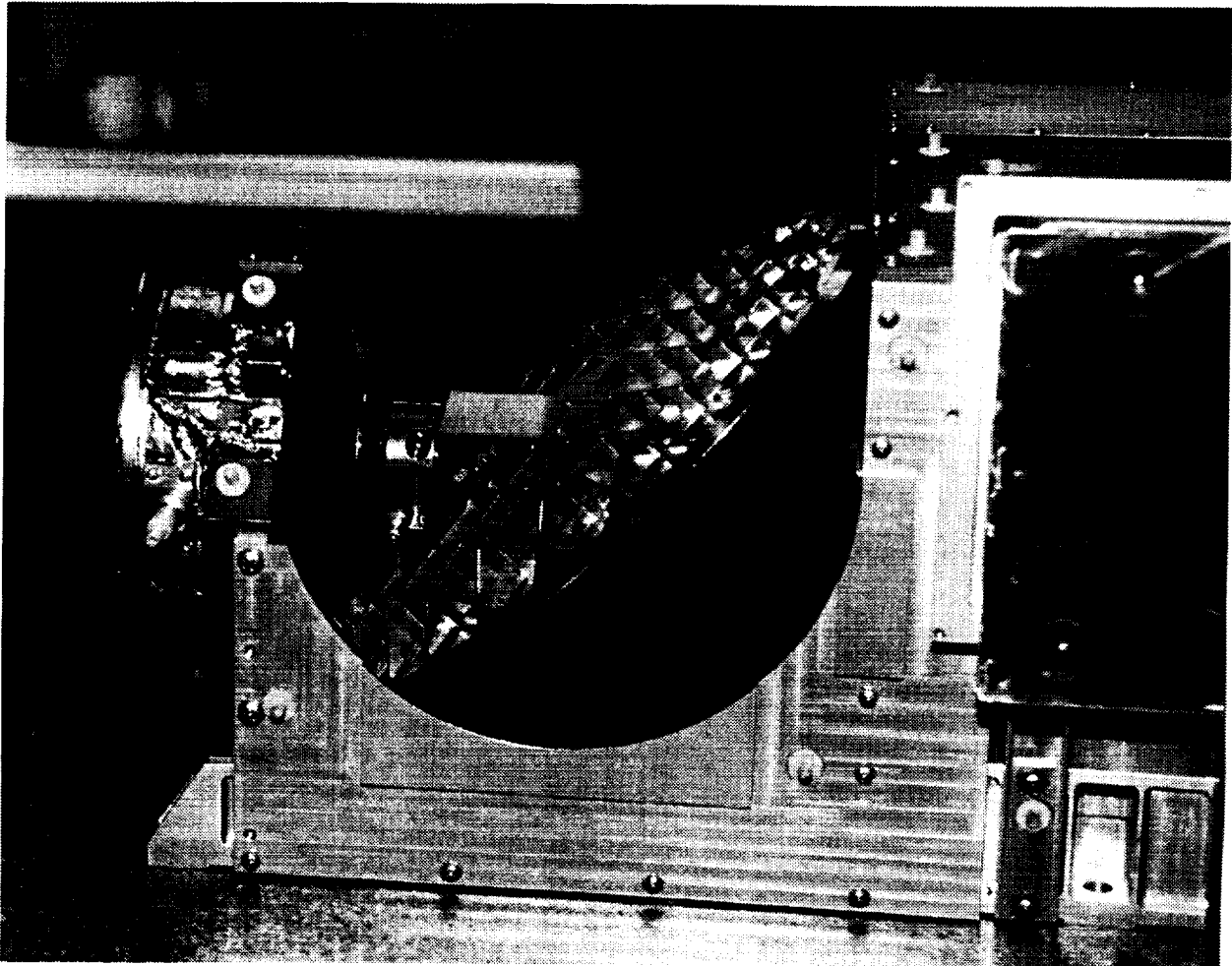


Figure 1. AVHRR Scanner

Table 1. AVHRR Scanner Cardinal Requirements

Requirement	Value	Comment
Free Body Torque, gross output torque delivered by motor without losing synchronism	> 0.508 N-m	When operated at a supply voltage of 20.5 to 24.5 volts
Maximum Allowable Power	7.5 W	Power measured at 0.565 N-m
Rotational Jitter	<34 microseconds	Peak-to-peak variation of rotational period for 98% of measurements over a 20 min period.
Synchronization Drift	< ±3 microseconds	Measured over a 24 hour period
Orbital Lifetime	3 years	
Natural Frequency	> 100 Hz	Requirement is for the complete instrument
Temperature	10 to 30 C	Operating temperature of Instrument, measured at the baseplate
Vibration	X axis: 11.44 GRMS Y axis: 19.40 GRMS Z axis: 8.12 GRMS	Titan II ELV levels

The relatively low torque output combined with the very severe drift and jitter requirements require very high precision bearings. The running torque and torque has characteristics of these bearings must remain consistent over time, temperature and vibration for the scanner to operate properly. The scanner is an open loop device. Thus, individual parameters must be carefully controlled. As a result of this, a great effort is made in the cleaning, lubrication, and setting of the preload and contact angle of the bearings and the installation of the bearings into the scanners.

Figure 2 shows a block diagram of the scanner. This is a simple but remarkably accurate model. This model is used to predict scanner performance, and has been verified by test results.

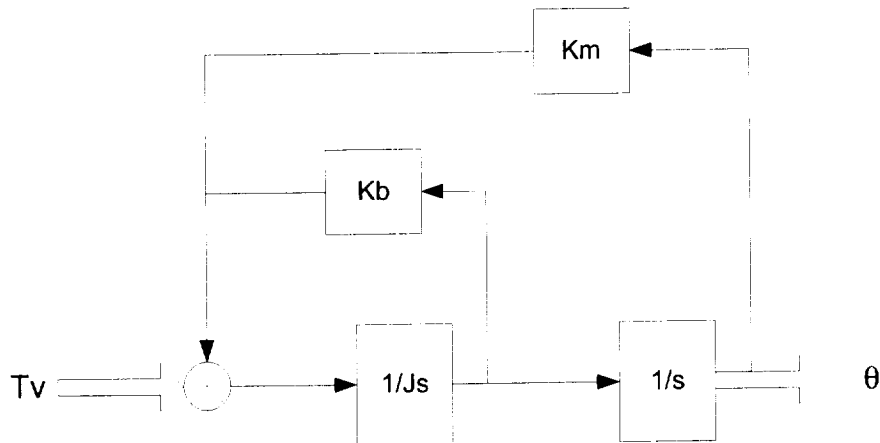


Figure 2. Block Diagram of Scanner

Based on "hunting" frequency measurements, taken on a scanner, the parameters shown in Figure 2 are defined in Table 2. The hunting frequency is the basic natural frequency at which the rotor oscillates relative to the rotating field.

Table 2. Scanner Motor Parameters

Parameter	Value	Units	Description
J	0.0067	kg*m ²	Scanner rotating inertia
Tv	N/A, input parameter	N-m	Torque variations from bearing torque hash*, load variations etc.
θ	N/A output parameter	radians	Slip angle variation between motor and rotating electric field in windings
Kb	0.0036	N-m-s/radians	System damping from friction magnetic hysteresis, etc.
Km	6.3251	N-m/radian	Electromagnetic "stiffness", essentially the restoring constant between the rotor and the rotating electric field

Based on measurements taken on A302 scanner

* Torque hash is defined as the non-repetitive torque variations that occur as a bearing rotates.

Utilizing the values shown in Table 2, a plot of the transfer function for the disturbance torque into the scanner versus frequency is shown in Figure 3. As can be seen, in Figure 3 the system is very lightly damped. In this the damping is approximately 1% of critical. Typical values range from 0.5% to 1.5%. This means that disturbances at low frequencies tend to greatly affect the jitter performance.

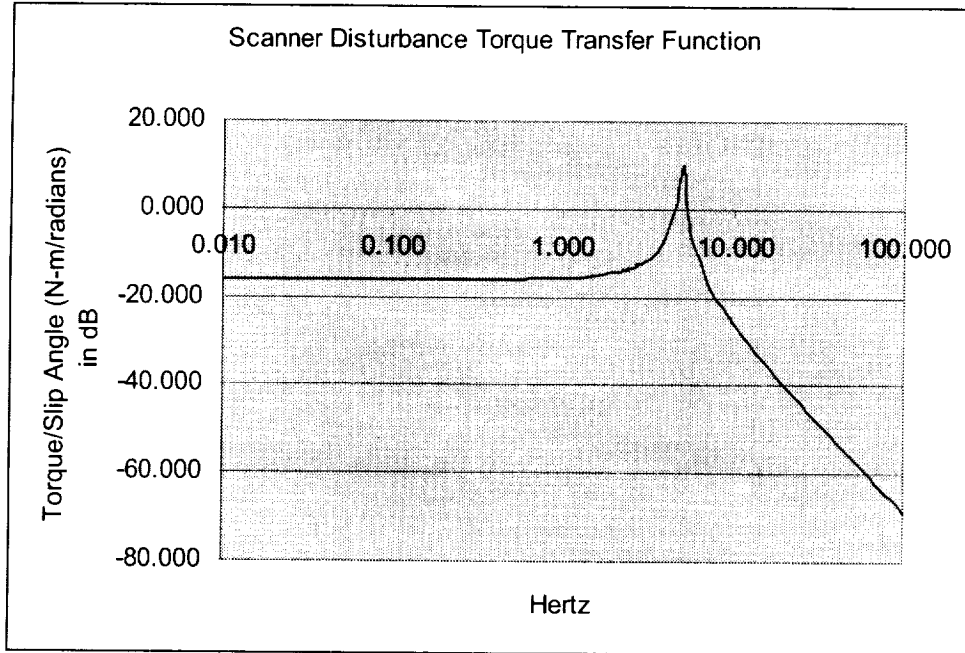


Figure 3. Scanner Disturbance Torque Transfer Function

Problem Statement

Despite the use of high precision bearing and careful assembly techniques with documented work instructions, variations in performance were noted. Scanner performance, in terms of jitter, was found to vary from bearing lot to bearing lot and even from assembly to assembly using the same sets of parts and the same assembly technician. An exploded view of the scanner is shown in Figure 4. A cross section of the scanner showing the bearing retaining system is shown in Figure 5.

Modal testing, on the assembled scanners, showed frequency shifts, as a result of scanner level vibration. The fundamental frequency would shift from approximately 275 Hertz prior to vibration to as low as 225 Hertz after the vibration. The loss of stiffness sometimes resulted in a condition known as "howling" based on the audible sound heard when the scanner was operated after a vibration. This change in modal frequency was indicative of a change of the loading on the bearing¹. The change in bearing loading resulted in a change in bearing running torque characteristics that affected jitter performance.

Given the stringent requirements for jitter, a change in the slip angle of 6.41×10^{-4} radians (0.04 degree) will result in 17 microseconds of jitter. Using the data from Table 2, this is equivalent to a torque variation of 4.05×10^{-3} N-m (0.57 oz-in) over a revolution. This torque calculation assumes no dynamic amplification, thus the actual allowable torque variation could be much less depending upon the frequency at which it occurs.

Analysis indicated that the vibration loads were resulting in the yielding of the bearing retaining system. As a result of this analysis, material changes were proposed in parts of the bearing retaining system. The bearing system part and the original and higher strength materials are shown in Table 3.

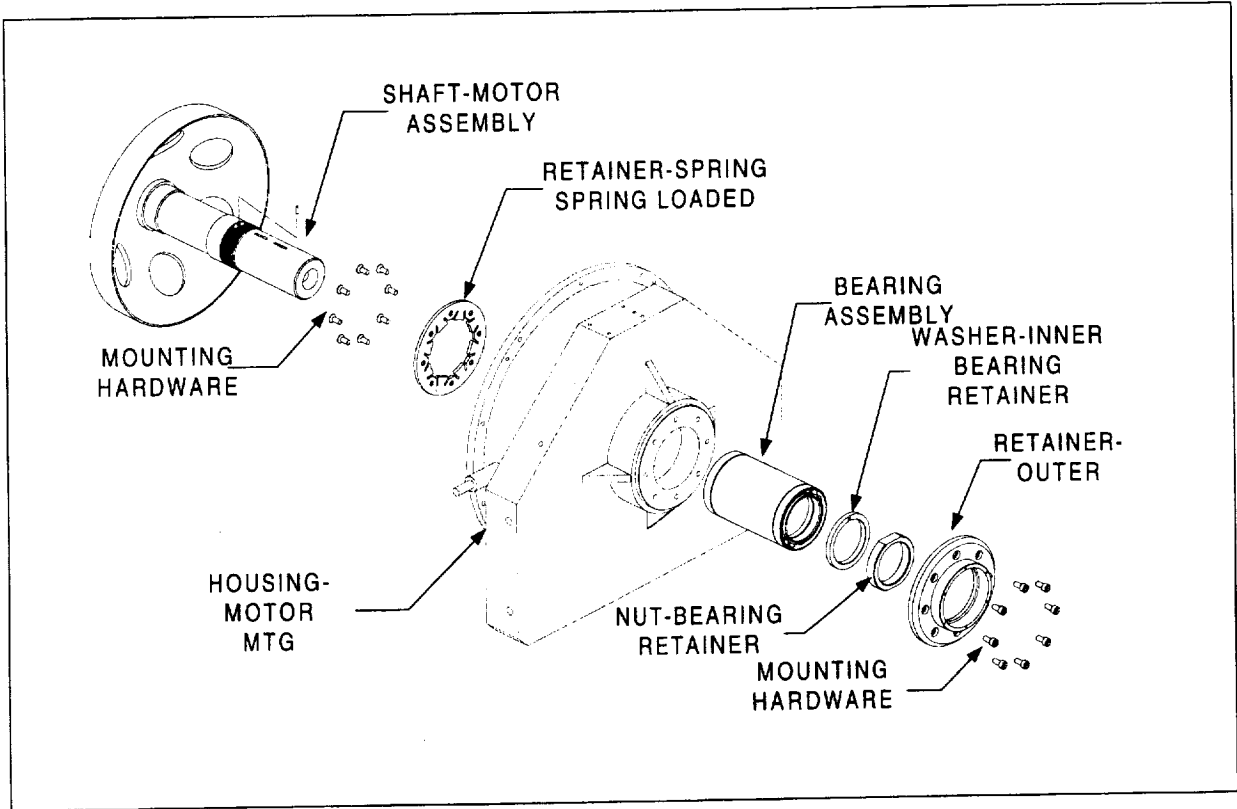


Figure 4. Exploded view of scanner Motor

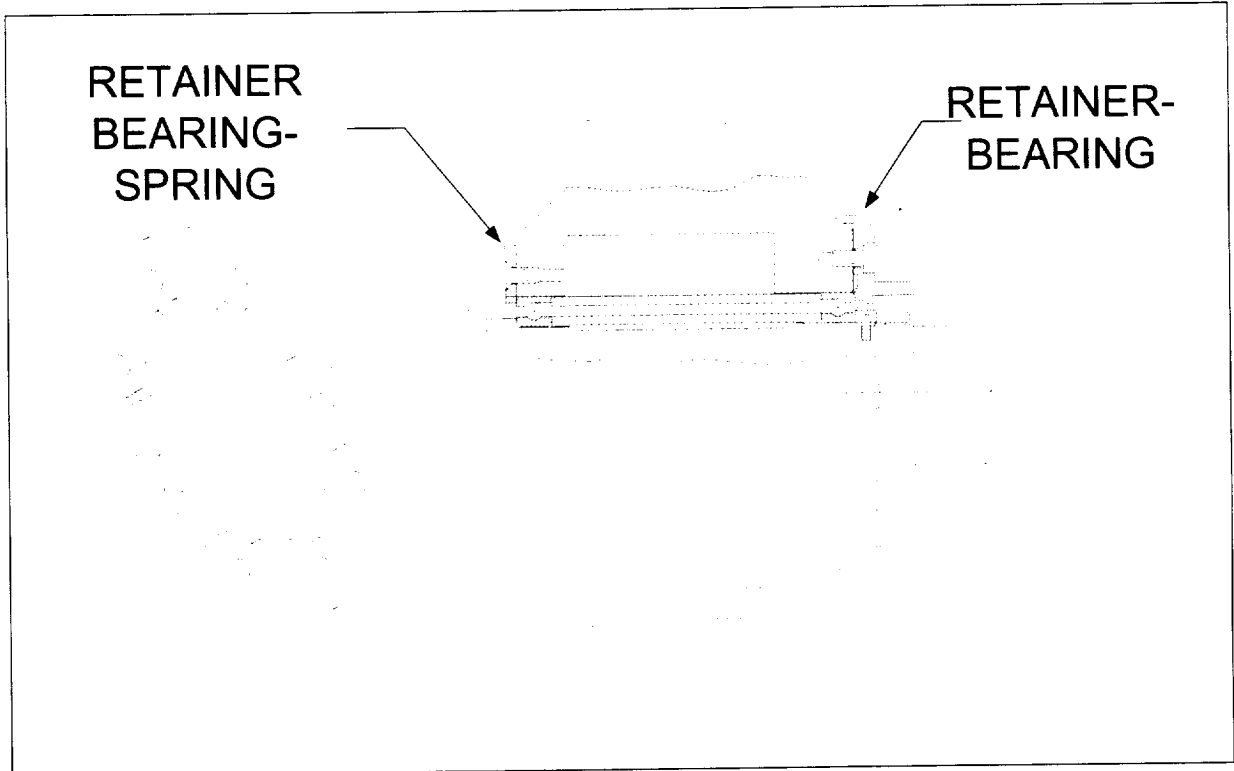


Figure 5. Scanner Cross Section, Rear Bearing Retainer, Spring Element & Bearing Retainer shown as Assembly

Table 3. Scanner Cross section Parts and Materials for Original and Higher Strength Designs

Item	Title	Old Material	New Material
1	Housing, Scanning Motor	Beryllium HP-20S-200	Beryllium HP-20S-200
2	Shaft Scan Motor	Inconel X-750	Inconel X-750
3	Outer Bearing Race	440C Steel	440C Steel
4	Inner Bearing Race	440C Steel	440C Steel
5	Outer Bearing Spacer	416 Steel	416 Steel
6	Inner Bearing Spacer	416 Steel	416 Steel
7	Washer, Inner Bearing	304 CRES	A286 Steel
8	Retainer-Spring	304 CRES	Custom 455 H1000
9	Retainer - Outer	6061-T6 Aluminum	7075-T7351 Aluminum
10	Nut, Bearing Retainer	304 CRES	A286 Steel
11	Screws-Spring Retainer	304 CRES	A286 Steel
12	Screws-Outer Retainer	304 CRES	A286 Steel

After the higher strength parts had been manufactured and installed into the scanner the scanner was retested. The material changes made the scanner much more robust with respect to vibration. There was very little change in natural frequency as a result of vibration. However, when tested over temperature, the jitter performance was found to vary greatly and in fact the scanner failed to meet the specification requirements at a temperature extreme.

Further analysis was performed and 2 root causes were discovered:

1. Tolerance stack-up and subtle assembly made the actual preload on the bearing very inconsistent on an assembly to assembly basis. The actual preload could vary beyond limits specified on the drawing as a result of these variations.
2. The coefficient of thermal expansion (CTE) mismatches resulted in a variation in bearing preload as the temperature changed.

The preload variations resulted in variations in bearing running torque and more significantly bearing torque hash over temperature. As can be seen from Figure 3, variations in torque will cause the slip angle and hence the rotational period to vary. This variation resulted in velocity jitter which, in this case, exceeded specification limits.

The analysis indicated that, for a bulk temperature change of as little as 10 degrees C, if the bearing is at the low end of the preload tolerance, the temperature change can result in zero preload.

Design Solution

A typical design solution for a high precision bearing mount such as this would be to add an element flexible element such as a wave washer. The wave washer or similar element would be much more flexible than the bearing spacers or rotor shaft. The purpose of this would be to allow for expansion and contraction due to bulk temperature changes while maintaining a constant preload on the bearing.

However, in this case the installation of an element such as a wave washer was not an option. The motor and bearings had already been purchased. The available axial space was not adequate for the installation of this type of element.

One of the other problems with the use of a wave washer or disk washer is their relatively low load capacity. During vibration, the AVHRR scanner bearing experiences loads approaching 1000 pounds. This is well beyond the load capacity of existing wave and disk washers, given the small amount of axial space available. Figure 6 illustrates a typical bearing installation utilizing a wave washer.

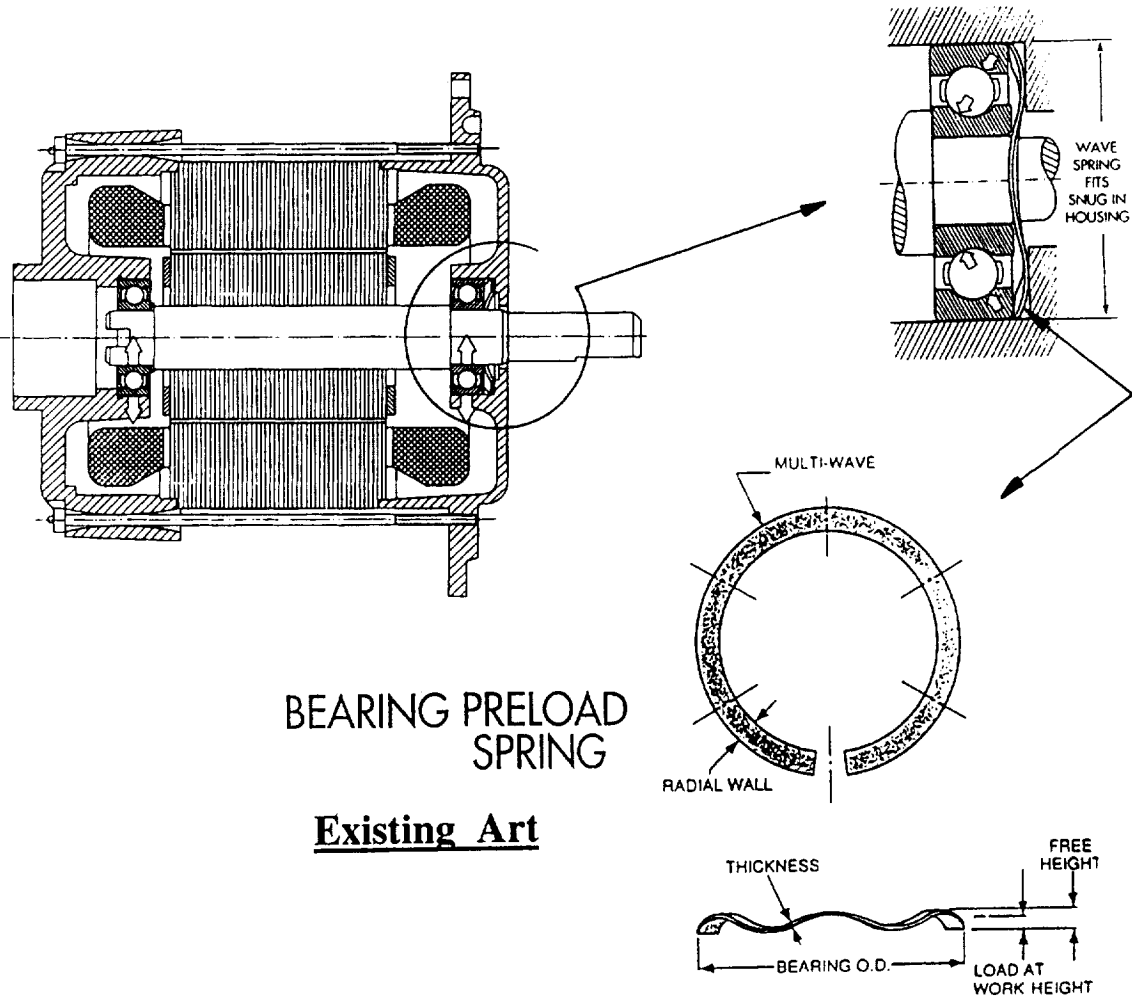


Figure 6. Typical Bearing Installation utilizing a Wave Washer

As shown in Figure 6, the duplex ball bearing mount device clamps the bearing axially. (Axially clamped is defined as applying a force along the axis of rotation to the races of the bearing). As the bearing is clamped the components of the retaining system will deflect.

As the bearing is clamped, the axial spring will deflect, applying a load to the race that is proportional to the deflection. Thus, variations in the deflection of the spring will result in variations in the load on the bearing. Thus, increased torque results in an increased load.

Disc springs, wave springs and finger disc springs from another manufacturer are also used, but the existing spring concepts design have a variation of load on the order of $\pm 25\%$. This is not acceptable for high precision mechanisms, which require stable performance, especially over a long period of time under severe environment condition, as required of space flight mechanisms.

If these springs were eliminated from the design in Figure 6 it would be impossible to clamp the bearing without changing the effective preload. The original design of bearing retainer for one of the ends of the AVHRR hysteresis scanner motor was a simple flat washer fastened to the motor housing with eight countersunk screws. This design produced spring rates in the shaft axial direction in excess of 875,000 N/mm. Thus there was little of the flexibility that is typically desired in a bearing retainer design.

A duplex bearing is preloaded by eliminating the "stick-out" present in the bearing³. The stick-out is produced by grinding the faces of the bearing rings during the manufacture of the bearing. The springs provide a relatively soft member to load the bearing and eliminate the stick-out.

Also, if the spring shown in Figure 6 were not present, the load applied, when the inner and outer retainers were clamped would result in deflection of other parts of the system such as the bearing races, any bearing spacers or the retainers themselves. If the resulting stress from this applied load were greater in the outer race than the inner race, the resulting strain would cause a change in the effective preload of the bearing. Thus, springs are used to provide a defined point of deflection in a bearing mount. Thus wave and disk washers are not effective for high precision applications, which are required to undergo severe vibrations.

Given these limitations and the requirement for large load capacity and a compact design, a different approach was developed. The basic idea behind the new design was to apply a controlled load (axial deflection) to the bearing while at the same time giving the bearing the ability to survive high vibration loads. The new design eliminates sensitivity to the torque applied on the retaining bolts of the bearing. The design challenge was to have a very compact design requiring little axial deflection while at the same time having a stiffness that was low relative to the rest of the system, and adequate strength with respect to yield.

The discussion of Figures 7 and 8 illustrate the bearing mount design that has been implemented and is also shown in Figure 4. Figure 7 shows the rear bearing retainer. This part is designed as a spring element.

Initial attempts were made to simply make the retaining washer thinner and to taper it. Effectively acting as a cantilever beam of decreasing thickness. These attempts could not reduce the spring rate to less than 350,000 N/mm. Subsequently, an idea was developed for a slotted retainer concept which enabled a much lower spring rate. Adjustments were then made to the design to reduce stress concentrations and to tailor the thickness to produce the desired spring rate.

Since the retainer possessed the type of symmetry known as cyclic symmetry, only a segment of the retainer needed to be modeled. Taking advantage of symmetry allows the use of a much higher level of detail for more accurate stress results while keeping overall model size small. Since there were eight fasteners equally spaced, there are eight "cycles" of symmetry. However, each of the eight cycles possessed bilateral symmetry which allowed further subdivision. The analysis model used a one-sixteenth segment of the whole (as can be seen in the Figure 7).

As appealing as a purely linear analysis would have been, the linear assumption breaks down badly for this part. The problem lies in the geometry of the part and the loading conditions. As in many mechanically fastened parts, this retainer is held against the surface of the motor housing (preload) by eight screws. Then, as the load is applied to the inner diameter of the retainer through the bearing spacer system, the retainer is pushed away from the motor housing. This creates a gap region in which there is no contact between the retainer and the motor housing. This gap is very small but it is nonetheless real and it changes the spring rate of the retainer. This change of spring rate is caused because the gap essentially makes a longer moment arm, which lowers the rate. The spring rate actually decreases for increasing load and deflection.

To analyze this condition it is necessary to model the contact surface. This was done by using contact surface analysis capability in PATRAN called Advanced Finite Element Analysis (AFEA). This program is an adaptation of the well proven ABAQUS finite element program. Because nonlinear solutions are very time consuming, the nonlinear solution was used to find the contact separation area and to learn how the nonlinear behavior affected the performance of the design. Then the contacting surface that was identified by the nonlinear analysis was constrained for a linear solution using the same loads. This essentially combined the best of both solution techniques by finding realistic boundary constraints through the nonlinear solution and applying those constraints in a much faster linear solution. This enabled many more design iterations than would have been possible with an exclusively nonlinear analysis.

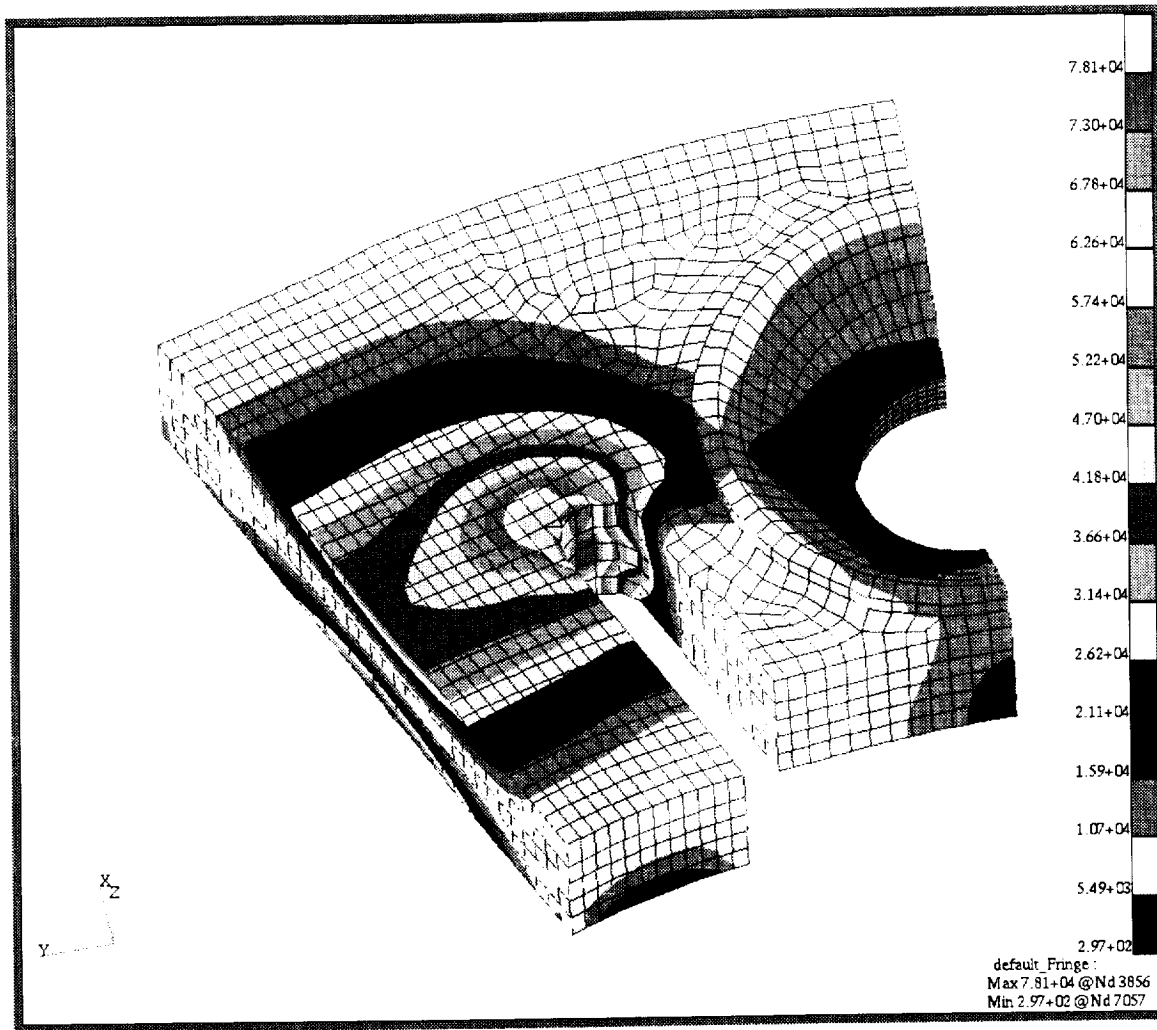


Figure 7. FEA Analysis of New Bearing Retainer

Compared to the alternatives such as wave washers and disc springs, this spring is just as compact while having a greater load capacity and a higher spring rate. Both of these features make this design capable of surviving high vibration loads, which would be well beyond the capability of the wave spring or disc springs. Table 4 presents an approximate summary of capabilities for a bearing used in the AVHRR scanner.

Table 4. Comparison of Spring Capabilities

Property	New Retainer Design	Wave Spring ²	Disc Spring
Working Load	1779 N	66.7 N	102.3 N
Working Height	1.91 mm	1.52 mm	0.51 mm
Spring Rate	70,050 N/mm	110.8 N/mm	179.7 N/mm

Numbers shown are approximate based on a 1 in OD bearing similar to what is used in the AVHRR scanner

The next aspect of the bearing mount design is shown in Figure 8. This is the ball bearing retainer. It applies the load to the outer race through the combined preload resulting from the torque on 4 bolts (a more uniform loading condition would be achieved by using 8 bolts or screws). This part is match machined to the "stick-out" of the specific bearing and housing used.

The basic approach is that as torque is applied to the retainer bolts, the rear retainer spring element deflects. This match machining is designed to provide a specific deflection in the spring shown in Figure 7. Once that deflection has been achieved the retainer seats against the housing and no further load is imparted to the bearing. This results in the force versus deflection curve seen in Figure 9 for the new design. This can be compared to the curve for the old design also shown in Figure 9. The reduction in variation provided by the new design is very apparent.

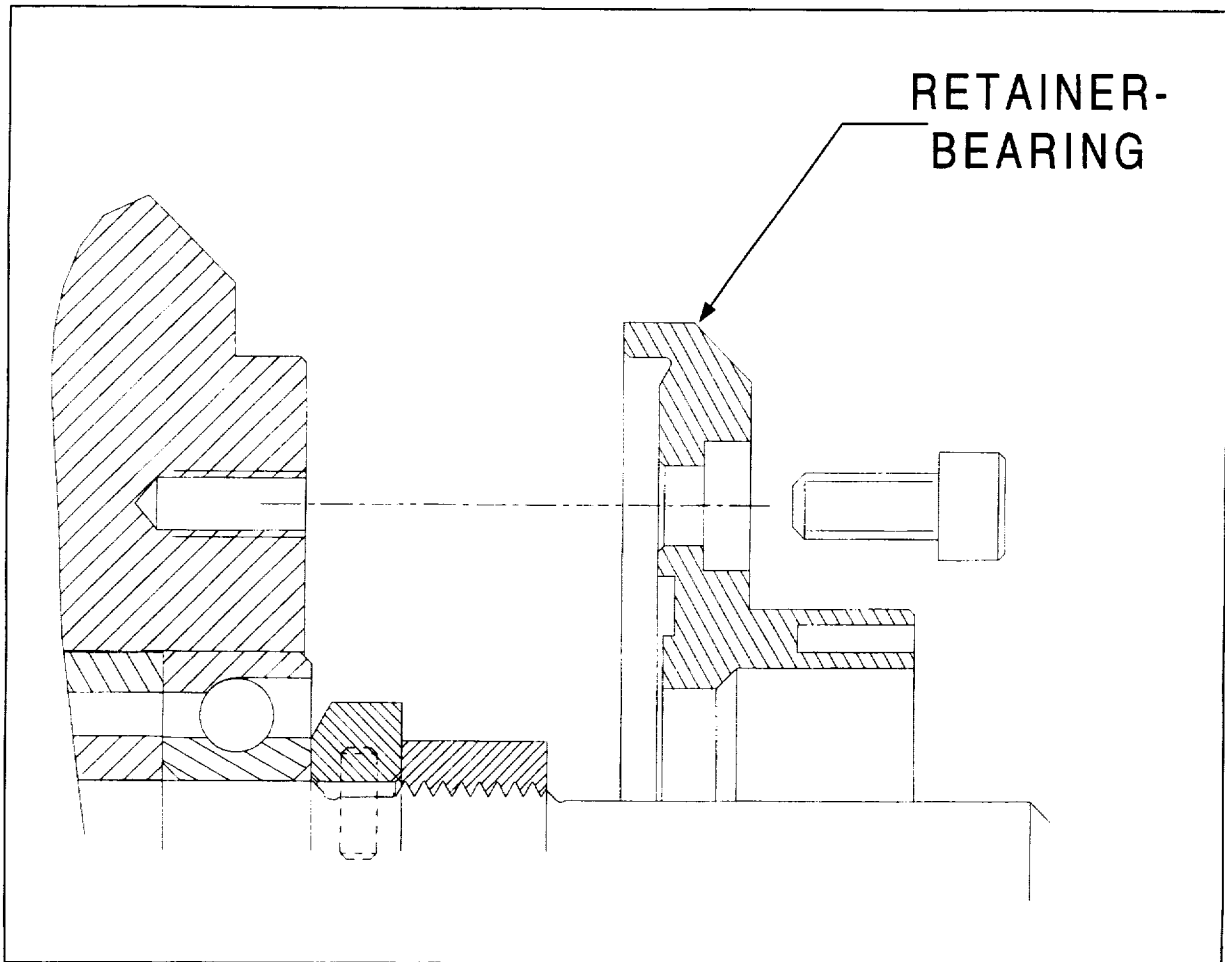


Figure 8. Ball Bearing Retainer

A cross section of the new design in the assembled condition is shown in Figure 5.

In the old design, the high stiffness of the rear retainer meant that other parts of the system would deflect. Thus the load on the bearing would be dependent upon the actual preload applied by the retaining bolts and the actual dimensions of the piece parts. The old design used shims to attempt to achieve a tailored fit (instead of match machining) however this allowed excessive variation given the high stiffness of the rear retainer.

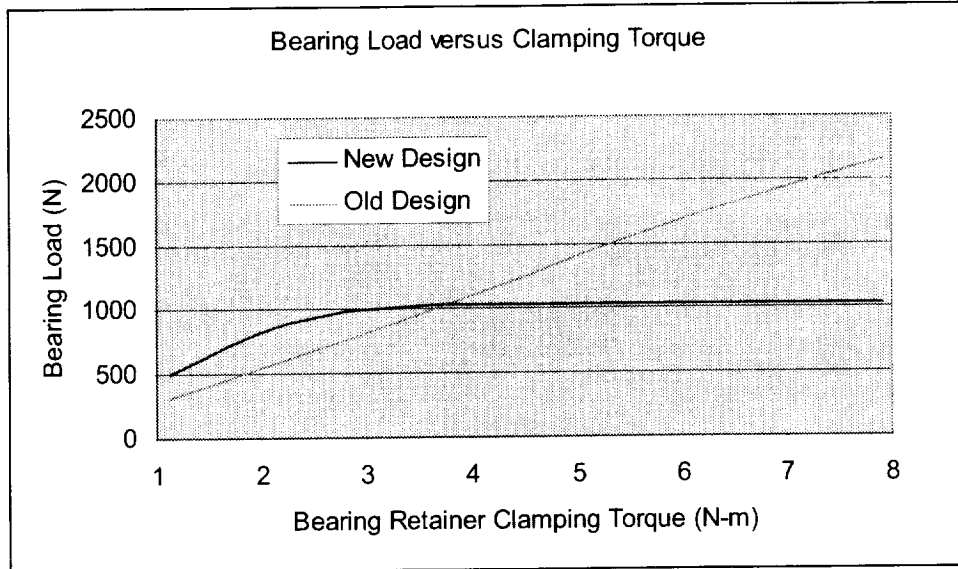


Figure 10. Bearing Load versus Clamping Torque Characteristics

The new design combined with match machining resulted in a consistent assembly, that was compact yet, flexible. The effectiveness of the new design has been proven by its successful implementation on the POES AVHRR scanner. Modal testing performed before and after vibration showed little changes in natural frequencies. Running torque data taken on the motor showed a consistent preload. A summary of the modal performance is shown in Table 5.

Table 5. Comparison of Modal Data New Design versus Old Design

	Old Design	New Design
First Mode prior to Vibe	290	270
First Mode after Vibe	240 - 220	270
Delta	50 - 70	0

Table Units are hertz

Measurement error of modes is estimated to be 5 Hz.

Numbers in Table are approximate, based on a number of "Old Design Builds."

Conclusion

When working with an existing design and attempting to trouble shoot or improve the existing design, improving one aspect can have unintended consequences, or indicate other short comings in the design.

A systematic systems engineering approach must be taken on any redesign effort to account for all the factors and requirements that affect the designs performance.

A very compact and flexible, yet strong, bearing retaining system was developed for the AVHRR scanner. The use of detailed finite element models and nonlinear analysis enabled the design to be successfully analyzed and implemented.

The new bearing mount design has the following features:

- The ability of the bearings to self align. Since the fingers shown in Figure 7 each support a section of the bearing they will independently adjust to provide the correct support. This provides repeatability of assembly.
- The high spring rate of the rear retainer (Figure 7) coupled with the solid mounting of the retainer (Figure 8) allows the assembly to survive high levels of vibration without a change in assembly position. As a result the design is able to achieve outstanding device performance.
- It provides a stable bearing preload over thermal variations

A patent on this approach has been applied for. The United States Patent and Trademark Office has issued Serial number 09/702,510 for the application filed on 31 October 2000.

References

1. Ball and Roller Bearings Theory, Design and Application, Johannes Brandlein, Paul Eschmann, Ludwig Hasbargen, Karl Weigand, John Wiley & Sons, New York, 1999, p. 311.
2. Smalley Steel Ring Company Catalog, Wheeling, Illinois, 60090.
3. Machine Design Theory and Practice, Arron D. Deutschman, Walter Michaels, Charles E. Wilson, Macmillian Publishing Company, New York, 1975, p. 454.

5/31

Retractable Trunnion Pin Mechanism

Wayne Jermstad* and Mark Landeck*

Abstract

The X-38 is a technology demonstration project for the proposed International Space Station Crew Return Vehicle. The project consists of several atmospheric flight vehicles and an unmanned spacecraft. This paper will discuss the design, development, and testing of a Retractable Trunnion Pin Mechanism used to mount the spacecraft in the payload bay of the space shuttle orbiter for launch.

Introduction

The X-38 Vehicle 201 is an unmanned spacecraft being developed in-house at NASA's Johnson Space Center (JSC) by a joint government/industry team. The V-201 spacecraft is launched in the payload bay of the space shuttle orbiter. Figure 1 shows the general arrangement of the V-201 spacecraft in the payload bay. The V-201 spacecraft is attached to the space shuttle orbiter at five points using 82.55-mm (3.25-in) diameter trunnion pins. Three trunnion pins are located on the De-orbit Propulsion Stage (DPS), which is attached to the rear of the V-201 spacecraft. Two trunnion pins attached to the orbiter longerons carry X and Z loads, and a keel pin carries Y loads. The remaining two trunnion pins are mounted to the forward bulkhead of the V-201 spacecraft and carry loads in the Z direction only. Because the nose of the V-201 spacecraft is quite narrow, an Airborne Support Equipment (ASE) cradle is used to provide a mounting point for the forward trunnion pins. The pins protrude from the V-201 spacecraft and are retained by Payload Retention Latch Assemblies (PRLAs). These pins must be retracted before re-entry of the V-201 spacecraft to provide the original outer mold line shape for aerodynamic purposes. A retractable trunnion pin mechanism has been developed to meet these requirements.

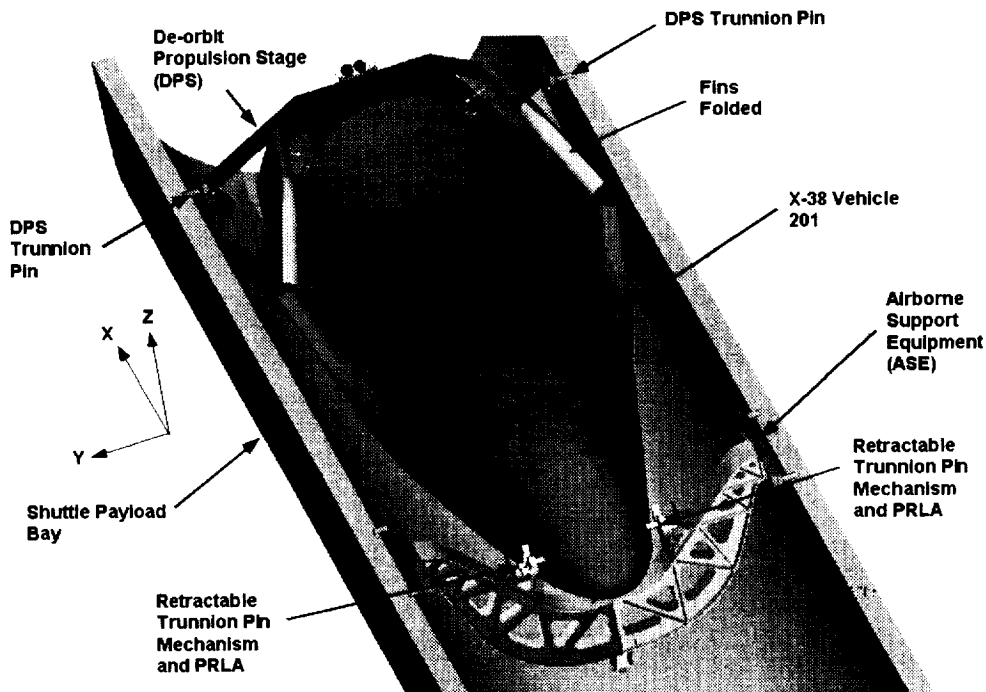


Figure 1. V-201 Spacecraft in Space Shuttle Orbiter Payload Bay

* NASA Johnson Space Center, Houston, TX

Background

The X-38 project is a demonstration of technology for the proposed International Space Station Crew Return Vehicle. The project consists of several atmospheric flight vehicles and an unmanned spacecraft. The design of the X-38 vehicles uses a lifting body shape originally developed by the U.S. Air Force X-23 (SV-5) and X-24A project in the mid-1960's. The X-38 spacecraft is launched by the space shuttle and deployed by the Remote Manipulator System. The DPS performs the de-orbit burn and is jettisoned prior to entry. The spacecraft enters the atmosphere as an unpowered glider like the space shuttle orbiter. When the spacecraft becomes subsonic, it deploys a large, steerable parafoil for its final descent to landing. The spacecraft landing gear utilizes skids rather than wheels.

Early on in the spacecraft design cycle the five-point attachment scheme described earlier was chosen. This configuration is nearly statically determinate, which simplifies loads calculations and reduces the interaction between the orbiter structure and the spacecraft structure. Once this basic layout was determined, the next big decision was whether to locate the forward pins on the spacecraft side or on the ASE cradle. Locating the pins on the ASE cradle simplified the spacecraft design and lowered the spacecraft weight, but made re-stowing the spacecraft in the payload bay very difficult. In order to carry the high launch and landing loads the pins would have had to go into tight tolerance holes on the spacecraft. Once the pins were pulled out of the spacecraft, re-inserting them would have been virtually impossible. Locating the pins on the spacecraft side greatly simplified the on-orbit operations. In addition, the already existing and proven PRLA could be used to retain the pins.

The original design concept used a trunnion pin that was jettisoned pyrotechnically. Packaging this concept was quite difficult. It quickly became apparent that the original pin interface location (on a cabin ring frame halfway down the length of the vehicle) did not have sufficient space or strength for the mechanism. A decision was made to move the trunnion pin interfaces to the cabin forward bulkhead where there was more space available. Moving the mechanism to the spacecraft nose also helped by reducing nose ballast.

Driving Requirements

The trunnion mechanism must be mechanically locked in both the extended and retracted positions. It must be able to carry an ultimate load of 200 kN (45,000 lbf). To accommodate vehicle deflections of ± 76.2 mm (± 3 in) the mechanism must have an extension distance of 355.6 mm (14 in). The mechanism must be able to function between -73°C (-100°F) and 66°C (150°F). The mechanism has a 3-mission life with a cycle life of 8 cycles.

Design Overview

The trunnion pin retraction mechanism is pneumatically actuated with nitrogen gas. The vehicle Attitude Control Subsystem provides the gas supply required for the mechanism to operate. A single N_2 line runs from tanks in the rear of the spacecraft and branches off to connect to the two retraction mechanisms. Having a single line synchronizes the two retraction mechanisms by supplying pressure to both simultaneously. The two retraction mechanisms are attached to the forward bulkhead of the V-201 crew cabin as shown in Figure 2. Each mechanism is attached using a combination of shear pins and bolts threaded into locking inserts. The trunnion pins protrude through the nose structure as shown in Figure 3. Once retracted, a Thermal Protection System cap on the end of the trunnion pin conforms to the original outer mold line shape of the vehicle (see Figure 4 and Figure 5). Each trunnion pin retraction mechanism is approximately 152 mm (6 in) in diameter and 965 mm (38 in) long in the extended position. Each mechanism weighs approximately 667 N (150 lbf).

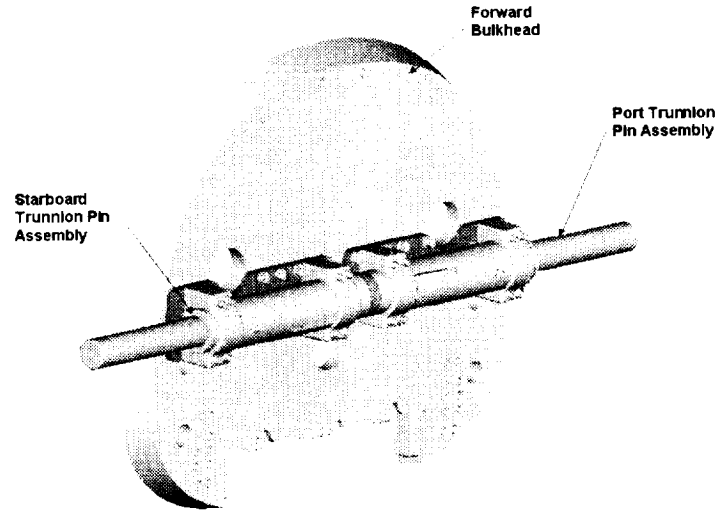


Figure 2. Trunnion Pin Mechanisms Extended

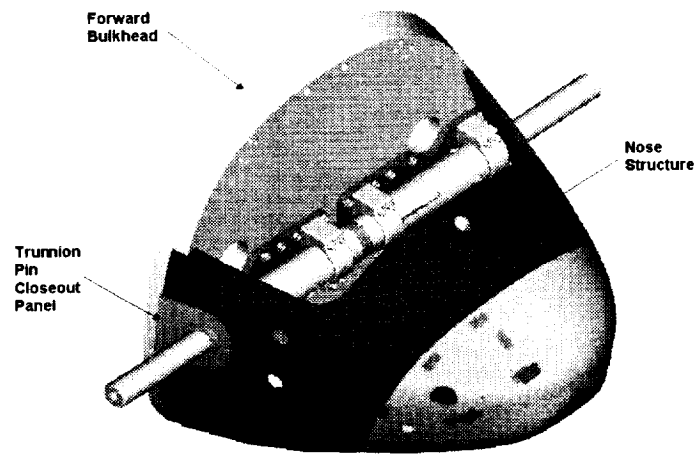


Figure 3. Trunnion Pins Extended Through Nose Structure

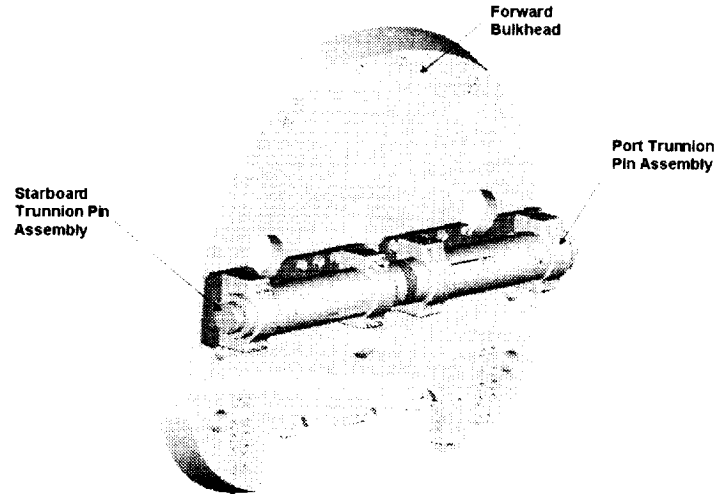


Figure 4. Trunnion Pin Mechanisms Retracted

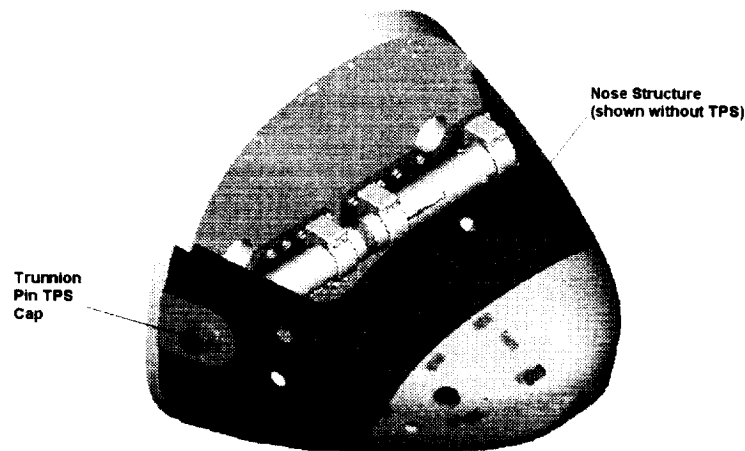


Figure 5. Trunnion Pins Retracted Through Nose Structure

The main parts of the retraction mechanism are shown in Figure 6. The housing is a hollow cylinder machined from Custom 455 stainless steel bar. The housing attaches to the base plate using the two mounts. The trunnion pin is cylindrical with a smooth bore throughout its length. It is made from Custom 455 stainless steel and is chrome plated with a surface finish of $0.2 \mu\text{m}$ ($8 \mu\text{in}$) to comply with shuttle payload requirements. The trunnion pin also has a notch (visible in Figure 6) used for latching the mechanism in the retracted position. An end cap bolts onto the housing and contains the silicone rubber bumper in a groove. A long rod screws into the end cap and fits inside the trunnion pin bore. On the other end of the rod is a stop. The piston slides on the rod. Three lock pins mechanically lock the trunnion pin and the housing together. All metallic parts, except for the trunnion pin and the housing, are made of 15-5 precipitation hardening stainless steel. The piston and the three lock pins have a titanium nitride coating for low friction and durability. Butyl rubber o-rings lubricated with vacuum grease are used extensively to prevent leakage.

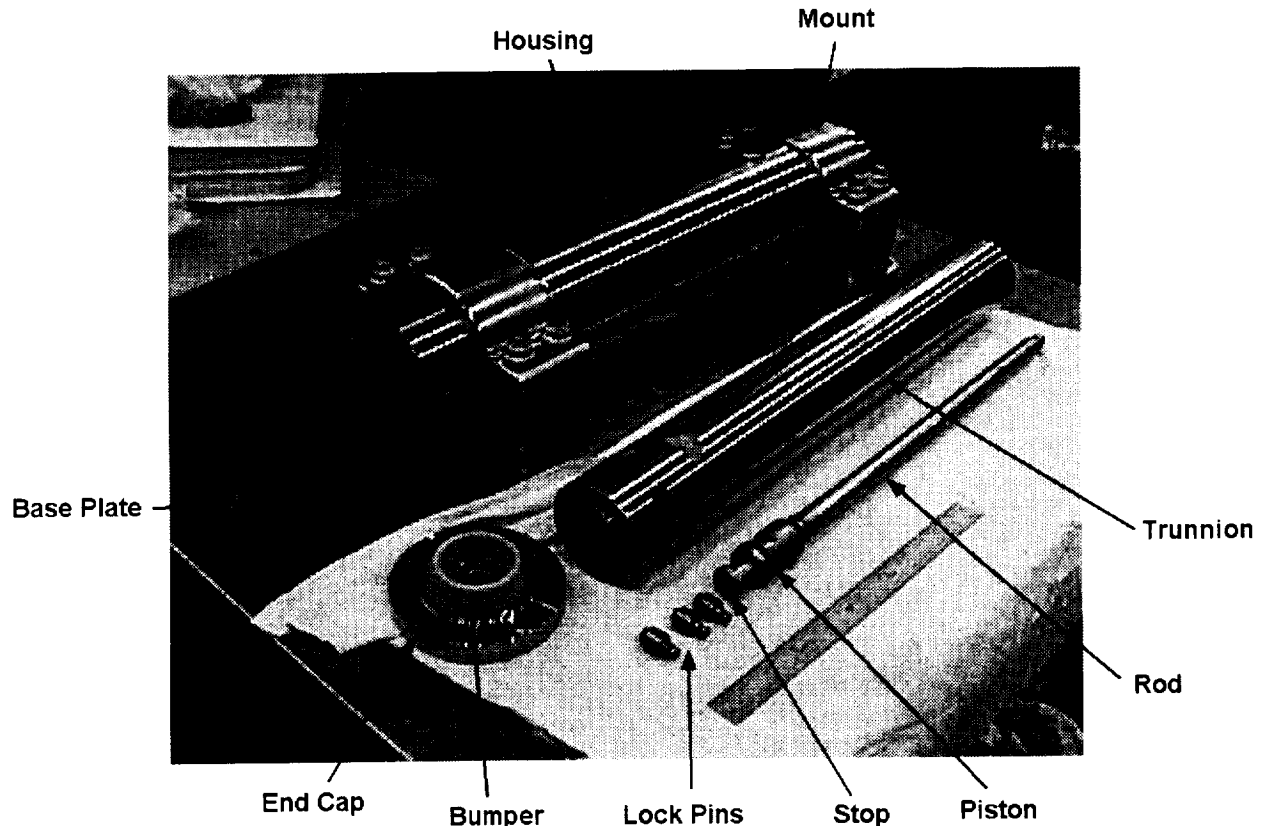


Figure 6. Trunnion Mechanism Parts

Mechanism Operation

During ascent in the payload bay of the space shuttle, the trunnion pin in each mechanism is mechanically locked in the extended position using three lock pins spaced 120° apart (see Figure 7). These lock pins are seated in lock pin receptacles located in the main housing of the assembly. The lock pins are held in position by a piston. The piston is kept in place with a spiral retaining ring and three spring plungers (see Figure 8). The three spring plungers are spaced 120° apart like the lock pins. The spring plungers can be adjusted to change the operating pressure of the mechanism.

Bending loads on the trunnion pin are reacted by the housing as a beam in a socket. The engagement length of the trunnion pin in the housing is about 200 mm (7.87 in). A generous radius on the corner of the housing prevents local stress concentrations at the trunnion pin to housing interface. Axial loads on the trunnion pin (which come only from friction at the pin to PRLA interface) are reacted by the three lock pins. Because of the angle of the lock pins and receptacles, axial loads on the trunnion pin generate an inward component of force, which is reacted by the lock pins bearing on the piston.

Once the V-201 spacecraft is deployed from the shuttle and the trunnion pins need to retract, nitrogen gas is supplied through the inner rod into the pressurized volume shown in Figure 8. When the pressure induced force on the piston overcomes the spring force of the spring plungers, the piston starts to move toward the stop. As soon as the piston clears the lock pins (see Figure 9), the lock pins move inward due to the inward component of force generated by the sloped surface on the lock pins and receptacles. The lock pins and receptacles have a generous 37.5° angle to avoid jamming. In addition small spring plungers in the lock pin receptacles assure inward movement of the lock pins. Once the lock pins clear the lock pin receptacles the trunnion pin can fully retract (see Figure 10).

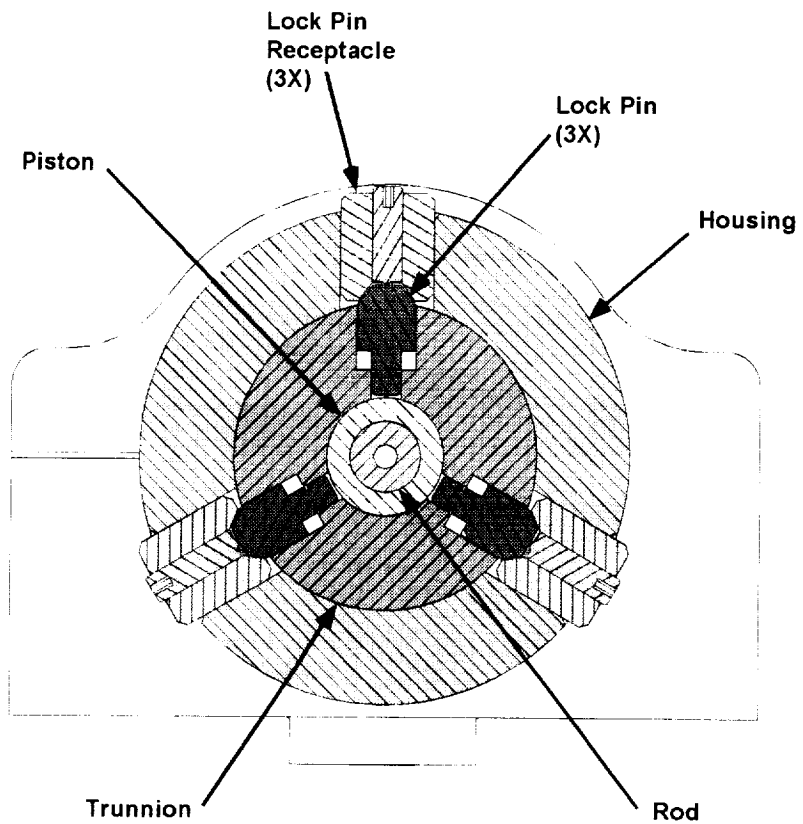


Figure 7. Cross Section of Mechanism Showing Lock Pins

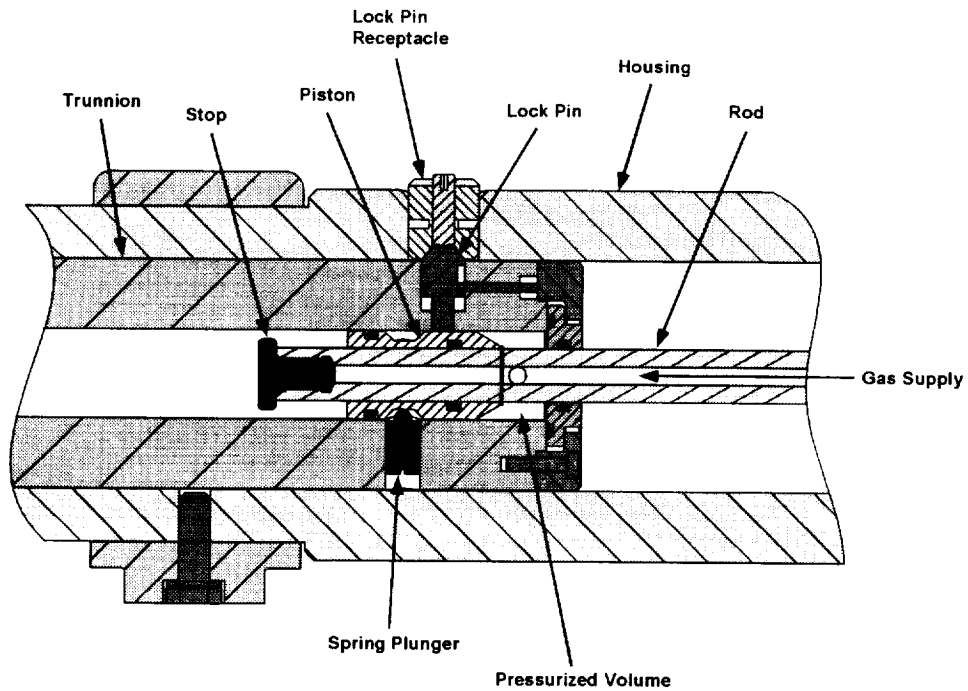


Figure 8. Cross Section of Mechanism in Locked Position

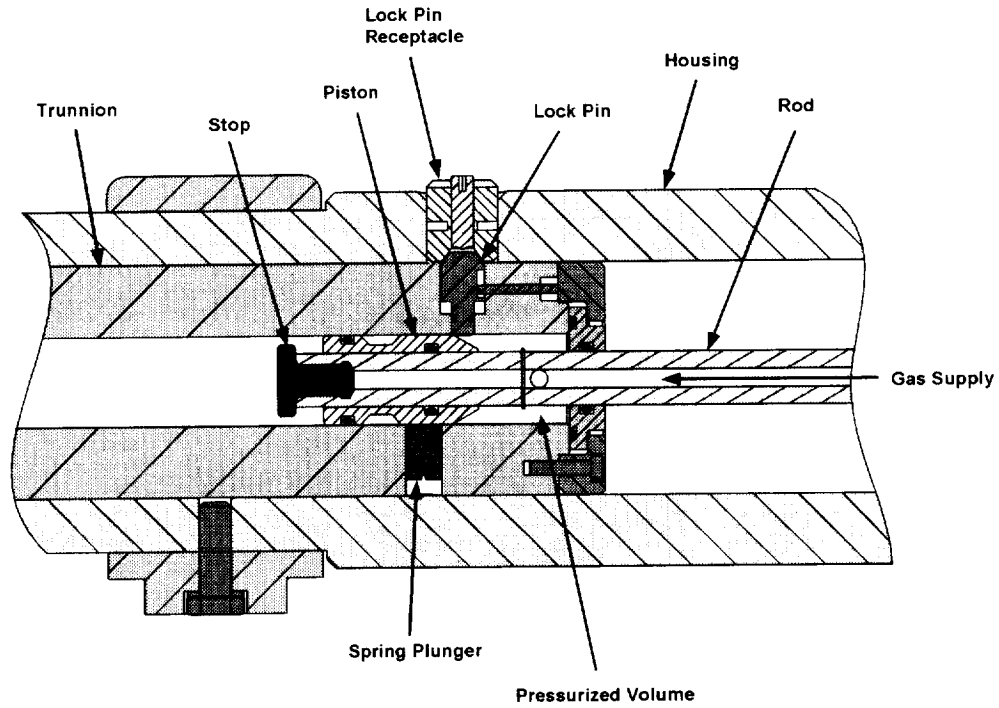


Figure 9. Cross Section of Mechanism as Piston Starts to Move

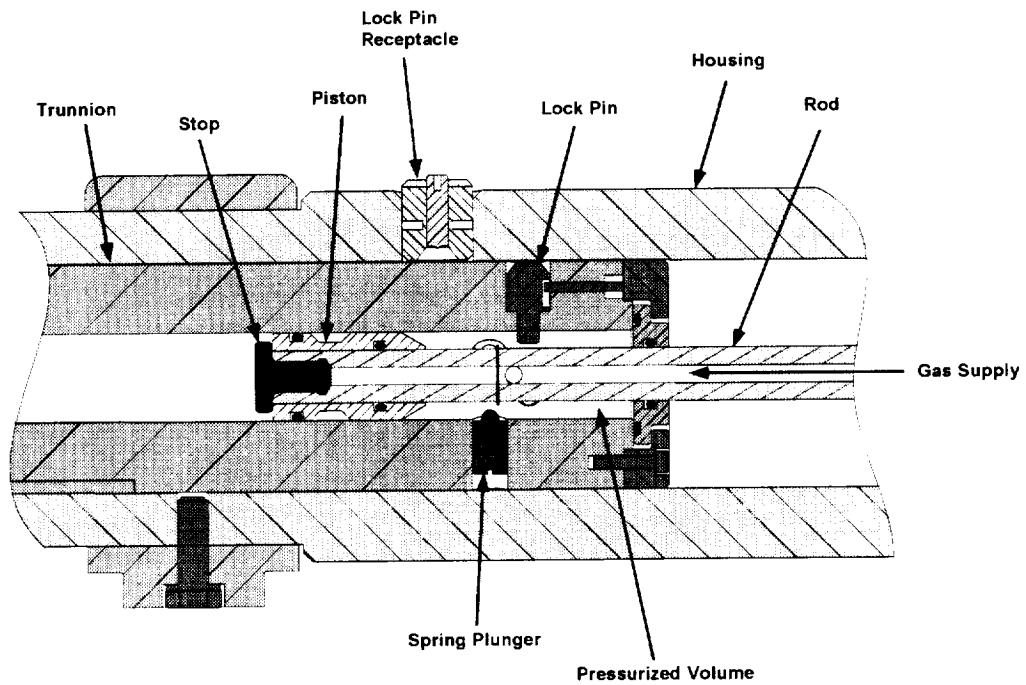


Figure 10. Cross Section of Mechanism Partially Retracted

To prevent rotation of the trunnion pin with respect to the housing, a slot is cut into the trunnion pin and a key is attached to the housing as shown in Figure 11.

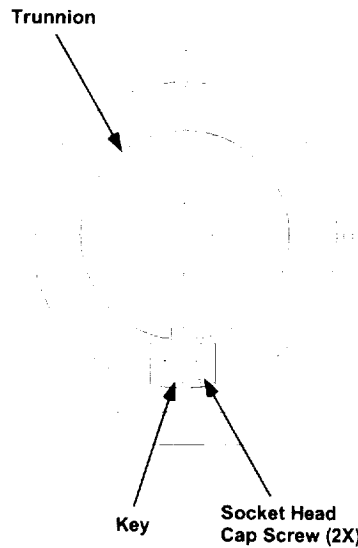


Figure 11. Cross Section Showing Key and Slot in Trunnion

The trunnion pin retracts rapidly (in less than one second). To absorb the energy of impact and to prevent rebounding, a silicone rubber bumper is used (see Figure 12). A notched groove in the trunnion pin and a cantilevered latch attached to the main housing are used to lock the trunnion pin in the retracted position (see Figure 12).

To unlock the trunnion pin mechanism for re-use, the key must first be removed from the trunnion pin slot. The trunnion pin is then manually rotated to lift the latch from the notch in the trunnion pin. The trunnion pin can then be fully extended and the key put back in place. A plunger is then used to push the piston back over the spring plungers into its locked position.

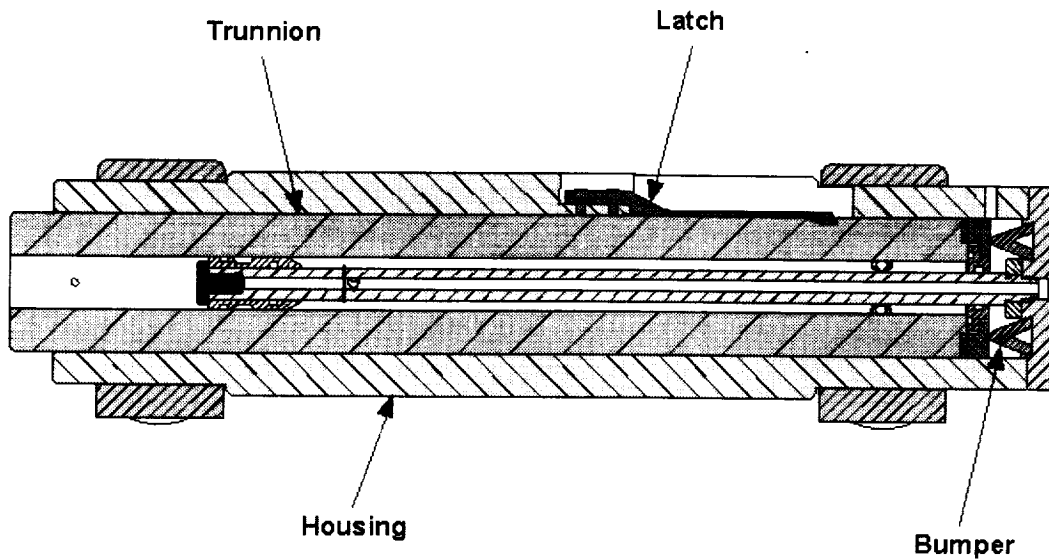


Figure 12. Cross Section of Mechanism Retracted and Locked

Testing

A dedicated qualification unit was built to perform developmental and qualification testing for the retraction mechanism. The developmental test program is complete. The qualification test program will take place during the spring and summer of 2001. The following paragraphs describe the testing that has already been performed, and the future testing planned for the mechanism.

Proof Pressure

Before functional testing could begin, a proof pressure test of the trunnion retraction mechanism to 1.5 times the maximum design pressure (MDP) was required by the JSC safety organization. The proof pressure test would also serve as a functional test since the mechanism was expected to retract at a pressure lower than the proof pressure. The initial proof pressure test revealed some defects in the mechanism. The mechanism was pressurized to 4.14 MPa (600 psi). The piston was heard to unlock, but the trunnion pin did not retract. The pressure was then reduced to a safe level of 517 kPa (75 psi). The trunnion pin was shaken by hand and it retracted. An audible leak was observed but the leak rate was not measured. A post-test examination of the mechanism drawings and tolerances showed that the leak was likely occurring around the three lock pins. The lock pins were subsequently modified to add an o-ring groove and o-ring.

A new proof pressure test was conducted after the additional o-ring was added to the three lock pins. This test was also used as a functional evaluation. The mechanism was again pressured to 4.14 MPa (600 psi). Once again the piston was heard to unlock. The trunnion pin appeared to move a small amount but it did not retract. This time there was no audible leak. The pressure was increased to the 5.17 MPa (750 psi) proof pressure and held for five minutes. After five minutes, leakage had reduced the pressure by 345 kPa (50 psi). The pressure was then reduced to 4.14 MPa (600 psi). The trunnion pin was shaken and it immediately retracted. A mechanical jam was now suspected.

After the test, the pin was disassembled. Small nicks were observed on the tips of the three lock pins and on the inside of the main housing. A subsequent examination of the drawings and tolerances showed that it was indeed possible for the tip of the lock pins to catch the edge of the lock pin receptacle hole on the housing if the lock pin receptacles were improperly adjusted. This explained why the trunnion pin moved a small amount and then stopped. The problem was solved by proper adjustment of the lock pin receptacles. The pin was re-assembled, this time tightening the receptacles until they came in contact with the trunnion pin. The receptacles were then unscrewed just enough to break contact. After this fix the mechanism retracted successfully. Most likely this adjustment problem, and not the leak, was the reason why the mechanism did not work in the original pressure test.

Function

A functional evaluation of the trunnion pin mechanism was performed with an initial pressure of 345 kPa (50 psi). The pressure was then raised to 4.14 MPa (600 psi) in increments of 345 kPa (50 psi). At each pressure the pin unlocked and retracted as designed. At high pressures the bumper came out of its groove due to the high impact energy. A design fix is in work to keep the bumper in its groove. After completion of this series of tests it was concluded that the new adjustment of the lock pin receptacles was correct. The procedure was documented in the mechanism rigging and repair manual.

Calibration

Adjusting the pre-load in the three spring plungers adjusts the mechanism operating pressure. A test was conducted to calibrate the three spring plungers. With the mechanism in the extended and locked position, the three spring plungers were adjusted to have the same pre-load. Pressure was slowly increased until the mechanism unlocked and retracted. This pressure was recorded. The mechanism was then disassembled so that the spring plungers could each be screwed in one-half turn. After re-assembly, pressure was again slowly increased until the pin unlocked and retracted. This procedure was repeated to determine the mechanism operating pressure as a function of spring plunger position. The same test was conducted using quick bursts of pressure with similar results.

Future testing

A complete qualification test program will be performed on the trunnion pin mechanism. The mechanism will be functioned in a thermal vacuum test at both the hot and cold temperature extremes. The mechanism will be static tested to 1.2 times limit load and then functioned. Qualification for Acceptance Vibration Testing and Qualification Vibration Testing will be performed, with functional tests of the mechanism after each. Life cycle testing will be performed on the qualification unit. After completion of life cycle testing the qualification unit will be static tested to ultimate load (1.5 times limit). The two flight units will be proof pressure tested, have a spring plunger calibration test, and be acceptance vibration tested in a vehicle level vibro-acoustic test.

Remaining Work

In addition to the completion of the qualification test program, some additional design work remains on the trunnion pin mechanism. Microswitches must be incorporated for both the extended and stowed positions. Redundant locking devices must be added for all threaded devices. This work will be done prior to the start of the qualification test program.

Conclusions

A retractable trunnion pin mechanism has been developed which can carry a high structural load in a locked extended position, then retract into a locked stowed position. Development testing indicates that the mechanism concept is sound. The mechanism can operate over a wide range of operating pressures. While there is more work to be done, so far the mechanism meets all its design requirements.

56/15

Design of the X-34 Speedbrake Mechanism Under Volume, Stiffness, Cost, and Schedule Constraints

William H. Kim*

Abstract

The X-34 Reusable Launch Vehicle (RLV) Technology Demonstrator has a split flap speedbrake mounted to an all-moving vertical tail for energy management during descent and for pitch trim during ascent. The speedbrake is deployed using a linear hydraulic actuator that drives a pair of torque tubes. The design of this speedbrake mechanism was constrained by the X-34 program goals of low cost and aggressive scheduling as well as limited volume for the speedbrake mechanism and a stiffness requirement to preclude aerodynamic flutter. The speedbrake mechanism has been designed, tested, and integrated on the first two X-34 flight vehicles. The mechanisms have been verified via fit checks, functional checkouts during flight simulations in the hangar, ground vibration testing, and runway tow testing. Upcoming unpowered approach and landing tests as well as powered flights will be the ultimate test of the mechanisms.

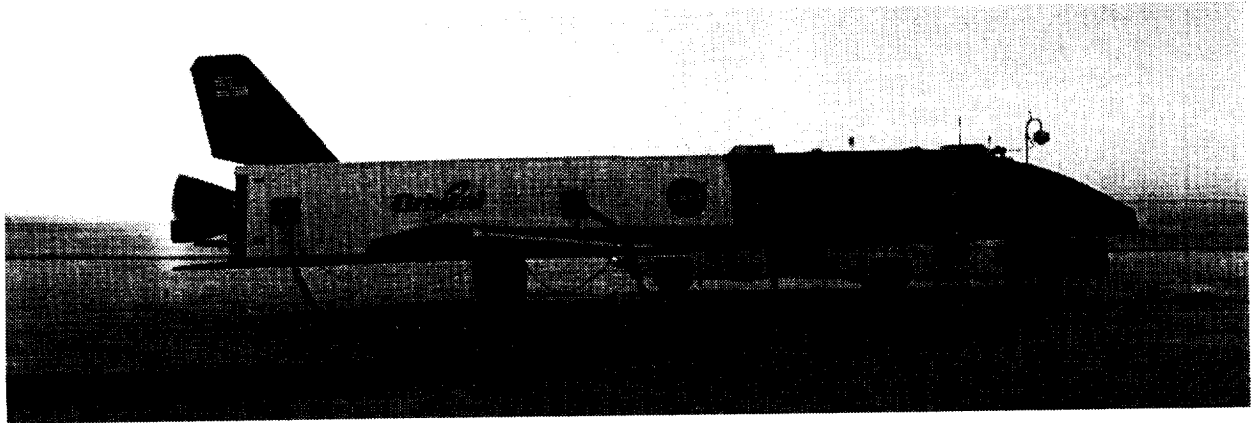


Figure 1. X-34 on Dryden Flight Research Center Lakebed Prior to Tow Testing

Introduction

The purpose of this paper is to provide an overview of the design of the X-34 speedbrake mechanism. How volume and stiffness constraints effected the design of mechanism will be discussed. In addition, how the cost and schedule constraints effected the execution of the design as well as the design itself will be discussed.

Background

The X-34 RLV Technology Demonstration program is a joint industry/government project to develop, test, and operate a small, fully-reusable vehicle with the objective of demonstrating technologies and operating concepts applicable to future RLV systems. Orbital is developing the unmanned X-34, shown in Figure 1, as an air-launched, liquid-fueled vehicle that draws heavily on Orbital's Pegasus and Taurus heritage and incorporates many RLV technologies including an all-composite primary airframe structure, composite RP-1 tank, SIRCA leading edge tiles, and autonomous flight control with safe abort capabilities. The X-34 is carried uprange by Orbital's L-1011 carrier aircraft and flies back to its base of operations at speeds of up to Mach 8 and altitudes of 76 km (250,000 feet). It lands horizontally on a conventional runway and is quickly readied for subsequent flights using aircraft-style ground operations.

* Orbital Sciences Corporation, Dulles, VA

Two complete airframes have been fabricated and assembled at Orbital's Dulles Integration and Test Facility. A third fuselage has been fabricated and is currently being assembled. System testing on the first airframe is underway with several captive carry flight tests on the L-1011 carrier aircraft completed and several runway tow tests at Dryden Flight Research Center completed as well. Unpowered approach and landing tests as well as powered flights will be performed upon completion of ground testing.

Requirements

The X-34 wing provides the required lift to change the vehicle flight path angle during the pull-up maneuver after separation from the carrier aircraft, and during the re-entry pull-up. The wing also provides cross range and maneuverability during the final approach and landing. Aerodynamic attitude control in pitch and roll is provided by elevons supported off the trailing edge of the wing. A fuselage mounted body flap also provides pitch control.

The all-moving vertical tail provides lateral stability and control for the X-34 during atmospheric flight. A split flap speedbrake mounted to the all-moving vertical tail provides drag which is used for energy management during descent [1]. The X-34 speedbrake mechanism is unique in that it is the first split flap speedbrake mounted to an all-moving vertical tail that is designed for transonic and hypersonic flight (up to Mach 8) and is actuated with a single linear hydraulic actuator. In addition to serving as a drag device, another unique feature of the speedbrake is that it is used as a pitch trim device both during ascent and descent. As shown in Figure 2, during the first 40 s of flight, elevon deflection, when the speedbrakes are opened to 75°, does not exceed -15°. If the speedbrakes are not opened (0° deflection), elevon deflection increases to -20°. Thus, the speedbrakes provide an additional 5° of elevon capability on ascent and keep the elevons well below the saturation level of -34° [2].

In contrast, the Shuttle speedbrake is a split flap mounted to a fixed vertical stabilizer and is actuated with multiple rotary actuators. The split flaps on Shuttle are used as speedbrakes between Mach 10 and 5. They are used as both a rudder and speedbrake below Mach 5 and are used for pitch trim only during descent [3].

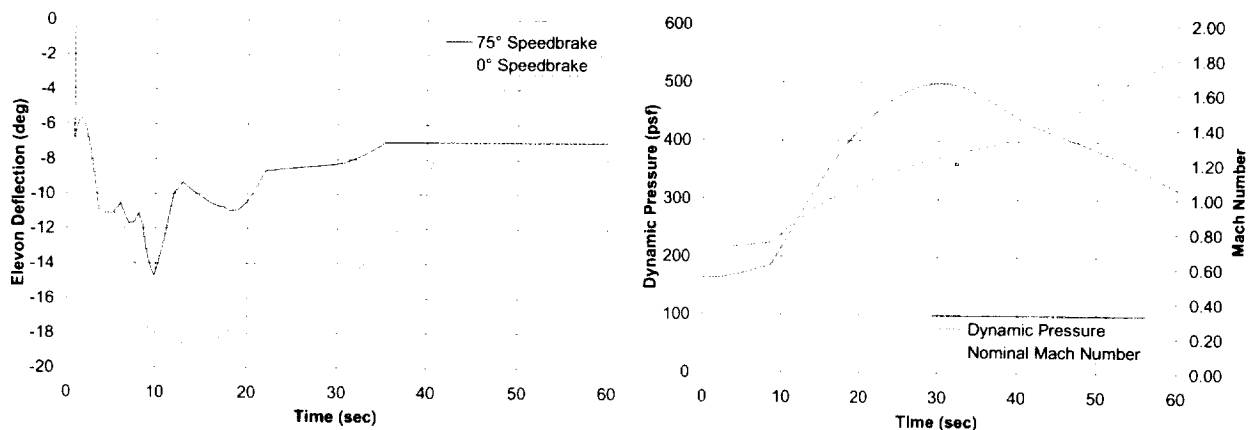


Figure 2. The Speedbrake is Used for Pitch Trim During Ascent to Offload Elevon Demand

The all-moving vertical tail consists of a rudder, rudder mechanism, two speedbrakes, and a speedbrake mechanism. The rudder is fabricated using graphite epoxy/aluminum honeycomb monocoque sandwich panel construction for the skins and ribs. The rudder mechanism consists of a steel torque shaft with two tapered roller bearings. The speedbrake panels are monocoque sandwich panel construction with graphite epoxy facesheets and aluminum honeycomb core. The speedbrake mechanism consists of several metallic components.

The driving load case for the speedbrakes occurs during ascent when the speedbrakes are deployed 75° to help pitch the nose of the vehicle up. As shown in Table 1, at Mach 1.25 and a dynamic pressure of

26.42 kPa (552 psf), 3,767 N-m (33,338 in-lb) of hinge moment is generated on each speedbrake panel. The resultant normal force on each panel is 17,263 N (3,881 lb). The resultant axial force on each panel is 5,698 N (1,281 lb). The resultant speedbrake actuator force is 54,388 N (12,227 lb) which corresponds to a 1,959 N-m (17,342 in-lb) moment on the torque tubes.

Table 1. Speedbrake Load Cases

	δ_{sb}	Mach	Q	HM	FN	FA
Ascent	75°	1.25	26.42 kPa (552 psf)	3,767 N-m (33,338 in-lb)	17,263 N (3,881 lb)	5,698 N (1,281 lb)
Entry	90°	6.60	15.61 kPa (326 psf)	1,417 N-m (12,543 in-lb)	6,494 N (1,460 lb)	2,144 N (482 lb)

The surface motion requirement for the speedbrakes is 0° to 90° and +/- 10° for the all-moving vertical tail. The slew rate requirement is 30°/s for the speedbrakes and 45°/s for the all-moving vertical tail. In addition to loads, the qualification temperature requirement for the composite speedbrake is 176°C (350°F). Thermal blankets and barriers are used to keep the composite structure below this limit. The speedbrakes are required to be interchangeable between airframes [4].

Constraints

The tail cross section geometry was constrained by the need to fit within the cavity in the fuselage of the L-1011 carrier aircraft. This cavity, which was originally designed to house the Pegasus vertical fin, was modified to accommodate the X-34 all-moving vertical tail and was kept as small as possible to minimize structural modifications to the aircraft. Because the tail is actually embedded within the fuselage of the carrier aircraft, the tail can potentially impact the carrier aircraft during the separation sequence. Extensive dynamic analyses were performed in order to verify adequate clearance between the tail and the cavity existed for safe separation. Figure 3 shows the path of the tail relative to the cavity in 0.10 s intervals after separation from the carrier aircraft. An area of the speedbrake was actually truncated at the intersection of the trailing edge and tip chord in order to increase the clearance margin between X-34 and the L-1011. The tail cross section geometry was also constrained by the desire to have as thin a tail as possible in order to minimize drag due to flow separation during transonic and supersonic flight of X-34. A tail cross section was selected ($t/c = 17\%$) that was large enough to accommodate the speedbrake mechanism but still fit within the L-1011 cavity.

A stiffness constraint is derived from the requirement that all control surfaces on X-34 be flutter free. This constraint drives the design of most of the speedbrake components. Cost and schedule constraints are derived from the overall X-34 program cost and schedule allocations set at the beginning of the program. These constraints drive the execution of the design in terms of the use of a small, highly efficient team, modular/common components, simplified assembly tooling, robust designs, and advanced design and analysis tools.

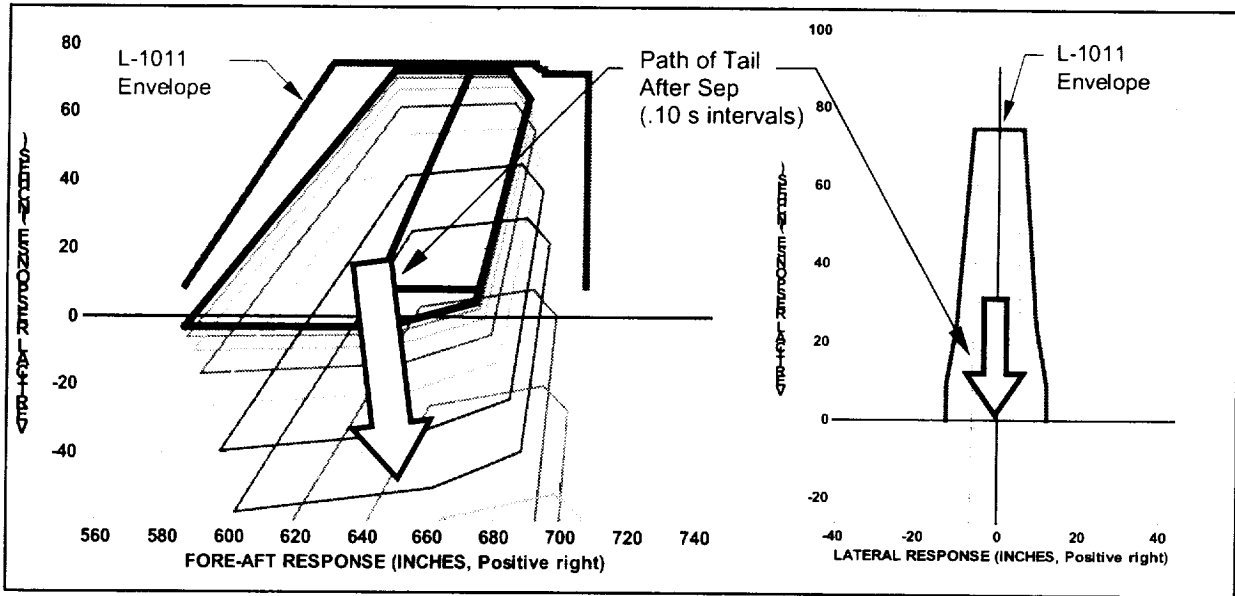


Figure 3. The All-Moving Vertical Tail was Constrained by the L-1011 Envelope

Volume Constraint

The design of the X-34 speedbrake mechanism demonstrated that it is possible to design a compact control surface deployment mechanism to fit into a small volume. The limited volume available for the mechanisms (defined by the trailing edge of the all-moving vertical tail and the inner mold lines of the two speedbrake panels) required that the mechanism be very compact. Figure 4 shows views of a partially integrated speedbrake mechanism in the open and closed position as well as a depiction of the available volume for the speedbrake mechanism.

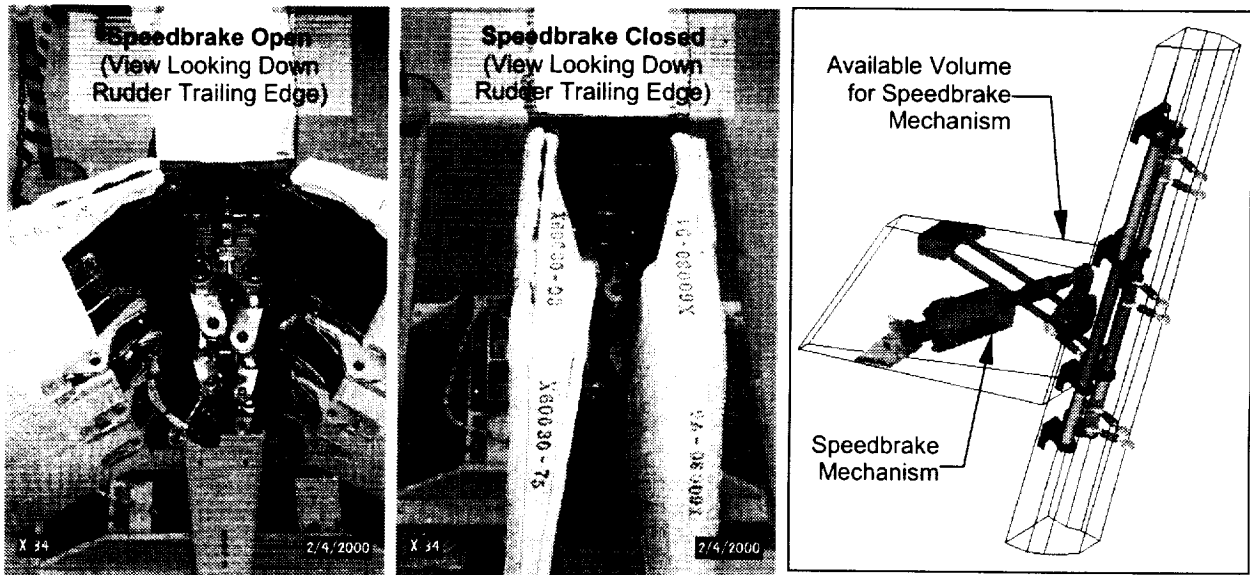


Figure 4. The Speedbrake Mechanism was Constrained by the Speedbrake Panels and Tail

The speedbrake mechanism consists of a speedbrake hydraulic actuator, speedbrake actuator clevis, crank arm, crank arm clevis, drive links, scissor links, torque tubes, pillowblocks, piano hinges,

smaller if the actuator was optimized for speedbrake requirements. The specifications of the control surface actuators are discussed further in the Cost and Schedule Constraints section of this paper.

The actuator's body diameter drove the spanwise location of the actuator in the all-moving vertical tail. The actuator was located as close to the tip chord of the rudder as possible while still maintaining clearance to the inner mold line (23.9 mm (0.943 in) skin-to-cylinder clearance). The use of graphite epoxy monocoque sandwich panel construction allowed for larger rib spacing than traditional metallic semi-monocoque skin-stringer construction since sandwich panel construction has a greater specific stiffness. The larger bay spacing (457 mm (18 in)) allowed for more room in the actuator bay for the hydraulic systems. The speedbrake actuator hydraulics are shown in Figure 7.

The speedbrake actuator is attached to a rib on the all-moving vertical tail with a stainless steel clevis and a stainless steel crank arm/clevis sub-assembly attached to the aft spar of the tail. While the design of the stainless steel fittings is conventional, the attachment of the fitting to the graphite epoxy structure required careful consideration. In order to transfer the actuator load into the rib, it was necessary to thicken the rib facesheets locally, add metallic thru-bushings to prevent bearing failure in the facesheets, and add a stainless steel backing plate to prevent fastener pull thru. Similarly, local doublers and a backing plate were added to the aft spar. A rudder brace assembly was also required to reduce loading into the skin-to-spar joints by transferring a portion of the load to the rib above the actuator via a pair of stainless steel struts. These reinforcements were made late in the design/analysis phase but were easily accommodated within the concurrent engineering environment. The ability of the concurrent engineering environment to handle these additions is discussed in the Cost and Schedule Constraints section of this paper.

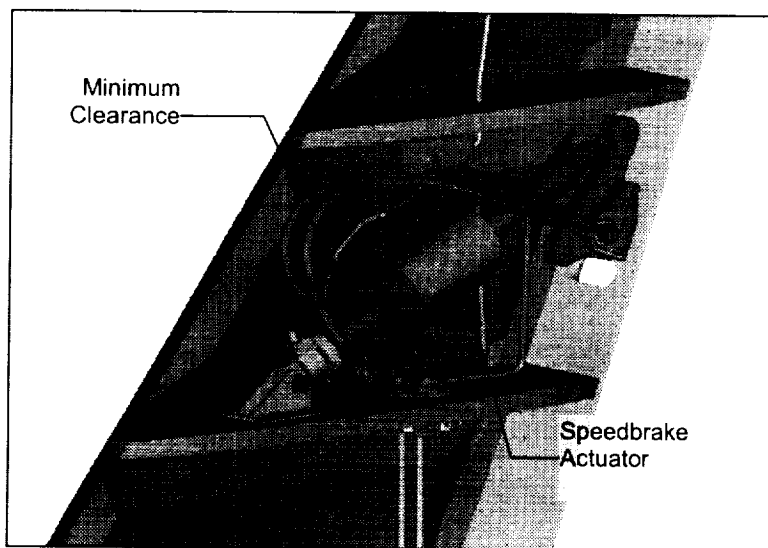


Figure 7. The Speedbrake Actuator was Located as Close to the Tip Chord of the Rudder as Possible

The crank arm/clevis sub-assembly is connected via two scissor links to the torque tubes. The scissor links have spherical bearings at each of their ends to adapt between the motion in the plane of the crank arm and the motion in the different planes of each torque tube. These 'narrow' profile bearings (P/N M81935/4-8) were not typically stocked by vendors and required lead times in excess of nine months. Vendors did stock 'wide' profile bearings (P/N M81935/1-8) but these bearings were less compact and had a lower load rating than the 'narrow' profile bearings. (Two shipsets of 'narrow' profile bearings were located after several weeks of searching.) The torque tube rotation axes are parallel to the hingeline rotation axes for simplicity. The hingeline axes are driven by the outer mold line (OML) of the all-moving vertical tail which is swept aft and tapers from root to tip chord. As a result of this sweep and taper, the torque tubes are not parallel to each other but 'toe-in' towards the tip chord. Because of this 'toe-in' and because the diameter of the torque tube was driven by stiffness concerns (discussed in the Stiffness

Constraint section of this paper) and because of the severe volume constraint on the mechanism, the output arms of the torque tubes are nested to prevent interference.

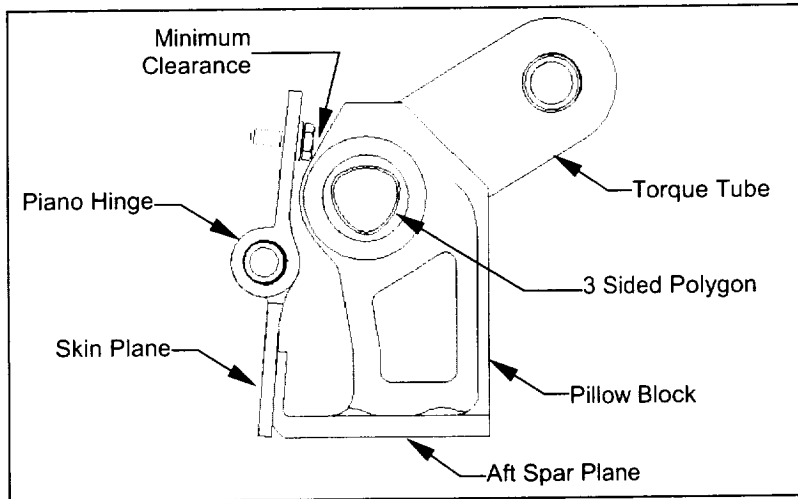


Figure 8. The Pillow Block Design was Constrained by the Piano Hinge

Each torque tube is made up of three stainless steel sections (total length = 1117 mm (44 in)). The need to minimize torque tube diameter for space reasons necessitated the use of a three-sided polygon section to connect the torque tube sections. The polygon section, shown in Figure 8, is more space efficient at torque transmission than a conventional spline. Breaking the torque tubes in three sections also allowed for a one-piece pillow block design as shown in Figure 9 because the individual segments of the torque tube could be fit into the pillow blocks and then assembled. A pillow block is located at each end of the torque tube and at the two joints in the torque tube. The stainless steel pillow blocks contain maintenance-free composite bushings. The minimum clearance between the pillow blocks and the piano hinge is .50 mm (0.02 in). Due to the limited footprint available on the aft spar to fasten the pillow blocks, it was necessary to fasten the pillow blocks to the piano hinge bolt pattern which is located on the skins. While it was undesirable to have one component fastened to two nearly orthogonal planes, this was the only way to fasten the pillow blocks adequately. The difficulties encountered while integrating the pillow blocks is discussed further in the Cost and Schedule Constraints section of this paper.

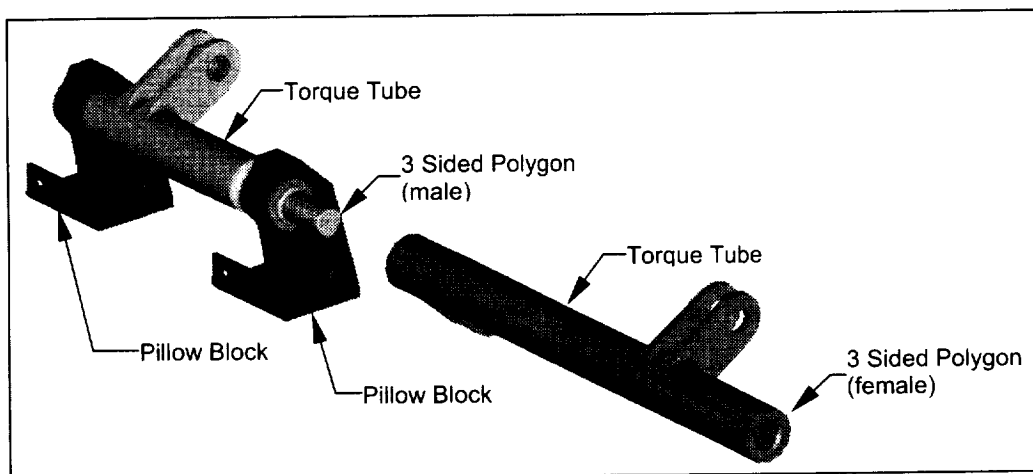


Figure 9. The Use of Multiple Torque Tube Sections Allowed for a One Piece Pillow Block Design

The output arms of the torque tubes are connected to the speedbrake clevises via drive links. The speedbrake clevises are attached to the speedbrake panels. Since the torque tube output arms are

nested, the corresponding speedbrake clevises are nested as well. These clevises employ a modular design which is discussed further in the Cost and Schedule Constraints section of this paper. This clevis underwent several design iterations in order to achieve a workable solution. In order to achieve adequate stiffness in the speedbrake panels, a honeycomb core thickness of 34.9 mm (1.375 in) was required. At that thickness, the last third of the trailing edge of the panels required tapering to fit within the OML. In order to maintain as much full height core on the remaining two-thirds of the panel, a 45° pandown angle was chosen to accommodate the speedbrake clevises as shown in Figure 10. This was the only location on any of the control surfaces that did not use the preferred 18° pandown angle. With the 45° pandown angle, the initial clevis design was unable to distribute the load into both facesheets. This problem was discovered in static load testing. Testing was halted until a new clevis could be designed, fabricated, and integrated. It was necessary to extend the clevis in the chordwise direction to account for the 45° pandown angle. This redesign/retest effort took three months.

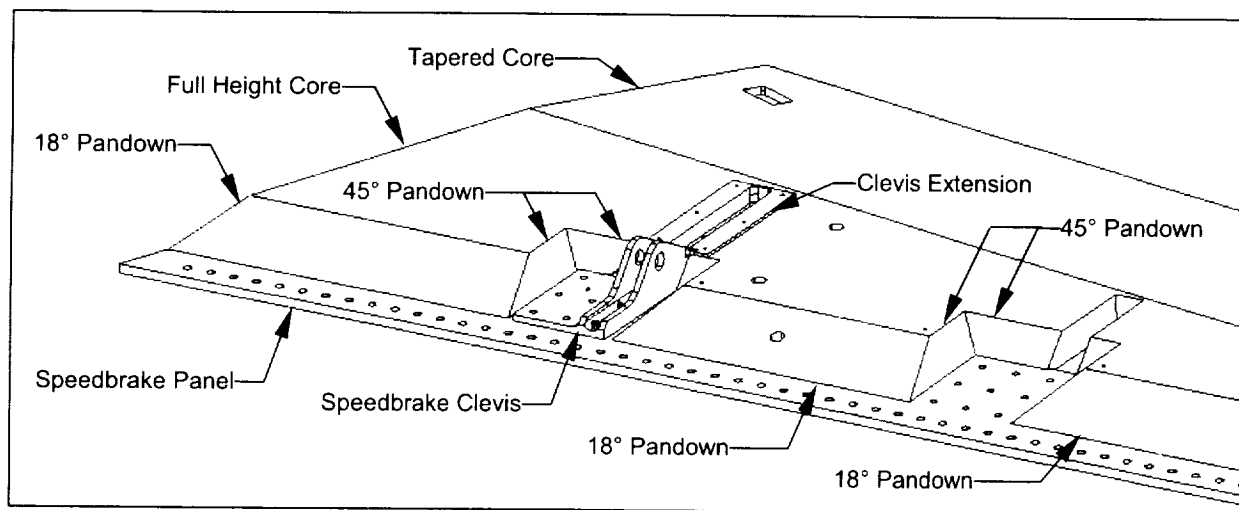


Figure 10. In Order to Achieve Adequate Stiffness, the Speedbrake Panels Required the Use of 45° Pandowns

The speedbrake panels are attached to the trailing edge of the all-moving vertical tail via the piano hinges. The piano hinge is comprised of modular titanium leaves and a stainless steel pin. The modular design of the piano hinge is discussed further in the Cost and Schedule Constraints section of this paper.

The speedbrake mechanism has been integrated with no interferences on two all-moving vertical tails for the first two X-34 flight vehicles. The mechanisms were static load tested at the system level during the all-moving vertical tail static load test by applying the flight hinge moment to the torque tubes and allowing the mechanism to react the load into the tail structure. Flight hinge moments were also applied to the individual speedbrake panels in separate static load tests. The mechanisms have been verified via fit checks, functional checkouts during flight simulations in the hangar, ground vibration testing, and runway tow testing at Dryden Flight Research Center.

Stiffness Constraint

The design of the X-34 speedbrake mechanism demonstrated that it is possible to design a compact control surface deployment mechanism with adequate stiffness to prevent aerodynamic flutter. It was recognized that aerodynamic flutter of the speedbrakes could occur if the stiffness of the deployment mechanism was below a certain value. After laying out the speedbrake mechanism using the available volume, preliminary hand calculations showed that the stiffness of the system was inadequate to prevent aerodynamic flutter. Further investigation revealed that although the speedbrake panels themselves were thin ($t/c = 6\%$) due to the severe volume constraints, they were not the primary contributor to the mechanism compliance since it was possible to make them stiff by constructing them with graphite epoxy facesheets over aluminum honeycomb core. The hydraulic oil column stiffness associated with the

actuator was a large contributor to the compliance, but it was not possible to alter its design because of the required commonality with the other control surface actuators.

Analysis showed that the next largest contributor to the compliance of the system after the oil column stiffness was the torque tubes. (The torque tubes initially accounted for 73% of the speedbrake mechanism stiffness.) Since the torque tubes were long and small in diameter, their rotational compliance relative to the other components was high. In order to reduce this undesirable compliance, the diameter of the torque tubes was increased from 25.4mm (1.00 in) to 38.1 mm (1.50 in). This increase in diameter reduced clearances between components (Figure 8) but decreased the compliance dramatically which increased the speedbrake mechanism stiffness by 58%. The design was finalized and given to Structural Dynamics Research Corporation (SDRC), the firm tasked to perform a detailed speedbrake flutter analysis.

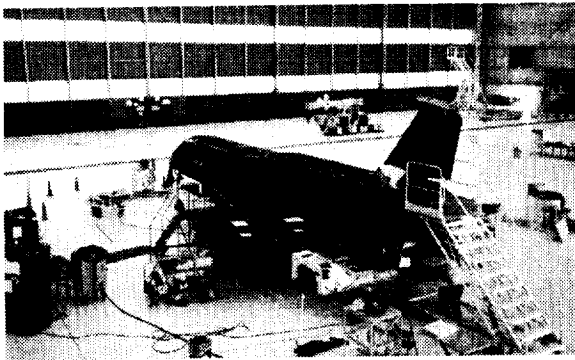


Figure 11. X-34 at Dryden Flight Research Center prior to Ground Vibration Testing, March 1999

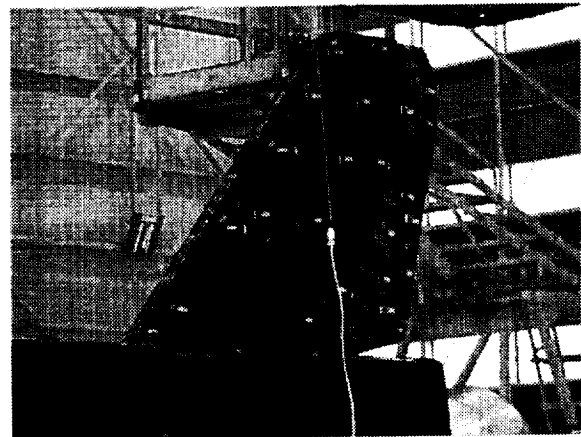


Figure 12. Rudder and Speedbrakes Instrumented with Accelerometers for Ground Vibration Testing

SDRC's initial modal analysis predicted a rigid body 'scissors mode' of the speedbrakes at 17.135 Hz. At that frequency, a potential flutter instability exists for the low supersonic portions of the flight envelope. This instability was found to be a single-degree-of-freedom (DOF) instability, not the classical bending/torsion coupling instability. Single DOF instabilities may result from asymmetric shock-boundary layer interactions. The instability could be eliminated by increasing the mechanism stiffness considerably (i.e.: increasing the torque tube diameter beyond 38.1mm (1.5 in)). However, the stiffness increase required was not feasible given the volume and mass constraints on the mechanism [5]. A modification to the control system involving active damping using pressure feedback was developed in order to deal with this problem.

SDRC's initial flutter analysis also revealed that aerodynamic loading increased the stiffness of the system. This loading occurs when the speedbrakes are deployed into the airstream [5] but not when the speedbrakes are closed. It was decided to preload the speedbrakes in the closed position by 'pinching' the trailing edge of the speedbrakes together. A set of elastomer pads was installed in three locations along the span of the speedbrake to provide a bearing surface, and the actuator is used to provide the preload force.

A Ground Vibration Test (GVT) was performed on the flight hardware at Dryden Flight Research Center (Figures 11 and 12). Data from that test were used to calibrate and confirm SDRC's analyses. The rigid body 'scissors mode', found at 37 Hz during GVT, was higher than the initial 17 Hz prediction (Figure 13). The initial modal analysis was refined by correcting modeling discrepancies and was able to predict the mode at 37 Hz. These data are summarized in Figure 14 [6]. With the mode at 37 Hz, the control system active damping modification actually decreased stability, and so, it was removed after GVT.

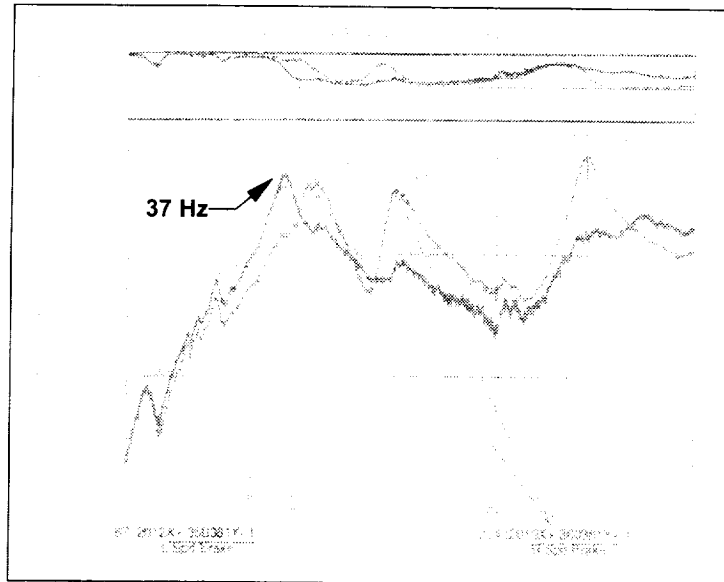


Figure 13. GVT Revealed That the Speedbrake Scissors Mode Was Higher Than Initially Predicted

The flutter analysis was rerun using the correlated model. A potential flutter instability still existed in the low supersonic portions of the flight envelope. It should be noted that the flutter analysis assumes it is analyzing single surface that is subjected to small disturbances. The speedbrakes are actually two surfaces that are both subjected to large disturbances ($\delta_{sb} = 60^\circ$). The analysis is extrapolating its results and may not be completely accurate. A wind tunnel flutter test may be required in order to verify that the instability does exist. Actual flight testing in the transonic regime where the system is most susceptible to flutter will be the ultimate test of the design.

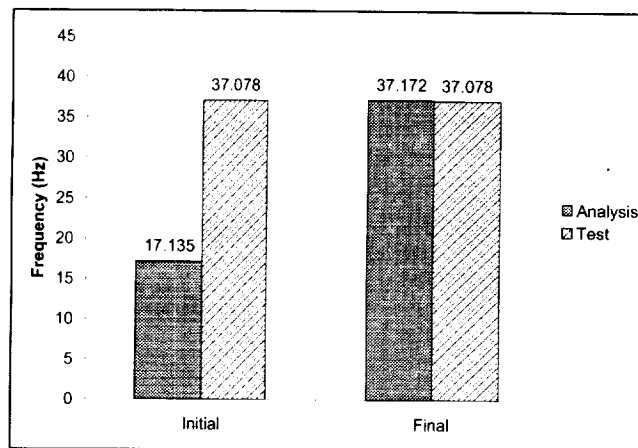


Figure 14. After Correcting Modeling Discrepancies, Predicted Frequencies Matched Test Results

Cost and Schedule Constraints

The design of the X-34 speedbrake mechanism demonstrated that it is possible to design a compact control surface deployment mechanism with adequate stiffness to prevent aerodynamic flutter for low cost in a short timespan. The original X-34 program was a fixed price contract valued at \$60 million over 30 months. The speedbrake mechanisms needed to be designed, fabricated, tested, and integrated under these constraints.

In order to minimize costs, the number of people working on the speedbrakes was kept to a minimum. At any given time, no more than three engineers were working on the speedbrake mechanism and they performed a large number of tasks including: design, modeling, analysis, drafting, project management, fabrication/integration/test support, test planning, test fixture design/analysis. Most components were fabricated out-of-house and were then integrated at Orbital's Dulles Integration and Test Facility. The system-level testing was performed at the all-moving vertical tail subcontractor test facility (Composite Optics, Inc., San Diego). The small team allowed for communication on a daily basis between team members. The primary design and analysis was performed by the same engineer. In keeping with the X-34 design philosophy, documentation was kept to a minimum.

Advanced design and analysis tools were also used to minimize cost. SDRC IDEAS Master Series 5 was used to produce a solid model of the mechanism, which is shown in Figure 6, that allowed the complex three dimensional mechanisms to be fit-checked on the computer before parts were fabricated and no interferences were found when the actual hardware was integrated.

In order to minimize the need for complex and time consuming analyses, the X-34 structural design philosophy was to produce a design that was robust enough to rely on simpler analyses using more severe load factors. The X-34 program applied safety factors of 1.25 for yield and 1.50 for ultimate to flight limit levels [4]. Having a robustly designed mechanism provided additional confidence in implementing an aggressive schedule.

Wherever possible, components were analyzed using simple hand calculations instead of detailed finite element models or not analyzed at all but verified in a system level test. For example, components with well-defined load paths such as clevises were analyzed using only hand calculations, MathCad worksheets, and MS Excel and were then verified in test. Components with more complex load paths such as the pillowblocks required finite element modeling in addition to testing.

Another cost reduction method was implementing modular design wherever possible. The X-34 program mandated the use of a common hydraulic actuator since this resulted in significant cost savings. The actuator was sized for the high bandwidth elevons and rudder in stroke and rate. The speedbrakes required a slower slew rate and had smaller stroke requirements, which are summarized in Table 2. The stroke, force, and slew rate requirements were derived from stability and control requirements. A common piano hinge design was used for all X-34 control surfaces (elevons, body flap, and speedbrake). The piano hinge design was selected for its inherent ability to serve as a thermal barrier along the control surface hingeline. The piano hinge assembly itself was designed using modular components in order to save cost by reducing unique parts. The speedbrake clevises also are modular in that they were designed to be used as either right hand or left hand parts requiring half as many dash configurations on the drawing. In order to maintain operational flexibility, all X-34 control surfaces were designed to be fully interchangeable. It is possible to exchange surfaces from vehicle to vehicle. Both the SN001 and SN002 all-moving vertical tails have been installed on the A-1 vehicle at different times. In the case of the speedbrakes, this meant using matched tooling to drill the hingeline bolt patterns on each serial number of the all-moving vertical tail and speedbrakes.

Table 2. Actuator Design Specifications vs. Requirements

	Stroke	Force	Slew Rate
Inboard Elevon Requirement	128 mm (5.061 in)	4,762 kg (10,500 lb)	45°/s
Outboard Elevon Requirement	95 mm (3.878 in)	4,762 kg (10,500 lb)	45°/s
Body Flap Requirement	106 mm (4.195 in)	3,815 kg (8,411 lb)	30°/s
Rudder Requirement	62 mm (2.466 in)	2,296 kg (5,063 lb)	45°/s
Speedbrake Requirement	114 mm (4.506 in)	5,546 kg (12,227 lb)	30°/s
Common Actuator Design Specification	180 mm (7.100 in)	10,069 kg (22,200 lb)	45°/s

A high degree of concurrent engineering was employed in the execution of the speedbrake mechanism design. It was necessary to release parts for production with minimal analysis in order to maintain schedule. When problems did occur, it was possible to retrofit solutions into the existing design.

In order to meet schedule, fabrication of the speedbrake mechanism commenced with the completion of hand calculations and limited finite element modeling. As the analysis was completed, it became apparent that the loads induced by the speedbrake mechanism on the aft spar of the all-moving vertical tail would over-stress the skin-to-spar joints. A rudder brace assembly that consisted of a pair of struts that spanned between the fitting on the aft spar and the adjacent rib was added to offload the skin-to-spar joints. A composite doubler and metallic backing plate were added to the aft spar and actuator rib to prevent fastener pull thru. These modifications were implemented with minimal impact to the mechanism and tail, which were already in production, and the speedbrake mechanism was delivered to static load testing on time.

In order to keep costs down, the amount of assembly tooling for the speedbrake mechanism was kept to a minimum. All components were designed to be assembled in place on the tail without fixturing. An aft spar simulator shown in Figure 15, which consisted of a flat aluminum plate containing the appropriate hole patterns, was fabricated to assist in assembling the torque tube sub-assembly. This sub-assembly required alignment between torque tubes which was easier to achieve using assembly tooling than by design. If a higher production rate was required, the assembly tool may have been designed differently to allow for easier setup. However, only two torque tube sub-assemblies were assembled using this tool and the additional time required to design the easier setup tool was not deemed necessary.

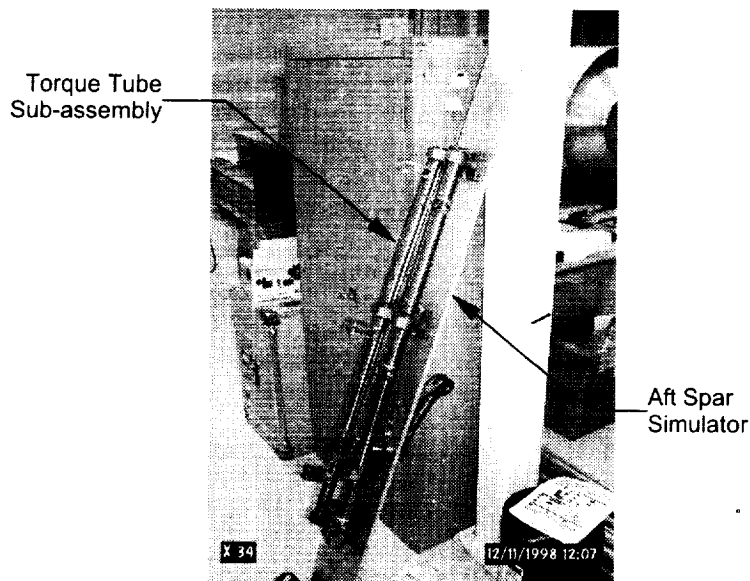


Figure 15. Simplified Assembly Tooling was Designed for the Torque Tube Sub-assembly

A set of pillow block simulators was also fabricated to assist in properly locating the aft spar relative to the tail skins. This is important for the pillow blocks since they have a bolt pattern on the aft spar as well as a bolt pattern on the skin whose plane is roughly 90° to the aft spar plane. Again, it was easier to fabricate simple assembly tooling to achieve the correct alignment than to fabricate more complex tooling. Unfortunately, the pillow block simulators were not used correctly during the first tail assembly and the alignment between the two bolt patterns was off. Extensive rework to the pillow blocks was required in order to account for this discrepancy. In hindsight, this was a case of not having adequate 'design space' to achieve a good solution. The pillow blocks were designed with bolt patterns at 90° to each other since that was the only way the reaction load could be passed into the structure given the severe volume constraints. In this case, taking the time to design the more complex tooling would have eliminated the time required to rework the pillow blocks.

After the design, analysis, fabrication, and integration were complete, it was necessary to load test the mechanism. The testing philosophy for the speedbrake mechanism and for all X-34 components was to verify the components using a system level test. Instead of testing its individual components, the

speedbrake mechanism was tested at the system level as part of the all-moving vertical tail static load test. The full flight integration of the speedbrake mechanism with the exception of the speedbrake panels, speedbrake clevises, and hydraulic actuator were installed into a flight tail (speedbrake simulator and actuator simulator were used in place of flight articles). The composite speedbrake panels and aluminum speedbrake clevises were protoflight tested individually in a separate static load test.

Since the interfaces between the metallic mechanism and the graphite epoxy tail were challenging to analyze, it was beneficial to test at a system level not only verify the integrity of the individual components, but also to verify the interfaces between the components. Most unforeseen problems occur at joint and interfaces. System level testing is a highly efficient way of discovering these problems [7].

As shown in Figure 16, the mechanism was verified by first protoflight testing to 125% of design limit. In order to verify that the protoflight test did not introduce any damage, the mechanism was then acceptance tested to 100% of design limit. The acceptance test was then repeated. The peak strains and deflections were required to be within 5% and the strains and deflections were required to return to within 5% of the peak value in order to verify that no damage was propagating thru the mechanism or structure. Designing and testing to 125% of the design limit ensures a robust structure and accounts for uncertainties in trajectories, loads, analysis methods, and manufacturing processes [7].

Two speedbrake mechanisms were fabricated for the X-34 program and each mechanism was subjected to protoflight testing. In contrast to a high rate production program, it is more efficient to test and fly each article to account for the inherent manufacturing and processing differences that arise in a low volume prototype program such as X-34 [7].

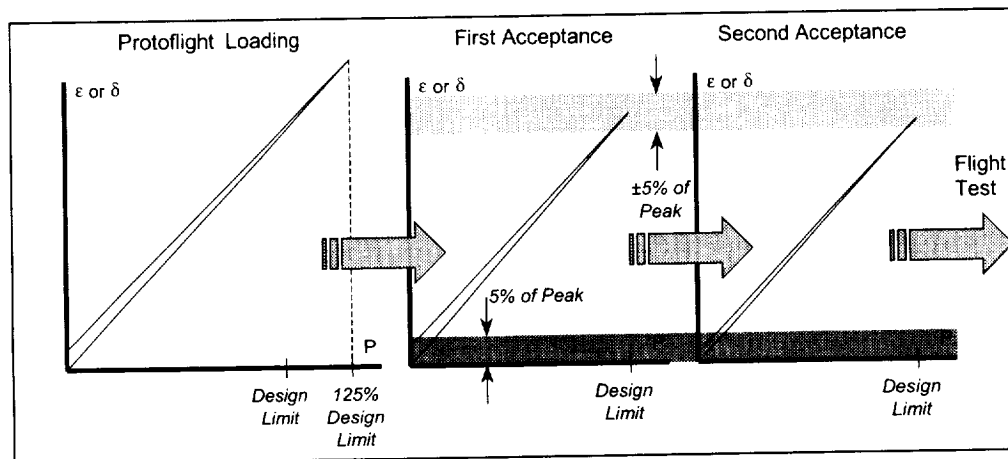


Figure 16. Protoflight – Acceptance Test Approach [7]

Conclusions

The X-34 split flap speedbrake mechanism is actuated with a single linear hydraulic actuator, is mounted to the all-moving vertical tail, and is designed for transonic and hypersonic flight. The speedbrake mechanism is used for energy management during descent and for pitch trim both during ascent and descent. The design of the mechanism was subjected volume constraints due to carrier aircraft compatibility and aerodynamic requirements as well as a stiffness constraint due to a no-flutter requirement. These constraints drove the layout and design of the mechanism. In addition, the execution of design was subject to cost and schedule constraints set by program goals. In order to accomplish the task, a small team employed advanced design and analysis tools in order to work as efficiently as possible but also recognized that certain analyses could be performed using simple hand calculations or not performed at all but verified in a system level test. Modular and robust designs were created as well as simplified assembly tooling to control costs. The team subcontracted with experts in certain subject areas and utilized a high degree of concurrent engineering. The X-34 speedbrake mechanism demonstrates that it is possible to design a compact control surface deployment mechanism with adequate stiffness to prevent aerodynamic flutter for low cost in a short timespan. This ability contributed significantly to the success of the X-34 program.

References

1. Pamadi, Bandu N., Gregory J. Brauckmann, Michael J. Ruth, and Henri D. Fuhrmann, "Aerodynamic Characteristics, Database Development and Flight Simulation of the X-34 Vehicle", AIAA 2000-0900.
2. Brauckmann, Gregory J., "X-34 Vehicle Aerodynamic Characteristics", AIAA-98-2531.
3. Jenkins, Dennis R., *Space Shuttle: The History of Developing the National Space Transportation System*. Motorbooks International. Osceola, WI, 1992.
4. *X10001, Load and Design Criteria X-34*. Orbital Document, Rev C, 6/30/99.
5. Blades, Eric L., Mike Ruth, and Henri D. Fuhrmann, "Aeroelastic Analysis of the X-34 Launch Vehicle", AIAA-99-1352.
6. Belloch, Paul, Eric L. Blades, and Thomas L. Dragone, "Modeling and Correlation of the X-34 Launch Vehicle", AIAA-2000-1777.
7. Dragone, Thomas L., "Structural Innovations in Design, Manufacturing, and Testing on the X-34 Reusable Launch Vehicle", AIAA-2000-5309.

Acknowledgements

The author would like to thank Tom Dragone, Henri Fuhrmann, Mike Ruth, and Bryan Sullivan of Orbital Sciences Corporation for their assistance with this paper.



37/44

Dust Cover for a Mars Lander Solar Cell Experiment

Scott Christiansen^{*} and Kurt Lankford^{*}

Abstract

A lightweight, low volume dust cover was required to protect three experiments located on the top of the Mars In-Situ Propellant Precursor (MIP) module on the Mars '01 lander. The need for a cover was not solidified until late in the design phase and, at that point in the project, there was no envelope planned for a cover. Additional space was apparently unavailable, given the very crowded lander deck. The purpose of the cover was to prevent accumulation on instrument surfaces of dust kicked up during the final phase of landing as the lander neared the Martian surface. This paper describes the difficult design process and the resulting design. Difficulties with performance and materials that occurred during manufacture and test are also discussed. Resolution of these issues led to successful qualification of the entire MIP module and cover system.

Introduction

One of the experiment modules to be flown on the '01 Mars Lander was the Mars In-situ Propellant Precursor (MIP) module. This module was designed and built by NASA JSC and Lockheed Martin. The top of the experiment was utilized for three additional experiments, Mars Thermal Environment Radiator Characterization (MTERC), Dust Accumulation and Removal Technologies (DART), and Mars Array Technology Experiment (MATE). The experiments consisted of several panel areas designed to characterize radiator panel and solar array performance in the Martian environment as well as assess the effects of dust accumulation and potential mitigation strategies after landing on the Martian surface. MIP, MTERC, DART, and MATE are part of NASA's planetary exploration program and are part of a series of experiments to assess resource capabilities and potential risks for manned exploration of Mars.

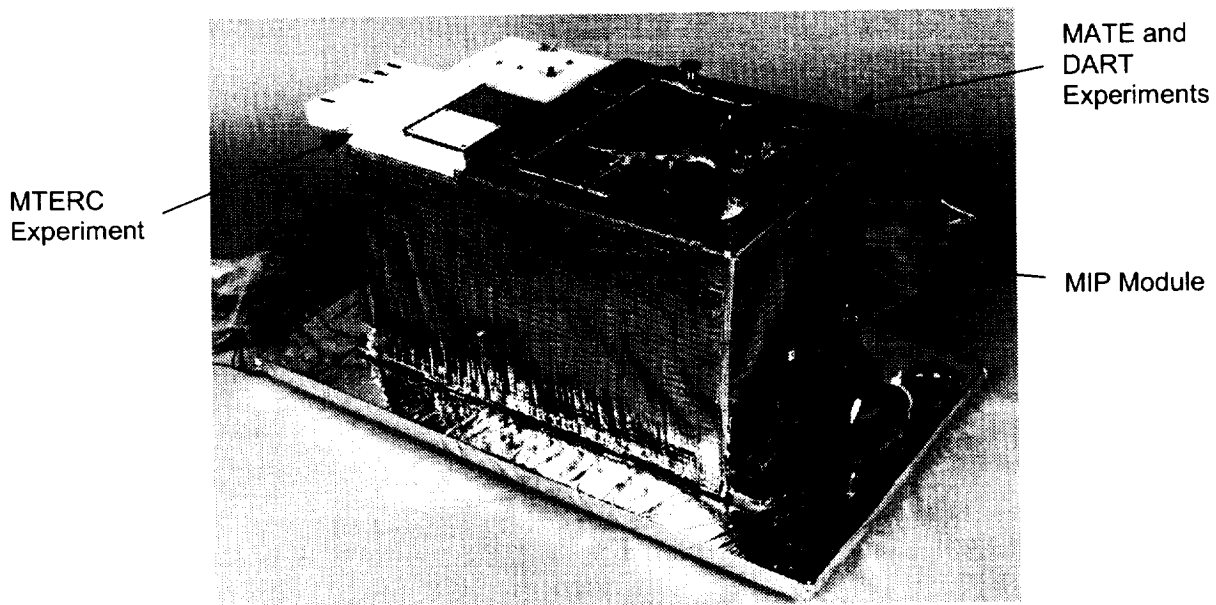


Figure 1. MIP Engineering model shown without cover system. (MTERC cover orientation was rotated 90 degrees in the Qualification and Flight units.)

^{*} Starsys Research Corporation, Boulder, CO

Background

It has been observed in past Mars missions that dust collecting on solar cells used on the Martian surface rapidly blocks solar energy and leads to eventual spacecraft failure. The experiments on the upper surface of MIP were designed to better characterize the dust collection phenomenon, and consisted of a number of small solar cells and radiator panels mounted on the upper, stepped surface of the MIP experiment enclosure. A number of solar cells and associated equipment were present to assess general cell performance and dust collection rates as well as to attempt dust mitigation techniques.

- Several different types of solar cells were included to assess their performance in the Martian environment and their sensitivities to dust accumulation. (MATE)
- Several cells were mounted on surfaces of different slopes to determine if the dust might slide off. Several cells were set-up near suspended wires such that small electrostatic fields could be used to attempt to repel dust from a specific area. (DART)
- Two small radiator panels were open to the Martian sky to assess thermal radiation characteristics and dust effects. (MTERC)

In all cases, the intent was to establish baseline operating performance for each experiment and then monitor performance and potential degradation as environmental dust collected on each cell.

In designing the experiments, it was very important to be able to have reasonable knowledge of initial dust loading and thereby to reasonably establish the initial operating conditions of the cells (initial dust loading was expected to be zero or near zero). Throughout the evolution of the design of the experiments, the possibility of the need for a cover had been raised and discussed several times. It was initially unclear whether or not a cover was needed and the added mass and cost pushed the cover into the “we really don’t need that” zone. In addition, the experiments were housed in a very tightly packed landing vehicle and, based on all the envelope constraints, there was not any room for a cover.

Late in the design process for MIP and the upper panel experiments the recurring cover conversation was, once again, renewed. In an attempt to resolve the issue more detailed analyses of the landing conditions were undertaken. While some still thought that the risk of dust accumulation during landing was minimal, a credible analysis indicated that the landing thrusters would stir up a very large dust cloud. Under certain conditions, this dust could settle and deposit up to a millimeter of dust on the upper surfaces of the spacecraft and instruments. If this were the case the uncovered experiments would be finished before they began. Based on this analysis several lander mission experiments (including the MIP module as well as the rover) that might be sensitive to this dust adopted the strategy that if there was any way to retrofit the experiment and still fit within the spacecraft, a dust cover was to be included. In the case of the MIP module, NASA-JSC, Lockheed Martin, and Starsys began working closely together to determine if a cover for the experiment was even feasible.

Design problems

Instrument requirements

The three experiments on the top surface of the MIP module needed to be protected from swirling dust during landing and settling dust after touchdown and engine shutdown. With all of the various solar cells and panels, the surface was very uneven and non-symmetrically shaped. In some ways the upper surface resembled a city block with buildings of differing sizes and heights. The cover would need to protect all of these instrument features without touching or damaging them. To make the problem more difficult, the surface consisted of separate sections at different levels. To maximize exposure to the Martian sky and view of the sun, the field-of-view for the experiments required that the cover not block the view above 15 degrees from the planes of the surface sections.

Because protection from swirling dust was necessary, the cover system also needed to protect the side aspects of the upper surface and experimental sections. The side sections needed to be tall enough to support the cover above the experiment components. In several areas side rails used to support the

cover and protect side aspects would remain in the field-of-view of cells near the edges if they weren't moved out of the way during deployment. During deployment, the cover was also required to control the disturbance or re-deposition of any dust that had collected on it during landing.

The MTERC experiment included a small, separate, spring-operated cover that protected a portion of the thermal radiators. This small cover was to remain closed until about halfway through the experiment, then be deployed to expose fresh radiator surfaces. The larger dust cover system had to pass over this smaller cover and then completely move away from it after deployment such that the smaller cover could operate without interference.

As with any cover system, the cover required some type of deployment mechanism and controllable release mechanism. Since the experiments would be useless if they were not uncovered, the entire system was expected to exhibit a high level of robustness and reliability.

Specific Envelope problems

The envelope volume for the MIP module was dependent on several configurations for the lander during the mission.

- The first configuration was the launch and flight mode. In this configuration, all hardware on the instrument deck was stowed and the aeroshell (a conical upper spacecraft cover) was present, enclosing the upper exposure of the spacecraft.
- The second configuration was the landing mode. In this configuration the aeroshell was jettisoned and the landing legs were deployed.
- The third configuration was the transition between the landing mode and the fully-deployed lander mode. During this process several experiments in the vicinity of MIP performed deployment events and the Rover was released and deployed.

This complex combination of configurations created a very restrictive and difficult to analyze mechanical envelope which made a cover initially appear impossible. Three areas of possible interference were the most significant in driving the shape and deployment aspects of the MIP cover system.

1. The MIP module was mounted such that a landing leg passed very near one edge and even slanted over a portion of the upper surface of the module. Prior to landing this leg was extended during deployment which meant that the leg would not be present during cover deployment, but also that the dynamic envelope for the leg motion required that any MIP components be well away from the undeployed leg.
2. One of the reasons that the upper surface of the MIP module was stepped was that it must fit under the conical shape of the aeroshell and maintain a minimal clearance for dynamic envelope. One corner of the lower surface was very close to the maximum envelope allowable to not contact the aeroshell during launch dynamic environments. During landing the aeroshell was to be jettisoned and this envelope constraint was not an issue for deployment.
3. The MIP module and Rover were mounted relatively close to each other in their flight and landing positions. Although the Rover was to move out of the way prior to deployment, the envelope in that area was considered off-limits in the event something went wrong and the MIP cover was required to deploy before the Rover could be moved. Several other instruments were near the MIP module and it was considered undesirable for the cover to dump dust on a nearby experiment during deployment.

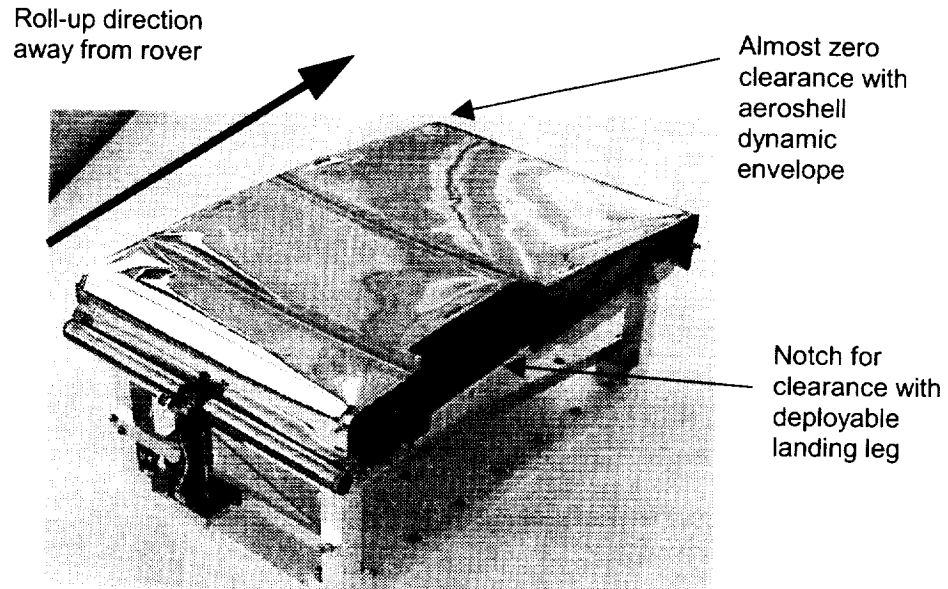


Figure 2. Qualification cover system shown on test fixture.

Design Process

Establishing Envelope / Interface

As discussed above, initially there was no space available (or mass budget) for a cover. Queries to the organizations involved in managing the mechanical envelopes all yielded responses that their envelopes were right up against their neighbor's and they did not have any spare space to give. The team was forced to try to look at the lander from a system point of view and identify available mechanical volumes that might not be evident when considering individual, simplified envelope definitions. In reviewing numerous views of the lander solid models, it appeared that there was room for a cover if it could be made to work around the unsymmetrically shaped structures and instruments near the MIP module. It took a meeting of personnel from NASA JSC, Lockheed Martin-Houston, Lockheed Martin-Denver, and Starsys to be able to identify that adequate space was, in fact, available. This group gathered around a CAD workstation and reviewed the actual lander models to identify components with their dynamic envelopes and find spaces in-between that could allow space for the cover. Ultimately the group concluded that there was room for an unusually shaped cover and the project moved forward.

A Unique Approach

A trade study for a potential cover for these experiments identified a unique, very light, simply released, self-deploying, roll-up, film-type cover as the best approach to meet the MIP system requirements. The roll-up cover provided several distinct benefits.

- It required very few mechanical elements to operate. This saved design time, development time, and reduced mass.
- The rolling action of the cover could capture dust as it rolled up, minimizing disturbances
- The fact that the cover rolled itself up meant that the cover would require minimal envelope after deployment.
- The minimization of mechanisms and driven elements reduced the power and complexity of control electronics required for operation.
- The shape and size of the cover made it extremely adaptable to the complex shape and functionality required
- Although some development was necessary the simple design allowed for very rapid design and development to meet the compressed schedule of a last minute cover program.

Basic components of cover

The final design included the following components:

- Self-rolling Kapton film cover – The main cover was a single sheet of Kapton film. On each edge a stainless steel constant torque spring was bonded to provide the rolling action. Across the moving end of the cover was an aluminum tube that served to interface with the release latch and hold the end of the cover during launch environments. To provide some structural stiffness and maintain the stowed cover shape the cover was designed to be shaped in a curve. Additionally two stiffening strips were bonded across the cover in two places.
- Self-retracting side rails – On the two sides of the cover several deployable side rails were mounted to the MIP module. The side rails were needed to support the Kapton cover above the sensitive solar cells. They were also required to move out of the field-of-view after deployment. Each side rail was mounted on a pair of pivots with torsion springs that would cause the side rails to flip out away from the upper surface experiments. The side rails had tabs on their edges to engage with slots in the cover to create a stable structure when the cover was stowed.
- Release Latch – The Release Latch was a simple paraffin actuator powered pin-puller mechanism. Two paraffin actuators were utilized to redundantly retract the release pin. When stowed, the release pin trapped the Tension Bar between the pin and a cradle on the latch body. Two additional cradles were present at the ends of the Tension Bar to support the Tension Bar during dynamic environments.

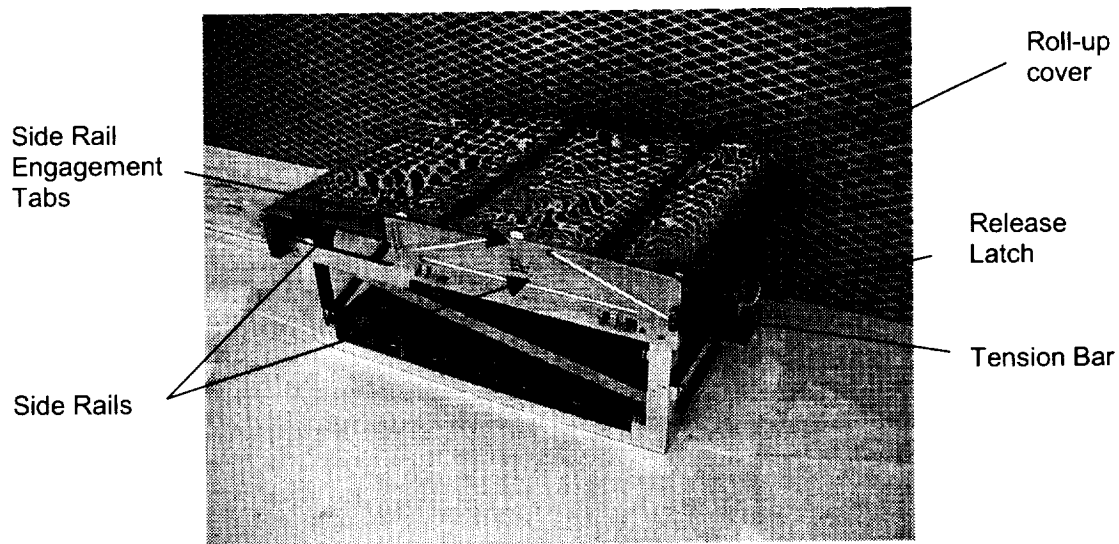


Figure 3. Basic cover system components shown in stowed position on test fixture. (Unit shown is the qualification unit in the final configuration.)

Lightweight materials

The original design did not include mass budget for a cover, and the mass of a cover system was not included in the module structural design or analysis. To make the cover as light as possible, mechanical components were minimized and lightweight materials were used wherever possible. The cover was fabricated from 0.125-mm Kapton coated with aluminum on one side. The side rails were fabricated from Ultem (polyetherimide) and used small aluminum pivots that mounted to existing MIP module structural elements. The two constant-torque springs were made from 6-mm wide by 0.1-mm thick 302 stainless steel strips. The latch was designed to be as light as possible while including redundant paraffin actuators. Total mass of the delivered flight cover system was 472 grams.

Operation

Stowed Configuration

In the cover-stowed configuration the side rails were maintained in their vertical positions. The tensioned cover contained several slots along each edge that interfaced with mating semi-circular tabs on the side rails. With the cover in place and tensioned slightly, the side rails were prevented from folding down. The cover tension was maintained by the clamping action of the Launch Latch on the tension bar. For launch and landing loads the ends of the tension bar were preloaded against a pair of small cradles out at the edge of the instrument. The Launch Latch also contained a pair of contacts that completed a circuit through a small conductive patch on the cover. When the cover was latched in place, the circuit was closed, indicating that the cover was still stowed in place.

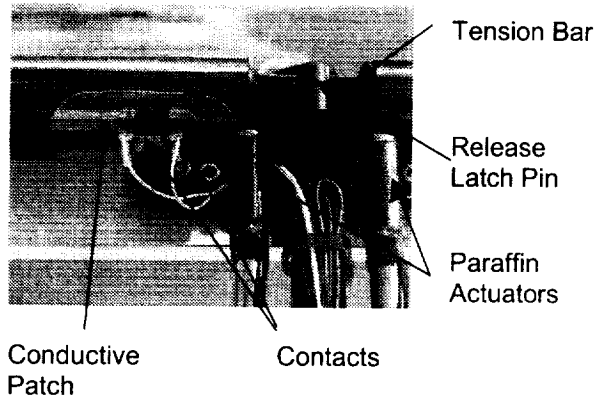


Figure 4a. Contact switch

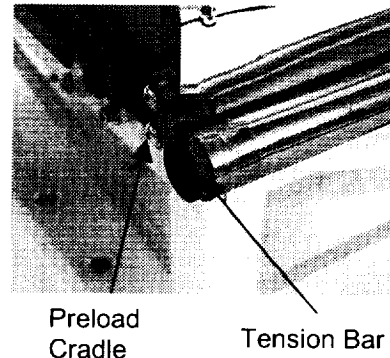


Figure 4b. Preload Cradle

Figure 4. Contact switch and preload cradle; cover shown in stowed position.

Deployment

When deployment was required a power signal was supplied to the paraffin actuators on the release Latch. The latch utilized redundant actuators to pull the retention pin (either actuator could independently retract the pin). Upon pin retraction, the tension bar would be released and the cover was free to begin rolling up. At the point that the spreader bar moved away from the latch the cover release indicator circuit would open, indicating successful release. The constant force springs then caused the cover to roll itself up. During rolling, the cover would tend to capture the majority of dust collected on it. With the cover no longer present to hold the side rails in their upright positions, the side rails "flipped" down into their deployed positions. After completely rolling up, the cover came to rest on the side panel on the outboard surface of the MIP module. At this point, the experiments were exposed and ready to perform their intended measurements.

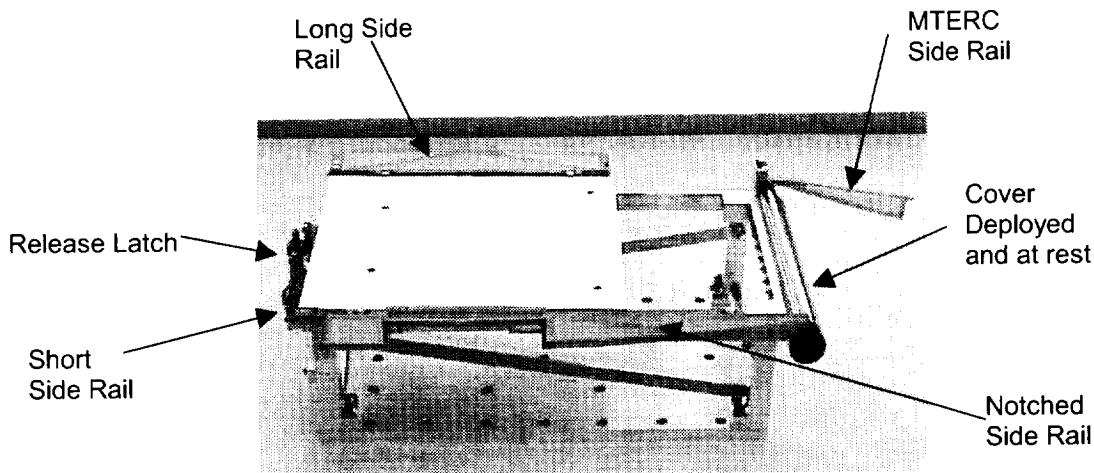


Figure 5. Cover system components shown in completely deployed configuration.

Development and Qualification

Cover and Spring design

The cover and roll-up spring design was arrived at by a primarily experimental process. General sizing of the key components was determined as a function of the system geometry and rough calculations. The intent was to balance adequate roll-up torque with minimization of system energy. Inadequate roll-up torque might create a functional problem while high system energy would cause higher dispersion of collected dust and potential impact problems at the end of travel during deployment. Damping features such as Velcro were considered, but the system energy was small enough that the additional risk of damping features was not deemed necessary.

Development tests

Several prototype cover systems were fabricated to assess the approach and provide additional design data needed to optimize the sequenced deployments of cover and side rails. Since the side rail deployment was dependent on the cover deployment, interactions between the moving parts needed to be studied experimentally. Results of the prototype testing led to several design decisions. To keep the side rails vertical and stowed small tabs on the Side Rails mated with slots in the cover (similar to the holes along the edge of photographic film). Key shapes and locations that led to a minimum number of tabs were identified. The final system configuration included four tabs along each edge of the cover. The final tab configuration was a flat, semicircular protrusion with the plane of the tab parallel to the direction of cover roll-up. The interface between the flat side of the tab and the slot in the cover provided adequate force to maintain engagement between the two parts when stowed. The semi-circular shape eliminated a sharp edge or corner for the cover to catch on as it rolled past the tab.

The number of side panels their size, shape, and orientation was also determined through prototype testing. A total of 4 deployable side panels were utilized to meet the combined requirements of full side protection, cover support, clearance of the field of-view, and no interference with neighboring envelopes or fields-of-view. The Notched Side Rail mounted along the edge closest to the landing leg. The notch was present to clear the landing leg dynamic envelope. The Notched Side Rail folded down approximately 110 degrees. At the latch end of the Notched Side Rail was the Short Side Rail. The Short Side Rail only deployed approximately 55 degrees and was necessary to keep from having the side rails on this side of MIP contact the APEX pin-puller. On the other side of the MIP module toward the latch was the Long Side Rail. This side rail extended from the latch end to the edge of the MTERC cover and folded down 90 degrees. These three side rails deployed outward along the sides of the MIP module. Because

the MTERC cover also deployed in this direction, the fourth side rail, the MTERC Side Rail, could not be mounted along this edge. The MTERC Side Rail was mounted on a pivot on the end of the module and deployed 180 degrees outward away from the module on the end where the cover was attached (see Figure 5).

Additional development testing involved assessing the dispersion of dust during deployment. Dust dispersion tests were performed under earth gravity and ambient air pressure. Analysis by JPL of previous mission data indicated that the texture of the dust is probably similar to that of talcum powder or flour. For our dust tests, flour was sprinkled over the cover to simulate a 1-mm layer collection of dust. The cover was then released and deployed. During the rolling action of the cover, most of the dust was captured between the Kapton layers of the roll. A relatively small amount (several percent) escaped out of the ends of the roll and was deposited on the Side Rail surfaces on either side of the test model. Swirling air effects caused some dust to swirl around behind edges of the moving cover resulting in an extremely small amount (much less than 1%) of dust being deposited on the edges of the experimental test surfaces (see Figure 6). The amount and location of possible dust that might be re-deposited on the MIP instruments was considered acceptable by the experiment principal investigators. As the roll reached its stationary attachment point it tended to overtravel and deposit dust from a portion of the cover at the base of the test model. This had been expected at some level and the direction of cover deployment had been chosen to assure that dust re-deposited in this way would fall harmlessly on the outer edge of the lander instrument deck.

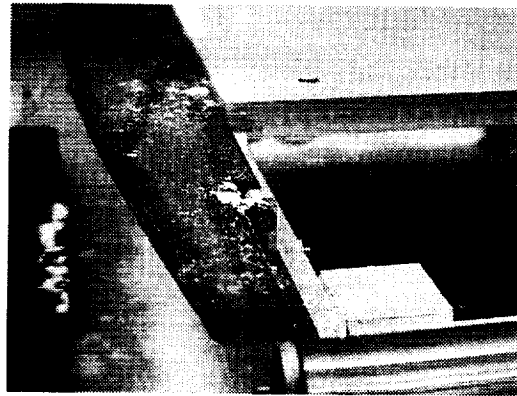


Figure 6. After dust-loaded deployment test, dust is present on deployed Notched Side Rail and a corner of the experiment area

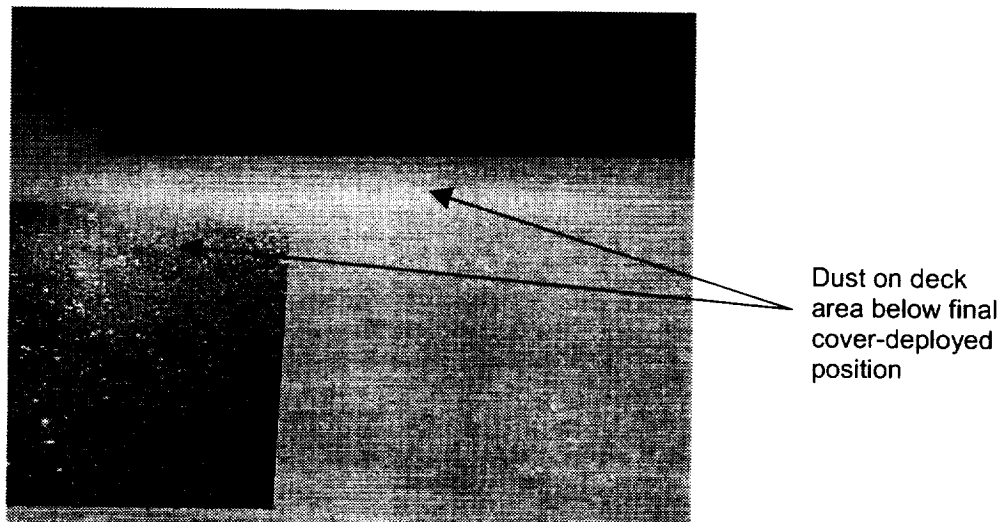


Figure 7. After dust-loaded deployment test dust is present on deck area below final deployed position of cover roll.

Qualification

Based on the prototype unit test results a qualification cover system was manufactured. A MIP module structural simulator was built to allow the proper configuration of the cover system. The system was made up of six separate subassemblies that relied on the MIP structure to support and properly locate them. This structural simulator was used for all tests including vibration, acoustics, and thermal/vacuum.

The qualification unit was tested according to a relatively typical spacecraft qualification plan. The tests included vibration, acoustic, thermal cycling (-98C to +55C), and thermal vacuum functional tests. The unit passed its functional tests, but several characteristics observed during the tests led to changes in the flight unit. During vibration testing the spring guide bushings were damaged due to interference with the pivot attachment features on the short side rail (see Figure 8). The bushing damage did not lead to a functional failure, but the design was changed to eliminate the interference and bushing damage.

During testing of this unit a small tear was noted at the edge on one of the slots where the cover wrapped around the corner of one of the Side Rails at the latch end of the cover (see Figure 9). This area is more highly stressed than the other engagement slots. The problem was resolved by bonding patches of Kapton film as doublers around the two slots at the Side Rail corners. The tearing did not reoccur during resumption of qualification testing.

After qualification testing at a component level at Starsys the qualification cover system was delivered to NASA JSC. There the system was mounted to the MIP module qualification unit and subjected to system-level testing with the module. The cover system functioned successfully throughout the qualification tests. After extended thermal cycling with operation at low temperature in reduced atmosphere (simulation of Mars atmospheric pressure of 6 Torr), cracking of several Ultem parts at bolted attachment points was noted (see Figure 10). While the system had functioned properly, the cracking of the parts was considered unacceptable. Investigation of the failure was inconclusive as to the cause. Differential expansion leading to overload of the parts was considered, although the system had been exposed to greater temperature extremes in previous tests. Low impact resistance of the Ultem was also considered, but the parts that exhibited cracking were not exposed to the highest impacts during deployment. Without causing excessive delays or increased costs due to an extensive investigation, the solution for this problem was to replace the Ultem parts at risk with aluminum parts of the same design. This maintained the functionality of the parts while increasing their strength and resistance to cracking. Subsequent tests were successful and the design was adopted for flight.

Flight

The flight unit was manufactured including important design changes based on results and observations obtained during qualification testing. The cover system has been delivered and has been integrated onto the flight model of the MIP module. The entire module is currently being stored in anticipation of a future flight mission.

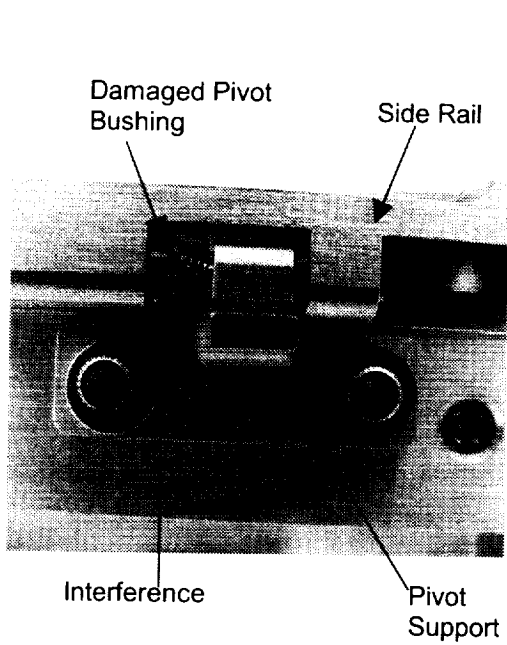


Figure 8. Vibration damage to pivot bushing.

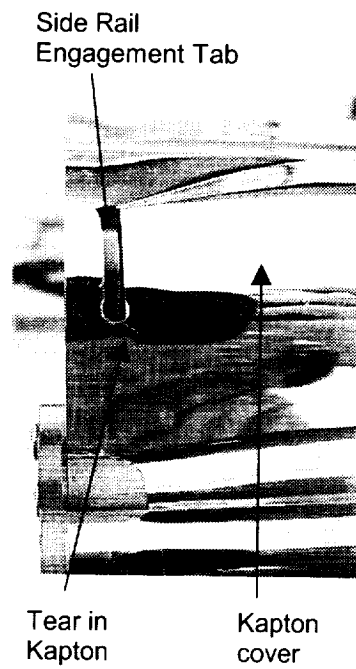


Figure 9. Tear at edge of hole in Kapton cover

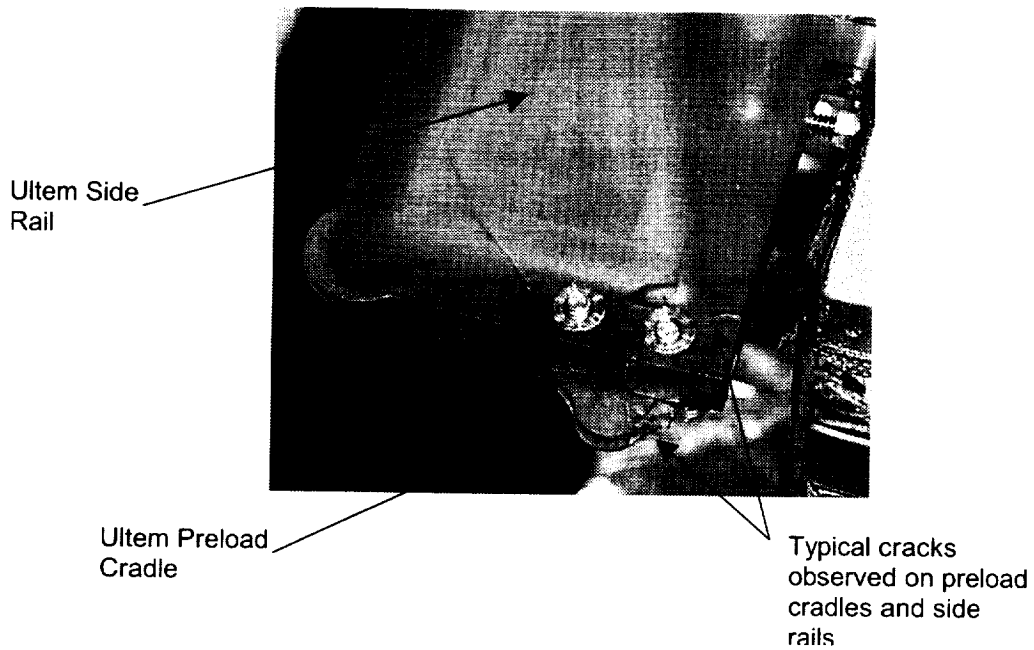
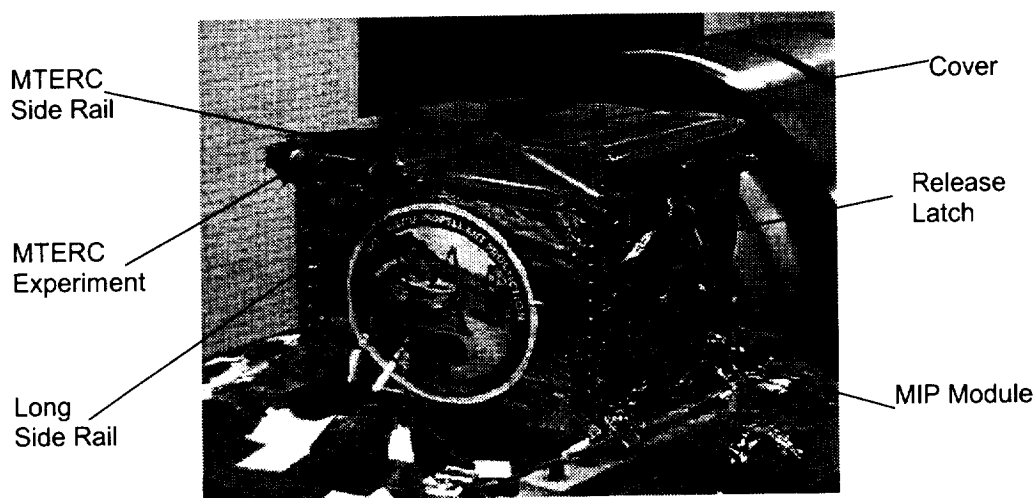


Figure 10. Typical cracks observed after system level thermal qualification testing.

Lessons

Spacecraft component mechanical envelopes are often simplified and do not necessarily reflect the shape or exact size of the component they define. In a spacecraft assembly there is often space to be found if an accurate system level model can be utilized. A major difficulty in working difficult envelope problems (especially from a subcontractor point-of-view) is to get all of the organizations responsible for the individual envelopes together to agree that the space actually exists.

While Kapton and Ultem are relatively well understood materials, additional care, analysis, and testing is extremely valuable when using them in applications that may induce unusual or uncharacteristic loading. Both Ultem and Kapton can be used in lightweight, structural/mechanical, spacecraft applications if proper precautions are taken assess their load conditions. In that these two materials are plastics and predicting thermal and impact affects is not exact, testing of the parts is extremely critical. Failure modes for these materials may be different than those typically considered in traditional analyses.



**Figure 12. Qualification unit MIP module with cover system.
Shown in stowed configuration during qualification vibration testing.**

Summary / Conclusions

Given a very difficult design problem the MIP cover system was designed and manufactured to meet the restrictive envelope and mass requirements. The MIP module and cover system have passed qualification testing and flight models have been fabricated and tested. The module was scheduled to fly on the Mars Surveyor 2001 mission that has been cancelled due to changes in NASA's Mars exploration program. The MIP module may be included in a future Mars mission, but it is not specifically scheduled to be aboard a specific mission at this time.

SRTM Mast Damping Subsystem Design and Failure Investigation

Jeffrey W. Umland*

Abstract

A mast vibration damping system was developed for the Shuttle Radar Topography Mission (SRTM). The damping system development is considered from both a system perspective, and a detailed mechanism design viewpoint. The requirements derivation approach is presented, starting from the general instrument requirements, and proceeds to the determination of specific mechanism design requirements. Key component failure modes and effects, as well as the design mitigations implemented, are discussed. The diagnosis of the damping system on-orbit failure is given. The root cause of the damping system failure is provided. Conclusions are drawn to provide guidance for future damping system implementations.

Introduction

The Space Radar Topography Mission (SRTM), illustrated in Figure 1, flew in February 2000 on the space shuttle Endeavor as the primary payload for STS-99. The objective of this joint project between the National Imagery and Mapping Agency and the National Aeronautics and Space Administration (NASA) was to generate a near-global high-resolution database of the earth's topography. This mission made use of Interferometric Synthetic Aperture Radar to digitally survey the Earth's surface from space. The primary product of this 11-day mission is a topographic database of 80% of the Earth's land surface, i. e., most land surfaces between $\pm 60^\circ$ latitude. The resulting digital terrain data set provides a significant improvement over currently existing global topography data sets.

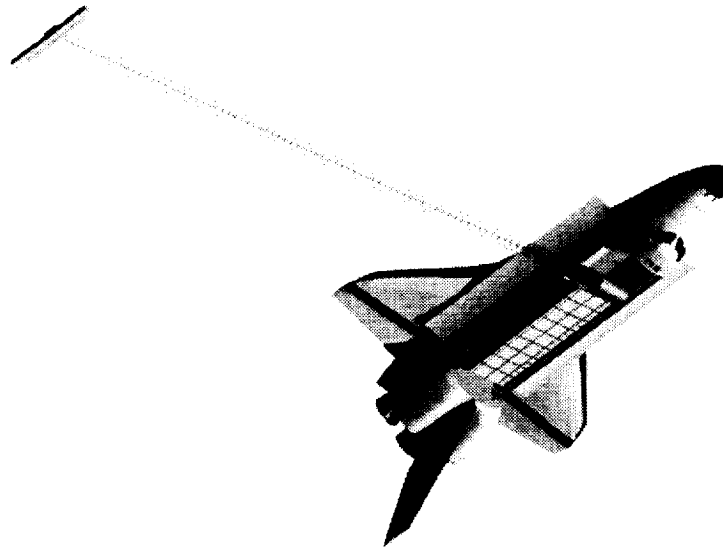


Figure 1. SRTM Mission Configuration

Instrument Overview

The SRTM architecture is based upon the Spaceborne Imaging Radar/X-band Synthetic Aperture Radar (SIR-C/X-SAR) instruments that flew twice on the Space Shuttle Endeavor in 1994 [Jordan, et al, 1995]. The SIR-C/X-SAR project was a collaborative effort between NASA, which developed SIR-C, and the German and Italian Space Agencies, which developed X-SAR. The SIR-C instrument was two separate SAR's, which operate in the C and L-bands. The X-SAR instrument operates in the X-band. The combined

* Jet Propulsion Laboratory, Pasadena, CA

SIR-C/X-SAR instruments including electronics essentially fill the shuttle payload bay. The primary objective of the SIR-C/X-SAR missions was the radar imaging of select "supersite" targets. SIR-C/X-SAR's secondary objectives, which enabled SRTM, included the demonstration of repeat pass interferometry and scan-SAR. The repeat pass interferometry data is then used to recover the topographical features of the target surveyed. Scan-SAR is a method of beam steering that is then employed by SRTM, in the C-band, such that the radar swath width is sufficient to achieve complete mapping coverage in 159 orbits. See Rosen, et al for a detailed treatment of Synthetic Aperture Radar Interferometry.

The modifications to the existing radar instrument required to collect the interferometric data included the addition of a second C-band antenna, a 60-meter mast, metrology, and additional avionics. Further, the German Space Agency provided a second X-band antenna. The fundamental SRTM instrument configuration is illustrated in Figure 1. Simplistically, SRTM makes use of two radar antennas separated by a fixed distance, or baseline, to form a fixed baseline interferometer. The in-board antenna, relative to the Orbiter payload bay, is used as both a transmitter and receiver, while the outboard antenna is only a receiver.

One of SRTM's significant features is the use of a 60-meter long deployable mast that serves to deploy an outboard antenna and create a stable baseline. The 60-meter deployable truss and its deployment mechanisms are described by Gross and Messner, 1999. An illustration of the various components that comprise SRTM is given in Figure 2. The structural dynamic issues associated with a 60-meter mast and large tip mass, i. e., the outboard antenna, deployed from the Shuttle required significant attention during the design and implementation of SRTM. Further, SRTM implemented a mast vibration damping system specifically to meet certain mast dynamic motion constraints, as well as to supplement the Orbiter reaction control system with regard to control system stability. The topic of this paper is the design of the mast vibration damping subsystem. Further, the mast vibration damping subsystem failed to function on-orbit, hence the failure diagnoses that occurred both during the mission, and post-mission are discussed.

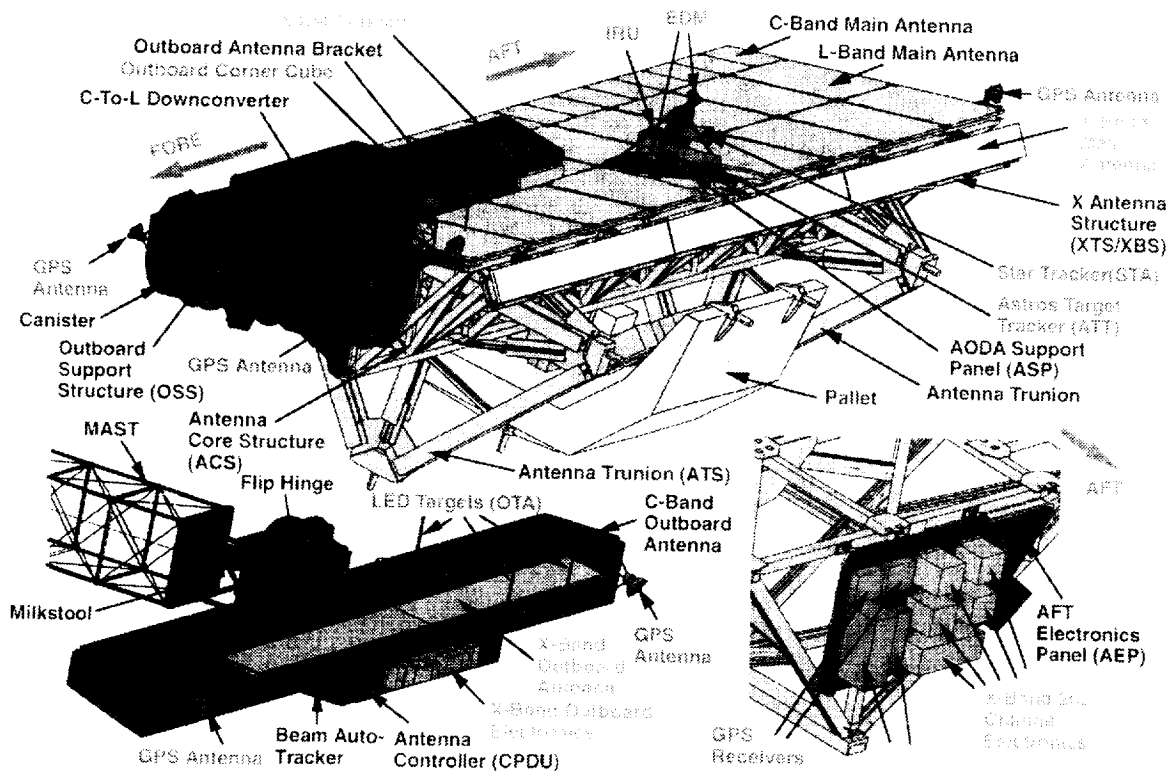


Figure 2. SRTM Instrument Component Layout

Mast Vibration Damping System

The mast vibration damping requirements were driven by several coupled factors, specifically: a) the metrology system's mast dynamic motion tracking capability, b) SRTM instrument pointing requirements, c) attitude control disturbance torques associated, and d) the Orbiter dynamic disturbance environment induced by the attitude control system. SRTM utilized a metrology system to provide relative outboard antenna position and attitude knowledge during radar interferometer operation. This metrology system consisted of two subsystems. The subsystem, which drove the damper design, consisted of the Astros Target Tracker (ATT), and three Optical Target Assemblies (OTA's). The ATT was essentially a star tracker that had been refocused to 60-m. Each OTA contained an LED, which was pointed towards the ATT, and acted as a pseudo-star that the ATT was able to track. The combination of the ATT and OTA's provided an accurate estimate for five of the outboard antenna's six rigid body degrees of freedom, the ATT and OTA constellation does not accurately measure range to the outboard antenna. A Leica range finder supplemented the ATT by directly measuring the distance to a retroreflector array mounted on the outboard antenna. With respect to instrument pointing, the nominal attitude during data acquisition was to: 1) fly the Orbiter with its tail pointed along the velocity vector, 2) rotate the Orbiter about its roll-axis such that the mast was 45 degrees from the local vertical, and 3) radar radiating surfaces oriented toward the ground. The Orbiter reaction control system was used to maintain SRTM pointing within a 0.1 deg attitude deadband, and 0.01 deg/sec attitude rate deadband. Given the attitude requirement and combined SRTM/Orbiter mass properties, the gravity gradient torque was the dominant disturbance torque to the Shuttle reaction control system. Specifically, the gravity gradient torque tended to rotate the combined Orbiter and mast system such that the mast longitudinal axis was oriented along the local vertical. The Orbiter's Digital Auto-Pilot was configured such that the 9-kg (24-lb) Vernier Reaction Control System jets were used for attitude control during radar operations. Based on the attitude control requirements, and configuration versus the disturbance torque applied to the system, the reaction control system generated positive roll commands that resulted in jet firings to counter the gravity gradient torque. As a consequence of these jet firings transient vibrations in the mast were generated. Mast tip motion was not a concern to the operation of the radar as an interferometer provided that the knowledge of the tip motion was acquired. Hence, the ATT and LED's were added to track the mast motion. The capability of the ATT to acquire and track the motion of the LED's defined a maximum rate of mast motion that could be tracked, this limit was defined to be 6 cm/sec (2.36 in/sec) at the tip of the mast. Additionally, in order for the ATT to acquire the LED the mast tip rates were required to be less than 6 mm/sec (0.24 in/sec) for ten percent of the time during data acquisition. Therefore a mast vibration damping system was implemented to enable the ATT to acquire and track the mast motion given the vibration environment generated by the attitude control system.

Vibration Damping Requirements

SRTM implemented a mast vibration damping subsystem in order to meet mast tip dynamic motion requirements. Early in the project design phase, a preliminary coupled Orbiter and deployed mast structural dynamic math model was created. This math model was employed in attitude control simulations to provide: a) propellant consumption estimates, b) mast tip dynamic motion estimates, and c) mast damping requirements. Given that the final damping system implementation was not determined, the preliminary math model was a "modal" model, i. e., the true complex modal behavior associated with discrete viscous damping elements was approximated. The results of these early simulations showed that the mast damping mechanisms should be designed to achieve "high", i. e., greater than 10%, damping ratios in the deployed mast's first orthogonal bending vibration mode pair and the first torsional vibration mode. These requirements were later confirmed via simulation of a final coupled model which included the complex modal behavior associated with the discrete damping elements.

Vibration Damping System Concept

Conceptually, the approach employed towards the design of the mast damping system was to concentrate sufficient modal strain energy at the mast interface to the inboard antenna such that only a few discrete damping elements are required to damp the mast. In practise, what this means is that, the structural elements which connect the mast to the to inboard antenna structure are softened, i. e., their stiffness is reduced, such that approximately half the modal strain of the deployed system's first modes of vibration is concentrated at these elements.

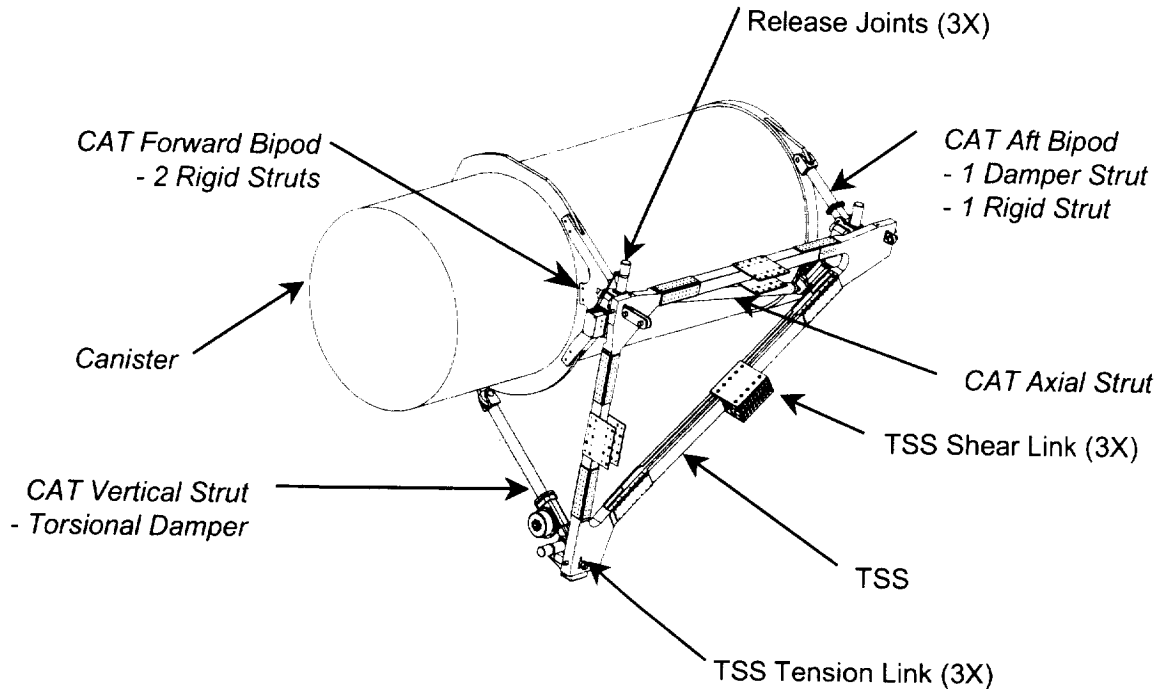


Figure 3. Mast Canister and Canister Attachment Truss (CAT)

The structural attachment of the mast, via the mast canister, to the inboard antenna structure is shown in Figure 3; this structure was called the canister attachment truss (CAT). The CAT is a kinematic, i. e., statically determinate, structure which serves to attach the mast and the mast canister to the inboard antenna structure. The CAT forward bipod and the CAT axial strut form a rigid tripod with a monoball, or spherical bearing, at its vertex. The monoball located at the vertex of this rigid tripod is a fixed rotation point about which the entire deployed mast rotates as a rigid body. The attitude of the mast relative to its fixed rotation point is controlled by the aft bipod, and the vertical strut. The mast damping elements were located at the aft bipod controlled the mast's first two orthogonal bending modes, while the damping element located in the vertical strut controlled the mast's first torsional mode. A conceptual model of the damping system implementation is given in Figure 4.

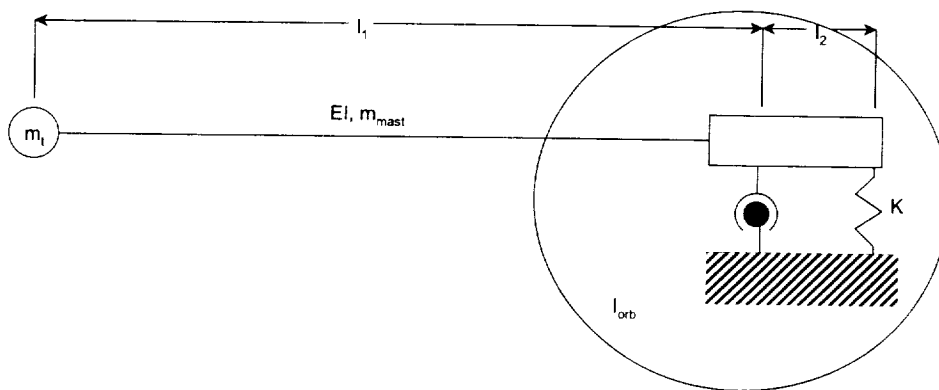


Figure 4. SRTM Conceptual Dynamic Model

Note that the CAT is the only structure, which connects the SRTM outboard equipment, i. e., outboard antenna, mast, and mast canister, to the Orbiter. The mass of the outboard equipment is on the order of 1340 kg (3600 lbm). Hence, the CAT was designed to meet structural requirements derived from launch and landing, i. e., specific loads and frequency requirements. Conceptually it was acknowledged that the

damping mechanisms embedded within the CAT would be required to be locked, i. e., "stiff", for launch and landing, and unlocked, i. e., "soft", during on-orbit operations.

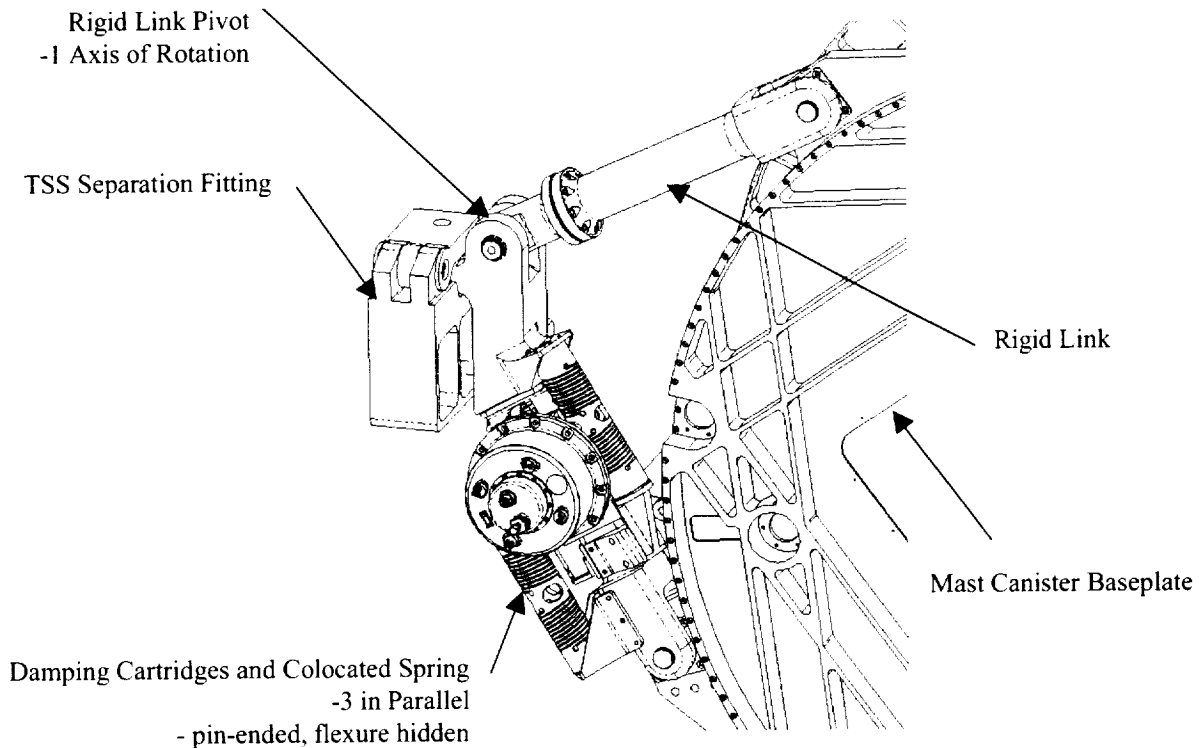


Figure 5. Bending Mode Damping Mechanism (CAT Aft Bipod)

Vibration Damping Mechanism Design

Two distinct damping mechanisms were developed for SRTM. The bending mode damping mechanism is shown in Figure 5; this mechanism is also the CAT aft bipod. The aft bipod upper strut is rigid while the lower strut contains three relatively soft springs and three viscous damping elements. The viscous damping elements are mechanically in parallel with the springs. Additionally, a caging mechanism is employed to lock out the soft springs for launch and landing. The torsional mode damping mechanism is also the CAT vertical strut. The torsional mode damping mechanism is similar to the bending mode damper, but uses only one damping element rather than three. The torsional damping mechanism is shown in Figure 6.

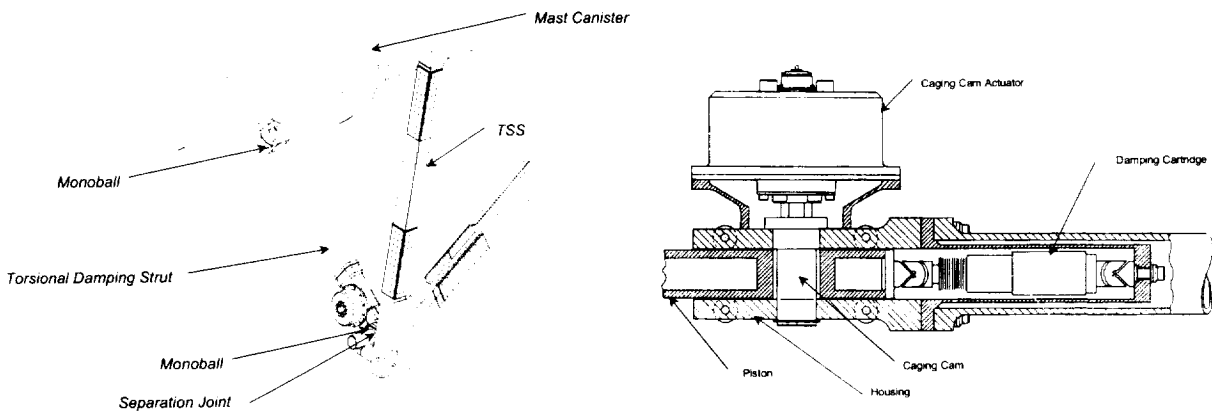


Figure 6. Torsion Mode Damping Mechanism

The dynamic impedances of the respective damping mechanisms were sized in a two-step process. Also, given the CAT geometry, and the mast mode shapes, the sizing effort for a given damper was uncoupled from the other. First, the static spring stiffness was determined as outlined above, that is the mechanical spring stiffness of the damping mechanism was adjusted, in this case reduced, until approximately half the modal strain energy for the mode or modes of interest was concentrated in the elements which represented the damping mechanism. Relative to the bending mode damper, variations on this approach were also tried and it was determined that acceptable results were achieved with the upper bipod strut rigid and the lower bipod strut soft. Specifically, the cumulative static spring stiffness of the bending mode damper lower strut was specified to be 87 kN/m (500 lbf/in). The cumulative static spring stiffness of the torsion mode damper was determined to be 4.4 kN/m (25 lbf/in). The second step in the damper requirement definition process was to determine the damping coefficient. A sensitivity analysis was performed by allowing the cumulative damping coefficient for a given damping mechanism to be analytically varied from zero to infinity. Once the root locus associated with the system's structural dynamics was known, the mechanism damping requirement was determined by selecting the desired set of structural dynamics, i. e., frequency and damping ratio, from the root locus plot. The root locus plot for the bending mode damping mechanism is given in Figure 7, see Umland and Eisen 2001 for a further discussion of the SRTM structural dynamic characteristics. Note that in the root locus diagram the radial grid lines represent constant damping ratio contours, while circles represent frequency given in radian/sec. Further the arrow shown next to the loci indicates the direction of increasing damping coefficient. The cumulative damping coefficient for the bending mode damping mechanism was determined to be 370 kN-s/m (2100 lbf-sec/in), implying that the damping coefficient for each of the three damping cartridges is 120 kN-s/m (700 lbf-sec/in). While the damping coefficient for the torsion mode damping mechanism was specified to be 4.4 kN-s/m (25 lbf-sec/in).

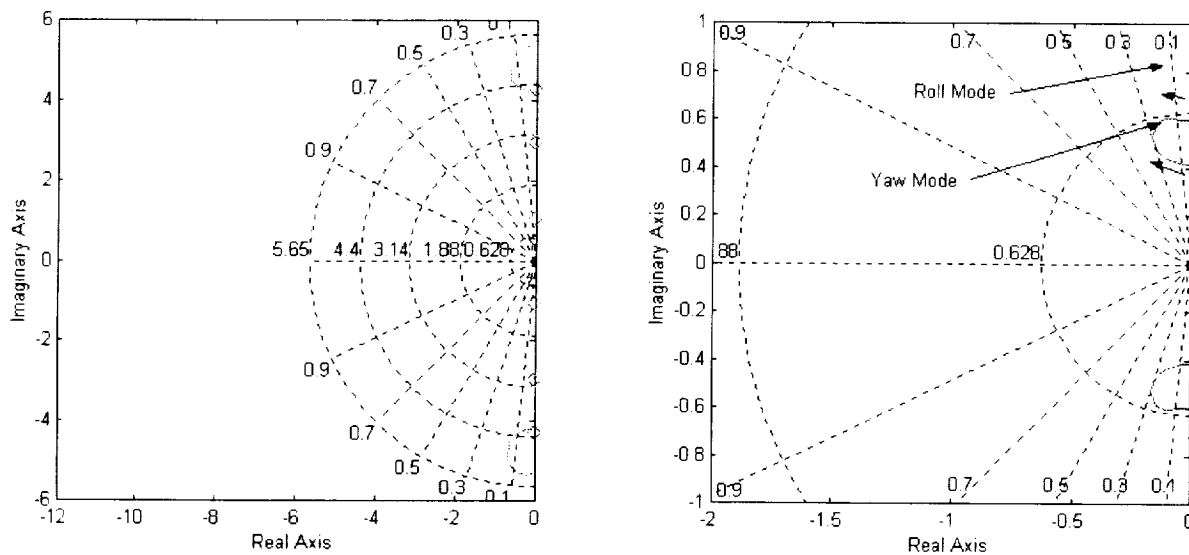


Figure 7. Bending Mode Damping Mechanism Root Locus Diagram

Damping Cartridge Design

A trade study was conducted early in the SRTM design phase, first to determine the necessity for a mast damping system, and then to determine an adequate damping system design concept. The mast damping approaches considered in the trade study included: active struts, Coulomb friction dampers, and linear viscous dampers. A linear viscous damping approach was selected based on several factors: 1) passive energy dissipation, 2) simple design concept, 3) amenability to existing analysis tools, and 4) design heritage. The viscous damping cartridges selected and used in both SRTM mast vibration damping mechanisms were a modification of a hermetically sealed vibration isolator previously described by Klembczyk and Mosher and U. S. Patent 4,638,895. The viscous damping cartridge contained within the vendor's vibration isolator readily met the SRTM damping approach selection criteria. It was expected that several modifications of the existing damping cartridge design would be needed in order to meet SRTM requirements, specifically the physical damping coefficient, and the overall stroke, i. e., length of travel. There are several differences between the SRTM damping cartridges as procured and the vibration

isolator described by Klembczyk and Mosher. First, both the helical spring and the universal, zero friction flexure, were not included as part of the damping cartridge definition, and hence part of the damping cartridge contract. Further, as the damping cartridge orifice matured it was determined that the orifices through the damping head were not required; rather the annular orifice between the damping head and the cylinder was sufficient.

The principles, which govern the damping cartridge operation, are straightforward. A damping head is placed within an essentially closed fluid filled cylinder. When the damping head is translated relative to the cylinder, a viscous shear stress is generated across the fluid that exists within the annular orifice created by the clearance between the damping head outside diameter and the cylinder head inside diameter. Wide ranges of viscous damping coefficients are achievable given such design variables as fluid viscosity, and annular orifice size. The damping head is supported on a piston rod. A set of labyrinth seals, which support the piston rod relative to the cylinder, provide two critical functions for proper damping cartridge operation. First the labyrinth seal is a dynamic seal, i. e., an infinite fluid resistance, such that as the damping head is translated in the cylinder, fluid flows between the two fluid chambers created on both sides of the damping head and not through the annular orifice created between the piston rod outside diameter and the labyrinth seal inside diameter. Secondly, the labyrinth seals act as linear journal bearings such that linear motion of the piston rod relative to the cylinder is possible. Finally, the entire unit is hermetically sealed. A pair of welded metal bellows is used as flexural seals such the entire damping cartridge is hermetically sealed relative to the external environment. The two fluid chambers created by the bellows assemblies are connected via a crossover port, such that the required fluid flow between these two chambers is accomplished. The fluid resistance of the crossover port is negligible.

The driving requirements for the SRTM damping cartridges are given in Table 1. The final damping cartridge designs for the bending and torsion mode damping mechanisms were mechanically identical. The only real difference between the two damping cartridges is that the torsion mode damping cartridge was filled with 10 cSt silicone fluid, while the bending mode damping cartridges were filled with 100 cSt silicone fluid.

During the damping mechanism design phase, possible damping cartridge failure modes were considered, as well as their effects on the overall system structural dynamics, the failure mode credibility assessed, and required failure mode mitigations were identified. Specifically, three cartridge operational states were determined: 1) nominal operation, 2) failure to a "soft" condition, and 3) failure to a "stiff", or seized, condition. Nominal cartridge operation was defined in the sense that, as the cartridge was "stroked", i. e., the damping head translated relative to the cylinder, the force required for relative motion was proportional to the rate of relative motion. Dispersions allowed for under nominal operation included a ten percent absolute tolerance on the cartridge physical damping coefficient such that the variation of the damping coefficient given the operating temperature range requirements was accounted for in the structural dynamic and attitude control assessments.

The "soft" failure condition was a generic failure mode created to describe the situation when the damping cartridge stroked readily, but failed to generate a damping force, i. e., a force that is proportional to the rate of relative motion. A hypothetical example of this failure mode is arrived if one assumes that the damping cartridge fluid leaks from the cartridge via a weldment crack. A damping cartridge "soft" failure due to a weldment failure was considered credible, based an inability to verify weldment workmanship. X-

Table 1. Damping Cartridge Requirements

Parameter	Bending Mode Damping Cartridge	Torsion Mode Damping Cartridge
Stiffness (lbf/in)	25	25
Damping Coefficient (lbf-s/in)	700	25
Stroke (in)	0.860	0.860
Frequency Range (Hz)	0.05 – 2 Hz	0.05 – 2 Hz

ray inspection of all cartridge weldments was considered inconclusive relative to weldment workmanship, given that any conclusion regarding the integrity of the convoluted bellows' inside diameter welds would be speculative at best. Standard leak tests were performed on the bellows assemblies to verify hermeticity, but a evaluation of the bellows inside diameter welds, for a measurement of such parameters as weld penetration, was considered impractical. Further, standard leak test evaluation of the cartridge final closure welds was also impractical. The final closure welds were visually and X-ray inspected. The soft failure of a damping cartridge was considered credible. Additionally, this failure mode was considered to be a random failure, rather than a failure common to all damping cartridges implemented on SRTM. Based on the soft failure mode coupled with a Shuttle payload safety two-fault tolerance requirements, in this case the concern was changes in the structural dynamic which could lead to attitude control instability, the bending mode damping mechanism was designed to incorporate three damping cartridges.

Gas bubble formation within a fluid filled damper is a significant concern; this concern is further exacerbated in space applications. Stewart, Powers, and Lyons, 1998, have discussed an example of this problem in regard to rotary dampers. This degraded performance condition is similar to the soft failure mode. Effectively, the gas bubble can act like a very soft spring that is in series with the damping element. The gas bubble effect can be so severe that from a dynamic perspective a deadzone or backlash is created within the damper when a gas bubble is formed within the fluid. The primary protection against gas bubble formation within the viscous fluid used here was a volumetric overfill, and the use of the bellows as an accumulator, such that pressure was maintained on the fluid once the cartridge entered a vacuum environment. The approach taken toward the over pressurizing the fluid was to fill the damper at a temperature below the specified operating temperature, in this case below -40°C . The silicone fluid has a positive volumetric expansion coefficient relative to temperature, i. e., as the fluid's temperature increases its volume increases as well. Further, in the damping cartridge application considered here the bellows were used as an accumulator, that is the bellows were a flexible container which could expand and contract with the fluid's volumetric changes. Given that the bellows are elastic with volumetric spring stiffness, then as the fluid expands due to a temperature increase, moderate fluid pressure increases are incurred due to the bellows accumulator effect. Finally, thermal control was applied to the damping cartridges such that the nominal minimum expected operating temperature was -17°C (0°F). Given this minimum expected operating temperature, the fluid volumetric expansion, and the bellows spring stiffness, the minimum expected fluid pressure was determined to be approximately 103 kPa (15 psi).

The silicone fluid was degassed prior to cartridge filling. Unfortunately, the fluid was only exposed to a vacuum of approximately 10^{-2} Torr. Further, the fluid was exposed to the ambient atmosphere during the filling process. Hence, the fluid was not considered completely degassed. Therefore, the possibility of bubble formation was considered highly unlikely, but credible. The issue of gas bubble formation within the damping cartridge was ultimately resolved by requiring a set of structural dynamic identification tests be performed during that SRTM on-orbit checkout phase. The success criteria of the identification tests was structured such that if the measured structural dynamics matched preflight predictions then the mission could proceed to its mapping phase, conversely if the measurements did not match the predictions then changes would be required to the attitude control design before mapping was authorized.

The "stiff" failure mode generically described any of the conditions where the damping cartridge was seized, i. e., it could not be stroked. The primary concern here was seizure of the piston rod in the linear journal bearings, i. e., the labyrinth seals, due particulate contamination that could cause this sliding surface interface to jam. The mitigations employed to protect against journal bearing seizure included silicone fluid filtration prior to the cartridge filling process, cartridge component precision cleaning prior to assembly, and cartridge assembly in a controlled clean environment, i. e., a flow bench. Given that the SRTM damping cartridges were a modification of a proven design that had not exhibited any in-service seizure type failures, the design heritage provided additional confidence that this design was not susceptible to seizure type failures. In an effort to minimize any friction force due to incidental contact of the piston rod with the labyrinth seals, tight concentricity tolerances were employed on the cylinder, and labyrinth seal assemblies. Further, cross-blade flexures, i. e., universal joints, were employed at each end of the cartridge such that end moments, which would be created due to various misalignments, would be minimized. Fluid freezing was also classified as a stiff failure. This type of stiff failure was protected against by thermally controlling the damping cartridges such that the nominal minimum cartridge temperature was -17°C (0°F) versus the silicone fluid freezing temperature of approximately -70°C . Further the minimum cartridge operating temperature without thermal control was -35°C . For the purposes

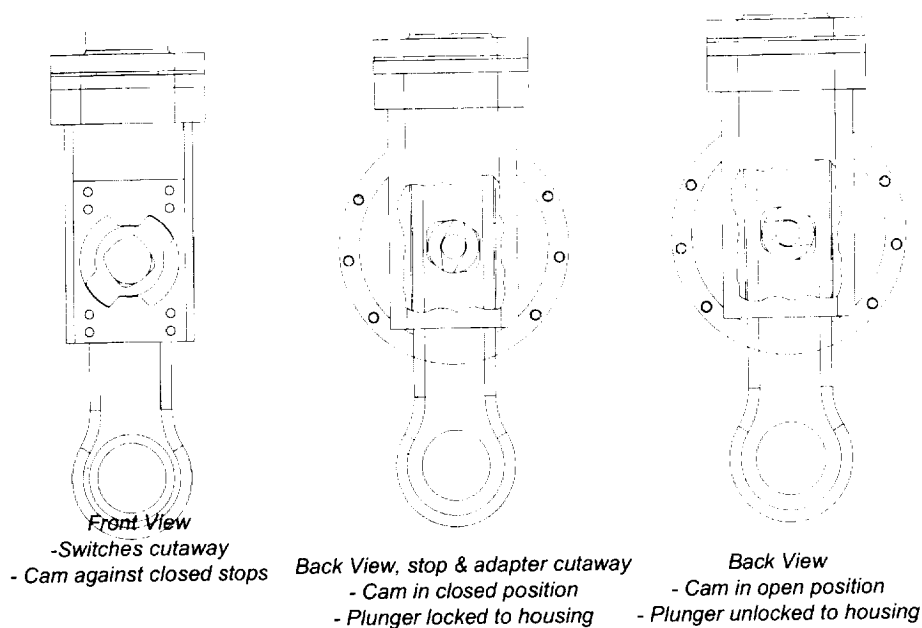


Figure 8. Caging Cam Conceptual Layout

of the overall damping mechanism design, the damping cartridge stiff failure mode was not considered credible based on the mitigations described. On the other hand, for the purposes of the attitude control system the damping mechanism stiff failures were considered credible, this assessment was based primary in regard to foreign object and debris type hazards to the overall damping mechanism and CAT articulation.

SRTM Damping Mechanism Design

Recall that the CAT is a kinematic (statically determinant) truss. It is noted that the CAT aft bipod upper and lower struts, i. e., the bending mode damping mechanism, and the vertical strut, i. e., the torsion mode damping mechanism, are axial force elements. The structural requirements on these truss elements are dependent on mission phase. In general for launch and landing these truss elements were required to be stiff and strong. The specific launch and landing limit load requirements were 49 kN (11,000 lbf), and 120 kN (27,000 lbf), for the aft bipod lower strut, and the vertical strut respectively. While on-orbit these dynamic impedance requirements imply that these struts were very compliant. A common lockable linear bearing design concept was implemented for both damping mechanisms (Figure 8). Supporting a piston with a housing with cam follower bearings created a linear bearing. The piston was locked and unlocked relative to the housing via a caging cam. In effect the caging cam is a diamond pin. The caging cam was actuated by a 565 N-m (5000 in-lbf) DC motor and gearbox assembly provided by American Technology Consortium. Knowledge of the linear bearing state that is, caged, fully un-caged, or in determinant, was provided by a set of limit switches that were actuated by mechanical features on the caging cam. The limit switches used here were the Honeywell 9HM1's. Payload safety considerations levied a two-fault tolerant requirement on knowledge of the caging cam position, and hence the linear bearing status. Therefore, two sets of three independent switches were integrated into each caging cam and actuator assembly, such that positive two-fault tolerant knowledge of the caging cam's position relative to being caged or fully un-caged was provided. Additional knowledge of the caging cam status was inferred via monitoring of the motor current draw during the act of caging or un-caging, and then comparing to similar ground test data.

A linear potentiometer was used to provide a relative displacement measurement for each of the two damping mechanisms. Betatronix, Inc provided the potentiometer. The damper linear displacement measurement was implemented in order to provide additional useful data regarding the state of each mechanism. Further the data obtained from the displacement sensor was considered a measure of the dynamic health of the device since this sensor was sampled at the rate of 1 Hz.

Damper Failure Investigation

Pre-Mission Investigation and Flight Rationale

Approximately two months before the eventual SRTM launch date the flight spare torsion mode damping cartridge was discovered to have seized, while the spare bending mode damping cartridge appeared to function normally. Further quantitative evaluation of both damping cartridges showed that: 1) the spare bending mode damping cartridge function normally, and 2) the torsion mode damping cartridge began to stroke only after a force of greater than 440 N (100 lbf) was applied. Normally, the torsion mode damping cartridge stroked once 1 N (0.25 lbf) was applied. Additional testing showed that once the torsion cartridge was cooled to 0°C the cartridge stroked readily. A trend was inferred based on these two data points in the sense that whatever caused the cartridge seizure was relieved as the unit's temperature was decreased. Based on this trend, a dimensional interference between the labyrinth seal inside diameter and the piston rod outside diameter was suspected to be the cause of the cartridge seizure. The piston rod was 15-5 stainless steel. While the labyrinth seal was made from Torlon material, and installed into a 302 stainless steel housing with a moderate interference fit. Based on the materials used for the labyrinth seal and the piston rod, as well as the residual stress created in the labyrinth seal due to the press fit, it was known that the clearance between the labyrinth seal and the piston rod would increase with a decreasing unit temperature. Hence, given the test data, a possible failure cause was suspected. The torsion mode damping cartridge was disassembled, and a dimensional interference of 0.005 to 0.007 mm (0.0002" to 0.0003") was measured between one of the labyrinth seals and the piston rod. Further it was determined that the piston rod outside diameter had not changed and that the inside diameter of the labyrinth seal was smaller than expected. The design data on the relevant assembly drawing showed that the normal clearance between the labyrinth seal and the piston rod should be 0.035 ± 0.005 mm (0.0014" \pm 0.0002"). Examination of the quality assurance paperwork for each damping cartridge set showed that a final machining operation instruction, where the clearance between the seal and rod was adjusted within the requirements, was omitted on the entire torsion mode damping cartridge lot. Consequently it could not be verified that the clearance between the seal and the piston rod was correct. The required final machining operation and the proper clearance was verified on the bending mode damping cartridges.

Yet, the torsion mode damping cartridges were verified to function properly during acceptance testing 10 months earlier, which implies that adequate, if not the required, clearance existed between the seal and piston rod. Therefore, a very serious concern was evident in that, the labyrinth seal was dimensionally unstable with respect to time. Two possible physical mechanisms were proposed to explain the temporal dimensional instability of the labyrinth seal material: 1) swelling due to silicone fluid absorption, and 2) stress relaxation driven by the residual stress associated with the press fit. Fluid absorption into the labyrinth seal material was not considered credible given the dissimilar chemistry of the silicone fluid and Torlon. Stress relaxation of the labyrinth seal material was postulated as the physical mechanism that led to the seizure of the torsion mode damping cartridge. Included in the damping cartridge assembly procedure is a labyrinth seal post-press fit stress relief heat treatment. During this investigation it was determined that the heat treatment performed was inadequate. This determination was based on a set of tests run on residual labyrinth seal assemblies, which had been previous heat-treated. A second heat treatment was performed on the residual hardware and typically a 0.0005" decrease in the labyrinth seal inside diameter was measured. Therefore, it was postulated that the labyrinth seal long term dimensional change was driven by a stress relaxation mechanism.

The seizure of the spare torsion mode damping cartridge was attributed to two factors: 1) the clearance between the piston rod outside diameter and labyrinth seal inside diameter was less than required on the assembly drawing; and 2) the clearance between these two parts was reduced to an interference via stress relaxation of the labyrinth seal. There was no justification that the flight torsion mode damping cartridge was any different than the spare, thus it was concluded that flight torsion mode damping cartridge was likely to be seized as well. On-orbit operation of the torsion mode damper was not required either for instrument performance or for payload safety. On the other hand, proper bending mode damper operation was required for instrument performance. Payload safety considerations required that the bending mode damper function within an expected and previously assess envelope. An acceptable for flight rationale was generated for the bending mode damper based on: 1) quality assurance paperwork verification that the clearance between the labyrinth seal and the piston rod was per the drawing callout, and 2) an adequate clearance between the seal and piston rod was estimated based on a worse case assumption of the stress relaxation driven dimensional change of the seal inside diameter.

On-Orbit Failure Diagnosis

As part of the SRTM on-orbit checkout procedure, flight rules required that the natural frequencies of the deployed mast's first vibration modes be measured. The rationale behind this requirement was that the stability of the Shuttle's reaction control system is assured by proper placement and sizing of notch filters which then serve to mask low frequency dynamics. This system identification was performed with the dampers locked, and unlocked. The system response was identical for both damper states. Further, during the pulse test with the unlocked damper, zero damper relative displacement was measured via the displacement sensor mounted on each mechanism. Based on comparison of the system identification results from the dampers locked versus unlocked tests it was concluded the dampers were inoperative. The dampers were re-locked, and the mission continued to a successful conclusion. Proper instrument operation was achieved without functional dampers by utilizing overlapping design performance margin contained within the other SRTM sub-systems.

Post-Mission Failure Investigation

Following the mission a failure investigation was conducted in order to determine the root cause of the SRTM damping mechanism failures. The conclusion of this investigation was that both damping assemblies failed due to a common mode failure attributed to the damping cartridge mechanical design. Specifically, it was found that all damping cartridges assembled for SRTM had seized. The SRTM damping cartridge seizure was traced to a dimensional interference between the piston rod outside diameter and the linear bushing inside diameter. It was further determined that the inside diameter of the linear bushing, made from Torlon, had changed dimensionally; i. e., the ID had reduced, thereby eliminating the required clearance between the bushing and piston rod. As discussed above, the two possible physical mechanisms which explain the temporal instability of the bushing inside diameter are: a) silicone fluid absorption by the linear bushing and b) long term creep of the labyrinth seal material was not considered a credible explanation for the dimensional change of the labyrinth seal material. It is noted that all the damping cartridges assembled for SRTM ultimately seized due to labyrinth seal interference with the piston rod; on the other hand, a labyrinth seal test unit that has not experienced long term fluid exposure has not seized. Therefore, it is possible that the assumption that, the dimensional instability of the labyrinth seal due to fluid absorption is incredible, is not valid. The conclusion reached to date is that the dimensional change of the labyrinth seal material is attributable to one probable cause and an additional possible cause, that is stress relaxation and fluid absorption, respectively.

A final technical conclusion reached here is that the material used for the labyrinth seal is inappropriate for this application. An understood but overlooked requirement for the labyrinth seal is that it must retain long term dimensional stability given the very tight clearance requirement between this dynamic seal and its mating part. A greater conclusion is reached regarding this mechanism failure when the design heritage of the damping cartridge is examined. It turns out that; a material other than Torlon was used in previous versions of the damping cartridge design for the labyrinth seal. Therefore the true root cause for the SRTM damping mechanism failure is that the damping cartridge design heritage was voided. An additional comment worth considering is that a protoflight development approach was followed with this system based on project schedule and cost constraints, and consequently specific engineering models were not developed. Hence, in order to meet shelf life requirements, similarity to existing designs was required. Unfortunately, the required similarity was lost due to a seemingly innocuous design change.

Conclusion

The mast vibration damping system implemented for SRTM was discussed herein. The system design followed a straightforward approach and used off the shelf components modified to meet specific performance requirements. Further, this system met all acceptance and performance test requirements, yet failed in-service, i. e., on-orbit. The technical root cause of the systematic failure of this system was identified and discussed. Additionally, a more general failure root cause was discussed. This data is presented in order to benefit future damping system applications.

Acknowledgments

The effort described in this paper was carried out at the Jet Propulsion Laboratory, California Institute of Technology, under contract with the National Aeronautics and Space Administration.

References

D. Gross, and D. Messner, 1999. "The Able Deployable Articulated Mast – Enabling Technology for the Shuttle Radar Topography Mission," Proc. of the 33rd Aerospace Mechanisms Symposium, NASA/CP-1999-209259, Pasadena, CA, pp. 15-30.

A. R. Klembczyk, and M. W. Mosher, 1998. "Applications of Hermetically Sealed Fluid Dampers for Low Level, Wide Bandwidth Vibration Isolation." Proceedings of the 69th Shock and Vibration Symposium.

A. Stewart, C. Powers, and R. Lyons, 1998. "Improvements for Rotary Viscous Dampers used in Spacecraft Deployment Mechanisms." Proc. of the 32rd Aerospace Mechanisms Symposium.

J. Umland, and H. Eisen, 2001. "SRTM On-Orbit Structural Dynamics," AIAA Paper No. 2001-1588, Proc. of the AIAA/ASME/ASCE/AHS/ASC Structures, Structural Dynamics and Materials Conference, Seattle, WA.

29/19

Fly Cast Maneuver for Shuttle Radar Topography Mission

Thomas A. Trautt*

Abstract

The orbital maintenance maneuver referred to as the fly cast maneuver was used in the Shuttle Radar Topography Mission to prevent a 60-meter boom supporting a radar antenna from vibrating excessively. The thruster burn sequence is derived in this paper. Analytical results of the boom response and actual flight data are presented.

Introduction

The Shuttle Radar Topography Mission (SRTM), which flew in February 2000, obtained data to map in three dimensions most of the earth's land surface between 56° south latitude and 60° north latitude. The mission was a joint project between the National Aeronautics and Space Administration and the U.S. National Imagery and Mapping Agency with the Jet Propulsion Laboratory serving as the prime contractor.

The main hardware components are the main antenna mounted in the cargo bay of the space shuttle, a 60-meter deployable boom, and an outboard antenna mounted at the end of the boom. The main antenna is both a radar transmitter and receiver. The outboard antenna is a radar receiver. Radar interferometry is used to compute heights of the earth's surface.

While taking data, the space shuttle was in a decaying orbit and required occasional orbital maintenance maneuvers to boost the shuttle back to the desired orbit. Typically, orbital maintenance maneuvers consist of a single pulse of one thruster or several thrusters fired simultaneously for the duration necessary to boost the space shuttle back to the desired orbit. With this approach, the dynamic response of the SRTM boom cantilevered from the space shuttle would not have had an adequate margin of safety.

To reduce the dynamic response, a firing sequence was derived for a single degree of freedom system. The derived firing sequence is referred to as the fly cast maneuver. The firing sequence consists of three pulses. The first pulse puts the correct amount of energy into the first mode so that a second pulse when timed correctly will cause a static deflection. Since the deflection is static during the second pulse, the duration of the second pulse can be adjusted without affecting the deflection. The correct timing and duration of the third pulse brings the first mode back to rest.

An analogy to a multiple degree of freedom system is derived. The fly cast maneuver derived for the single degree of freedom system is applied to an analytical model of the space shuttle and boom and flight data is presented.

Deployable Boom

The deployable boom was built by AEC-Able Engineering. The boom is composed of 86 collapsible bays and one solid bay at the free end. The length of each bay in the deployed configuration is 0.6975 meter. In the stowed configuration, 85 bays are fully collapsed and 1 bay is partially collapsed. The collapsed bay length is 0.0159 meter. The boom is stowed in a canister with a maximum diameter of 1.36 meters and length of 2.92 meters. During orbit, the boom was deployed one bay at a time from the canister. After the data was taken, which took about 10 days, the boom was retracted into the canister, collapsing one bay at a time while still in orbit.

* AEC-Able Engineering Company, Goleta, CA

Pictures of the boom are shown in Figures 1 through 10.

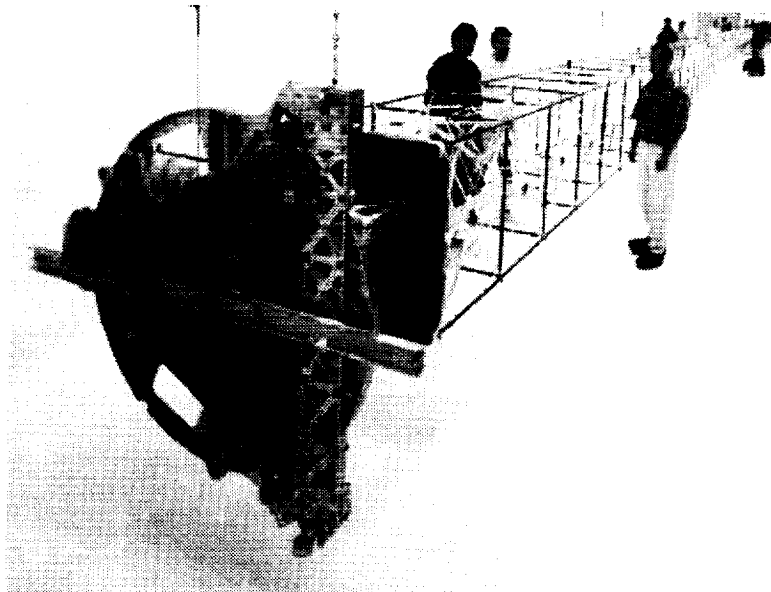


Figure 1. Deployed 60-meter boom

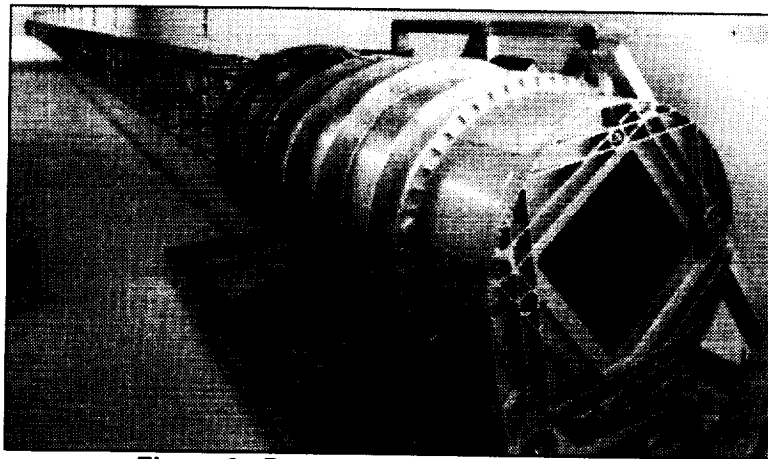


Figure 2. Boom deployed from canister

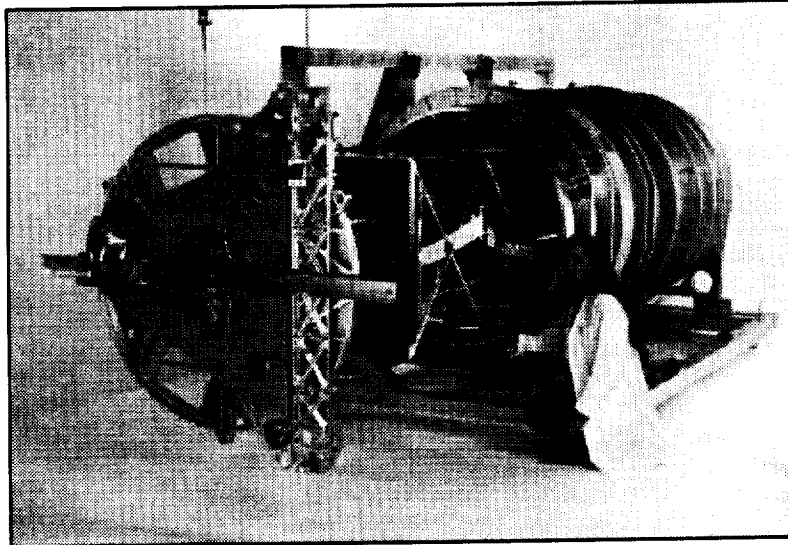


Figure 3. Beginning of deployment

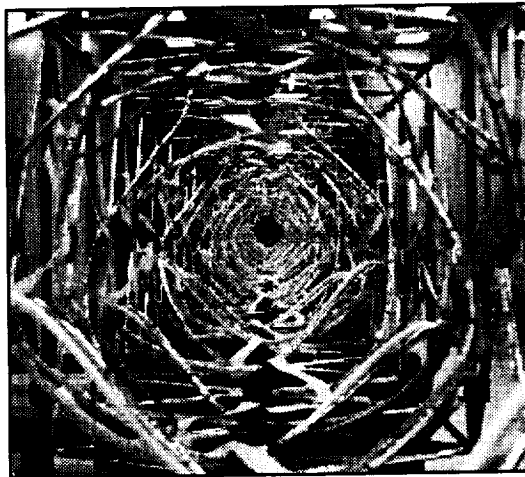


Figure 4. View down the centerline of the deployed boom

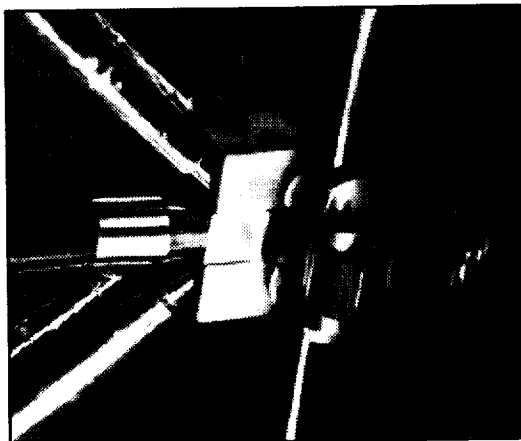


Figure 5. Corner fitting

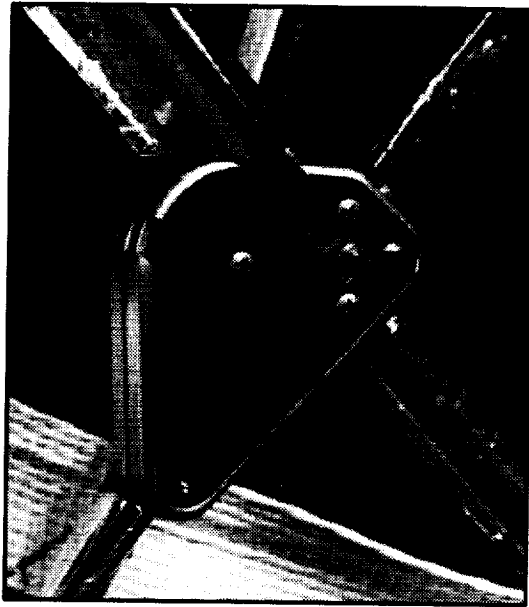


Figure 6. Diagonal latch

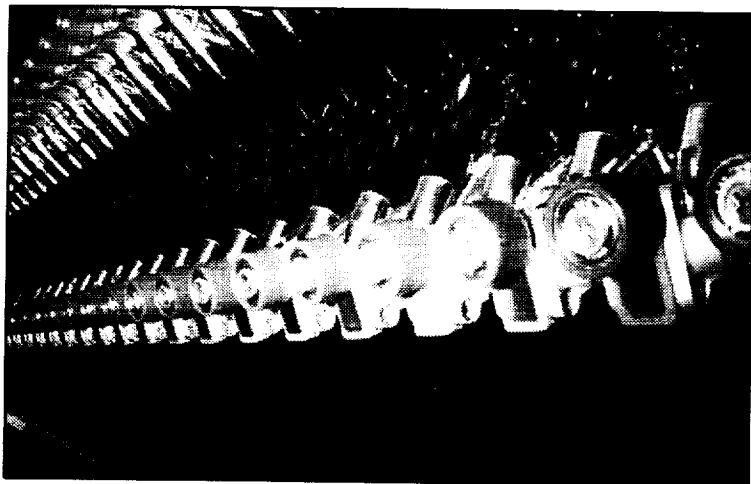


Figure 7. Stowed boom



Figure 8. Boom deploying from space shuttle

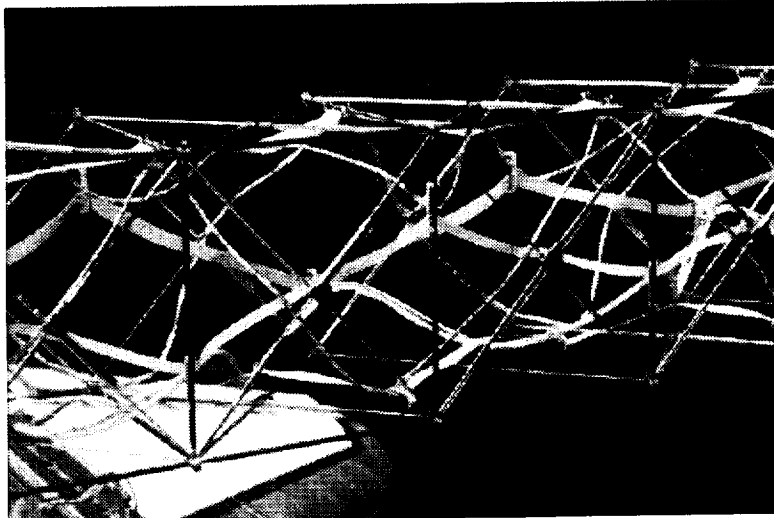


Figure 9. Portion of deployed boom viewed from space shuttle



Figure 10. Antenna and end of boom viewed from space shuttle

Firing Sequence Derivation

The fly cast firing sequence is derived for a single degree of freedom model as shown in Figure 11.

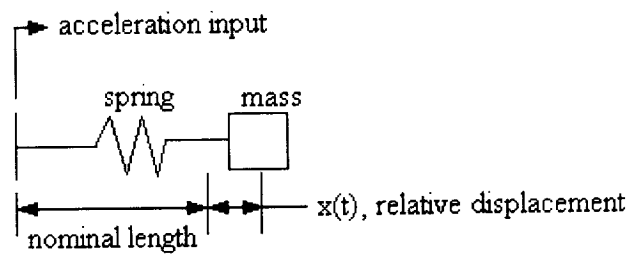


Figure 11. Single degree of freedom model

The equation of motion for this system is

$$\ddot{x} + \omega^2 x = -a \quad (1)$$

where x is displacement of the mass relative to the moving support, ω is the circular natural frequency of the system in radians per unit time, ' a ' is the acceleration input at the support, and the dots indicate derivatives with respect to time. The solution to this equation with constant acceleration is given by the following equations.

$$x(t) = -a/\omega^2 + (x_0 + a/\omega^2)\cos(\omega t) + (v_0/\omega)\sin(\omega t) \quad (2)$$

$$v(t)/\omega = -(x_0 + a/\omega^2)\sin(\omega t) + (v_0/\omega)\cos(\omega t) \quad (3)$$

In these equations, v is relative velocity, x_0 is the initial relative deflection, v_0 is the initial relative velocity, and t is time. We assume the initial displacement and velocity are zero. At the end of a constant acceleration pulse of duration, t_1 , the relative displacement and relative velocity are

$$x_1 = -a/\omega^2 + (a/\omega^2)\cos(\omega t_1) \quad (4)$$

$$v_1/\omega = -(a/\omega^2)\sin(\omega t_1) \quad (5)$$

Turning the pulse off for a duration, t_2 , after the initial pulse will result in the following relative displacement and relative velocity at the end of the t_2 duration.

$$x_2 = x_1\cos(\omega t_2) + (v_1/\omega)\sin(\omega t_2) \quad (6)$$

$$v_2/\omega = -x_1\sin(\omega t_2) + (v_1/\omega)\cos(\omega t_2) \quad (7)$$

From these two equations, the following equations can be obtained.

$$x_2\sin(\omega t_2) + (v_2/\omega)\cos(\omega t_2) = v_1/\omega \quad (8)$$

$$x_2\cos(\omega t_2) - (v_2/\omega)\sin(\omega t_2) = x_1 \quad (9)$$

Applying another pulse at the end of the t_2 duration results in the following response of the system during the pulse.

$$x(t) = -a/\omega^2 + (x_2 + a/\omega^2)\cos(\omega t) + (v_2/\omega)\sin(\omega t) \quad (10)$$

For $x(t)$ to be constant, the following conditions must be satisfied.

$$x_2 = -a/\omega^2 \quad (11)$$

$$v_2 = 0 \quad (12)$$

Substituting equations (4), (5), (11), and (12) into equations (8) and (9) and canceling some terms, we obtain

$$\sin(\omega t_2) = \sin(\omega t_1) \quad (13)$$

$$\cos(\omega t_2) = 1 - \cos(\omega t_1) \quad (14)$$

The solution to these equations with the shortest duration of time is as follows.

$$\omega t_1 = \omega t_2 = \pi/3 \quad (15)$$

$$t_1 = t_2 = (\pi/3)(1/\omega) = (\pi/3)(T/2\pi) = T/6 \quad (16)$$

In the last equation, T is the natural period of the system. At the end of the main pulse of arbitrary duration, t_3 , the relative displacement and relative velocity are

$$x_3 = x_2 = -a/\omega^2 \quad (17)$$

$$v_3 = v_2 = 0 \quad (18)$$

The pulse is turned off for a duration, t_4 , and on again for a duration, t_5 , resulting in the following relative displacements and relative velocities at the ends of the t_4 and t_5 durations.

$$x_4 = x_3 \cos(\omega t_4) = (-a/\omega^2) \cos(\omega t_4) \quad (19)$$

$$v_4/\omega = -x_3 \sin(\omega t_4) = (a/\omega^2) \sin(\omega t_4) \quad (20)$$

$$x_5 = -a/\omega^2 + (x_4 + a/\omega^2) \cos(\omega t_5) + (v_4/\omega) \sin(\omega t_5) \quad (21)$$

$$v_5/\omega = -(x_4 + a/\omega^2) \sin(\omega t_5) + (v_4/\omega) \cos(\omega t_5) \quad (22)$$

Combining equations (21) and (22), the following equations can be obtained.

$$x_5 \sin(\omega t_5) + (v_5/\omega) \cos(\omega t_5) = v_4/\omega - (a/\omega^2) \sin(\omega t_5) \quad (23)$$

$$x_5 \cos(\omega t_5) - (v_5/\omega) \sin(\omega t_5) = x_4 + a/\omega^2 - (a/\omega^2) \cos(\omega t_5) \quad (24)$$

At the end of the t_5 duration, we want the system to return to zero relative deflection and zero relative velocity. Setting x_5 and v_5 to zero results in the following equations.

$$0 = v_4/\omega - (a/\omega^2) \sin(\omega t_5) \quad (25)$$

$$0 = x_4 + a/\omega^2 - (a/\omega^2) \cos(\omega t_5) \quad (26)$$

These equations are combined with equations (19) and (20) to obtain the following equations.

$$0 = \sin(\omega t_4) - \sin(\omega t_5) \quad (27)$$

$$0 = \cos(\omega t_4) + 1 - \cos(\omega t_5) \quad (28)$$

These equations are similar to equations (13) and (14). The solution with the shortest duration is

$$t_4 = t_5 = T/6 \quad (29)$$

Figure 12 shows the pulse sequence and response of a single degree of freedom system with a 0.1 Hz natural frequency. The response to a single pulse is shown in Figure 13 for comparison. The response to a single pulse has twice the amplitude of the response to the fly cast pulse sequence.

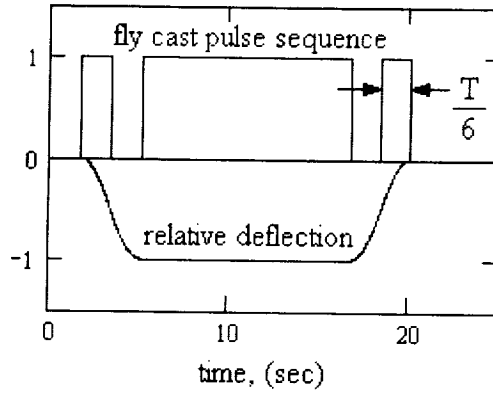


Figure 12. Fly cast sequence and response of single degree of freedom system (normalized to static condition)

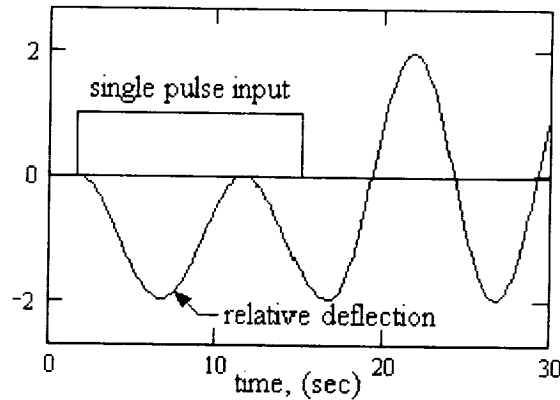


Figure 13. Single pulse input and response of single degree of freedom system (normalized to static condition).

The firing sequence was derived for a single degree of freedom without damping. The error from neglecting damping is analyzed below. The equation of motion for the single degree of freedom with damping is

$$\ddot{x} + 2\zeta\omega\dot{x} + \omega^2x = -a$$

where ζ is the damping ratio and ω is the undamped natural frequency in radians per unit time. The relative displacement and relative velocity responses are given by the following equations.

$$x(t) = \frac{-a}{\omega^2} + e^{-\zeta\omega t} \left[\left(x_0 + \frac{a}{\omega^2} \right) \cos(\omega_d t) + \frac{\frac{v_0}{\omega} + \zeta \left(x_0 + \frac{a}{\omega^2} \right)}{\sqrt{1-\zeta^2}} \sin(\omega_d t) \right] \quad (30)$$

$$\frac{v(t)}{\omega} = e^{-\zeta\omega t} \left[\frac{v_0}{\omega} \cos(\omega_d t) + \frac{\left(x_0 + \frac{a}{\omega^2} \right) + \frac{v_0}{\omega} \zeta}{\sqrt{1-\zeta^2}} \sin(\omega_d t) \right] \quad (31)$$

where

$$\omega_d = \sqrt{1 - \zeta^2} \omega \quad (32)$$

The damping ratio of the first mode of the boom is approximately 0.005. Applying the firing sequence to a single degree of freedom system with this damping ratio results in the relative displacement profile shown in Figure 14. The maximum deflection magnitude is 0.89% greater than without damping. This error is similar to the amount of decay of a damped system over a period, $T/3$, as follows.

$$1 - e^{-\zeta\omega t} = 1 - e^{-(0.005)(2\pi/T)(T/3)} = 0.0104 = 1.04\% \quad (33)$$

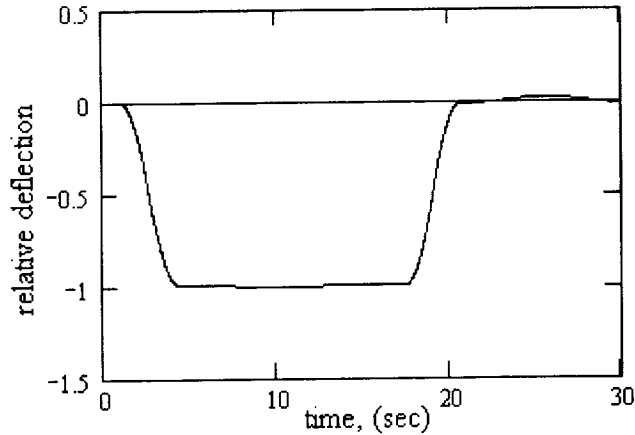


Figure 14. Response of damped system to fly cast sequence (normalized to static condition).

Multiple Degree of Freedom Analogy

Neglecting damping, a multiple degree of freedom system can be modeled in the following form.

$$\mathbf{M} \cdot \ddot{\mathbf{x}} + \mathbf{K} \cdot \mathbf{x} = \mathbf{B} \cdot \mathbf{f} \quad (34)$$

In this equation, \mathbf{M} is the system mass matrix, \mathbf{K} is the system stiffness matrix, \mathbf{x} is a vector of degrees of freedom, \mathbf{B} is a loading matrix, and \mathbf{f} is a vector of forcing functions. The vector, \mathbf{x} , can be related to the modal amplitudes, \mathbf{u} , by the equation,

$$\mathbf{x} = \Phi \mathbf{u}, \quad (35)$$

where the columns of Φ are eigenvectors of the system. The eigenvectors are normalized with respect to the mass matrix to obtain the following result where \mathbf{I} is the identity matrix.

$$\Phi^T \mathbf{M} \Phi = \mathbf{I} \quad (36)$$

Substituting equation (35) into equation (34) and multiplying by Φ^T results in the following equation.

$$\mathbf{I} \cdot \ddot{\mathbf{u}} + \Omega \cdot \mathbf{u} = \Phi^T \mathbf{B} \cdot \mathbf{f} \quad (37)$$

where

$$\mathbf{\Omega} = \mathbf{\Phi}^T \mathbf{K} \cdot \mathbf{\Phi} \quad (38)$$

The matrix, $\mathbf{\Omega}$, is diagonal and the diagonal terms are squares of the natural frequencies of the system. In equation (37), the modal amplitudes are uncoupled from each other. The equation for mode i can be written as follows.

$$\ddot{u}_i + \omega_i^2 \cdot u_i = (\mathbf{\Phi}^T \mathbf{B} \cdot \mathbf{f})_i \quad (39)$$

This equation is analogous to equation (1) for the single degree of freedom. By tuning the firing sequence to a particular mode, the response of that mode will be similar to the single degree of freedom response in Figure 14.

Analytical Results

The boom coordinate system and orientation of the boom relative to the space shuttle are shown in Figure 15. A finite element model is shown in Figure 16.

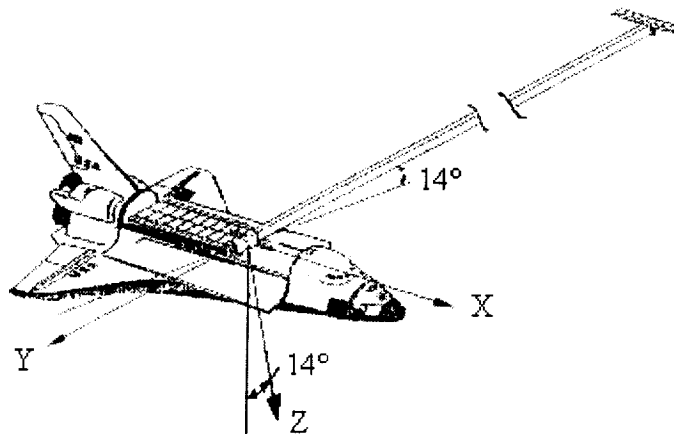


Figure 15. Space Shuttle and boom

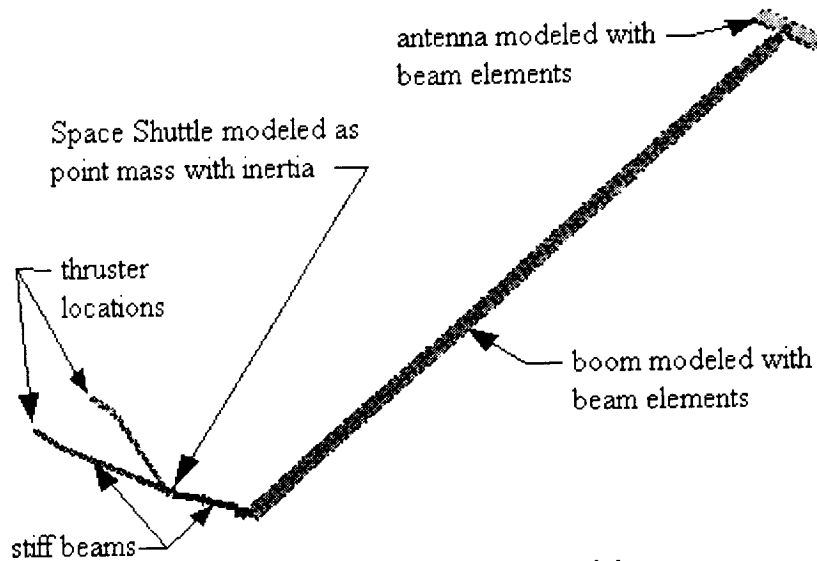


Figure 16. Finite element model

The lowest natural frequency from the finite element model is 0.1 Hz due to bending of the boom about the Z axis. This mode is the most affected by the thrusters used for orbital maintenance. The period, 10 seconds, of the first mode is used to compute the fly cast pulse sequence for the finite element analysis. The pulse durations on the space shuttle can be adjusted in increments of 0.08 second. To compute the worst case response accounting for the time increments of the thrusters, durations of 0.08 second are added to the short pulses and to the durations between the pulses. The short pulse duration for the finite element analysis is then calculated as follows.

$$\text{short pulse duration} = (10 \text{ sec})/6 + 0.08 \text{ sec} = 1.75 \text{ sec}$$

The firing sequence applied to the finite element model is as follows.

on for 1.75 sec
off for 1.75 sec
on for 13.0 sec
off for 1.75 sec
on for 1.75 sec

The boom tip deflections due to the firing sequence are shown in Figure 17. The bending moments at the root of the boom are shown in Figure 18. The bending strength of the boom is 9200 N-m. The two bending moments combined will meet the required safety factor of 2.0.

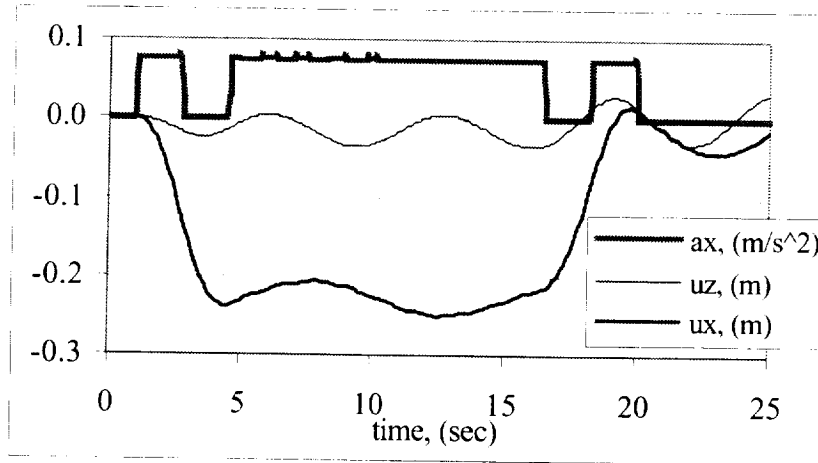


Figure 17. Boom tip deflections and space shuttle x-acceleration

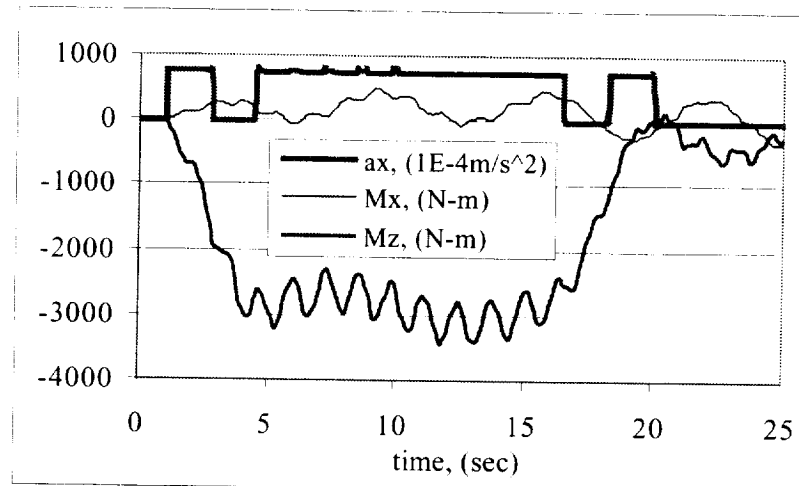


Figure 18. Boom bending moments and space shuttle x-acceleration

Flight Results

During orbit, the first natural frequency of the boom was measured prior to applying the fly cast maneuver. The period for the first natural frequency was 10.53 seconds. As mentioned in the previous section, the pulse durations can be adjusted in increments of 0.08 second. Dividing the period by 6 and rounding to the nearest multiple of 0.08 second results in a duration of 1.76 second. This duration was used for the short pulses and durations between pulses in the fly cast maneuver. Boom tip deflections scaled from camera scenes taken during a fly cast maneuver are compared with the finite element results in Figures 19 and 20. The fly cast maneuver starts at time, 1.0 second, in the plots. The actual deflections are similar to the deflections obtained from the finite element model.

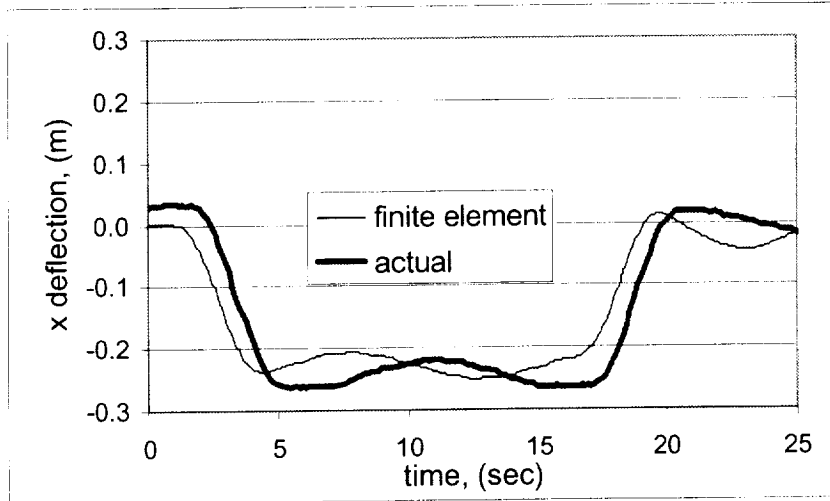


Figure 19. Boom tip x deflections during fly cast maneuver

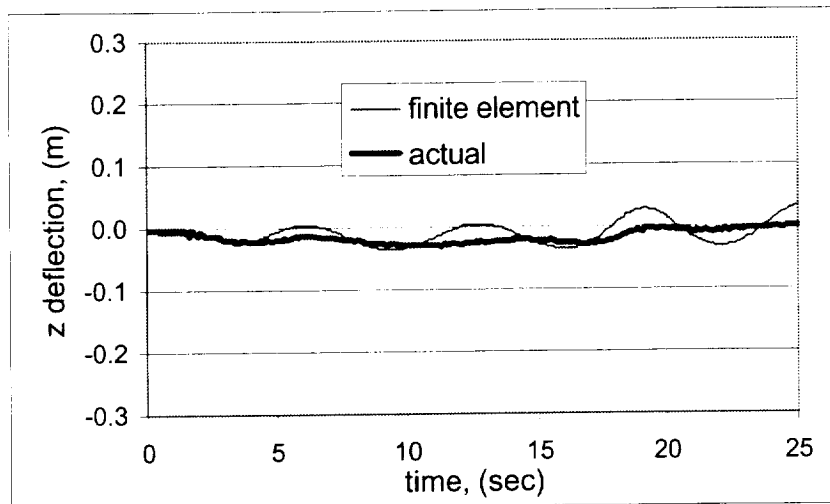


Figure 20. Boom tip z deflections during fly cast maneuver

Conclusion

The typical single pulse orbital maintenance maneuver would have required the boom to be retracted before each maneuver. The boom takes about 20 minutes to retract and 20 minutes to deploy. Using the fly cast maneuver, the loads on the boom were low enough that the boom did not have to be retracted prior to the maneuver and allowed more time for taking data.

Acknowledgments

The author would like to acknowledge Bill Layman from JPL for suggesting that a pulse sequence could be found to deflect the boom in a static deflected shape similar to fly casting a fishing pole.

Development of "Super-Flat" Strain Wave Gearing

Yoshihide Kiyosawa^{*}, Yoshihiro Tanioka^{*} and Keiji Ueura^{*}

Abstract

Strain wave gearing, also known as harmonic drive gearing, has been used in many space applications where lightweight and compact mechanical components are essential. To meet these requirements, a new type of strain wave gearing, the "Super-flat" component set CSD-type, has been developed. There were many issues to be resolved in order to realize the super-flat design. New ideas and new technologies were applied to develop CSD-type gearing. Its exceedingly flat shape has never been seen before in a precision speed reducer. This new gear will allow a new generation of solar array drives and antenna pointing devices to be developed.

Introduction

Strain wave gearing has been used in many space applications since it was first deployed on the Apollo 15 mission 30 years ago. Solar array drives, antenna-pointing devices and robot arms are other examples. In space applications, lightweight and compactness are essential. These requirements led to the development of a new type of the strain wave gearing, the "Super-flat" CSD-type component set.

Development to reduce axial length has been continuing for a quite some time. In 1991, a 40% reduction of the axial length as compared to the conventional type of strain wave gearing CS (or HDUC)-type was developed. The CSF (or HFUC)-type gear was introduced to the market. The CSF-type gear also employed a new tooth profile ("S" tooth profile) and a new diaphragm shape, which can achieve increasing torsional stiffness and torque capacity. It allowed the possibility to design compact space mechanisms. Now, the CSD-type gear has been developed, using also the technology of "S" tooth profile and new diaphragm shape, to reduce the axial length even further. This paper will present the design methods for the super-flat harmonic drive gear.

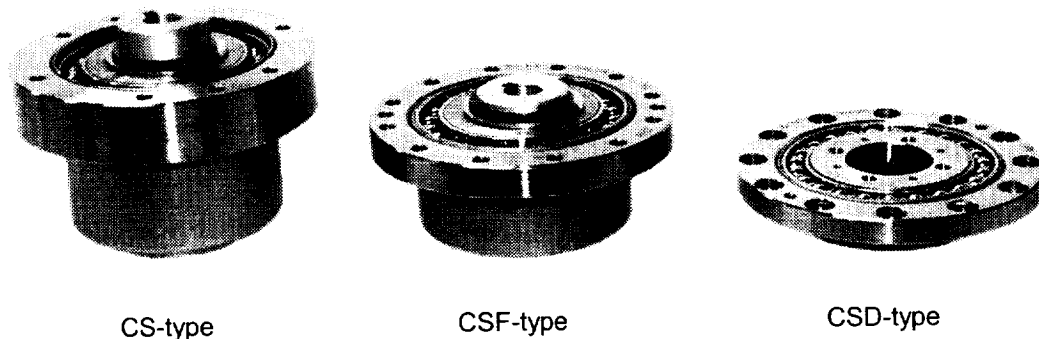


Figure 1. Cup-type strain wave gearing

^{*} Harmonic Drive Systems, Inc., Hotaka-machi, Minamiazumi-gun, Nagano, Japan

Design of "Super-flat" Strain Wave Gearing

The strain wave gearing principle is unique in transmitting high torque through an elastically deformable component. The gear has just three concentric elements:

- The Circular Spline (CS) is a solid cylindrical ring with internal gear teeth.
- The Flexspline (FS) is a non-rigid, thin cylindrical cup with external teeth at the open end of the cup. The closed end of the cup is provided with a mounting flange for connecting machine elements.
- The Wave Generator (WG) is comprised of a thin-raced ball bearing fitted onto an elliptical plug, serving as a high efficiency torque converter.

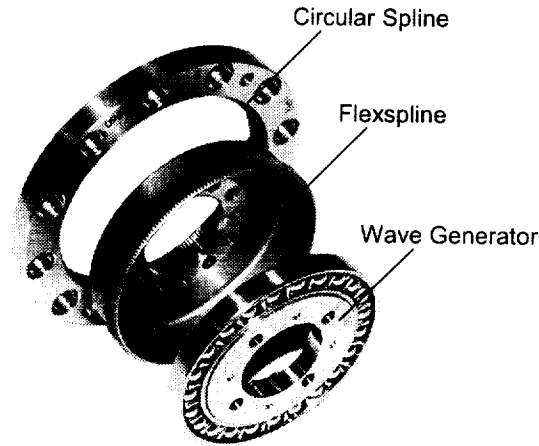


Figure 2. Basic gear components

To reduce the overall length of the gear, a new super-flat shape FS and thin WG bearing were designed. The width of the CS was also reduced to fit to the FS tooth width. Figure 3 shows a comparison between design dimensions of the conventional model (CS-type), the current model (CSF-type), and CSD-type gear. All gears are size 20. This new type of gear is approximately 50% of the length of the CSF-type gear and 30% of the CS-type gear. There were many issues to be resolved in order to realize the super-flat design.

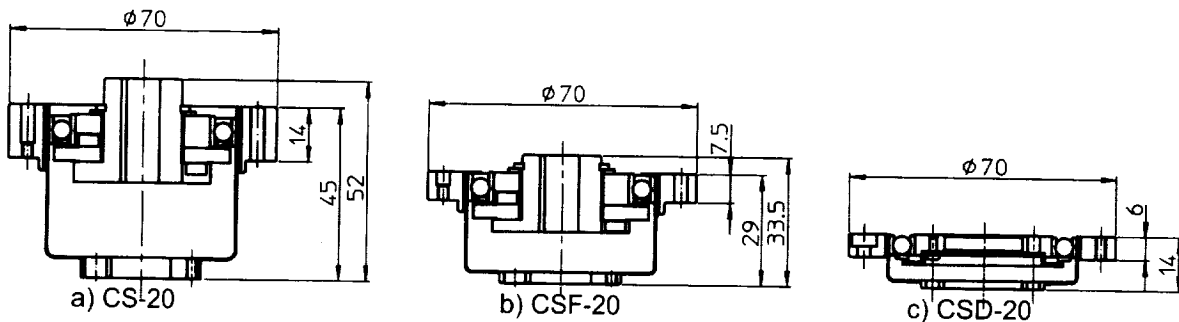


Figure 3. Dimensions of CS-type, CSF-type and CSD-type gear

Technical Challenges Related to the Super-flat Design and their Solutions

Fatigue strength of FS tooth bed

To reduce the overall length of the gear, a new 50% shorter FS was designed. The tooth width itself was reduced by 50% compared to the CSF-type. The reduction of tooth width causes decreasing fatigue strength of the FS tooth bed. This was confirmed by the results of prototype testing at the early stages of development.

The CSF-type FS tooth shape was designed with tooth relief to prevent tooth interference. Figure 4 shows an example of the tooth shape with relieving. In designing the CSD-type FS, the relieving was eliminated to increase tooth contact area as much as possible. A method other than tooth relief was used to solve tooth interference, as will be discussed later. The success of this design was confirmed by the result of prototype testing.

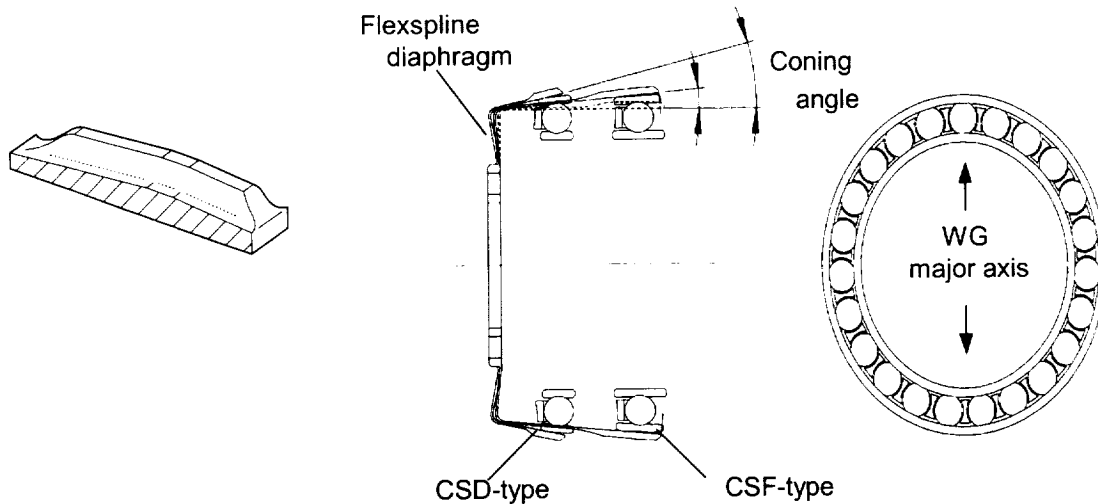


Figure 4. Relieving

Figure 5. Coning of Flexspline

Fatigue strength of FS diaphragm

When the FS and WG are assembled, the FS is elastically deformed into a conical shape by the elliptical shape of the WG. This elastic deformation is called “coning”. The coning angle increases as the FS length is shortened. (Figure 5). The increase in the coning angle will cause an increase in the repeated bending stress at the diaphragm and a reduction in the fatigue strength. Furthermore, as shown in Figure 6, a substantial effect on the fatigue strength is also anticipated if there is a mounting error.

Based on the stress values obtained by finite element analysis, the limit for mounting errors for the FS as a function of the fatigue fracture of the diaphragm were calculated. Figure 7 shows an example of a gear size 50 with gear ratio 100:1. This calculation confirmed that the allowable mounting error, when considering repeated peak torque, exceeds the recommended assembly tolerance of the gear. This provides evidence of the robustness of the CSD-type design.

Starting torque

The larger coning angle poses a challenge to smooth rotation of the gear due to increased tooth interference and a decrease of the gap within the bearing raceway. This causes the starting torque of the gear to increase. To prevent tooth interference, a new elliptical shape for the WG plug has been developed. This new shape is optimized for the CSD-type gear. The new elliptical shape adjusts a moving locus of the FS tooth. It was successfully applied to the CSD-type gear of size 50 and ratio 100:1 with this larger coning angle.

The coning of the FS deforms the outer race of the WG bearing, with larger coning angles causing larger conical deformations. This deformation generates an axial translation between the WG outer race and the inner race causing interference between the races and balls. This tends to increase the starting torque of the gear. To prevent this undesired effect of coning, the radial clearance of the bearing was optimized for the CSD-type gear. As a result of these optimizations, the increase of starting torque was kept at a minimum.

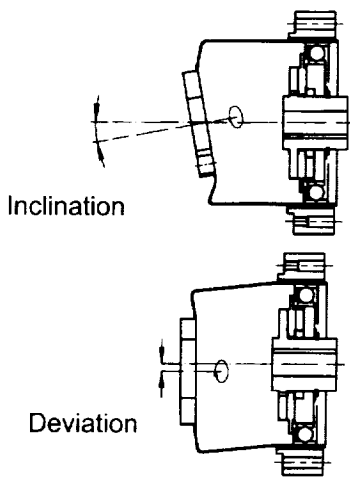


Figure 6. Mounting error of Flexspline

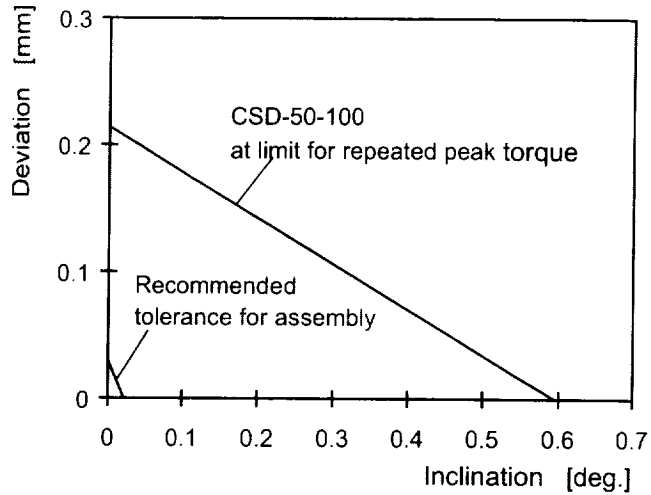


Figure 7. Misalignment limit for Flexspline

Torsional stiffness

The larger coning angle requires larger clearances between the inside of the FS and the outside of the WG bearing. This accommodates the larger conical deformation of the FS. Additionally, the WG bearing has a larger radial clearance optimized for the CSD-type gear. These clearances have an influence on the torsional stiffness of the gear. When a torque is applied to the gear, the clearances within the gear are reduced as the result of elastic deformation of each element of the gear.

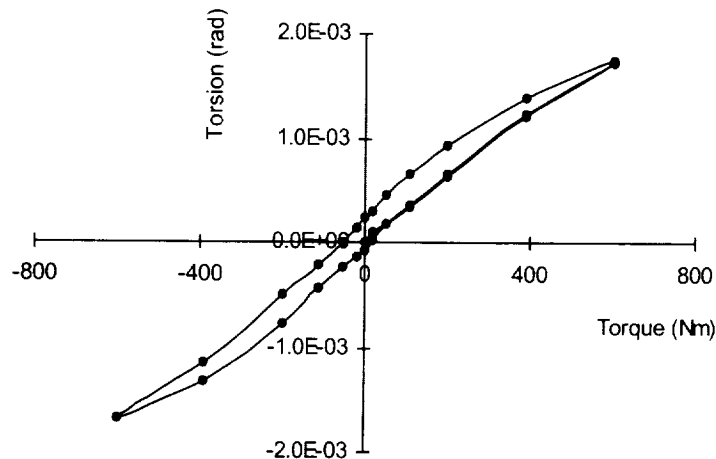


Figure 8. Torque-torsion Curve of CSD-50-100

Figure 8 shows the torsional characteristics viewed from the low speed shaft when the load torque is applied to the low-speed shaft with the high-speed shaft fixed. There is no noticeable decrease in stiffness in the low torque region. This shows that optimizing the clearances within the WG for the CSD-type gear does not degrade the torsional stiffness.

Durability

Figure 9 shows an example of a durability test for the CSD-type gear size 50, ratio 100:1. The test was performed under a sinusoidal load torque of $\pm 686\text{Nm}$ and input speed of 3000 rpm. Harmonic drive grease 4B No.2 was used for lubrication. The durability was evaluated by measuring the increase in lost motion against the total number of revolutions of the WG.

The value of the lost motion is the torsional angle viewed from the low speed shaft when a small torque (approximately 4% of the rated torque) is applied to the low-speed shaft with the high-speed shaft fixed. The angles measured by performing this test in the clockwise and counterclockwise directions are added together. By reviewing the increase in the trend of lost motion versus the number of WG revolutions, it is possible to predict the subsequent wear with additional WG revolutions. As the result of the test, virtually no increase in the lost motion value was found at the total of 4×10^8 WG revolutions. The test results illustrate the high durability of the CSD-type gear under conditions indicated.

Wear life of the gear depends on the operating condition and lubrication. In space applications, a special vacuum-suitable lubricant is normally used. These durability test results can not be applied directly to space applications. Instead, extensive testing must be conducted to verify the suitability of other greases and under other operating conditions. These durability tests should be conducted for both the gear set and spacecraft as a whole.

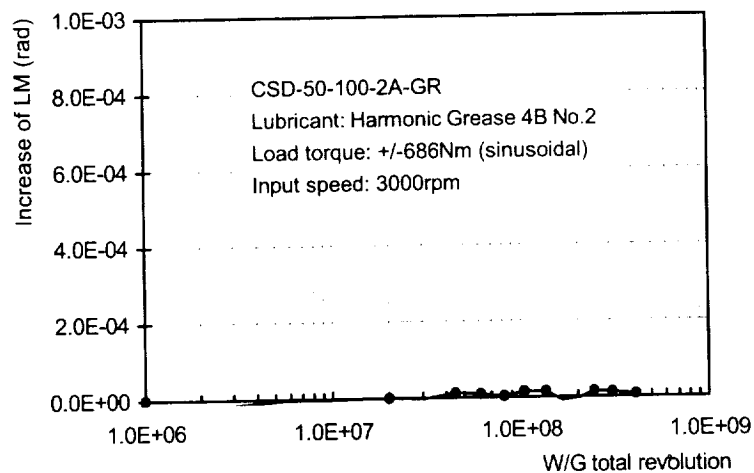


Figure 9. Durability test result

Further Development

The CSD-type gear was designed to have an axial length that is as short as possible. The next step in developing lightweight and compact gears involves the utilization of an aluminum alloy for the WG plug and CS. The CS can consist entirely of an aluminum alloy or feature a composite design using aluminum and either cast iron or stainless steel. This would greatly improve power density by reducing weight. A version of this gear is under development for industrial applications. A prototype with an aluminum alloy WG plug and a composite CS made from aluminum alloy and cast iron has achieved an equal wear life as the current model of the same size. A version for space applications would feature a CS composite using an aluminum alloy and stainless steel. However, there are technical issues to be resolved for joining stainless steel and aluminum components. These issues are left as a further development subject.

Conclusion

CSD-type strain wave gearing realizes an exceedingly flat shape that has never been seen before in a precision speed reducer. Despite many technical challenges to achieving this flat design, the decrease of

torque capacity can be held to 30% in comparison with CSF-type. However, the advantages in compactness and weight savings are still maintained. Figure 10 shows the relationship between volume and rated torque. Figure 11 shows the relationship between mass and rated torque for each type of strain wave gearing. The CSD-type is approximately 27% smaller than the CSF-type and approximately 60% smaller than the CS-type in volume. It is also approximately 20% lighter than the CSF-type and approximately 37% lighter than the CS-type in mass per rated torque. These results show that the power density of CSD-type is higher than the other types of strain wave gearing. The size and mass savings will be amplified when the design of the entire spacecraft is considered. This new gear will allow a new generation of solar array drives and antenna pointing devices to be developed.

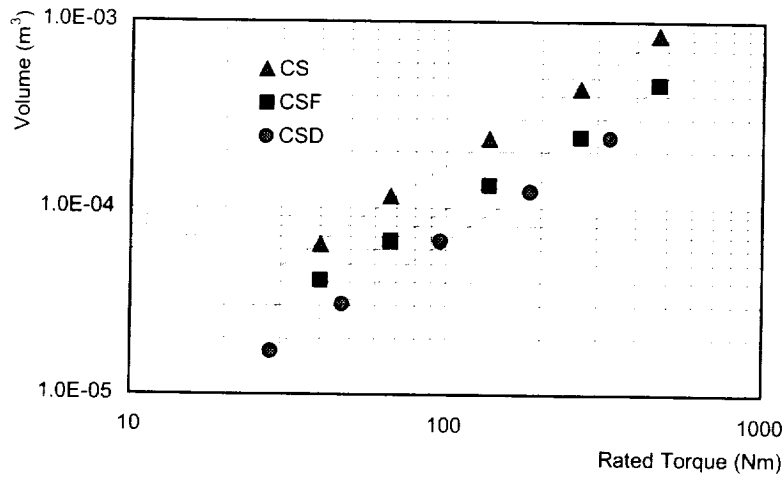


Figure 10. Relationship between volume and rated torque

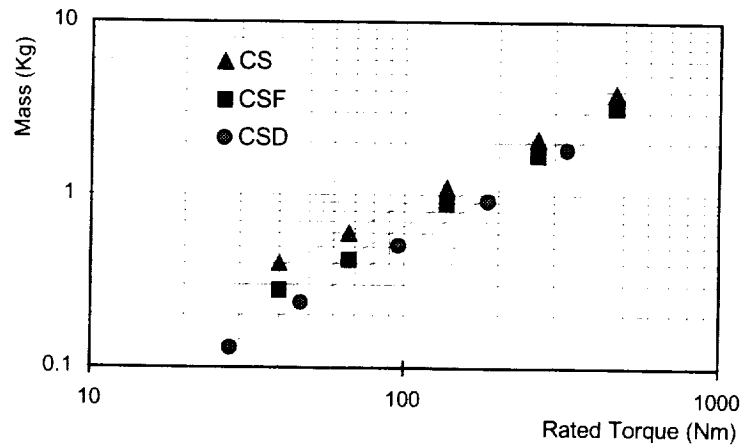


Figure 11. Relationship between mass and rated torque

References

1. Kiyosawa, Y., Sasahara, M., and Ishikawa, S., "Performance of a Strain Wave Gearing using a New Tooth Profile", ASME, Proc. International Power Transmission and Gearing Conference, April 1989, Vol.11, pp. 607-612.
2. Kiyosawa, Y., Takizawa, N., Ohkura, T. and Yamamoto, Y. "A New Strain Wave Gearing: Performance Evaluation", JSME Proc. MPT,'91 International Conference on Motion and Power Transmissions, November 1991, P.1132-1136
3. Keiji Ueura, Dr. Rolf Slatter "Development of the harmonic drive gear for space applications", ESA Proc. 8th European Space Mechanisms and Tribology Symposium, September 1999, pp. 259-264

2/3/01

Zero Play Hinge Latch

Mike Cabiran

Abstract

A zero play hinge latch was designed by using a tapered latching pin to stop the hinge from returning from its unfolded position. The tapered latch pin would hold the hinge without any play by wedging it against a backstop. Any play caused by tolerances is taken up by additional axial movement and therefore wedging by the spring-loaded tapered latching pin. This particular idea should be widely useable in space structures since many stiff, long, and light structures are used in space as often it is necessary to keep play at a minimum. Some reasons for this would be the need to hold a camera steady to focus, to hold stowage in precise volumes, etc.

Introduction

This paper presents a description of the design, manufacture, testing, and problems of a zero play latch design using a tapered latch pin. The zero play hinge latch was designed to provide a small, stiff, minimum play hinge and latch arrangement for folding, then unfolding a tubular frame, as shown in Figure 1, which would support a cloth cover as shown in Figure 4. Figure 4 shows the frame and cloth cover but not the cord that goes through the holes and around the frame and ties at the end. This frame and cloth cover were originally designed to be folded into a compact shape, transported to the International Space Station (ISS), then through several hatches to the Zarya module, (formerly known as the FGB module), unfolded, then clamped in position in the Zarya module while on-orbit as shown in Figure 5. Figure 5 shows FGB enclosure 17 clamped to the Zarya frame. Some dimensions are shown. Also the Crew Transfer Bag (CTB) is shown in the frame. This frame with the cloth cover was called the FGB enclosure. The FGB enclosures were too large to fit through the entry hatches of the modules of the ISS at their full volume and therefore had to be folded to fit through when on-orbit. When they were unfolded, they had to be precisely sized and stiff since any extra play would result in violating the imposed boundaries of 1 cm (0.394 in) outside of the defined volume. This was to prevent interference by the stowed items with delicate avionics and clearances used for ventilation. Other requirements were that the FGB enclosure had to be able to be assembled into a larger space than it could fit through meaning that it had to easily expand into place. It had to be able to be easily clamped into place in zero gees and without any tools. See Figure 5. Also, there could be no pinch points in the hinge mechanism. The hinge needed to be about as stiff as the tubing, however, much of the stiffness of the enclosure assembly was provided by the cross bracing from corner to corner of the assembly with Nomex webbing as shown in Figure 4. Two main features of the enclosure then was that it had to be foldable and compact, and once unfolded, it had to be stiff. One of the problems with making complex mechanisms stiff is the accumulation of clearances due to tolerances from manufacturing. This problem was solved by using a tapered latch pin, which by axial movement could hold the hinge open and take up any accumulation of clearances.

Description of a Zero Play Hinge Latch

The actual loads on the FGB Enclosure were relatively low since they were caused by stowed goods in a micro-gravity environment. The maximum load the frame would encounter from acceleration would be .11 g's from a berthing maneuver for a duration of 1 second. During this maneuver the frame would need to restrain the mass of its contents, i.e., CTBs, to within 1 cm. The CTBs have a mass density of 400.5 kg/m³ or about 22.7 kg for 1 full size CTB. The FGB volumes are numbered from 1 to 22 and the volumes we were designing for, 1-4 and 14 and 17 were calculated to deflect at most 0.292 cm (0.115 in) from the

Lockheed Martin Space Operations, Houston, TX

1 second of .11g berthing acceleration. The size of the FGB enclosures varies from 0.481 to 0.065 cubic meters (17 to 2.29 cubic feet) and in length from 32.5 to 1388.4 cm (12.8 to 54.7 in). Since every kilogram of mass is expensive to launch and since the loads were low, the frame was made with relatively small, 1.27-cm (0.5-in) outside diameter x 0.953-cm (0.375-in) inner diameter aluminum tube. The hinges were then made as small as reasonably possible or 1.78 x 2.29 x 5.84 cm (0.7 x 0.9 x 2.3 in) not including the pins used to connect with the tubing. Enclosure 17's mass is 3405 g (7.5 lb) and the hinge assembly mass is 81 g (0.178 lb).

The FGB enclosure is transported to the FGB volume in the Zarya module of the ISS and unfolded into the volume while the panel door is being held open. When possible, one side of the enclosure is clamped to the Zarya frame and this side and frame serves as a stable base the astronaut can hold onto and from which they can unfold the rest of the frame. Then, the opposite side of the enclosure is clamped to the Zarya frame. Finally, the back part of the FGB enclosure is pushed out into the empty volume and the hinges lock into place. The spring loaded panel door is allowed to close. The FGB enclosure assembly was briefly tested by an astronaut and her comments helped guide the development of the enclosure.

The hinge is expected to be folded then unfolded at least once and possibly more times if the enclosure is removed and stored or reinstalled. The hinge is unlatched by pressing in on the latch pins with the thumb or forefinger from inside the enclosure. It can also be unlatched from outside of the enclosure by pulling on the back of the latch pin with the latch pin grip (Figure 2).

The hinge is made up of a double hinge piece with holes for two hinge axles and corresponding holes for two hinge latch pins. Hinge axles are placed in the hinge axle holes in the double hinge and held in place with retaining rings. Springs are placed in the hinge latch pin holes before the hinge latch pins are placed in the holes. The single hinges are fit over the hinge axles while pressing the hinge latch pins in the latch pin holes by compressing the springs. A latch pin screw then attaches the tapered latch pin to the latch pin grip assembly which has two spring pins. These spring pins are used to hold the latch pin in the fully retracted position so that it will not interfere with closing the hinge assembly. The latch pin grip assembly is not necessary for the zero play hinge latch assembly to work, but it makes it easier to use (Figures 1 and 2).

The effect of the tapered hinge latch pins is that the single hinges on the foldable tubes are wedged between the backstop of the double hinge and the tapered wedge of the latch pin. The tapered latch pin will not allow any play. It will do this by springing axially forward to take up any gap that would be opened by play in the hinge assembly. This gap is usually caused by clearances due to tolerances.

Tests and Results

The object of this test was to see whether the tapered latch pin assembly truly has removed all of the play from the mechanism. Table 1 shows the play at the end of a typical zero play hinge latch for side 1 and side 2 with the hinge latch assembly locked in the open position. Figure 3 shows the setup of the measuring equipment. Play was measured in the rotational direction. This is the direction that the hinge would normally rotate. The play in the opened, rotational direction is a very low value 0.00254 - 0.00381 mm (0.0001-0.00015 in) but is not zero. This was caused by the fact that in testing it a certain amount of force was applied to the hinge, about 30 g (1 oz), so that some reading would appear on the dial indicator. It was necessary to do this to make sure the weight of the hinge was not preventing the hinge from moving freely. When the force was applied, it probably pushed the latch pin backward in an axial direction, causing some looseness. The reading would be closer to zero if less force were used. After the play in the hinge was measured, each side of the hinge was taken apart and the axles and holes were measured. These results are given in Table 1. Using basic geometry and trigonometry, the play was calculated in the hinge assembly assuming no wedging action of the latch pins, but just a straight latch pin from one end to the other. These results are also given in Table 1. When comparing the play in the hinge latch in the opened and locked position with the calculated play from the relatively loose fit of the hinge axles in the holes in the rotational direction, one can conclude that the tapered hinge pins are preventing a large amount of play in the hinge assembly in a rotational direction. Theoretically the play should be zero with the tapered latch pins.

Table 1 also shows the play at the end of a typical zero play hinge latch for side 1 and side 2 perpendicular to the direction of rotation with the hinge locked in the open position. The amount of play in this direction will depend on the interaction of the clearance between the hinges, and the clearances between the holes and axles of the hinges. The clearance between the hinges is listed as axial space between the hinges in Table 1, as well as the clearance between the hinge axles and the hinge axle holes. All of these clearances cause play in the hinge when the hinge is not using the wedged latch pin. An attempt was made to measure the play perpendicular to the direction of rotation and that is listed in Table 1 also. There were problems in this regard because when attempting to measure the play in the unlocked position, the hinge tended to move not only in the direction of measurement, but also perpendicular to it. In addition, the indicator tended to slip off the top of the circular rod where the play was being measured. The result shown in the table is from attempts to measure the play on each side. Each side was added up proportionally so that the result would show the play from one end to the other.

In retrospect, on the single hinge, it would be better to use a sharper edge with a taper on it to match the taper on the latch pin, and to use a much stronger and harder material without a coating that could flake off. On the latch pin, it would be better to use harder material, and no coating and to reduce tolerances. On the double hinge it would have been better to use closer tolerances.

Lessons Learned

1. Hard anodized surfaces and hard low friction surfaces will flake off if the contact stress is high enough.
2. Contact stress could have been reduced by making the mating hinge face tapered like the hinge pin.
3. Frictional coefficients vary widely and depend among other things upon the finish of the mating surfaces, the humidity, the speed of loading, the duration of loading, etc. Since coefficients vary so widely, it is necessary to test the device under exactly the same conditions that you expect it to see in service.
4. Use hard surfaces and underlying materials on both bearing parts.
5. The latch pin will tend to back out slowly if a low friction coating and taper is used on the pin. One may consider locking the pin in place to counteract this.

Advantages of the Zero Play Hinge Latch

1. Zero or near zero play in the direction of rotation of the hinge.
2. Zero or near zero play in the direction perpendicular to the hinge due to the wedging action.
3. Wedging action is available to pre-load the hinge in the open position.
4. The taper helps the latch to unlatch by tending to push out the tapered pin.
5. A twisting action with a pulling or pushing action tends to make the tapered latch back out even more easily under load.

Areas of Concern

1. Sliding out of the hinge pin especially when a hard nickel/Teflon coating is used on the mating surfaces.
2. Working out of the latch pin when the hinge part is oscillated especially in an axial direction or rotary axial direction to the latch pin when using low friction coatings.
3. Overloading the contact area between the hinge and the tapered pin to beyond the contact stress limit, whether it is a hard coating or the underlying material.

Conclusion

In conclusion, the zero play hinge latch will reduce any play in its hinge mechanism to virtually zero when it is carefully designed. Areas of concern are the loads on the hinge, the contact area of the tapered latch on the hinge, the coatings on the mating surfaces and designing them so they do not flake off, and the tendency of the tapered hinge pin to work itself out under continued load if it is not restrained. All of these issues should be successfully addressed in the design. There remains more applications and areas that can be studied in regards to this mechanism and its use in space.

Table 1. Zero Play Hinge Latch

Results and Measurements from Test on the Zero Play Hinge Latch	mm (in)
Play In the Direction of Rotation	
Side 1 Play at the end of the Zero Play Hinge Latch from 30 gm force	<.00254 (<.0001)
Side 2 Play at the end of the Zero Play Hinge Latch from 30 gm force	<.00381 (<.00015)
Side 1 Latch Pin Outside Diameter	6.322 (0.2489)
Side 1 Latch Pin Hole Inside Diameter	6.388 (0.2515)
Side 1 Latch Pin/Latch Pin Hole Clearance	0.066 (0.0026)
Side 1 Hinge Axle Outside Diameter	6.337 (0.2495)
Side 1 Hinge Axle Hole Inside Diameter	6.363 (0.2505)
Side 1 Double Hinge Axle Hole Inside Diameter	6.388 (0.2515)
Side 1 Hinge Axle/Hinge Hole plus Hinge Axle/Double Hinge Hole Clearance	0.077 (0.003)
Side 2 Latch Pin Outside Diameter	6.337 (0.2495)
Side 2 Latch Pin Hole Inside Diameter	6.388 (0.2515)
Side 2 Latch Pin/Latch Pin Hole Clearance	0.051 (0.002)
Side 2 Hinge Axle Outside Diameter	6.337 (0.2495)
Side 2 Hinge Axle Hole Inside Diameter	6.363 (0.2505)
Side 2 Double Hinge Axle Hole Inside Diameter	6.363 (0.2505)
Side 2 Hinge Axle/Hinge Hole plus Hinge Axle/Double Hinge Hole Clearance	0.052 (0.002)
Calculated amount of play without the wedging action due to loose fit between axes, pins and holes in the rotational direction at 35.56 mm (1.4 in) from axle axis.	1.27 (.050)
Play Perpendicular to the Direction of Rotation	
Side 1 Play at the end of the Zero Play Hinge Latch from 30 gm force	<.00508 (<.0002)
Side 2 Play at the end of the Zero Play Hinge Latch from 30 gm force	<.00508 (<.0002)
Axial Space Between Side 1 Hinge and the Double Hinge	.3175 (0.0125)
Axial Space Between Side 2 Hinge and the Double Hinge	.2413 (0.0095)
Measured then calculated amount of play from one end to the other without the wedging action due to loose fit between the parts and the holes and axes at 35.56 mm (1.4 in) from axle axis.	1.1684 (0.046)

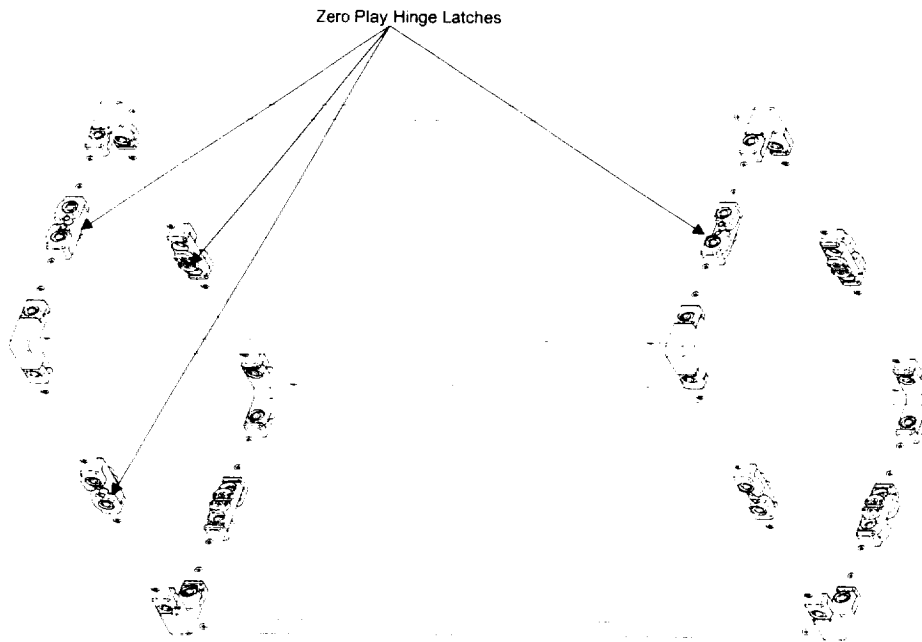


Figure 1. FGB Enclosure 17 Frame with Zero Play Hinge Latches

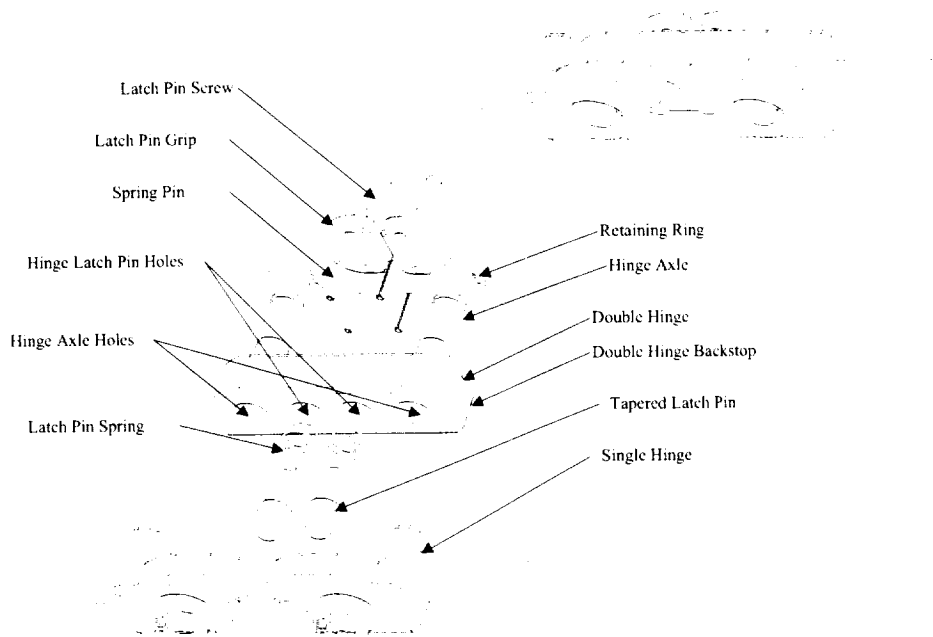


Figure 2. Zero Play Hinge Latch - Exploded and Assembled Views

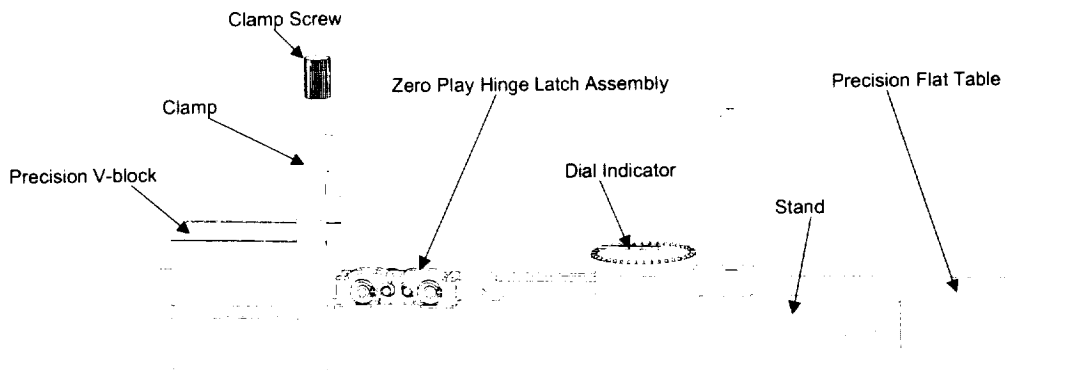


Figure 3. Zero Play Hinge Latch Test Assembly - Rotational Direction

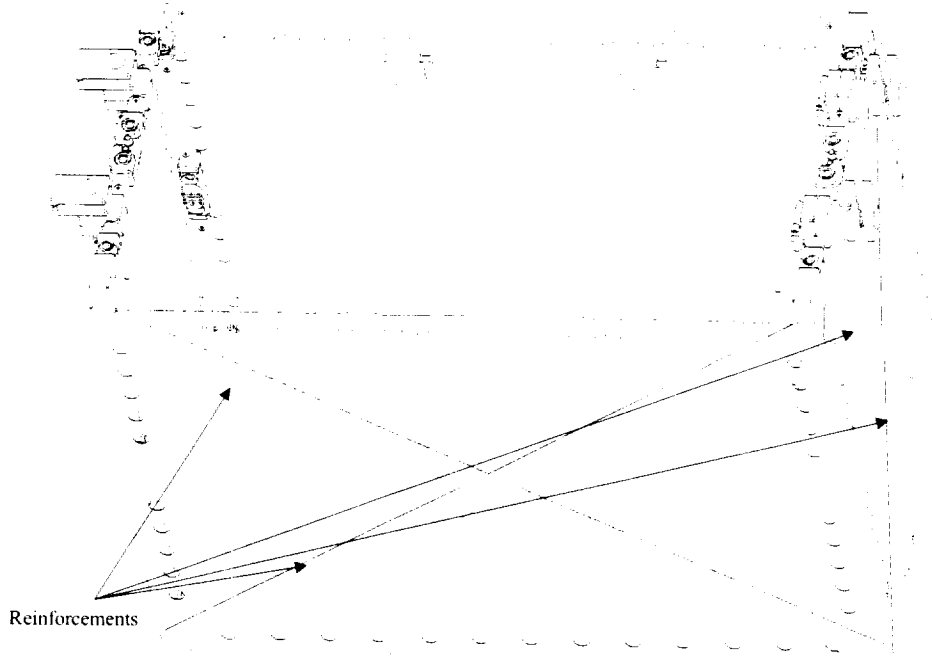


Figure 4. FGB Enclosure Frame 17 with Cover and Reinforcement

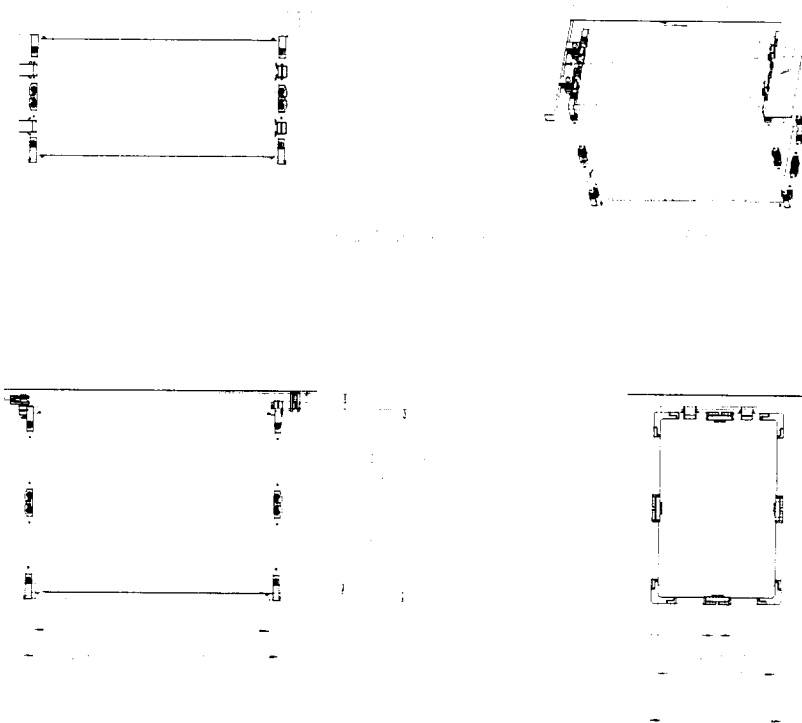


Figure 5. FGB Enclosure 17 Frame Interface Control Drawing showing where and how it attaches to Zarya Frame

S12/27

Non-Metallic Hold Down and Release for an RF Antenna

David J. Hernandez Jr.*

Abstract

Quick release mechanisms typically use metallic rods as preload-carrying members. This is often not a viable solution for restraint and release components that are connected to an RF Antenna. This is because metal extensions remaining after release can interfere with the antenna's communications signals.

Astrium Ltd. (formerly Matra Marconi Space) required an antenna release mechanism that incorporates a quick release with negligible source shock output. However, the mechanism could not disrupt the antenna's transmission after the antenna was released from the stowed position. In addition, a tensile preload had to be maintained for a 6-month period with a rod elongation not to exceed 5% of the rod length.

NEA met these requirements by integrating a Glass Fiber/Epoxy Laminate 10G/40 ("Tufnol") rod into the NEA-patented split-spool hold down and release mechanism. The combination of the non-metallic rod and the split-spool device (SSD) provides an effective method of applying and maintaining the necessary preload for launch as well as providing a "virtually" shock-free release.

Introduction

Release mechanisms are devices that allow release of a device that is initially stowed during launch and, later, to be deployed when in space. These devices include, among others, solar arrays, reflectors, various instruments, covers or antennas.

Astrium Ltd. required such a release device to be used in conjunction with the deployable antennas for the MetOp spacecraft. Two different tensile preloads for antenna restraint, and the location of the hold down points, forced the development of two release systems.

A preload of 3700 N was to be applied at the elbow of the antenna. At this location the antenna was restrained by a SSD integrated with a titanium rod. A tensile preload of 2000 N was to be applied at the antenna end. At this location the antenna was restrained by a SSD integrated with a Tufnol rod. The antenna and the hold down points are shown in Figure 1. In the figure, release assembly (RA) 001 refers to the location of the SSD with the titanium rod and RA 002 refers to the location of the SSD with a Tufnol rod.

A 4.5-amp current pulse over a duration of 35 milliseconds was required to activate both SSDs. Furthermore, the configuration of each mechanism had to remain identical per the Astrium specification. The ability to incorporate both titanium and Tufnol rods is possible with the SSD release mechanism. The SSD's preload-carrying capability varies with the diameter and material of the rod used in conjunction with the mechanism.

The SSD's strength capability is important. With its present design the Model 9101P SSD, independent of the rod diameter and rod material, will withstand up to 20000 N. Consequently, any potential creep from the SSD would come directly from the rod. This is because the SSD is used at a fraction of its load carrying capability (less than 25%).

* NEA Electronics, Inc., Chatsworth, CA

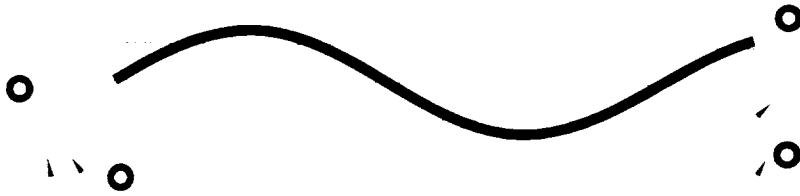


Figure 1. Antenna Hold Down Points

Mechanism Actuation

The release of the mechanism requires activation through a fuse wire initiator assembly. The release time of the fuse wire is approximated by the following equation:

$$Ws \geq c_p \rho V_{wire} * 1.25$$

W = Watts ($I^2 * R$)

s = Time in seconds to actuate

c_p = Thermal Capacitance of fuse wire

ρ = Density of fuse wire

V_{wire} = Volume of fuse wire between contacts

When the value of the left side of the equation exceeds the melting point value on the right, the actuation time can be approximated within 2 milliseconds. The 25% additional thermal mass (1.25 coefficient) accounts for any potential losses from conduction, convection, and radiation. While the wire does not melt during actuation, it does reach temperatures close to the melting point. It is the pull of the restraining wire on the fuse wire that separates or opens the fuse wire circuit. For analysis in determining the mechanism actuation time it is safe to assume the melting temperature of the wire. At this temperature the wire would no longer be a solid capable of resisting the force of the restraining wire.

The fuse wire length used in this mechanism was optimized. It was optimized to allow for a margin of greater than 10 milliseconds to the lowest time the actuation current was supplied by the MetOp power supply.

SSD Shock Output

The source shock from the mechanism's release of the rod was also an important requirement. The mounting and location of the hold down points, in addition to the antenna's sensitivity, necessitated a very low shock output. Astrium Ltd. required that the SSD mechanism emit shock levels less than $0.8 \times$ frequency of emission. The shock was to be measured by accelerometers (10 – 10000 Hz) in the Z axis on a 61 cm x 61 cm x 19 mm (2' x 2' x $\frac{3}{4}$ ") aluminum plate at 127 mm (5 inches) and 254 mm (10 inches) from the source.

During actuation the source shock produced a peak level of 160 g's at 7000 Hz using a 42-mm long Tufnol rod. The tensile preload on the rod was 2500 N. The negligible source shock is attributed to the split-spool restraint and release principal. The test data demonstrated that the mechanism with the Tufnol rod exhibited a greater shock emission than their titanium counterparts. It is believed that the reason for the greater shock emission is because the Tufnol material has a higher elastic modulus than the titanium.

NEA engineers assume that the slow release of the rod's strain energy is the reason for the overall negligible shock emitted. The measured preload drop over time in milliseconds after actuation would seem to confirm this hypothesis.

Non-Metallic Rod Development

A significant challenge for NEA in developing the Hold-Down and Release Mechanism for Astrium Ltd. was selection of the non-metallic rod material. The properties that are important in the material selection include:

- High tensile strength
- High electrical resistance
- RF transparency
- High modulus of elasticity
- Low creep characteristics

The more common non-metallic materials used in space were eliminated because they did not sufficiently meet the requirements above. These materials include but are not limited to ULTEM, Delrin, TORLON and PEEK.

After a thorough review of the above parameters, Astrium Ltd. recommended using a material named Tufnol. A rod diameter of 7.95 mm, with a tensile strength of 300 MPa, was more than capable of withstanding the 4000-N maximum preload requirement. The operational preload of 2000 N would be maintained at the MetOp spacecraft level by means of a flexure plate as shown in the Astrium design in Figure 2. What remained was the creep behavior of the Tufnol under preload over an extended period of time.

In this configuration the flexure plate maintains the preload via bending. For this reason elongation in excess of 0.18 mm would cause an unacceptable non-preload condition.

The practical application for the SSD mechanism is to preload it during assembly of the MetOp satellite bus and stow it for a period of six months. It was necessary for Astrium Ltd. to specify that the Tufnol rod survive a preload of approximately 2500 N for this six-month period. Furthermore, Astrium added a temperature requirement of 30°C +5°C/-0°C for the six-month condition. This would represent the conditions that the MetOp bus would be stowed in.

NEA constructed a test to simulate the stowed conditions. Assembled in hardware made to the flight configuration, the Tufnol rod was preloaded to approximately 2450 N. This load was the maximum operational preload case in ambient conditions (room temperature of 15°C to 20°C).

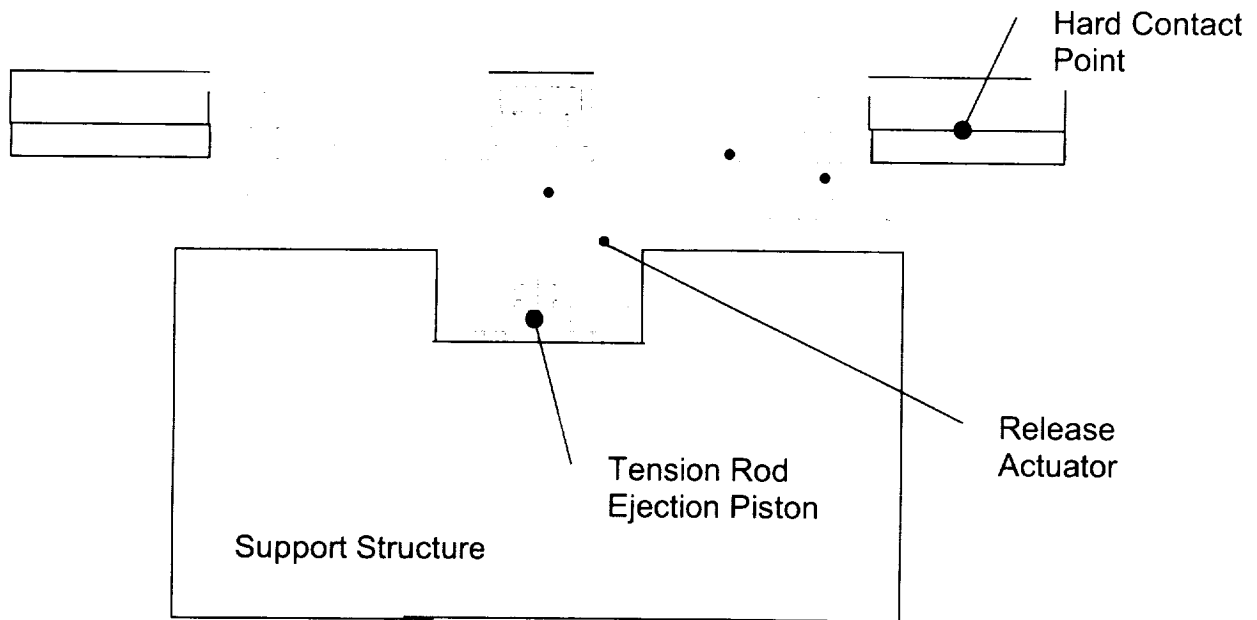


Figure 2. MetOp Antenna Configuration

When the SSD mechanism was placed in the oven, the preload increased to approximately 2465 N. The preload was adjusted to maintain a constant load. However, the time for adjusting the constant load was for a period of 60 days. After that time, the load was allowed to decay at its own rate without adjustments. A graph depicting the load as measured by a load cell in compression is shown in Figure 3.

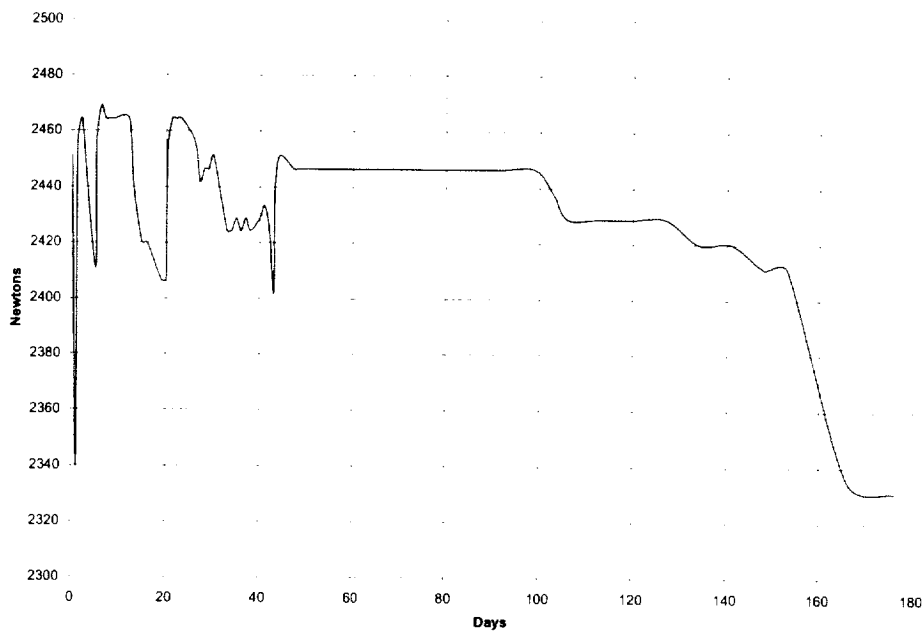


Figure 3. Tufnol Rod Load vs. Time

The elongation over time, while under load, shows a total creep of 0.076 mm over the final four (4) month period. Once the load was removed and the rod examined, it was found that the rod length had increased 0.05 mm in plastic deformation.

As seen in Figure 4, the rod length increased at increasing time intervals. The behavior of the rod was expected to be in this condition, reaching an asymptote-like curve. Although the creep test was scheduled to run for two months, NEA continued the test for another four months. After one year, the elongation of the rod under constant load would approach 0.11 mm, well within the elongation requirement of Astrium's flexure plate.

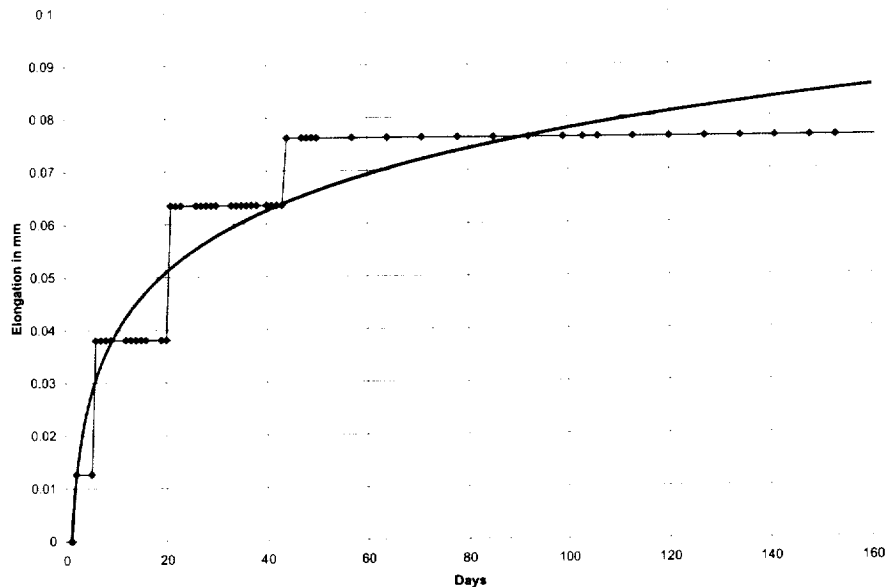


Figure 4. Elongation of Tufnol Rod vs. Time

Conclusion

The release mechanism, integrated with a Tufnol rod, succeeded in holding a constant load over an extended time with minimal creep. The co-action of a glass composite rod and a metallic restraining device to retain a load over an extended time has proven successful to both Astrium Ltd. and NEA.

Plastic deformation of the Tufnol rod occurs at loads above 2400 N, while maintaining an ultimate load of approximately 14000 N. Uses of the Tufnol rod in tension over extended periods of time should be possible when the nominal force is between 14 and 17% of the composite material's ultimate strength.

Shock emissions from the mechanism may be minimized using release rods of higher modulus of elasticity. Provided the rod material does not interfere with the application one should consider using a less elastic material.

Fuse wire assembly provides consistent actuation. The analytical model provides a consistent means of predicting the actuation time. Depending on the amount of power available for actuation, the correct wire diameter and length can be utilized to fit the needs of different applications.

Acknowledgements

Stephen Bamford, Astrium Ltd., for providing the application responsible for the antenna and hold down design. A.M. Kiley, Astrium Ltd., for the hold down concept and Tufnol rod design.

5/3/07

Fault Tolerant Magnetic Bearing for Turbomachinery

Benjamin Choi* and Andrew Provenza*

Abstract

NASA Glenn Research Center (GRC) has developed a Fault-Tolerant Magnetic Bearing Suspension rig to enhance the bearing system safety. It successfully demonstrated that using only two active poles out of eight redundant poles from each radial bearing (that is, simply 12 out of 16 poles dead) levitated the rotor and spun it without losing stability and desired position up to the maximum allowable speed of 20,000 rpm.

In this paper, it is demonstrated that as far as the summation of force vectors of the attracting poles and rotor weight is zero, a fault-tolerant magnetic bearing system maintained the rotor at the desired position without losing stability even at the maximum rotor speed. A proportional-integral-derivative (PID) controller generated autonomous corrective actions with no operator's input for the fault situations without losing load capacity in terms of rotor position. This paper also deals with a centralized modal controller to better control the dynamic behavior over system modes.

Introduction

Magnetic suspension is now a competitive technology for aerospace applications such as gas turbine engines and energy storage flywheels. Despite their many benefits, active magnetic suspension systems may sustain failures in any one of many complex components: displacement probes, DSP control boards, power amplifiers, communication buses, wiring, etc. A failure in any one of these could mean a complete failure of the entire system. Because of this, concerns about overall system reliability have arisen. For some applications, double or even triple redundancy in mechanical systems is required. Redundancy in a typical magnetic system may require extra duplicate components powered up and ready to go with a voting mechanism in place to choose (see Field, et al., 1998). This can work with amplifiers, probes, DSP boards, and perhaps even wire bundles, but not necessarily for electromagnetic coils.

Maslen, et al. (1998) showed that symmetry of poles in a magnetic bearing is not required for control. Appropriate coil currents can be determined to prescribe an arbitrary force for many combinations of faults in coils, amplifiers, or connectors. Na, et al. (2000) developed optimized solutions for fault scenarios for an 8-pole heteropolar magnetic bearing. They found that an 8-pole bearing with up to five failed coils can maintain control over a rotor provided there was sufficient position stiffness and damping. Chen (2000) has also shown that a magnetic bearing can operate without all of its coils functioning.

In this paper, a fail-safe controller for a fault-tolerant magnetic suspension test rig was demonstrated. Without changing the initial control gain parameters, the controller successfully enabled a rotor to spin up to the maximum allowable speed of 20,000 rpm with only two controlled poles out of eight from each radial bearing.

Fault-Tolerant Magnetic Bearing Rig

The NASA Glenn Research Center has a facility to study a fault tolerance in magnetic suspension systems. The test rig and associated hardware are shown in Figure 1. The rotor is 68.6 cm (27") long, weighs 10.4 kg (23 lb), and is driven by an air turbine. The air turbine can spin up to 60,000 rpm, but the rotor can only be spun up to 20,000 rpm due to the stress limitations in the Hyperco 50 rotor laminations. The rotor is attached to the air turbine with a helical flexible coupling, which provides some axial rotor

* NASA Glenn Research Center, Cleveland, OH

support. There is no thrust bearing, but the two radial magnetic bearings provide additional axial restoring forces through reluctance centering effects. The static predicted load capacity of each radial bearing is 113 kg (250 lb). In typical applications, a radial bearing system is designed with a load capacity of three times the rotor weight. In this case the bearings are grossly oversized and almost an order of magnitude stronger than required. Fault tolerant bearing designs will most likely be oversized, but not this much. Oversized bearings eliminate a potential source of non-linearity during fault tolerance testing. As shown in Figure 2, each bearing has 8 coils (including four redundant coils), which are individually controlled by their own dedicated PWM transconductance power amplifiers. For this configuration, a decoupler is required for each bearing (see Meeker, 1996). The bearing near the air turbine (in-board) is powered by two-state amplifiers and the outboard bearing is powered by three-state amplifiers. Ten eddy current displacement probes in three different planes monitor the motion of the rotor.

There are several ways to simulate circuit faults in this facility. There are mechanical switches and voltage controlled switches in the circuits both in front of the each amplifier and each coil. The mechanical switches can be controlled manually from the control panel (Figure 3). The voltage-controlled switches can be opened and closed with a 0 and 5 volt signal, respectively. Circuit faults can also be simulated by controlling the command signals from the magnetic controller to the PWM amplifiers.

System Dynamics

For proportional-integral-derivative (PID) feedback control the following relation is represented the decentralized dynamics of the suspension system:

$$m_{eq}\ddot{x} + K_d K_d \dot{x} + (K_i K_p - K_s)x + K_i K_i \int x dt = 0 \quad (1)$$

where K_p is the proportional control gain, K_i is the integral control gain, K_d is the derivative control gain, and, m_{eq} is the equivalent lumped mass of the rotor.

For centralized control force from each radial bearing, the following equation represents the centralized dynamics of the fault-tolerant magnetic suspension system

$$F_{1,2} = -\frac{(k_1 + k_2)(x_1 + x_2) + (k_1 + k_2) \cdot l \cdot \theta + (c_1 + c_2) \cdot l \cdot \dot{\theta}}{4} \quad (2)$$

Control System

The control system uses a proportional-integral-derivative (PID) control algorithm, which is implemented with the MATLAB/Simulink software. A real-time ANSI C code was generated, compiled, and downloaded to a dSPACE control system (Figure 4), which is an integrated software and electronic control unit combination (MATLAB software and ds1003/ds1004 alpha-combo, multiprocessor board). It found that fundamental shortcoming exists in the block diagram based controller as applied to the event-driven fault-tolerant control application. The number of blocks used in the overall control system drastically increased the loop time (or sample time). To overcome this deficiency, a customized block was used to incorporate a fault-tolerant control algorithm written in ANSI C with the control hardware. It reduced the loop time by about 45%, reducing a lot of Simulink blocks to implement a fault-tolerant control algorithm.

Unlike other magnetic suspension test rigs at GRC, the fault-tolerant test rig had severe sensor noise, which caused an intolerable operating noise. To cancel sensor noise, a moving average (MA) filter was implemented to smooth out five running points. Since a MA filter is a Finite Impulse Response filter, which cannot be implemented in real time fashion (the next two future values are unknown). To make this non-causal filter causal, we had to shift the index back by two (that is, two sample times).

Figure 5 shows a controller cockpit window that allows modification of magnetic bearing parameters such as bias, stiffness, damping, and integral. Also it includes a feature for various fault-tolerant situations for multiple coil and amplifier failures. It has a switch for a decentralized PID controller or centralized modal controller. At critical modes, a centralized modal controller was sufficient to suppress the vibration

amplitude. Since a different type of PWM power amplifier was used in inboard (air turbine side) and outboard bearing, a gain adjustment block was added to compensate the different gain used. A safe gain feature will be triggered to protect the bearing system at higher speed when the rotor orbit exceeds the predefined orbit size. Also, a whirling feature was implemented to investigate the dynamic behavior of the magnetically suspended rotor system as well as to check backup bearings. Whirling orbit size, starting angle, and the center point of orbit are all user defined to investigate bounce mode and tilting mode. All the above-mentioned features can control inboard and outboard bearings separately.

Coils or/and amplifiers failing situations are simulated by manually shutting down their control current commands from the controller cockpit. This eliminated a bunch of mechanical switches shown in Figure 2. A simple data acquisition system window was added to the next to the control cockpit window to monitor the system performance.

Experimental Results

Figure 6 shows that current inputs to compensate the pole 1 (one of top two poles) failed operation at 0 rpm. The adjacent pole 2 (the other top pole) needed a more control force and two bottom poles 5 and 6 had reduced control forces to compensate the less attracted force caused by pole 1 failure, while four horizontal poles 3, 4, 7, and 8 had little impacts.

Figure 7 shows that current inputs to compensate the consecutive 1-4-6th poles failed operation at 0 rpm. When pole 4 failed, the adjacent pole 3 needed a little more control force and the other opposing horizontal poles 7 and 8 had little impacts because horizontal poles didn't take account of rotor weight. When pole 6 failed, a top pole 2 had reduced control force to compensate the less attracted force caused by pole 6 failure, while two horizontal poles 7 and 8 had little impacts.

Now we increased the rotor speed up to the maximum allowable speed of 20,000 rpm without changing gain set done in experiments at 0 rpm described in Figures 6 and 7. Figure 8 shows that current inputs to compensate the consecutive 2-3-5-7th poles failed operation at 20,000 rpm. When pole 2 failed, the adjacent pole 1 needed a little more control force (same as in Figure 6) and two bottom poles 5 and 6 had reduced control forces to compensate the less attracted force caused by pole 2 failure, while four horizontal poles 3, 4, 7, and 8 had little impacts. When pole 3 failed, the adjacent pole 4 needed a little more control force and the other opposing horizontal poles 7 and 8 had little impacts because horizontal poles didn't take account of rotor weight. When pole 5 failed, a top pole 1 had reduced control force to compensate the less attracted force caused by pole 5 failure, while two horizontal poles 7 and 8 had little impacts. Even failed pole 7 didn't affect the remaining active poles 1, 4, 6, and 8.

We continuously killed poles 6 and 8 to see if only two active poles 1 and 4 can handle the worst scenario of multiple coil and amplifier failures. Figure 9 shows that current inputs to compensate the consecutive 6th and 8th poles failures with poles 2, 3, 5, and 7 pre-killed. When pole 6 failed, only remained top pole 1 needed a little more control force to handle the rotor weight, while horizontal poles 4 and 8 needed slightly reduced control forces. Finally, pole 8 failure affected a little impact on pole 4.

A variety of failed situations was investigated and all the results agreed with those shown in Figures 6 through 9. Figure 10 shows another case of using only two active poles. It shows that current inputs to compensate the consecutive 2nd and 4th poles failures with poles 5, 6, 7, and 8 pre-killed. When pole 2 failed, only remained top pole 1 needed a relatively large control force to handle the rotor weight, while horizontal poles 3 and 4 needed slightly increased control forces. Finally, pole 4 failure affected a large impact on pole 3, while pole 1 was barely affected.

Also, it was demonstrated that for any failed situations, the predefined desired rotor position was maintained because an integrator successfully generated a corrective force to compensate the steady state position error. Figure 11 shows that a transient sensor signal plot of the failed situation of the case of Figure 10. When pole 2 failed, the rotor was moving down, but an integrator was triggered immediately to generate a corrective force, which enabled the rotor to move back to the original position in less than 0.3 second. When pole 4 failed, the rotor was moving to right because of strong attractive force caused by pole 3. However, the rotor recovered its desired position within less than 0.5 second.

Conclusions

In summary, as far as a controller gain value set of proportion, integration, and derivative of a PID controller is within a stability limit, any combination of the three stable gains guaranteed to spin the rotor up to the maximum allowable speed of the fault-tolerant magnetic bearing test rig. For a variety of multiple component (coils and amplifiers) failures, the integrator of a PID controller generated autonomous corrective forces to compensate those failed situations. Also, the controller doesn't require any operator's input to change the gain value set for failed situations. The demonstration was highlighted when using only two active coils and amplifiers from each radial bearing (that is, twelve out of sixteen coils and amplifiers were failed) levitated the rotor and spun it without losing stability and desired position up to the maximum allowable speed of 20,000 rpm.

This valuable demonstration proved that a safe fault-tolerant bearing design is possible and an oil-free magnetic bearing can have multiple coil or/and amplifiers failures before causing an entire system shutdown. This work helped to eliminate the controversial safety issue of using a magnetic suspended turbomachinery for future engines to carry people safely.

The future work will include a complete dynamic analysis of a fault-tolerant bearing system and develop a more enhanced PID controller by using a Kalman filter, which can estimate state variables to overcome the sensor noise and unknown process noise.

Acknowledgements

This work was carried out under a fund, which was mainly provided by the Turbomachinery and Combustion Technology Program (Robert Corrigan, Program Manager), and also in part by the Flywheel and Energy Storage System Program.

References

1. Chen, H. M., 2000, "A Self-Healing Magnetic Bearing," 5th International Symposium on Magnetic Suspension Technology, pp. 25-34, July.
2. Fedigan, S. J., Williams, R. D., Shen, D., and Ross, R. A., 1997, "Design and Implementation of a Fault Tolerant Magnetic Bearings Controller," Proceedings of the Fifth International Symposium on Magnetic Bearings, Kanazawa, Japan, pp. 307-312.
3. Field, R. J., Iannello, V., 1998, "A Reliable Magnetic Bearing System for Turbomachinery," Proc. 6th Int. Symp. Magn. Bearings, Cambridge, MA, pp. 42-51, August.
4. Lyons, J. P., Preston, M. A., Gurumoorthy, R., and Szczesny, P. M., 1994, "Design and Control of a Fault-Tolerant Active Magnetic Bearings System for Aircraft Engine," Proceedings of the Fourth International Symposium on Magnetic Bearings, ETH Zurich, pp. 449-454.
5. Maslen, E. H., Meeker, D. C., 1995, "Fault Tolerance of Magnetic Bearings by Generalized Bias Current Linearization," IEEE Transactions on Magnetics, Vol. 31, No. 3, pp. 2304-2314, May.
6. Meeker, D. C., 1996, "Optimal Solutions to the Inverse Problem in Quadratic Magnetic Actuators," Ph.D. Dissertation, Mechanical Engineering, University of Virginia, May.
7. Na, U. J., Palazzolo, A., 2000, "Optimized Realization of Fault-Tolerant Heteropolar Magnetic Bearings," ASME Journal of Vibrations, Vol. 122, pp. 209-221, July.

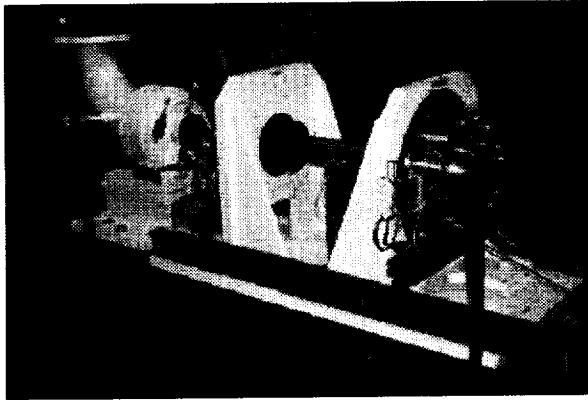


Figure 1: Fault-Tolerant Magnetic Suspension Test Rig.

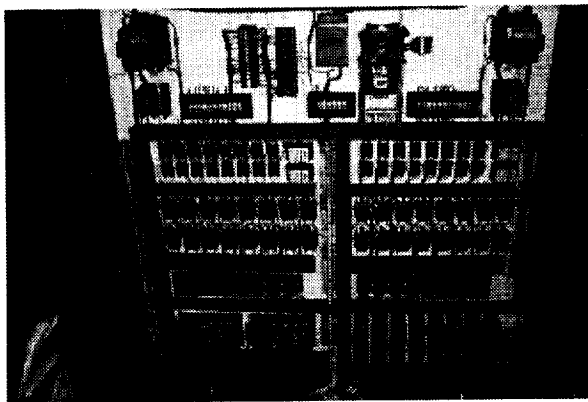


Figure 2: Associated hardware for Fault-Tolerant Magnetic Bearing Suspension Test Rig.

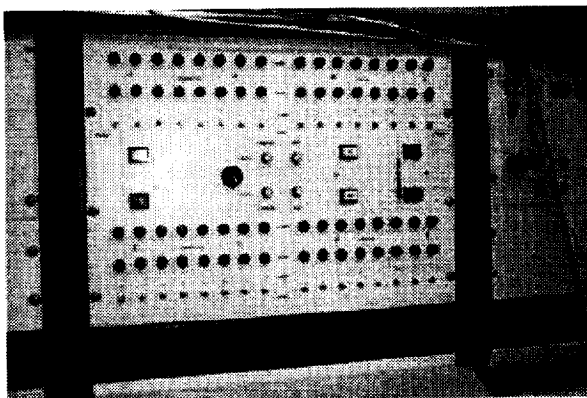


Figure 3: Fault-tolerant control panel that simulates coil or/and amplifier failures by using manually controlled mechanical switches.

Fault Tolerant Magnetic Bearing Modal Controller with Safe Gain and Power-off Switch Features (11-10-99)

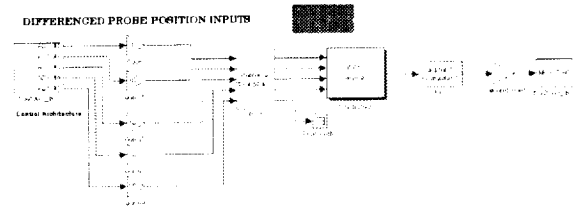


Figure 4: Controller block diagram for the Fault-Tolerant Magnetic Suspension Test Rig.

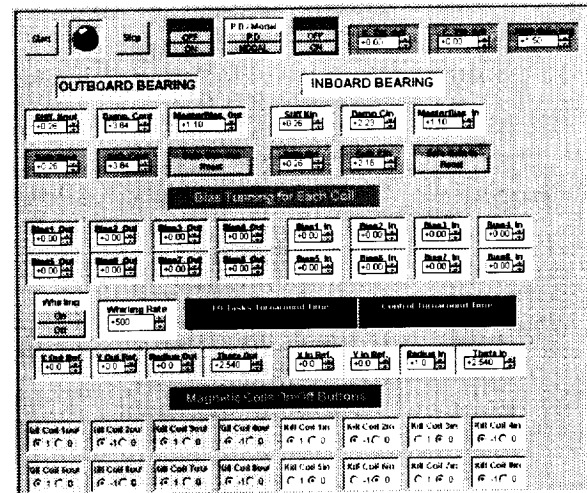


Figure 5: Control cockpit window that adjusts system parameter values and simulates multiple component failures.

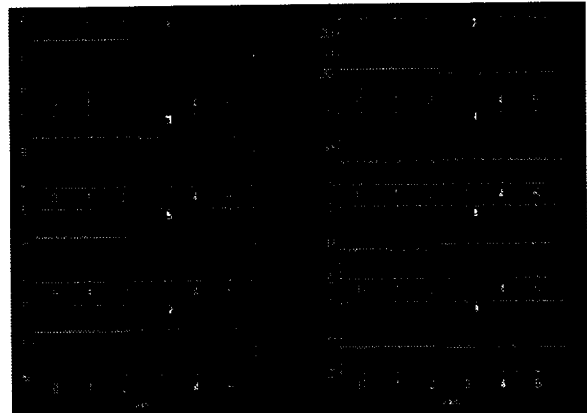


Figure 6: Current inputs to compensate the first pole failed operation at 0 rpm.

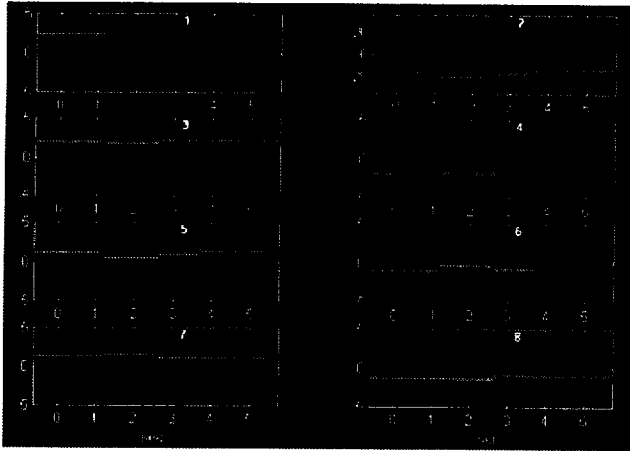


Figure 7: Current inputs to compensate the consecutive 1-4-6th poles failed operation at 0 rpm.

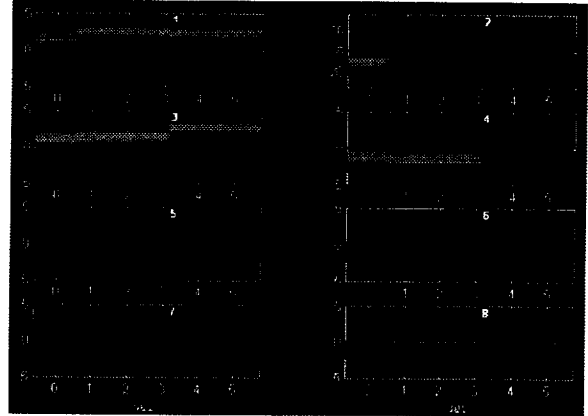


Figure 10: Current inputs to compensate the consecutive 5-6-7-8-2-4th poles failed operation at the maximum allowable speed of 20,000 rpm. Only two active coils of 1 and 3.

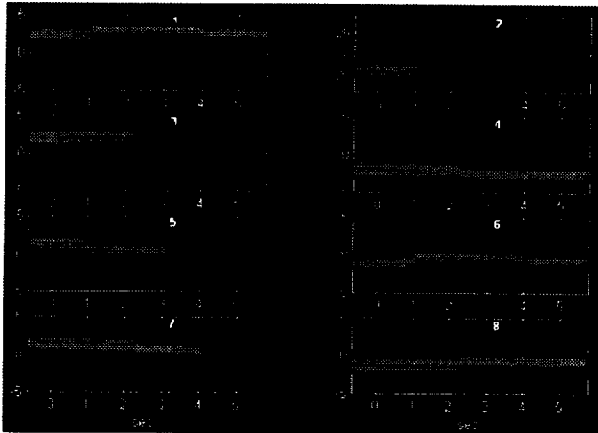


Figure 8: Current inputs to compensate the consecutive 2-3-5-7th poles failed operation at the maximum allowable speed of 20,000 rpm.

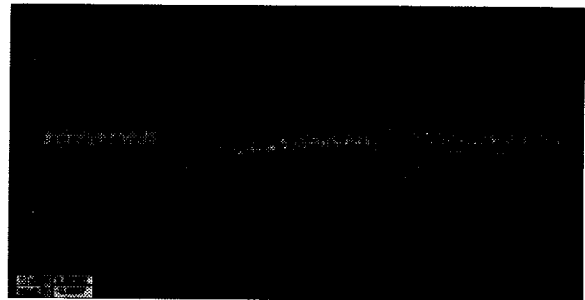


Figure 11: Transient sensor plot of the failed situation of Figure 13. The 5-6-7-8th poles pre-failed, followed by the 2-4th poles failed case. Only two active coils of 1 and 3 at 20,000 rpm.

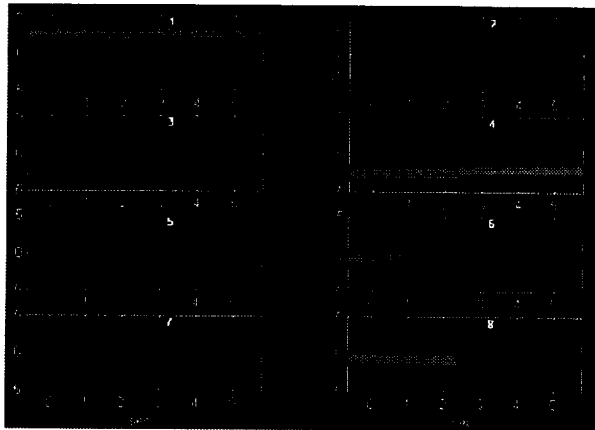


Figure 9: Current inputs to compensate the consecutive 2-3-5-7-6-8th poles failed operation at the maximum allowable speed of 20,000 rpm. Only two active coils of 1 and 4.

7/25

Methods for Improving Yield of Liquid Salt Bath Nitrocarburized 13-8 PH Steel Components

Irwin Hochler*

Abstract

Liquid salt bath nitrocarburizing (LSBN) is a thermochemical diffusion surface treatment technique that can produce excellent case hardened stainless steel gears and pinions. However, the process did not yield consistent results for a 13-8 PH stainless steel, fine tooth pitch pinion. Aeroflex Laboratories had been experiencing spalling (flaking) problems with the case produced on this pinion, but has been able to improve yields from 50% to 95% of each processed lot by working in conjunction with Kolene Corporation, the U.S. manufacturer of the salt baths, to tightly control the process parameters of temperature, time, and surface preparation.

This paper will present the theory and practice of LSBN, and offer suggestions on how to improve process yield. Aeroflex's case history of a 19-tooth, 4.7-mm (0.185 in) diameter, 13-8 PH shaft pinion for a space-quality step motor will be discussed.

The pinion in question underwent LSBN before lead plating. The plating lab observed highly reflective spots on the shaft, indicating that spalling had occurred. Discussions with the original nitriding vendor suggested that this is a common situation with fine pitch gears because the hardened layer becomes excessively thick at the gear edges, causing embrittlement. In addition, PH steels were said to undergo a structural change after LSBN that increases the possibility of damage to the hardened surface.

Cross sections of unacceptable shafts revealed that case depths were in fact thick (approximately 0.01 mm to 0.02 mm (0.0005 in to 0.001 in)), but within the vendor's limits (approximately 0.005 mm to 0.02 mm (0.0002 in to 0.001 in)). In addition, visits to the vendor's facilities revealed that difficulty in controlling the degree of air agitation is a problem associated with using large commercial tanks for processing small, precise parts. Poor air agitation results in non-uniform case depths for these small parts.

Discussions with Kolene Corporation revealed that the parts should be treated in a laboratory environment, and case depth controlled for uniformity by adjusting residence time and bath temperature. In addition, improved surface preparation of the parts prior to LSBN helped assure depths no greater than 0.0127 mm (0.0005 in). Implementation of these methods produced the 95% acceptance rate for every lot processed.

Introduction

Aeroflex Laboratories was contracted to design and build a space flight quality 90 degree stepper motor with a 19-tooth 4.7-mm (0.185-in) diameter, 13-8 PH stainless steel pinion on the end of the rotor shaft. The customer specified the shaft to be case hardened with a liquid salt bath nitrocarburizing (LSBN) process prior to final assembly in the motor. The customer specified all process parameters, including a suggested LSBN processor. After sending the shafts to this source for LSBN processing, the shafts were then sent to the customer for lead ion plating of the pinion. The operator noticed approximately 50% of the pinions had shiny spots on the teeth (LSBN should produce a uniform flat black to gray finish), and reported to Aeroflex that spalling (flaking) of the case had occurred. Figure 1 shows spalling at the tip of the pinion (Area C). Subsequent investigations concerning ways to improve the yield led Aeroflex to contract Kolene Corporation, the manufacturer of the LSBN salts, to treat the pinions in a laboratory environment in order to better control the critical process parameters. This effort resulted in 95% of newly processed lots of pinions showing no spalling.

* Aeroflex Laboratories, Farmingdale, NY

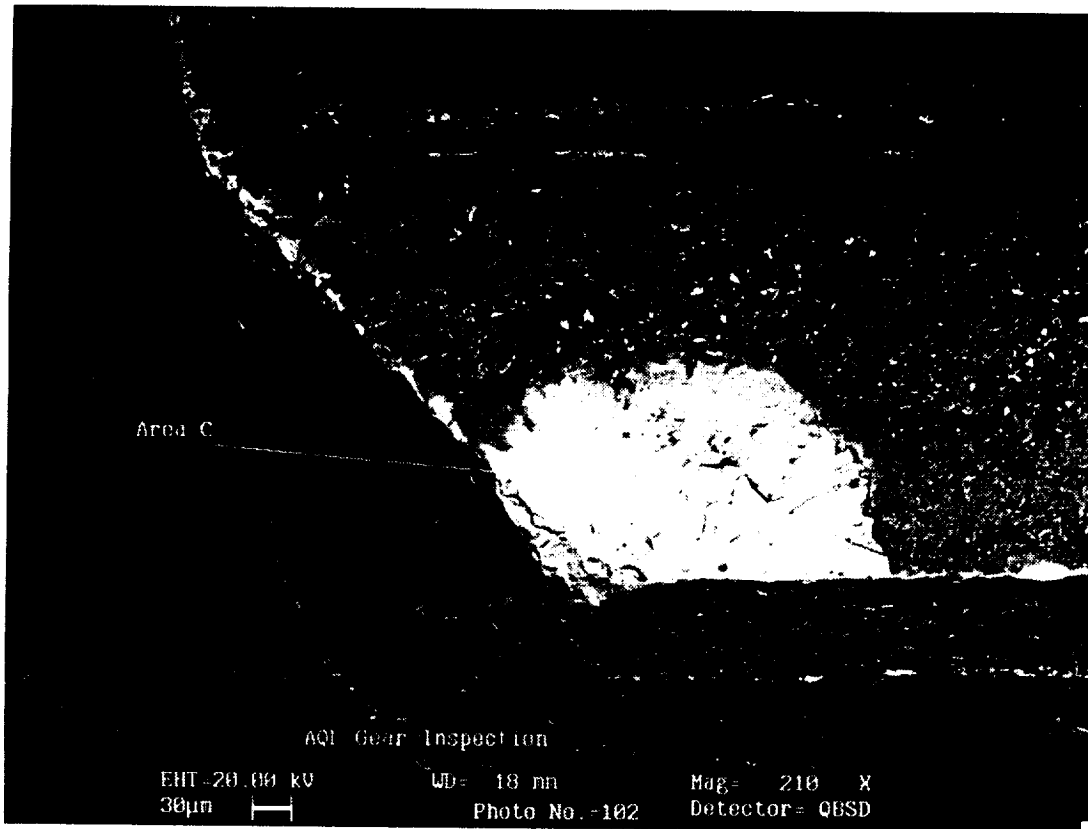
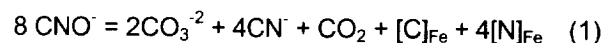


Figure 1. Spalled Gear Pinion (Area C)

Process Background

In order to understand the reasons for the problems encountered in this process, a description of LSBN is presented. LSBN uses a combination of potassium and sodium cyanate salts (KCNO and NaCNO) in a molten state, typically at 580°C (1075°F). These salts react with the iron at the steel surface and release carbon and nitrogen as follows:



The desired product in this reaction is the $4[\text{N}]_{\text{Fe}}$, or epsilon iron nitride. This compound improves the wear resistance of steels.

The reaction and subsequent diffusion of the carbon and nitrogen is represented schematically in Figure 2. On the left is the KCNO salt, which releases the C and N at the surface to produce the compounds shown in Equation 1. The zone where reaction occurs is called the compound layer, and is the area where spalling problems may occur. Compound layers range in thickness from 0.005 mm to 0.025 mm (0.0002 in to 0.001 in), depending on residence time, bath temperature, and the alloy composition of the treated steel. Unreacted nitrogen will diffuse below the compound layer, producing a solution of nitrogen in iron. This layer, called the diffusion zone, can impart improved fatigue strength on the processed part if it is aged at 300°C (570°F) in order to precipitate Fe_4N ¹. This layer is much deeper than the compound layer, measuring up to 1.02 mm (0.040 in)². Figure 3 shows a typical low carbon steel after LSBN treatment, showing the relative thickness of the compound zone and the diffusion zone, as well as the iron nitride needles formed in the diffusion zone after aging.

¹Wensing, Donald, et al, "Liquid Nitriding," ASM Committee on Liquid Carburizing, p. 254.

²Wensing, p. 254.

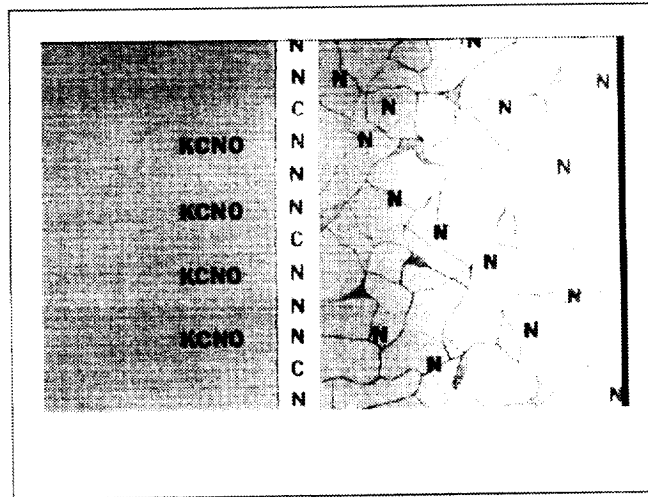


Figure 2. Schematic of the Nitrocarburizing Process³

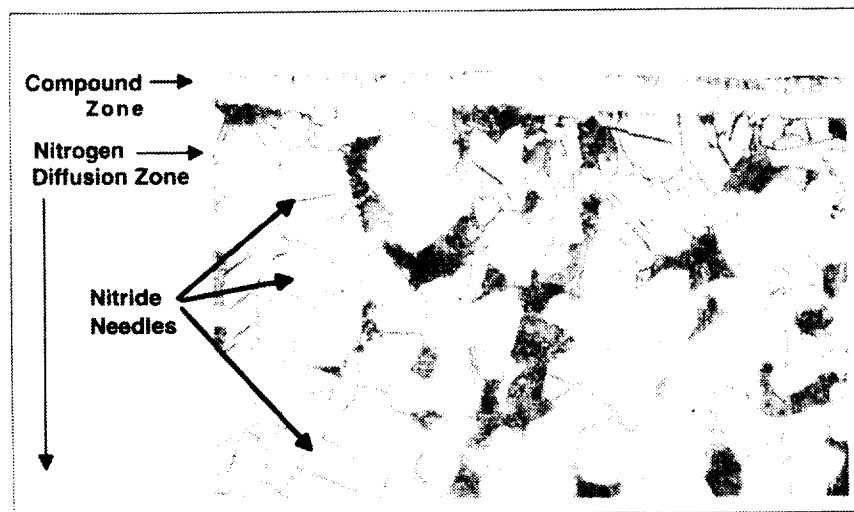


Figure 3. Nitrocarburized Low Carbon Steel⁴

Engineering Properties of Nitrocarburized Steels

The enhanced engineering properties of steels processed with LSBN involve improved wear resistance, reduced coefficient of friction, and improved fatigue strength. The improved wear resistance is primarily due to increased surface hardness (640 minimum Knoop KH_{100} for 13-8 PH steel). In addition, the surface of the compound layer during processing develops microporosities which act as reservoirs for lubricant⁵. These micropores make the surface ideal for holding lead plating, which help improve wear resistance. The reduced coefficient of friction is also due to the increased surface hardness, and generally results in a coefficient of

³Easterday, James R., "Salt Bath Ferritic Nitrocarburizing," Kolene Corporation Technology Update (1996), p.2.

⁴Easterday, p. 3.

⁵Easterday, p. 3.

0.3⁶. The improved fatigue strength, as mentioned previously, is a result of iron nitride formed in the diffusion zone, and generally results in an improvement of 25% to 35% in stainless steels⁷.

LSBN Process Description

The parts are usually cleaned first in an alkaline rinse to remove any surface oxides. They are preheated to approximately 400°C (750°F) in order to reduce the possibility of thermal shock and to dry the parts completely.

The parts are then placed in the salt bath, generally kept at 580°C (1075°F). The critical parameter to control at this stage is the cyanate concentration, which must be kept at 34%-38% for proper compound layer formation⁸. If the concentration falls below this range, a proprietary nitrogen-bearing polymer is added, which reacts with the carbonate in the bath to form cyanate. The residence time in the bath depends on the material processed and the required compound layer thickness, and is usually 15 minutes minimum, 30 minutes maximum for 13-8 PH and 17-4 PH steels. The last factor to be considered in the bath is aeration, which is accomplished by using air spargers on the bottom of the tank. The air to the spargers is dried and filtered, and its function is to improve surface contact with the parts and the liquid.

The parts are then removed from the salt bath, and are placed in a quench tank. This tank is kept at 400°C (750°F) and contains oxidizing (nitrate) salts. The oxidizing salts convert any remaining cyanide and cyanates to carbonates, thus stopping any further surface reactions. In addition, the lower temperature of the quench bath prevents any distortion of the parts due to thermal stress. The parts are usually kept in this bath for 5 to 20 minutes.

After removal from the quench tank, the parts are air cooled to room temperature, and residual salts are rinsed off with water. At this stage, the parts should have a uniform black finish. One piece is usually sectioned and tested for hardness and thickness of the compound layer, as well as hardness of the diffusion zone.

Problems Associated with LSBN Processed Stainless Steels

The LSBN process usually provides predictable and uniform results for a wide range of steels and even cast iron. However, some difficulties arise when processing stainless steels. The chromium and nickel in stainless steels are also nitride formers; therefore, the compound layer contains chromium and nickel nitrides in between grain boundaries. This results in a very brittle compound layer, which increases the chance of spalling. The molybdenum in 13-8 PH steel also scavenges nitrogen, thus adding to the possibility of spalling in this alloy. In addition, the nitriding reactions occur very quickly, so residence time is critical in order to prevent formation of an excessively heavy compound layer. Furthermore, the diffusion zone is not as deep as in non-alloyed steels because a great deal of the free nitrogen is scavenged by the alloying elements; therefore, the nitrogen cannot diffuse well into the steel. Finally, corrosion resistance is compromised due to the reactions of the alloying elements chromium and nickel.

Case History

The 13-8 PH pinions that were initially processed were done according to the customer's specifications, which were based on their years of experience using LSBN. The parts were required to be heat treated to RC 42-45 prior to LSBN processing. The salt bath temperature was specified to be less than the heat treat temperature in order to prevent any degradation in the hardness, and the residence time was to be adjusted to produce a compound layer between 0.005 mm and 0.025 mm (0.0002 in and 0.001 in). However, when this specification was followed for the Aeroflex pinion, a chromium nitride embrittled compound layer close to 0.025 mm (0.001 inch) resulted in too much buildup on both sides of the fine pitch tooth, and spalling occurred. In other words, the specification tolerances on the compound layer thickness for this particular part had to be tightened.

⁶Easterday, p. 9.

⁷Easterday, p. 9.

⁸Easterday, p. 4.

Another problem specific to this pinion was the size of the parts. Most commercial LSBN processors use tanks approximately 1-m long by 1-m wide by 3-m deep. If large loads of parts are processed before the small pinions, carbonate precipitation (Equation 1) causes sludge to develop at the bottom of the tank, resulting in reduced air agitation. The small pinions placed in a large tank with reduced air agitation resulted in poor surface contact with the salts, causing uneven compound layer formation. Therefore, smaller vessels with improved air agitation will produce a more consistent compound layer.

Problem Resolution

The U.S. manufacturer of the salt baths, Kolene Corporation, was contacted to use laboratory scale LSBN processing in order to control the aforementioned factors that led to the spalling problem. The first parts run through the lab used the previous LSBN processor's parameters. The pinions showed gold colored areas where the salt bath solution did not penetrate, possibly due to inadequate removal of surface oxides (usually chromium oxide) prior to LSBN. This group was immersed in the salt bath for an additional 10 minutes, and the pinions showed complete blackening of the surface. However, the compound layer ranged in thickness from approximately 0.01 mm to 0.02 mm (0.0005 inch to 0.001 inch), a range that Kolene agreed was too deep for pinions of this configuration.

A second group of pinions was first precleaned for 10 minutes in an ultrasonic bath containing a proprietary alkaline cleaner heated to 70°C (160°F) in order to remove surface scale. The parts were then rinsed with water and preheated. The next operation, salt bath immersion, is critical to control compound layer depth, and the lab determined that a 25 minute ±1 minute exposure at 550°C ±10°C (1020°F ± 20°F) was sufficient to produce a compound layer of 0.0038 mm to 0.0127 mm (0.00015 in to 0.0005 in). Table 1 compares the parameters from the first LSBN processor and Kolene Corporation's laboratory. When compared step by step, there does not appear to be a significant difference, but taken together there was a great improvement from the 50% yield seen previously. When these controls were implemented on subsequent production runs, 95% of the parts showed no sign of spalling, and have been used successfully on flight qualified motors. The improved product yield resulted in a change in our customer's LSBN procurement specification to reflect these process changes.

Table 1
Comparison of Commercial Shop LSBN and Kolene Lab LSBN Parameters for 19 Tooth, 4.7-mm (0.185 in) Diameter, 13-8 PH Pinion

Process Step	Shop LSBN	Kolene Lab
Pre-Clean	Water at Room Temperature	Alkaline, Ultrasonic, 160°F, 10 Minutes
Pre-Heat	370°C to 400°C (700°F to 750°F), 30 minutes	370°C to 400°C (700°F to 750°F), 30 minutes
Salt Bath Nitriding	560°C ± 5°C (1040°F ± 10°F), 30 minutes ±1 minute Air agitation was not consistent from lot to lot.	550°C ± 10°C (1020°F ± 20°F) 25 minutes ± 1 minute Vigorous air agitation
Quench Bath	425°C to 440°C (800°F to 825°F) 10 minutes	400°C to 425°C (750°F-800°F) 10 minutes
Air Cool	As required (Until parts are cool to touch)	As required
Water Rinse	As required (Until most of the salts are removed)	10 minutes
Secondary Water Rinse (Ultrasonic)	As required (Until all visible salt is removed)	Not used
Compound Layer Cross Section Analysis	0.0127 mm to 0.025 mm (0.0005 in to 0.001 in) case depth, 640 HK ₁₀₀ at surface	0.0038 mm to 0.0127 mm (0.00015 in to 0.0005 in) case depth, 640 HK ₁₀₀ at surface

Conclusions

The process parameters shown in Table 1 are only applicable for this particular part; however, some general guidelines for successful yields when using PH stainless steels can be summarized as follows:

- Pay close attention to the part geometry. If there are fine threads, fine gear teeth, or other small details present on the surface to be nitrided, specify a case depth of 0.013 mm (0.0005 inch) maximum. The temperature and residence time will be determined by testing sample pieces until the desired case depth is achieved.
- Make sure the LSBN processor thoroughly cleans the parts before nitriding, preferably by using a heated alkaline ultrasonic bath. Any scale on the surface will prevent uniform compound layer formation.
- Make sure the processor maintains vigorous air agitation in the salt bath tank when processing parts with fine surface geometries.

References

1. Wensing, Donald, et al. "Liquid Nitriding." *ASM Handbook Volume 04: Heat Treating* (1991).
2. Easterday, James R. "Salt Bath Ferritic Nitrocarburizing." *Kolene Corporation Technology Update*, 1996.

5/5/06

Wear and Corrosion Resistant PM Tool Steels for Advanced Bearing Applications

B. Hann*, P. Kilonsky*, D. Smith** and M. Sperber*

Abstract

A need exists for new bearing materials that possess properties not attainable with conventional bearing materials such as M50, 52100, and 440C. These materials must have a combination of the following: high attainable hardness, high hot hardness, dimensional stability at high temperature, wear resistance, corrosion resistance, toughness, and rolling contact fatigue resistance. With Powder Metallurgy (PM) technology, higher alloy contents with greater volume fractions of fine ($< 5 \mu\text{m}$) primary carbides may be achieved, without the adverse segregation inherent in conventional materials. Various PM alloy materials are in development to address the current and future needs of the bearing users.

Several papers have been published discussing CPM[®] VIM CRU[®] 20[™], a cobalt-free PM high-speed steel, which has exhibited some significant property advantages compared to M50 and 52100. Though CPM[®] VIM CRU[®] 20[™] shows promise for many bearing applications, the need for a high hardness, corrosion resistant bearing material has yet to be addressed. Several high hardness, corrosion resistant PM tool steels have recently been developed. New materials have been developed with corrosion resistance properties comparable to commercially available bearing grade stainless steels, but with substantially improved wear resistance.

Introduction

An issue that still exists for the aerospace designer is the need for a corrosion resistant material that may be used to produce critical bearings requiring high hardness, dimensional stability, and toughness. More and more aerospace bearings are operating in a more open environment than was required in previous designs. In some instances, bearings are not only exposed to hard abrasives in the lubricating media, but also to corrosive attack by moisture, acids, or lubrication breakdown constituents.

A secondary, but equally important issue that needs to be addressed is shelf life. A conventional bearing material may be suitable for a given application, but often corrosion takes place while in inventory that precludes the material from being used for its intended application. Corrosion resistant bearing materials exist, but the attainable hardness, and therefore compressive strength and wear resistance, are not equivalent to their conventional counterparts, like 52100 or M50. Bearing candidate materials with excellent corrosion resistance, good toughness, and hardness level greater than 62 HRc have been developed.

Employing the same principles used to develop CPM[®] VIM CRU[®] 20[™], the PM process has been applied to develop a new advanced bearing material that is both wear and corrosion resistant.

Background

PM materials have been successfully commercialized for non-corrosive bearing environments. CPM[®] VIM CRU[®] 20[™], a vacuum induction melted (VIM) version of M62 high-speed tool steel, has been discussed in various papers [1-3]. CPM[®] VIM CRU[®] 20[™] has exhibited rolling contact fatigue life comparable to silicon nitride and superior to conventional bearing grades, like M50 and M50NiL [1]. CPM[®] VIM CRU[®] 20[™] has also been used in bearing raceways with silicon nitride balls, to provide for a hybrid bearing design with higher load capacity and longer life than 52100 [2,3]. Currently four life tests of Reaction Wheels and Control Moment Gyroscopes are running using these hybrid bearings. One of the CMG tests

* Crucible Compaction Metals Division, Oakdale, PA

** Honeywell Satellite Systems Operation, Phoenix, AZ

has completed four years of its planned 10-year life. Though CPM® VIM CRU® 20™ has shown a higher compressive yield strength than 440C materials, the material is limited to non-corrosive environments.

The advantage of PM materials is that they may be manufactured with higher alloy contents than conventional steels, since cooling rates from the molten state are on the order of 10^4 to 10^8 °C/second, compared to 10^{-1} °C/second, typical for conventional ingot metallurgy. This fast cooling rate allows for a fine grain size, a highly alloyed matrix, and the formation of fine (< 5 μm) homogeneously dispersed primary carbides. Essentially, the gas atomized powder particle may be considered a micro-casting. Higher levels of carbide formers may be added to the initial melt, producing a greater volume fraction of primary carbides. After melting and atomization, the powder metal is classified by screening (250 μm maximum particle diameter is typical), blended to homogenize the particle size distribution, encapsulated in a mild steel mold, evacuated and hermetically sealed, and then consolidated to full density via hot isostatic pressing (HIP). From this point, conventional steel-making processes may be used to convert the consolidated powder to bar form. PM materials typically exhibit improved hot workability due to the inherently fine grain size and lack of alloy segregation.

Screening classifies the powder such that the maximum theoretical inclusion size is limited to the sieve opening size, important for rolling contact fatigue resistance. In some cases, non-metallic inclusion levels are capable of meeting specifications for vacuum induction melted plus vacuum arc remelted (VIM-VAR) quality bearing steel [1]. A given PM tool steel alloy displays a toughness advantage over conventional tool steel, due to the absence of carbide banding, coarse carbides, and carbide angularity [4]. Another advantage inherent with PM materials is in non-destructive testing (NDT). Higher levels of resolution are possible in ultrasonic inspection, which decreases the likelihood of a large inclusion from getting into service.

A secondary benefit seen in PM tool steels is the attainable surface finish, which is considerably finer than conventional tool steels due to the small, evenly dispersed carbides, which have less effect on the surface roughness when pullouts occur. This has benefits in reducing noise in operation and initial run-in contamination. However, it must be kept in mind that the improved wear resistance makes it more difficult to achieve a near finish dimension, so specialized machining and grinding equipment is often required.

VIM CRU® 60™ Development

Two chemistry modifications of CPM® VIM CRU 80™, a commercially available corrosion resistant tool steel, were developed. By increasing vanadium carbide contents of these steels, metal-to-metal, abrasive and corrosive wear resistance properties improve [5]. Nominal compositions for the CPM® VIM CRU 80™ chemistry variations (CPM® VIM CRU® 60™ and 98VN084) and other corrosion resistant bearing materials may be found in Table 1.

Table 1. Corrosion Resistant Bearing Material Compositions and Hardness Levels

Material	C	Cr	Mo	Ni	V	Other	Carbide Volume %	Attainable Hardness (±1 HRC)
440C	1.05	17	0.5	---	---	---	~16	59
440 N-DUR™ [6]	0.65	14.5	---	---	---	.1 N	< 16	61
BG42®	1.15	14.5	4	---	1.2	---	16	62.5
Cronidur 30® [7]	0.33	15.5	1	---	---	.3 N	4.5	59
Pyrowear® 675 [8]	0.07	13	1.8	2.6	0.60	5.4 Co	?	64 (case)
CPM® VIM CRU® 80™	2.35	14	1	---	9	---	23	62
CPM® VIM CRU® 60™	3.25	14	2.5	---	12	---	28	64
98VN084*	3.4	14	1	---	14.5	---	31.5	63
CPM® MPL-1	3.75	24	3	---	9	---	46	64

Compositions are reported in wt.%. *Experimental Grade

Three pilot-size heats each of CPM® VIM CRU® 60™ and 98VN084 were melted and atomized to yield enough powder to produce a large, commercial-size compact. The compacts were HIP, GFM radial

forged, and hot rolled to produce bar. Samples were cut and evaluated for heat treat response, retained austenite content, corrosion resistance, and wear resistance as summarized in the following sections.

Heat Treatment Response

Heat treatment response was initially evaluated by austenitizing at 1121°C (2050°F), 1149°C (2100°F), and 1177°C (2150°F), oil quenching, and then double tempering between 260°C (500°F) and 593°C (1100°F).

A second heat treatment response study was performed using the same austenitizing, tempering, and quenching procedures, but incorporating refrigeration at -75°C (-103°F) for one hour between tempers. The results of both heat treatment surveys are presented in Figure 1.

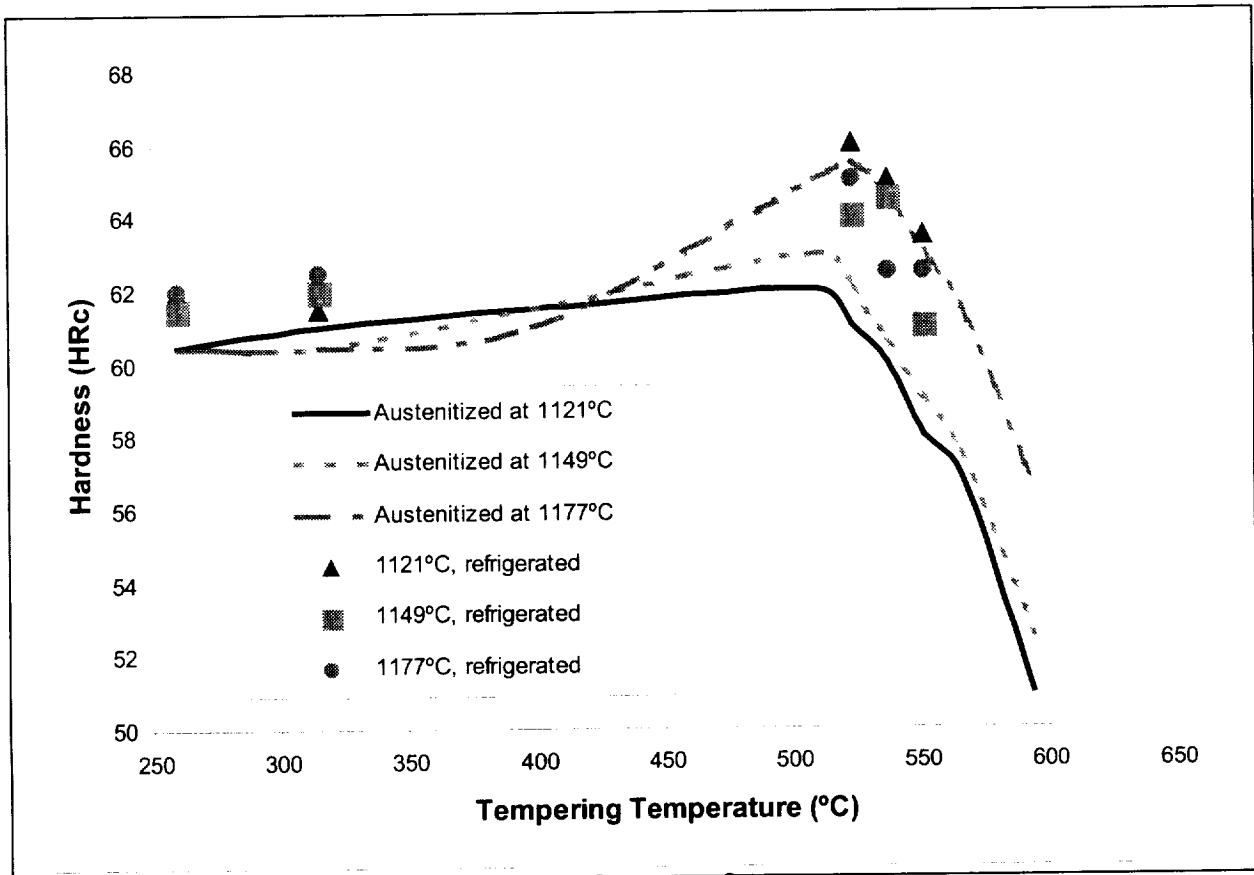


Figure 1. Tempering Curve for CPM® VIM CRU® 60™ (two hour double-temper)

Retained Austenite Content

Results of x-ray diffraction retained austenite (RA) determinations are presented in Table 2. CPM® VIM CRU® 60™ contained approximately 16% RA when oil quenched from 1177°C (2150°F) and 5% RA when quenched from 1149°C (2100°F). Tempering at 510°C (950°F) after oil quenching from either temperature eliminated all retained austenite. Tempering at 260°C (500°F) also eliminated most or all of the retained austenite, defying the conventional wisdom that austenite to martensite transformations will not occur at low temperatures (< 315°C).

The results for refrigeration treatments for CPM® VIM CRU® 60™ were mixed. Cooling to -75°C (-103°F) immediately after the oil quench significantly eliminated or reduced the as-quenched retained austenite contents to below 2% RA (the detection limit of the x-ray diffractometer) for both 1149°C (2100°F) and 1177°C (2150°F) austenitizing. However, applying the refrigeration treatment between a double temper at only 260°C (500°F) resulted in 3% RA for 1149°C (2100°F) austenitizing and 13% RA for 1177°C

(2150°F) austenitizing - i.e. relatively little change from the as-quenched numbers. This implies that some stabilization of the austenite content had occurred.

Table 2. Retained Austenite in CPM® VIM CRU® 60™

Austenitizing Temperature →	1149°C (2100°F)			1177°C (2150°F)		
	As-Austenitized	Tempered 2 + 2 hours		As-Austenitized	Tempered 2 + 2 hours	
260°C		510°C	260°C		510°C	
Heat Treatment						
OQ	5%	<2%	<2%	16%	---	<2%
OQ + refrigeration before tempers	<2%	<2%	---	<2%	<2%	---
OQ + refrigeration between tempers	---	3%	---	---	13%	---

Wear Resistance

Two types of wear tests were performed on CPM® VIM CRU® 60™: crossed cylinder and pin abrasion (Table 3). Other materials evaluated were 440C, CPM® VIM CRU® 80™, and 98VN084. These same tests have been used in the past to evaluate wear resistant materials [9]. The crossed cylinder wear test (metal-to-metal) was performed with stationary samples oriented perpendicular to a rotating tungsten carbide cylinder, in a manner similar to ASTM G 83. A higher wear number is better in this particular test. The wear resistance of CPM® VIM CRU® 60™ in this test is significantly greater than to that of 440C, especially when CPM® VIM CRU® 60™ is multiple tempered at 538°C.

The pin abrasion wear test consists of rotating cylindrical specimen pressed at a fixed load against an abrasive cloth. The test apparatus operates in such a way that the sample is exposed to fresh cloth for the entire duration of the test. A lower weight loss value is better. Again VIM CRU® 60™ exhibited wear resistance significantly greater than that of 440C.

Corrosion Testing

Corrosion testing results from VIM CRU® 60™ were compared to those of 440C, CPM® VIM CRU® 80™, and 98VN084. Results may be found in Table 3. When double tempered at 260°C (500°F), CPM® VIM CRU® 60™, CPM® VIM CRU® 80™, and 98VN084 all exhibit corrosion resistance characteristics at least comparable to that of 440C hardened from 1040°C (1904°F) and double tempered at 200°C (392°F). Tempering CPM® VIM CRU® 60™ or 98VN084 at 538°C (1000°F) reduces the corrosion resistance compared to 260°C (500°F) tempering, but we would expect similar or perhaps somewhat worse results for 440C using high temperature tempering.

Table 3. Wear and Corrosion Resistance of Corrosion Resistant Tool Steels

Material	Austenitizing Temperature (°C)	Tempering Temperature (°C)	Hardness (HRc)	Wear Test Results		Corrosion Test Results	
				Crossed Cylinder Wear Resistance* (x10 ⁷ kg/mm ²)	Pin Abrasion Wear Resistance Weight Loss** (mg)	Dilute Aqua-Regia 24°C-3 hr. (mm/yr.)+	10% Acetic Acid Boiling - 24 hrs. (mm/yr.)++
440C	1040	200	57.5	4	66	109.0	29.0
CPM® VIM CRU® 80™	1121	260	58	9.5	57.9	117.0	17.0
CPM® VIM CRU® 80™	1177	260	58.5	11.9	50.5	102.0	9.0
CPM® VIM CRU® 60™	1149	260	61	38.6	30.5	110.9	57.3
CPM® VIM CRU® 60™	1149	538	62.5	50.9	27	355.1	141.4
98VN084	1149	260	60.5	41.8	30	70.1	15.2
98VN084	1149	538	60.5	40.4	29	309.1	121.0

*higher number is better

**lower number is better

+Specimens exposed for 3 hours in a 24°C aqueous solution containing 5 vol. % HNO₃ and 1 vol. % HCl

++Specimens exposed for 24 hours in a boiling aqueous solution containing 10 vol. % acetic acid.

Discussion/Conclusions

It has been demonstrated that the PM process may be used to manufacture wear and corrosion resistant steels [1-5,9]. With proper heat treatment, CPM® VIM CRU® 60™ is capable of attaining 63-65 HRC after multiple tempering in the range 524-538°C (975°F-1000°F) for maximum secondary hardening and optimum stress relieving. This is significantly greater than the attainable hardness capability of 440C, and also somewhat better than that of BG42® bearing steel. Although some corrosion resistance is sacrificed compared to laboratory results obtained for low temperature tempering, the corrosion resistance of CPM® VIM CRU® 60™ tempered at 524-538°C (975-1000°F) is still significantly better than that of non-corrosion resistant bearing steels. High attainable hardness also results in optimum compressive strength and wear resistance, which were two of the primary objectives of the alloy design. High compressive strength is important for static load capacity and fatigue strength in some advance bearing designs.

Acknowledgements

The authors would like to recognize Robert Dixon, William Stasko, and Maria Sawford of Crucible Research Center for their ongoing support of this program.

References

1. Pearson, P.K., Moll, J.H., Hannigan, C.J., Atwell, D.R. "Evaluation of P/M Tool Steels for Bearing Applications," *Specialty Materials and Composites Advances in Powder Metallurgy and Particulate Materials - 1994, Volume 5*, Metal Powder Industries Federation, Princeton, NJ, 1994, pp. 155-163.
2. Smith, D. W., Leveille, A.R., Hilton, M.R., Ward, P.C., "Rex 20 / Si₃N₄ Control Moment Gyroscope Bearing Development," 32nd Aerospace Mechanisms Symposium, 13-15 May 1998.
3. Hilton, M.R, Ward, P.C., Leveille, A.R., Park, W., McClintock, D.A., Smith, D.W., "Rolling Contact Fatigue and Load Capacity Tests of M62 Bearing Steel", 32nd Aerospace Mechanisms Symposium, 13-15 May 1998.
4. Stasko, W., Pinnow, K.E., Eisen, W.B., "Development of Improved PM Wear and Corrosion Resistant Tool Steels," 4th *International Tooling Conference*, Bochum, Germany, 1996.
5. Dixon, R.B., Stasko, W., Pinnow, K.E., "Particle Metallurgy Tool Steels," *ASM Handbook, Volume 7, Powder Metal Technologies and Applications*, ASM International, Materials Park, OH, 1998, pp. 786-802.
6. Tomasello, C.M., Maloney, J.L., Ward, P.C., Materkowski, J.P., "A New Corrosion Resistant, Martensitic Stainless Steel For Improved Performance in Miniature Bearings," *Bearing Steels: Into the 21st Century*, ASTM STP 1327, J. J. C. Hoo and W. B. Green, Jr., Ed., American Society for Testing and Materials, West Conshohocken, PA, 1998, pp. 437-446.
7. Trojahn, W., Streit, E., Chin, H.A., Ehler, D., "Progress in Bearing Performance of Advanced Nitrogen Alloyed Stainless Steel, Cronidur 30," *Bearing Steels: Into the 21st Century*, ASTM STP 1327, J. J. C. Hoo and W. B. Green, Jr., Ed., American Society for Testing and Materials, West Conshohocken, PA, 1998, pp. 447-459.
8. McCaffrey, T.J., and Wert, D.E., "Development of a Stainless Corrosion Resistant Carburizing Bearing Steel," *Creative Use of Bearing Steels*, ASTM STP 1195, J. J. C. Hoo, Ed., American Society for Testing and Materials, Philadelphia, 1993, pp. 137-148.
9. Stasko, W., Pinnow, K.E., Eisen, W.B., "Development of Ultra-High Vanadium Wear Resistant Cold Work Tool Steels," *Advances in Powder Metallurgy & Particulate Materials - 1996, Volume 5*, T.M. Cadle and K.S. Narasimhan, compilers, Metal Powder Industries Federation, Princeton, NJ, 1996, pp. 16-179 - 17-188.

Crucible, CPM®, VIM CRU®, CPM® VIM CRU® 20™, CPM® VIM CRU® 60™, and CPM® VIM CRU® 80™ are trademarks or service marks of Crucible Materials Corporation.
440 N-DUR™ is a trademark of Timken Latrobe Steel Company.
BG42® is a registered trademark of Timken Latrobe Steel Company.
Cronidur 30® is a registered trademark of FAG Kugelfischer Group.
Pyrowear® 675 is a registered trademark of Carpenter Technology Corporation.

A Low-Shock Stage Separation Mechanism

S. Vara Prasad Rao¹ and Deepak Agrawal*

Abstract

A low-shock pyrobolt-actuated stage separation mechanism for multi-stage aerospace vehicles has been designed, developed and successfully tested. The mechanism is found highly reliable, easy to assemble and disassemble, and generates very low operational shock. This stage separation mechanism is very useful for the applications in which the separation plane is very near to shock sensitive packages. Design, development and testing experiences, which the authors have come across during the development of this low-shock stage separation mechanism, are presented.

Introduction

Various mechanisms can be employed for stage separation of a large multi-stage vehicle, depending on the space availability, ease of integration, and most important of all, the permissible shock levels generated due to stage separation. Very large vehicles employ flexible linear-shaped charge cords, where large shocks (of the order of 50,000 to 100,000 g) are produced, do tolerate the same, since the shock duration is of the order of few tens of microseconds. Moreover in such vehicles, shock sensitive devices like relays and computers are configured in such a way (distance as well as with special mountings) that they do not remain vulnerable. But for vehicles where such high shocks are not permitted, separation mechanisms with very low shock are specially designed to suit the specific purpose. One such low-shock stage separation mechanism is the "pyrobolt-actuated stage separation mechanism". Two stages are fastened together with six or eight pyrobolts. When all the pyrobolts are operated simultaneously, the stage separates.

Pyrobolt-Actuated Stage Separation Mechanism

The key element in this stage separation mechanism is the pyrobolt, which is specially designed for this purpose. Pyrobolt consists of an electro-explosive pyro cartridge, piston, cylinder, a round-head release bolt, and four collets with an arrester as shown in Figure 1. This assembly is kept locked before operation by a locking pin. The release bolt head is engaged in the four collets and can come out when the collets are allowed to move radially outwards. The arrester stops the radial outward movement of the collets. The arrester is locked to the casing by a locking pin. When the pyro cartridge is fired, the arrester moves up due to pyro pressure after shearing the locking pin, hits the check nut and stops. The arrester thus makes the collets free to move out. Pyro cartridge pressure acts on the piston also. The piston pushes the release bolt out. Pyrobolt release operation is shown in Figure 1.

Two stages have a flanged interface and are joined together with a number of pyrobolts. The number of pyrobolts required to join the two stages depends upon the load, bending moment, and space available to mount pyrobolts. More pyrobolts in the joint requires more firing current. Less pyrobolts in the joint needs a bigger diameter of each pyrobolt, and so a pyrobolt requires more mounting space and wider interface flange. The designer has to select number of pyrobolts to join two stages based on the firing current supply source limitations and space available to mount pyrobolts.

Interface Bolted Joint

Loads at the separation interface are mainly axial force, bending moment, and shear force. The bolted joint is designed for these loads. Tensile force on a pyrobolt is estimated for these loads. The joint may open in two possible ways as shown in Figure 3. It may open about the neutral axis as per beam bending theory or it may open about the edge of the stage. Pyrobolts at one side of the axis will experience tensile

¹ Defense Research & Development Laboratory, Hyderabad, India

force when the joint opens about the neutral axis. All the bolts in the joint will experience tensile force when the joint opens about the edge of the stage.

Tensile forces have been calculated for both possible ways of joint opening, and the release bolt is designed for the higher tensile force out of these. For the joint opening about the neutral axis as shown in Figure 2(a), the maximum force will be in the bolt, which is farthest from axis of opening and it is given by

$$F_1 = (BM \cdot PCD \cdot A_b) / (2 \cdot I_{sy})$$

where PCD= pitch circle diameter

A_b = bolt cross-section area

$$I_{sy} = I_b + A_b \sum x_i^2$$

I_b = moment of inertia of the bolt

x_i = distance from neutral axis

For the joint opening about the edge of the stage, it is assumed that the tension in bolt developed due to the bending moment is proportional to the distance of the bolt from the edge of the section. Assuming n (even number) number of bolts are necessary to withstand loads, all the bolts of the joint will be in tension and the joint will try to open about the N-A axis as shown in Figure 2(b). Maximum tensile force will be in the bolt that is farthest from axis of opening and given by

$$F_n = 8 \cdot BM / 3 \cdot n \cdot PCD$$

Separation Dynamics

The pyro cartridge generates high-pressure gases (order of 80 MPa) in the free volume between the piston and pyro cartridge. Gas pressure acts on the pyro cartridge and piston. Since the pyro cartridge is mounted on the arrestor, the arrestor moves and makes the collets free. Once the collets are free, they move radially outwards with the force transferred by the release bolt on collets, and at the same time the piston moves ahead and pushes the bolt out. The force acting on the piston is sufficient to move the bolt against friction forces. The stroke length of the piston is sufficient to push the bolt out of the pyrobolt casing. Since the arrestor and release bolt move in opposite directions, the net recoil force on the pyrobolt mounting is less and so recoil shock is less. Major shock in pyro devices is due to recoil forces, which is very low in pyrobolt. So the separation shock is less. The pyrobolt is assembled with two stages as shown in Figure 3. The pyrobolt after firing is shown in Figure 4. A guide is provided all along the circumference as shown in Figure 4 to avoid lateral movement of the spent stage just after the pyrobolts are fired. The spent stage can separate when it rotates about its edge as shown in Figure 5. The bolt head may interfere with the on-going stage as shown in Figure 5. This may lead to a disturbed stage separation. This can be avoided if the guide length is sufficient and local flange thickness of on-going stage is minimum. The tapered hole in the flange will also allow the bolt head to come out without interfering as shown in Figure 5.

Separation Shock

Separation shock is measured by placing accelerometers at different locations on the spent stage and the on-going stage. Bruel & Kjaer model 8309 accelerometers are used. Three sensors 1, 2 & 3 are placed to measure axial shocks and 4, 5, & 6 are placed to measure radial shocks. The shock levels at the locations are given in Table 1.

Table 1: Separation Shock Levels at Different Locations

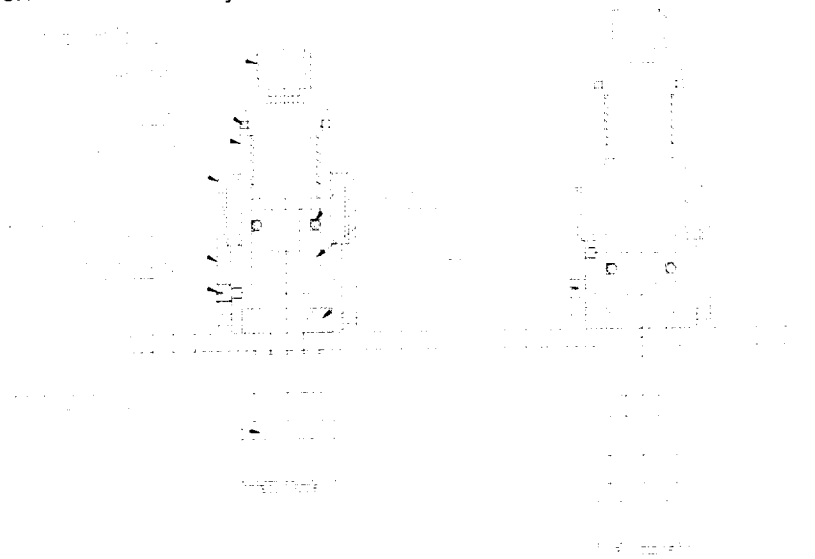
Location	Shock Level
1	600g, for 20 ms
2	500g, for 20 ms
3	200g, for 10 ms
4	100g, for 10 ms
5	500g, for 20 ms
6	500g, for 20 ms

Conclusion

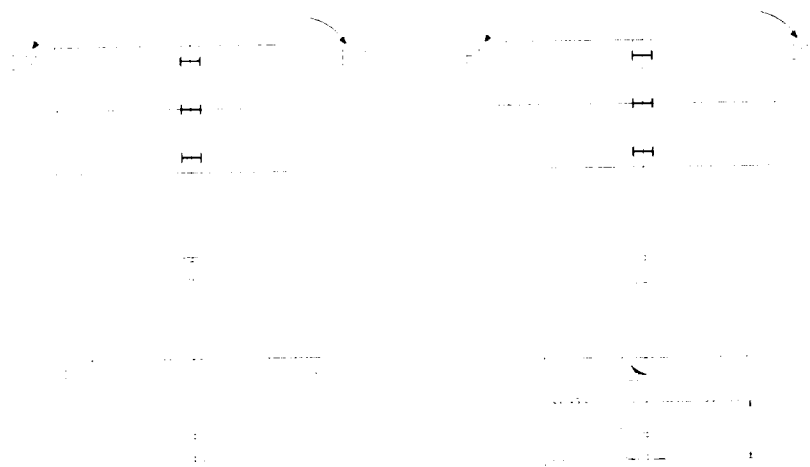
Stage separation shock in pyrobolt-actuated stage separation is very low and so this stage separation mechanism is very useful for applications where the separation plane is close to shock sensitive packages/passengers. The assembly and disassembly of stages are easy and safe. Maintenance of the separation system is easy and safe. The functionality of a pyrobolt can be confirmed by pneumatic pressure before it is assembled to the flying vehicle.

References

1. S. Vara Prasad Rao, Deepak Agrawal. "Pyrobolt for Low Shock Stage Separation Mechanism". National Seminar on Aerospace & Related Mechanisms, Paper 13.
2. Neil Butterfield. "Pyrotechnic Release Devices". Space Vehicle Mechanisms Elements of Successful Design edited by Peter L. Conley.
3. Karl O. Brauer. "Handbook of Pyrotechnics"



Before operation After operation
Figure 1. Pyrobolt before operation and after operation



(a). Joint opening about Neutral axis (b). Joint opening about edge
Figure 2. (a), (b): Possible ways of joint opening



Figure 3. Pyrobolt before firing



Figure 4. Pyrobolt after firing

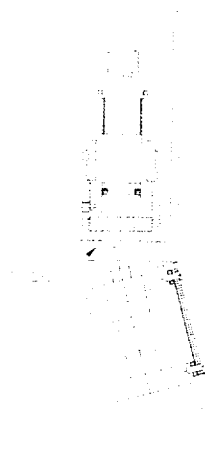


Figure 5. Released spent stage

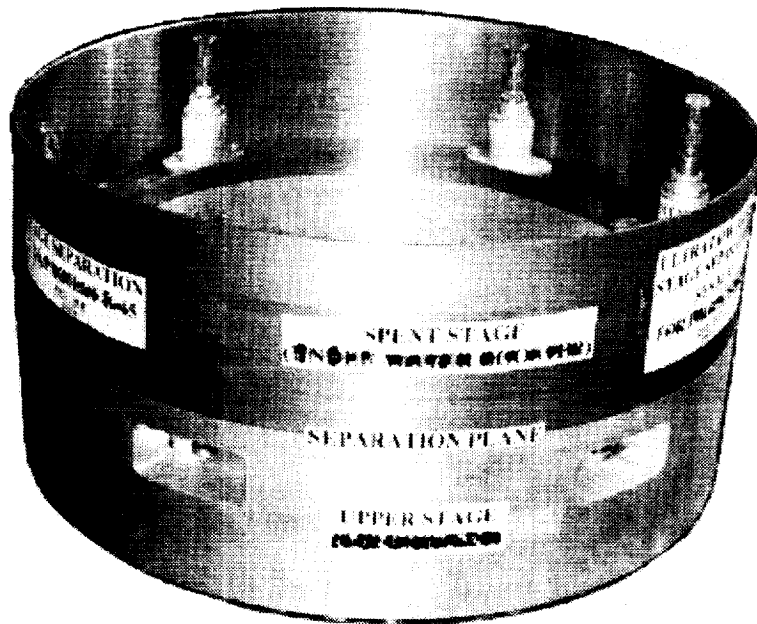


Figure 6. Stage bolted joint assembly

219/37

Design of a High Resolution Hexapod Positioning Mechanism

Jamie Britt*

Abstract

This paper describes the development of a high resolution, six-degree of freedom positioning mechanism. This mechanism, based on the Stewart platform concept, was designed for use with the Developmental Comparative Active Optics Telescope Testbed (DCATT), a ground-based technology testbed for the Next Generation Space Telescope (NGST). The mechanism provides active control to the DCATT telescope's segmented primary mirror. Emphasis is on design decisions and technical challenges. Significant issues include undesirable motion properties of PZT-inchworm actuators, testing difficulties, dimensional stability and use of advanced composite materials. Supporting test data from prototype mechanisms is presented.

Introduction

Large, active-optics systems for space are pushing the limits of positioning mechanism design. Active optics mechanisms require increased motion resolution and position stability, often in multiple degrees of freedom. The DCATT telescope is a ground-based example of this type of system. Figure 1 shows a model of the DCATT testbed. The vertical structure is DCATT's Cassegrain telescope, standing 4.6 m (15 feet) tall. Figure 2 shows DCATT's one-meter-diameter primary mirror, which consists of seven hexagonal, aluminum segments. As part of the testbed's experimental plan, these segments must be actuated in six degrees-of-freedom (6-DoF) with nanometer and arc-second resolution over a range of millimeters and degrees. Once in position, the mechanisms must hold position for one or more hours.

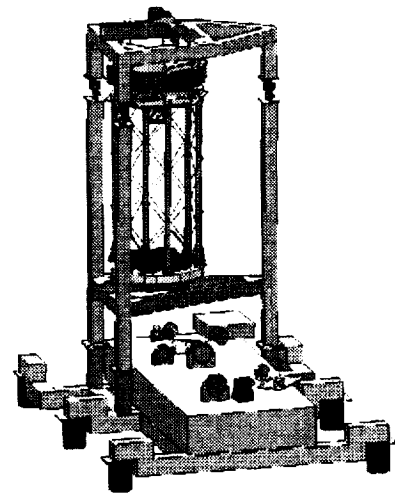


Figure 1. DCATT Testbed Model

The result is the DCATT hexapod positioning mechanism. Based on the Stewart platform concept, the DCATT hexapod provides 6-DoF motion using a truss-like arrangement of linear actuators. This arrangement is both compact and rigid. Commercially available, piezo-electric, PZT-inchworm actuators provide the hexapod's high-resolution motion. Materials with low and negative coefficients of thermal expansion (CTE) are used in the legs to provide maximum dimensional stability.

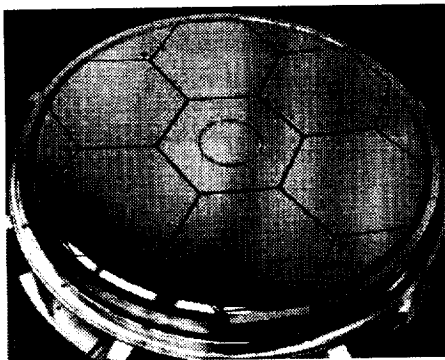


Figure 2. DCATT Primary Mirror (shown in polishing fixture)

A number of obstacles had to be overcome during development of the mechanism. The first challenge involved motion tests of the selected actuators, which revealed undesirable motion properties. Developing a high-resolution, 6-DoF motion test was the next challenge. This test brought to light problems with the dimensional stability of both the mechanism and the test setup. These were addressed with new designs incorporating low-CTE metals and negative-CTE composites. All of these issues, along with their solutions will be presented in this paper.

Prior to integration and testing of the final hexapod design, the DCATT project was cancelled due to a shift in focus of the NGST project. Thus, final performance testing of the hexapods was never performed.

* NASA Goddard Space Flight Center, Greenbelt, MD

DCATT Hexapod Requirements

General Requirements

The DCATT testbed was created to test optical wavefront control for NGST. The goal was to use these methods to achieve diffraction-limited performance in the DCATT telescope. This required active control of the telescope's segmented primary mirror. The DCATT hexapod was designed to perform this task.

The segments were constructed from machined aluminum with mirror surfaces of polished-nickel. Each outer segment weighed 2.3 kg (5 lb). The center segment weighed 1.4 kg (3 lb). All seven segments had to be actuated in 6-DoF from beneath the mirror. Thus, each mechanism had to support and actuate the weight of a segment. In addition, light passing through center segment's hole could not be obstructed.

Actuation Range and Resolution

Table 1 gives the range and resolution requirements for the DCATT hexapod in three critical degrees of freedom. Tip and tilt are rotations perpendicular to the optical axis of the mirror. Piston is linear motion parallel to the optical axis of the mirror. Although the other degrees of freedom were required, they did not have specific resolution or range requirements attached to them. They simply had to be of the same order of magnitude as the critical three.

Table 1. Actuation Requirements: Resolution and Range

Tip/tilt resolution	+/- 0.01 arc-sec
Tip/tilt range	+/- 0.5°
Piston resolution	+/- 0.1 μm
Piston range	+/- 0.05 mm

The DCATT hexapod's resolution requirement is driven by the need to align the segments of the primary mirror. The range requirement is driven by the need to misalign the segments by optically large values at the start of an experiment.

Position Stability

A minimum requirement for jitter motion was not given at the start of the design process. Jitter stability was implied by a 100-Hz minimum-stiffness goal for the hexapod's first mode of vibration.

Long-term stability was implied by a requirement that the telescope be "self-compensating" for dimensional changes caused by thermal expansion. This mandated that the structure have the same CTE as the mirrors. Since the mirrors were made of aluminum, the structure and hexapods were to be aluminum as well.

DCATT Hexapod Concept

Figure 3 shows a computer model for the aluminum DCATT hexapod. Each leg contains an IW-700 PZT Inchworm linear actuator manufactured by Burleigh Instruments¹. All parts are aluminum except for the actuators and three flexures in each leg. Figure 4 shows an exploded view of a leg assembly. The flexures provide the same degrees of freedom as ball-and-socket joints in an ideal Stewart platform, but without the frictional problems of real ball-and-socket or universal joints.

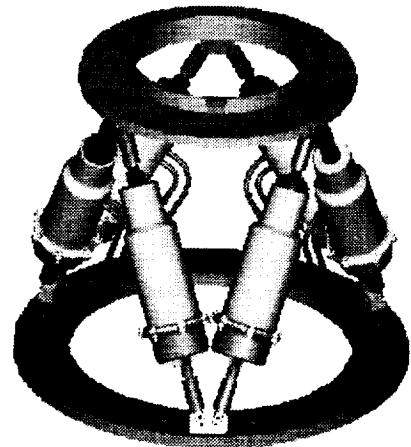


Figure 3. Hexapod Model

¹ Burleigh Instruments, Inc., Burleigh Park, Fishers, New York, 14453-0755

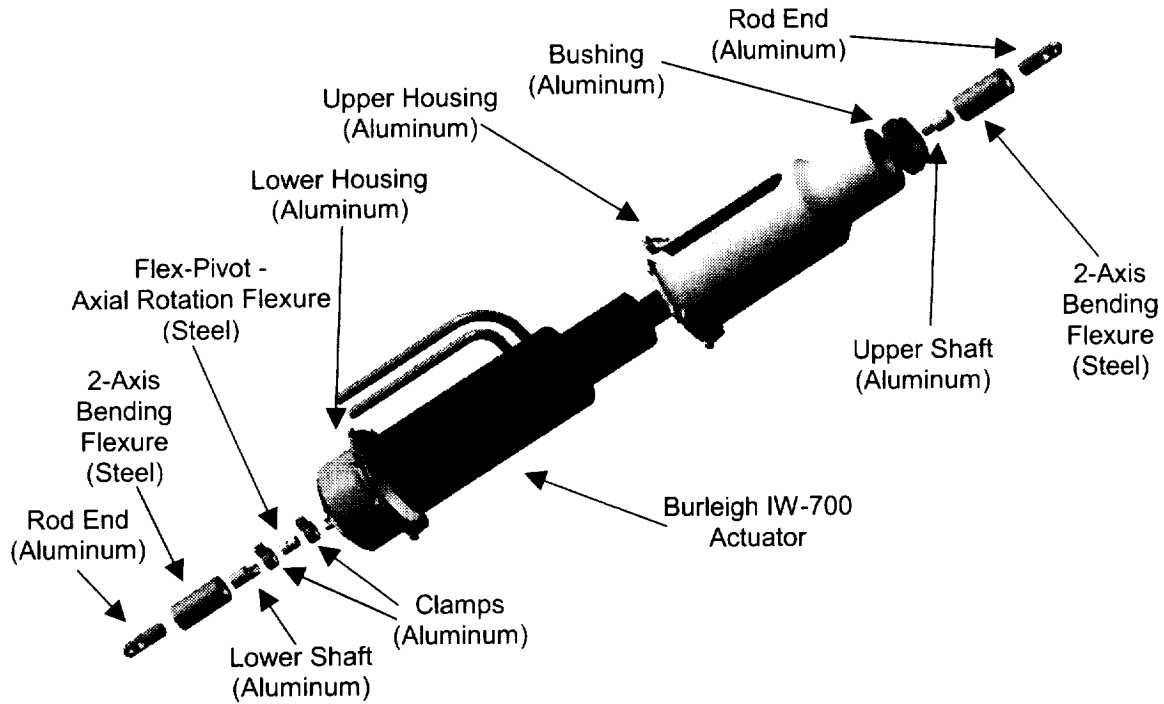


Figure 4. Exploded View of Hexapod Leg

Table 2 shows the stated performance of the IW-700 actuators. Table 3 shows the predicted performance of the hexapod compared to the requirements. These predictions were calculated using the IW-700 performance numbers and a kinematics model based on the geometry of the hexapod.

Table 2. IW-700 Performance

Minimum Step Size:	4 nm
Actuation Range:	6 mm

Table 3. Predicted Hexapod Performance

Motion	Requirement	Predicted Performance
Tip/Tilt Resolution	+/-0.01 arc-sec	+/-~0.002 arc-sec
Tip/Tilt Range*	+/- 0.5 deg	+/- 1.0 deg w/+/-1.0 mm piston
		+/- 1.7 deg w/+/-0.5 mm piston
		+/- 2.0 deg maximum range
Piston Resolution	+/- 0.1 μ m	+/- ~0.005 μ m
Piston Range*	+/- 0.05 mm	+/- 0.5 mm w/+/-1.7 deg range
		+/- 1.0 mm w/+/-1.0 deg range
		+/- 3.4 mm maximum range

*NOTE: Maximum ranges for all degrees of freedom are coupled. Sample extremes within the motion envelope are given.

PZT-Inchworm Actuator Motion Issues

For a good portion of the design process, the assumption was made that the IW-700 actuators would move with the resolution stated in Table 2 over their entire range of motion. This would allow the actuators to be operated in an essentially open-loop fashion. Control software would determine how far each actuator had to move to position the mirror segment and then command a certain number of

actuator steps to achieve that motion. Characterization of the actuator motion was not done until later in the program. This was a mistake, as characterization turned up a significant design issue.

The IW-700 inchworm consists of a moving shaft, two PZT clamps, and a third PZT element that changes the distance between the two clamps. Figure 5 shows how these elements work together to move the shaft. First, PZT Element 1 clamps the shaft while PZT Element 2 extends. This causes the shaft to move to the left. The distance moved is determined by the voltage applied to Element 2. A 1 V increment causes a single step of 2-4nm. After 665 steps, Element 2 becomes fully extended. Then Element 3 clamps the shaft followed by the release of Element 1. In this configuration, the shaft will continue to move to the left as Element 2 contracts. This process is repeated to move the shaft through the actuator's entire range of motion.

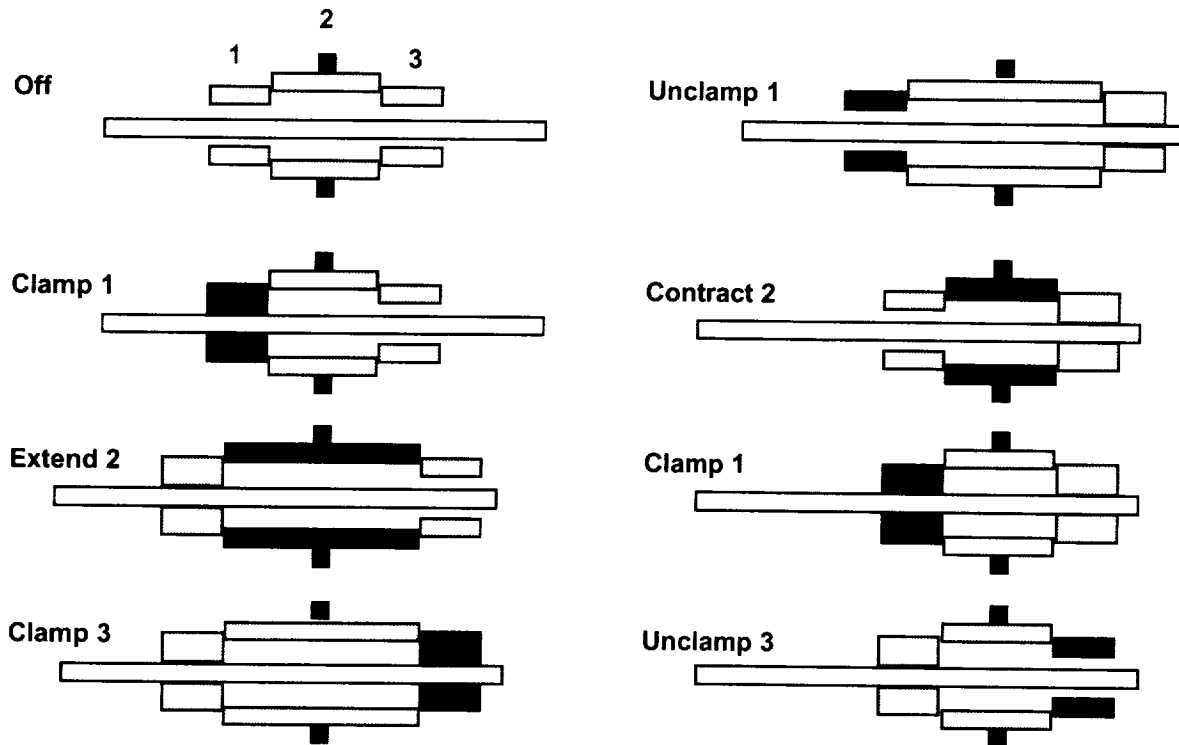


Figure 5. Inchworm Actuator Motion

Characterization tests of the actuators revealed that a motion discontinuity occurs when the clamps exchange. Imperfections in the way the clamps grip the shaft cause the shaft to move forward or backward by an uncontrolled amount. Tests showed this discontinuity to be as large as 215 nm. Since thousands of clamp changes occur throughout the actuator's range, this prevents the actuator from being accurately commanded in an open-loop fashion. Furthermore, it was feared that the actuator could have "dead-zones", positions within the length of a discontinuity that the actuator could never reach.

Figure 6 shows a graph of commanded actuator position plotted against measured position determined using a Zygo laser-ranging interferometer. The actuator has been run back and forth repeatedly through the same clamping cycle. That is, the actuator was run through 1330 steps, causing element 2 to go through full expansion and contraction, and causing both clamps to open and close on the shaft. Then the actuator was run backwards to its starting position, and the process was repeated.

The discontinuities can be clearly seen every 665 steps. It is important to note that discontinuities occur in both the forward and reverse directions, but with different magnitudes. Discussions with the manufacturer suggest that the magnitudes vary depending on the actuator's loading condition. This result suggested that by moving back and forth across a discontinuity, the actuator could achieve any position within its

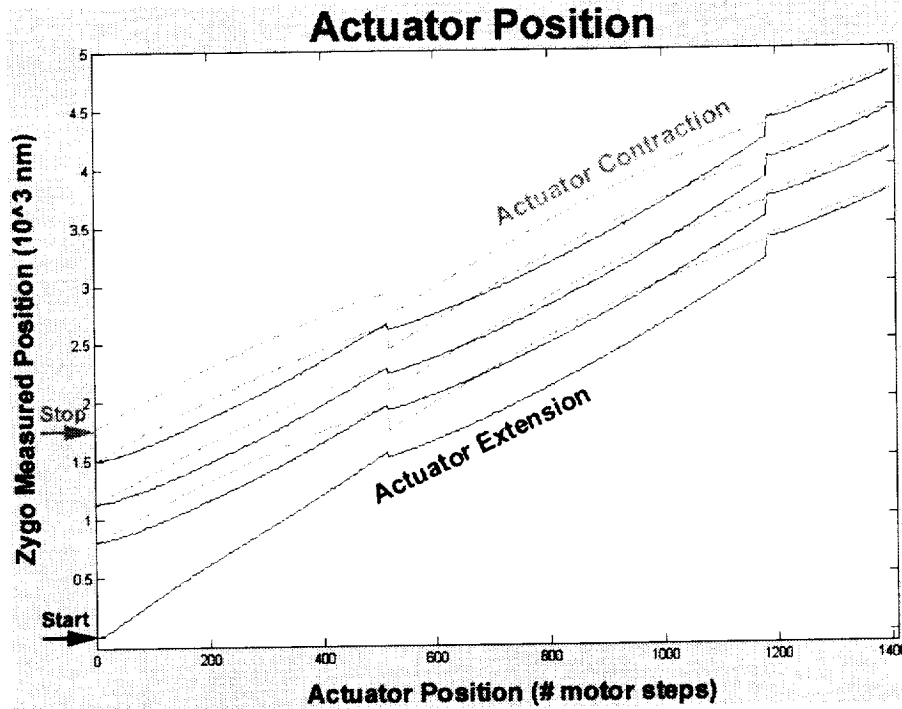


Figure 6. Actuator Motion Discontinuities

range. Thus, the discontinuities do not cause any “dead-zones”. In order to operate the actuator in this fashion, however, high-resolution position feedback must be provided to the control system. The DCATT controls team made efforts to address this problem, but that work is beyond the scope of this paper.

Anyone considering the use of high-resolution inchworm actuators should be aware of these potential discontinuities, and design their system accordingly. Discuss this issue with vendors before selecting actuators for a design. Early actuator characterization is also strongly recommended.

6-DoF Motion Testing

The 6-DoF Test Facility

In the hexapod mechanism, all six actuators move in combination to achieve motion along one degree of freedom. The required motion from each actuator is calculated using the hexapod kinematics model. Deviations from the geometry used in that model, including machining and assembly errors, will introduce errors into that calculation. Early in the design it became clear that characterizing and calibrating the motion of each assembled hexapod would be critical. In order to accomplish this, a test was required that could measure the hexapod’s motion in all six degrees of freedom simultaneously. Devising this test with the required resolution was not trivial.

Laser-ranging interferometers were selected to make most of the measurements. By reflecting off a mirrored cube attached to a hexapod, three beams could be used to measure linear motion of the hexapod. Parallel beams hitting the same cube face could be used to measure rotation over a small range. As long as rotations remained small, all the interferometers could make measurements simultaneously. An autocollimator reflecting off another mirror provided 2-axis rotational measurements with greater range than the interferometers but less resolution.

Figure 7 shows a prototype hexapod that was used to help develop the 6-DoF testing facility. Figure 8 shows the prototype in the facility. A flat “dummy segment” has been bolted to the prototype to provide a mounting surface for the mirrors. In this picture, two lasers have been split to feed three interferometers.

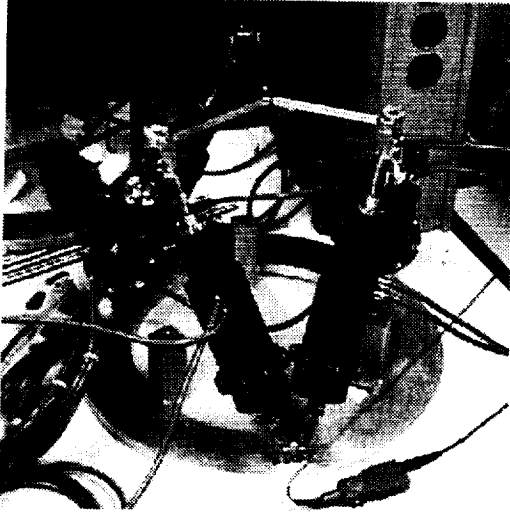


Figure 7. Prototype Hexapod

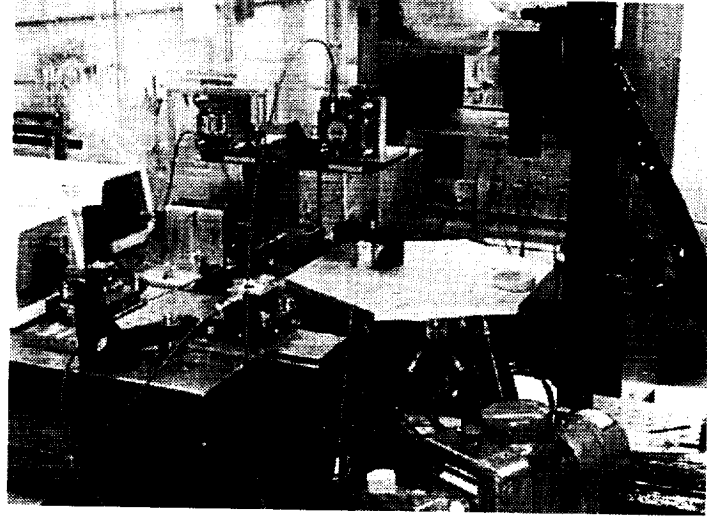


Figure 8. 6-DoF Testing Facility

These interferometers are measuring the three linear degrees of freedom as well as rotation about the piston axis. An autocollimator is being used to measure tip and tilt rotation.

6-DoF Testing Results

The 6-DoF facility was never used to fully characterize a hexapod. During testing with the prototype, the design team discovered significant dimensional stability problems. Part of this instability was thermal expansion in the hexapod, which is discussed in the following section. The rest of the problem was attributed to thermal expansion of the test setup. It became clear that dimensional stability of the test setup was imperative for measuring the high-resolution motion that was desired from the hexapod. Machined aluminum parts traditionally used to mount optical elements were unacceptable for this test. Plans were made to replace the aluminum parts in the test setup with low-CTE metals such as Invar or Super Invar. This effort was not completed before the project was cancelled.

Although 6-DoF tests were performed on the prototype hexapod, that data will not be presented here. In addition to dimensional stability errors, these tests occurred before the inchworm motion discontinuities were discovered and addressed. With multiple sources of error in the measurements, the data from these tests is considered unreliable.

Despite errors in the data, the 6-DoF testing effort is considered a partial success. The facility was sensitive enough to detect both dimensional stability problems and systematic errors that resulted from inchworm discontinuities. It is believed that DCATT's 6-DoF testing facility is a good model for similar testing endeavors. As will be described in the following section, designers of similar facilities should carefully examine the dimensional stability of their potential test setup. When attempting to measure movement on the scale of nanometers, thermal expansion of the test setup can be as large or larger than the motions that are being measured.

Dimensional Stability and New Requirements

Discovery of the Dimensional Stability Problem

In keeping with the early goal of a self-compensating telescope, the dimensional instability of aluminum was at first seen as a bonus. As the temperature changed, it was desirable to have the telescope structure expand or contract at the same rate that the mirror's figure was changing. Experiments with the prototype hexapod in the 6-DoF testing facility brought to light serious flaws with this thinking. Initial discussions of thermal expansion assumed that the structure would expand or contract as a unit. Testing,

however, showed how the hexapods could behave as individual structures growing at different rates. Worse still, individual hexapod legs might grow at different rates, causing the mechanism's position to drift in all 6 degrees of freedom.

Prototype tests showed that the hexapod's position was drifting. In an attempt to isolate this motion, tests were run with the hexapod in a static position. The test facility monitored changes in the hexapod's position over time. Figure 9 is an example of this data taken by the autocollimator. As can be seen, the measurement drifts in tilt by about 1 arc-second and then back during the course of the test. The bottom axis of Figure 9 is given in the number of measurements taken. The total time of the test is about 1 hour.

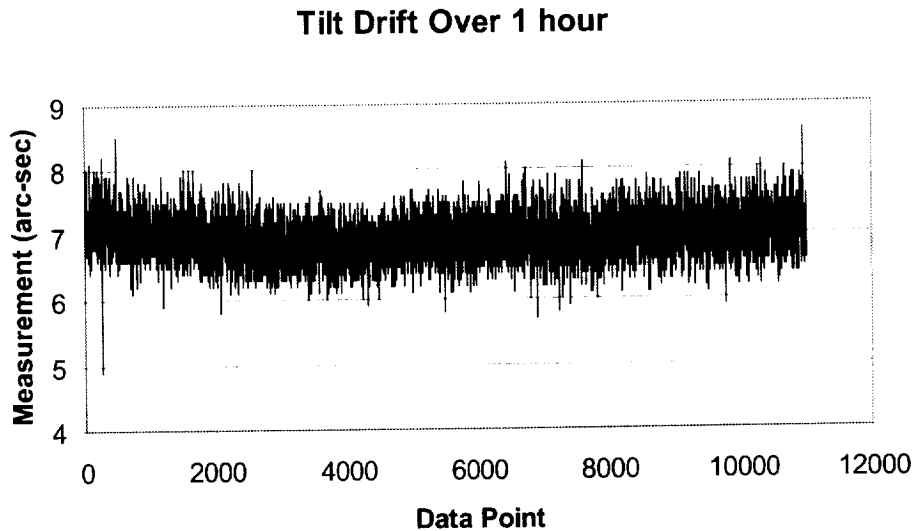


Figure 9. Position Drift in Prototype Hexapod

After ensuring that there was no data drift caused by the measuring tools, it was hypothesized that this drift was the result of thermal expansion within the hexapod and/or the test setup. The next step was to analyze the hexapod's dimensional stability in more detail.

Hexapod Dimensional Stability Analysis

A simple thermal-expansion model was created to analyze the dimensional stability of the hexapod. The analysis focused only on the hexapod legs, not the base or mounting platform. This was done for several reasons. First, the legs comprise most of the height of the hexapod, so their contribution to growth is much larger than either the base or the platform. The parts in the legs are also less massive than the base or platform, so they are likely to change temperature faster. Lastly, the actuators themselves are a source of heat, and fluctuations in that heat will effect the legs more than the base or platform. Since all legs are identical, only one hexapod leg was modeled.

In the model, each part was represented by an effective length (L), a coefficient of thermal expansion (α), and a temperature differential (ΔT). Only parts that added to the growth of the leg were included in the model, and L represents only the portion of that part which contributes to leg growth when it expands. The value ΔT represents a static, bulk temperature increase in the leg. The growth (ΔL) of each part was calculated by multiplying these three characteristics together:

$$\Delta L = L * \alpha * \Delta T$$

The total growth of the leg was calculated by adding the growths of all the parts. Thermal expansion coefficients were based on part material, with the exception of the actuator itself. For the actuator, the

value of $L \cdot \alpha$ was determined experimentally. In the model, the growth contribution of the actuator is determined by multiplying this $L \cdot \alpha$ by ΔT .

Two extreme cases were used to equate leg growth to hexapod position drift. In the first case, all legs on one hexapod are assumed to grow the same relative to another hexapod in the system. Thus, ΔT is a difference in temperature between two hexapods. The resulting leg growths produce a piston error between the two segments. The size of this piston error was calculated using the hexapod kinematics model. The second case assumes that two adjacent legs on the same hexapod grow relative to the other legs on that hexapod. This produces a tilt error. The size of this error was also calculated using the hexapod kinematics. It should be noted that both of these cases are conservative. In reality, differential leg growth will be random, resulting in less segment drift than predicted for most cases.

Table 4 shows the spreadsheet thermal model for a single hexapod leg with a 1°C ΔT applied. The hexapod drift uncovered by this analysis was large enough to prompt a closer look at the dimensional stability requirements for the hexapods.

Table 4. Thermal Expansion Analysis of Hexapod Leg

Part	Number Per Leg	Length (mm)	Material	α at 20 C (/C)	ΔT (deg C)	Growth (nm)	Total Growth (nm)
Rod end	2	12.07	303 Stainless Steel	1.55E-05	1	186.77	373.53
Flex couple	2	6.02	303 Stainless Steel	1.55E-05	1	93.19	186.37
Upper shaft	1	9.14	303 Stainless Steel	1.55E-05	1	141.55	141.55
Upper housing	1	107.44	Al 6061-T6	2.29E-05	1	2456.12	2456.12
Actuator	1	NA	Steel and Al	2.38E-07 m ^o C	1	238.37	238.37
Lower housing	1	30.48	Al 6061-T6	2.29E-05	1	696.77	696.77
Flex pivot	1	7.62	420 Stainless Steel	9.90E-06	1	75.44	75.44
Lower shaft	1	11.94	303 Stainless Steel	1.55E-05	1	184.80	184.80
Hexapod Height change if all actuators grow:						5005.90 nm	4352.96
Hexapod tilt if 2 actuators grow:						8.22 arc-sec	

New Dimensional Stability Requirements

DCATT's largest concern with position stability was that once the primary mirror was aligned, it should stay aligned for the remainder of the experiment. The length of an experiment was unclear, but was expected to be between 1 hour and 8 hours. During that time, the DCATT scientists defined two new requirements that the hexapods had to meet.

First, no hexapod could grow in piston more than 10 nm relative to any other hexapod. All the hexapods could move together by more than this amount, but their relative piston positions had to stay within 10 nm. Thus, significant thermal growth in the hexapods was allowed. Differential thermal growth, however, would violate the new requirement.

Second, no hexapod could tilt more than 0.025 arc-second from its commanded position. Tip and tilt drift would result from differential growth of individual hexapod legs. Again, all the legs in a hexapod could grow significantly without causing enough drift to violate the requirement. Only differential leg growth posed problems.

The hexapod-leg thermal model was used to calculate the temperature difference between legs that would exceed these new requirements. That value is 0.002 deg C.

Characterizing the Thermal Environment

With the thermal model in hand, the next step was to determine the actual temperature variation that was likely to exist between hexapod legs. Thermocouples were attached to each leg of a prototype hexapod, and that hexapod was placed on the DCATT testbed. Additional thermocouples were placed on the hexapod's base, a dummy segment mounted to the hexapod platform, and the telescope baseplate. After the legs came to equilibrium in the environment, the actuators were turned on and temperature data was taken for a period of 24 hours. This data included a one to two hour period during which the legs rose to a new equilibrium temperature due to actuator heating. The remainder of the data showed how the temperature of the legs varied with time.

Figure 10 is a graph of the raw data from this test. Note that leg #2 appears to be significantly colder than the other hexapod legs. Examination of the test setup revealed that leg #2's thermocouple had become partially unattached during the experiment. For this reason, leg #2's data was not included in the analysis.

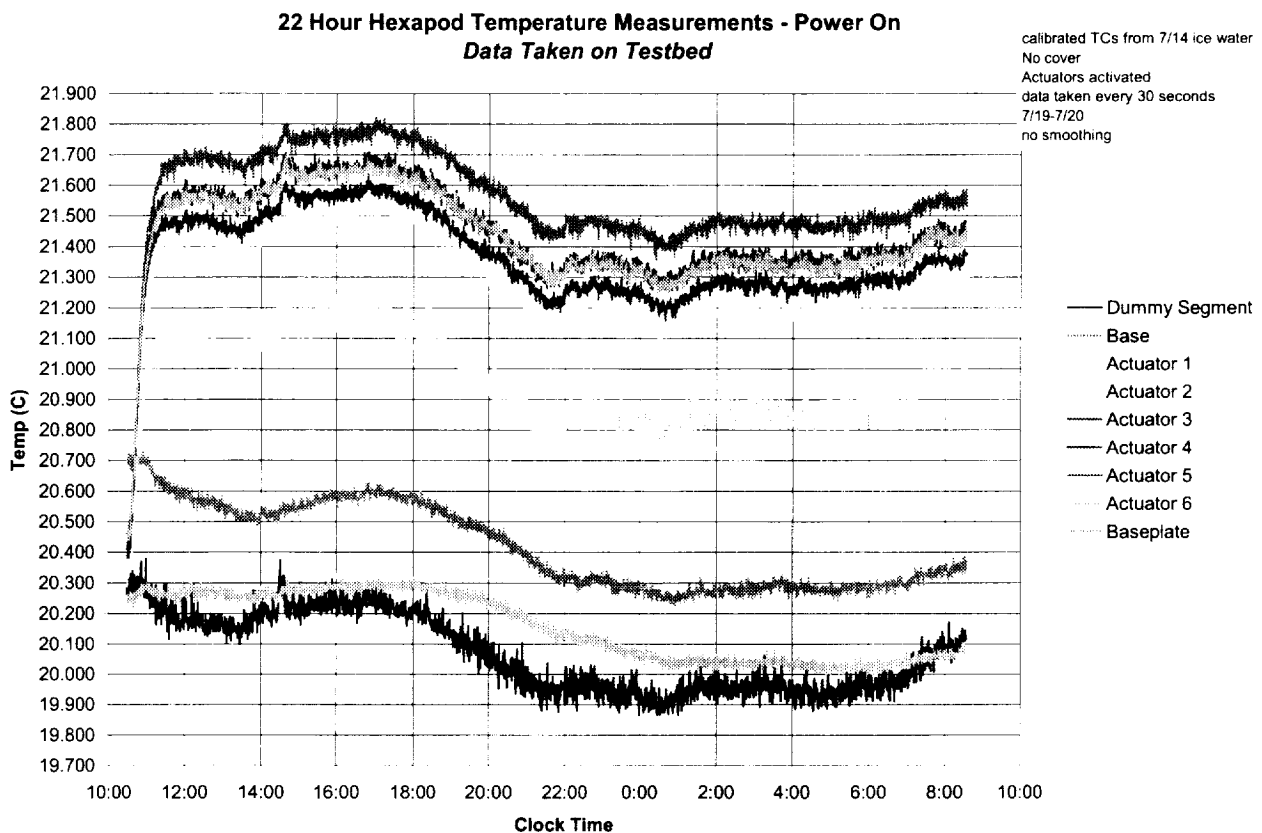


Figure 10. Hexapod Temperature Measurements

Analyzing the Hexapod in the DCATT Thermal Environment

Because the dimensional stability requirements are effected by relative leg growth, it is necessary to compare the temperatures of one leg with another. Figure 11 shows three curves derived by subtracting one leg's test results from another, after those results were smoothed with a running average. Ideally, it would be desirable for these curves to be constant at zero. This would produce no segment drift. If the curves were constant but non-zero, the segments would move in piston, but would have no relative drift or significant tip/tilt drift. This would still meet the long-term stability requirements. As can be seen in Figure 11, however, the difference curves are not constant. Therefore, undesirable drift will occur. The

worst variation in the test occurs in the difference between leg#5 and leg#4. This curve was used for the rest of the analysis, and was referred to as the 5-4 curve.

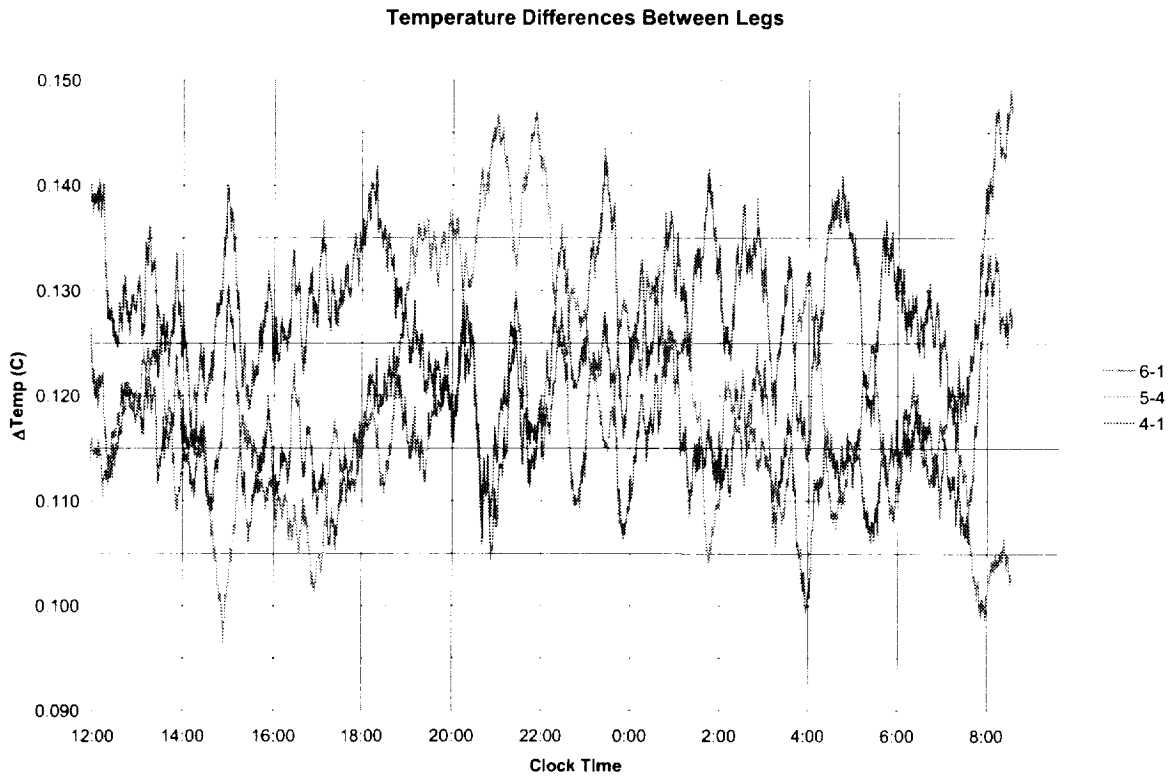


Figure 11. Temperature Difference Curves for Selected Pairs of Hexapod Legs

To examine the hexapod’s response, the 5-4 curve was treated as a leg temperature vs. time curve and variations in it were considered to be ΔT values which could be input into the hexapod-leg thermal model. The largest variations in the curve for 1, 2, 3, 4, and 8-hour intervals were determined. These values are given in Table 5. Recall that the requirements will be exceeded if the differential change in temperature between hexapod legs is larger than 0.002 deg C. Table 5 shows that the requirement will be exceeded during any of the time intervals considered.

Table 5. Maximum Variation in 5-4 Curve for Selected Time Intervals

Time Interval	Time Range for Largest ΔT	ΔT (deg C)
1 hr.	18:30 – 19:30	0.026
2 hr.	21:52 – 23:52	0.032
3 hr.	16:55 – 19:55	0.035
4 hr.	21:52 – 01:52	0.043
8+ hr.	14:00 – 22:00	0.05

Table 6 shows how the thermal growth model responds to the ΔT values in Table 5. Again, the requirements are exceeded in all of the time intervals by at least an order of magnitude. Controlling the temperature of the hexapod legs to 0.002 deg C was considered unreasonable, so it was decided that the aluminum hexapod design would not meet the new requirements.

Table 6. Predicted Drift of Hexapod in DCATT Environment

Time Interval	ΔT (deg C)	Piston Error (nm)	Tip/Tilt Error (arc-sec)
1 hr.	0.026	130	0.214
2 hr.	0.032	160	0.263
3 hr.	0.035	175	0.288
4 hr.	0.043	215	0.353
8+ hr.	0.05	250	0.411
Requirements:		10	0.025

Dimensionally Stable Design for a Hexapod Leg

Proposed Design

The goal of the new design was to maximize the dimensional stability of the hexapods legs by using materials with low or negative CTEs. The first iteration used only low-CTE metals: Invar and Super Invar. The final design incorporated graphite-epoxy composites with a negative CTE along the axis of the leg. Figure 12 shows the final leg design.

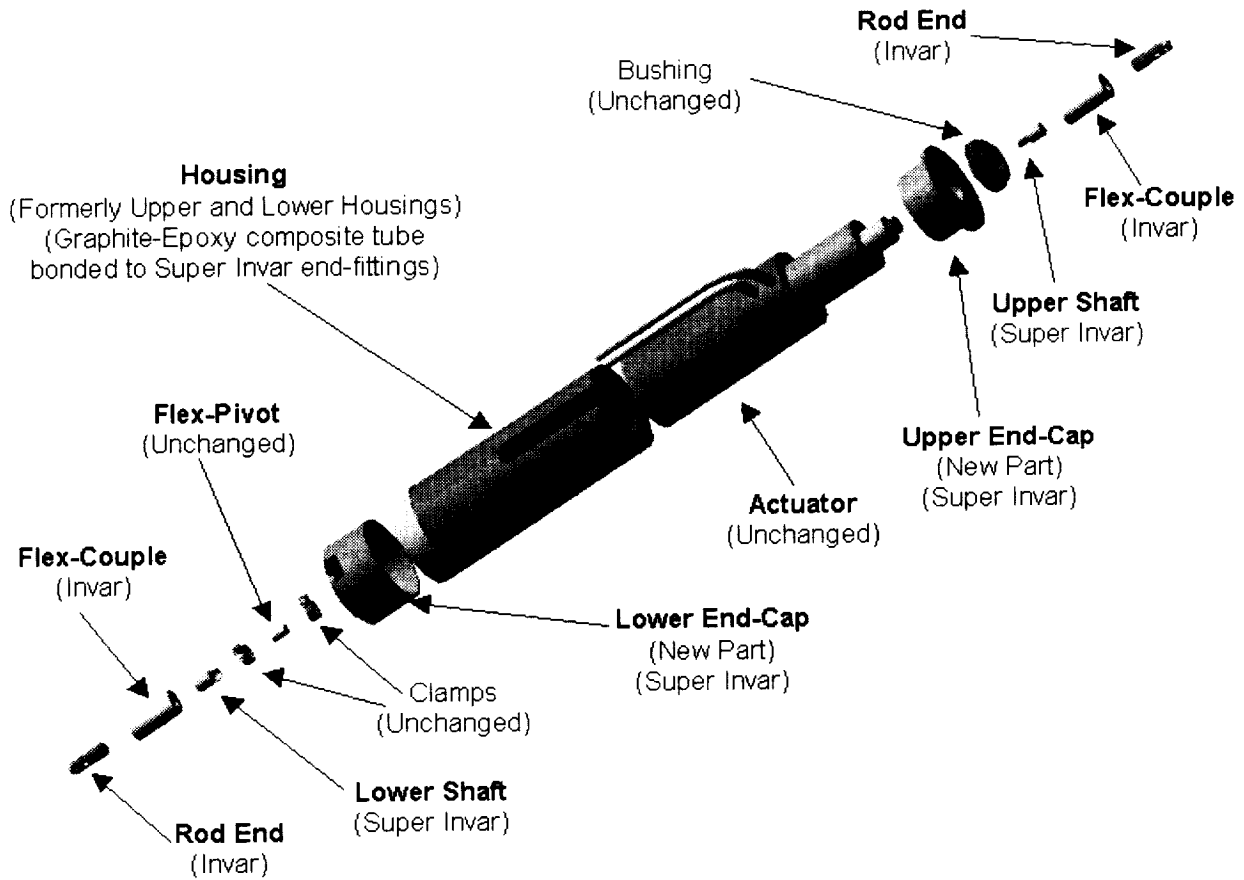


Figure 12. Dimensionally Stable Hexapod Leg

Composite Design Effort

The design of the composite tube required its own effort, with assistance from a materials engineer specializing in composites. Analysis suggested that with the proposed leg concept, a composite tube could be designed that would provide the leg assembly with a near-zero CTE in the axial direction. The goal for the tube was to have a CTE in the axial direction of $-4.4E-6$ per deg C. Specific analysis was also required to estimate the effective CTE of the overlap between the tube and the Super Invar end-fittings that were bonded to it.

The composite material designed uses 9 layers of Amoco's T50 graphite fiber with Cytec Fiberite's 954-2A cyanate ester resin. A layup of 30/30/-30/-30/0/-30/-30/30/30 was predicted to provide the desired CTE of $-4.4E-6$ per deg C. This layup takes advantage of the large Poisson's ratio of the material to amplify the negative thermal expansion of the tube. As the temperature increases, the tube expands in diameter, and this causes the tube to shrink in the axial direction. This is in addition to axial shrinking caused by the negative CTE of the composite fibers themselves. This layup design has reduced strength and stiffness compared to other layup options. In this application, however, the strength and stiffness properties were determined to be adequate. This was an acceptable trade.

Since the hexapod would be in a terrestrial environment, dimensional changes caused by moisture absorption in the composite were a concern. The composite selected had a large coefficient of moisture expansion (CME). This effect had to be minimized, or the new hexapod would be just as dimensionally unstable as the old one. This problem was solved by applying a moisture barrier. Parylene-C, a polymer commonly used for conformal coating electronics, was selected. This vapor-deposited coating is easy and inexpensive to apply and has a very low rate of moisture transmission. The coating itself is thin and compliant, so it was not expected to change the thermal expansion properties of the part.

Final Design

Table 7 shows the predicted expansion of the dimensionally stable hexapod design with a 1 deg C ΔT applied. Table 8 shows how the model behaves when the temperature variations from Table 5 are applied. The analysis predicted this design would meet the requirements with significant margin. A 1.53 deg C temperature change between legs is necessary to cause this model to exceed the drift requirements.

Table 7. Expansion of Dimensionally Stable Hexapod Design

Part	Number Per Leg	Length (mm)	Material	α at 20 C (/C)	ΔT (deg C)	Growth (nm)	Total Growth (nm)
Rod end	2	12.065	Invar	1.25E-06	1	15.08	30.16
Flex couple	2	6.0198	Invar	1.25E-06	1	7.52	15.05
Upper shaft	1	9.144	Super Invar	3.00E-07	1	2.74	2.74
Upper cap	1	6.48	Super Invar	3.00E-07	1	1.94	1.94
Upper bond	1	15.875	Invar-to-Comp. Joint	-1.60E-06	1	-25.35	-25.35
Housing	1	70.74	Graphite-Epoxy	-3.83E-06	1	-270.93	-270.93
Actuator*	1	NA	Steel and Al	2.38E-07	1	238.37	238.37
Lower Cap	1	28.94	Super Invar	3.00E-07	1	8.68	8.68
Lower bond	1	15.875	Invar-to-Comp. Joint	-1.60E-06	1	-25.35	-25.35
Flex pivot	1	7.62	420 Stainless Steel	9.90E-06	1	75.44	75.44
Lower shaft	1	11.938	Super Invar	3.00E-07	1	3.58	3.58
							54.33
Hexapod Height change if all actuators grow:				62.48 nm			
Hexapod tilt if 2 actuators grow:				0.10258 arc-sec			

Table 8. Predicted Response of New Hexapod Design to Measured Temperature Environment

Time Interval	ΔT (deg C)	Piston Error (nm)	Tip/Tilt Error (arc-sec)
1 hr.	0.026	0.17	0.00028
2 hr.	0.032	0.22	0.00034
3 hr.	0.035	0.23	0.00038
4 hr.	0.043	0.28	0.00046
8+ hr.	0.05	0.33	0.00054
Requirements:		10	0.025

Invar Considerations

Before incorporating Invar or Super Invar into the mechanism, the design team did considerable research to fully understand these complex metals. Invar's CTE varies non-linearly with temperature, so the operating thermal environment must be well understood. Achieving the listed properties for Invar requires specific heat treatment, and machining Invar after the heat treatment will alter these properties. Therefore, heat treatment is required again for finished parts. Lastly, Invar is subject to dimensional creep over long periods. Consider all these properties carefully before deciding to use Invar or Super Invar. The primary source of Invar information used by the DCATT team was "The Invar Effect"².

Final Status of DCATT Hexapods

Fabrication and Assembly Status

The DCATT project was cancelled shortly after the dimensional stability design effort. Limited funds were made available to fabricate parts for one hexapod in the interest of verifying design elements that might be useful to future projects. At this time, all parts have been fabricated, but the hexapod itself has not been assembled. Thermal expansion tests have been performed on some of the components to verify design predictions of their CTE. Final assembly and testing of a hexapod is not currently being pursued due to funding and manpower limitations. It is possible, however, that renewed interest in the future may revive this development effort.

Component-Level CTE Testing

CTE tests have been performed on several of the composite tubes. The results show an average CTE of $-3.83E-6$ per deg C over a temperature range of 7-31 deg C. This is within 13% of the design value. One measurement was made on each of two sub-assemblies consisting of composite tubes bonded to their Super Invar end-fittings. Both CTE measurements were $-1.9E-6$ per deg C. More measurements on the sub-assemblies were not possible on the restricted budget, so the sub-assembly CTEs carry less confidence than the tube CTEs.

Dimensional Stability Predictions with Measured CTEs

If the measured CTEs are included in the hexapod thermal models, the design performance degrades by nearly a factor of 10. This still meets the drift requirements, however. Worst case 8-hour drifts are 6 nm in piston and 0.01 arc-second in tip/tilt. Drift requirements are exceeded by a 0.09 deg C differential temperature change. Table 9 further details these results.

² "The Invar Effect: A Centennial Symposium." International Symposium on the Invar Effect (1996: Cincinnati, Ohio). ed. Jerry Wittenauer. Warrendale, PA: Minerals, Metals & Materials Society, 1996

Table 9. Hexapod Drift Predictions with Measured CTEs

Model Description	Predicted 8-Hour Drift		ΔT to Exceed Req. (deg C)
	Piston (nm)	Tip/Tilt (deg C)	
Analytical model with no measured CTEs	0.33	0.00054	1.53
Model with measured CTE of composite tubes	3.1	0.0051	0.17
Model with measured CTE of tube sub-assemblies (low confidence in measurement)	5.9	0.0096	0.09

Conclusions

The DCATT hexapod is a response to the need for a high-resolution, 6-DoF positioning mechanism for use in a large, active-optics system. Although the final design has not been assembled or tested, the development brought to light several challenging obstacles which were analyzed and overcome. With active optics being proposed for increasing numbers space flight missions, the experiences of the hexapod design team may prove relevant to future aerospace mechanisms.

The most important lessons learned from the hexapod design effort are as follows:

- High-resolution inchworm actuators may have unacceptable motion discontinuities caused by the clamping and unclamping of the inchworm mechanism.
- High-resolution, 6-DoF motion tests require significant design effort. Analyze dimensional stability in the test setup.
- Relative dimensional stability may be more restrictive than absolute dimensional stability in active-optics systems.
- Large negative CTEs can be achieved with graphite epoxy. Tube structures can amplify this by taking advantage of the Poisson's ratio of the material.
- Composites with a large, negative CTE may have reduced strength and a large CME.
- If a composite's CME poses a problem, Parylene-C can be a simple, cost-effective moisture barrier.

5.3.37

Lessons Learned from the Design and Implementation of a Potentiometer Assembly for an Antenna Pointing Mechanism Application

Bradley Arkwright^{*}, Pietro Di Leonardo^{*}, Colin Francis^{**} and Richard Gahart^{**}

Abstract

Potentiometers are often used as position sensing devices for positioning mechanisms. They have proven to be a low-cost, reliable telemetry device when used in the correct environment and fabricated using controlled processes. Several lessons learned were realized from a development effort in which rotary potentiometers were used in an antenna positioning mechanism. In this application, each actuator makes use of two rotary type potentiometers: one for fine telemetry and one for coarse telemetry. The units are required to operate between -45°C and $+105^{\circ}\text{C}$, with a required life (for the fine potentiometer) in excess of 1,800,000 revolutions.

Lesson learned and issues that will be discussed include:

- Dealing with potentiometer noise at low temperature
- Workmanship, cleanliness, and handling issues associated with fabrication of potentiometers
- Material selection for the potentiometer wiper assembly
- Resistive track deadband geometry and size
- Test equipment and flight electronics design precautions and recommendations that should be employed when testing or operating potentiometers

The following performance parameters and trend data resulting from qualification and life testing will also be discussed in the paper:

- Potentiometer element resistance values as a function of life and temperature
- Potentiometer accuracy as a function of life and temperature
- Wiper preload

Introduction

Figure 1 illustrates an exploded view of a rotary actuator assembly that utilizes a coarse potentiometer and fine potentiometer in tandem to indicate the precise position of the actuator output. The design issues discussed herein have all been resolved and the units have completed full qualification, life testing and production, and are currently accumulating on orbit life aboard several commercial communication satellites.

In the standard actuator design, a redundant potentiometer assembly is integrated directly on the back end of the motor that serves as the fine telemetry output. The fine potentiometer is a two piece unit mounted directly on the back end of the motor shaft. In the final design, the primary and redundant resistive tracks each have an approximate 15-degree deadband with the primary and secondary deadbands oriented 180° apart. This configuration ensures continuous electrical readout over 360 degrees when both tracks are monitored. When used in conjunction with the coarse potentiometer (of similar construction) on the output shaft of the actuator, the fine potentiometer provides precise positional output. The coarse potentiometer and fine potentiometer on the motor are different in diameter but very similar in construction and materials. The coarse potentiometer is non-redundant but it only provides rough positioning data in order to specify which revolution the fine potentiometer is on.

^{*} Honeywell Aerospace Electronic Systems, Glendale, AZ

^{**} Space Systems / Loral, Palo Alto, CA

Due to the more severe life and environment requirements, this discussion will focus on the fine potentiometer (shown in Figure 2 and Figure 3) which is integral to the stepper motor assembly. However, all of the lessons learned discussed herein are also applicable to the coarse potentiometer design.

The rotary potentiometer being discussed herein is of the conductive plastic type. Precious metal wiper fingers contact a co-molded conductive plastic resistance element to complete a circuit and indicate a rotary location of a shaft as shown in Figures 2 and 3. The output of the potentiometer is a voltage trace that is linearly proportional to the rotary position on the resistive track. The fine potentiometer schematic is presented in Figure 4. The output of the position sensor is a saw tooth type waveform. The secondary signal is of the same form but offset by approximately 180 degrees. A more complete description of potentiometer operation is included in Reference 1.

Although the rotary potentiometer is simple in concept, there are many design and manufacturing issues to be considered when incorporating this type of telemetry into an actuator. The following sections describe some design, handling, and manufacturing issues that were encountered during the project and were found to be very critical to proper unit operation.

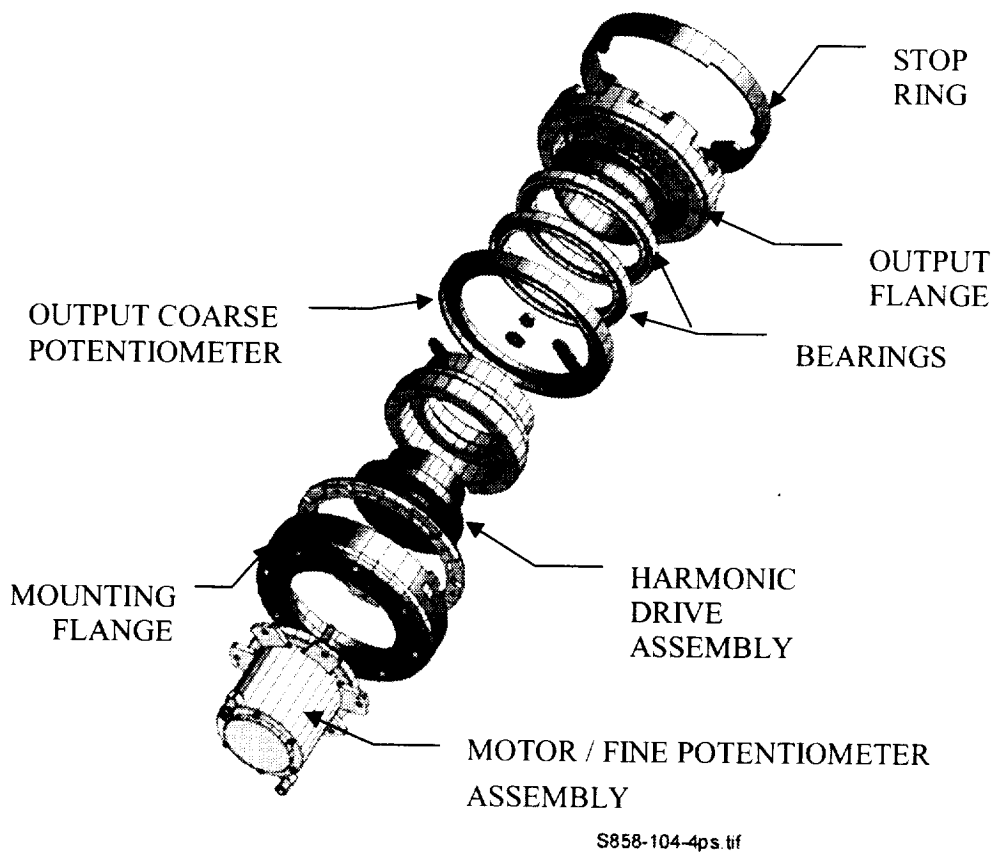


Figure 1. Rotary Actuator Exploded View

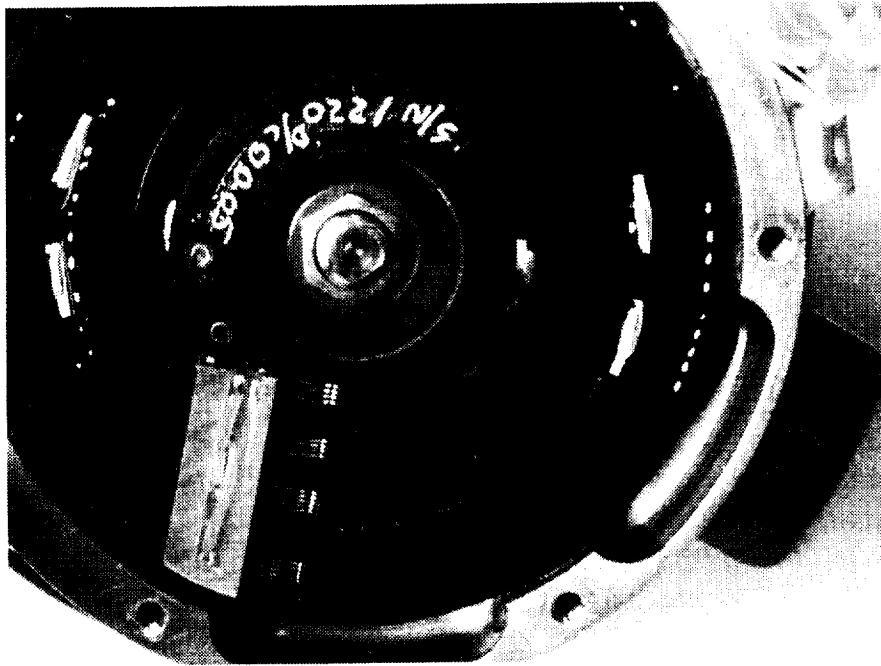


Figure 2. Fine Potentiometer Assembly (Part of Stepper Motor Assembly)
{The fine potentiometer assembly is mounted directly to the back end of the stepper motor assembly.
It is easily accessible for inspection via the removal of a back cover.}

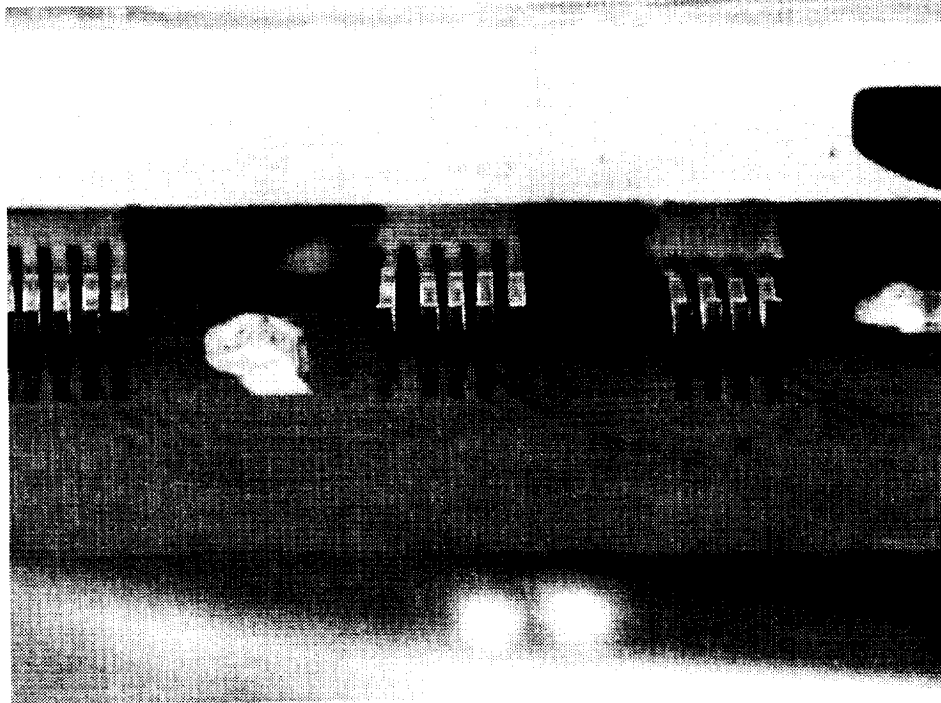


Figure 3. Fine Potentiometer Assembly – Wiper Detail

Potentiometer Noise at Cold Temperature in Vacuum

During life testing, after approximately 45,000 motor revolutions, the fine potentiometer began exhibiting noise traces as shown in Figure 5 during cold thermal vacuum testing.

With each successive cycle, the minimum temperature at which the noise began slowly increased (i.e., the noise appeared at a warmer temperature). A thorough cause and effect investigation was initiated to determine the root cause of the anomaly. The investigation focused on several possible causes:

Dynamic Instability: The noise could have been caused by dynamic instability of the motor as it steps through its detent positions.

Mechanical Interference: The noise could have been caused by interference between the motor back cover and the rotating wiper assembly on the fine potentiometer.

Surface Contamination: The noise could have been caused by the introduction of contaminants between the contacting surfaces.

The investigation proceeded to demonstrate that the noise was actually caused by the dynamic formation of an electrical insulator at the interface of the wiper and the resistive element of the potentiometer. This phenomena lead to a thorough examination and characterization of the electrical interfaces and their surrounding materials.

The baseline wiper material was PALINEY[®]7 (Ref. 2), a precious metal alloy comprised of palladium, silver, copper, gold and platinum. The potentiometer substrate material is Diallyl Phthalate (DAP) with a resistive track co-molded into the substrate material. The literature in Ref.2 (see Table 1) cites Palladium and Platinum as the two most highly catalytic metals in the formation of frictional polymers. This supports the theory for polymer formation since PALINEY[®]7 contains large amounts of Palladium and Platinum.

During operation, this very reactive surface rides on short chain polymers from the DAP resistive glaze formulation along with lithium sterates used as mold releases by the potentiometer manufacturer. This creates an ideal environment for the formation of a polymeric film. The unit sensitivity to this film is increased at cold temperature when the film solidifies and creates an insulating barrier between the wipers and resistive track. Under these conditions it is not unexpected to observe noisy or nonlinear voltage output from the potentiometer due to this lack of intimate wiper contact with the element surface.

A design change was then instituted which changed the wiper material from PALINEY[®]7 to NEYORO[®] G, which is a gold alloy. The literature in Ref. 2 cites Gold as several times (~20X) less catalytic than Palladium or Platinum (see Table 1).

Based on surface analyses results which showed evidence of general debris and contamination on the elements, it was also deemed necessary to implement stricter cleanliness precautions while handling or viewing potentiometers. All personnel within the immediate area of an exposed potentiometer are now required to wear clean room hats and masks. The hat and mask are in addition to the general requirement of smocks and lint free gloves. The potentiometers are handled within a Class 100,000 rated area and a Class 100 flow hood. Only when the potentiometers are closed up inside a unit is the hat and mask requirement relieved.

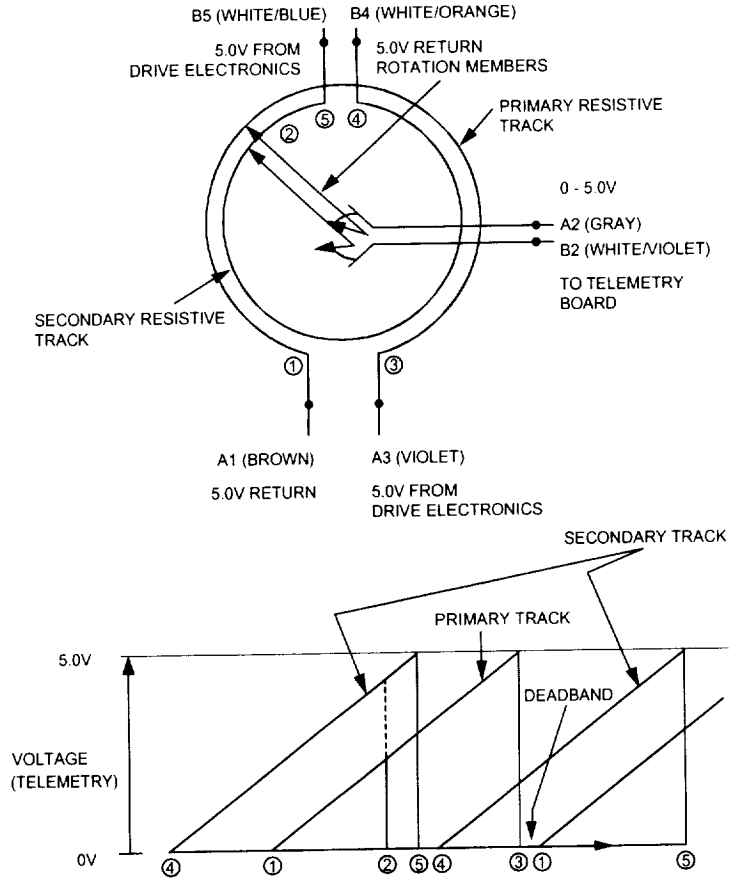


Figure 4. Fine Potentiometer Schematic

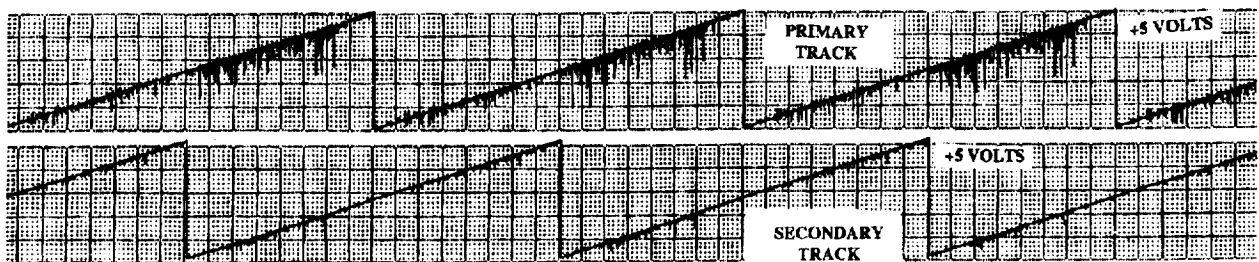


Figure 5. Noise Event Traces Detected During Life Testing (After 45,000 motor revolutions) – PALINEY® 7 Wipers

{Example of a fine potentiometer “noise” event while the unit is operating at cold temperature (-45 °C). Wiper material is PALINEY® 7. Noise traces were attributed to polymer formation at the contacting surface. These events were eliminated by changing the wiper material to NEYORO® G (See Table 1).}

Table 1. Relative Polymer Formation of Selected Metals and Alloys (Ref. 2)

{This table was very useful in helping make a decision to change the wiper material from PALINEY® 7 to NEYORO® G}

SLIDER	MATING SURFACE	RELATIVE POLYMER PRODUCTION
Platinum (in PALINEY® 7)	Platinum	100
Palladium (in PALINEY® 7)	Palladium	95
Ruthenium	Ruthenium	55
69 Au, 25 Ag, 6 Pt	Palladium	50
75 Au, 25 Pd	75 Au, 25 Pd	37
Quartz	Palladium	30
70 Au, 30 Ag	Palladium	20
Gold	Palladium	16
69 Au, 25 Ag, 6Pt	69 Au, 25 Ag, 6Pt	12
Gold (in NEYORO® G)	Gold	5
Silver	Silver	0
Copper	Copper	0
Zinc	Zinc	0

Ultimately the change to NEYORO® G wipers proved to be successful. Figure 6 illustrates part of a strip chart recording taken during final cold functional testing (-45 °C), under vacuum conditions, at the conclusion of the required life test duration of 1,825,000 potentiometer revolutions.

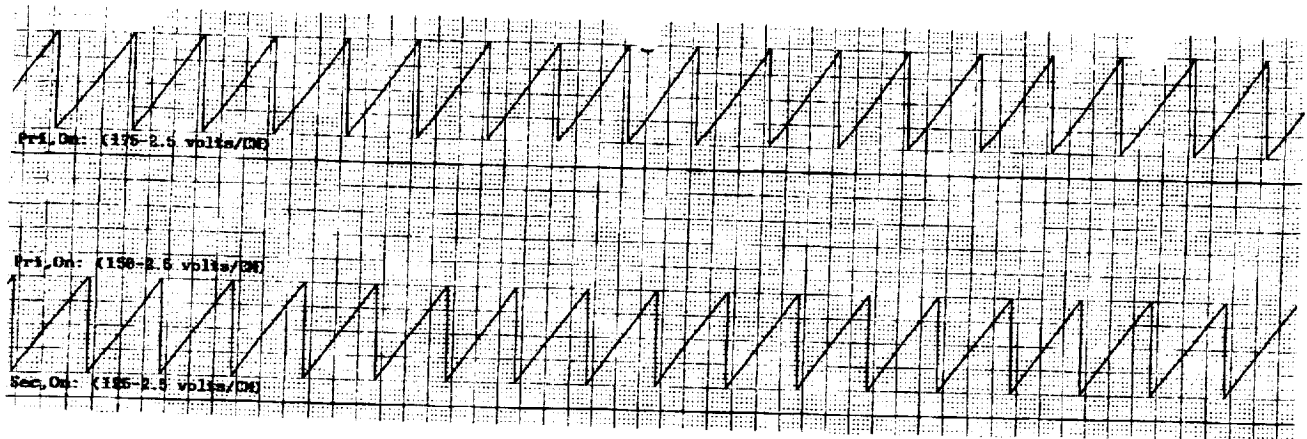


Figure 6. End of Life Fine Potentiometer Traces – NEYORO® G Wipers

{Strip chart example of the fine potentiometer output while the unit is operating at cold temperature (-45°C). Wiper material is NEYORO® G. This reading was taken during final functional test at the end of life (after 1,825,000 potentiometer revolutions). Nominal output signals from the potentiometer observed. Note: The chart speed is different than the one shown in Figure 5.}

Fine Potentiometer Failures Caused by Deadband Shorting

The actuator fine potentiometers experienced another catastrophic type failure during life testing. The failure manifested itself early with sudden and complete output signal loss from two fine potentiometers. Furthermore, the signals were not lost simultaneously.

Upon disassembly, inspection and failure analysis of the potentiometer it was determined that the dead band area had shorted. Figures 7 and 8 illustrate very clearly the extent of the damage in the dead band

areas. Further observation of the other fine potentiometer tracks on the unit revealed a "smearing" phenomena (as shown in Figure 9), which was deemed as one of the causes of the failure. The tendency over time is for the conductive material and DAP to smear across the dead band area. This phenomena is actually expected to occur over many revolutions, but other contributors also made the situation worse.

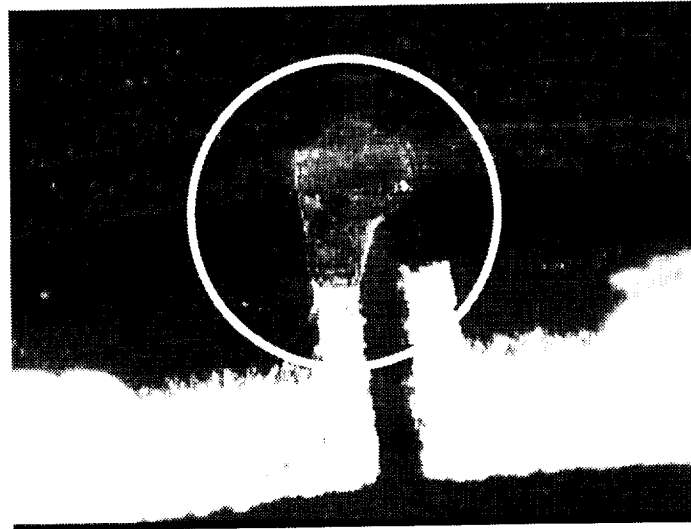


Figure 7. Shorting in Dead Band Area – Example 1

{Catastrophic failure of one potentiometer track caused by shorting across dead band. The failure was triggered by wiper wear and "smearing" of conductive material over the gap area.}

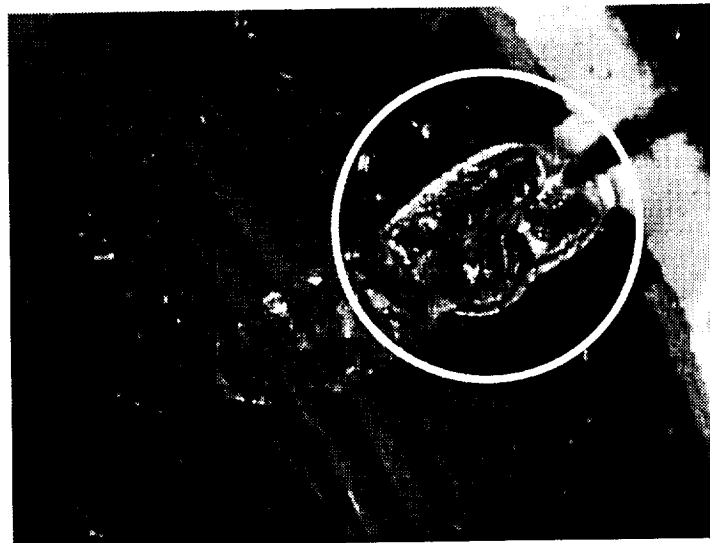


Figure 8. Shorting in Dead Band Area – Example 2

{A more severe example of shorting across the dead band. Failure of the conductive track could have been avoided by using a current limited power supply.}

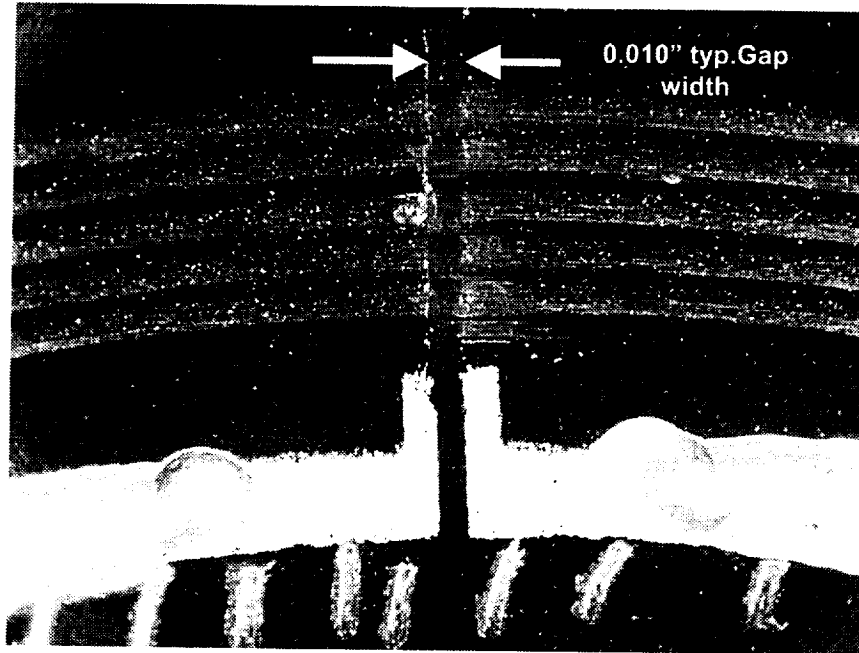


Figure 9. “Smearing” Effect of Conductive Track Across Dead Band Area
 {Over many revolutions (1,825,000) this is an expected effect. But with a small dead band gap and expected wiper wear, this phenomenon proved to be catastrophic. (See Figures 7 and 8)}

Normal wiper wear over many revolutions causes a flat patch formation on the contact area of the wipers as shown in Figure 10. As the wiper traverses across the dead band area over life and the wear patch gets larger, the wipers actually can bridge across the dead band as the wear patch exceeds the gap width. The dead band gap therefore needs to be large enough to accommodate the normal, expected wear patch on the wiper assembly.

Workmanship issues were also identified with the dead band manufacturing process as shown in Figure 11. The small dead band requirement caused the manufacturing process to be very difficult and not repeatable. The process involved a mechanical removal of the conductive material, which caused the quality of the required dead band gap to be less than acceptable and certainly very uncontrollable in terms of size and geometry. This process also caused the exposure of silver epoxy used to create the wire tab connections for the potentiometer. Exposed silver epoxy is visible along one edge of the gap. Although it was never determined that the exposed silver epoxy in the dead band area actually was a partial cause of the failure, it certainly was undesirable.

Furthermore, the investigation revealed that the 5V power supply being used to power up the potentiometers was not current limited low enough to protect the potentiometers. During nominal operation this would not be an issue. However, this added to the catastrophic type failure since the test equipment did not offer sufficient protection against mis-wiring or against inadvertent current draws by the unit. A current limited supply was then implemented to protect the hardware from excessive current going through the unit.

Figure 12 shows a sample of a strip chart output that captures the shorting phenomena across the dead band. By monitoring the current limited supply line on the strip chart channels it was possible to capture the shorting events on one potentiometer track. The hash marks indicate additional current draw from the supply. This only became visible when a current limited supply was used since the added current draw is relatively small.

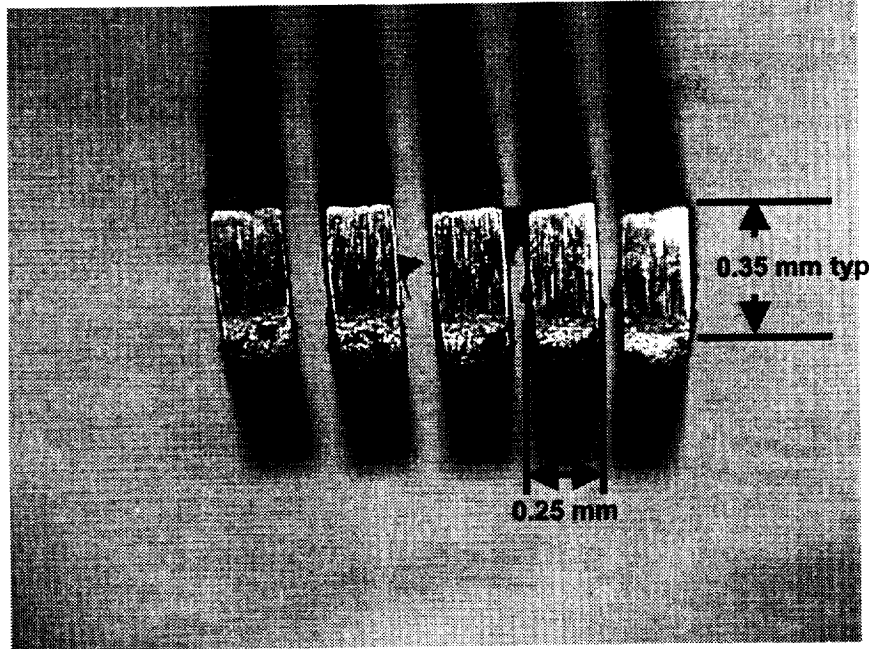


Figure 10. Typical Wiper Wear Patch

{As the life testing progressed, the width of the wiper wear patch (0.35 mm or 0.014" typ) approached and exceeded the width of the dead band (0.25 mm or 0.010" typ) on the conductive tracks.}

Figure 12 shows indications of shorting across the dead band of the primary fine potentiometer. This is proof that the wiper is actually bridging across the dead band as it travels over the resistive track material. Two strip chart channels were used to monitor the power supply voltage to each potentiometer. The vertical hash marks indicate additional current draw for that particular power supply.

Figure 13 shows the results of running the "small gap" fine potentiometer with a current-limited power supply over approximately 300,000 revolutions. While the unit exhibited bridging across the dead band, the potentiometer element was protected by the current limited supply. The power supply was not as effective in protecting the wipers. As shown in Figure 13, both the primary and secondary wipers were damaged. The repeated arcing at the deadband location created local heating on the wiper fingers such that they were essentially melted over time. Notice that in Figure 13, the two wiper bundles on the left have been shorted due to the repeated wiper melting. In contrast, the wiper bundle on the right, which is associated with the slip ring, did not experience the local arcing phenomena and is in nominal condition at end of life. This test proved that, although the output signals of the potentiometer were nominal, the dead band bridging was still detrimental physically to the component. A performance compromise was necessary to alleviate the problem. The solution was obtained by being able to open the specification requirement for the dead band gap width.

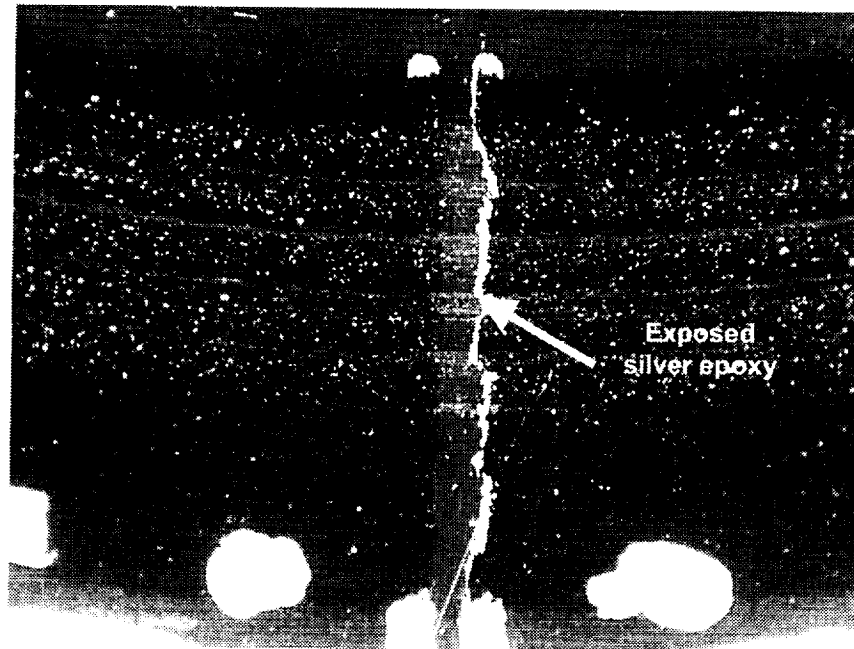


Figure 11. Workmanship Issues Caused by Small Dead Band Requirement

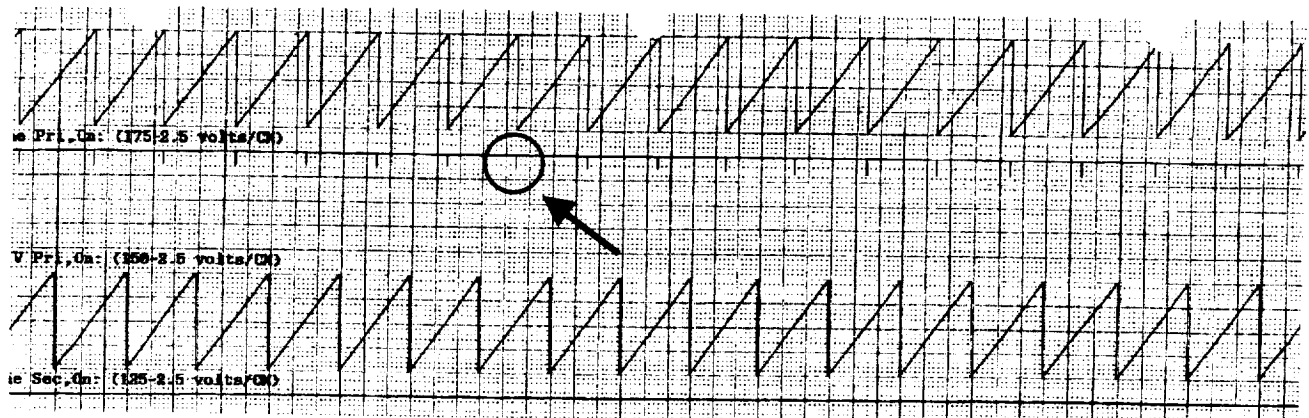


Figure 12. Dead Band "Shorting" Phenomena as Seen on a Strip Chart Printout



Figure 13. Wiper Wear After Running a Life Test With a Current Limited Supply

The new configuration shown in Figure 14 opened the gap width from 0.25 mm to 1.5 mm (0.010" to 0.060"). This width had substantial margin over the predicted wiper wear patch (shown in Figure 10). This wide gap configuration proved to be easy to manufacture and control. The vendor was now able to use a very repeatable and proven masking technique to generate the larger gap.

A final life test was conducted to validate the final gap configuration. Figure 15 shows the same dead band crossing at the completion of over 1,825,000 cycles.

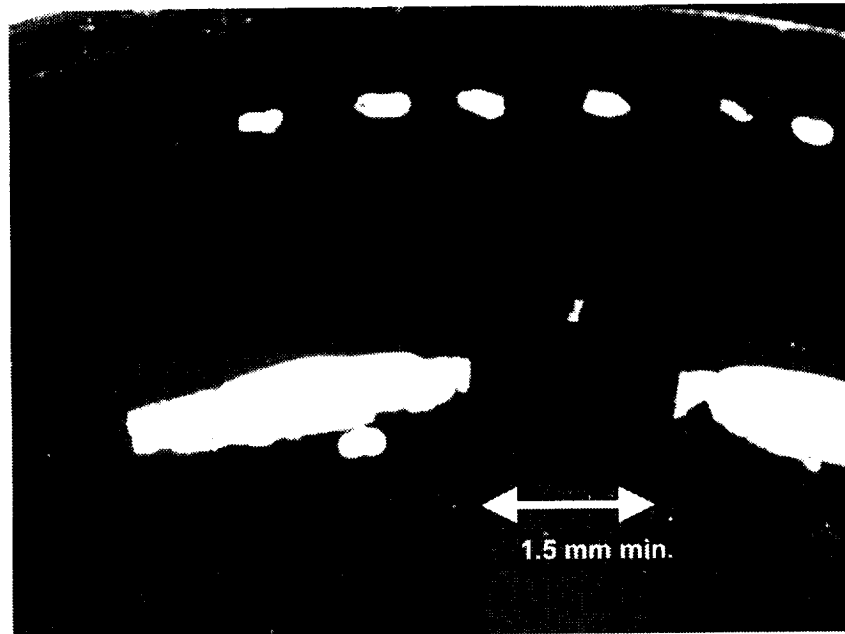


Figure 14. Corrected Dead Band Configuration – Pre Life Test

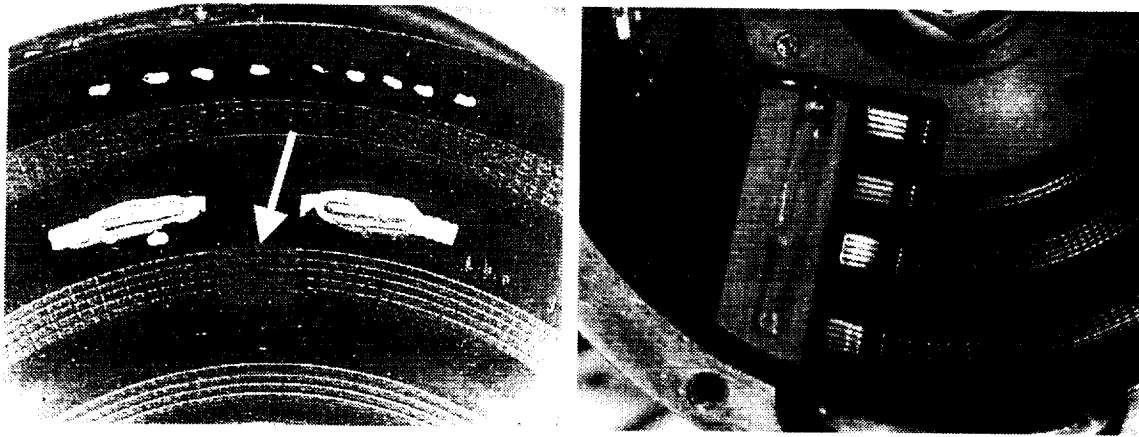


Figure 15. Final Dead Band and Final Wiper Condition – Post Life Test

Potentiometer Performance Trends

Due to the multiple life tests performed on this project, there was considerable potentiometer performance trend data available. The final life test using NEYORO® G wipers and the large dead band gap design was performed for final assurance that the corrective actions taken were indeed valid. Once the design, workmanship, and handling issues were resolved, the potentiometers were found to behave very accurately and consistently.

Potentiometer Element Resistance

Table 2 summarizes the potentiometer's track resistance as measured at different phases of the life test. The results demonstrate that the resistance remains relatively constant over life, even under vacuum and thermal conditions. As shown in Table 3, the maximum deviation from the initial resistance value was only 3.5% over the tested temperature range in thermal vacuum conditions during a 2-month life test.

Table 2. Potentiometer Element Resistance Trend During Life Testing

Test Point	Primary Fine Pot. Element Resistance (ohms)	Secondary Fine Pot. Element Resistance (ohms)
Pre Life Test Functional Test at Ambient	8926	9444
Initial Hot (105°C) Thermal Vacuum (T/V) Functional	8914	9386
Initial Cold (-45°C) T/V Functional	9073	9587
Post 912,500 Revolutions – Cold (-45°C) T/V Functional	9169	9671
Post 912,500 Revolutions – Hot (105°C) T/V Functional	9035	9584
Post 1,825,000 Revolutions – Hot (105°C) T/V Functional	9110	9695
Post 1,825,000 Revolutions – Cold (-45°C) T/V Functional	9239	9783
Post 1,825,000 Revolutions – Functional Test at Ambient	9121	9684

Table 3. Potentiometer Resistance Maximum Deviation

Case	Primary Potentiometer Percent Resistance Change	Secondary Potentiometer Percent Resistance Change
Maximum Negative Deviation from Initial	- 0.5 %	- 0.6 %
Maximum Positive Deviation from Initial	+ 3.5 %	+ 3.5 %

Potentiometer Accuracy

Potentiometer linearity or accuracy over life was also a parameter of primary concern. The output value of the potentiometer at one prescribed motor detent position was measured at various points during the life test. The data in Table 4 shows the variation of the potentiometer read-out at different phases of the life test. The reference position is a mechanical scribe mark located on the motor output shaft and motor mounting housing. The primary and secondary fine potentiometer readings were very repeatable over life. As can be seen from the voltage readings, the accuracy drift over life did not vary by more than 0.01 volt, which is equivalent to 0.46 degree at the motor. Going through the gear ratio, this converts to only 0.003 degree at the output of this particular actuator design.

Table 4. Potentiometer Accuracy Drift Over Life

{A scribe mark was used as a reference position. The data indicates the variation of the fine potentiometer readings for the same baseline scribe position, over life.}

Case	Primary Fine Potentiometer Voltage (V)	Secondary Fine Potentiometer Voltage (V)
Baseline Scribe Reading	3.832	1.245
+105°C Pre-life test Functional Scribe Position	3.834	1.245
-45°C Pre-life test Functional Scribe Position	3.833	1.243
1,200,000 Revolutions +105°C Functional Scribe Position	3.836	1.244
1,200,000 Revolutions -45°C Functional Scribe Position	3.831	1.241
1,200,000 Revolutions Ambient Scribe Reading	3.839	1.240
1,825,000 Revolutions Final +105°C Functional Scribe Position	3.842	1.239
1,825,000 Revolutions Final -45°C Functional Scribe Position	3.838	1.237
1,825,000 Revolutions Ambient Scribe Reading	3.840	1.239

Note: Average Potentiometer Performance: 69 degrees/volt or 0.0145 volt/degree

Linearity of the potentiometer was also found to be well within specification over life. Table 5 tabulates the linearity error that was measured over the course of one of the life tests. It shows that the potentiometer was very accurate over all temperature ranges, during the life test and at the end of life. Table 5 shows that the end of life linearity error is only 0.0274 volt or 1.89 degrees at the motor shaft. Note that this error also includes a maximum error of 0.2 degree attributed to motor step error. Going through the gear ratio, this converts to only 0.012 degree at the output of this particular actuator design.

Table 5. Potentiometer Linearity Error during Life Testing

Case	Temperature (°C)	* Primary Fine Potentiometer Linearity Error (°)	* Secondary Fine Potentiometer Linearity Error (°)
Pre Life Test Functional Test	Ambient	0.911	0.897
Initial T/V Functional	105	4.347	4.416
Initial T/V Functional	- 45	0.214	0.193
Post 912,500 Revolutions T/V Functional	- 45	0.145	0.386
Post 912,500 Revolutions T/V Functional	105	0.200	0.276
Post 1,825,000 Revolutions T/V Functional	105	3.105	3.036
Post 1,825,000 Revolutions T/V Functional	- 45	3.064	3.098
Post Life Test Functional Test at Ambient	Ambient	1.891	1.435

* **Note that this is the linearity error at the motor shaft as read by the potentiometer**

Wiper Preload

Wiper finger preload on the element can effect both nominal performance and wear life. If wiper preload is too low, then it is possible that the wiper fingers can lose contact with the element at certain temperature extremes and the output signal would be lost. If wiper preload is too high, then wiper wear can be accelerated and total operational life will be compromised. However, during this project a rather broad range of preloads was found to perform successfully. Figure 13 presented earlier, shows how the wiper tips were melted due to the local arcing at the deadband. Clearly the wiper preload was drastically effected due to this wiper damage and yet the potentiometer output signal showed nominal performance at end of life.

Conclusions

One of the first considerations to be taken when selecting a component to be incorporated into a mechanism or any design, should be heritage of that component. Specifically, it is important that the proposed application be very similar to past heritage and should be supported by qualification and life testing. It is necessary to scrutinize any performance requirements that are not supported by heritage experience or applications. One such example in this project was the initial small deadband size. Although it was a heritage size for a deadband for the potentiometer vendor on some past designs, those applications did not actually have the wipers travelling over the deadband during actual operation. It is very important to make sure that a vendor clearly understands the application of their component in the end product even if it appears to be well defined in the procurement specification. Typically, whatever component is scrutinized the least in a design usually has the most risk related to it.

There were a number of technical and producibility type lessons learned on this project. Because of the relative simplicity of the rotary potentiometer, it is very easy to overlook all the details of the design that can have a very real effect on the performance of the unit.

Electrical output noise from a rotary potentiometer has been an issue that many have experienced. Wiper material choice and element cleanliness has a definite effect on the tendency for electrical output noise to occur. The formation of any insulating polymer layers on the element surface seems to be much less prevalent when a gold alloy type wiper like NEYORO[®] G is utilized instead of a palladium or platinum type alloy like PALINEY[®]7. However, these potentiometers seemed only to be sensitive to this polymerization formation at relatively cold temperature. It is recommended that these types of potentiometers not be utilized at temperatures less than approximately -20°C unless the design is proven by significant life testing.

The size of the resistive track deadband is particularly critical if the application requires the wipers to travel over the deadband during normal operation. It is important that the size of the deadband is a minimum of 3 times bigger than the length of the wear patch on the wiper fingers at end of life. This margin will account for wiper wear rate variability, deadband geometry consistency, wiper preload variation, and temperature effects, etc. Although the size of the wiper wear patch will vary in each configuration and application, the wear patch length in this application was found to grow from 0.025 mm (0.001 inch) at beginning of life to 0.35 mm (0.014 inch) (Figure 10) at end of life after 1,825,000 revolutions (≈ 1.75 diameter track). The size of the wear patch at end of life was consistent over multiple life tests. The larger deadband was also found to be much more producible and consistent in terms of fabrication.

Related to the deadband shorting issue, it was determined that is also good practice to utilize a current limited power source when testing potentiometers to protect the units from damage due to inadvertent mis-wiring. This lesson learned extends to the design of actual spacecraft electronics also.

Because of the delicate nature of the wipers and the relatively low wiper preload, great care has to be taken in terms of handling and cleanliness of potentiometers. It is recommended that the potentiometers be handled like bearings in terms of cleanliness requirements until contained inside a unit or covered. Special shipping precautions must be taken with the wiper assemblies to ensure that the delicate wipers do not get damaged simply due to the shipping process.

Although wiper preload was found to have a rather wide acceptable range for successful performance, it is still important to measure/inspect the wiper preload accurately both at the vendor and prior to installation into a unit. Without adequate dimensional inspection of the wiper preload, performance can be affected in an extreme situation where the preload is very low.

Despite all the design issues encountered with rotary potentiometer as discussed herein, the units performed exceptionally in both qualification testing, life testing, acceptance testing and ultimately on-orbit over a rather large temperature range. The units proved to be very physically robust and never encountered any issues associated with structural loading or vibration testing. In addition to the data presented herein, a considerable amount of test data was amassed for various life tests and over 20 flight units which supports the use of potentiometers for this type of application. When the design and handling precautions recommended herein are instituted, these rotary potentiometers yield very linear and repeatable positional output.

Rotary potentiometers have been utilized successfully for decades as the telemetry device for precision rotary actuators. While potentiometers are rather simple devices, there are many basic design parameters to be considered as discussed herein. Great care should be taken when operating potentiometers in cold environments and in long life applications. However, rotary potentiometers are still a relatively low-cost, lightweight telemetry option that yields accurate and repeatable results even over extreme environments, and they should still be considered a viable option as a telemetry device in future precision actuators.

References

1. Conley, Peter L., Space Vehicle Mechanisms, 1998.
2. Pitney, Kenneth E., Ney Contact Manual, The J.M. Ney Company, Bloomfield, Connecticut, 1973

5/9/19

MIRO Calibration Switch Mechanism

Jason Suchman^{*}, Yuki Salinas^{*} and Holly Kubo^{*}

Abstract

The Jet Propulsion Laboratory has design, analyzed, built, and tested a calibration switch mechanism for the MIRO instrument on the ROSETTA spacecraft. MIRO is the Microwave Instrument for the Rosetta Orbiter; this instrument hopes to investigate the origin of the solar system by studying the origin of comets. Specifically, the instrument will be the first to use submillimeter and millimeter wave heterodyne receivers to remotely examine the P-54 Wirtanen comet. In order to calibrate the instrument, it needs to view a hot and cold target. The purpose of the mechanism is to divert the instrument's field of view from the hot target, to the cold target, and then back into space. This cycle is to be repeated every 30 minutes for the duration of the 1.5 year mission. The paper describes the development of the mechanism, as well as analysis and testing techniques.

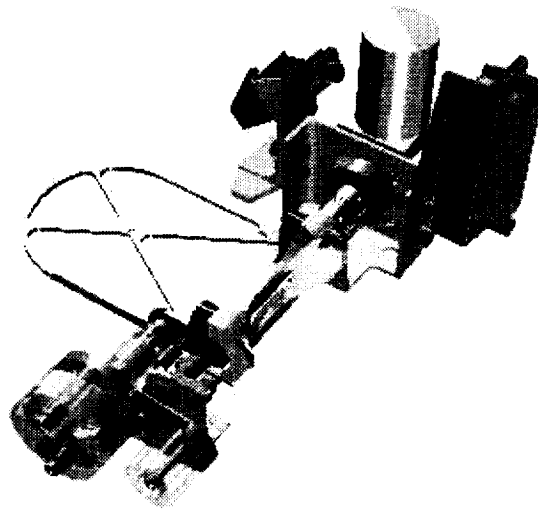


Figure 1. CAD Model of the MIRO Calibration Switch Mechanism

Design

The design features a stepper motor with planetary gearhead manufactured by CDA Intercorp. The power is transmitted from the output shaft of the gearhead to a flex coupling made by Helical Products Company, Inc. The flex coupling is pinned to both the gearmotor's output shaft and a shaft that runs across the mechanism to a bracket that holds a counterweight and the SMA pinpuller by TiNi Aerospace, Inc. The pin of the SMA pinpuller engages the side of the mirror, which is held in place by Vespel[®] SP-3 journal bearings on the transverse shaft described above. Vespel[®] SP-3 is a low-friction polyimide manufactured by the DuPont Corporation. The mirror is under a moment load due to a torsion spring that, when the SMA Pinpuller is actuated, slams the mirror down towards the bracket and against a Vespel[®] SP-3 hardstop. The off-axis mass of the mirror is balanced by the mirror counterweight. All counterweights are manufactured from tungsten class 4 (MIL-T-21014) to provide a high-density material to minimize volume, which would adversely effect the configuration. Feedback to the MIRO computer is provided by three Infrared reflective object sensors that provide information as to the position of the mechanism. Upon testing of the instrument we found that using these sensors in this configuration was troublesome, and the paper will address this issue as well as what the correct implementation should be. Figure 2 shows a 25 pin connector; however, this connector was removed due to mass considerations, and a pigtail design was adopted.

^{*} Jet Propulsion Laboratory, Pasadena, CA

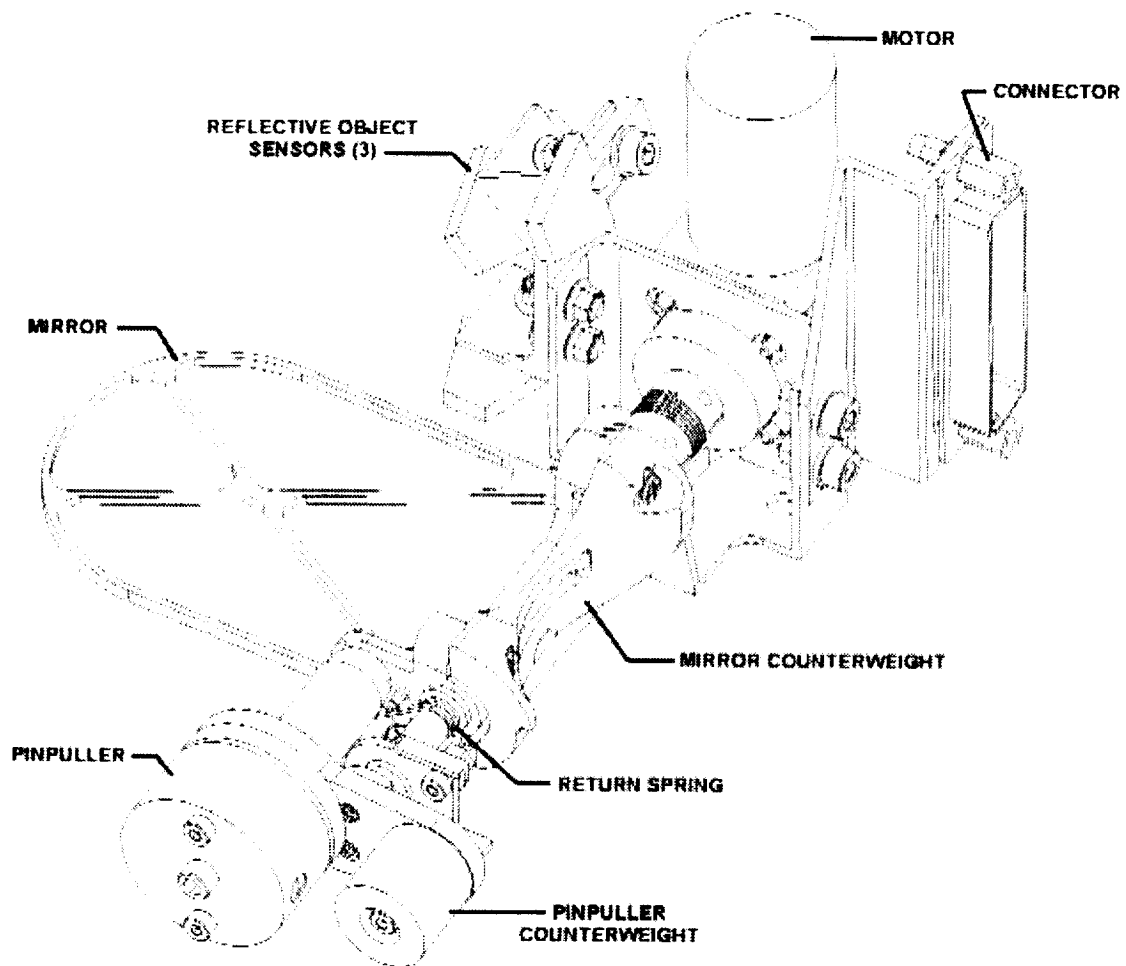
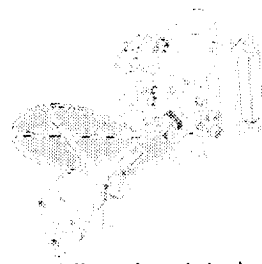


Figure 2. Overall Configuration of the MIRO Calibration Switch Mechanism

One complexity of the system was its need for a repeatable failsafe device. A shape memory alloy (SMA) pinpuller, developed through a partnership between TiNi Aerospace, Inc. and JPL, was chosen to perform this function. The pinpuller features a primary and a redundant circuit to provide added reliability. The device is good for smaller applications where a small stroke and a small pull force is adequate. Another consideration in selecting this device was its cleanliness. A great deal of high precision instruments are in very close proximity to the mechanism, so outgassing of materials and lubricants is of great concern (total mass loss < 1%; volatile condensable mass < 0.1%).



The Pinpuller is activated, allowing the mirror (shaded gray) to rotate independently. The pinpuller is pushed against a hard stop on the bracket as the mirror is pushed toward the safe position by the return spring.



The Mirror is rotated against the RTV stop (on the far side of the mirror) in the safe position. The return spring will keep the mirror in this position indefinitely.



The Fail-safe Mechanism is reset by driving the pinpuller around until it can re-engage the mirror in the safe position. During the reset cycle the motor must overcome the torque of the return spring and the friction at the pinpuller/mirror interface caused by the pinpuller pin extension spring. The mirror lip is angled to allow the pinpuller to engage the mirror more easily.



The Pinpuller is fully reset and the Calibration Switch is fully operational.

The Pinpuller is reset in the event that the pinpuller is dislodged from the mirror during launch, or if the motor begins to operate again after the Failsafe has been activated.

Figure 3. Sequence of operations for pinpuller failsafe actuation and reset

Testing

Testing of the device included acceptance testing of the externally provided components as well as qualification testing of the completed mechanism. The test environment includes temperatures of -30 to 60°C (operating) and -40 to 70°C (non-operating). The dynamics environment included sine vibration in all three axes (5.0 Hz to 21 Hz = ± 7.5 mm (0 to peak), 21 Hz to 60 Hz = 13.5 g, 60 Hz to 100 Hz = 4.0 g) as well as three axes of random vibration (20 Hz to 100Hz = +3 dB/Oct, 100 Hz to 300 Hz = 0.05, $(M+20)/(M+1)*g^2/Hz$, 300 Hz to 2000Hz = -5 dB/Oct). The vast majority of the environmental testing was performed at the MIRO instrument level.

The life testing of the device was performed as well. The life test cycles were calculated by adding two times the number of flight cycles plus four times the anticipated ground test cycles, which resulted in 52,790 cycles. The life test ended after over 250,000 cycles, far in excess of the requirement. However inspection of the test setup showed that the failed component was the motor driver electronics, a ground support equipment non-flight component that simulated the flight electronics. Upon further inspection of the test setup, it was noted that these electronics, as well as the mechanism itself, were bolted to a plexiglass base. (We thought it looked nice!) Unfortunately plexiglass can accumulate a static charge fairly easily, but as it is not a good conductor it has difficulty getting rid of this charge through grounding. Therefore we feel that electrostatic discharge probably occurred and ended our test. Figure 4 shows some photographs of the test setup.

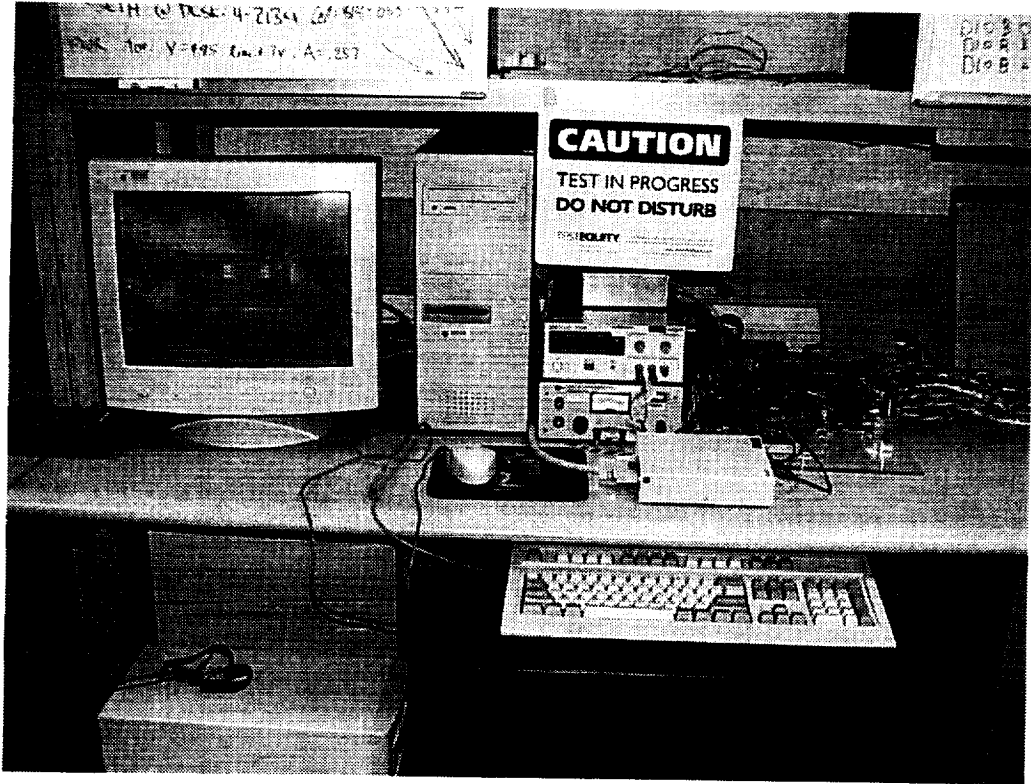


Figure 4. Life Test Setup

The final mechanisms have been built and two flightworthy units (flight and flight spare) have been delivered to the project. The flight mechanism has been integrated into the flight model for MIRO. Rosetta is scheduled for launch in January of 2003.

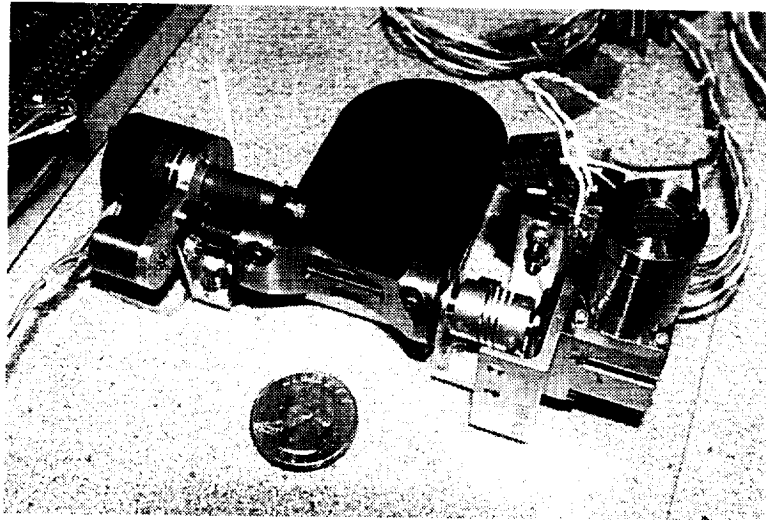


Figure 5. Photo of the mechanism during life test

Issues and Concerns (Lessons Learned)

Fragility of the SMA Pinpuller (Failure #1): On the qualification mechanism (integrated to the qualification instrument), an electrical engineer inadvertently reversed two connectors and then turned the system on. This resulted in a lot of current being applied to the pinpuller for too long a time. The pinpuller's Nitinol wires significantly surpassed their transition temperature for a considerable time, rendering the pinpuller inoperable. The mechanism had been delivered with no connector (i.e., with wire pigtails). Due to extremely tight mass requirements, the project elected to drop a little mass by removing the mechanism's connector. The cabling engineer, at the system level, used two identical connectors of the same gender in the same area. This created the confusion that led to the mistake. Thankfully, the unit had already gone through the necessary system-level tests needed to prove the design was robust. Lesson learned: Resist the request of a project to remove your connector, and work with the cabling engineer to ensure that your connector is different from those in the surrounding area. Truthfully, we (the mechanical team) were not sure how to prevent such electrical-team-induced failures from occurring. However, TiNi has since recommended that we could have incorporated a microswitch that would shut off power to the pinpuller, eliminating the possibility of the SMA wire overheating (and re-annealing).

Fragility of the SMA Pinpuller (Failure #2): After the flight mechanism had been mechanically integrated into the optical bench of the instrument, a long period of time had transpired before the cabling was integrated to its flight connector. Due to the pauper-like funding for this instrument, various integrations occurred at spread-out intervals. This made Quality Assurance (QA) coverage difficult, and due to the financial situation QA was reduced to a bare minimum. Eventually, the wiring for the flight unit was being connected to the appropriate connector. As the cabling engineer was about to solder the connector in place, he checked the resistance of the pinpuller's primary and redundant circuits. On the primary circuit, he noted 2.4 ohms, on the redundant side he found an open circuit. The mechanism had previously gone through a diminished flight acceptance test with success, and the redundant circuit had passed. The mechanism was removed, the pinpuller was replaced, and the mechanism returned to flight integration. Analysis of the failed pinpuller found that a wire on the pinpuller's redundant circuit had broken at a solder joint internal to the pinpuller. Several design flaws were found. (Although the pinpuller had been built at TiNi Aerospace, the design was a JPL design that TiNi helped bring into production.) First, there was no strain relief for this connection. Second, there was no conformal coating used to insulate the wiring. Third, a grommet that was originally in the design had been removed. Fourth, the wire used was fairly stiff. Lesson learned: Run your electrical connections by an experienced packaging engineer, even for devices built out of house, and get their approval of the design before allowing its use. This pinpuller is undergoing rework at TiNi per our direction. Strain relief has been added to the wiring and conformal coat has been added to the area. A grommet is being added to the pinpuller housing. Finally, the wire will be changed to one that is less stiff (same gage, but more strands).

Fragility of the SMA Pinpuller (Failure #3): This incident is still under investigation, but the speculation is that a floating ground may have led to a failure of the FPGA internal to the MIRO electronics. This failure resulted in current being applied to the pinpuller for longer than intended (see failure #1). Assuming that this is the cause of the anomaly, we're unsure as to what a mechanisms engineer could do to safeguard his/her design from a failure of the electrical system. Because the pinpuller requires between 120 and 150 milliseconds to activate, an electrical fuse would not be an appropriate solution. A microswitch, as referred to in failure #1, should always be incorporated in the SMA pinpuller design to protect from such failures.

Position Sensing of the Mirror (not a failure): The requirements for this mechanism dictate that there must be a way to provide feedback to the MIRO computer that indicates when a mirror is at appropriate reflective positions. Reflective object infrared sensors were chosen to perform this task. The side of the mirror was polished to provide high reflectance. During characterization of the mechanism, we faced a dilemma. During assembly one can set the sensitivity of the sensors by changing the resistance values of a resistor in series with the infrared transmitter. (Changing the resistor to a lower resistance results in increased current flow through the transmitter, and more light is transmitted). Characterization proved that at different light conditions, and at different temperatures, the sensitivity changed some more. Therefore at cold temperatures some sensors could not find the mirror when they should have, and at hot

temperatures the mirror was detected by some sensors approximately 5 degrees away from the desired position. In my opinion, we picked the wrong sensor for the job. That aside, we did not implement the sensors we chose in an appropriate way. Instead of detecting the entire side of the mirror, we should have placed a 10-mm long dowel pin normal to the surface of the side of the mirror, with its end polished. Therefore, the sensor would only see the pin when it was placed in front of its nose, but when the pin moved out of the way the surface that is left would not be at an appropriate focal length for good sensing. But we feel a better sensor configuration would have used the infrared emitter / detector pair that was direct, but not reflective. (They're positioned in a U-shape). The device senses when the beam is blocked and when it is not. Although we have no experimental data to back this up, it looks to us that this configuration would prove to be more accurate and more reliable. (You could dramatically increase the sensitivity of the sensor, making ambient light and temperature effects less significant.) A potentiometer may also have been worth investigating, although reliability concerns frightened us away. Lesson learned: There are many ways to sense position – talk to other engineers and listen to their past experiences with such devices.

Conclusion

We'd like to take a moment to point out that this experience in no way diminished our belief that the SMA pinpuller is the appropriate device to handle the failsafe function of the design. A lot of the problems we had came as a direct result of human error, some of which an improved design could have compensated for. Other areas could not have been compensated for in the design while still maintaining high reliability, low complexity, and low mass. As mechanism engineers we have to accept some of the risk levied on us by the other disciplines on the team.

But to review some areas that would have helped the design:

- 1) Never deliver hardware with pigtails – always incorporate your own connector
- 2) Ensure that the connector you place on your mechanism is different from those surrounding it
- 3) Work with your vendors to make sure all aspects of their hardware is consistent with the high standards you have set for your own work
- 4) Be sure to incorporate a microswitch to shut off an SMA device upon appropriate displacement to ensure overheating of the SMA does not occur.

Note:

This work was performed at the Jet Propulsion Laboratory, California Institute of Technology, under a contract with the National Aeronautics and Space Administration. Reference herein to any specific commercial product, process or service by trade name, trademark, manufacturer, or otherwise does not constitute or imply its endorsement by the United States Government or the Jet Propulsion Laboratory.

200/91

A Robotic Rover-Based Deep Driller for Mars Exploration

T. Ylikorpi^{*}, G. Visentin^{**}, and J. Suomela^{***}

Abstract

VTT Automation has developed an advanced rover-based mobile drilling device for planetary exploration. The mobile Robotic Sampling System has been designed to perform deep (up to 2 meters) soil sampling on the surface of Mars or other planetary objects. Due to the complexity of the task, very strict mass and volume limitations, and the need for complete automation of all its operations, the system demands a very ambitious mechatronic design. In this paper, the design of the system is described as well as the first functional prototype to be manufactured and now under testing. This work is being performed under European Space Agency funding by Space Systems Finland Ltd. as the prime contractor, together with the Technical Research Center of Finland (VTT, Finland) (the drill system) and Helsinki University of Technology (the roving system and drill electronics).

Introduction

In the past few years the world has witnessed the discovery of life forms thriving in extreme environments such as rocks several kilometers underground or underwater thermal vents where temperatures exceed +100 degrees Celsius. These environments were previously considered to be too hostile to sustain any form of life. One of the possible implications of this unexpected proliferation and survivability of life forms is that some sort of life could have possibly also evolved on other planets and moons like Mars or Europa. In order to develop instruments for searching for any signs of such extraterrestrial life, the European Space Agency has funded a technology research contract called "Micro Robots for Scientific Applications 2". Under this contract, a Robotic Sampling System (RSS) consisting of an automated drilling device and a tracked roving vehicle has been designed and constructed. The RSS consists of the following components: 1) A Mobile Drilling Platform that is basically a small (10 kg) tracked rover whose function is to house the drilling and sampling subsystem and transport it between the lander and the sample acquisition locations. 2) A Drilling and Sampling Subsystem (DSS) to perform the actual drilling and sampling. 3) A Docking and Sample Delivery Port on the lander where the RSS can deliver the collected samples for further processing. Figure 1 illustrates the mission scenario.

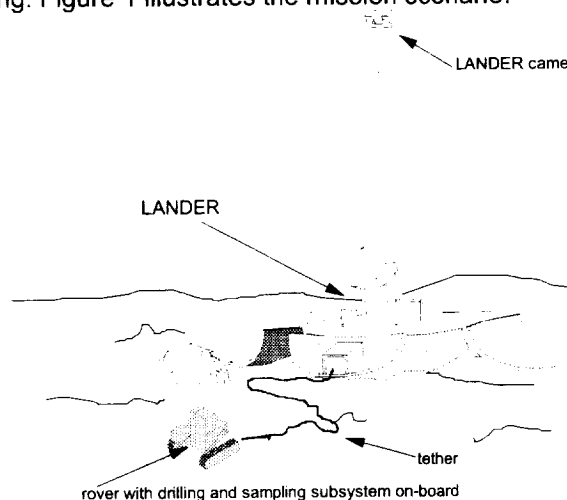


Figure 1. Robotic sampling system scenario.

^{*} Technical Research Center of Finland, Helsinki, Finland

^{**} European Space Agency, Noordwijk, The Netherlands

^{***} Helsinki University of Technology, Helsinki, Finland

Specifications

The search for possible extinct or extant life is the primary goal of the exobiology investigations during future Mars missions. As learned from the NASA Viking and Pathfinder missions to the Moon and Mars, sampling of surface soil and rocks can gain only limited scientific information. Any sensible Martian exobiology investigation requires pristine samples that have never been exposed to the lethal effects of Martian surface environment. Two types of samples have this characteristic: 1) samples extracted from surface stones/rocks by coring at a depth of a few centimeters, 2) deep soil samples acquired vertically from a depth of more than 1 meter.

For an extensive search for life, a Robotic Sampling System to be used as part of an exobiology investigation facility has to accommodate the following list of operational requirements, as set at the beginning of the project:

1. Drill at depths ranging from 0 to 2 meters into regolith with 5 mm depth accuracy
2. Drill up to 2 centimeters into surface rocks/stones
3. Drill into non-homogeneous material of density and hardness ranging from loose sand to hard rock
4. Drill at commanded elevation angles from 0° to 90° (drill into surface rocks or directly into the ground)
5. Drill with independent rotation and thrust actions
6. Allow control of drill depth (0-2 m), rotation speed (0-30 RPM) and thrust force (0-30 N)
7. Acquire cylindrical samples (radius 5 mm and height 2 cm) of non-homogeneous material of density and hardness ranging from loose sand to hard rock
8. Ensure that the sampled material belongs to the specific depth of sampling (i.e., do not carry down material from upper layers)
9. Preserve the morphology of the sample (i.e., do not scramble, compress or stretch it)
10. Preserve the purity of the sample (i.e., do not mix it with other material)
11. Allow acquisition and storage of at least 10 samples per trip
12. Carry out 3 trips at minimum
13. Size of DSS is restricted in volume of 110 x 110 x 350 mm
14. Mass of DSS is restricted to 5 kg.

Concept

Lay-out

The robotic sampling system consists of a tracked roving vehicle (110-mm tall, 400-mm wide, 400-mm long and weighs 10 kg) and a drilling system (110 mm x 110 mm wide, 350-mm long and weighs 4 kg) (Figure 2).

Drilling and sampling system should reach a depth of at least 2 m. It is obvious that rover mobility would suffer greatly from any drill parts longer than 0.5 m no matter how they are carried; vertically, horizontally, or perhaps dragged behind the rover. Therefore the drill string must be assembled on the rover from shorter sections that are stored inside the drilling system. Since a total of 30 samples are expected, several holes must be drilled. Therefore, the drill string must be reused from hole to hole and the drill-string sections shall be assembled, disassembled and reused on the rover in an automatic way. The extendable DSS drill string is assembled from up to 10 separate pipes in a similar manner that is used on terrestrial automatic rock drilling machinery.

The 10 drill pipes are stored in a rotating pipe carousel, and 11 drill tools are stored in another carousel. Linear slides and ball-screw that give drilling thrust and guidance for a moving rotation actuator are located inside the pipe carousel, which saves lots of volume and gives the DSS its compact appearance. Another visible feature is a clamping system that is used for holding the drill string during addition or removal of a drill pipe.

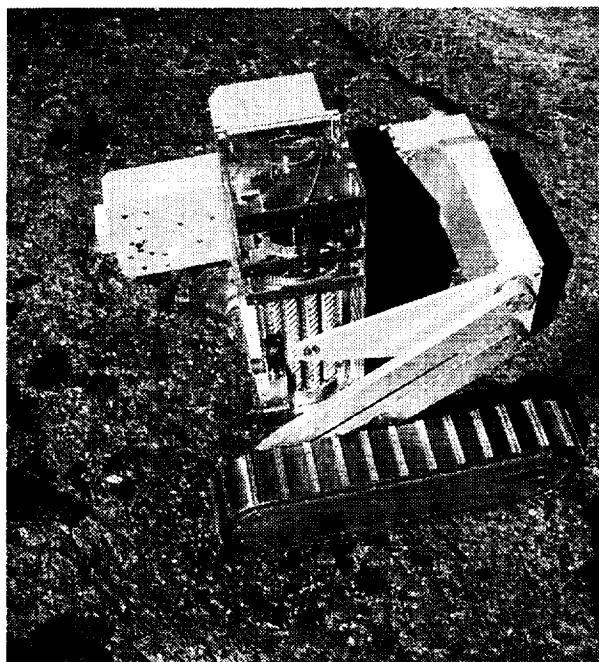


Figure 2. RSS in drilling position.

The Roving Vehicle

The roving vehicle procured by Helsinki University of Technology; Automation Technology Laboratory, is a tracked tethered vehicle, serving as a platform for the DSS. Its function is to enable the DSS to sample at desired locations and to deliver these samples back to the lander. During its mission, the rover makes multiple trips between the lander and the various sampling locations. The rover is commanded and supplied with power from the lander via a tether. A special feature of the tether system is that it can be rewound. When returning to the lander, the rover follows the tether left behind earlier and winds it back to the reel after cleaning excess dust from it. This way, the length of the tether stored does not limit overall travel length of the rover, and a danger of damaging the tether by over-riding it is avoided. The rotating axis of a payload cab holding the DSS allows drilling/ sampling at angles ranging from the vertical to the horizontal. Moreover the lifting bridge allows adjustment of the rover's ground clearance. This feature significantly improves the rover cross-country ability.

Operation

Drill operation is similar to that for conventional automated drilling machines using an extendable drill string. Two independent actuators, one for rotation (0-30 rpm, 1 N·m) and one for thrust (0-100 N) perform the drilling. Drilling and sampling procedure consist of the following actions:

1. Selecting the drill head from storage,
2. Assembling the drill string from sections,
3. Drilling to the desired depth (in the soil, or in a surface rock),
4. Acquiring the sample inside the drill head,
5. Elevating and disassembling the drill string, and
6. Storing the drill head -with the sample- in the sample storage.

The rotation actuator -or spindle- is mounted on a sledge moving in and out along linear guides propelled by the thrust actuator and ball nut and screw. The spindle is equipped with a trihedron coupling, similar to ones used for industrial robots, and with the necessary electrical feed-through.

First the spindle is connected to one drill pipe on the pipe carousel, after which a tool from a tool carousel is connected to the lower end of the pipe. Then drilling, which continues for the length of the pipe, is

started. As the spindle reaches the lower limit of its travel, a clamping system crabs on the pipe and the spindle is separated from the drill string. As the clamping system holds the drill string steady, the spindle is elevated back to the upper end of the linear feed and a new pipe is selected from the pipe carousel. After the spindle is connected to the new pipe that is further connected to the drill string held by the clamping system, the clamp can be opened and drilling can be continued for another length of the pipe. The procedure is repeated until the desired drilling depth is reached. Retraction of the tool and storing the pipes in the pipe carousel is a sequence opposite to the assembly and drilling.

Tool bit design is such that as the tool penetrates through terrain, soil can flow through it, entering from the lower end and exiting from holes in the upper end of the tool. This is how the tool always holds a sample representing the current depth in terrain. Upon retrieval of the tool, internal wedges or flaps inside the tool hold the sample and prevent it from falling out of the tool.

The RSS does not contain any means for anchoring to prevent rotation or moving of the system during drilling operations. Initial requirements, and also selection of the motors and hardware design, limit the drill thrust to 30 N and torque to 1 N•m. Simulated tests using off-loading methods indicate that the weight of the RSS on Mars would hold it still on sandy surface during drilling, but for example, on the Moon's surface additional holding methods would be needed.

Passive and active operations

During system design, a trade-off between passive and active operations had to be made several times. Active operations are operated with actuators, like motors and solenoids, and thus provide high controllability and flexibility of these actions.

Passive operations, however, rely on geometry and movement of other parts of the system to provide the desired action. Passive operations do not need separate actuators or any sort of power or information transmission, and so they have less effect on volume, mass and control needs. Passive operations can not be re-programmed though, and they produce a risk in case something should go wrong, in case of jamming of movement, for example.

Since the DSS already has many degrees of freedom and power feed to motors and actuators appeared quite challenging already in the beginning, it was decided to utilize passive operations as much as possible. Active operations were selected where operation was required independent from current operational state of drilling system.

Active operations:	
Carousel rotation	Two independent carousels. Any of the tools or pipes can be selected.
Spindle rotation	Independent drill rotation.
Drill feed	Independent drill thrust.
Spindle locking solenoid	The spindle must be connected to and separated from the drill string in the lower end and in the upper end of travel. In the case of string emergency release, the spindle must be released also in the middle of travel.
Clampers	The clampers must be able to operate together with the locking solenoid, i.e., anytime in the drilling phase.

<u>Passive operations:</u>	
Connection between the pipes and between a pipe and the spindle	Connection happens by pushing the couplings together, and is held by the spring force of a locking ring. Separation force (pull) of couplings is roughly three times larger than nominal drilling thrust. It was found very difficult to use any kind of an actuator to realize an active coupling system. Also delivering external power to the coupling for active operations appeared very challenging. The passive solution selected does not appear very repeatable and requires re-work or alternative solutions.
Separation of a pipe from the spindle at the upper end.	As the spindle with a pipe (the locking solenoid opened) reaches the upper limit of travel, mechanical forks separate the pipe from the spindle and leave the pipe in the pipe carousel. Solution is simple and reliable.
Tool locking inside tool carousel	Tools are locked inside the tool carousel with a sort of bayonet. Locking in happens by rotating and pushing the tool past flexible spring blades that snap over a shoulder formed by cutting bits of the tool. The lock is released by rotating the tool so that due to geometry the blade becomes lifted above the cutting bits and the tool can be removed from the carousel. Locking system is functional but requires sophisticated control of spindle rotation and axial feed during procedure.
Core cutting and sample holding.	Although pipe connections provide a possibility to route electrical energy to tool bits, a passive operation method was selected. The core is cut from the base material by combined rotation and push/pull of the tool. Core cutter operates in a similar manner as the core cutters for conventional core drills.

Sample storage and delivery

The tool bit is designed such that as the tool penetrates through terrain, soil can flow through it, entering from lower end and exiting from holes in the upper end of the tool. Upon retrieval of the tool, internal wedges or flaps inside the tool hold the sample and prevent it from falling out of the tool. Thus the samples are collected inside the coring tool. After a sample is captured inside the tool, the string is retracted from the borehole. The coring tool where the sample is stored is transferred to the tool carousel in the end of a drill pipe.

The samples are transferred from the carousel to the lander with the aid of the drill string by connecting a pipe to the spindle; and to the tool to be transferred to the end of the pipe. The DSS is then aligned towards the sample receipt port (SRP) of the lander and the string is extended to insert the tool into the SRP. If the distance to the SRP exceeds the reach of a single pipe, connecting more pipes to it with the aid of the string holding device can extend the string farther.

Mechanical design

Spindle and couplings:

The spindle gives the drill string the needed drilling rotation, and provides an electrical feed-through for spindle locking system and active drill tools. Coupling of the spindle, that connects to drill pipes, is similar to robotic couplings with round-edged trihedron design. This geometry fluently allows passive coupling of mating parts and has an ability to transfer torque too. Electrical connections for active tools are located concentric in the middle of the pipe cone using a coaxial plug, see Figures 3 and 4.

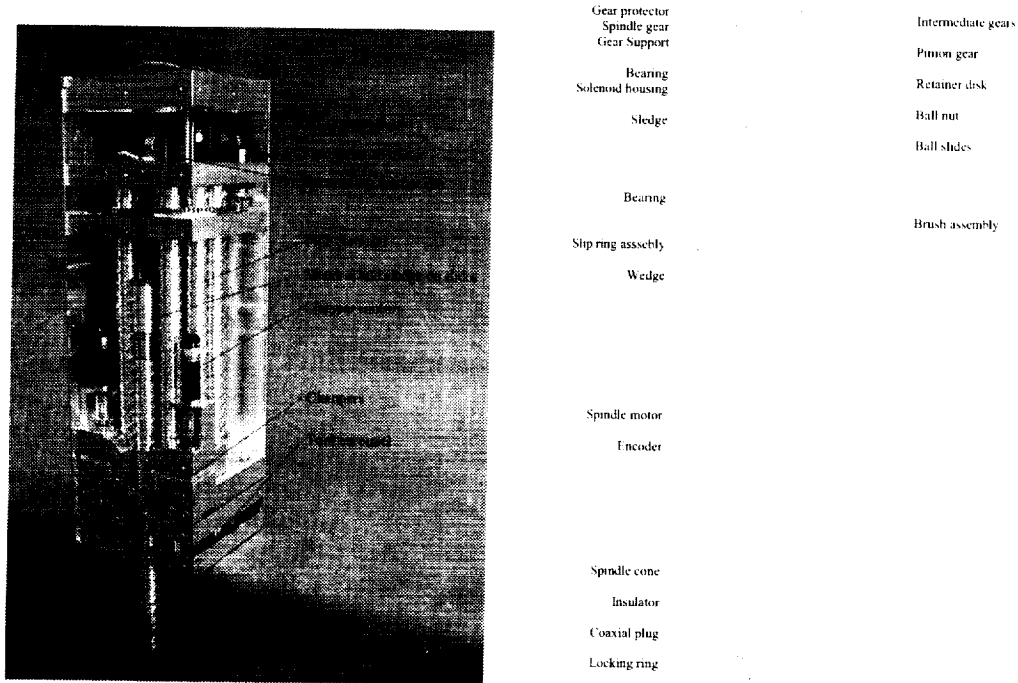


Figure 3. DSS and an exploded view of the spindle.

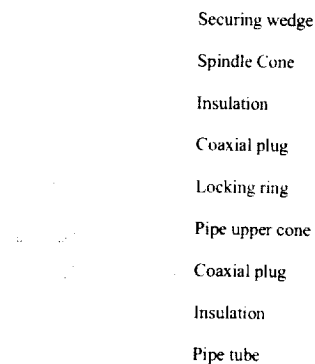


Figure 4. Design of the coupling.

The coupling is locked with a split ring, or a C-ring, on the spindle part (male), the female coupling on the pipe upper ends has a mating groove for the ring. Shape of the groove is made non-symmetric with different conical angles such that coupling by pushing happens easily, but de-coupling by pulling requires a force close to 100 N, which is close to the linear drive capacity. It was soon learned that the C-rings needed to have a special design to operate with the desired forces. Several different designs were incorporated and tested. The groove for the C-ring has angled surfaces so that the slightly contracted ring causes some pre-load for the coupling.

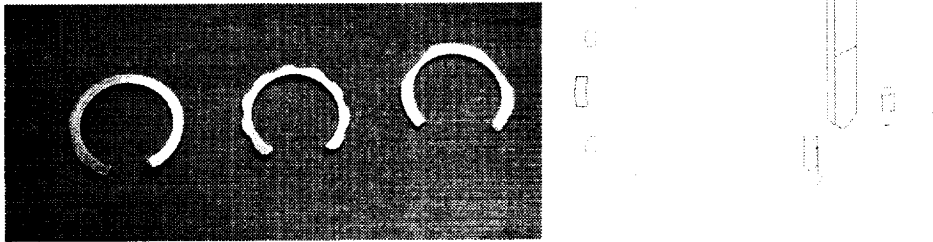


Figure 5. Prototypes and final design of the C-ring. Diameter of the ring is ~9 mm.

An in-house developed spindle solenoid (or an electromagnetic flip-flop)(Figure 6) is used to operate a wedge that can prohibit contraction of the locking ring and thus control disconnection of the spindle coupling when separating pipes from each other and from the spindle. When the wedge is located between the ends of the C-ring, its contraction is prohibited and de-coupling requires very high forces. De-coupling may happen nominally when the wedge is removed from between the ends of the C-ring. The solenoid is a flip-flop-type using a permanent magnet core to maintain each of its two positions and thus does not require any springs, separate locking mechanisms, or continuous power input. Power feed is realized with a capacitor that can produce a high short-term output power for solenoid, while collecting energy for the next operation with a low input power.

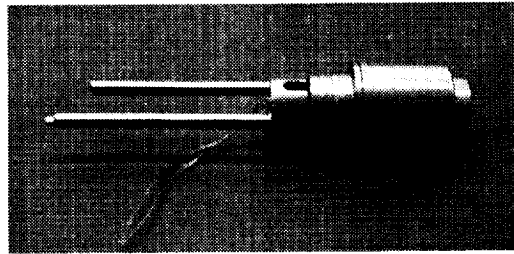


Figure 6. Electromagnetic flip-flop and a wedge.

A disadvantage with circular C-rings was also found. Prior to coupling, the C-ring is in a free state and can rotate freely during coupling. The ring may rotate so that it slightly touches thin end the securing wedge. After the coupling is performed, however, the ring is in slightly stressed state to provide some preload for the coupling. In the stressed state the ring can cause extra friction, which prevents moving of the securing wedge and thus prevents securing action or release of the lock. A couple of designs were tested to reduce movement of the ring. First, a single axial spring wire was mounted on the ring opposite the split to give some guidance. Later the ends of the ring were shaped so that two stationary pins would define the position of the unstressed ring. This enhanced action of the ring slightly. A larger ring would allow larger tolerances and would make use of the moving wedge easier. It was also noted, that the hardened steel ring has a tendency to dig into softer steel, which makes separation force unrepeatable. Further external torque or bending has some effect on release forces, which may be due to non-symmetric modified rings or minor geometrical errors in ring-groove geometry. Altogether the system seems to be very sensitive to the accuracy of the geometry.

A simple in-house developed slip-ring assembly (Figure 7) is used to transfer electricity to the rotating spindle for the spindle solenoid and active drill tool functions. There are five isolated lines in the slip ring. For prototyping purposes the rings are made of brass and brushes are made of spring steel. One ring has a split to be used for absolute spindle position detection.

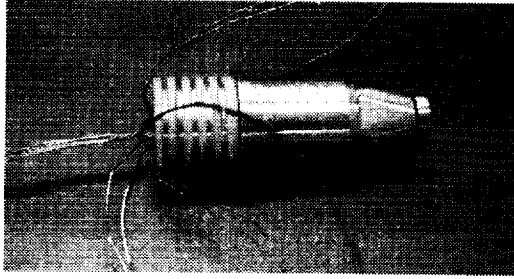


Figure 7. Slip-ring assembly.

The spindle, manufactured mainly from steel, is mounted on a sledge (manufactured of aluminum) that moves up and down along a linear slide. For effective use of volume, the drilling motor is located aside the spindle and below the sledge and the motion is transmitted with a gear train. Absolute spindle position is detected with the aid of a split in the slip ring. The split in the ring is detected as a break in electrical current. After this, signal spindle position is calculated from incremental encoder mounted to the end of the spindle motor.

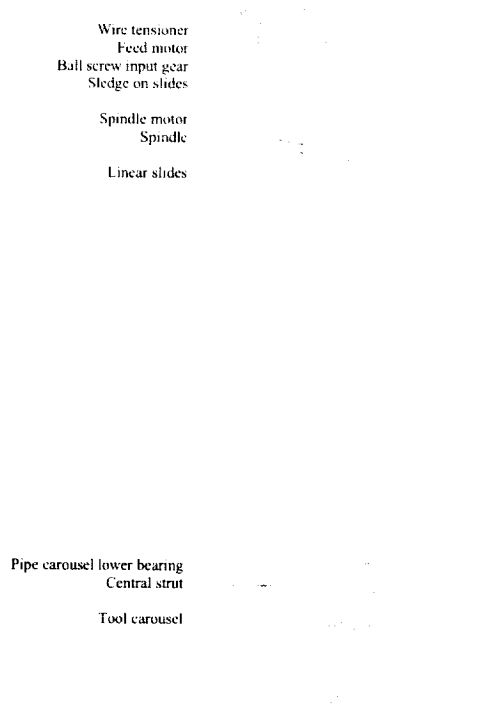


Figure 8. Linear feed system.

Linear Feed:

Linear feed, moving the sledge and spindle up and down, is realized with a thin ball screw, rotated with an electric motor, and a ball nut that is mounted on the spindle sledge. The sledge is guided by four ball splines that run along four guide rods. Drilling force ± 100 N is measured with a load cell attached to the lead screw. The load cell can measure only compressive force and therefore the lead screw is pretensioned to 100 N. Axial load on the screw is carried by two thrust bearings and radial load is carried with two needle rollers (Figure 8).

Axial position of the sledge is measured with the aid of a linear potentiometer constructed of 0.3-mm thick stainless steel wire giving resistance approximately 0-8 ohms over the measuring range. To maintain constant tension in the wires they are tensioned with two compression springs.

Drill Pipes:

The drill pipes, constructed of aluminum, are located in a pipe carousel. Inside diameter of the pipes is 13 mm, outside diameter is 15 mm, and the three-ended helical flute outside the pipe has a 17-mm outer diameter. Couplings in the ends of pipes are made of steel and present the same design as the spindle coupling, but without any securing means.

Connection between the pipes happens by pushing them together until the locking ring snaps into the groove. The three-ended flute is symmetric and so the pipes can be connected in any of the three possible orientations. Disconnection of two drill pipes from each other happens when the clamping mechanism holds the lower pipe and spindle pulls the upper pipe apart. Then the locking solenoid in the spindle is opened by a command and the sledge is driven to the upper position. During elevation of the spindle, a mechanical de-coupling mechanism separates the pipe from the spindle, leaving it in the pipe carousel. A tool is separated from the pipe by first driving the tool into the tool carousel and locking it in there. Then the pipe is pulled with the aid of the sledge apart from the tool.

For enhanced or special sampling actions, two power lines are routed through drill pipe couplings to allow use of possible active drilling tools in the end of drill string. These possible tools include, for example, percussive tools and ultrasonic tools. Dr. T. C. Ng and Holinser Group have already developed a design for a suitable active percussive tool in University of Hong Kong. Special measuring instruments can be mounted in the tools for measuring temperature, contact force, etc.

Pipe carousel:

The pipes are located in a pipe carousel, which has a skeleton-like appearance with thin vertical bars and slotted disks at both ends. The design allows the spindle to be located and move inside the carousel, which saves a lot of volume. The pipes are not mounted positively to the carousel, but sit in the slots surrounded by structures above the upper disk and around and below the lower disk. The rotation of the carousel is actuated with a Maxon d13 motor located outside the carousel and a gear rim connected to the upper end of the carousel. The carousel is positioned to the correct angular positions with two limit switches and index pins; one for each pipe indexing and one for absolute position indicator. In the bottom of the carousel there is a slot through which the drilling happens. In order to prevent inadvertent falling of a pipe into the slot, two spring-loaded pushers add some friction between the pipe and pipe carousel.

Tool Carousel:

The tools, which also double as sample containers, are stored in a tool carousel. There are 11 storage cups for the tools. The tools are mounted to the cups with a bayonet-like passive mechanism. The tool is inserted to the carousel with combined and controlled feed and tool rotation. With the aid of an aligning pin the tool finds correct position in the carousel and three flat springs snap over upper edge of drilling bits holding the tool. For removing the tool it is rotated so that a bulge in the side of the tool lifts the spring above the edge and sets the tool free. Coupling between the tool and string is similar to the pipe connections. The locking between the carousel and the tool makes it possible to disconnect the tool from the string simply by pulling. Actuation and position sensing of the tool carousel is similar to that of the pipe carousel, except that the Maxon d10 motor is located inside the carousel support (Figure 9).

Upper bearing
Indexing pins
Lower bearing

Figure 9. Pipe carousel and tool carousel.

String holding device:

A string holding device, located between tool carousel and lower end of linear slide system, is used to hold the lower pipe in place during pipe connection or disconnection. Clamping of the pipe is done at both sides of the string with two paws, shown in Figure 10, are coated with soft rubber-like high-friction material to accommodate helical flute of the drill pipes. The paws are attached to linear slides and the linear movement and clamping force are provided with two independent cam mechanisms located on both sides of the string. Geometry of the cam is such that the clamping force approaches infinity as the travel approaches its maximum. The two clamping motors are driven in an electronically synchronized way to guarantee that the paws will clamp the string with equal forces and in the middle of drilling axis. Position of each slide is measured with a linear potentiometer.

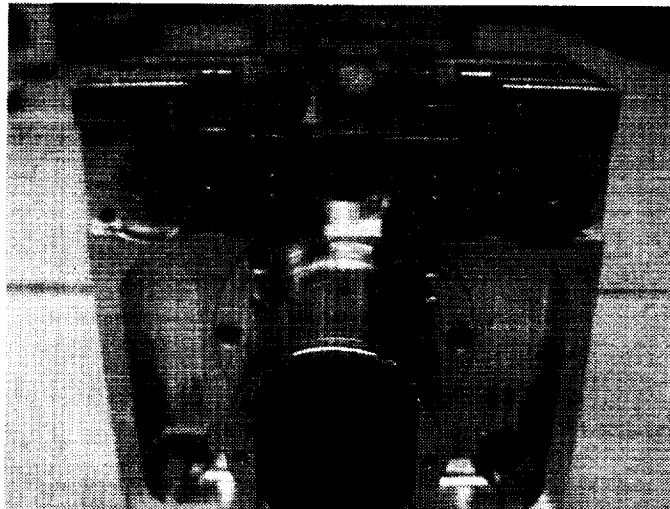


Figure 10. String holding mechanism.

For coupling and de-coupling of the pipes, the string holding device must provide a 100-N linear holding force, which, with a friction coefficient of 0.25, needs a clamping force of 400 N. The arm of the clamping

force will remain a minimum 0.5 mm, which gives the needed torque in the cam axle of 0.2 N•m. With a Maxon RE d13 118430 motor and Maxon 110 316 gear (max. torque 0.3 N•m), a 400-N clamping force is reached with a 0.75-mm force arm, or with 0.5-arm, a 600-N clamping force is achieved.

Tools

In the beginning of the project it was considered whether to use hammering action to chip the material or not. From a mechanical point of view, it was considered whether to develop a hammering system on the drill - even two meters and 10 couplings above the drill bit, or to fit a miniature hammering device inside a drill pipe. From an electrical point of view, the power need for such a hammering device was considered. From a scientific point of view, it was considered whether the interesting remains of possible fossils would be found from sediment layers of sandstone and limestone-like materials, or do we really need to drill into hard rock like granite. After these considerations, it was decided to produce this first prototype without hammering action and rely on cutting and grinding based removal of material. For this purpose, very hard and sharp diamond-like drill bits would suit the best. If for scientific reasons carbon-based materials can not be used, boron-nitride hard-alloy would provide a good replacement. For this prototype the tool bits are made of industrial hard-alloy Sandvik DZ05 having HV30 hardness on Vickers scale.

The tool used for sampling duplicates as a drilling bit and a core drill, as shown in Figure 11. The tool is designed to drill a 17-mm-diameter hole into rock material and to contain a 9-mm diameter and 20-mm-long core inside it. A crown that carries out the cutting is constructed of six cutting bits made of hard alloy. During drilling a core develops inside the drill while the bit crown chips material. Chips are conveyed to the surface by the external helical profile. Once the coring section is full, the head cutter chips the core top. The effect is that the bit penetrates deeper into the material always holding a 20-mm core of the current depth. When the desired depth has been reached, the core is broken apart from the base material with the aid of a wedge-shaped core lifter by lifting and turning the drill. This action is similar to that used with conventional rock-core drills. For sampling of sand or other similar loose soil, specially designed flaps will be mounted next to the core lifter to hold sample inside the tool during lifting. A total of nine tools are stored in the tool carousel and they are intended to penetrate into rocks of hardness similar to limestone and sandstone. In this configuration, the DSS will carry individual tools for each sample to be acquired during a single trip between the lander and the sampling location. A fresh tool will be attached to the drill string before each sample acquisition, and then subsequently detached with the sample inside.

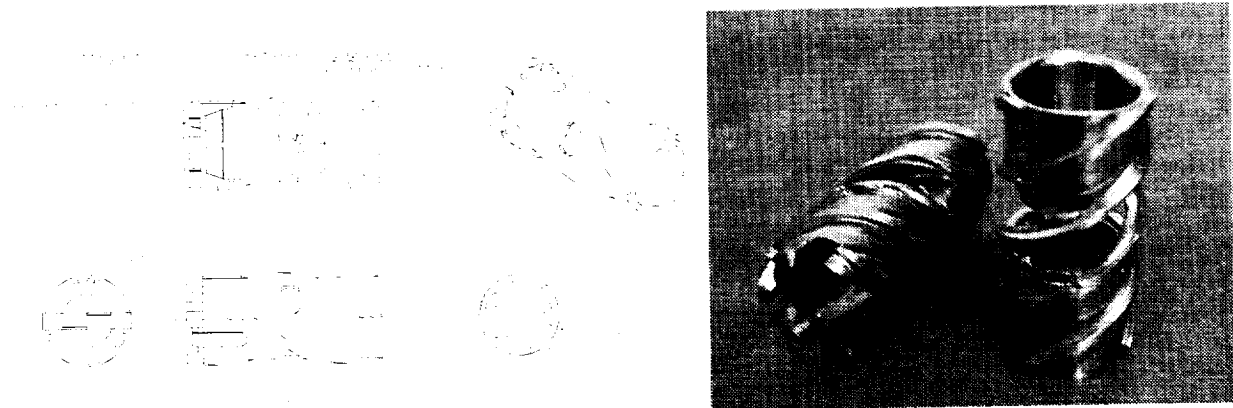


Figure 11. Tool design and prototypes (missing drill bits here).

Preliminary tests with different types of cutting tools were carried out in early stage of project. The tests show cutting power that would collect a rock core 10 mm in diameter and 15 mm in height within a few hours. Quick tests on very hard and abrasive Finnish granite indicate that with given thrust and power it would be possible to collect similar rock core in a time frame of tens of hours, however, durability and selection of drill bit material will be a critical issue. The tools that were tested were (Figure 12):

- 6 and 16 mm impregnated diamond core drills for cutting of glass
- 16 conventional hard-alloy-tipped drill for hand-held hammering drills (Hilti)
- 16 mm hard-alloy tool for metal cutting (4-mm core)
- 16-mm custom-made hard alloy core drill (Terätrio)
- a concept of two surgical knife blades rotating at 16-mm radius (~14-mm core)
- some tools were tested also with the aid of sonic vibrations, but without any success

Hole	Drill bit	Material	Speed RPM	Force N	Hole depth/mm	Speed mm/h	Duration h
1	diamond Ø16	Marble	30	24	8.8	0.3 .. 2.5	4
2	hard alloy	Marble	30	25	12.1	2.6	5
3	"Hilti"	Marble	30	25	17.6	1.9	14
4	diamond Ø16	Marble	30	24	16.6	1 .. 2.2	8
5	hard alloy	Marble	30	25	17.8	2.6	6.5
6	diamond Ø6	Marble	30	24	11.1	0.5 .. 2.1	6
7	diamond Ø6	Marble	60	24	13.2	0.7 .. 2.4	6
8	diamond Ø16	Marble	60	24	15.1	1 .. 2.2	8
9	diamond Ø6	Limestone	30	24	6.7	0.3 .. 3.9	4.5
10	diamond Ø16	Limestone	30	24	10.6	1.7 .. 3.4	5
11	knife blades	Limestone	30	25	3.4	6	0.5
12	sonic hard alloy	Limestone	30	12	4.3	1.5	Different sonic vibration
13	sonic hard alloy	Limestone	30	12	6.1	1.5	
14	sonic hard alloy	Limestone	30	12	2.3	1.5	
15	Terätrio	Limestone	30	27	9.8	18	0.5
16	Terätrio	Granite	50	high	0.9	3	10 minutes
17	Terätrio	Granite	120	high	6.2	36	10 minutes
18	Terätrio	Granite	120	27	2.3	2.2	1.3
19	sonic knife blades	Granite	30	12	1.5	0.2	2
20	knife blades	Granite	30, 120	12	1	0.2	3
21	Terätrio	Granite	120	45	3.1	2.0	1.5
22	Terätrio	Granite	120	45	12.9	0.2 .. 1.8	14

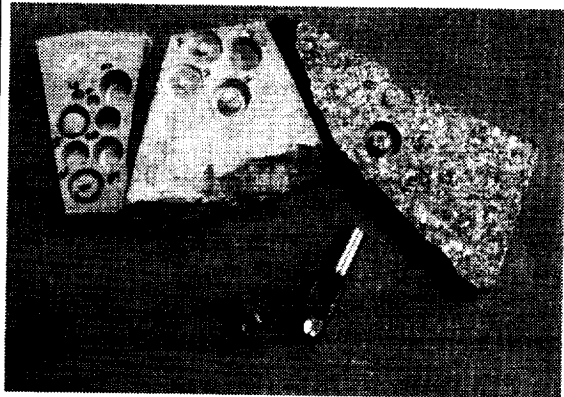


Figure 12. Some preliminary drilling test results, materials and tools.

For enhanced or special sampling actions, two power lines are routed through drill pipe couplings to allow use of possible active drilling tools in the end of drill string. These possible tools include, for example, percussive tools and ultrasonic tools. Dr. T. C. Ng and Holinser Group have already developed a design for a suitable active percussive tool in University of Hong Kong. Also special measuring instruments can be mounted in tools for measuring temperature, contact force, etc. A concept to utilize ultrasonic vibration to enhance cutting action was also developed and tested. An ultrasonic transducer was developed to fit inside the drill pipe. The results show, however, that with given volume it was not possible to gain reasonable mechanical amplification for vibration and the required electrical input power requirement became too high. An ultrasonic transducer in this size turned out to be useless.

Preparation for anomalies

The worst case accident to happen for the drill would be the one that would seize entire rover preventing it from returning back to the lander or carrying out any other tasks. This can happen if the drill string gets stuck in the borehole, or the drill system fails to separate drill pipes from each other.

To be prepared for such an accident, the drill system is capable of leaving the entire drill string into the borehole as the rover backs away from the borehole. This is possible since the DSS has a long vertical slot in the front side of the structure, right in front of the active drill pipe. Also designs of the pipe carousel, clamping system, pipe holders, and tool carousel are such that the pipe can be abandoned and the rover can be backed away.

1. In case the drill string should get stuck in the ground, the drill first pulls with full power in hope to separate one of the couplings on the string. If one coupling opens, the string retraction can proceed in the preplanned manner. If none of the couplings open, it means that the uppermost pipe is stuck in the ground. Then the securing wedge on the spindle is released and the spindle is separated from the string, after which the rover can back away.
2. If a coupling between two pipes is stuck, those can not be stored in the carousel. In that case both of them must be abandoned by releasing them from the spindle and leaving them into the borehole.

3. If the coupling on the spindle is stuck, only one pipe can be used and the length of the pipe limits the possible sampling depth.
4. In case the tool gets stuck on the pipe, only this one pipe and this one tool can be used, but the rover maintains its moving capability.

Development and prototyping

The entire drilling system was designed with IDEAS 3D modeling software, which was of a great help when fitting all moving parts and components inside the limited volume. At certain stage of development and modeling it was decided that instead of continued visual modeling a hardware-model would provide a more concrete playground and faster progress. The 3D model was translated into an STL-file that was used to produce a plastic model of the most important parts (roughly 30 pieces) with fused deposition modeling (FDM) method. This plastic prototype was fitted with all mechanical motions, not electrically driven though, which clearly exposed potential interference and tight places.

Some of the part placement, like the micro switches, was done first with the plastic model and only then transferred to the computer model. Also all of the mountings and screws were designed with the prototype first. This approach appears to be very fast and efficient. However, a couple of things that should have been done in this time were left to wait for the final model, which later turned out to be a mistake. Details like the pipe holder (that prevents a pipe from dropping from the carousel into the drilling hole), tool cleaning brushes and complete wiring design, turned out to be extremely difficult and took a lot of time at the stage where there was not the time reserved. In general details like these, and also all new features, should be prototyped and tested simultaneously during designing to avoid surprises in assembly and integration phase.

Testing

The drill performance is to be tested on a set-up constructed of a platform and a 2-m-long transparent plastic tube. The soil sample to be drilled into is prepared into the tube and the drilling system sits on the platform, mounted either on a separate jig or on the roving vehicle. Drilling speed and thrust are measured with the drill's own instrumentation, while torque-measuring system is mounted to the jig. The sample to be prepared will consist of dry sand with varying grain size and compactness, added with occasional boulders of marble, lime stone and sand stone. The aim of the tests is to determine drilling speed, power and forces, and to demonstrate capability to obtain samples from the desired depth and from the desired materials.

Vacuum compatibility and qualification for space

This device is merely an advanced proof-of-principle model; operations of which still require development for better efficiency and reliability. The model is constructed of commercial and self-manufactured components, but its operation does not rely on any special parts or materials that could not be made space-qualified.

On a mechanical point of view, the design lacks launch locks that might be necessary for a space instrument, and mass can still be reduced by another ~0.5 kg with optimized structural design. Effects of thermal expansion, thermal balance, and protection against dust must be studied carefully to guarantee operation of the drill in space environment.

Lessons Learned

Pipe Couplings

Round-edged trihedron design familiar from robot wrist/tool interfaces appears to suit well for automated connections between parts. A split ring, or a C-ring, for securing of the coupling, although simple in design and easy to use, has some disadvantages related to clinging and possibly to ring orientation.

Drilling tests

With a rotary core drill, 30-N thrust, 30 RPM, without hammering action, core diameter ~10 mm and depth ~15 mm, using hard-alloy cutting tool bits, it takes a few hours to take a sample from a soft rock like marble or lime stone. For hard rock like granite it takes a time frame of tens of hours, but durability and selection of drill bit material would be a critical issue. For hard rocks rotation speed has a great effect, the faster the better.

General

3D volumetric development together with rapid prototype modeling techniques is a very efficient and fast way to design complex systems with moving parts.

Prototyping and testing of mechanical subsystems already during design phase is very important. Nothing should be left to be invented with the final hardware.

Pay attention for design of wire harness, especially if it is moving.

Conclusions

The work presented here produced the first prototype of a small mobile robotic drilling device capable to extend and retract an extendable drill string reaching up to two meters into soil. Scaling the device smaller a lighter and smaller drill can be developed, or if desired to drill deeper, a bigger scale drill with similar actions could be constructed. With this size, and especially with scaled-down devices, volume available for drill motors sets certain limits for applicable drilling power and speed. The lessons learned section indicates some of the development targets that should be considered for the next generation of the prototype.

References

1. 'Exobiology in the Solar System and The Search for Life on Mars' ESA SP-1231, ISBN 92-9092-520-5
2. 'Nanokhod Microrover Heading Towards Mars' Fifth international Symposium on Artificial Intelligence and Automation in Space, I-Sairas '99, ESA SP-440 August 1999
3. 'A Robotic Deep Driller for Mars Exploration' J.Suomela, Helsinki University of Technology, Helsinki, Finland; G. Visentin European Space Agency, Noordwijk, The Netherlands; T.Ylikorpi, Finnish Technical Research Center, Helsinki, Finland; M.Zelikman Space Systems Finland, Helsinki, Finland; Invited session on "Mechatronic Applications in Aerospace", IFAC-2000

521/37

Design and Verification of Space Station EVA-Operated Truss Attachment System

Gabriel Katell*

Abstract

This paper describes the design and verification of a system used to attach two segments of the International Space Station (ISS). This system was first used in space to mate the P6 and Z1 trusses together in December 2000, through a combination of robotic and Extra-Vehicular tasks. Features that provided capture, coarse alignment, and fine alignment during the berthing process are described. Attachment of this high value hardware was critical to the ISS's sequential assembly, necessitating the inclusion of backup design and operational features. Astronauts checked for the proper performance of the alignment and bolting features during on-orbit operations. During berthing, the system accommodates truss-to-truss relative displacements that are caused by manufacturing tolerances and on-orbit thermal gradients. After bolt installation, the truss interface becomes statically determinate with respect to in-plane shear loads and isolates attach bolts from bending moments. The approach used to estimate relative displacements and the means of accommodating them is explained. Confidence in system performance was achieved through a cost-effective collection of tests and analyses, including thermal, structural, vibration, misalignment, contact dynamics, underwater simulation, and full-scale functional testing. Design considerations that have potential application to other mechanisms include accommodating variations of friction coefficients in the on-orbit joints, wrench torque tolerances, joint preload, moving element clearances at temperature extremes, and bolt-nut torque reaction.

Introduction

The construction of the ISS presents many challenges due to its large size and complexity. Multiple segments are brought to orbit via the Space Shuttle. Once on-orbit, the segments must be unberthed from the Orbiter's cargo bay, moved to the ISS, then attached to the ISS. In other applications, it makes sense to accomplish these tasks solely via autonomous and robotic tasks. Due to the critical nature of the ISS power system segments, however, a new attachment system was designed to be operated by spacewalking astronauts who could quickly react to any problems encountered during assembly. The system was first used to mate the P6 and Z1 trusses together. This paper describes the many design considerations associated with the new attachment system and the unique verification approach used to gain confidence in system performance.

The P6 Long Spacer is an integrated truss structure that will provide the ISS with power, using solar arrays and batteries, and communications for voice and telemetry. The P6 was carried into orbit on STS-97, ISS flight 4A, where it was attached to the rest of the ISS through the Z1 Truss. The Z1 is an integrated truss structure that provides a mating location for the P6 Long Spacer, attitude control hardware, and communication hardware for the ISS. The Z1 was carried into orbit on STS-92, ISS flight 3A, where it was attached to Node 1 of the ISS. Figure 1 shows the Z1 element in its launch configuration while Figure 2 shows the P6 element in its launch configuration. Figure 3 is a photograph of the ISS at the conclusion of STS-97, showing the P6 attached to the Z1.

Design and Operations Overview

The truss attachment system is the hardware used to align, mate, and attach the P6 Long Spacer to the Z1 Integrated Truss Assembly. The mating is accomplished with the use of the Shuttle Remote Manipulator System (SRMS) and Extra-Vehicular Activity (EVA). The system, shown in Figures 4 and 5, consists of four sets of coarse alignment cones/receptacles, four sets of fine alignment cones with integral bolt mechanisms and nuts, and a capture latch/capture bar mechanism to pull the interfaces together. Figure 4 shows the Z1 side of the interface plane. The Z1 zenith bulkhead supports the Capture Latch Assembly (CLA), four coarse alignment receptacles, and four fine alignment bolt mechanisms. Figure 6

* The Boeing Company, Canoga Park, CA

shows the P6 side of the interface plane. The P6 nadir face contains the capture bar, four coarse alignment cones, and four fine alignment nut assemblies.

Operating Phases

The truss berthing and attachment has four distinct operating phases: Phase I-SRMS positioning, Phase II-interface alignment, Phase III-bolt down, and Phase IV-demating. Phase I consists of manipulating the P6 into position near the Z1, using the SRMS. The P6 is positioned using the Space Vision System so that all four P6 coarse alignment cones have their cylindrical tips at or below the plane of the Z1 coarse alignment bushing faces. Meeting that Ready to Latch (RTL) criteria ensures that the P6 segment's capture bar is placed within the capture envelope of the Z1 capture latch. The EVA astronauts visually verify that the ready to latch condition has been achieved, completing Phase I operations.

In Phase II, astronauts use the electric wrench to close the Z1 capture latch. As the latch claws close upon the P6 capture bar the Z1 and P6 segments are pulled together, the fine alignment features engage, and the P6 moves laterally with respect to the Z1. The SRMS is placed in its Test mode during Phase II to reduce resistance to the fine alignment. SRMS Test mode is a "limped" mode in which the joint servos have no control authority and the SRMS joints are relatively compliant to end effector motion. The Z1 fine alignment/bolt mechanism is shown in Figure 6. The P6 long spacer nut installation is shown in Figure 7. When the fine alignment cones (shear cylinders) on the Z1 side fully seat in their receptacles on the P6, the capture bar is approximately 6 mm from fully seated in the capture latch. Continuing to close the capture latch deflects the capture bar's backup structure, which produces a small preload between the Z1 and P6 structures.

To complete Phase III, the EVA astronauts first verify the fine alignment features are fully seated by checking the gap between the P6 and Z1 housings, using a convenient tool of a known width. Next, the crew tightens the primary structural attach bolts to fasten the truss segments to each other in the sequence noted in Figure 5. The resulting configuration is shown in Figure 8. The bolt design incorporates a "self-feeding feature" which provides a small axial force to initiate bolt thread engagement so that the crewmember does not have to push on the end of the bolt during tightening. During tightening, the crew checks that the bolt is turning, advancing, and the running torque is low. The bolt preload is controlled by torque alone. Primary bolt installation torque is reacted by two pins in the Z1 shear cylinder engaging matching slots in the P6 primary balls. After the bolts are fully tightened, the preload applied by the capture latch is released by EVA actuation, the SRMS ungrapples the P6, and the attachment process (Phase III) is complete. Later in the ISS assembly sequence, the P6 is removed from the Z1 and moved to a permanent location on the outboard truss, at P5. The Phase IV tasks associated with the demating operation are the reverse of Phases I through III.

Where possible, the three phases associated with truss berthing and mating are separate and have distinct, identifiable beginning and ending points. In addition, confidence for proceeding with the next phase can be gained by establishing specific verification criteria. For example, the interface alignment phase is verified complete prior to initiating bolt operations, by checking that the fine alignment features have accomplished the lateral positioning, and that the capture latch has accomplished the axial positioning. The practical means of determining that the alignment has been achieved to within the design limits of the system is by having the EVA crew check the Z1 to P6 housing distance. The gap check confirms that the lateral offset is within the capability of the bolt threads to engage the nut, even with the nut rotated within its spherical bearing.

Capture Latch Description

The Capture Latch Assembly, mounted on the Z1 truss, consists of two opposing claws connected to a series of linkages, a drive screw, and a geared drive train (Figure 9). The input shaft to the drive train, when driven at a constant 15 RPM, will cause the claw to rotate from fully open to fully closed in approximately 6 minutes 45 seconds, although it may be driven faster or slower. Assuming the capture bar, a solid steel cylindrical shaft mounted on the P6 truss, is within the sweep area of the claws, the claws will then pull the bar, and the attached P6 truss, towards the Z1 truss, forcing the two interfaces to comply. For use on the Z1, the CLA's input is extended by a tube to the outer edge of the truss where the astronaut has good access.

Contingency Design and Operational Features

In Phase II, if the capture latch fails to close, the astronauts have contingency procedures for routing special straps between the trusses and with a winch, they temporarily hold the interface together during bolt engagement¹. To accommodate failures in Phase III, bolt-down, each fine alignment device incorporates two contingency attachment bolt/nut combinations to allow a structural connection to be made in the event the primary bolt cannot be engaged (see Figure 8). At each corner of the truss, the mechanism is two fault tolerant for achieving structural integrity. Therefore if the primary bolt cannot be engaged, one contingency bolt can be engaged. If that contingency bolt cannot be engaged, the second contingency bolt can be employed.

Specific operational procedures were prepared through the development of flowcharts that addressed potential anomalous on-orbit conditions². Manufacturing tolerances and thermal-structural deflections may create an offset between the capture bar and the capture latch (see Figure 10). These offsets affect latch preload and the ability to fully seat the shear cylinders at the shear carrying corners of the truss. Procedures were devised to loosen the capture latch if the bar/latch offset causes excessive Z1 bolt to P6 nut misalignment, as detected by the truss-to-truss gap check. An analysis was conducted to derive the number of turns the latch would need to be loosened.

Contingency bolts and associated threaded spacers are launched with the Z1 in the position shown in Figure 6. EVA astronauts extend the spacer sleeve. The spacer serves to maintain the gap between the Z1 fine alignment housing and the P6 corner fitting so that no bending moments are created due to the distance between the fine alignment shear cylinder's centerline and the contingency bolt's centerline. A special lock tool is installed over the spacer sleeve to keep it from turning during contingency bolt operations (see Figure 11). The tool incorporates an additional feature for use in contingency operations to measure the gap between Z1 and P6 housings³. If needed, the tool's tapered protrusion is placed between the housings until the edges contact the housings. The housing gap is indicated by graduated lines on the protrusion, which are visible to the crew.

All contingency nuts in P6 fine alignment device slide in Y-Z plane. Even if the primary bolt fails to engage, shear is transferred through the shear cylinders on primary bolt at the two truss corners that are intended to react shear. Operational procedures ensure the shear cylinder is seated even if the primary bolt is not completely engaged.

Contingency bolt installation torque is reacted by a locking plate on the P6 assembly (see Figure 12). After contingency bolt torquing, this plate is removed by EVA and stowed for future use. A pry bar can be used to assist in plate removal while the contingency ball flats press against the plate's slotted hole. Plate removal allows the contingency ball/nut races to slide and rotate as required to accommodate thermal-structural deflections.

If the capture latch cannot be released nominally, there are backup means to release the preload by turning the P6 capture bar in its eccentric bushings, and releasing the Z1 capture latch claws via EVA handles on the Z1 zenith bulkhead².

For demating (Phase IV), the device includes a release mechanism, an EVA operated lock pin, to allow disconnect of the P6 from the Z1 should the primary EVA bolt become stuck in the P6 sleeved nut (see Figure 12) during engagement. If the nut gets stuck, contingency tools and means exist to replace the nut (threaded sleeve) in the P6 fine alignment assembly, thereby restoring the original fault-tolerance of the joint for connection of P6 to P5. The self-feeding nut in the Z1 bolt assembly is made of plastic which will shear off as the bolt/nut together are unscrewed, if the bolt has stuck to the nut at a significant engagement depth. This feature is required because there is a small difference in thread pitch between the outer and inner diameters of the P6 sleeve/nut.

Thermal-Structural Analysis

The accommodation of structural deflections caused by the temperature gradients was one of the most important considerations in designing the truss attachment system. Estimates of the temperature distributions were made using ISS thermal models of both the pre-mate and post-mated conditions. Transient thermal analysis was used to determine truss temperatures at the point in time when the mating was expected to occur. Numerous flight attitudes, sun angles, hardware configurations, shadowing, and

truss thermal properties were evaluated in the analyses. Once temperatures were determined from the thermal models, they were mapped onto the corresponding elements of the structural finite element models. Finite element analysis was then performed to determine structural deflections. Through further processing, the relative deflections of corresponding P6 to Z1 attach points were calculated. To determine the deflections in a relative sense, the fixed corner was the origin of a coordinate system that was positioned angularly by +/-Y sliding corner⁴.

Attachment Restraint

Figure 5 indicates the degrees of freedom in the fine alignment assembly's primary nuts located at each corner of the P6. Figure 8 shows a cross section of a fine alignment mechanism with the Z1 primary EVA bolt engaged into the P6 long spacer primary nut. Spherical bearings are used around both the primary and contingency nuts to provide a limited rotational freedom about the Y and Z axes. This bearing arrangement provides relief for on-orbit differential thermal expansion and distortion that may occur between the Z1 and P6 during on-orbit operations. The arrangement also accommodates angular misalignments due to manufacturing tolerances.

In addition to the rotational degree of freedom in the primary nut assemblies, there are provisions for sliding in the Y-Z plane to allow for differential thermal expansion of the P6 and Z1. One corner of the P6 incorporates a fine alignment nut assembly that is fixed from sliding in the Y-Z plane. A second corner incorporates a nut assembly that is allowed to slide in the Y-direction only. The two remaining corners incorporate nut assemblies that are allowed to slide in the Y-Z plane. This arrangement allows the bolts to react shear and torsional loads, while still allowing the structures to expand and contract thermally.

The sliding degrees of freedom in the P6 nut side of the fine alignment mechanism is accomplished by incorporating a gap between the bearing race and the truss corner fitting. The magnitude of these gaps is established based upon both part tolerances and predicted thermal displacements. All of the contingency nuts in the P6 fine alignment device are allowed to slide in the Y-Z plane. The shear cylinder at the primary bolt locations still carry shear loads even when the contingency bolt is installed.

After the structural connection is made, loads are transmitted across the Z1-P6 interface as follows:

- +/- Z in-plane shear load - reacted by fixed truss joint & truss joint that is free to slide in the +/-Y direction
- +/- Y in-plane shear load - reacted by fixed truss joint only
- +/- X axial load - reacted by all four truss joint corners

Race-Nut Centering

The P6 primary races contain springs that keep the ball/nut elements centered for entry of the Z1 fine alignment shear cylinder (see Figure 13). The P6 ball opening, Z1 shear cylinder tip, and the P6 centering spring geometries ensure fine alignment feature engagement when lateral misalignments are present, as limited by coarse alignment feature clearances. Such misalignments may be due to thermal gradients and manufacturing tolerances. The P6 contingency races contain springs that keep the ball/nut elements centered for Z1 contingency spacer seating (see Figure 14).

Bolt Installation Torque Reaction

Primary bolt installation torque is reacted by two pins in the Z1 shear cylinder engaging matching slots in the P6 primary balls. These features keep the P6 nut from turning during installation of the Z1 bolts. In addition, the nut is free to slide and rotate after full torque is applied. The torque reaction features were designed to engage with the P6 primary ball/nut rotated to its limits, translated to its limits, and with the maximum gap predicted from the thermal and manufacturing tolerance studies. Figure 15 shows a layout of the Z1 shear cylinder entering the P6 ball/nut with the Z1 torque reaction pin capable of resisting torque against the P6 ball's slot. The layout shows the shear cylinder axially separated from the P6 ball a distance equal to the maximum expected gap predicted from the thermal and manufacturing tolerance studies. The shape of the slot in the P6 ball and the positioning of the pin in the Z1 shear cylinder were critical, having been derived from a series of layouts reflecting the expected relative misalignments. Those layouts ensured that the Z1 pin would enter the P6 primary ball even with the ball rotated to its limit.

Joint Preload Considerations

The primary and contingency bolts must be tightened to a sufficiently high torque to create a preload that prevents joint separation under the influence of external loads. The maximum torque is limited by strength, fracture and fatigue considerations. With upper and lower limits defined, a range of permitted torque values is therefore determined. Typically, another factor must be taken into account- the change in preload associated with tightening the bolt at the various predicted on-orbit temperatures, due to the difference in thermal expansion coefficients between the bolt and clamped materials. In the case of the subject attach system, however, the bolt, shear cylinder, retaining nut, and threaded sleeve are all stainless steel alloys with similar coefficients of thermal expansion. Variations in bolt-nut interface friction coefficients are examined in the joint analysis that place additional constraints on the bolt torque allowable range. Development tests were conducted to characterize the friction coefficients associated with the specific materials, sizes, surface finishes, and lubricants of the truss attach system joints⁵. These tests were conducted in air, and at vacuum, over the expected temperature range. The attach bolts, races, balls and nuts are dry film lubricated with Molybdenum Disulfide.

The primary bolt sizing calculations included misalignment loads associated with closing a maximum axial gap that may exist at the time of bolt-up, due to truss-to-truss interface out-of-plane manufacturing tolerances and thermal-structural deflections. The contingency bolt sizing did not include this misalignment load because the contingency spacer sleeve bridges, but does not close, the axial gap. On-orbit mechanical loads are also part of the joint design loads.

After the preload range was computed, the torque range was determined and a wrench with adequate torque accuracy was selected⁶. In the case of the subject truss attachment system, the final tightening of the bolts was accomplished using a manual torque wrench that had an accuracy of +/-10% in the expected operating and torque ranges.

Design Tolerance Studies

A large number of tolerance analyses were performed to ensure that the selected design dimensions of the truss attachment system features provide the required performance in the different operating phases⁷. This section describes the evaluations of truss in-plane differential displacement, out-of-plane relative displacement, and relative rotations due to warpage. In addition, studies of the clearances of the moving elements are addressed. During and after mating, temperature gradients exist within the P6 and Z1 trusses. Such gradients cause the structure to deflect from its nominal shape. The tolerance assessment included thermal conditions that exist during pre-mate and post-mate configurations.

In-Plane Differential Displacements

Analysis was performed to predict the maximum thermal-structural displacements in the mating plane, across the Z1-P6 interface. Relative displacements were predicted between each of the four corner fine alignment features, between each of the four coarse alignment features, and between the coarse and fine alignment features.

A check was made to ensure radial clearance exists between the coarse alignment P6 cone's cylindrical body and Z1 coarse alignment bushing inside surface when displacements are at their extremes. The coarse alignment features must have clearance post-mating, so that shear loads are only transmitted at the fine alignment connections. The analysis was repeated for both nominal and worst case detail part dimensions, and overall positional tolerances. Clearances for pre-mate and post-mate thermal conditions were examined.

The clearance between the P6 fine alignment primary ball/race and the P6 corner fitting bore for each of the four corners, one to another, was analyzed as well. Race clearances must exist, post-mating to ensure that shear loads are reacted by the intended statically determinate system.

A calculation was made to determine the radial clearance between the fine alignment Z1 shear cylinder and the P6 receptacle (nut) when these two items first begin to engage (by capture latch closure). The calculation was repeated with the items displaced by thermal-structural gradients and manufacturing tolerances. A detailed layout revealed that the shear cylinder would enter the ball properly.

Selection of the minimum clearance between the coarse cone and bushing was driven by the thermal-structural displacements between the coarse alignment features that are furthest from the fixed fine alignment nut. Once this selection was made, a calculation showed that entry of the fine alignment features would always occur with the maximum clearance between the coarse alignment features.

Analysis confirmed that with the predicted thermal displacements, dimensional tolerances, and positional tolerances, when the coarse alignment features engage, the fine alignment always begins to engage, even considering the potential for free play associated with the primary race centering springs.

Out of Plane Relative Displacements

Manufacturing tolerances and temperature gradients in and between the Z1 and P6 trusses shift the out-of-plane (X-direction) positions of the fine alignment features when the Z1 capture latch is closed on the P6 capture bar, prior to structural bolt engagement. Stated another way, three of the four shear cylinders will seat, but the fourth might not be seated. The primary attach bolt's stroke, bolt strength, contingency attach sleeve stroke, and contingency attach bolt strength were found to be sufficient to seat the fine alignment Z1 shear cylinders in the P6 receptacles (nuts). For this truss attachment system, the capture latch preload is not sufficient to seat the fine alignment Z1 shear cylinder in the P6 receptacle (nut).

With the shear cylinder not fully seated, there could be a bolt to nut centerline offset that must be accommodated by attach bolt's lead-in. Analysis and test confirmed the capability to engage the threads in this offset condition.

Relative Rotations Due to Warp

Temperature differences between the Z1 and P6 might produce warp that creates relative rotation between the Z1 bolt and P6 nut assemblies. The amount of the rotations due to thermal effects was analytically predicted. Rotational freedom was provided in the design, in the form of spherical bearings for both the primary and contingency nut assemblies sufficient to accommodate the predicted rotations due to thermal gradients and manufacturing tolerances. In addition, an analysis concluded that the on-orbit mechanical loads do not rotate the bearing to its travel limit, thereby confirming that local moments remain released.

Moving Element Clearances

Analysis was performed to ensure clearance exists, with worst case predicted temperatures, and with worst case dimensions, between the following components: Z1 shear cylinder outer surface to P6 primary ball inside surface, Z1 contingency bolt spacer to contingency bolt, Z1 microconical fitting to primary bolt, Z1 spring retainer nut to primary bolt, Z1 shear cylinder to primary bolt, Z1 launch restraint cap to housing, Z1 launch restraint cap to shear cylinder, Z1 shear cylinder to self-feeding nut, P6 ball to race spherical diameters, P6 race width to housing, and Z1 primary bolt to self-feeding nut. The Z1 launch restraint nut, shown in Figure 16, secures the primary bolt from rattling during launch, and is removed by the EVA crew on the mission prior to berthing.

Verification Program

Confidence in system performance was achieved through a cost-effective collection of tests and analyses, including thermal, static loads, vibration, misalignment, contact dynamics, underwater simulation, and full-scale functional testing⁸. A balance between tests and analyses at the component and system levels resulted in an integrated verification approach. The relationship between component level testing and system level characteristics is described for each test in the following sections.

Qualification Vibration Test

A qualification vibration test was performed to demonstrate the ability of Z1 & P6 fine alignment assemblies to withstand the maximum expected launch vibration environment with a qualification margin. This component level test correlated to system level performance in that the vibration spectrums used for the test were derived from system (cargo element) level acoustic tests. The fine alignment bolt and nut assemblies passed all functional tests after being exposed to the vibration environments⁹.

Qualification Thermal Cycle Test

A qualification thermal cycle test was performed to demonstrate the ability of the fine alignment assemblies to perform in the ISS space environment, meeting all thermal and mechanical performance requirements¹⁰. This component level test correlated to system level performance in that the temperatures used for test were predicted from system level (truss) thermal analysis. The component test partly verifies ability of the P6 primary and contingency nuts to comply with the predicted system borne misalignments relative to Z1 fine alignment features. The test also evaluated bearing rotation and race sliding at temperature extremes.

With regard to nut rotation/sliding performance, results of this ambient pressure test correlate well with results of an earlier Human Thermal Vacuum (HTV) test¹¹. In the HTV test, a misalignment test was performed at temperature extremes, simulating both overall truss thermal-structural deflections and local mechanism thermal-structural deflections (clearance changes due to differential coefficients of thermal expansion between mechanism moving elements). Functional testing at several points of this test was successful, including confirmation that the primary bolt did not loosen as a result of thermal cycling, and visual inspection revealed no change occurred. The test also verified that the fine alignment features, bolts, launch restraint cap, etc. have sufficient clearance to engage/disengage at temperature extremes.

Qualification Misalignment Test

A qualification misalignment test was performed to verify that the Z1 and P6 fine alignment interfaces engage and can be bolted together when there is an angular misalignment between the two structures, when there is a lateral offset between the Z1 and P6 assemblies, and when there is a gap between the Z1 shear cylinder and the face of the sleeve in the P6 ball/receptacle¹².

This component level test correlated to system level performance in that the thermal-structural deflections that the mechanism's degrees of freedom are designed to accommodate, are the truss deflections. These truss deflections are due to overall Z1 to P6 truss temperature differences, not local temperatures of the mechanisms themselves. Test gaps and misalignments simulate those that may occur between the P6 and Z1 due to worst case system level on-orbit thermal effects and manufacturing tolerances. This component test also correlated to system level performance in that the test fixture simulated the P6 truss backup structure stiffness. The P6 finite element model was used to calculate required fixture stiffness. Fixture stiffness was test verified prior to use in the misalignment test. A graphical view of the misalignment test setup is shown in Figure 17.

In the qualification misalignment test, performed at room temperature, only simulated overall truss thermal-structural deflections were addressed. However, in the HTV test, the misalignment test was performed at temperature extremes, simulating both overall truss thermal-structural deflections, and local mechanism thermal-structural deflections (clearance changes due to differential coefficients of thermal expansion between mechanism moving elements). Therefore results of both the qualification and HTV misalignment tests provided confidence that the mechanism would perform as required in the space environment.

Qualification Static Loads Test

The qualification static loads test was performed to verify the functionality of the test articles after the application of 1.0 times the design limit on-orbit loads¹³. An additional objective was to measure the force required to slide the P6 assembly under applied limit loads. The strength of the test article was verified for 1.5 times the design limit on-orbit loads. This component level test correlated to system level performance in that the structural test load values were derived from system-level analyses. These loads include on-orbit mechanical loads, thermal loads, and misalignment loads due to manufacturing tolerances. Test cases included configurations with only the primary bolt engaged, and cases with only the contingency bolt engaged. After the application of limit loads, no damage was found and the units passed the mechanical functional tests. No failure occurred after application of ultimate loads. Load versus deflection data was recorded for each load case and was used to determine joint stiffnesses.

Qualification Contact Dynamics Test

A special contact dynamics test was performed to validate the mathematical model of the truss attachment's fine alignment features, comprising the ball-nut and shear cylinder at one truss corner¹⁴. This model, together with the SRMS and CLA models made up the system level model, or full simulation as it

has been called. The intent of the simulation, using the system model, was to predict the behavior of the truss interface and the SRMS as the CLA draws the P6 and Z1 trusses together to a mated, pre-loaded condition, after which the primary bolt attach features are engaged. The testing of a single corner's fine alignment feature, i.e., the component level, allowed identification of detailed alignment characteristics that would otherwise be masked by system level testing.

A specially designed test setup was created consisting of a platform supported by struts that were each instrumented with a displacement and axial load transducer. The platform held the ball-nut half of the fine alignment feature and an XYZ table held the shear cylinder feature above the ball-nut (see Figure 18). The XYZ table was used to create a lateral misalignment between the two features while they were apart from each other. The table was then driven down, causing the two features to engage and forcing the platform to comply via displacement of the struts. Strut loads and displacements were recorded as a function of time for correlation with a simulation of the entire test setup.

After being correlated to the contact dynamics test results, the system model was developed and used for several studies¹⁵. First, hand selected initial misalignment conditions were used to examine the boundaries of the capture envelope. Then, treating the maximum misalignment values as three-sigma conditions generated probabilistic initial conditions. The initial conditions were screened for meeting the ready to latch criteria. The RTL criteria itself was determined through a series of studies which ultimately resulted in the one used on-orbit, i.e. that all four P6 coarse alignment cone tips be placed at or below the plane of the Z1 coarse alignment bushings. In all the simulated cases, the P6 and Z1 trusses were successfully brought together by the CLA and the interfaces fully seated, even with the SRMS in Brakes On Mode. The coarse and fine alignment features of the interfaces were always able to remove initial misalignments completely, followed by pre-loading of the interface by the CLA. The worst case travel paths defined by the simulations were used to perform a computer aided design clearance study. This analysis confirmed that no interference to berthing exists. Additional berthing simulations were performed to show that berthing can be achieved using the straps and winches, mentioned earlier, in the event the capture latch cannot be operated¹.

Underwater Testing

Full scale Z1 & P6 segment mockups were built to physically simulate truss module interfaces and the capture mechanism. These mockups were made neutrally buoyant and placed underwater in a massive tank. Space suited astronauts demonstrated they could conveniently reach and operate the truss attachment mechanisms in simulated weightless conditions¹⁶. This demonstration provided confidence that the mechanism would work in the Z1 to P6 application.

Acceptance Phase Component Testing

Functional tests were performed during assembly of the individual Z1 bolt assemblies. Checks on the Z1 bolt assemblies included verifying lock pin operation in the primary bolt launch restraint, operation of the contingency spacer lock, and operation of the contingency spacer. Because the P6 nut elements are integral with the truss corner fitting, they were verified after installation in the P6 truss. Careful dimensional inspections during detail part fabrication and during assembly ensured mechanism performance was as intended. Such inspections were possible, and therefore the usual mechanism thermal vacuum and vibration acceptance tests were not needed.

Acceptance Phase Full Scale Testing

Functional tests and inspections were performed after the bolt assemblies were installed on the Z1 and after the nut elements are installed in the P6. Many of these checks were performed using the Mating Mechanism Simulators (MMS). The Z1 MMS is an inspection tool that contains simulated Z1 features for checking the P6 flight article (see Figure 19). The P6 MMS is an inspection tool that contains simulated P6 coarse and fine alignment features and is used to check the Z1 flight unit features (see Figure 20). Measurements taken using the MMS units verified that the manufacturing tolerances on the flight article's alignment features were within the allocated values. With that confirmation, confidence was gained that there would be sufficient race float and coarse alignment feature clearance to accommodate the expected on-orbit thermal deflections. The MMS measurements were augmented with laser theodolite and camera-computer system measurements¹⁷.

Conclusions

This paper reviewed the design and verification of a Space Station truss attachment system that was successfully used for the first time to mate the ISS Z1 and P6 segments, in December 2000. The mechanisms were designed and used in a manner that, as much as possible, kept the berthing, interface alignment, and bolt-down phases separate. Contingency procedures were developed for the EVA astronauts to use in response to on-orbit anomalies. A robust system was developed which accommodated interface misalignment caused by manufacturing tolerances and thermal gradients. The verification approach resulted from a balance between tests and analyses at the component and system levels.

References

1. "Z1 to P6 Berthing Using Payload Retention Devices", Gabriel Katell, The Boeing Company, Rocketdyne Propulsion & Power, April 16, 1999, EID-03968.
2. "Evaluation of Z1 Capture Latch to P6 Capture Bar Preload", Gabriel Katell, The Boeing Company, Rocketdyne Propulsion & Power, November 22, 1999, EID-05257.
3. "Rocketdyne Truss Attachment System (RTAS) Design/Verification Technical Interchange Meeting", Gabriel Katell, The Boeing Company, Rocketdyne Propulsion & Power, April 29, 1999, EID-03899.
4. "Z1-Stack Flight 4A IDR3 Z1/P6 and P6LS/P6IEA Interface Loads", Robert Rudd, The Boeing Company, February 16, 1998, A92-J195-STD-M-RAR-9800016.
5. "Rocketdyne Truss Attachment System (RTAS) Bolt Development Torque-Preload Test", George Raquelsantos, The Boeing Company, Rocketdyne Propulsion & Power, May 17, 1999, ETD-MD4-C01178.
6. "RTAS Mechanism- Z1 Side (P6 to Z1) Stress Report", Bill Ng, The Boeing Company, Rocketdyne Propulsion & Power, June 23, 1999, EPS-S-PV-16-01-017.
7. "Rocketdyne Truss Attachment System (RTAS) Design Tolerance Analysis", Gabriel Katell & Stanley Gordon, The Boeing Company, Rocketdyne Propulsion & Power, July 12, 2000, EID-03256.
8. "Rocketdyne Truss Attachment System (RTAS) Verification Plan", Gabriel Katell, The Boeing Company, Rocketdyne Propulsion & Power, March 26, 1998, EID-02267.
9. "Rocketdyne Truss Attachment System Fine Alignment Bolt/Nut Qualification Vibration Test Report", Frank Chang & Keli Asato, The Boeing Company, Rocketdyne Propulsion & Power, March 12, 1999, ETD-PQ4-C01180.
10. "Rocketdyne Truss Attachment System Fine Alignment Bolt/Nut Qualification Thermal Cycle Test Report", Gabriel Katell & Keli Asato, The Boeing Company, Rocketdyne Propulsion & Power, March 31, 1999, ETD-PQ4-C01181.
11. "HTV #7 Test Results- BMRRM Dual Latch, RTAS Bolts, Z1 Keel, Russian Tools", John Maddux, The Boeing Company, Rocketdyne Propulsion & Power, October 15, 1999, EID-00722-103.
12. "Rocketdyne Truss Attachment System Fine Alignment Bolt/Nut Misalignment Qualification Test Report", Gabriel Katell & Keli Asato, The Boeing Company, Rocketdyne Propulsion & Power, April 8, 1999, ETD-PQ4-C01189.
13. "Rocketdyne Truss Attachment System Fine Alignment Bolt/Nut Qualification Static Test and Z1 Contingency Spacer Lock Tool Strength Test Report", Gabriel Katell & Alfred Lewis, The Boeing Company, Rocketdyne Propulsion & Power, May 13, 1999, ETD-PQ4-C01191.
14. "Rocketdyne Truss Attachment System Fine Alignment Hardware Contact Dynamics Test/Analysis Correlation Report", Gabriel Katell, The Boeing Company, Rocketdyne Propulsion & Power, April 20, 1999, EID-03970.
15. "Rocketdyne Truss Attachment System Full Simulation Report", Teri Krene, The Boeing Company, Rocketdyne Propulsion & Power, August 2, 1999, EID-03954.
16. "Crew Consensus Test Report", Cathy Therrien, The Boeing Company, Rocketdyne Propulsion & Power, June 22, 1998, EID-00722-51.
17. "P6 RTAS Race Concentricity Assessment", Gabriel Katell, The Boeing Company, Rocketdyne Propulsion & Power, October 10, 2000, EID-05780.

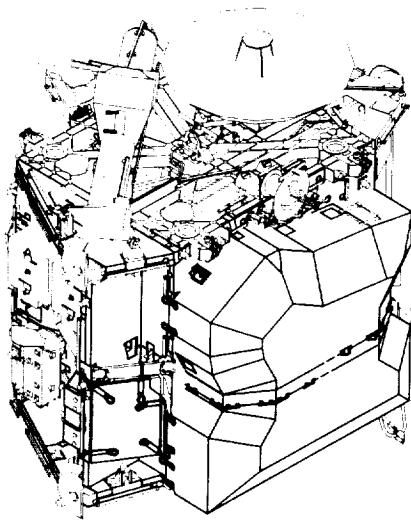


Figure 1. Z1 Cargo Element

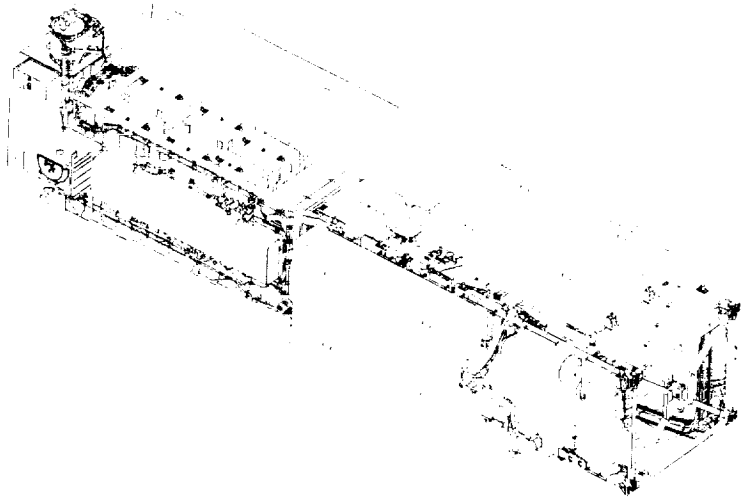


Figure 2. P6 Cargo Element

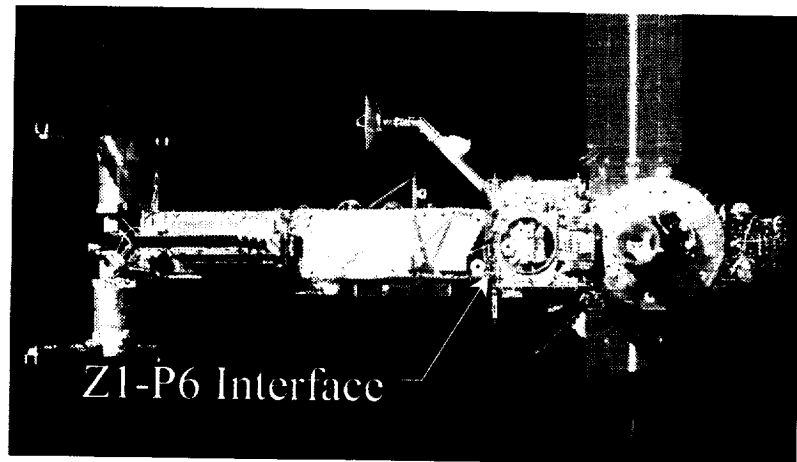


Figure 3. ISS at STS-97 Conclusion

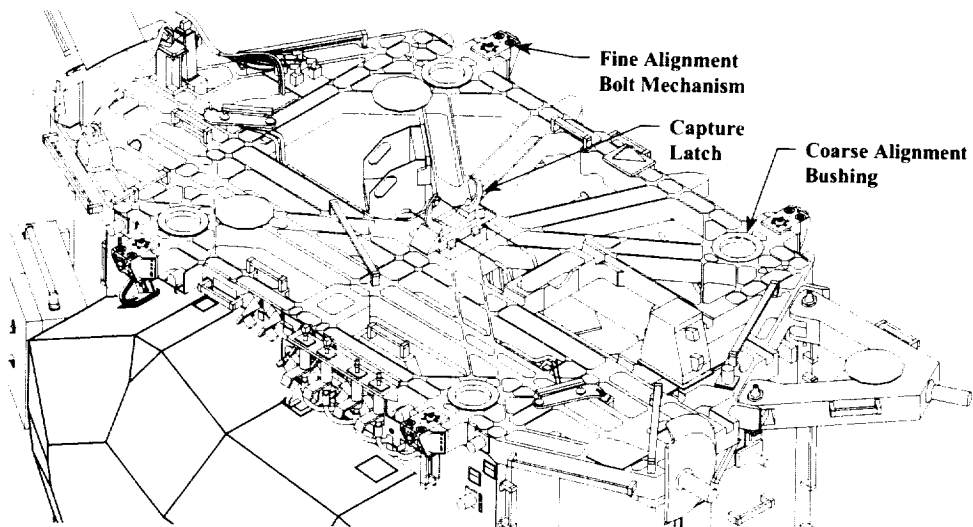


Figure 4. Z1 Zenith Bulkhead Truss Attachment Features

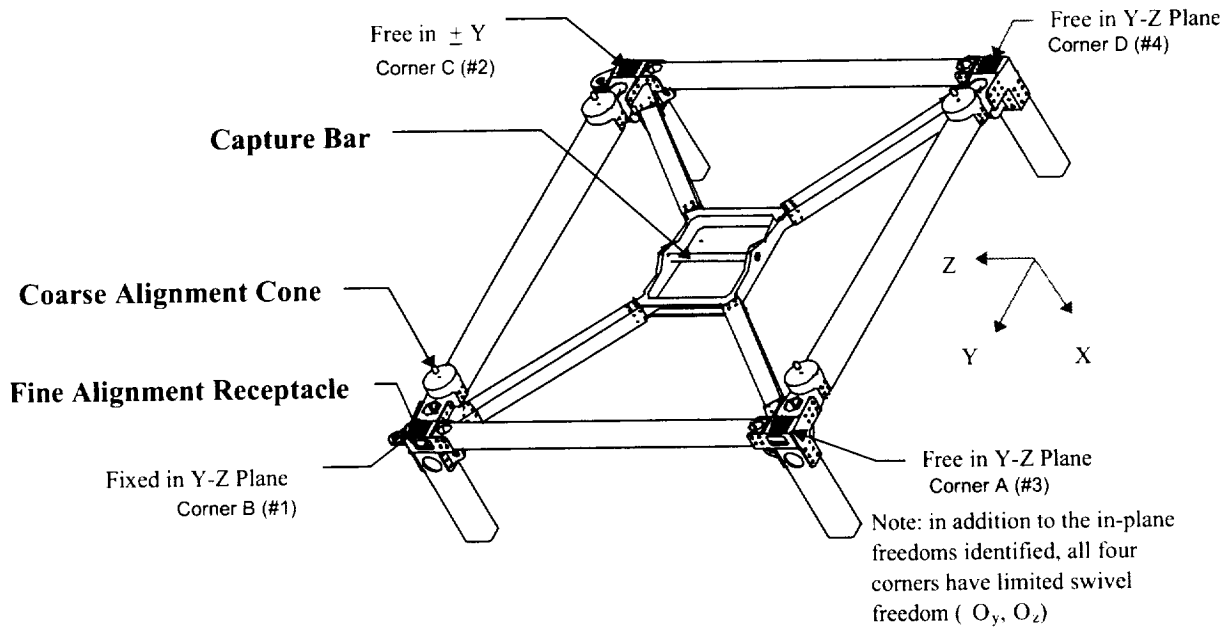


Figure 5. P6 Long Spacer Truss Attachment Features

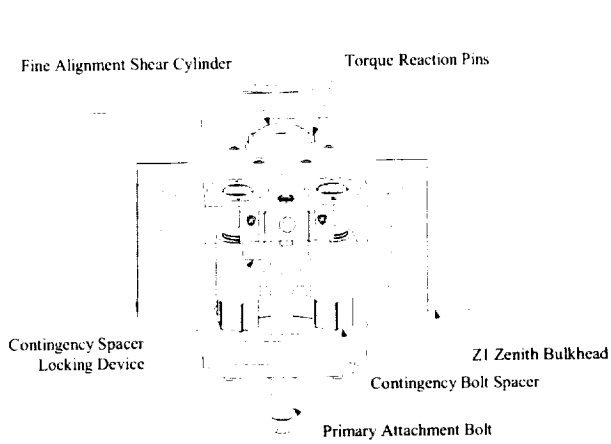


Figure 6. Z1 Fine Alignment/Bolt Installation

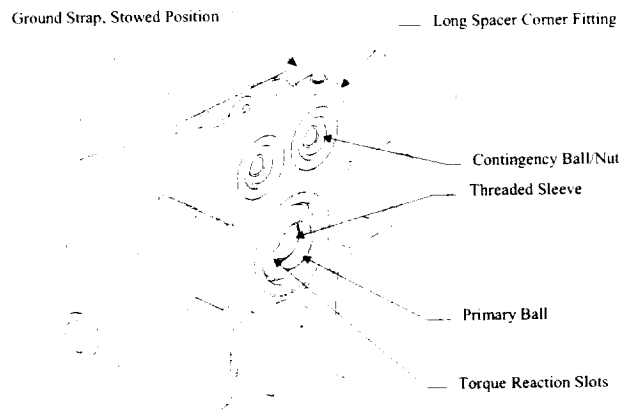


Figure 7. P6 Fine Alignment/Nut Installation

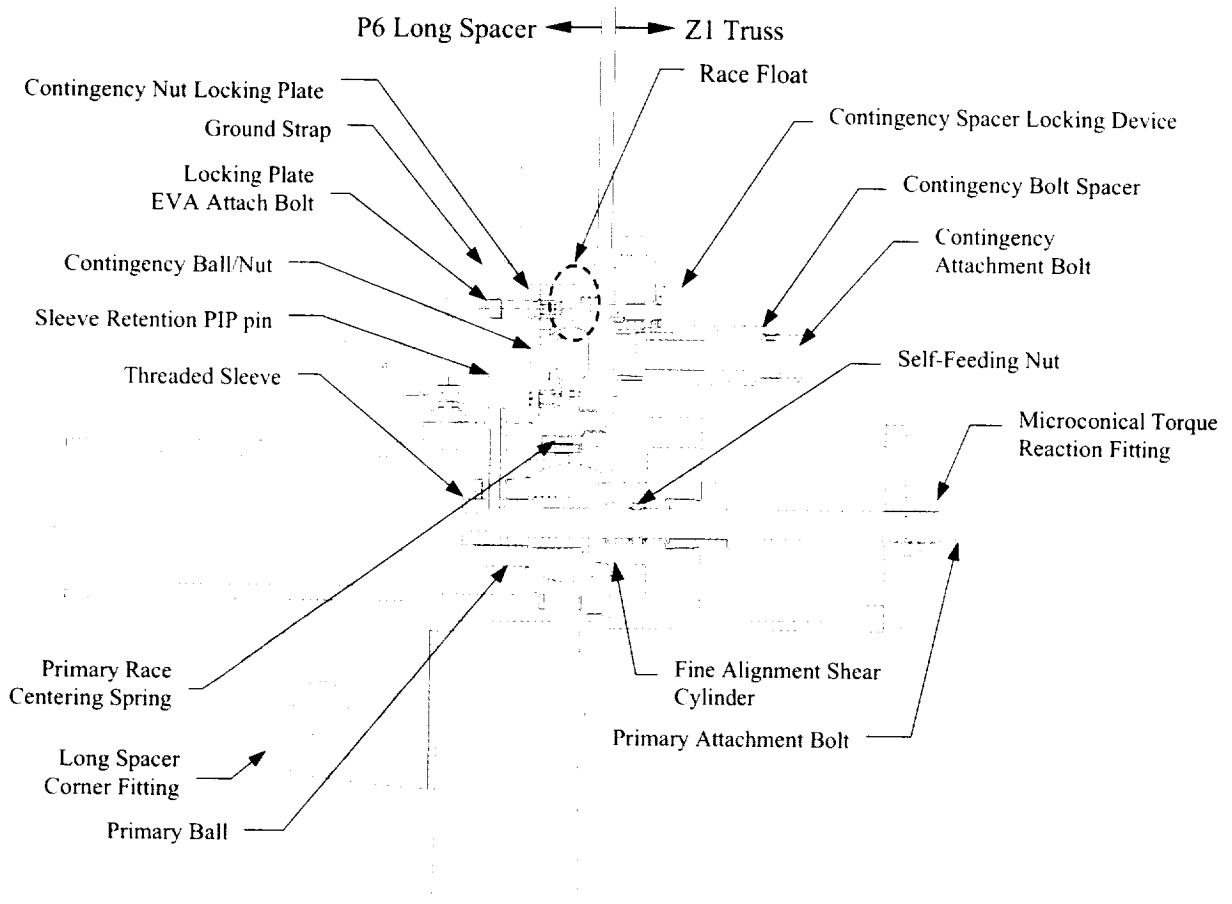


Figure 8. P6-Z1 Mated Configuration



Figure 9. Capture Latch Assembly

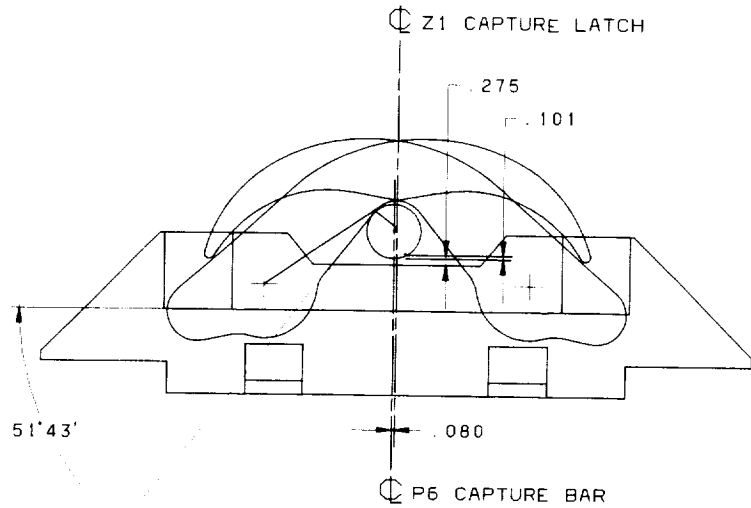


Figure 10. Capture Latch-Capture Bar Offset

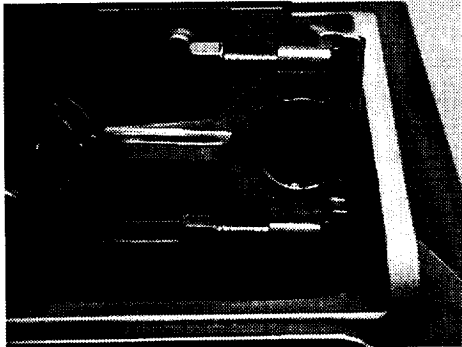


Figure 11. Z1 Congingency Spacer Lock Tool

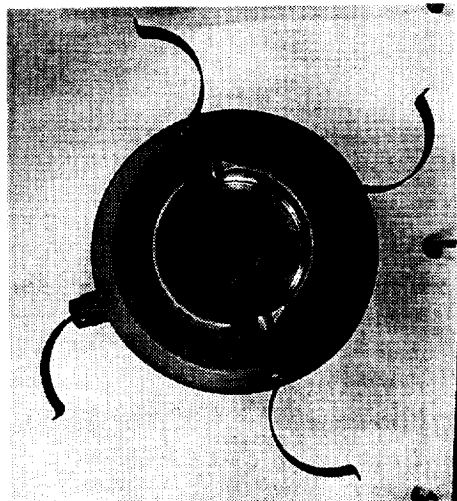


Figure 13. P6 Primary Race with Centering Springs

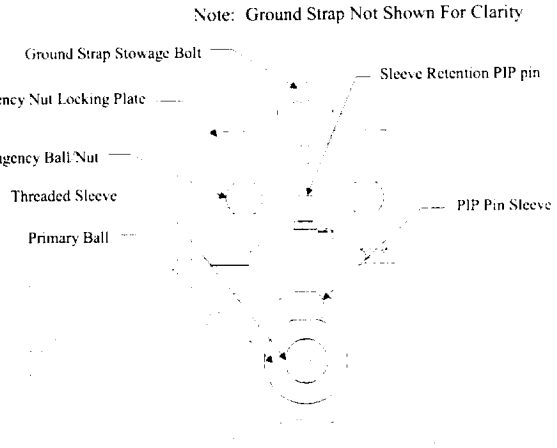


Figure 12. P6 Fine Alignment/Nut Installation Rear View

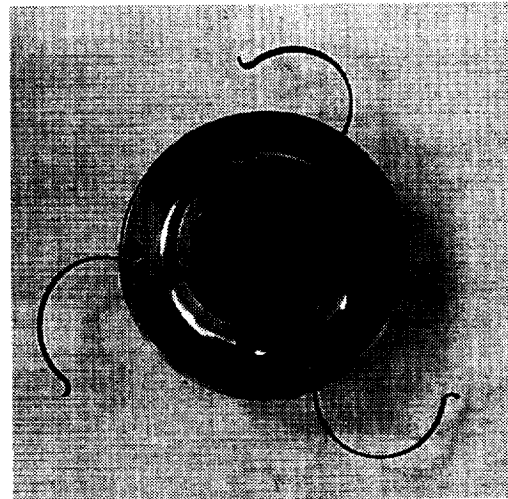


Figure 14. P6 Contingency Race with Centering Springs

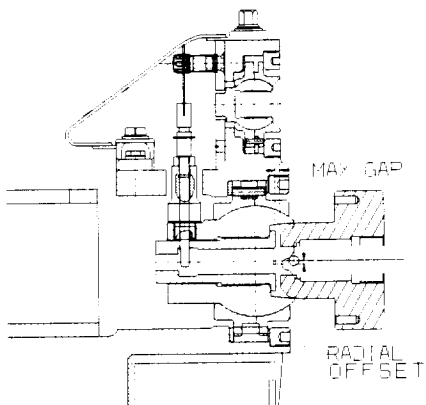


Figure 15. Z1 Shear Cylinder Entering P6 Ball/Nut, at Ready to Bolt Configuration

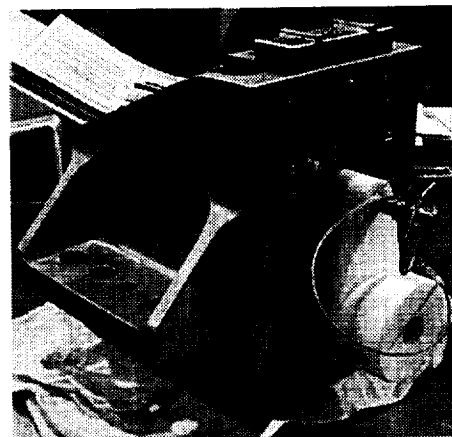


Figure 16. Z1 Fine Alignment/Bolt Assembly

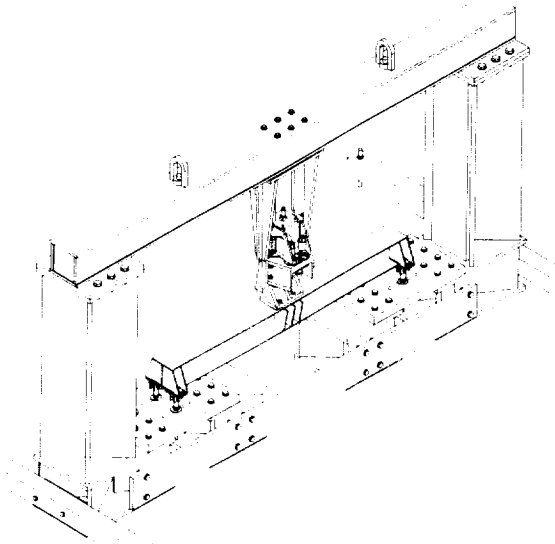


Figure 17. Misalignment Test Setup

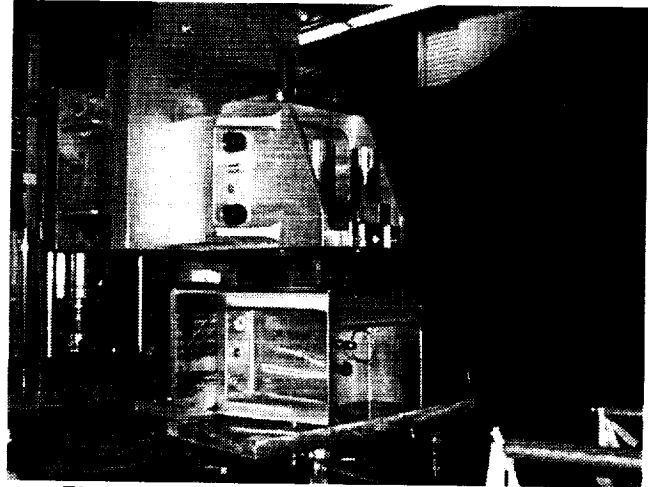


Figure 18. Contact Dynamics Test Setup

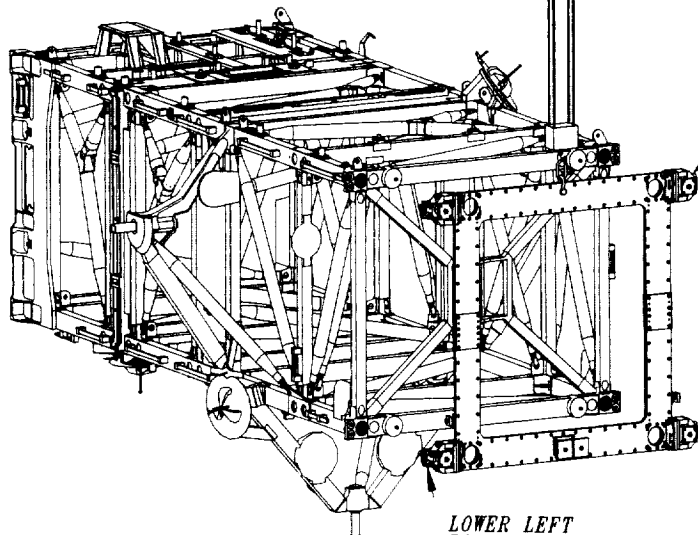


Figure 19. Z1 MMS Checkout of P6 Flight Article

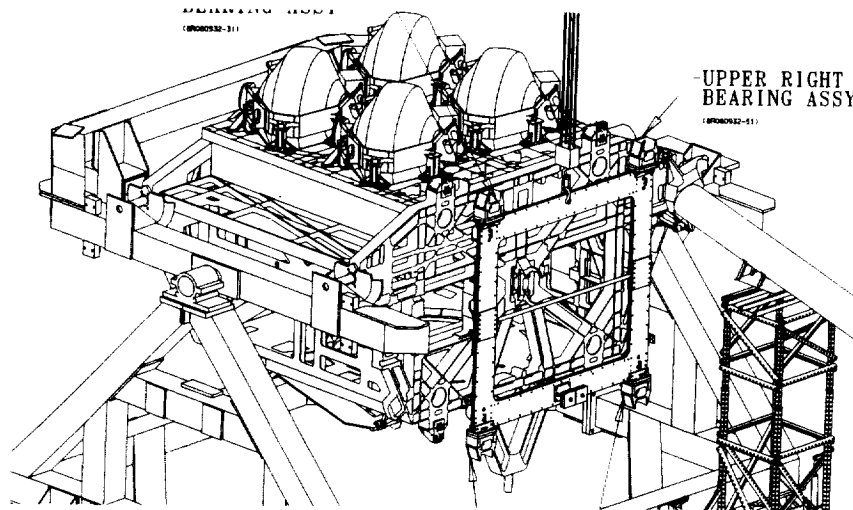


Figure 20. P6 MMS Checkout of Z1 Flight Article

522 137

A Four Panel, Rotating Solar Array Wing for the TIMED Spacecraft Mechanism Design, Development and Test Results

Steven R. Vernon* and David F. Persons*

Abstract

The TIMED (Thermosphere, Ionosphere, Mesosphere, Energetics and Dynamics) spacecraft is the first science mission sponsored by the NASA Office of Space Sciences in the Sun Earth Connections program and is being developed by the Johns Hopkins University Applied Physics Laboratory (JHU/APL). Requirements for the field-of-view (FOV) of the instruments, pointing accuracy, jitter requirements, the requirement for an anti-sun, cold side of the spacecraft, and sun angle variations during the year placed severe limitations on the design of the solar array. Presented is a timeline of system concept evolution to illustrate the many design iterations required as the design team reacted to changes in key spacecraft and program requirements. Also given are several of the mechanism trades off studies performed, along with a detailed description of the final design. The mechanical ground support equipment, analysis (dynamics and stress), mechanism materials and finishes, and flight qualification testing are covered in detail. Flight array deployment test results are presented and the "lessons learned" during the engineering model development and testing program are summarized.

Introduction

The Applied Physics Lab (APL) of the Johns Hopkins University has a long and successful history of spacecraft, sensor and mechanism design for a wide variety of space missions and sponsors. Since the early 1960's many government agencies such as the Navy, Air Force, BMDO and NASA have approached APL for consultation and solutions to problems of national interest.

The APL system design philosophy is probably best stated as one tailored to each individual mission. APL specializes in unique and "one of a kind" types of missions where a fast response is required. One constant throughout every mission APL has undertaken is to establish a close association between the lead engineers and the hardware they are responsible for producing. The lead engineers are empowered to make technical as well as schedule decisions in a close team environment where they are exposed to the requirements and challenges facing the program office and the other subsystem engineers. The lead engineer of a subsystem is expected to be involved in the project from "cradle to grave". Formal reviews are also held and are of a high quality, utilizing outside and internal reviewers. The APL panel members are often the most critical and difficult reviewers the technical lead engineers face.

For the TIMED mission, the two decisions that had the most impact upon the solar array design were made at the system engineering level. The first decision was to allow unlimited power system growth to occur in order to meet the science instrument requirements for continuous operation (24 hours per day, 7 days a week) from the start of in-orbit initial operations until the conclusion of the mission. The orbit and the precession rate chosen created a solar array and associated power system that on the surface appears far in excess of the typical spacecraft of this size and class. The second decision was to co-manifest TIMED with a second spacecraft to minimize launch costs. This decision created an immediate mass problem for the array that influenced the design throughout the development effort.

Program Requirements Evolution

For the TIMED solar array, evolving program and system requirements drove three major design iterations in 18 months between the CoDR (Conceptual Design Review) and the CDR (Critical Design

* The Johns Hopkins University Applied Physics Laboratory, Laurel, MD

Review). These iterations provide an interesting example of the effects of 'requirement creep' on mechanical design.

Nonetheless, several basic requirements and their effects remained relatively constant throughout the design process and are as follows:

- Spacecraft Orbit: 625 km circular, 74.1° inclination, 2°/day precession rate, 12000 eclipses. This environment set solar array temperature excursions to +/- 100° C.
- Spacecraft: 3 axis stabilized, nadir pointing.
- SABER Instrument Radiator FOV: Required a cold side of the spacecraft to constantly point anti-sunward and limited solar panel width to 122 cm to eliminate reflected sunlight onto the radiator.
- TIDI Instrument Telescope FOV: Additional requirements by the 4 telescopes that limited the Solar array width to 122 cm.
- Rotation Angle: Arrays must rotate 0-100°, single axis after deployment (0° position).

For the CoDR, held December 1994, a 300 W maximum orbit average power, 11.14 meters² array was chosen. Consisting of 2 wings, each wing consisted of two aluminum honeycomb panels angled with a 10° droop, using silicon BSFR cells with 0.15-mm CMX cover-glass. With an OSC Taurus launch vehicle baseline, the 950 kg allowable spacecraft launch mass provided plenty of available mass for the array. To reduce program costs after this review, spacecraft design efforts were reduced to a low level to allow time for the science instrument designs to 'catch up' and firm up their requirements through continued design efforts.

During this down time, an experienced array design team was chosen, consisting of the TIMED lead spacecraft mechanical engineer, a structures and kinematics analyst, the TIMED lead spacecraft thermal engineer, a senior designer, and a junior designer. Up through delivery of the flight wings to the spacecraft, none of these team members worked full time on the solar array due to budget and manpower constraints. The analyst (at 75%) and the junior designer (100% from EDR to CDR) spent the most time.

By the spacecraft preliminary design review (PDR), held February 1997, significant changes were made as requirements firmed up and new issues surfaced. As of January 1997, TIMED was co-manifested with the JASON spacecraft on a Delta 7920-10 launch vehicle to minimize launch costs. As a result, the maximum TIMED spacecraft launch mass was reduced to 660 kg. Mass immediately became a significant issue for the solar array design. Exacerbating the mass issue was the growth in the required maximum orbit average power from 300 W to 410 W. Packaging constraints increased the number of panels per wing from two to four, increasing the parasitic hinge, damper and release masses proportionally. In response to these significant changes, the 12.8 m² baseline array at spacecraft PDR consisted of two rotating wings, each with four GrCE (graphite/cyanate ester) face sheets and aluminum honeycomb sandwich panels, GaAs cells, each wing with a 30° droop.

Table 1: Evolving Power System Requirements Summary

Program Milestone	Power (BOL)	Cell Type	Allowable Mass, Total Kg.	Cell Area (meters ²)	Droop Angle
CoDR	1200 Watts	Silicon	90+ Kg.	11.1	10°
PDR	2240 Watts	GaAs	110 Kg. Max	12.8	30°
S/A EDR	2412 Watts	GaAs	110 Kg. Max	11.1	20°
CDR	2412 Watts	GaAs	110 Kg. Max	11.1	20°
Flight Hardware	2453 Watts	GaAs	80.9 Kg.	11.1	20°

Deployment System and Individual Mechanism Trade Studies Performed

After spending approximately 30 days searching available sources in the literature, it became apparent that there were six competing deployment system designs that might satisfy our requirements. These systems are briefly summarized below with their associated advantages and disadvantages:

1. Free deployment system, no rate dampers.
 - a. Advantages: Lowest cost and mass, simple to design and fabricate.
 - b. Disadvantages: Control challenge, high velocity deployment, motion path control not within acceptable limits, no heritage or information available with other missions or organizations, very large lockup loads.
2. Single motor driven system with synchronized panel-to-panel deployment.
 - a. Advantages: Robust, large motor torque margins available, momentum control using motor, predictable motion path, array retraction in flight possible (not a requirement), similar flight systems in use.
 - b. Disadvantages: Highest mass and cost, multiple parts and failure points, long lead time for engineering model motor, motor drive and control electronics are high \$ and mass cost for a "one time" event.
3. Spring driven system with synchronized panel to panel deployment using eddy current dampers for momentum dampening.
 - a. Advantages: Lower cost, similar mass to "2" above, single damper at the yoke controls system momentum, eddy current damper requires no power.
 - b. Disadvantages: Mechanically complex, many single point failure points, no recent flight history found on available eddy current dampers, high mass and size for damper, system mass very high, small adjustment range of damper.
4. Free deployment system with "saloon door" hinges and over travel dampers.
 - a. Advantages: low cost and mass, long APL history with this style of hinge, minimal complexity, and minimal power to operate.
 - b. Disadvantages: Control challenge, high panel deployment velocity, challenging to lock panels in place, totally unpredictable motion path control.
5. Free deployment with viscous damper velocity control (PDR Baseline).
 - a. Advantages: communication satellite heritage, acceptable mass and cost, good momentum control, acceptable motion path variability, dampers have wide range of adjustment.
 - b. Disadvantages: Temperature control of dampers required, additional damper test, qualification and characterization program required.
6. "Off the shelf" purchase from an outside vendor.
 - a. Advantages: Shift substantial risk and headaches to the vendor.
 - b. Disadvantages: No "off the shelf" design realistically available, modification to existing designs required, substantial investment of time to monitor contract and technical issues with travel involved of key personnel at often inopportune times (personnel availability).

We evaluated each option in detail and chose option "5", the free deployment system using viscous dampers at each hingeline. The relatively simple design coupled with acceptable mass and cost weighed heavily.

The team recognized early on that with the manpower and schedule constraints present, make or buy decisions for individual mechanisms leaned heavily toward the buy side. As a result, the decision was made to investigate and buy commercially-available damper and release mechanisms and adapt heritage hinge, ball & socket, and bearing designs to the purchased items. Briefly summarized here are the results of the trade studies:

1. Choice of eddy current vs **viscous fluid damper**.
 - a. Viscous dampers have flight heritage at APL and GSFC.
 - b. Large range of adjustment available for viscous damper.
 - c. Air bubble concerns with viscous damper.
 - d. Concern with high-speed gearing in eddy current damper.

The DEB Manufacturing Model 1025 viscous rotary damper was chosen with several modifications suggested by DEB and GSFC in fill and testing procedures to minimize concern over the development of an air bubble in the fluid during vacuum operation.

2. Choice of release mechanism.

- a. Pin puller: Extensive heritage at APL, high shock, hard to adapt to this configuration, relatively high mass.
- b. **Release nut:** Low mass, low shock, easily adaptable to separation bolt configuration.
- c. Thermal knife: High power in comparison with other options, concern about simultaneous deployment of each pair.
- d. Cable cutter: Extensive heritage at APL, high shock, cable would replace separation bolt, would need load cell in place of strain gage in the bolt.

The Hi-Shear 9321 low shock series separation nut was chosen combined with a strain-gaged BeCu bolt as the release system for each wing.

Design Timeline and Concept Evolution

The major features of the array deployment system gradually matured as the program progressed. Summarized below is the design as it stood at selected program milestones. Since much of the spacecraft design had been completed, more time could be spent on the array design, enabling a good deal of progress to be made in one year.

Solar Array Baseline Design at Spacecraft PDR, February 19, 1997

- Four (123 cm x 132 cm x 1.59 cm thick) panels per wing.
- Aluminum core panels with GrCE face sheets to eliminate 'thermal twang' of the panels during transitions in and out of eclipse.
- Two torsion spring hinges with viscous dampers per inter-panel hinge line.
- Torsion spring actuated yoke also with viscous damper.
- 4 ball & socket supports per wing to take shear during launch.
- 2 pyro pin pullers with long bolts with load washers that control panel preload and release each wing.
- Pin pullers located on spacecraft side to minimize pyro shock to solar cells.
- Heated dampers (8 W max) to control damper temperature.
- Panels lock at the end of deployment.
- Cells on outside panel face outward during launch.
- Solar array deployment actuator (SADA): Schaeffer Magnetics Type 3 actuator motor.

Due to manpower constraints, the solar array baseline design was very immature at the spacecraft PDR. After PDR, the updated four panel/wing Pro-Engineer layout was completed, allowing the NASTRAN structural analysis of the wing in both the stowed and deployed conditions to proceed. By the end of March, 1997, completion of the initial kinematic deployment analysis using 2D Working Model v4.0 provided the flight baseline spring and damping coefficients, uncovered lock-up loads, facilitated damper procurement, and permitted the flight hinge design to start. As the flight mechanism designs matured, a separate solar array engineering design review (EDR) was held in July 1997 to review the progress made to that date. GSFC mechanism experts served on the review board and suggested changes that significantly improved the JHU/APL wing design. First-cut deployment test plans and very preliminary ground support equipment designs to support the wing deployment testing also were reviewed. Solar array design changes from the spacecraft PDR are summarized below:

Solar Array Design at Sub-System EDR, July 1997

- On-orbit SADA rotation set at 0°-100°.
- 20° droop angle chosen to minimize solar pressure torques (for PDR it was 30°).
- Low-shock separation nuts substituted for heritage pin pullers, nuts mounted on backside of outermost wing panel for accessibility.

- Instrumented (strain-gauged) release bolt chosen over load cell design to save mass.
- Constant force leaf spring replaced torsion spring at yoke hinge to solve packaging problems and save mass.
- Cells moved to opposite sides of panels to reduce the angle of rotation into the sun required during initial deployment and to protect cells from damage during integration.
- 4 Support points (2 release, 2 ball & socket) substituted for 6 points (at PDR) based on NASTRAN stowed frequency analysis.

Solar Array Design at Spacecraft CDR, December, 1997

The solar array design was essentially complete at the spacecraft critical design review (CDR), held in December 1997. Solar array design changes from the solar array EDR are summarized below:

- Four (199.6 cm x 125.2 cm x 1.3 cm thick) panels per wing (11.1 m² total array area).
- Aluminum face sheets replaced GrCE facings. Thermal twang of aluminum faces was evaluated and deemed acceptable under the TIMED jitter requirements. Use of aluminum faces allowed use of magnesium inserts, representing a large mass savings over the titanium inserts required for coefficient of thermal expansion (CTE) compatibility with GrCE facings.
- Two self-aligning spherical bearings at each inter-panel hinge line replaced the two Envex bushings.
- One spring/damper assembly per inter-panel hinge line instead of two to save mass.
- Hi-Shear 9321 low-shock separation nut chosen.
- Retraction spring on release bolt added to increase clearance between bolt and panel based on detailed kinematic analysis.
- Four point wing interface to the spacecraft modified to two flats at the release bolts, one ball and socket, and 1 'V' groove to accommodate the difference in temperatures between the spacecraft body and the wing assembly after the approximately two hour time span between launch and wing deployment.
- Modified damper cover from aluminum to magnesium to save weight.

Concern was expressed at the CDR concerning the number of eclipse cycles, the large size of the cells, and the CTE mismatch between GaAs cells and aluminum face sheets. In addition, in-depth conversation with the launch vehicle manufacturer indicated that 53 kg additional spacecraft launch mass was available by making various minor changes to the launch profile. It was decided to initiate another structural iteration on the substrates, using GrCE cloth face sheets with downsized titanium inserts. This was accomplished with drawing release in February 1998.

Summary of Solar Array System Milestone Dates:

- Conceptual Design Review (CoDR): December, 1994; Spacecraft design activities halted.
- Preliminary Design Review (PDR): February 19, 1997.
- Solar Array Engineering Design Review (EDR): July 19, 1997.
- Critical Design Review (CDR): December 3, 1997.
- Substrate Contract Fabrication Start/Finish: 2/98 to 7/30/98
- Cell Vendor Lay down Contract Start/Finish: 8/98 to 9/20/99
- APL Mechanical Assembly Start: 9/30/99.
- SC Environmental Test Start: 10/18/99.

Flight Design Configuration

Figure 1 illustrates the TIMED spacecraft in the orbital configuration. Figure 2 shows a solar array wing in the launch configuration.

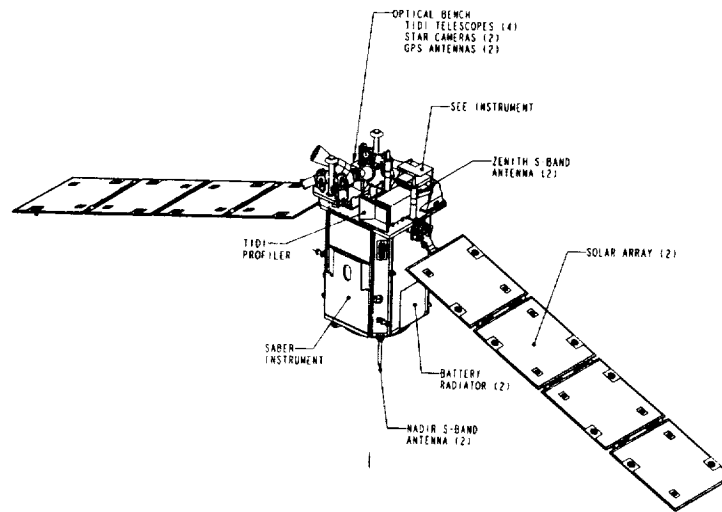


Figure 1

Panels /Substrates

Each 1.31-cm thick panel consists of Nippon SF-50A-75/Bryte EX1515 GrCE spread fabric face sheets on 1.3-cm thick, 3/16-5056-.001P aluminum honeycomb core. \Face sheets consist of three plies angled as (0,45,0) and are bonded to the aluminum core using Bryte EX1516 film adhesive. A 0.0076-cm thick Kapton Type VN film is co-cured with the top side face sheet to serve as an electrical insulator for the solar cells. Inserts for highly stressed areas are 6Al-4V machined titanium. Lightly loaded fasteners use AEP and Rosan floating nut inserts potted with Fiber Resin SLE-3009 adhesive.

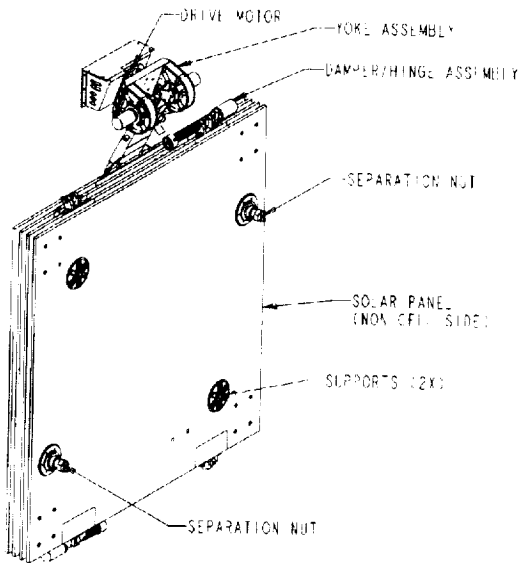


Figure 2

Yoke

Figure 3 shows the yoke, which provides the interface between the SADA and the panel assembly. Machined almost entirely of ZK60A-T5 magnesium, each yoke has a mass of 4.0 kg in full flight configuration

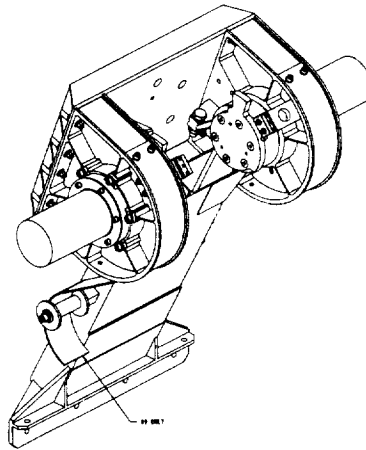


Figure 3

Energy for the 70° deployment of the yoke attach arm is provided by a 2-ply beryllium copper (BeCu) constant-force leaf spring that provides drive torque that is >5.0 times the measured friction torque. The arm rotates by virtue of four Kaydon preloaded angular contact bearings lubricated with Braycote 601 grease. Two DEB viscous rotary dampers provide velocity control for the yoke deployment arm. Two adjustable stops precisely locate the array at the end-of-travel (EOT), with a limit switch to sense proper deployment. Having no latch at the yoke enables each wing to fold during re-entry, providing the proper burnup/debris scenario.

SADA

The SADA provides the 110° of rotation required by the wing during orbital operations. It is a standard MOOG/Schaeffer Type III harmonic drive actuator. A rotary potentiometer provides 180° of position data. A typical rotation angular velocity for this actuator will be ~1°/sec. A Type III actuator provides the desired shaft/bearing stiffness for the deployed array wing. The torque margin on the motor is calculated to be much greater than 5.0.

Hinges

Panel hinge lines consist of two stainless steel, self-aligning spherical bearings, one of which is joined to a single spring/damper assembly. Each bearing is lubricated with Braycote 601 grease. The hinge, shafts and bearing housings are made of ZK60A-T5 magnesium hard coated with a proprietary 'Mag-oxide' coating provided by Luke Engineering. The single DEB viscous damper is mounted to the main shaft through a flexible coupling and provides velocity control over the entire 180° of travel. At each spherical bearing housing, a small leaf spring rides up and over a wedge and provides a solid lockup of each panel hinge line at the EOT. Each hinge line of a wing has a custom Elgiloy helical torsion spring whose variable preload is set based on the results of kinematic analysis and ground test. The spring provides drive torque that is >5.0 times the measured friction torque.

Viscous Dampers

The DEB Manufacturing Model 1025 viscous rotary damper was chosen to provide deployment rate control for each wing. Building on Goddard Spaceflight Center (GSFC) experience with this damper, extensive testing was performed to characterize typical damper performance under various temperature and load conditions. The damper uses a rotating vane to force CV-7300 silicone fluid of chosen viscosity through an adjustable orifice, providing up to 1411 N-cm of torque in a package weighing ~0.5 kg.

For this model damper, the damping coefficient was found to vary nonlinearly with needle valve setting, temperature, direction of rotation, and surprisingly, with applied torque. The latter characteristic influences the testing sequence for setting up and testing the flight wings. To accurately predict the behavior of a particular damper under temperature and various needle valve settings, the net torque that each damper sees must be accurately measured. Therefore, the spring torque and drag torques from pin friction,

harness, and air tubing must be measured for each hinge line before individual flight damper characterization can be performed.

Release & Spacecraft Interface

A wing assembly (minus the yoke) attaches to the spacecraft at 4 points. To allow for the difference in thermal expansion coefficient between the aluminum spacecraft and the GrCE array, two support points, shown in Figure 4, use a ball & socket and a 'V' groove in a flexure mounting system to react shear but allow expansion along the axis of the 'V' groove. The two release points of the mounting system interface between panels through flats that take no shear. As illustrated in Figure 5, a hole through each panel series separation nuts attached to the outboard panel. The bolt is strain-gaged to permit an accurate measurement of the bolt preload, and it spring loaded to partially retract after release. A small gap to the spacecraft is provided at each release bolt interface to obtain a 'pop' release using stowed strain energy from bending of the panel assembly.

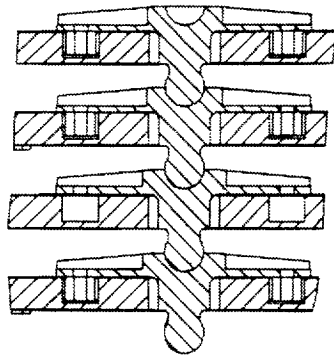


Figure 4

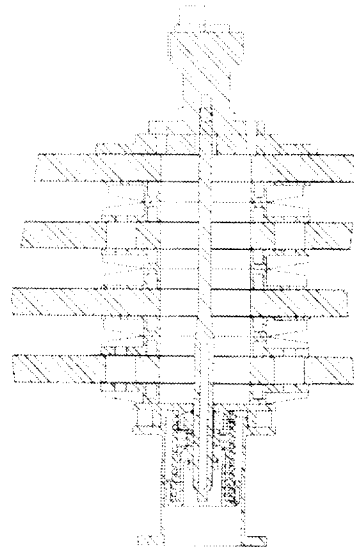


Figure 5

Mechanical Ground Support Equipment

The APL mechanical systems group has a very strong philosophy dating to the 1960's era that "you fly what you test". The design team was certain from the beginning that due to the size of this array and the limited integration time available, that we would not be able to deploy and test the array on the spacecraft. To reduce risk, the team insisted early on that a high fidelity, full-scale engineering model be fabricated and tested prior to spacecraft level CDR. However, to perform the engineering model and flight testing, unique deployment/G-negation ground support equipment (GSE) would have to be designed. It was obvious that the available manpower would not allow us to develop the GSE from scratch and maintain the tight GSE development schedule. Our NASA sponsor, Goddard Spaceflight Center (GSFC), offered design drawings of their air bearing deployment system used on the TRIMM and XTE missions. After a quick review of the drawings, some additional design changes were made and we set out to fabricate the system. In addition, GSFC was very familiar with the DEB Manufacturing damper design chosen for TIMED and graciously offered their damper characterization thermal chamber for our use. The help provided by GSFC jump started our GSE design effort and was instrumental in maintaining schedule.

Deployment Table System

The deployment table system shown in Figure 6 consists of a series of aluminum honeycomb panels mounted on an aluminum support frame. These tables were joined together to form a smooth air bearing

compatible surface flat to within 0.38 mm overall. These tables were approximately 1.2 m x 2.4 m (L x W) x 0.6 m in height.

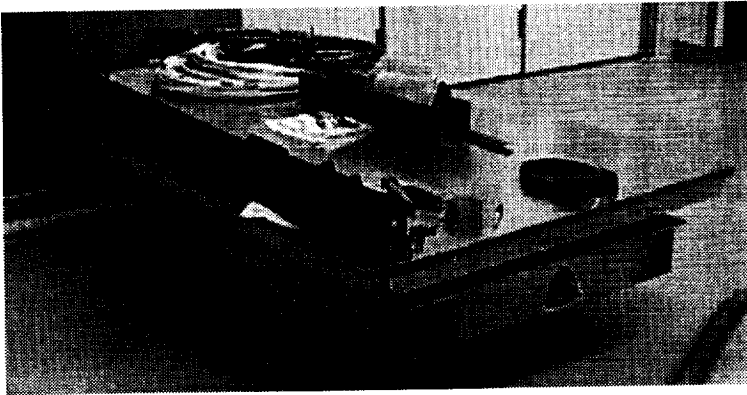


Figure 6

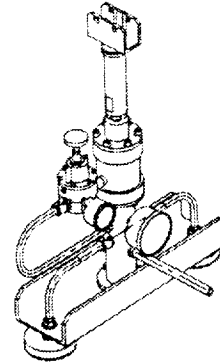


Figure 7

The frame consisted of welded tubular aluminum 6061 alloy rectangular sections 10 x 15 cm with a 0.64 cm wall. The welded frame was supported off the clean room floor with a four-point machine-tool type of leveling foot. The aluminum honeycomb panel (deployment surface) interfaced to the frame via 10 adjustment screws. The concept was that by employing the adjustment screws, local leveling of the honeycomb surface could be achieved regardless of the honeycomb panel flatness. This unique feature proved quite valuable later on when we received "less than optimum" honeycomb panels. The schedule identified the need to quickly manufacture the table system. A panel vendor was located via the Thomas Register who could deliver within a week. The vendor specialized in flooring systems for Navy ships and was not connected with the aerospace industry. The panels procured were 2.5-cm thick with 0.38-mm thick face sheets and cost \$340 each. The entire table design and drafting process took one man week with procurement of all components about three weeks.

Finding the proper support points for the air bearing system was probably the most challenging aspect of the deployment GSE setup. Stability during deployment had to be traded with the crowding of the supports when stowed. Three different air bearing designs were fabricated, mono-pods (1 air puck), bi-pods and tri-pods, in sufficient quantities to support multiple combinations. The final combination and location of the supports was determined empirically on the full-scale engineering model and carried over onto the flight array. Figure 7 presents the bi-pod version of the air bearing, and Figures 13 and 14 show the air bearing arrangement chosen along the length of the array.

Structural Dynamics, Stress and Kinematic Analysis

Kinematic analysis was performed using the 2D version 4.01 of Working Model software by Knowledge Revolution, Inc. Choice of damper capacity, spring size and preload depended squarely on the results of the design analysis performed using Working Model.

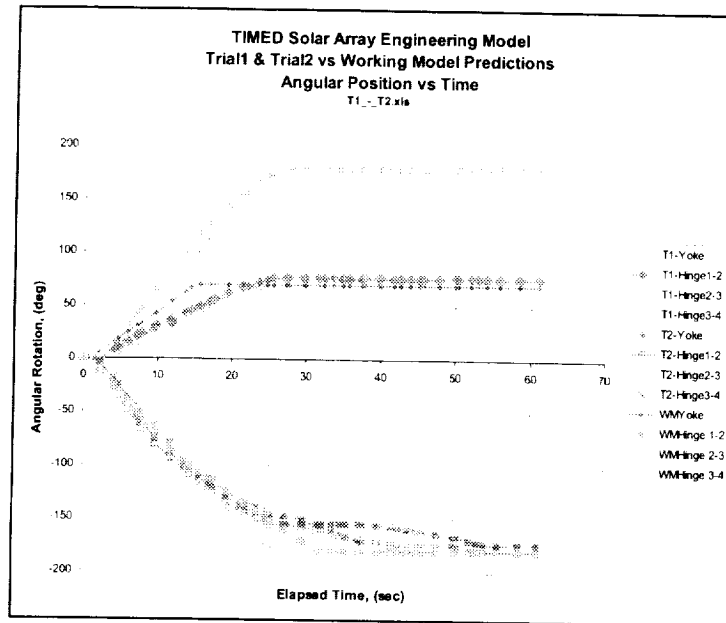


Figure 8

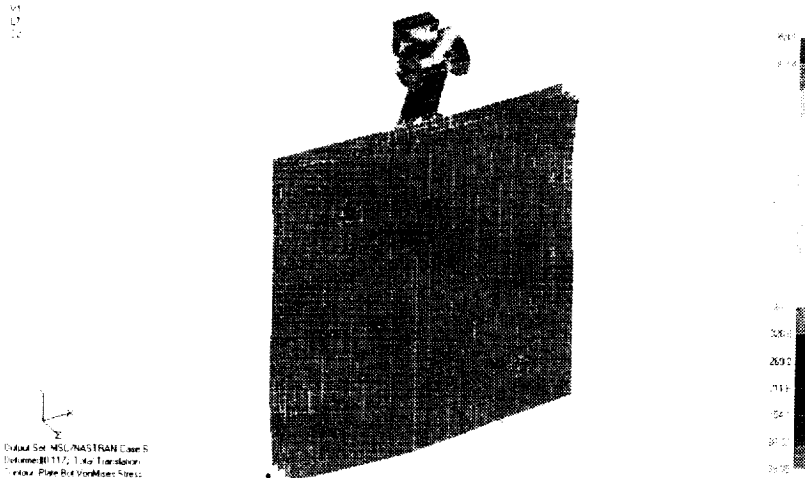


Figure 9

Lockup loads were derived from the velocities uncovered from the deployment analysis. The engineering model deployment test results were used to verify the rigid body kinematic model. Figure 8 gives the deployment angle vs. time curves generated for each joint for both the engineering model test and analysis model. Agreement is quite good given the accuracy that joint friction was known during ground-based deployment. The curves with * and square icons also illustrate the ability of the analysis to diagnose GSE problems, in this case an uneven floor section that slowed the deployment of hinges 1-2 and 3-4. The diamond icon curves show a slower deployment during test than predicted by analysis for the yoke dampers. Further investigation uncovered that the yoke dampers, which were loaded with a more viscous silicone fluid than the panel dampers, required a more sensitive adjustment procedure than

a hand adjustment could accomplish. For flight, the yoke damper viscous damping coefficient was adjusted using the GSFC thermal chamber for confirmation.

Structural and dynamic analysis was performed using MSC NASTRAN finite element software for both the stowed and deployed configurations. Quasi-static load cases were run consisting of ± 15 G's in thrust (X), ± 15 G's normal to the panels (Z), and ± 7.5 G's in (Y), along with a case that enforced a 2.1-mm preload (gap) at the release bolts. Strength margins of safety were all positive for the five stowed load cases run. Figure 9 shows a typical stress distribution pattern of the stowed array under quasi-static loading.

As shown in Figure 10, the wing deployed first bending natural frequency is 0.26 Hz. When stowed, the wing first natural frequency is 39 Hz. Fixed base sine testing of each array stack returned a fundamental frequency of 37.9 Hz, verifying the dynamic FE analysis.

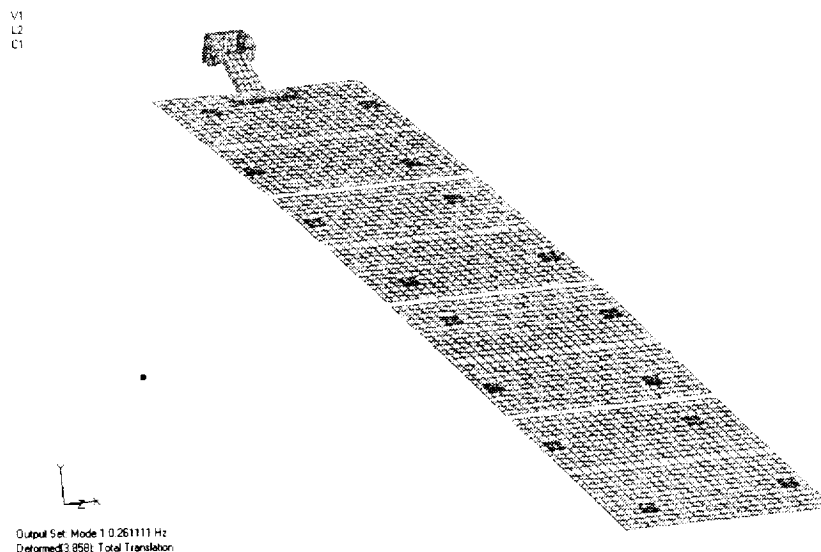


Figure 10

Engineering Model Test Program

The engineering model test program was the most significant effort undertaken in the development of the array system. The plan going in was to complete all full scale engineering model testing prior to spacecraft CDR. The engineering model was designed to be full scale and of a high fidelity with the following requirements imposed:

- A. Panels/substrates: Physical size and mass identical to flight. Inserts included for hinges and release mechanisms
- B. Wiring Harness: All wiring service loops were to be flight like in size and composition.
- C. Hinges and Release Mechanisms: Flight-like as well.
- D. Viscous Dampers: Flight design without full qualification testing.

The single DEB Manufacturing, Inc. Model 1025 viscous damper is flex mounted to the shaft between panels and provides velocity control over the entire 180° of travel. Extensive testing was performed to characterize typical damper performance under various temperature and load conditions. The tests used a custom-built thermal chamber borrowed from GSFC.

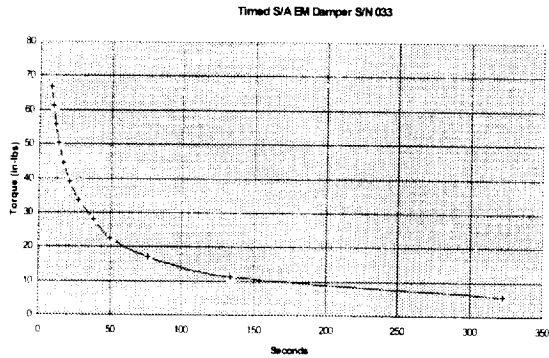


Figure 11

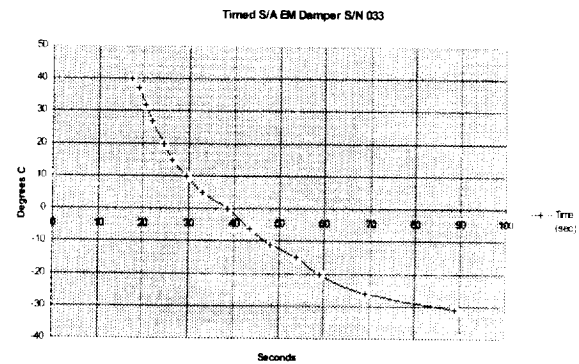


Figure 12

The damper uses a rotating vane to force CV-7300 silicone fluid of chosen viscosity through an adjustable orifice, providing a very wide range of adjustment up to 1400 N-cm of torque in a package weighing ~0.5 kg. For this model damper, the damping coefficient was found to vary nonlinearly with needle valve setting, temperature, direction of rotation, and with applied torque. Typical performance curves for an engineering model inter-panel hinge damper are presented in Figures 11 and 12.

The engineering model yoke and hinge hardware was fabricated to flight quality drawings (level 2) but fabrication and process requirements were held to a minimal level 1. The lead engineer was responsible for tracking changes made from the drawings to the as built hardware and ensuring these changes were incorporated into the flight design. Waiving inspection requirements, material certification processes and allowing minor blemishes and insignificant defects to pass speeded up fabrication efforts. Material finishes were allowed to deviate from flight where function was not affected. The identical assembly tooling, handling processes and deployment system used for the engineering model was also to be used for flight.

Assembly of the deployment table surface proved quite difficult and time consuming. The tables were bolted together loosely and a grid pattern was established. Gross leveling was progressively accomplished starting with a carpenter's level and progressing to a machine tool level. A theodolite and height gauge was then employed to finish the leveling process. After the tables were completely leveled, the bolts were tightened that fastened them together and the seams were taped with Kapton tape to ensure the air bearings would travel over the joints. The initial deployment test revealed that the air bearings would occasionally hang up on the joints. Further inspection discovered that the joints did not quite match up in height even though adjacent areas were leveled within tolerance. The adjustment system on the tables did not have enough adjustment points to correct this problem. A second floor surface, commercial floor tiling, was applied without success. We then decided to apply 0.64-cm thick aluminum sheeting in a pattern that ensured the seams did not match up with the existing seams. We then set up a finer grid and shimmed the sheets where needed and repeated the leveling process. This method was successful and provided repeatable deployments.

The engineering model array deployment testing started by trying many combinations of air bearing design and location. Use of three of the di-pod bearings, in the locations shown in Figures 13 and 14, was judged to be optimal. An upgrade to the compressed air system in the building was required when the airflow through the air bearing pucks proved to be less than anticipated. Stable and repeatable deployments were finally achieved with a nice "W" pattern deployment with all hinge points locking up within 1-2 seconds of each other. Actual spring tension and damping rates on the dampers were measured and the results worked back into the kinematic software model. Data from non-flight optical encoders at each hingeline were acquired through a Labview-based data acquisition system. The deployment angle-vs-time results were used to correlate the software model. At this point, we had achieved our objectives and felt we truly understood our system and were ready for the spacecraft CDR and subsequent fabrication and testing of flight hardware.

Flight Array Test Program

To accurately predict the behavior of a particular damper under temperature and various needle valve settings, the net torque that each damper sees must be accurately measured. Therefore, the spring torque and drag torques from pin friction, harness, and ground support air tubing must be measured for each flight hinge line before individual flight damper characterization can be performed. Since the dampers' damping coefficient varies greatly with temperature, for flight, redundant heaters are mounted on each damper to control the housing temperature within the range of +15°C to +20°C.

Due to a very late delivery of the fully populated flight substrates from the vendor, we were limited to only two weeks to assemble, deployment test, vibrate, deployment test again and integrate each wing into the spacecraft for spacecraft-level environmental testing! The lessons learned on the engineering model proved invaluable and more than paid for the investment during this difficult period. The fabrication tooling, data acquisition system and the deployment system performed flawlessly. Sine vibration testing of each wing went smoothly with no gapping observed at the release bolts, verifying the preload in the strain bolt was correct. Post-vibration deployment testing, shown in Figures 13 and 14, noted no changes in the damper settings or in deployment behavior. The yoke was integrated first to allow for a full 180° of rotation of the SADA, verifying proper harness loop routing and tiedown. Integration of each wing with the spacecraft went well without any modification of interface components required. The following test matrix details the entire test program implemented for the engineering model and flight solar array hardware.

Table 2

TIMED Spacecraft													
TIMED Solar Array Testing Plan Chart													
Assembly/Component	Engineering Model						Flight Hardware						
	TV Cold	TV Hot	Vib.	Torque Measure	Release Test	Deployment Dynamics	TV Cold	TV Hot	Vib.	Torque Measure	Deployment Dynamics	Release Test	
Hinge Assy/damper, spring	Performed	Performed		Performed		Performed				5/17/99	10/13/99		
Damper(component)	7/27/97	7/27/97	3/18/98	Performed		Performed	10/21/98	12/21/98		5/17/99	10/13/99		
Spring (component)				Performed		Performed				5/17/99	10/13/99		
Release Mechanism Assy						Performed	7/23/97	7/23/97	7/20/99				
Separation Nut							7/23/97	7/23/97			10/13/99	10/31/99	
Ball & Socket							7/23/97	7/23/97			10/13/99	10/31/99	
Support Flats							7/23/97	7/23/97			10/13/99	10/31/99	
Retraction Mechanism Assy											10/13/99	10/31/99	
Yoke Assembly	Performed	Performed		4/15/98	11/24/98 Hot and Cold	5/22/98	5/3/99	5/3/99		4/28/99	10/13/99	10/31/99	
Bearings				4/25/98			5/3/99	5/3/99		4/28/99	10/13/99	10/31/99	
Negator Spring				4/25/98			5/3/99	5/3/99		4/28/99	10/13/99	10/31/99	
Harness				4/25/98			5/3/99	5/3/99			10/13/99	10/31/99	
Service Loop				X (hot&cold)		5/22/98			10/13/99	5/3/99	10/13/99	10/31/99	
Inter-Panel Harness				X (hot&cold)		5/22/98			10/13/99	5/3/99	10/13/99	10/31/99	
Complete Array Wing						5/22/98			10/7/99		10/13/99	10/31/99	

Once the arrays were integrated, the spacecraft underwent sine vibration testing at JHU/APL, and acoustics, mass properties, and self-induced shock testing at GSFC. As part of the shock test, each wing's separation nut pyrotechnics were fired, and each tethered wing was allowed to swing a few degrees from the spacecraft. This 'pop & catch' test demonstrates that sufficient clearances exist between the array and last minute additions during the integration process such as thermal blankets and harness.

Conclusions and Lessons Learned

- As we have learned on other JHU/APL mechanism designs as well, an engineering model is an incredible resource, provided it simulates all important aspects of the flight design such as function, behavior, lubrication and surface finish, GSE handling fixtures, tooling, etc. *We were able to develop the actual flight assembly and handling processes and procedures on the engineering model, allowing the flight arrays to be assembled, deployment tested, environmentally tested, and delivered to the spacecraft in two weeks!*



Figure 13



Figure 14

2. Encourage outside reviewers. Fresh eyes provided valuable design suggestions during the array EDR. The GSFC reviewers remained helpful contacts, sharing experiences on similar designs and providing insight into design intent (not always reflected) on the air bearing GSE drawings that were provided by GSFC.
3. Be willing to toss out a really "bad" idea even late in the game where risk to the flight hardware is possible. Unfortunately the one assembly we could not test out was the wing integration fixture. It was an offset CG-compensating fixture used solely for flight integration on the spacecraft, and thus could not be accurately tested using the engineering model array. When we tried to use it for flight integration, the fixture was too massive to safely handle the much lighter weight flight wing. We then substituted 4 men for one fixture, greatly reducing the risk.
4. Establish good personal relationships with peers in other organizations. We developed good relationships with suppliers and GSFC employees thus allowing us to "cut through the red tape" when quick responses were needed to problems.
5. Design and implementation of deployment GSE can be as much of an effort as the flight array design. As such, cost, schedule and manpower resources must be allocated in sufficient quantities or the test program can be jeopardized.

Validation of TSX-5 Solar Array Deployment by Correlated Simulation and Test

Brian W. Gore*

Abstract

An innovative spacecraft hinge mechanism has been analyzed and flight qualified by a unique method that joins various DADS simulations and complementary lab testing, since The TSX-5 solar array subsystem is incapable of being deployed in the Earth's gravitational field. Results from sub-scale testing and corresponding validated models exposed detrimental deployment effects in a full-scale simulation that would not have otherwise been detected using standard aerospace qualification techniques. Those deficiencies were fixed, and the spacecraft solar arrays recently deployed successfully on-orbit. The methodology used and the subsequent results are presented and explained in detail.

Introduction

The **T**ri-**S**ervice **E**xperiment-5 (TSX-5) spacecraft is a U.S. Air Force program that provides a platform for two technology experiments to be launched on a lower cost, higher risk, and faster schedule basis. The only deployable on board is a non-articulated solar array, consisting of two wings, each containing six solar panels (see Figure 1).

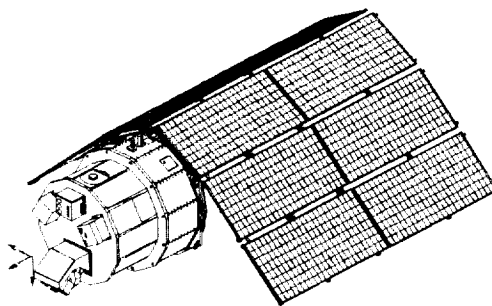


Figure 1. TSX-5 Spacecraft (Courtesy of Orbital Corp.)

Since complete mission failure may result if the array fails to deploy, it is of paramount importance that the system deploys successfully. In order to ensure that success, the standard procedure is to subject such a moving mechanical assembly to rigorous testing in a laboratory environment so that its kinematic and dynamic behavior are well-understood and comply with all requirements. However, the innovative solar array hinge design used by Orbital Corporation on TSX-5 can not support the gravitational weight of the solar array. This design is satisfactory when there is no gravity, but it poses a particularly complex problem for engineers who wish to test its behavior on the ground.

Moreover, this problem can be readily solved in most spacecraft deployment systems since they usually consist of a single, or even two parallel, hinge lines. In such cases, various methods of gravity off-loading are generally employed. In this unique case, each of the wings (which deploy individually) possesses multiple and moving hinge lines about which deployment occurs simultaneously, thus ruling out standard off-loading fixtures.

As such, engineers were faced with three possibilities:

- 1) deploy the system in a simulated zero-gravity field -- the KC-135 aircraft can provide this during parabolic flight paths

* The Aerospace Corporation, El Segundo, CA

- 2) employ a gravity off-loading fixture using balloons, cables, etc.
- 3) use a combination of analytical and sub-scale testing techniques to evaluate the validity of the deployment system

The first choice was completely cost-prohibitive given the low budget of the program. The second choice was attempted but with questionable results since the balloons had a significant aiding or hindering effect on individual panels. Hence, the latter was chosen as the course of action. This paper shall discuss the testing and analytical procedure as well as the lessons learned throughout the evolution of this evaluation process.

Three organizations took part in this testing: Orbital Corporation (TSX-5 prime contractor), Planetary Systems Corporation (TSX-5 solar array expert), and The Aerospace Corporation (customer technical representative).

Background

In order to understand the issues involved with this deployment system, it is first necessary to understand the design of the hinge, since it serves as the structural link between panels, as well as the motive force to deploy them. Figure 2 depicts the hinge of interest, which was invented by Walter Holemans and patented by Orbital Corporation (Patent # US05715573).

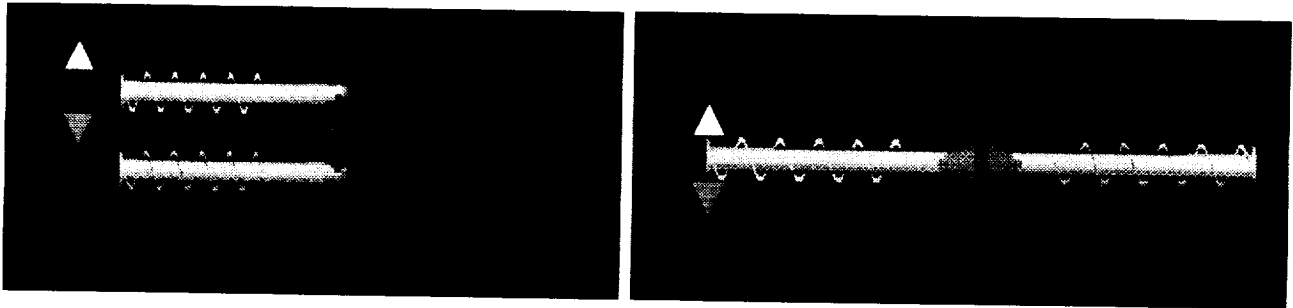


Figure 2. Hinge, Stowed & Deployed

One can see that the link (the diamond-shaped piece between the plungers) has a plunger attached on each side via a revolute joint. On the other end of each plunger, which resides within the interior volume of its respective panel, is a seat against which the deployment springs actuate. When the compressed spring releases its energy, the plunger is pulled into the panel, and the link rotates and slides along the panel edge and up into its seated position, also inside each panel. One of the most important features to note about this hinge is that it has virtually no capability to support shear loading when not latched, thus gravity offloading becomes a major necessity.

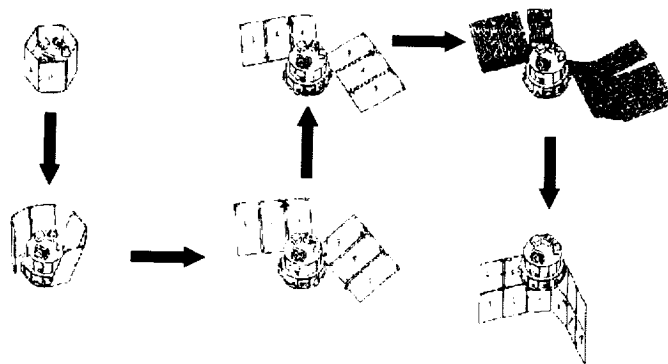


Figure 3. Solar Array Deployment Sequence (Courtesy of Orbital Corp.)

On a larger level, Figure 3 shows how the hinges act to move the solar arrays from their stowed configuration to their deployed configuration.

Two additional points should be identified at this time: 1) during deployment, the hinges allow a certain amount of over-travel of the panels before settling in the deployed configuration, and 2) the deployed configuration of the two wings is not planar (see Figure 1). At the outset of the program, it was argued that a wing deployment staggering mechanism should be employed so that the two wings would not hit each other. In addition, it was suggested that energy dissipating soft stops be added to prevent damage should either wing hit any part of the spacecraft bottom core plate. Once the technical experts embraced these ideas, several major questions remained:

1. How long should the deployment staggering device wait to release the second wing?
2. Does 2nd wing deployment cause a "tail-wagging-the-dog" disturbance sufficient to unseat the 1st deployed wing?
3. Does over-travel of either wing induce excessive bending stress in the panels or spacecraft core plate?
4. Will any other panel over-travel (within a particular wing) cause detrimental contact of the deploying solar array?
5. Do core plate soft stops necessarily prevent detrimental over-travel of the deploying solar wing?

Note that there are a total of 12 panels and hinge lines, very few of which are parallel during deployment. As such, it is nearly impossible to effectively offload the effects of gravity during a wing deployment test. This same subject was mentioned in Reference 1 (but with highly questionable ground test results), and this effort strove to find a solution. It was clear that a validated model would be necessary to satisfactorily address all of these issues, thus **the sole remaining option to qualify this deployment scheme design was a correlated analysis and test.**

Modeling and Testing

Figure 4 illustrates the overall procedural flow that will be discussed in this section; note the three different box styles for each step of testing, output, and modeling, and the fact that this is a highly integrated methodology.

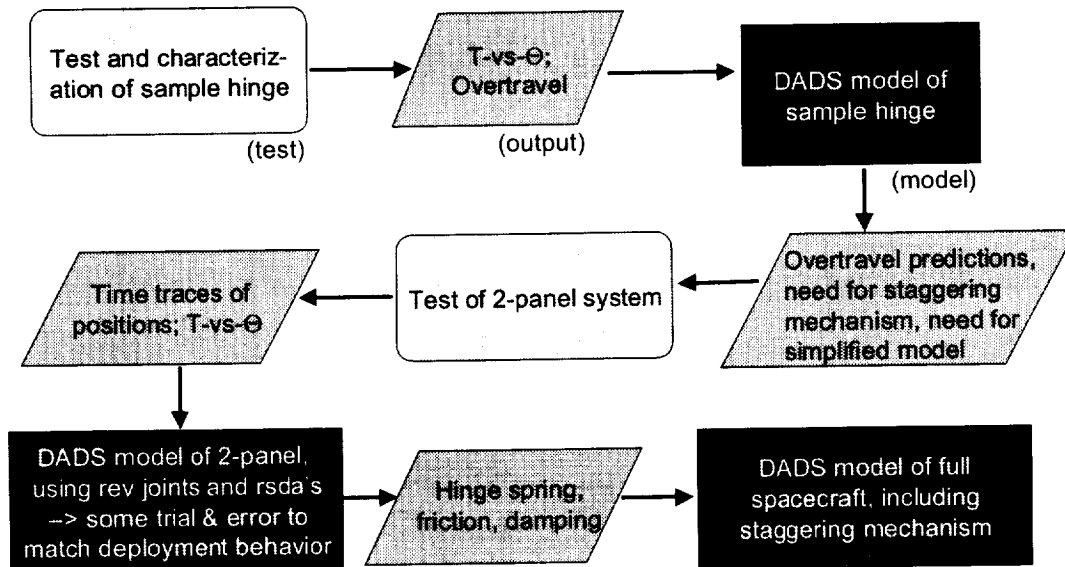


Figure 4. Integrated Correlation Methodology

The first step was to perform a series of tests on a single hinge that was connected to two small coupons of honeycomb panel substrates. This test was done to characterize the spring properties, friction, and over-travel tendencies of the hinge design. Those properties were then used to correlate a DADS (Dynamic Analysis and Design System; LMS-CADSI, Coralville, IA) model of that same sample hinge setup.

The model contained a very high level of fidelity by including not only the spring, mass properties of the panel coupons, and air drag resistance forces on them, but also the geometric rolling/sliding contact behavior between the link and the hinge housing. With the friction coefficient between the link and the panel housing being the only real unknown, it was varied within normal expected ranges until the over-travel shown in the model was very near what was found in the sample hinge test.

At that time, the need to incorporate a wing staggering mechanism into the spacecraft design was beginning to become clear. With the light sample substrate, an over-travel angle of 20-30 degrees was observed in test. As stated above, with the two wings possessing a non-planar deployed configuration, this level of over-travel would certainly produce an impact between the wings during a simultaneous deployment. This is a highly undesirable condition given the fragile nature of the solar cells mounted to the panels.

Another conclusion drawn at this point in the procedure was that a simplified hinge model would be necessary in order to create the eventual goal – a correlated spacecraft model. Due to the high level of calculation necessary during the model solving process (primarily due to the rolling/sliding contact elements in the hinge model), it became evident that it would be unfeasible to duplicate this setup in the 32 necessary locations in a spacecraft model. The run-time for this sample hinge model was approximately 40 minutes for 1.25 seconds of simulation of one hinge. The spacecraft model was expected to take approximately 60 seconds and contain 24-32 hinges, and the relationship is non-linear when combining such sets of elements in a comprehensive model. Hence, it was decided that the full spacecraft model would need to have simplified revolute joint/spring hinges, while still capturing the correct behavior of these innovative devices.

The next step in the process was probably the key to the entire effort – performing a meaningful sub-scale test to be used as a platform from which the entire spacecraft model would be extrapolated. Figure 5 illustrates the setup used for this 2-panel test. A grounded-body spacecraft mockup was used, along with two dummy panels which had large holes cut out to minimize the effects of air resistance. The core/root hinge line had four hinges across it, similar to the corresponding location on the flight unit; the root/outer hinge line had two hinges across it, simulating the most outboard hinge lines on the spacecraft. Wiring harnesses similar to those used in flight were routed across both hinge lines.

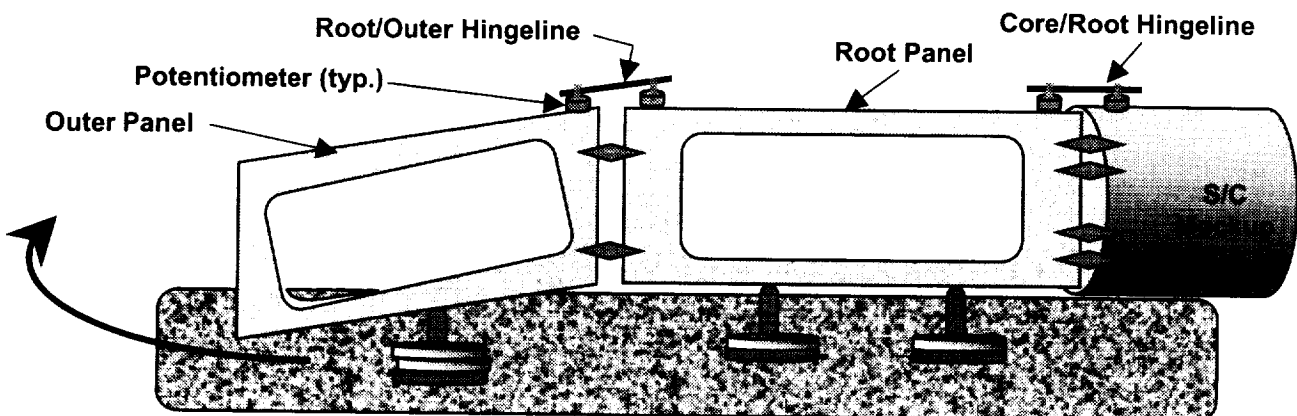


Figure 5. 2-Panel Test Setup Schematic

The entire assembly was supported using air bearings on a granite table – recall that these hinges have no capability to provide lateral stiffness (vertical direction here) until they are latched. The air bearing

paddles had the capability to support various steel weights such that the mass properties of the wing could be varied. The reason for that accommodation was an unresolved discussion regarding the distribution of wing weight. One argument was that the wing weight should be divided equally among the inboard and outboard panels (proper distribution relative to the core/root hinge). The other said the weight of one panel should be left to the outer panel and the remaining five panel weights lumped at the inboard panel (proper distribution relative to the root/outer hinge). The compromise was to test both configurations and attempt to correlate both with the same set of simulated hinge parameters.

In addition, a potentiometer measurement system was used to gather the time history data of the deploying panels. This data was used to refine and correlate the ensuing DADS model. That model included all of the correct mass properties and geometric features of the 2-panel test setup, including contact/interference between the panels and the spacecraft and contact/stiffness between the deployed panels and the core plate. The simplified hinges now consisted of basic revolute joints, driven by Rotational Spring/Damper/Actuator (RSDA) elements.

Torque-vs-angle data was used to fine-tune the non-linear spring characteristics of the hinge for the RSDA's, as well as the friction and cable harness resistance inputs. The third energy dissipation factor used was a "buckling factor." When these hinges pass through their deployed position, there is some energy loss during that transition, very similar to the behavior exhibited by carpenter tape hinge deployments. Figure 6 illustrates the reversible step function that was assumed for this factor, which was also assumed to act only within ± 10 degrees of the deployed position based on observed hinge geometry. The magnitude of the ordinate (torque) was essentially found using a trial and error approach until it resulted in a close match of the behavior for the both of the aforementioned mass properties cases.

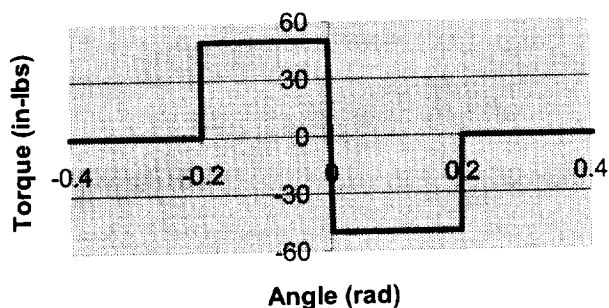


Figure 6. "Buckling Factor" Resistance Step Function

There were many more sensitivities in the system than initially assumed. The dynamics and timing of one panel definitely had non-linear effects on the deployment behavior of the other. As such, extremely good correlation could be achieved for *either* of the chosen representative cases (Tests 17 and 18), but the best *overall* correlation is shown in Figures 7 and 8 for both respective cases simultaneously. This was achieved by splitting the difference for some of the parameters so that the errors in both cases were minimized simultaneously.

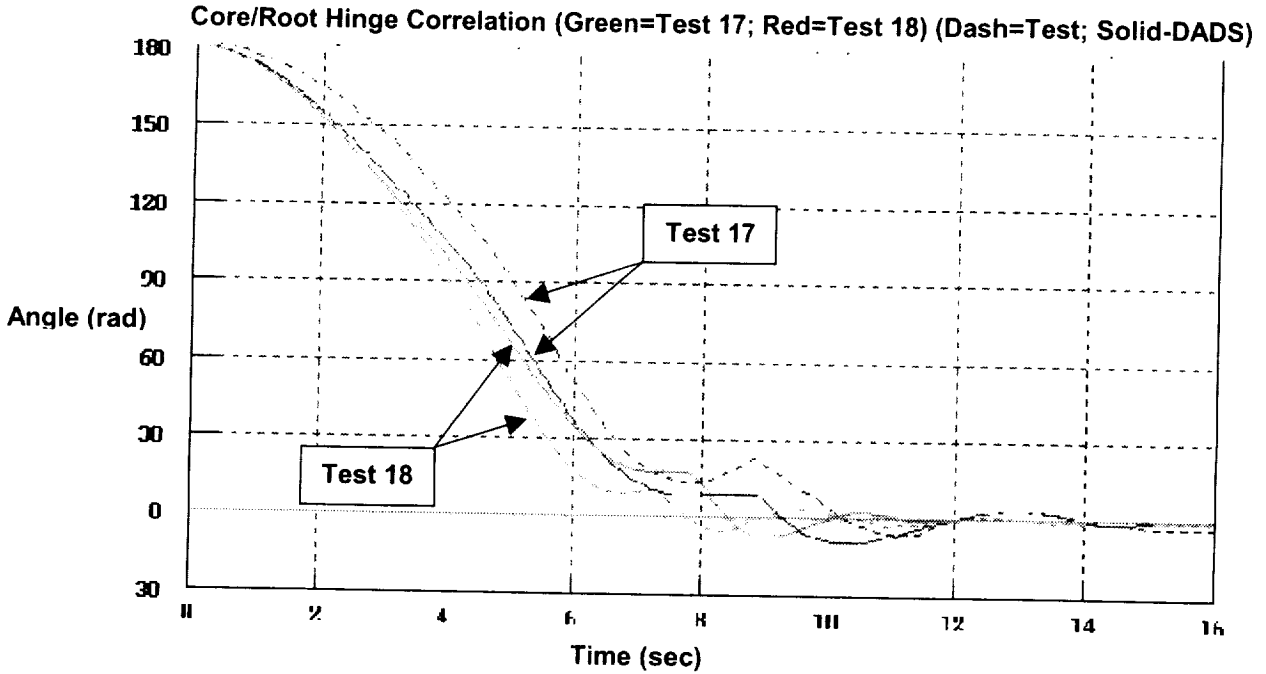


Figure 7. Core/Root Hinge Test and Analysis Correlation

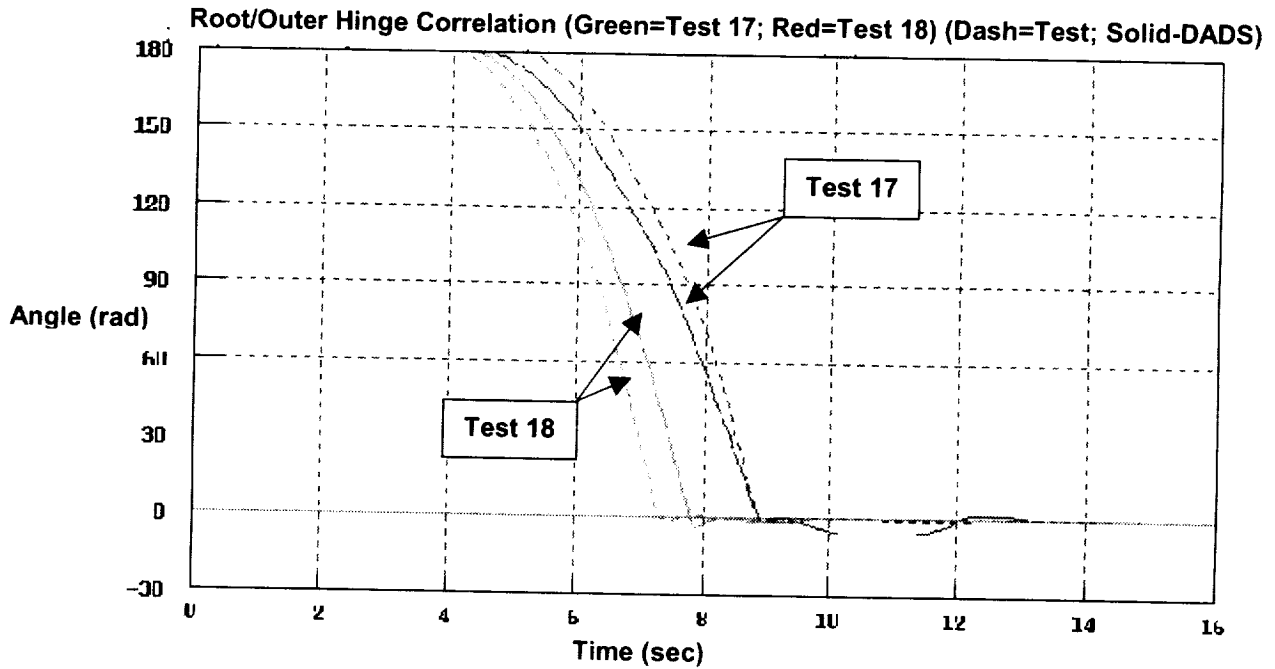


Figure 8. Root/Outer Hinge Test and Analysis Correlation

One can see that the overshoots match well between the tests and the model. Also, all of the significant timing of events is within 0.5-1.0 second or better between computer prediction and test. After review of these results, the model was deemed by all parties to have sufficient correlation to proceed to the extrapolation of the entire spacecraft configuration.

With the proper spring and damper parameters obtained, the next step was to use those values in a DADS model of the entire spacecraft. This model is comprised of a bus, two wings with six solar panels on each, the wing deployment staggering mechanism, and other features to represent the realistic nature of the deployment behavior. One such feature are two "mousetrap" springs, or articulation fingers, on each wing between the outer panels to control relative panel motion and speed (see Figure 9). An AVI format animation file exists in Reference 2 that shows the solar array deployment event, from the fully stowed to the fully deployed configuration.

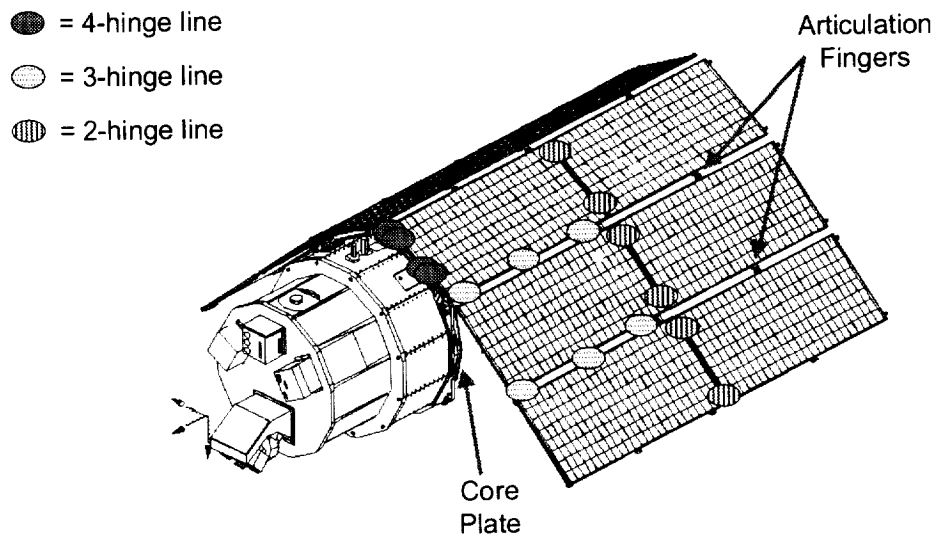


Figure 9. Hinge and Articulation Finger Locations on Spacecraft (Courtesy of Orbital Corp)

Results

In the analysis, the second wing is released after 25 seconds, rather than 60 seconds, which was arbitrarily chosen when the program decision needed to be made. It has been proven that keeping the 60-second delay was not only prudent and conservative, but it also prevented the need for additional software changes at that late date in the program schedule.

There were other minor issues uncovered through the use of this model that might never have been rectified otherwise. The biggest issue was the fact that the articulation finger that controls the two outer panels closest to the spacecraft centerline (the upper one pointed out in Figure 9) was ineffective on the staggered wing (and maybe both). Those panels separated approximately 25.4 cm (10 inches) at the tips, and the spring finger is only a few (5-8) centimeters long. The reason for the separation is the fact that their respective inner panels, when deployed, are not planar, but instead form a 12-degree angle with each other.

Two out of four of these articulation mechanisms that are used to keep the panels under a semi-controlled deployment were shown in the model to lose contact with their respective panels. Depending on the actual level of variability in the hinge torque, the leading panel can become the lagging panel due to a loss of contact. If that occurs, the mousetrap spring would interfere with the latch-up of the panels, much like a broomstick across a doorjamb would prevent the door from fully closing. The hardware was evaluated prior to flight and it was discovered that the fingers were placed in the wrong locations, too close to the outboard tips of the wings. Based on a geometric calculation, they were relocated to a more effective location further inboard along their respective hinge lines.

Also due to the 12-degree offset between these panels, it was discovered that this location has the potential for creating the same re-contact scenario as between the two deploying wings, which was solved

by adding the staggering mechanism. Since that solution is not feasible in this location, engineers discussed adding foam to the areas that could possibly contact; however, it is unclear whether the contractor ever incorporated this feature.

At this point, the team reflected back on the five major questions to be answered at the outset of this project, and assembled the following answers:

1. *How long should the deployment staggering device wait to release the second wing?*
The DADS model predicted that the vibrations of each wing were sufficiently settled after approximately 25 seconds. It is believed that keeping the accepted 60-second delay was not only prudent and conservative, but it also prevented the need for additional software changes at a late date in the schedule.
2. *Does 2nd wing deployment cause a "tail-wagging-the-dog" disturbance sufficient to unseat the 1st deployed wing?*
No. The deployed wing and joint stiffness is sufficient to preclude contact between panels on different wings during deployment.
3. *Does over-travel of either wing induce excessive bending stress in the panels or spacecraft core plate?*
No. The maximum moment caused by the core plate interference was 6.2 N-m (55 in-lb) for both wings. Although this may appear counter-intuitive since the wings deploy slightly differently, it is because the final, roll-out motion is nearly the same for both, with the same moments of inertia and very nearly the same speeds.

A calculation was done, applying this moment to the root panel in order to see the effects. The stress induced in the face sheets resulted in less than 6.2 MPa (900 psi), maximum, and the corresponding overall face sheet elongation due to bending is about 0.01 mm (0.4 mils) – hardly worth a concern, given the compliant adhesive used to bond the cells to the panels.
4. *Will any other panel over-travel (within a particular wing) cause detrimental contact of deploying solar array?*
Possibly. Due to the non-planar nature of the 12-degree offset at two hinge lines, it was discovered using the DADS model that these locations have the potential for creating the same re-contact scenario as between the two deploying wings, the latter of which was solved by adding the staggering mechanism.
5. *Do core plate soft stops necessarily prevent detrimental over-travel of the deploying solar wing?*
No. During the test, there was little or no effect given by rubber foam placed along the edge of the core plate. In fact, it actually appeared as though a larger over-travel angle was exhibited with the soft stop present. There is no explanation for this phenomenon, except for the possibility that the foam slows the inner panel at the end of its travel range, thus changing the dynamics of the wing as a whole. It was readily seen using the DADS model that the interaction between the two panels of a single wing can have a large impact on the over-travel angle.

Conclusion

The foremost conclusion brought about by this entire task is that it is desirable to design a system that can be tested on Earth so the extensive methodology discussed herein is not necessary. However, it is not always possible to do so, and in those instances, it has been shown that iterative correlated test and analysis CAN work. The TSX-5 program accepted many items based on this process:

- The wing staggering mechanism and its time delay
- The placement / relocation of "mousetrap" articulation fingers
- The removal of foam on the core plate due to lack of need
- The lack of detailed FEM modeling for solar cell cracking at end-of-travel

It should be noted that the support of management to execute proper testing is essential in this process, because if this methodology is chosen, one must remember that the computer model is only as good as the data going into it. Although this may not be a revelation, it is indeed one more valid argument proving the need of an extensive a meaningful testing program.

The ultimate proof? TSX-5 successfully deployed its solar array on-orbit June 7, 2000...



Lessons Learned

- Design a system that can be effectively tested within Earth's gravitational field
- When using an air bearing system, ensure sufficient stiffness laterally (so paddle doesn't cock over) and provide for adjustment vertically.
- In areas of possible hardware contact/collision, test configuration with rubber/foam/etc. installed, since it may have dramatically different effects than expected.
- Test, Test, then Test some more...

Acknowledgements

The author would like to express extreme gratitude toward Walter Holemans, who designed the subject hinge while at Orbital and displayed an energetic and unwavering commitment to excellence throughout this entire procedure. After leaving Orbital, Walter acted as a gratis consultant in order to ensure this work was completed. It should also be noted that these efforts would not have been possible without Orbital's technical expertise provided by Michael Whalen and management support provided by Pat Davis. All illustrations of the TSX-5 spacecraft used herein (Figs. 1, 3, & 9) are reprinted with the permission of Orbital Corporation.

References

1. Daniel, Walter K., and Bidinger, G. Michael, " Deployment Dynamics of Solar Arrays with a Link-in-Slot Hinge/Latch Mechanism," 34th Aerospace Mechanisms Symposium, May 2000.
2. TSX-5 spacecraft website at <http://www.te.plk.af.mil/stp/tsx5/craft/craft.html>
3. Holemans, Walter and Gore, Brian, "TSX-5 Solar Array Deployment Test Plan and Report," October 1999.

204/37

Milstar Solar Array Boom Deployment

Thomas B. Pace^{*} and Steven M. Honodel

Abstract

The Milstar Solar Array Boom is a mature design that has been successfully deployed in test dozens of times and has been successfully deployed on orbit six times. On June 7, 2000, one of the Booms did not fully deploy during its thermal vacuum ground test at cold temperatures. The problem was caused by a piece of ground test equipment, a restraint mechanism that had developed excessive friction. This restraint mechanism had been used for over 100 test deployments and had never been refurbished. The anomaly had a positive effect in that this restraint mechanism was reexamined to determine where design improvements could be made to increase friction margins. A significant lesson learned is that even relatively low cycle deployment test equipment can experience wear-out problems and must be routinely inspected during long multiyear programs like Milstar.

Introduction

There are two Booms on each Milstar satellite. Each pair of Booms serves three basic purposes. First, they move the two solar arrays away from the vehicle so that the arrays can be safely deployed. Second, they rotate the two solar arrays so that the arrays can track the Sun. And third, they transfer the power generated by the two solar arrays to the vehicle.

The Milstar Solar Array Boom is a large electro-mechanical device that is approximately 23 cm (9 in) wide by 23 cm (9 in) thick by 171 cm (67.5 in) long and weighs about 32 kg (70 lb). The Boom has two hinges on it, an inboard hinge and an outboard hinge (Figure 1). Each hinge contains two sets of negator leaf springs that provide 32 N-m (286 in-lb) of torque. One eddy current damper on each hinge provides damping. The inboard hinge connects the Boom to the vehicle and upon deployment, it rotates the Boom away from the vehicle. The outboard hinge supports a flexible substrate solar array (FSSA) and upon deployment, it rotates the FSSA away from the vehicle and positions it for deployment. The range that the inboard hinge deploys in the first part of the deployment is critical. If the inboard hinge deploys too far too fast, there is the possibility that the FSSA Deployment Canister could be driven into the vehicle payload (Figures 2 & 3). Therefore, a device called a Tripwire Mechanism (TM) is used to restrain the motion of the inboard hinge during the first part of the deployment.

The TM consists of a spring-loaded spool that pays out a stainless steel cable (Figure 4). When installed, the TM is bolted to a fixed point on the vehicle. Then its cable is pulled off of its spool and bolted into another fixed point 140 cm (55 in) away. Midway across the span of the cable, the cable is placed on a hook that is mounted to the base of the FSSA. The springs in the TM ensure that the cable is under tension across this span. Upon being released from its stowed position, the inboard hinge wants to fully deploy but it is restrained by the tripwire cable. Although the inboard hinge is restrained, the outboard hinge is free to rotate. In fact, the tripwire force aids the deployment of the outboard hinge. This allows the FSSA to rotate clear of the vehicle payload and thus eliminates any possible interference. As the outboard hinge rotates the FSSA, the hook also rotates as it is mounted to the FSSA. After the outboard hinge rotates far enough, the angle of the hook changes enough so that the cable is able to slide off of the hook. At this point, the inboard hinge is free to rotate and complete the deployment (Figure 5).

^{*} Lockheed Martin Space Systems Company, Missiles and Space Operations, Sunnyvale, CA

Deployment Test Anomaly

The Boom did not fully deploy in test because an interference occurred between test hardware representing the L-bracket on the FSSA and the Solar Array Release Mechanism (SARM) bracket on the vehicle bus. This interference halted the deployment and left the system stuck in a half-deployed position. In a nominal deployment, the Boom begins in its stowed position (Figure 6). During the first part of the deployment, the TM allows the inboard hinge to travel 9° before the tripwire cable is pulled taut and halts the motion of the inboard hinge (Figure 7). The outboard hinge then rotates 114° (Figure 8) at which point the tripwire cable slides off of the hook (Figure 9). At that point, both hinges are free to deploy and the deployment continues to the end (Figure 10). In the anomalous deployment, the inboard hinge did not travel its initial 9° and the tripwire cable never slid off of the hook, thus causing the two brackets to interfere with one another (Figure 11). Insufficient inboard hinge rotation was caused by excessive friction in the TM. During deployment tests, a TM designated as a test unit was used. This test unit had been used since the inception of the program and had never been refurbished. Friction increased over time and ultimately prevented the inboard hinge from rotating enough to clear the release mechanism bracket. Similarly, a worn hook and a worn tripwire cable caused the tripwire to not release from the hook.

This test anomaly led to a more in-depth investigation that revealed that the deployment design margins to friction could be improved. Elevated levels of friction in the TM components could lead to an on-orbit deployment failure. This potential interference had not been recognized as a problem before this incident. To ensure that the friction levels were minimized, the TM components were redesigned and new test procedures were written to verify that the components met the new friction requirements.

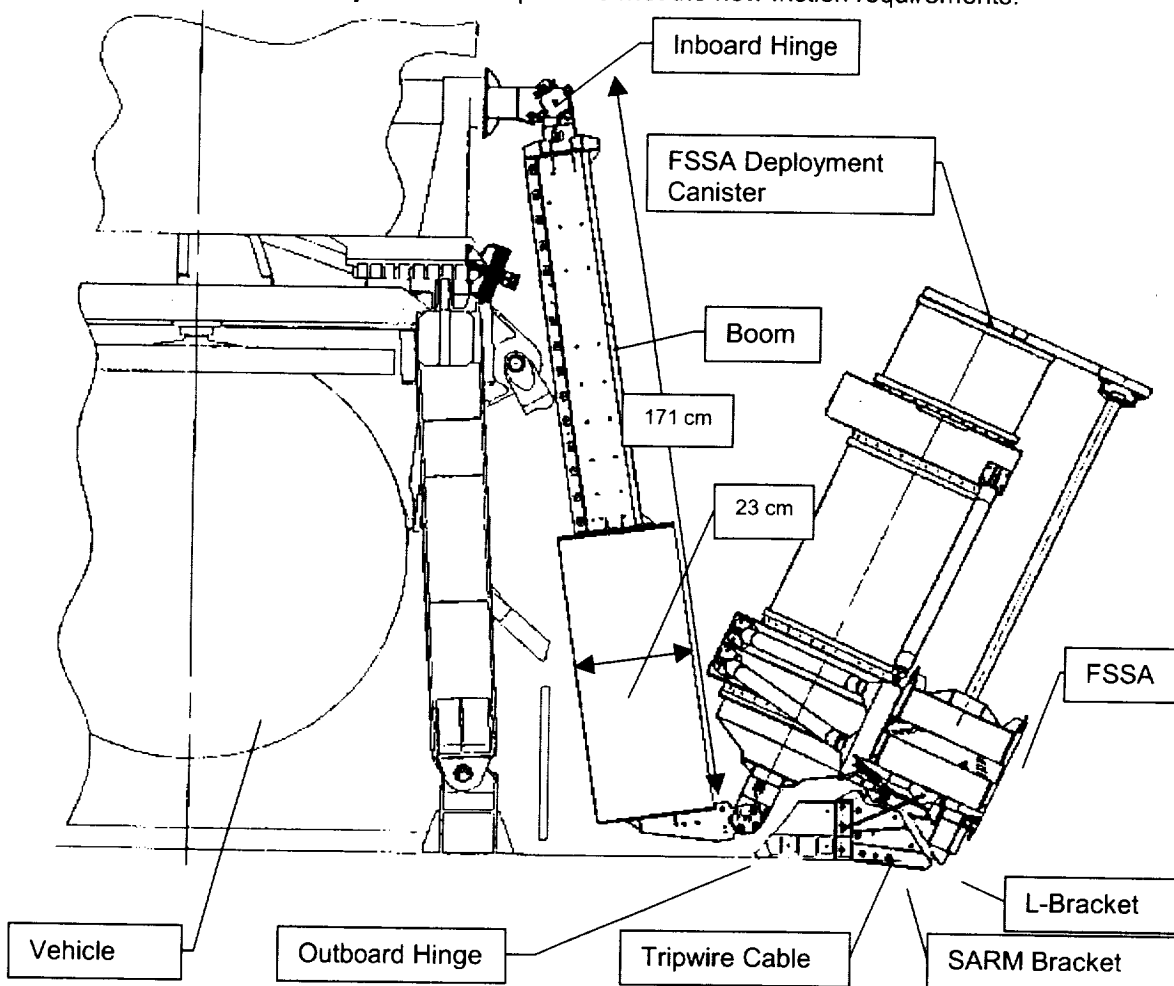


Figure 1. Boom and FSSA in Stowed Position

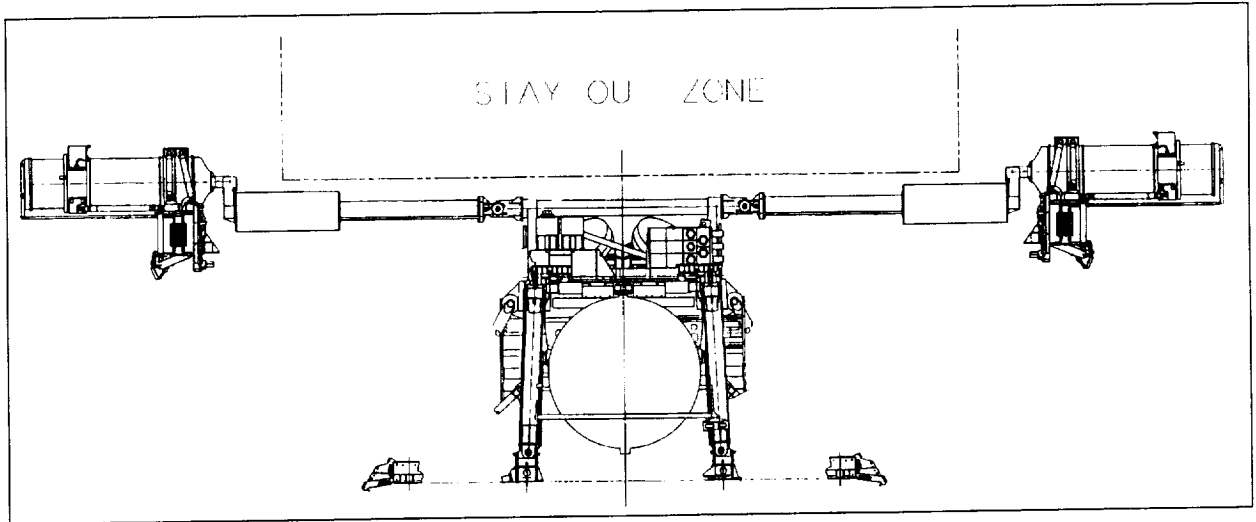


Figure 2. Successful Deployment with TM

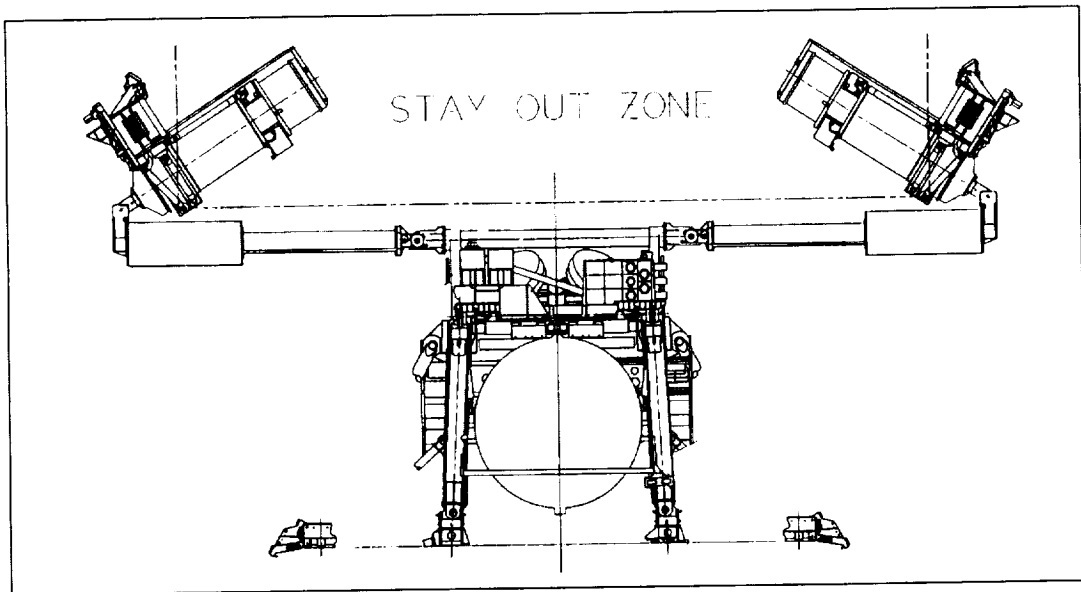


Figure 3. Possible Interference without TM

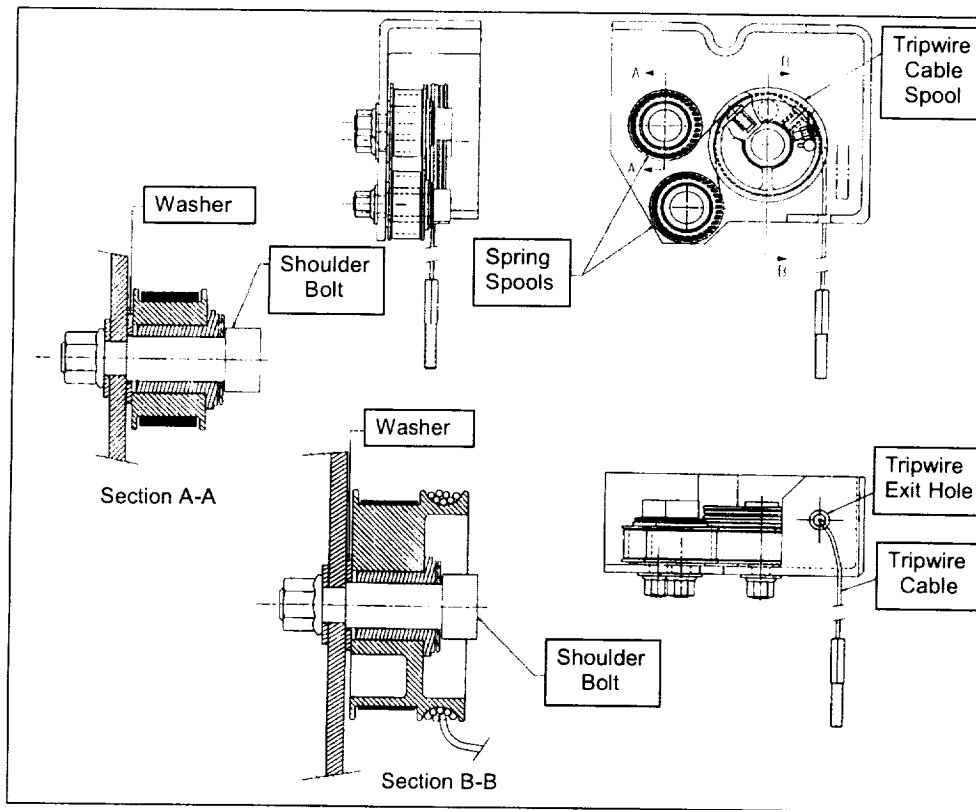


Figure 4. Tripwire Mechanism Drawing

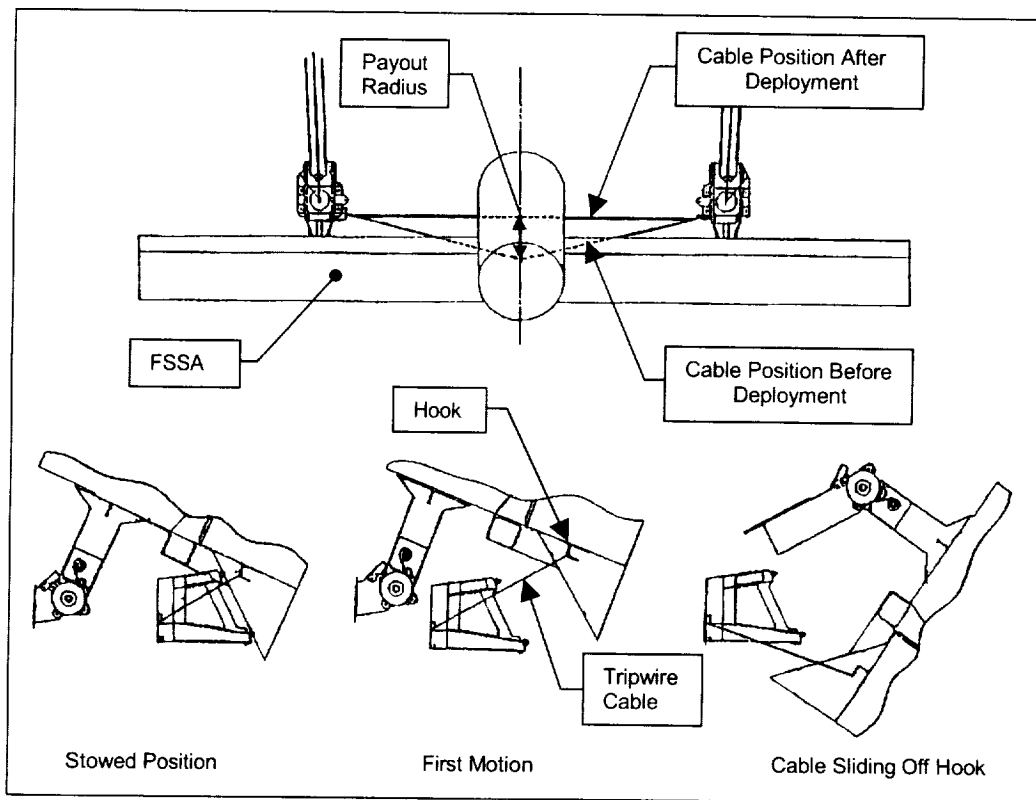


Figure 5. Tripwire Mechanism Function

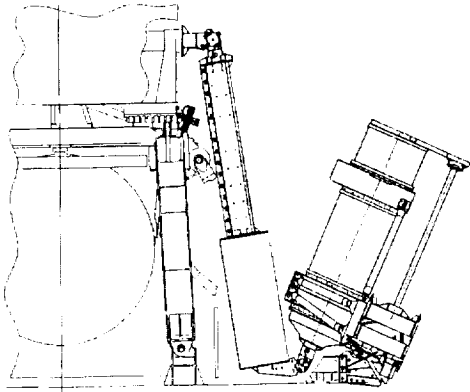


Figure 6. Stowed Position

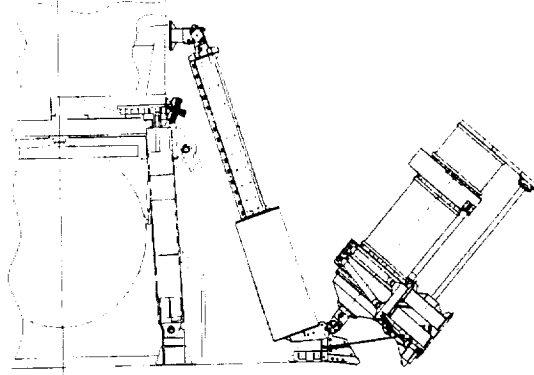


Figure 7. TM Restrains Inboard Hinge

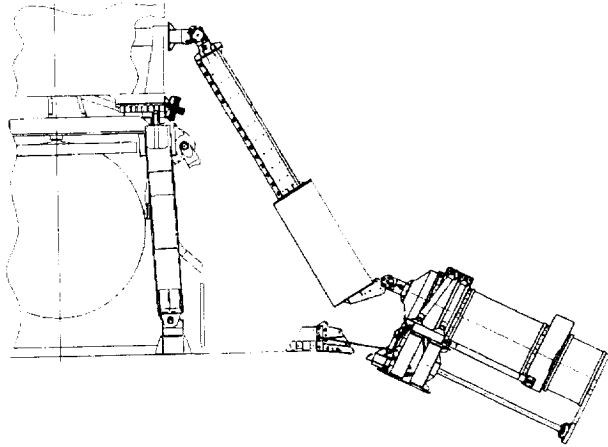


Figure 8. Outboard Hinge Rotates 114°

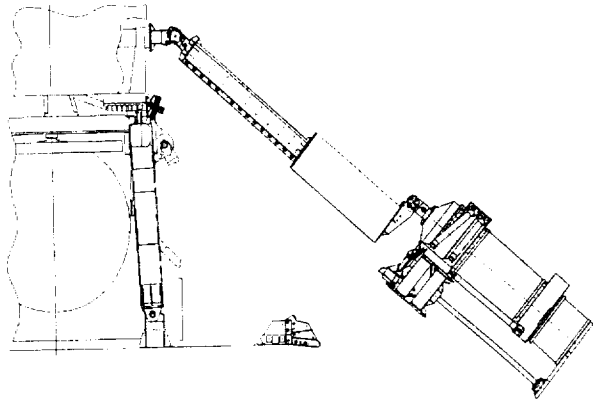


Figure 9. Tripwire Releases Inboard Hinge

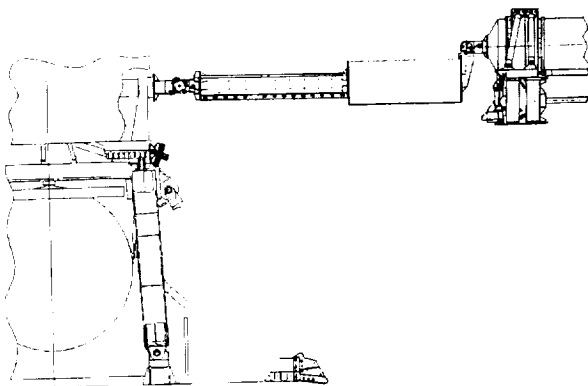


Figure 10. Deployed Position

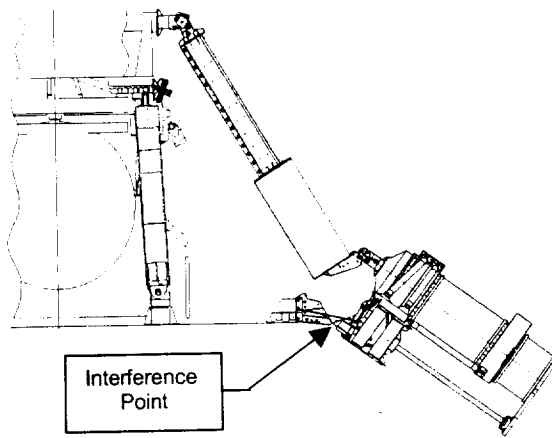


Figure 11. Stuck Position

Cause of Test Anomaly

The Boom deployment anomaly was caused by excessive friction in the TM components. The components used during the test were designated as non-flight Special Test Equipment (STE) and were used during every deployment test. A separate set of flight TM components is reserved for each vehicle and they are not used for Boom deployment tests. The problem was that the STE components had been subjected to approximately 100 deployment cycles without ever being refurbished. Inspection of the STE TM components revealed significant signs of wear. This wear caused two things to happen. One, the tripwire was not able to completely pay out of the STE TM. And two, the tripwire was not able to release from the STE hook.

TM Washers

The TM consists of three spools mounted on an aluminum chassis (see Figure 4). The central spool contains the tripwire cable. The two smaller spools contain the springs that provide the tension for the tripwire cable. All three spools are mounted to the chassis by a shoulder bolt and nut combination. In order to provide a redundant rotating surface between the shoulder bolt and the chassis, a washer was added to the bearing surface. However, like the chassis, the washer was made from aluminum and created an ideal situation for galling to occur as like materials were bearing upon one another. Furthermore, it was discovered that the STE TM was assembled incorrectly as the washer was trapped under the shoulder bolt. Instead of being free to rotate, the washer was pinched between the shoulder bolt and the chassis and damaging itself and the chassis with each subsequent cycle (Figure 12 and Figure 13). The friction created by the improperly installed washers and the improperly selected washer material were significant reasons as to why the tripwire did not completely pay out of the STE TM.

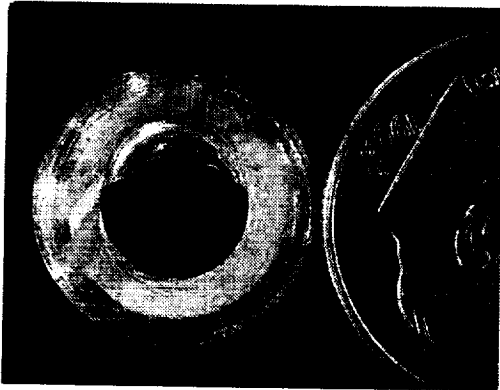


Figure 12. Pinched Washer

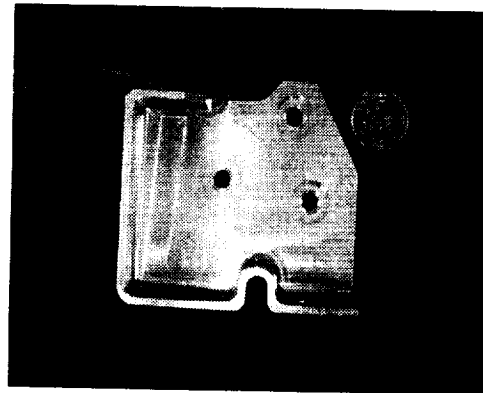


Figure 13. Galling Caused by Washers

TM Exit Hole

As the tripwire cable unwinds off of the central spool, it exits the TM through a small hole in the chassis. Due to the geometry of the system, the tripwire cable is pulled to one side of the exit hole and makes contact with the chassis as the cable is pulled off of the spool. Since the cable is stainless steel and the chassis is aluminum, the cable acted as a saw and cut a significant groove into the side of the exit hole (Figure 14). This groove inhibited the motion of the cable and contributed to the tripwire not completely paying out of the STE TM.



Figure 14. Groove Cut in TM Exit Hole

Tripwire Cable

Upon examining the STE tripwire cable, kinks were found in the section of cable that feeds through the exit hole in the TM (Figure 15). In the anomalous deployment configuration, one of these kinks was located in the groove that was worn in the exit hole of the STE TM. Additional force is required to pull these kinks through the exit hole but the Boom was not capable of providing this extra force. Therefore, the tripwire cable was not allowed to completely pay out of the STE TM.

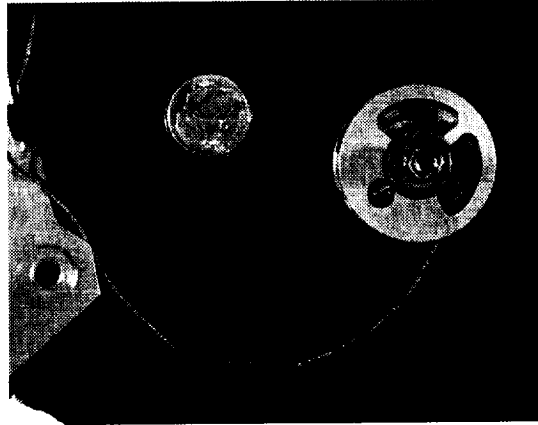


Figure 15. Kinks in Tripwire Cable

Hook

The final piece of the puzzle was the hook. Like the TM chassis, the hook was also made of aluminum. When the stainless steel tripwire cable was dragged over the aluminum hook repeatedly, a groove was cut in the STE hook (Figure 16). With a pristine hook, the tripwire cable should slide off the hook at a hook slip angle of 12 degrees. With the groove cut in the STE hook, the tripwire never released from the hook even though the hook slip angle was 43 degrees. Subsequently, this caused the motion of the inboard hinge to be restrained longer than normal.

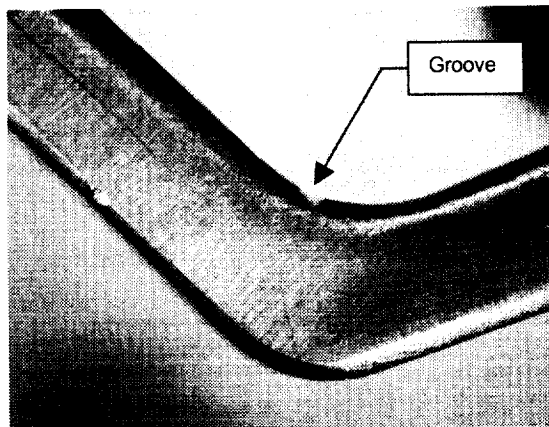


Figure 16. Groove Cut in Hook

Corrective Action

Because the deployment anomaly was caused by worn components, fixing the STE system would have simply required replacing the worn parts with new parts. But the STE components duplicate what is used on the flight vehicle, so the anomaly prompted the design team to determine the system's sensitivity to TM friction. Therefore, the goal of the investigation was to not only fix the problem but to ensure that this anomaly would never occur again.

Design Changes

The initial TM design used aluminum washers to provide a redundant rotating surface between the shoulder bolts and the aluminum chassis. In order to eliminate the galling produced by bearing aluminum washers against an aluminum chassis, the aluminum washers were removed and replaced with stainless steel washers. In addition, the new stainless steel washers were coated with a dry film lube in order to reduce friction even more.

To reduce the amount of wear on the TM exit hole, the entire TM chassis was coated with a teflon impregnated anodic coating. Previously, the TM chassis was coated with just an alodine coating which only provided protection from corrosion, not wear. The new anodic coating is much more wear resistant and protects the TM exit hole from the sawing motion of the stainless steel tripwire cable. Furthermore, the impregnated teflon in the anodic coating serves to lubricate the TM exit hole, reducing the amount of wear caused by the cable. The contact between the tripwire cable and the exit hole could not be eliminated because due to the geometry of the system, the exit hole acts as a pulley for the tripwire cable.

Like the TM chassis, the hook was also coated with the same teflon anodic coating, thus reducing friction and increasing wear resistance.

Finally, the kinked tripwire cable in the STE TM was simply replaced.

Test Changes

The original TM acceptance test did not apply "Test As You Fly" principles. It simply measured the spring force in the TM by pulling the tripwire cable straight out of the exit hole and then letting it retract. This is an important measurement but this is not how the TM is used during flight. During flight, the tripwire cable is pulled out of the mechanism with a side load and the cable rubs on the surface of the exit hole. Therefore, a new acceptance test was written that tested the TM in this manner. A special set of STE was built that allowed the force required to extend the cable to be measured versus payout radius (Ref Fig 5). All TMs were required to test below a maximum force requirement at ambient, cold, and hot temperatures. The STE TM that was used in the deployment anomaly failed this test. All of the redesigned flight TMs passed this test easily.

Through this investigation, it was also discovered that the hook slip angle, i.e., the angle at which a tensioned tripwire cable slides off of the hook, was critical. Therefore, a simple incline test was designed to measure this slip angle. An analysis of the deployment (discussed below) determined that the slip angle should be no greater than 20 degrees. The STE hook that was used in the deployment anomaly and that had the groove cut in it had a slip angle of over 43 degrees and failed this test. All of the redesigned flight hooks measured no greater than 12 degrees and easily passed this test.

Results

Prior to these design changes, the critical clearance between the L-bracket and SARM bracket for a nominal deployment measured 6.0 cm (2.4 in). With the new design changes, the critical clearance has been more than doubled to 12.7 cm (5 in).

Analysis

The deployment tests are an important method of verifying workmanship and performance in thermal vacuum extremes. As in most programs, such testing is constrained by technical limits, cost, and the risk of damaging flight hardware. Deployment analysis and simulation were used to complement testing and further verify the Boom performance on-orbit. An analysis was performed for the Boom system with the objective of predicting hardware clearance on-orbit with a reliability of 0.999999.

A computer model of the Boom deployment including the offload system for testing was developed using an in-house, multi-body dynamics solver called Ezydyn. The model represents the Boom as 2 rigid bodies with springs, dampers, joints, and various forcing functions to simulate friction, deadband, etc. The overhead counterbalance system is represented with 4 rigid bodies tied with joints and cable forces. The model duplicated the hang-up when the payout radius of the tripwire cable (Ref Fig 5) was limited to 34.5

cm (13.6 in) and the cable was not allowed to slide off the hook. The model also matched the 43-degree slip angle that was held with the cable trapped in the groove. Figure 17 shows a close-up of the hang-up, as predicted by the model.

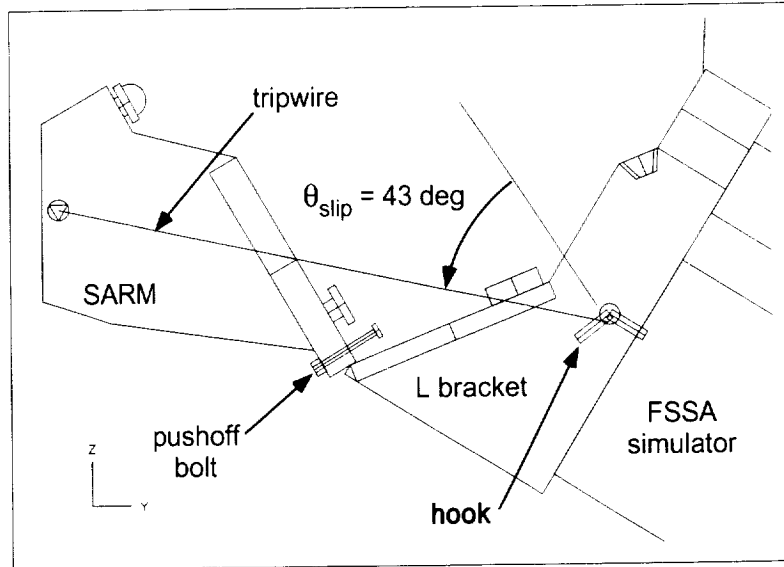


Figure 17. Close-up of Predicted Bracket Hang-up

Many inputs to the model were varied between their nominal and worst-case values to determine their effect on clearance between the SARM and L brackets. Some parameters required better definition and, in some cases, prompted new component tests to determine nominal and worst-case values. After several iterations of model prediction and parameter refinement, it became clear that the tripwire hook force (similar to the arrow force on a bow and arrow) and hook slip angle were critical to clearance. This led to a pass/fail requirement for the tripwire of 15.6 N (3.5 lb) max hook force at a hook radius of 31.0 cm (12.2 in). The 31.0 cm (12.2 in) radius represents minimum payout that ensures a static bracket clearance of 2.5 cm (1.0 in). More payout is needed for dynamic clearance, depending on the slip angle that the tripwire releases at. This is because the brackets are still approaching one another even after the tripwire has released. After tripwire release, the relative strength and damping at inboard versus outboard hinges affects the minimum clearance. The hook slip angle pass/fail was set at 20 degrees. The process of quantifying the parameter values and correlating the model led to some discoveries.

One of the discoveries was that the deployment during the cold deployment anomaly was greatly assisted by a test harness that was tie-wrapped too tightly between the support post and the rotating offload beam. Figure 18 shows the large aiding torque and friction caused by the test harness when comparing the 6/5 test with later tests where the test harness was re-routed.

One of the functions of the Boom is to transfer power generated by the solar array to the vehicle. This is accomplished by utilizing a large cable harness that is approximately 5.0 cm (2.0 in) in diameter. This thick, stiff cable harness is routed over the inboard hinge and makes the hinge harder to deploy. Typically, a cable harness aids deployment for roughly the first half of deployment then starts resisting thereafter. The aiding torque at the start of deployment is usually similar in magnitude to the resisting torque at the end of deployment. By comparing the tests after 6/5 to the hinge-only test in Figure 18 it is clear that this harness resists deployment through most, if not all, of deployment. This is consistent with the results during development tests of the harness. Therefore, the routing and tie-wrapping of the cable harness, as designed, tends to reduce the deploy torque and thus, the clearance between the brackets.

#1009 Cold Deploy Data

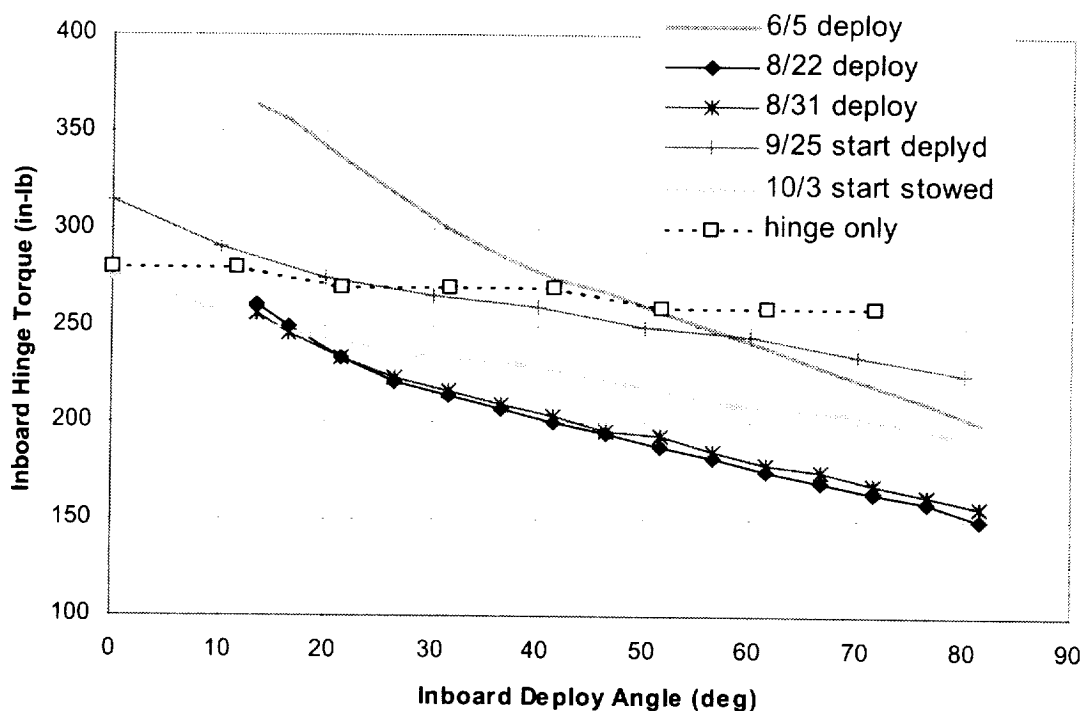


Figure 18. Comparison of Deploy Torque over Various Tests on a Single Boom

Comparing the 9/25 and 10/3 results in Figure 18 shows that the cable harness takes a significantly different set depending on the Boom orientation during cool down. If the Boom is cooled in its stowed position, the cable harness takes a cold set in that stowed position and significantly decreases the available torque of the hinge, compared to the torque when the cable is cooled in the deployed position. The starting orientation of the Boom was not precisely specified during testing, and at least one torque margin test is known to have started from the deployed position instead of stowed.

Another discovery was the large unit-to-unit variation in inboard hinge torque. Figure 19 shows the deploy torque measured from several Booms. Simulation of the Booms with lower torque values shows that there is very little clearance margin even after matching the weakest tripwire to that Boom. The only requirement levied on the torque tests is to demonstrate 100% minimum torque margin, which all the Booms in Figure 19 (without the tripwire) possess.

Cold Deploy Data - All Booms

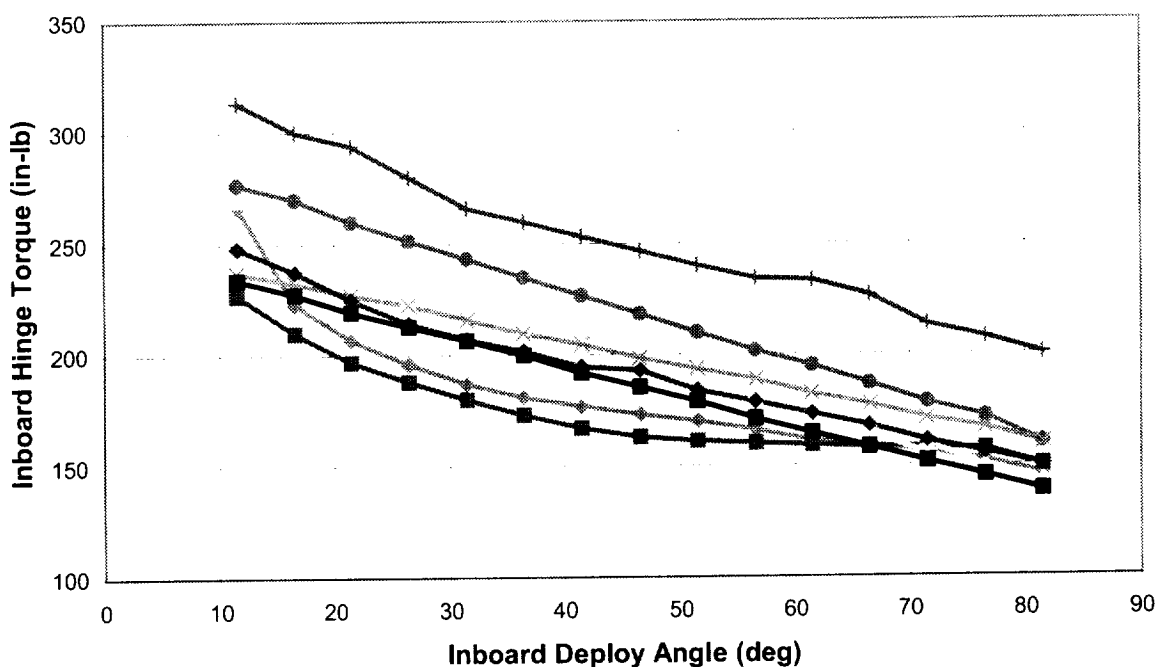


Figure 19. Unit-to-Unit Variation in Inboard Deploy Torque

A third discovery is that the torque margin of the inboard hinge while the tripwire is engaged was not performed at the beginning of the program. With the tripwire engaged, the torque margin of the inboard hinge is well below the program requirement of 100%. At first glance, torque margin might seem irrelevant here since the purpose of the tripwire is to hold back the inboard hinge temporarily. However, the inboard hinge must deploy the Boom sufficiently to maintain clearance for the outboard hinge as it deploys. Failure of the inboard hinge to provide this clearance results in a hang-up as seen in the deployment anomaly. Therefore, the torque margin must be at least greater than zero through some payout distance of the tripwire to prevent a hang-up. The torque margin must be large enough to accommodate variations in the tripwire force among others. As the STE tripwire force increased with wear the torque margin of the inboard hinge dropped. Therefore, a torque margin analysis early on might have tipped the scales against using a tripwire by highlighting the Boom's sensitivity to it.

The torque margin for the Boom depends on the trajectory because there are two degrees of freedom in the Boom, the two hinges. A minimum torque margin of 50% was determined at first, based on a static analysis of the Boom where the tripwire payout was adjusted to maintain 2.5 cm (1.0 in) of clearance between brackets for all achievable hinge angles. This method was dropped because the clearance continues to drop for a period after the tripwire is released. The current analysis method determines torque margin directly from the worst-case dynamic clearance simulation for each Boom. This analysis indicates that a torque margin of 38% when the tripwire is released is needed to prevent a hang-up during a dynamic deployment. This number is lower than the earlier method because the tripwire is paid out further in the dynamic analysis and creates a larger resisting force on the inboard hinge.

A fourth discovery during this analysis was that the deadband in the dampers is a significant factor for clearance, and the stowing procedure influences the amount of deadband available for the next deployment. At the beginning of hinge motion, the Boom accelerates away from the release bracket

quickly until the damper deadband is taken up. At this point the deployment slows considerably. If the hinge torque is low and the deadband is small, the tripwire may not pay out fully by the time the SARM and L brackets approach each other. The damper deadband can vary with each installation of the Boom on the vehicle, making the prediction of deadband stroke very uncertain for on-orbit deployment.

Once the model was correlated to the deployment tests with the improved tripwire and hook, the nominal and worst-on-worst flight simulations were performed. The nominal cold-temperature performance for all Booms had a predicted clearance on the order of 10.0 to 12.7 cm (4 to 5 in). With 15 parameters being varied, the worst-on-worst performance, not surprisingly, resulted in a hang-up. A sensitivity study of the parameters was then performed and the dominant parameters were determined. When only the four most dominant parameters were set to worst-case, the objective of predicting clearance with a reliability of 0.999999 was achieved.

Lessons Learned

This deployment anomaly provides many lessons to the design team. Some of them are obvious and reaffirm basic aerospace practices while others are less obvious and perhaps more valuable because of that.

The first lesson is that any STE used during testing should be inspected and refurbished at appropriate intervals. The Boom deployment tests have been occurring for about a decade and the TM components had no planned maintenance procedure. Some of this can be attributed to the fact that several engineers have been responsible for the Boom over the years. This turnover tends to drain knowledge and familiarity with the hardware. A well written test procedure should identify possible problems and instruct the team to conduct the appropriate inspections prior to reuse of STE. Everything from inspecting for component wear to performing torque hysteresis plots of the offload system are items to be considered when writing a test procedure.

Ground test anomalies are not all bad. In this case, the deployment test anomaly alerted the design team to a failure mode that was never fully appreciated before this incident. This led to design improvements to increase margins. The lesson to be learned here is that the cost required to conduct extensive tests on every single piece of flight hardware can be well worth it if the tests identify a potentially serious problem. The Milstar program was required to perform deployments at hot and cold thermal vacuum conditions with every Boom. In contrast, many programs are under pressure to qualify a design with a qual unit and then do abbreviated flight tests in order to save money. If that had been the case here, the design team may have never discovered this failure mode. In the long run, eliminating tests could end up costing more money rather than saving it.

An important way to reduce the risk of an on-orbit failure is through deployment analysis. Deployment analysis and simulation is helpful in identifying design sensitivities that may not show up in test or are difficult to verify by test. Perform, as appropriate, a torque margin, kinematic, dynamic, and/or clearance analysis early. This will help to identify sensitive parameters, determine if other tests, procedures, or requirements are needed, catch problems with a design, or anticipate test-related problems before it is too late or too costly to make changes.

Special care and keen insight must be used when deciding which tests are value-added; keep in mind all of the variables that could affect the test. In the case of the Boom, there are several variables such as the level of friction in the TM, the amount of torque in the hinge springs, the damping in the dampers, etc.

One critical variable is the routing of cable harnesses, especially when they are routed over hinge lines. Special care must be taken to ensure that harnesses are not overstressed or improperly routed and that they are representative of flight geometry and constraints. Also, cable harnesses used during test must be inspected to ensure that they are properly routed and thermally controlled as needed to minimize their influence on the test. Tie-wraps are often used to control the routing of cable harnesses but care must be taken not to overuse tie-wraps. Tie-wraps are great for making neat and well-maintained harnesses, but they also make the cable a lot stiffer. If this cable is run over a hinge line, the available torque of the hinge

may decrease significantly, especially at cold temperatures. Unless the deployment margin is large, use the minimum number of tie-wraps or tape that will adequately control the working space and dynamic motion of any harnesses crossing a deployable joint, and control the routing and constraining in a drawing.

And finally, special care needs to be taken when designing test equipment. Requirements for test equipment aren't always less demanding than for flight equipment. In this case, all of the STE TM components passed their component test. However, this component test was designed with flight hardware requirements that assumed that the TM components would see relatively few cycles. However, the TM components were subjected to over 100 cycles at the time of the anomaly. In addition, the TM was not tested in the (bow and arrow) geometry that is seen at the system level where the highest forces and wear occur. The design team needs to consider that test conditions can be more of a design driver than the actual flight conditions.

Conclusions

The wear-out failure mode of the Boom test equipment had a positive outcome in that it taught the design team many valuable lessons. These lessons were learning how to improve test equipment inspection procedures, realizing the importance of in-depth testing of every unit, recognizing the value of analysis as a design tool, learning that cable routing is a critical variable, and understanding the factors that are involved in test equipment design. But the most important outcome of the deployment anomaly was that it led to design improvements that increased Boom deployment margins. A previously unknown point of failure was quickly remedied, thus improving the probability of success in Solar Array Boom deployments for the remaining Milstar satellites.

525/44

The "Curwin"® Design: A Novel Solar Array Concept for Constellations

Henk J. Cruijssen* and Gerard J.A.N. Kester*

Abstract

Within Fokker Space a study was undertaken during the period 1998 to 1999 to investigate solar array designs for instance for the constellation markets. In close co-operation with Boeing and MMS (now Astrium), several solar array design options were investigated for the Teledesic and Celestri programs but also other future initiatives could benefit from our study effort. One of the solar array concepts studied in more depth was the "Curwin"® solar array. This paper discusses the evaluations made, which have led to this novel concept. Also, the preliminary performance characteristics are provided. A breadboard model at 50% scale was made to correlate hardware with the theory. A brief overview is given of the breadboard test results.

Introduction

For constellations, it is mandatory to keep the total system cost down. Therefore, the launch costs are to be decreased, for instance by implementing multiple launch options. For this reason, the tight stowage volume requirement for the solar array implies a considerable design driver. For future spacecraft concepts, this may be required as well, as the power demand is expected to increase whereas the available stowage volume may become critical.

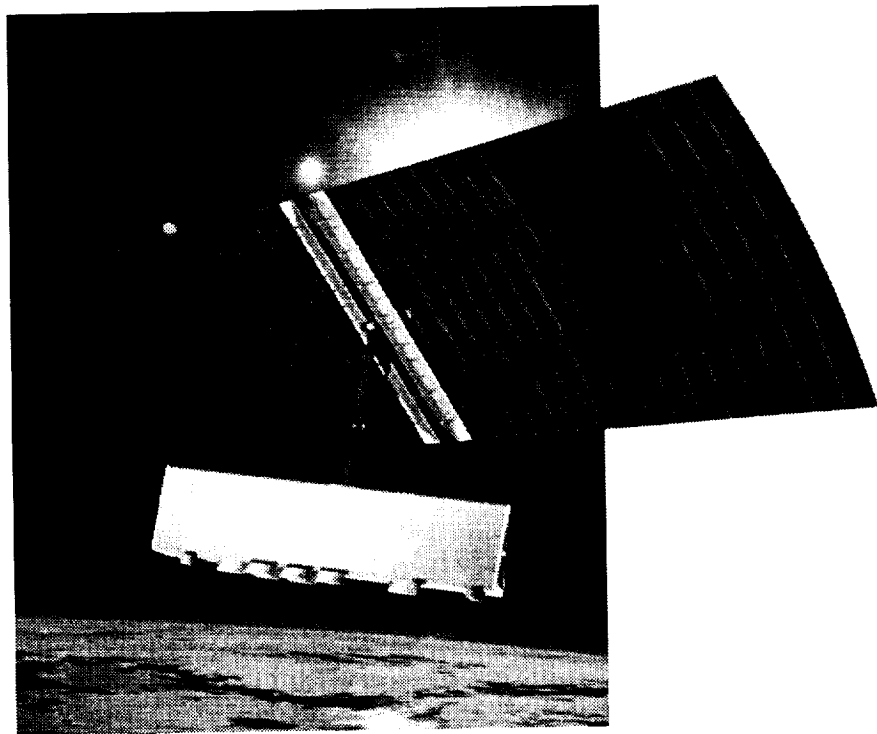


Figure 1. Curwin solar array in fully deployed configuration with panels curved (rear view)

* Fokker Space BV, Leiden, The Netherlands

Solar Array Technical Requirements

The following table provides the technical requirements. These requirements were not firm and changed several times during the course of the study. These were triggered by the merger between the Teledesic and Celestri project, which resulted in an increased power demand.

Table 1: Major technical requirements (typical for constellation type solar arrays)

Parameter	<i>Teledesic</i>	<i>Celestri</i>
Power at End of Life (EOL) conditions	4.3 kW later increased to 8.4 kW	7.6 kW up to 8.4 kW
Drop-off orbit	~ 300 km	~ 300 km
Operational Orbit	1375 km, $i = 84.7^\circ$	1375 km, $i = 48^\circ$
Lifetime	9 -10 years	12 years
Architecture	2 wings on a central extension arm from top side of the S/C	2 separate wings on a yoke from either side of the S/C
Volume	250 mm tapering off to 150 mm	250 mm height
Overall Mass target (specific)	> 35 W/kg	> 35 W /kg.
Max deployed area / Moment of Inertia	N/A	Less than 10500 kg-m ²
Sun tracking mechanism	Double rotation axis SADM / gimbal mechanism	Double rotation axis / gimbal
Field of View	Visual line of sight / contact with the neighboring S/C	no details available
Stowed resonance frequency	$f_1 > 35$ Hz	$f_1 > 40$ Hz
Deployed resonance frequency	$f_1 > 0.3$ Hz	First mode to be $f_1 > (6/I)^{0.5}$ with $I =$ inertia
Deployment shock	N/A	< TBD N-m

A high degree of design commonality was strived for from the beginning of the study. For both the Teledesic / Celestri solar array this has lead to the following technical design drivers

- End-of-Life (EOL) power (4.3 kW up to 8.4 kW).
- Stowage volume on spacecraft (S/C) (150 mm tapering to 250 mm)
- Deployed resonance frequency $f_1 > 0.3$ Hz
- Deployment trajectory to reach the fully deployed configuration must be controlled and within certain constraints (i.e. stay-out zones)
- Total solar array mass (> 35 W/kg)
- Field of view and moment of inertia in deployed configuration

Specific Programmatic requirements:

Typical programmatic constraints were implemented to verify the proposed technical designs against the schedule and cost constraints.

- Development schedule: first demonstration launch in 2003, thereafter regular launch rate
- Launch rate: every week one launch, resulting in a delivery rate: one array per 2 weeks for Celestri (maximum case): one array per 2 working days for Teledesic (maximum logistic case)
- Non-recurring cost: TBD to initiate and endorse to a maximum extent lowering of the recurring cost, recurring cost: < \$1M per array. (4.3 kW EOL), based on a production lot of 180 satellites to be produced in 4 years

Solar Array Design Options

The tight volume requirements in combination with the required on-orbit stiffness led to some very constraining features. The required on-orbit stiffness can be achieved in 3 ways:

1. Thick rigid panels
2. Mast supporting structure with blanket
3. Geometric stiffness with semi-rigid panels

Option 1 was discarded as it did not fit in the tight volume constraints. Option 2 could not meet the stowage volume requirements and/or the frequency requirement. Although the blanket specific mass looks very attractive, one must realize that all supporting structures and deployment and restraint mechanisms are to be included to get the actual number for the specific mass at EOL condition (i.e., W/kg). Furthermore, Fokker Space BV had experience with flexible blanket technology (Ref.: Olympus²) to lead to relative complex and costly mechanisms with a disappointing specific power (< 20 W/kg at EOL). Hence, also this option was discarded.

It became quite clear that a novel concept was required, allowing a very compact stowage method while still providing a stiff backbone in the fully deployed configuration. The idea was to introduce curvature in the deployed configuration, by curving the thin panels by special tension wires. The "Curwin[®]" concept was born [1]. As such, a complicated mast could be avoided, also allowing a good solar cell area coverage as the full panel area could still be used effectively.

Curwin[®] Overall Design Description

The "Curwin"³ concept is quite different from conventional solar array concepts in the way that it uses geometric stiffness to reach higher deployed Eigen frequencies instead of a separate backbone structure. The fully deployed wings are slightly curved like a measuring tape, the actual curving occurs after the wings have been deployed. Not only the deployed bending stiffness is ensured, also the torsional stiffness of the array is covered. The tension wires form a kind of shear web, which closes the open C-structure, providing the required on-orbit torsional stiffness. Note that the panel curving has no noticeable detrimental effect on the power, as the solar incidence angle, i.e., the cosine effect, is negligible.

For Teledesic, the "Curwin[®]" solar array consists of two wings on top of the Primary Deployment Mechanism (PDM) boom. A double solar array drive mechanism (SADM) links the two wings to the boom, in such a way that the two wings can rotate about the same axis, so they always stay in the same plane together, perpendicular to the sun's rays. Between each of the wings and this SADM, there is a structure in the form of an open Carbon Fiber Reinforced Plastic (CFRP) frame. This snubber frame is located behind the first panel and houses the primary curving system in addition to the tensioning parts of the primary and secondary system. During launch, it also supports the SADM and part of the PDM boom.

Every solar array wing of Teledesic is identical and has 14 panels of 4.3 m x 0.50 m to meet the power demand of 4.3 kW at EOL. The thin panels are made of CFRP carbon fiber face sheet with an aluminum honeycomb. The panel sandwich thickness is 4 mm. In the stowed position, the 14 panels are stacked with a spacing of about 3 mm each. This leads to a total stack height of about 100 mm. The inter-panel hinges at the long edges and a number of cups and cones distributed over the panel surface assure this spacing. Through 6 of these cups or cones at each edge of the individual wing package, an element is running from the hold-down bracket on the spacecraft to the snubber frame that is on top of the panel stack. The other cups and cones are held under compression by this snubber frame on one hand and a so-called snubber frame on the other hand. This snubber frame is meant to increase the number of support points for the panels to meet the stowed resonance frequency requirements of $f_1 > 35$ Hz.

² Olympus solar array was successfully deployed in orbit in 1987

³ Curwin concept and principle has been granted a patent: No: US 6,091,016 and EP No EP 0926 068 by G.J.A.N. Kester ; Fokker Space BV

A dedicated synchronization system [3] guarantees that the deploying panels stay within a certain deployment trajectory. The torque rods of this system are located on the back of the deployed panels. In stowed position they fit within the panel spacing. The deployment phases of a typical Teledesic type array are given in Figure 2.

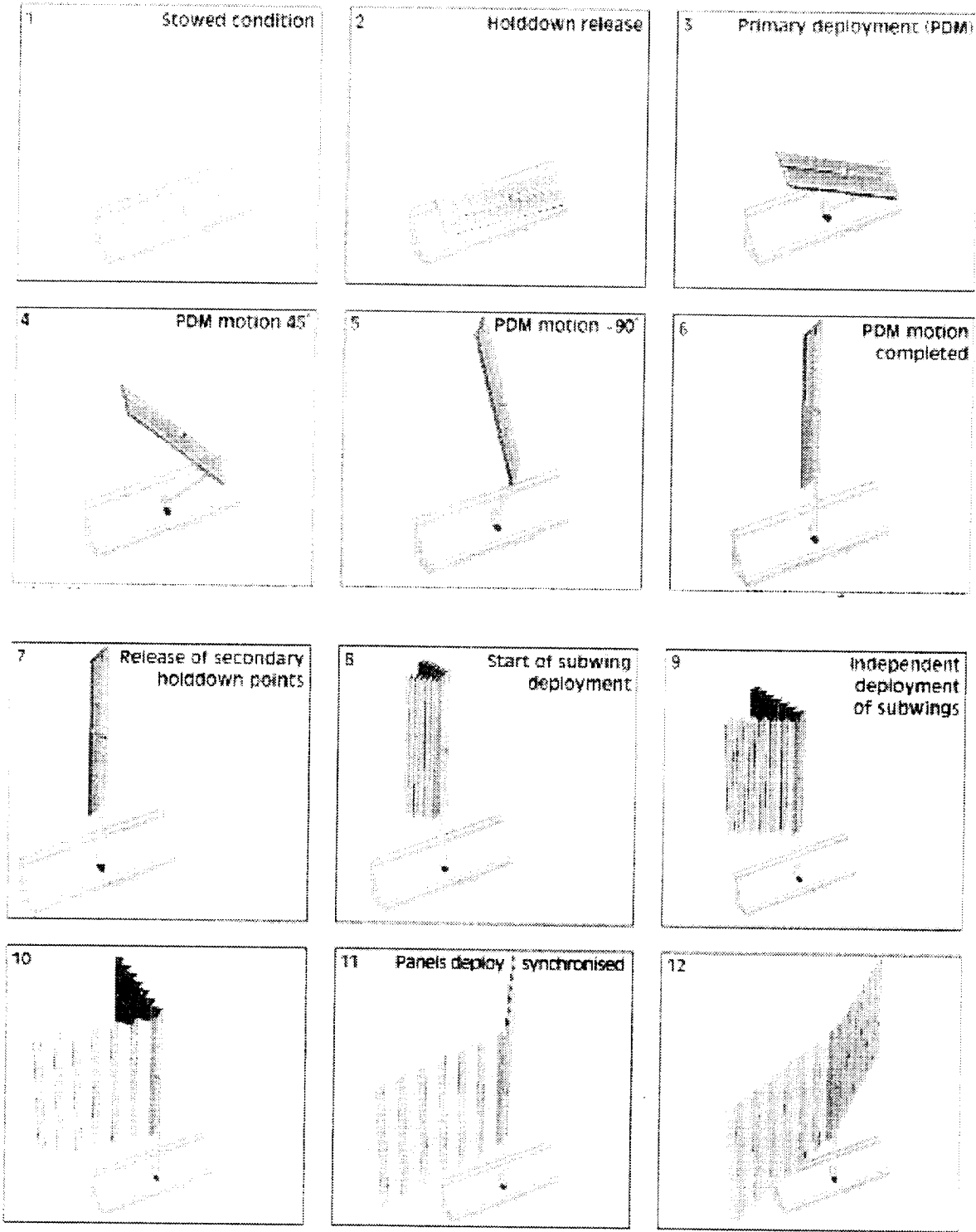


Figure 2. "Curwin" deployment (typical for a Teledesic design case)

Detailed Array Description

The solar array consists of the following major elements:

1. Primary Deployment Mechanism (PDM)
2. Wing solar panel structure with Photo Voltaic Assembly (PVA)
3. Wing Deployment mechanisms
4. Hold down and release mechanism

The following sections provide some details of the wing concept design. Emphasis has been put on the design of the wing hardware, as it contains a high degree of design commonality and design modularity with both programs, being the items 2, 3 and 4 of the above list.

Primary Deployment Mechanism (PDM)

The purpose of the primary deployment mechanism is to create sufficient clearance between the rotating wing and the baseline spacecraft structure. In addition, it ensures minimisation of shadow lines and also provides adequate clearance from the exhaust plumes of the S/C thrust motors. The primary deployment motion is quite different per concept. Still, modular elements such as the limbs and the individual hinges are foreseen. A typical design concept is shown in Figure 3. The PDM also needs to be restrained during launch by 2 of the Advanced Rigid Arrays (ARA)-type hold downs, as it is considered a relative heavy structure mechanism.

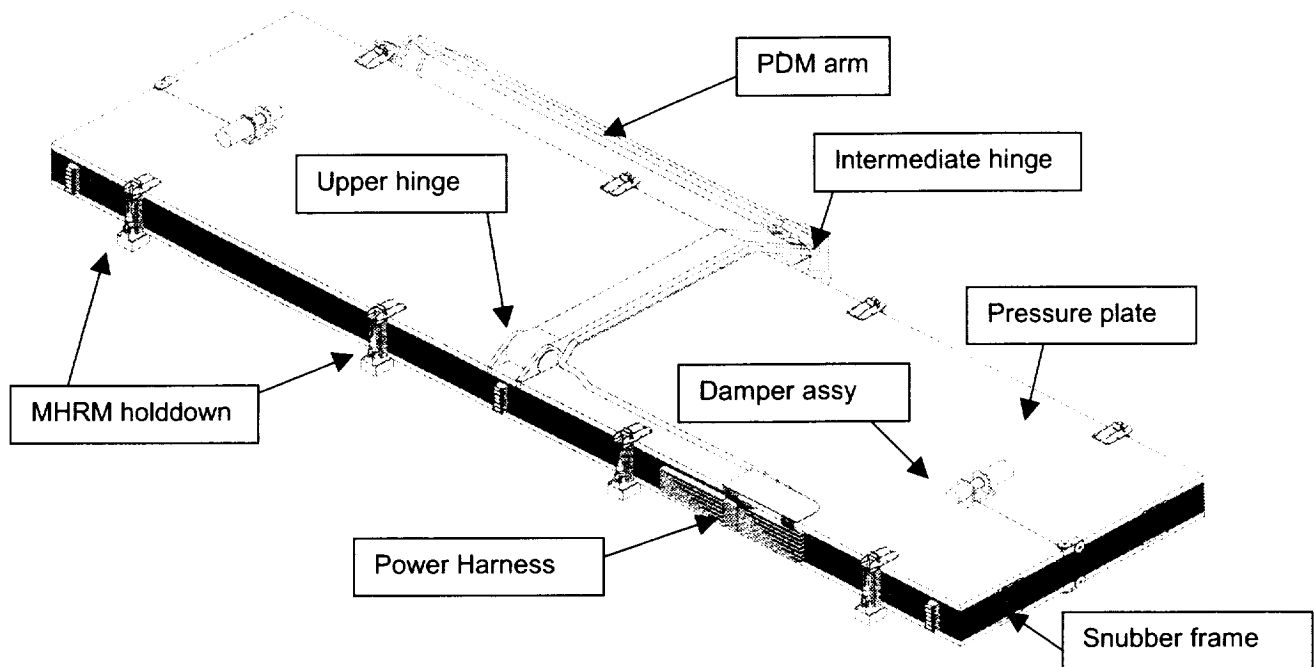


Figure 3. Solar array in stowed configuration with PDM; (Celestri typical)

The Wing Panel Package: The wing solar panel packages structure (2-off)

Each wing package consists of:

- Fourteen (14) thin semi-rigid CFRP panels
 - equipped with thin film type solar cells
 - electrical inter panel power transfer harness
- Pressure plate
- Snubber-frame interfacing with the S/C including the jack curving mechanism
- 2 x 6 primary ARA-type hold-down points
- 2 secondary modified ARA-type hold-down points

Thin semi-rigid CFRP solar panels with PVA

The wings consist of a number of relatively thin sandwich panels, measuring 4.3 m x 0.50 m. The sandwich is Aluminum honeycomb with CFRP face sheets on both sides. The baseline panel thickness is 4 mm. The photo-voltaic assembly is based on the application of large thin film cells such as amorphous Silicon or the novel Copper Indium (Di) Sulphide (CIS) type cells are now emerging. The front side of the panels are equipped with solar cells, while the backside is used for the electrical wiring and the synchronization system. The design of the cell substrate is aimed to accommodate two cell types, i.e., the 'conventional' but heavier and more expensive mono-crystalline Silicon or GaAs type cells as well as the much lighter and cheaper thin film, e.g., amorphous Silicon cells.

Thin film Solar Cell Technology

The concept to be selected should allow the use of novel thin film solar cell technology. The Amorphous Silicon thin film (a-Si) cell is resistant to high radiation environment [2]. An additional reason for implementing this cell type is the low associated cost and low mass. Typically, the manufacturing process allows for bulk production as required for constellations.

Panel and inter-panel electrical harness

The rear side of the panel is equipped with a flexible electrical harness in order to minimize the resistance torque during deployment, especially under the extreme temperature conditions. A single uninterrupted flex-print is design baseline to eliminate the 'conventional' inter-panel power transfer harness and connectors. This will result in a lower mass, compact flat stowage, low cost and a reliable performance. This flex-print design also reduces the multiple ohmic losses at the 'conventional' inter-panel connector junctions. Redundancy requires that there are 2 uninterrupted flex-print harness.

Snubber frame:

The purpose of the snubber frame is to obtain a stiff interface towards the spacecraft structure. As the thin panels have a relative high flexibility, it is required to have a stiff frame such to meet the stowed resonance frequency requirement of $f_1 > 35$ Hz. The CFRP frame has interface points towards the 12 hold down points. It includes the "jack mechanism". (see: deployment mechanisms section)

Pressure Plate (optional)

To close the box, a pressure plate of CFRP is foreseen. The total panel package is kept tight together by means of the earlier mentioned snubber frame and the pressure plate. The pressure plate interfaces with the last life panel. The pressure plate can be deleted in case the spacecraft acts as a supporting structure. This means a close interaction with the S/C builder. As such, 25 mm of stowage height could be saved.

Deployment Mechanisms of Wings

The following deployment mechanisms are foreseen for the wings:

1. Secondary deployment system, i.e., panel hinges
2. Panel curving system with tension wires
3. The hold-down element based on existing and proven ARA design.
4. Deployment damper for speed control

Secondary Deployment System

The panels are equipped with three (3) hinges along their fold lines. The actual deployment of the solar panels starts after the last and central connecting element has been cut. Spring motors actuate the solar panels fold-out. At every hinge line there is a deployment spring in the form of a torsion rod. The deployment of the panels is synchronized by a "soft" synchronization system [3]. Between two adjacent hinge-lines there is a torque tube instead of a pulley and cable system. The synchronization tube is made of stainless steel, but in case the bending stiffness has to be less, carbon fiber is an option. Figure 4 shows some details. The panel hinges only have a stop but no lock. This means that there is hardly any deployment shock. Still, at least one damper is required to better control the deployment trajectory [4]. A small eddy-current or viscous damper is foreseen unwinding a cable pulley system. Hinge backlash is inherently eliminated when the hinge line is curved. The panel hinges are pre-loaded via the curving mechanism and are "forced" to one side of the hinge edge.

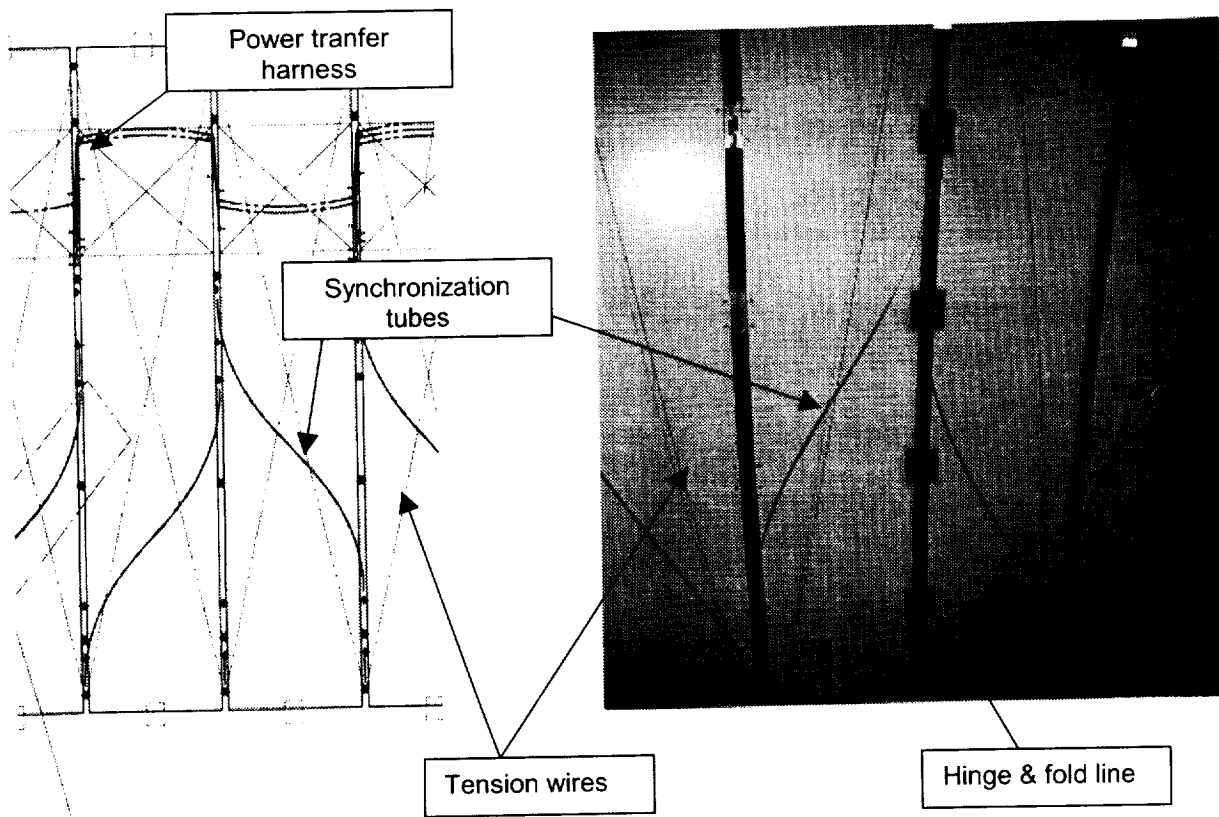


Figure 4. Design of the secondary deployment mechanism (incl. the synchronization "tubes")

During deployment, the panel hinge/fold lines are stiff, because the panels are in different planes. As soon as the panels have lined up at the end of the secondary deployment phase, the panels can be curved to form a curved wing. In addition to the primary curving system, the curvature of the panels is

initiated and maintained by a number of spring loaded rigging wires or straps, which run diagonally behind each panel to all four corners.

When the panels are flat, the wires are stretched for about 25 mm, but as soon as the panels are allowed to curve, the wires shorten 25 mm and pull the panels in a defined curvature. A diagonal layout of the wires is selected to increase the torsion stiffness of the deployed wing. Existing, space qualified and low-mass Kevlar cables are foreseen to be used as panel rigging wires. The tension at start is about 100 N per cable. At the final position, once the panels are curved, the remainder of the pre-tension is about 60 N

The primary root curving system (i.e., "jack" mechanism)

At the root of the wing, embedded in the snubber frame, several provisions are required to allow the wing to change from a flat surface to a curved one. The function of this "jack" mechanism is to initiate panel curving once the deployment is completed.

The number and the design of these provisions are a function of the required curved shape of the wing after deployment. This curving system is sandwiched between the snubber frame and the first panel. Figure 5 shows some details of the design concept. The first panel is fixed to the snubber frame at its tip and base with two shear webs. One shear web is equipped with only one hinge/fold line and the other shear web with two hinge/fold lines. In this way, the panel is allowed to have excursions in the center, in a similar way as a suspended leaf spring.

The concertina structure pushes the in-board panel in the center away for about 200 mm. Hence, the remainder of the wing panels is urged to follow, because of the panel curving system. The hollow side of the curved wing is normally pointing away from the sun. From later breadboard testing it turned out that the mechanism could be avoided, as the curving motion was initiated by the strain energy induced from the tension cables to the individual panels.

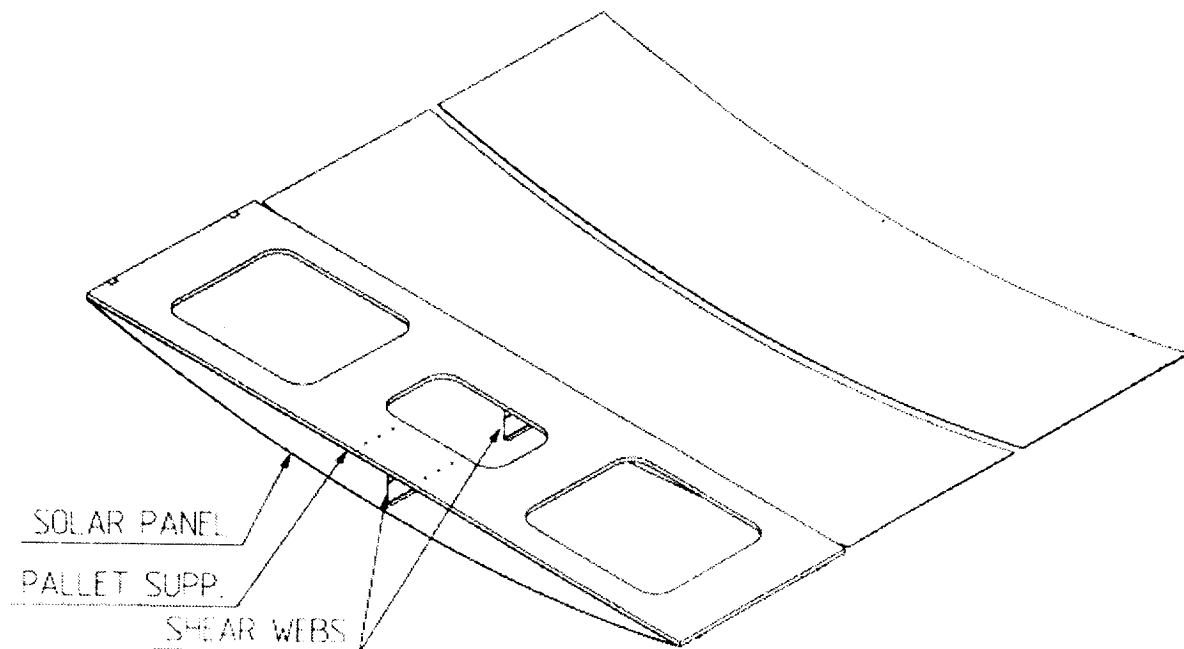


Figure 5. Panel primary root curving mechanism.

The hold-down system

The hold-down system is divided into two systems:

- The primary hold-down system
- The secondary hold-down system

The primary system restrains the 2 stowed wing stacks and the PDM during launch, while the secondary hold-down system functions in the first part of the operational orbit to keep the still stowed panels tied to the snubber frame and prevent premature secondary deployment.

The PDM boom and the two wing stacks of concertina-wise folded panels, are held stowed by two (2) hold-down elements in addition to the twelve (2 x 6) points for each wing, including the restraint elements. The other 'hard points' are not equipped with a restraint element; they act as 'snubber' points. In case the number of points on the spacecraft is not sufficient to support the two panel stacks, a frame-like adapter can be used. This frame will provide the required extra hard points for the solar panel stacks against the S/C sidewall. This snubber-frame itself is fixed to the brackets on the sidewall of the satellite.

A hold-down point consists of a bracket, a hard point in the panels, a restraint element, a tensioning element and a set of 'Thermal Knives'. The restraint element will be based on existing and proven ARA-type technology [5] (Figure 6).

Also, a new hold down mechanism is being developed to achieve a more compact stowage volume. It is called the Multipurpose Hold down and Release Mechanism (MHRM). The cutting action is achieved by a thermal (redundant) knife. The cable type is Dyneema[®], which has a lower melting point than the Kevlar cable used in the ARA type holddown. Also, the cable is now configured in a closed loop, allowing a more compact stowage volume. The location of the MHRM would be along the long edge, as each wing panel package is rather slender. Figure 7 shows the design concept of the MHRM, typical for one panel option. Extension to a larger panel stack will be implemented in the follow on study.

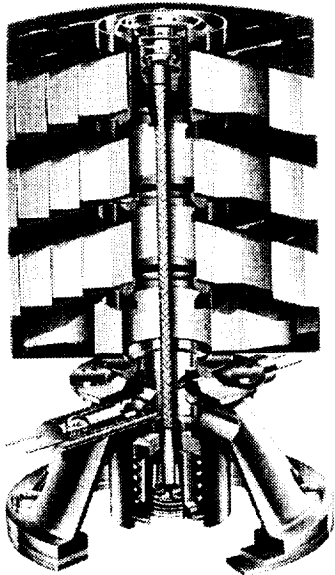


Figure 6. ARA restraint based on a Thermal Knife [5]

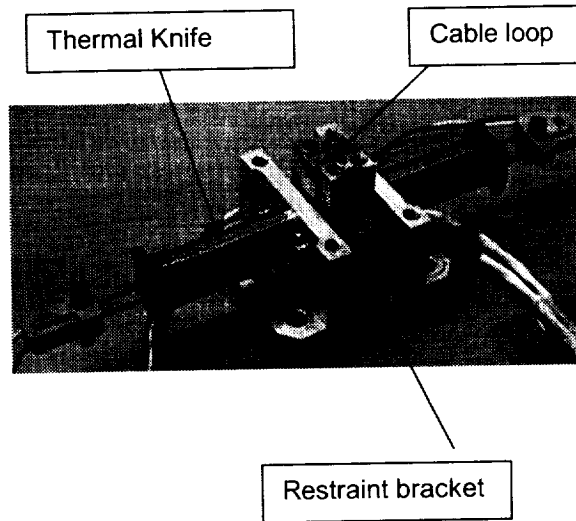


Figure 7. MHRM: Multipurpose Hold down & Release Mechanism [7].

Structural Performance

Deployed Wing Analyses:

Both for the stowed as well for the deployed wing, structural analyses was executed (FEM /NASTRAN). For the deployed wing, also a non-linear analysis was done, in which the sensitivity against the following three parameters was investigated:

- Tension loads in the straps / tension wires
- Amount of curvature of the semi-rigid panels
- Stiffness of the tension wires or straps

It was found that the stiffness of the (sub) wing could be tuned with the above parameters. The lowest frequency was a torsion mode ($f_1 \sim 0.278$ Hz), followed by a bending mode ($f_1 \sim 0.577$ Hz). Increase in torsion rigidity could be achieved by increasing the stiffness of the tension straps in combination with the panel curvature. Also, the PDM-stiffness determines the overall deployed wing behavior greater than expected. This can be tuned by the geometry of the CFRP tube of the primary linkage.

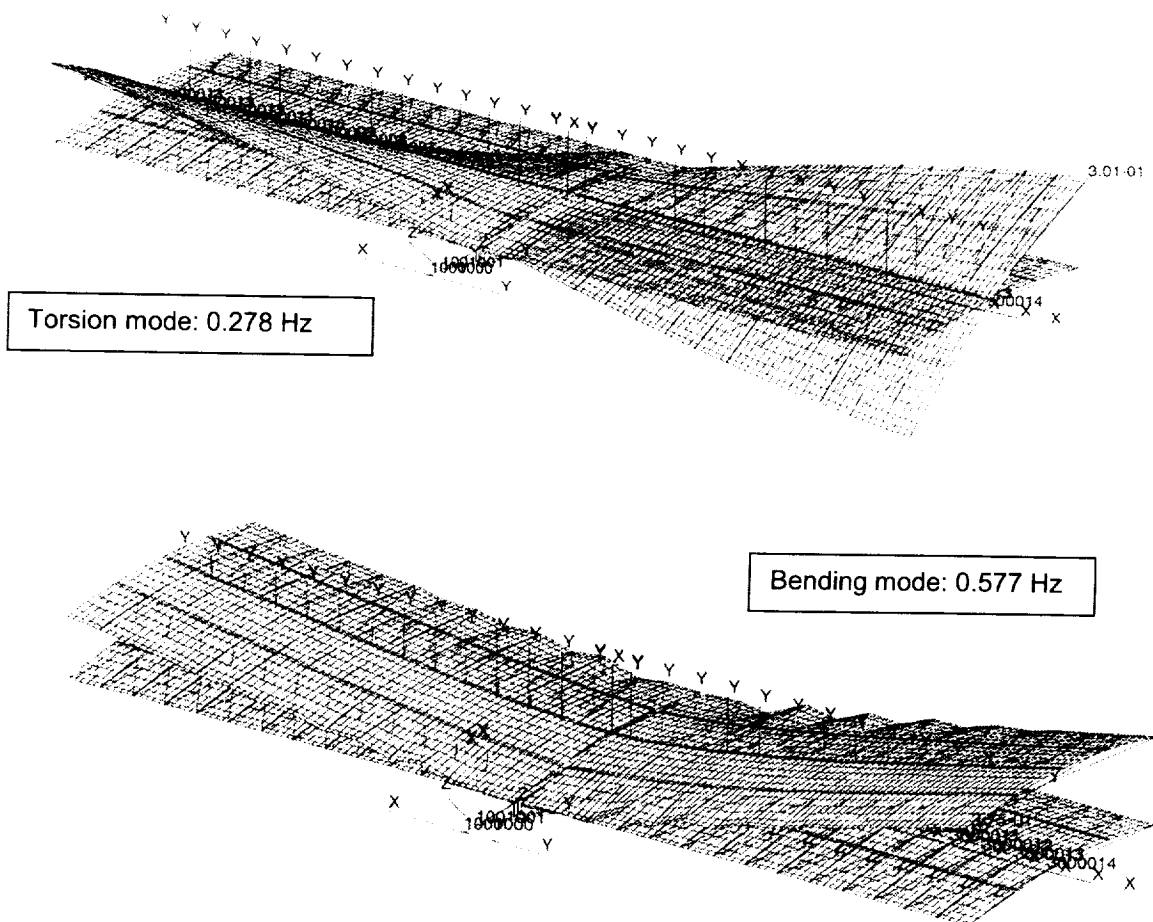


Figure 8. Typical mode shapes of a fully deployed wing (Ref: Teledesic)

Mass performance:

A preliminary mass table (See Table 2) is provided showing the typical masses involved (based on the relative low value of about 8% cell efficiency at EOL conditions). The PDM and all mechanisms are included which contribute to ~30% of the overall mass. Especially, the PDM with the double gimbal SADM is a heavy structure, and is fully driven by the constellation requirements. But in case a normal V-yoke structure is used, and no active motorized PDM hinges are used, considerable mass saving is foreseen.

Note, that in case transfer is made to the much more efficient CIS type thin film cells (i.e., with a predicted efficiency of 15% EOL), the power to weight ratio would increase to about 70-80 W/kg EOL for the 2 individual wing structure(excluding the PDM, excluding 20% margin).

Table 2: Predicted mass performance of a typical solar array (Ref 2; Teledesic)

Assembly	Item	Unit mass typ. (kg)	No	Mass (kg)	
Wing	Solar panel structure CFRP	1.599	14	22.386	
	PVA (based on 8% a-Si cells, 70 W/m ² EOL)	0.540	14	7.560	
	Pressure Plate	5.626	1	5.626	
	Snubber Frame	3.511	1	3.511	
	Inter panel hinges	0.030	40	1.200	
	Inter panel snubbers	0.003	285	0.855	
	Primary hold-down system (per 2)	0.385	6	2.310	
	Snubber frame shear webs	0.146	1	0.146	
	Synchro / panel curving system	2.495	1	2.495	
	Wing damper system	0.920	2	1.840	
	Power transfer harness	1.143	1	1.143	
	Telemetry deployment / wing status	0.120	1	0.120	
	Telemetry / sunsensing	0.500	1	0.500	
					49.692
				2	99.384
	Wings				
	EOL Watts / kg (excl. PDM etc)	43 W/kg			
Solar Array	Primary Deployment Arm	14.187	1	14.187	
	PDM Hold down System	0.266	2	0.532	
	PDM Power Transfer Harness	2.407	1	2.407	
	SADM / gimbal mechanism	15.000	1	15.000	
					131.51
	EOL Watts / kg (with PDM etc)	32 W/kg			

Deployment characteristics:

To predict the deployment behavior, a special purpose program that is normally used for our standard ARA-type solar arrays was updated (SMX-Deploy). Also, the damper effect was included. A sensitivity study was done to investigate critical behavior. It appeared rather quickly that the calculation method with SMX Deploy could not be used. A new deployment program was required that could deal with the highly non-linear behavior. This analysis activity was initiated with the Multi-Body software code called ADAMS, and is now in process.

Bread boarding as part of D & D

A 50% scale model was built comprised of 15 panels of 2.2 m x 0.25 m. A special deployment rig was manufactured to simulate zero gravity. This air bearing deployment rig was based on a previous Fokker Space in-house development [6]. The following tests were performed:

- Functional deployment and life testing
- Torque surplus measurements (indicative)
- Stiffness and backlash (qualitative & quantitative)

The model was stowed and deployed several times (>20x). The wing deployment was initiated by the torsion springs in combination with the synchronization tubes. Initial reservations concerning the deployment initiated were taken away. During the deployment, some panels already curved to their final curvature while others still remained flat. This was not expected and could also not be predicted as it was considered to be a highly non-linear kinematics deployment behavior. It could be expected however, that

any premature curving of the panel would impose excessive friction forces at the hinges. In reality, this was not the case. On the contrary, it helped the deployment motion by the energy released from the contracting tension cables.

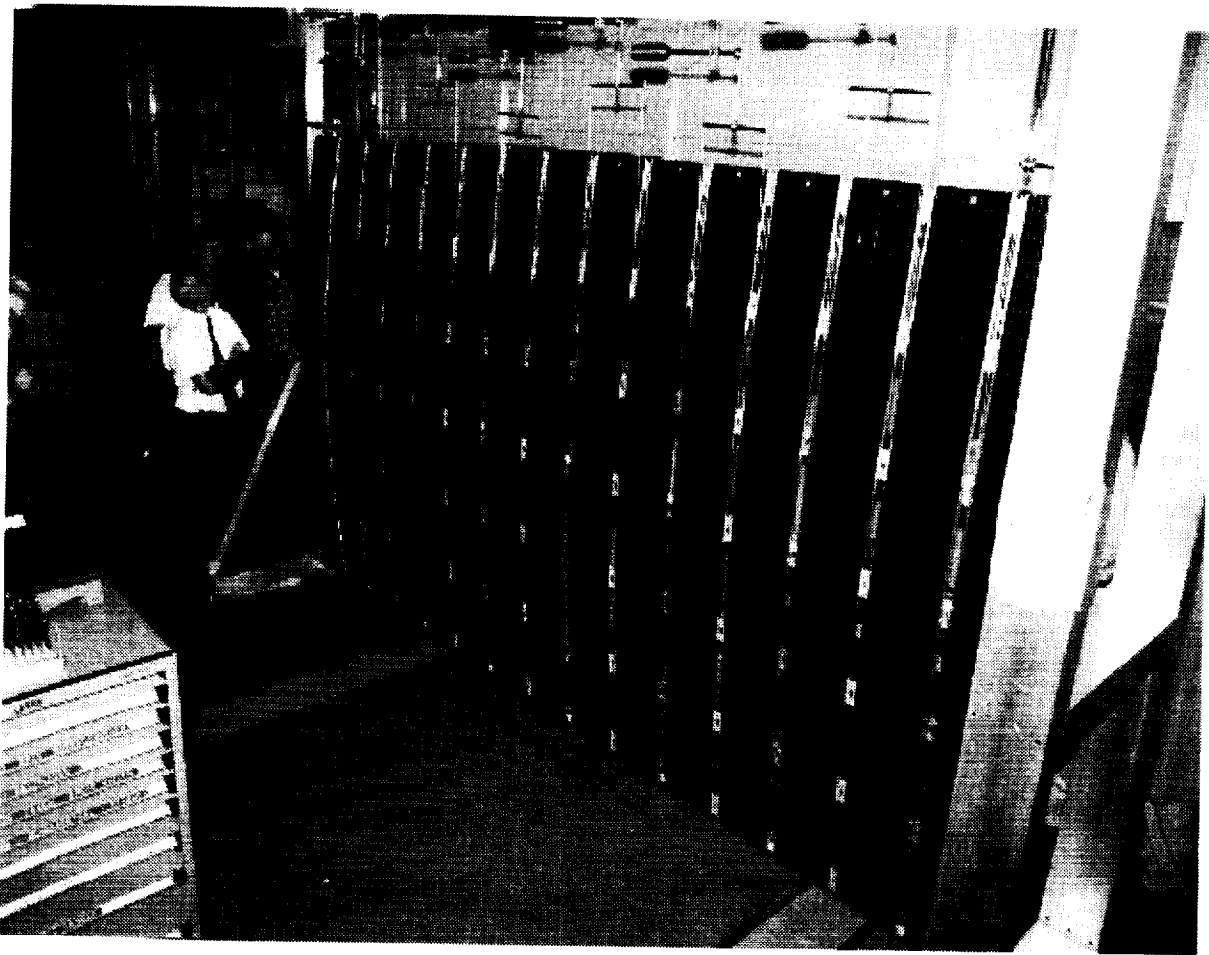


Figure 9. The scale model (50%) of the Curwin in fully deployed state (one wing)

A restart of the deployment was always possible, even when a certain amount of the panels had already reached their curved (=deployed) position. It was observed that the curving of the panels near the deployed condition is not a potential resistance source, but instead stimulates the further deployment of the remaining panels. During the wing BB testing it was clearly demonstrated that some form of damping would be required to control the additional deployment energy coming from the curving panels and also to control the deployment trajectory.

Table 3: Stiffness performance of a typical 50% scale wing (Ref 2; Teledesic)

Out of plane stiffness	EI average	1600 Nm ²
In plane stiffness	EI average	20000 Nm ²
Torsion stiffness	GIp average	740 Nm ²

The stiffness as measured fulfilled the requirement. An expected knock-down of 4 was observed in bending and torsion, however, still meeting the anticipated requirement of $f_1 > 0.3$ Hz for the flight design case. Life testing showed no observable degradation; the tension wires remained intact with no degradation. Although no large shocks occurred, it was considered mandatory to implement a

deployment damper in order to limit the off-axis trajectory of the secondary deploying solar array. The relative soft synchronization requires some type of damper to coordinate the deployment behavior. This was implemented in the update design sketches. The design sketches and their inputs were used for a complete Phase C/D costing and to determine the feasibility of the \$1M / array. Unit developments were identified for further detailing and costing for phase C/D. More effort is required for the AIT streamlining as this determines the bulk costing for the recurring phase.

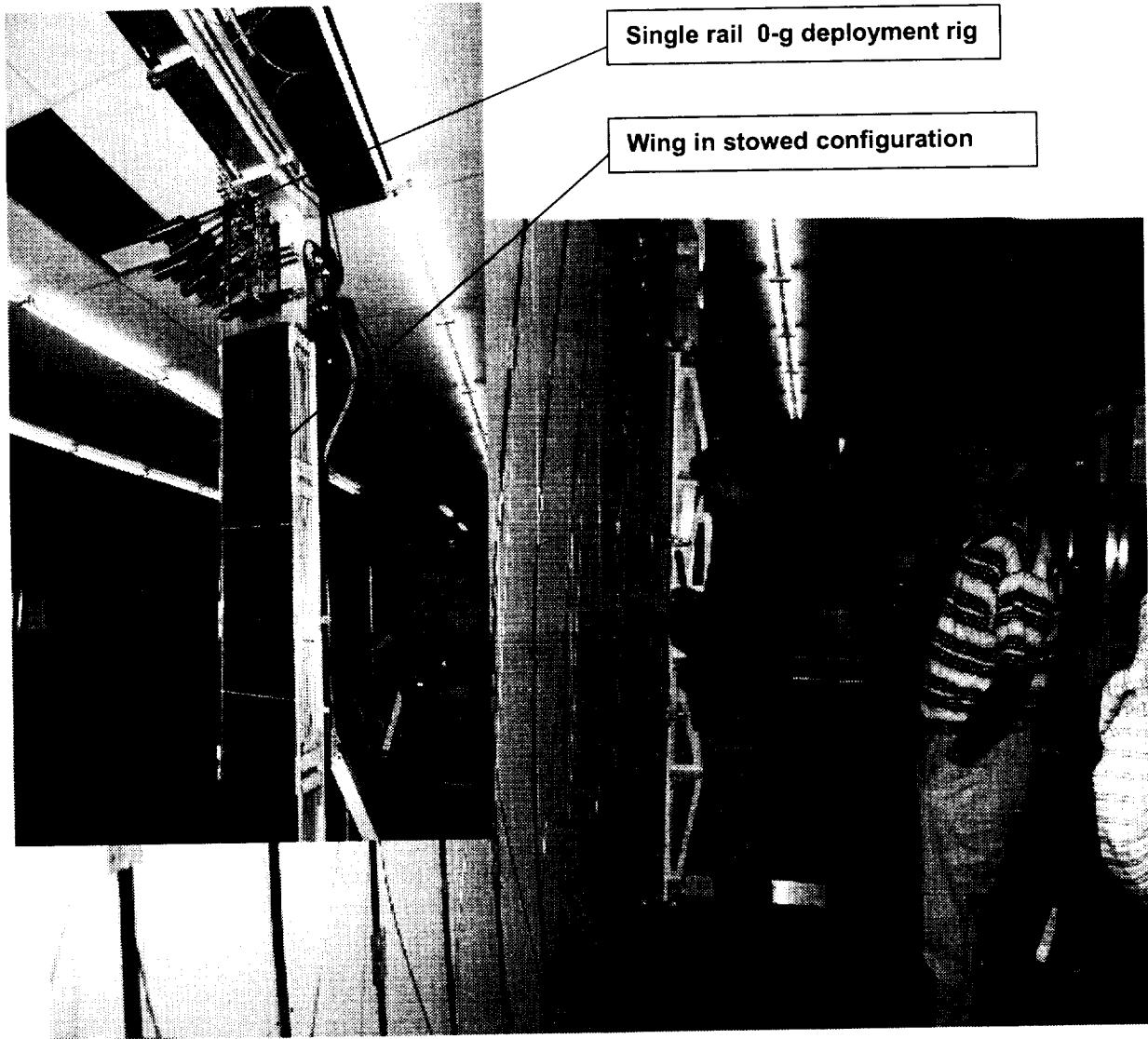


Figure 10. Curwin fully deployed, shown from rear side showing synchronization tubes and tension cables

Conclusions

The reservations concerning the deployment feasibility and associated deployment principles were fully covered by the 50% scale breadboard model. Deployment was feasible despite first reservations. Stiffening of the deployed array by bending the ultra-thin panels not only worked on paper, but was also proven in extensive BB-testing.

Summarizing:

1. Compact stowage of the thin panel stack can be achieved, still meeting the frequency requirements for both the stowed configuration as well as the fully deployed configuration.
2. The mechanism complexity such as HDRS and hinges are well known and therefore are not considered a large risk (Fokker Space BV design heritage).
3. The PDM is a relatively complicated and costly mechanism due to the required deployment trajectory. Commonality for Teledesic and Celestri could still be achievable.
4. A power-to-weight ratio of 35 W/kg at EOL for MEO and also under a relative high radiation environment after 10 years seems achievable. This is the case for the thin film cells, but even more for the CIS type cells, which offer better performance. (i.e., 70 to 80 W/kg at EOL conditions)
5. Implementation of thin film technology on ultra thin panels was selected as the most favorable cell technology. This could be either a-Si type cells, new CIS type cells presently under development or even ultra thin GaAs cells which are now also emerging.

Acknowledgements

I want to thank the Dutch NIVR for funding this study. Without their help, a "jump start" would never have been possible. They realized the importance to be there in time. Also, the phase-A and phase-B team, which created a tremendous output in such a short time. This helped the design team to establish a baseline relatively quickly. Last but not least, the hardworking BB-team, which, with their enthusiasm, were able to create, build and test this 50% scale model in just 3 months.

References

1. Curwin Solar Panel System: Patent No: US 6,091,016 and Europa 97204099.2
2. Phase B1 data package to NIVR CONSA and a-Si developments: CONSA-SER-SER-095
3. Solar Panel Synchronization System patent No US 6,031,178 and EP 98200951.6
4. BB test results of ½ scale Curwin[®] model: Phase B1 study note CONSA-FS-SER-094
5. Thermal Cutting Hold-down & Release Mechanism. *Second European Space Mechanisms & Tribology Symposium*, Meersburg, Germany, Symposium Book ESA SP-231.
6. Fokker Space Solar Array Deployment Rigs (A. P. Eggers and H. J. Crujissen; *33rd Aerospace Mechanisms Symposium*, Pasadena, California May 1999; NASA/CP-1999-209259.
7. System for holding together and separating parts of a construction: US patent: 5,716,157 and EP:0716982

536/10

Hitchhiker Marman Band Interconnect Linkage

Gary R. Slebzak* and Gene Barrett*

Abstract

The Hitchhiker (HH) project offers experimenters the ability to eject small satellites into orbit from the Space Shuttle's cargo bay. During launch the satellite is secured to the HH ejection system using a pyrotechnically releaseable marman band assembly. Due to an on-flight anomaly, the actuation of the marman band assembly was examined using high speed video. The video showed a potential for re-contact of the marman band assembly with the satellite from rebound effects before the satellite was sufficiently deployed, thereby creating a hazardous satellite tip-off situation. This paper describes how the energetic release and subsequent motion of the assembly is controlled through the use of a clamp interconnect linkage system in conjunction with a system of pull down springs. The linkage system was selected as opposed to a more conventional "catcher" system due to hardware specific interfaces and adaptability to existing band hardware. The linkage system controls the releasing band motion by supporting and decoupling the pyrotechnic cutter mass from the clamp portion of the assembly, allowing unrestricted motion of the clamps until the system is in the fully expanded condition at which point the linkage acts as an over-center mechanism inhibiting rebound and collapse of the assembly back toward the satellite. In addition, the entire assembly is pulled down and away from the satellite and separation plane by the pull down spring system that also secures it in the post deploy configuration. Since the entire actuation takes place in less than 30 milliseconds, successful functional testing of the newly developed mechanism was documented and verified using high-speed video at 1000 frames/second.

Introduction

The Hitchhiker project is sponsored by the Shuttle Small Payloads Project (SSPP) at Goddard Space Flight Center (GSFC). The SSPP has been providing the technology and hardware for ejecting small satellites into orbit using the Space Shuttle as a platform since the mid 1980's. This service began with the NUSAT satellite in 1985 as part of the Get Away Special (GAS) program. NUSAT became the first satellite to be ejected from a shuttle carried GAS canister using the GAS Ejection System, which later evolved into the Hitchhiker Ejection System (HES). The latest series of satellite deployments during 1998-1999 has used a combination of the HES and the more versatile Pallet Ejection System (PES). It was during one of these deployments, MightySat-01 on STS-88 in December of 1998 that standard orbiter video taken during the satellite ejection also detected debris apparently generated during the deployment. It was determined that the debris was, in fact, one of the components of the ejection system and that prompted an extensive investigation into the cause of the anomaly. The investigation proved to be both educational and enlightening. The cause of the debris was not that dramatic and was traced to a workmanship issue. However, the investigation further revealed deficiencies in the ejection system configuration only detectable by the use of high-speed photography. The Hitchhiker (HH) marman band interconnect linkage is the design improvement developed to correct the inherent deficiencies discovered in the ejection system marman band used in both the HES and PES.

Ejection System Background

The SSPP ejection systems (Figure 1, PES shown) are similar in design and use the same basic technique for deploying satellites. Essentially, the satellite is placed onto a spring-loaded push plate, which is compressed and secured to the ejection system base using a marman band clamp assembly (Figure 2). The marman band assembly was developed in the early 1970's by Rockwell for deploying satellites from Delta rockets and the design has been used without change. The assembly consists of two halves of the marman band, which clamp the satellite and base together using separation bolts. The halves are also connected to each other by means of leaf springs, which assist in band separation and keep the released band as a single assembly following deployment. The released

* Swales Aerospace, Beltsville, MD

assembly is captured using a series of retaining springs, which secure it in the post deployment position. To deploy the satellite the separation bolts are cut with pyrotechnically actuated bolt cutters

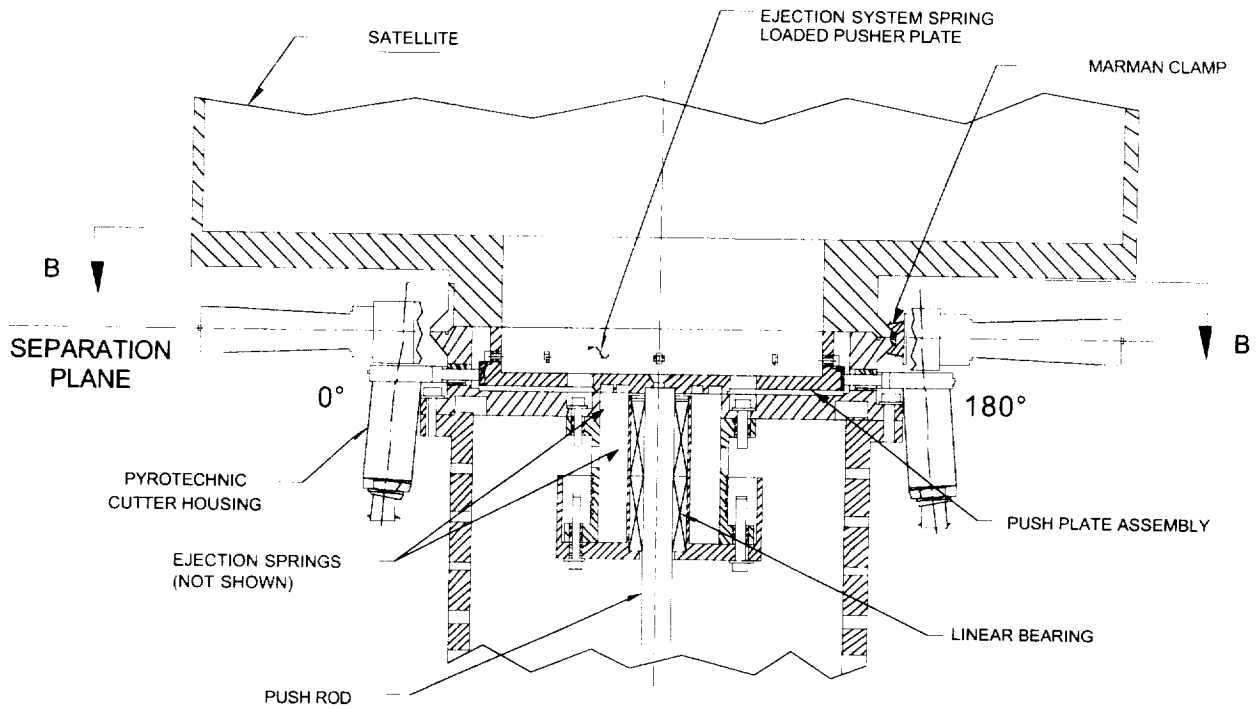


Figure 1. Integrated Satellite, PES, Marman Band Assembly Section

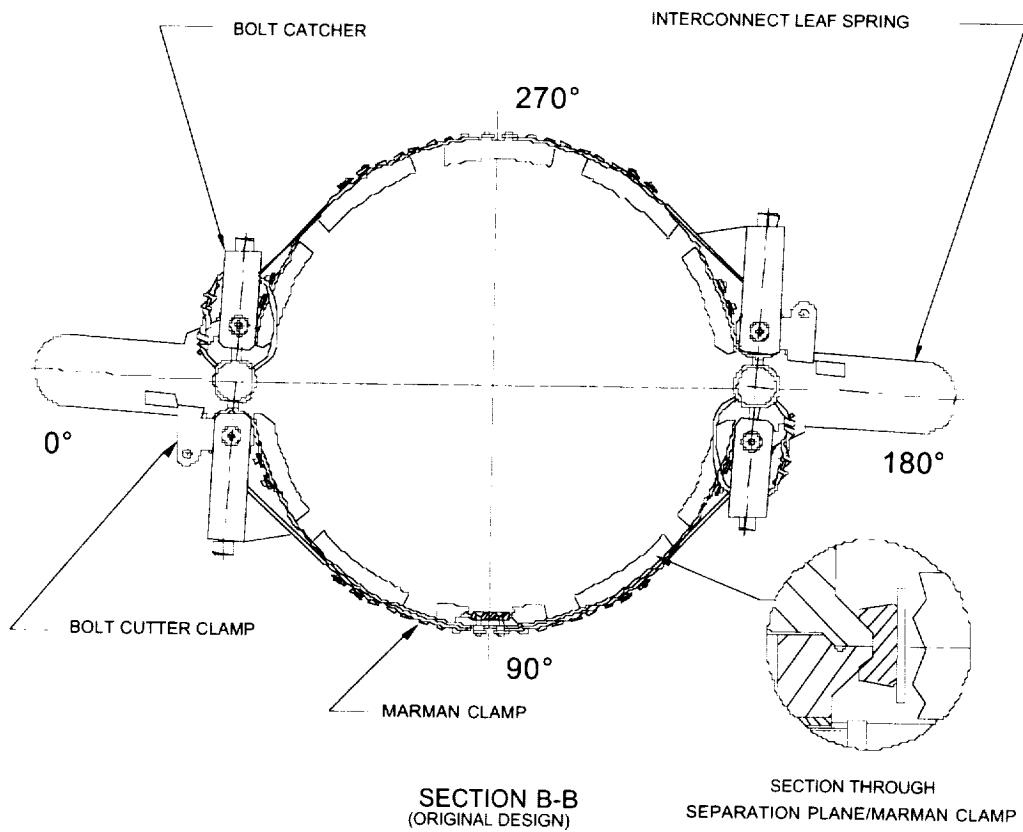


Figure 2. Original SSPP Marman Band Assembly

releasing the marman clamp and thereby, allowing the spring loaded push plate to eject the satellite into orbit.

During the investigation connected with the on orbit debris issue, the motion of the marman clamp assembly was studied using video recorded at 1000 frames per second. When viewed at a playback rate of one frame per second, this video revealed that the marman clamp assembly would separate, reach the end of travel, rebound back and re-contact the separation plane before the satellite could be deployed. Any re-contact with the satellite prior to being fully deployed could result in a hazardous "tip-off" and mission-compromising situation. It was also apparent that the basic configuration of the assembly had a tendency to exacerbate separation plane re-contact. Design improvements were required to eliminate the hazardous condition and improve overall system reliability.

Marman Clamp Design Improvement

Design Requirements

The following goals were established to guide the design improvement effort:

1. Eliminate the re-contact of the marman band assembly with the satellite and/or separation plane, thus, avoiding a safety hazard.
2. Prevent any change to the marman band clamping load path, which would invalidate previous analysis, and testing.
3. Improvements must be retrofittable and compatible with both the HES and PES.

To meet the design requirements, it was necessary to do a more in depth study of the high-speed video and attempt to isolate problem areas in the existing design. Several points were identified:

1. When released the marman clamp assembly reacted in a very uncontrolled and undesirable manner.
2. The bolt cutter assemblies comprised a large portion of the overall mass of the marman clamp assembly. Their method of attachment to one end of each clamp inhibited the free motion of the band as it expanded in a "tail wagging the dog" fashion. The cutter assembly immediately pivoted about the end of the clamp bumping and slapping the separation plane during release. The design of the clamp used to secure the bolt cutter was inadequate and in need of improvement.
3. The interconnect leaf springs which joined the two marman clamps, were determined to have little effect in band separation compared to the strain energy in the band due to the bolt preload. The leaf springs, in fact, contributed to the rebound effects of the band due to their stored energy when fully expanded at the end of travel.
4. The stops that the marman clamp assembly come to rest on after separation were located such that they would direct the rebounded assembly back toward the separation plane. A more robust design was needed to accommodate impact loading.
5. The retaining springs that secure the marman clamp assembly after separation, if redesigned, could act as "pull-down" springs and contribute to the controlling of band motion.

Design Trade-offs

Based on the design requirements and the existing hardware configuration and deficiencies, design approach trade-offs were performed. Two approaches were considered:

1. The more conventional method for marman band applications, which would involve adapting the ejection systems to incorporate a "band catcher".
2. The hardware specific approach in which a series of design improvements to the existing hardware is used to meet the requirements.

Conventional approach - Band Catcher

Preliminary concepts for a band catcher revealed that any type of mechanism that would meet the safety requirement for fail safe operation of the dual bolt cutters involved complex configurations. In addition, the mechanism would have to adapt to the ejection systems such that they could be integrated into the SSPP standard 141 liter (5 ft³) canister which has a 50.8-cm (20-inch) inside diameter. Since the marman clamp assembly has approximately a 25.4-cm (10 inch) outside diameter in the clamped configuration, there would be limited space for the assembly to actuate during deploy and still be captured by a second mechanism. There were also reliability issues concerning an additional mechanism of that complexity. Finally, the catcher mechanism would have to adapt to both the HES and PES, which have substantially different base configurations that would involve design(s) of separate interface mounting hardware.

Hardware specific approach

The hardware specific design approach, which was adopted, involved modifying the existing hardware only as needed to control the motion of the marman band assembly to meet the requirements. By minimizing and delaying rebound effects, as well as translating the assembly down and away from the separation plane, the motion of the assembly could effectively be controlled. Thereby, satisfying the requirement of eliminating re-contact with the separation plane. Also, since the modifications only affected the marman band assembly, they were easily adapted to both the HES and PES. It was determined that the bolt cutter housing(s) contributed only negative effects to the marman clamp assembly actuation. Decoupling the mass of the bolt cutter housing from the marman clamps would permit the clamps to freely separate during actuation and redirect the energy that was causing the cutter housing to impact the separation plane. It was decided that a linkage could be adapted to the existing load clamping components of the assembly allowing the clamps to freely separate and, in addition, support the bolt cutter housing. In addition to the incorporation of the linkage to control the marman clamp assembly movement, the existing retaining springs could be redesigned to have greater capacity and function as pull down springs as well. By also redesigning and relocating the stops well below the separation plane, the springs could pull the band down and away during actuation.

Marman Band Interconnect Linkage

The linkage named the, **Marman Band Interconnect Linkage (MaBIL)**, was designed such that it could use the excess energy of the expanding clamp assembly to move the bolt cutter radially away from the separation plane and then when fully extended act as an over center latch to minimize rebound.

The MaBIL (Figure 3) replaced the leaf springs as a clamp interconnect feature eliminating the stored energy effects contributing to rebound. Additional benefits of MaBIL are the relatively large mass of the links compared to the total marman clamp assembly and linkage joint friction, both of which contribute to the slowing of the energetic separation.

Design

As with many hardware designs, cost and schedule are always of concern and this was no exception. In particular, schedule was in the forefront. The SSPP ejection systems were essentially grounded due to the safety concerns until the satellite re-contact issue was resolved. It was highly desirable to develop a sound design with as little iteration as possible.

The linkage configuration that was developed consists of a central bolt cutter clamp connected on each side to the existing marman clamps through a series of two links. Using the parametric 3D modeling capability of Pro Engineer™ to model the existing marman clamp components and develop the new design, it was made possible to assure correct interfacing with the existing hardware and avoid interferences in the newly designed components. The modeling also made it relatively easy to assess the linkage in the pre-deploy (clamped) and post-deploy (open) condition. Configuring the linkage to collapse into the small volume available when the marman band assembly was in the clamped condition became the starting point for the design. It was essential that the links and bolt cutter clamp were able fold up without interference, providing access to the bolt cutters and other components. Once configured in the closed position the length of the links were optimized in the expanded configuration to function within the envelope of the 50.8-cm (20") diameter canister while providing the greatest amount of expansion for deployment.

The details of the design were added to the basic linkage configuration. Link connections were designed as clevis joints to assist in load transfer and minimize binding effects. The completed design was structurally analyzed to provide positive safety margins using factors of safety of 2.0 on yield and 2.6 on ultimate material strength. These factors of safety were used in lieu of structural testing as specified in the **HH Cars Accommodations & Requirements Specifications (CARS)**, 740-SPEC-008, thereby, minimizing testing and reducing cost and schedule impact. The analysis was also used to optimize component features. Thermal compatibility between linkage component materials and other interfacing components was required to assure that the mechanism would actuate properly at all environmental extremes. Based on these factors corrosion resistant steels from the Table I of "Design Criteria for Controlling Stress Corrosion Cracking", MSFC-SPEC-522B, were selected, 15-5 PH condition H1025 for the links and cutter clamp, and A286 hardened to RC 30 min for the clevis pins.

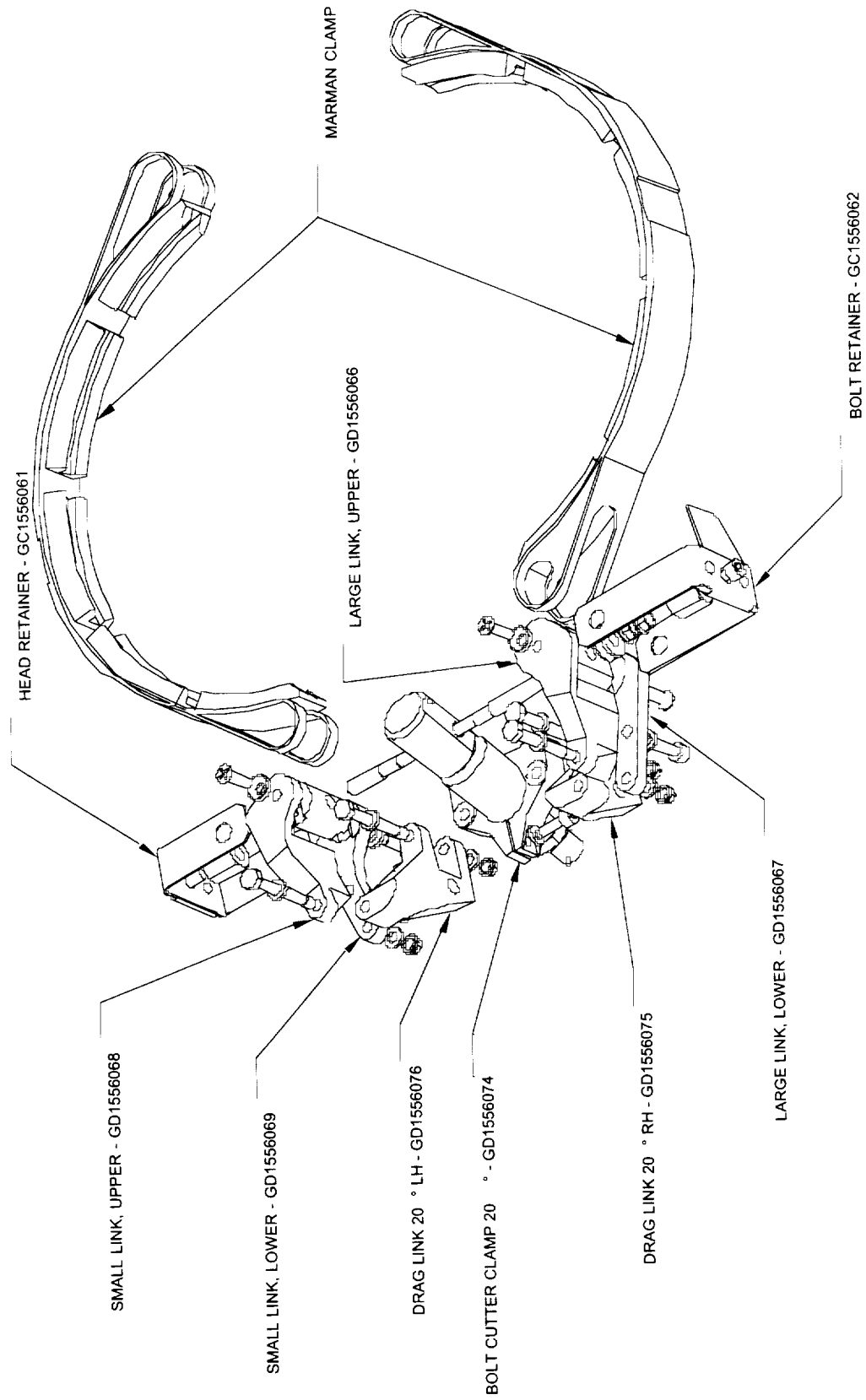


Figure 3. Exploded View - Marman Band Interconnect Linkage

Preliminary Test & Evaluation

Since the unproven linkage design was being fabricated from relatively costly materials requiring a longer procurement cycle and considerable machining time due to the material toughness, the decision was made to develop an Engineering Test Unit (ETU) using readily available, easily machinable materials. The ETU (Figures 4, 5 & 6) provided many benefits:

1. Development and verification of component fabrication programs using less costly materials
2. Design verification tool for form, fit and assembly techniques
3. Low level functional testing of linkage assembly via manually releasable separation bolt
4. Increased confidence level in design

The ETU assembled easily, requiring no additional procedures or processes. When assembled a few design improvements became apparent. Most notably, by threading the bolt cutter clamp screw access hole in two of the links, setscrews could be installed after assembly to eliminate the free movement the bolt cutter assembly, which was a concern under launch vibration conditions. When assembled using a manually releasable separation bolt, functional tests with up to a 10% separation bolt preload could be repeatedly conducted, filmed at normal and high speed and reviewed without the expense and availability of using pyrotechnically actuated bolt cutters. Numerous tests were performed and in all cases the mechanism actuated nominally. As a final test of the ETU, the opportunity became available to perform a single test with the full 8896-N (2000-lb) separation bolt preload and record it using high-speed digital video.

With the increased level of confidence in the linkage design provided by the ETU and testing, materials were ordered and fabrication of the protoflight unit authorized.

Protoflight Test & Evaluation

As was learned during the investigation into the on flight anomaly, viewing the playback of the assembly's actuation recorded on high speed video proved to be the only acceptable method of verifying that MaBIL met the requirements. For the protoflight functional testing the opportunity became available to use high-speed digital video as opposed to high-speed film cameras used during the previous investigation. The digital video, while not having the resolution of the film cameras, provided other advantages. Before performing a test, the setup could be verified to be functioning properly, and following a test, the recording was available for immediate playback without having the delay due to film processing. The immediate playback feature provided the ability to tweak or change the setup based on what was viewed in the previous test. The overall test time was also reduced improving cost and schedule. The HH Marman Band Interconnect Linkage Test Procedure, SSPP, 870-PROC-587, was developed to specify the test article configuration, functional tests, thermal tests and vibration tests required for the flight qualification of the MaBIL.

Functional Test

The functional tests consisted of assembling the protoflight units to the PES in a full flight configuration (Figures 7) and taking high speed video at 1000 frames per second from the top and side of both the nominal dual pyrotechnic bolt cutter and single bolt cutter firings. The videos were then reviewed at a playback rate of 1 frame per second to determine if the requirements were met. Real time observations of each test gave the indication that the linkage controlled the motion of the actuating mechanism as expected. Review of the video playback confirmed that in each case the MaBIL performed as designed, permitting the marman band to release independent of the bolt cutter (mass), while the supported bolt cutter was moved radially away from the separation plane. Then, once the band expanded to the end of travel, the bolt cutter remained in the "locked out" configuration (Figures 5 & 7), allowing minimal rebound of only the marman clamps. The pull down springs effectively pulled the assembly below the separation plane and to rest on the stops. Incidental contact was limited to contact between the marman clamp shoes and the ejection system support base with said contact occurring below the separation plane. Based on these observations the MaBIL was determined to have met the functional design requirements and could be subjected to environmental testing.

Thermal Testing

The thermal testing consisted of subjecting the test article to one thermal cycle, from the hot case at +70°C to the cold case at -50°C, with a four-hour soak period at each extreme. Then back to each temperature extreme for a final four-hour soak and mechanism demonstration. The mechanism demonstration consisted of a worst case single cutter firing and only visual observation since the

facility precluded the taking of video. In both the hot and cold case the mechanism was observed to actuate nominally and in a controlled manner as in the functional tests.

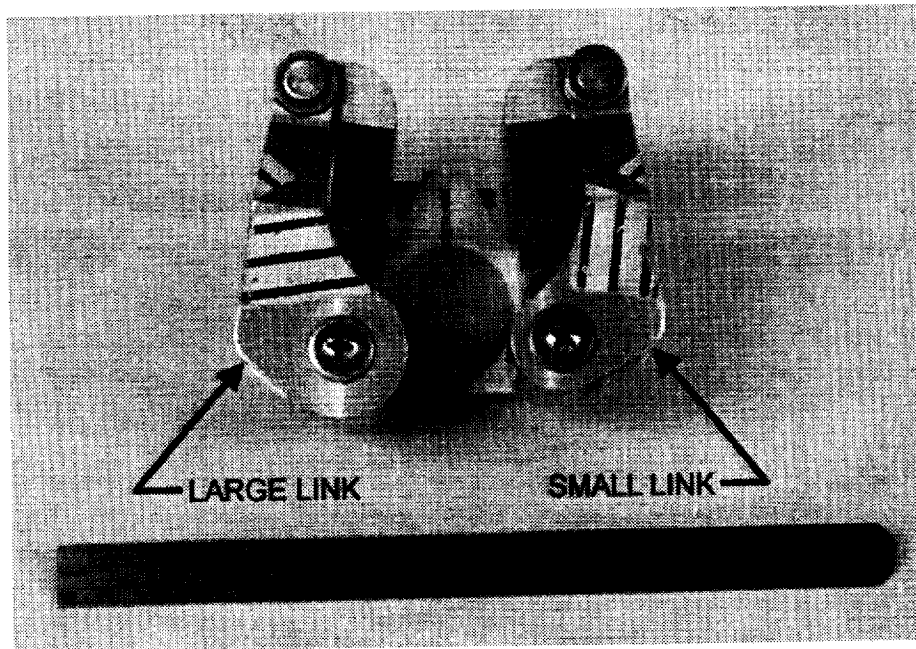


Figure 4. Linkage ETU - Clamped Configuration (Top View)

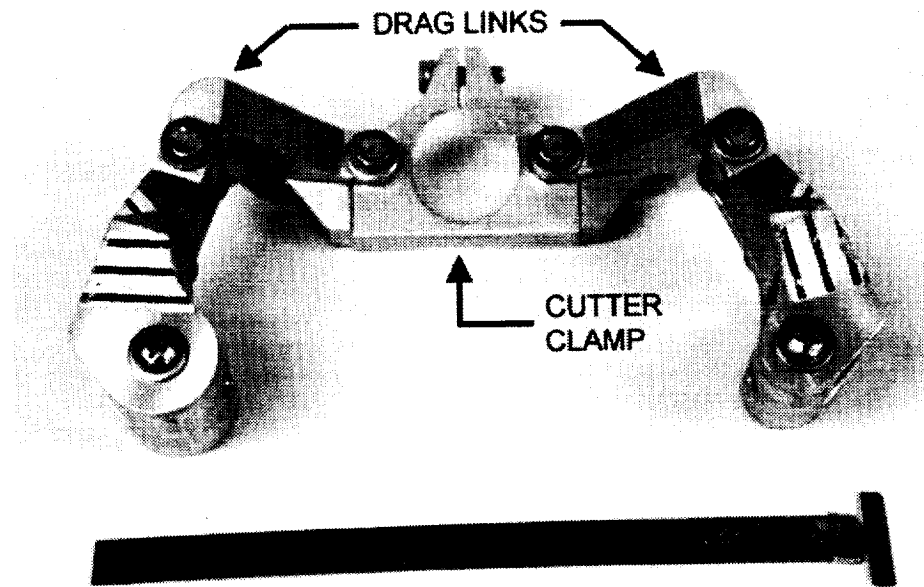


Figure 5. Linkage ETU - Expanded "Locked-out" Configuration (Top View)

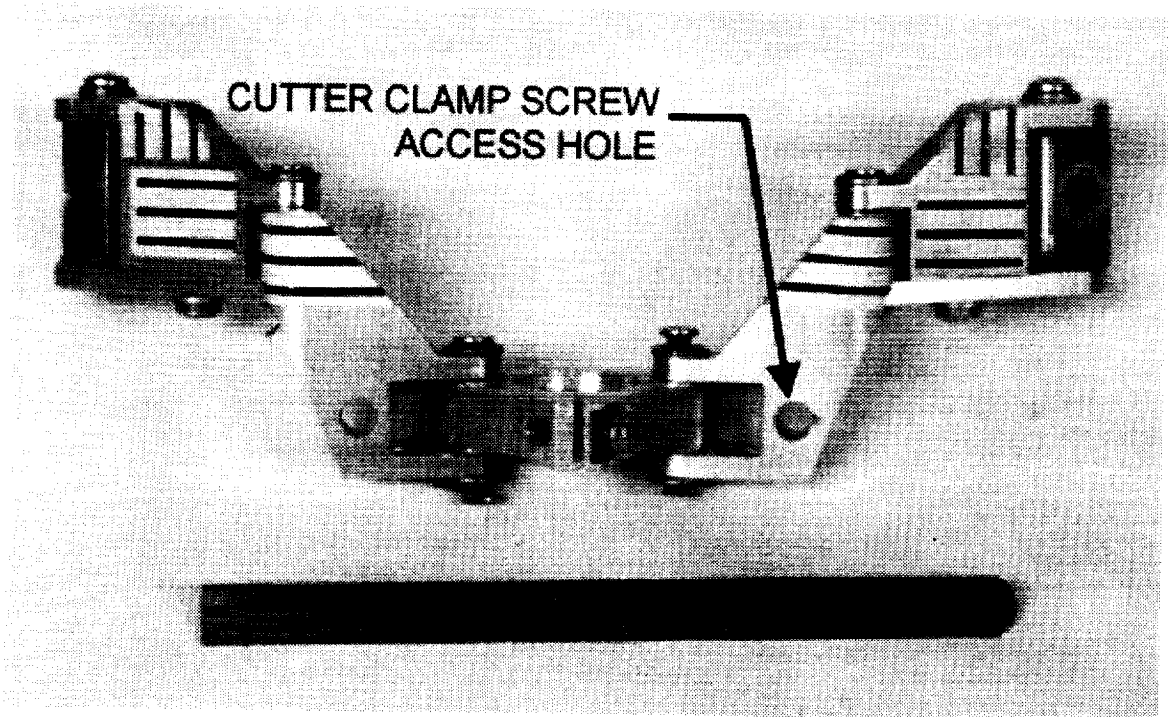


Figure 6. Linkage ETU - Unfolded (Side view)

Vibration testing

The test article was subjected to random vibration testing to the General Environmental Verification Specification for STS & ELV Payloads, Subsystems & Components, GEVS-SE, protoflight levels of 14.1 G_{rms} for one minute in each of two axes. The first was the "Z" or vertical axis and the second a "X/Y" composite or horizontal axis. Ironically the only anomaly noticed during vibration testing was the backing off of improperly staked setscrews used to eliminate vibration in the clamped configuration of the linkage. A post vibration functional test consisting of dual pyrotechnic bolt cutter firings was conducted to verify results. The post vibration functional mechanism demonstration was observed to actuate nominally and in a controlled manner as in the functional tests.

Conclusion

The marman band interconnect linkage mechanism permits the existing SSPP ejection system marman clamp assembly to meet the primary requirement of eliminating satellite re-contact during deployment by channeling the stored energy present in the system to actuate and control assembly motion. Compatibility and adaptability requirements are simply met since the linkage is a one-to-one replacement for the existing assembly components. It demonstrates a significant improvement to the well used, tested and analyzed mechanism.

Utilizing the 3D modeling capability of Pro Engineer™ for design development provided an efficient and accurate method for meeting the design goals.

The use of high-speed video recording as a test and investigation tool has proven to be an important development for SSPP in mechanism evaluation and documentation. Since its initial use during the HH on flight anomaly investigation, high-speed film and high-speed digital video have been used extensively for the test and evaluation of mechanisms on the HH, Triana, and SHELS projects. The video playback is also an effective tool for demonstrations and presentations.

The first scheduled application and flight for the new linkage will be during the summer of 2001. The SimpleSAT experiment will be deployed using the PES aboard Discovery STS-105.

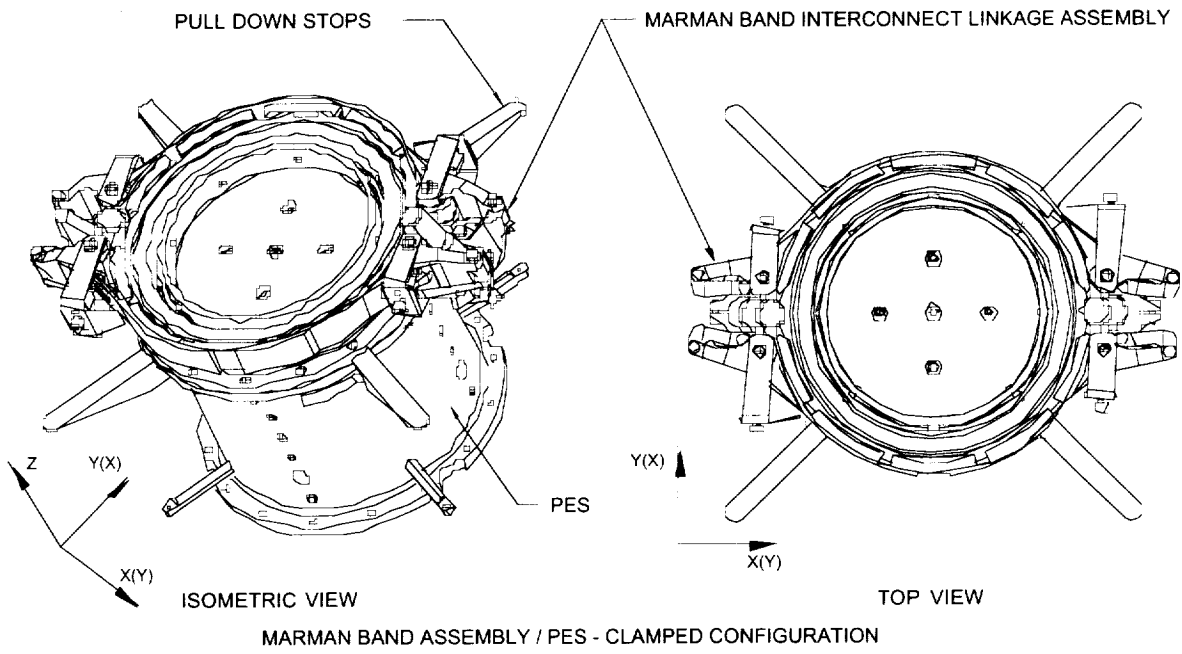


Figure 7

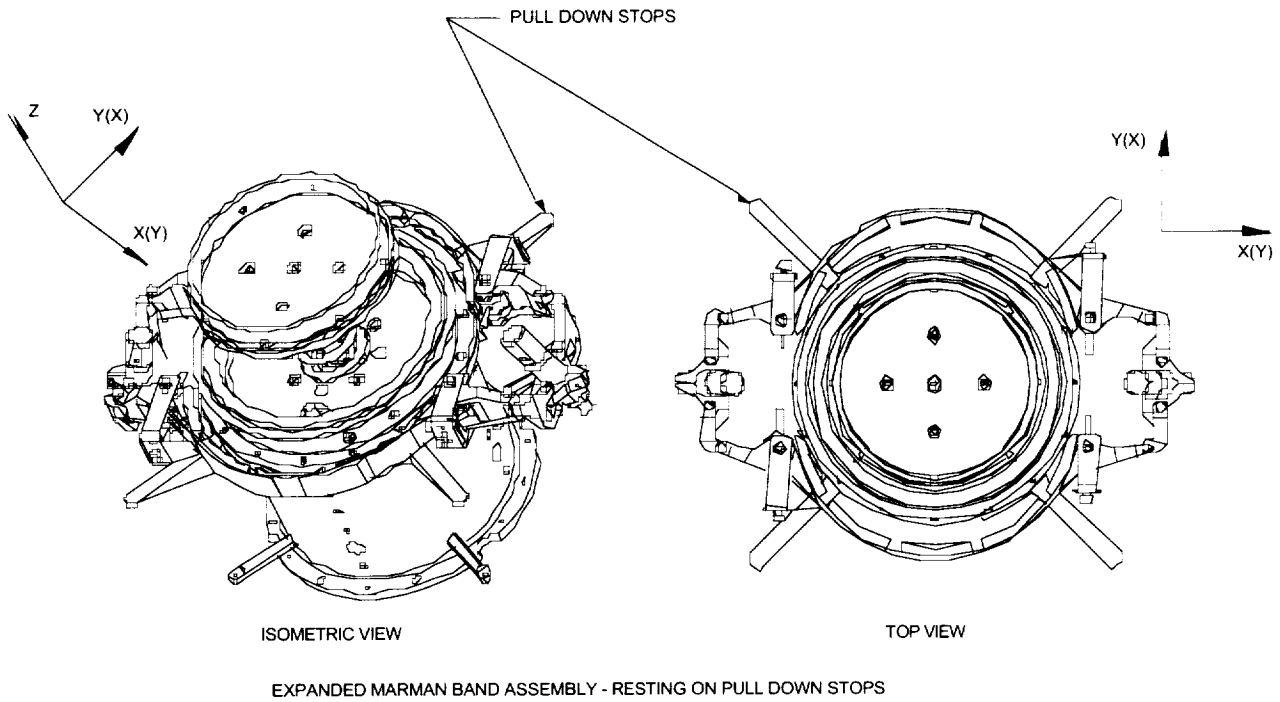


Figure 8

References

1. NASA GSFC, "Hitchhiker Customer Accommodations & Requirements Specification", 740-SPEC-008, 1999.
2. NASA MSFC, " Design Criteria for Controlling Stress Corrosion Cracking", MSFC-SPEC-522B, 1987.
3. Slebzak, G.R., "Hitchhiker Marman Band Interconnect Linkage Test Procedure", SSPP, 870-PROC-587, 2000.
4. NASA GSFC, "General Environmental Verification Specification for STS & ELV Payloads, Subsystems, and Components" GEVS-SE, 1996.

2/17/18

Taking Spacecraft Commercial Practices Too Far

Chuck Lazansky¹ and Scott Christiansen*

Abstract

In the radically changing, commercially driven spacecraft market emphasis has been placed on driving the price of components to an absolute minimum. This paper considers the question: How does the push for simple, low-cost devices effect the risk of failure in the use of the device? Starsys Research developed a paraffin-powered pinpuller for the Iridium[®] program. The design was very successful in its simplicity, reliability, and low cost. However, costs to integrate, operate, and control the pinpuller on orbit were higher than expected as a result of the design simplicity. Ultimately, the problems were addressed and flight operation of the mechanisms was successful.

After the program, the pinpuller was re-designed to address the limitations of the Iridium device. The simplified control, integration, and ground use of the new pinpuller have won wide appeal despite a slightly higher unit cost. In retrospect, we learned some important lessons and potential pitfalls in high-volume spacecraft component design.

This paper will describe the specific problems encountered with the Iridium pinpuller, and how they came about. How those problems were addressed in the improved design will also be presented. Finally, a discussion of how the lessons of Iridium have effected our design process will be included.

Introduction

The Iridium Program

In 1994, Starsys Research won a contract that would transform the company into a high-volume manufacturer of space-flight hardware. Starsys was chosen as supplier of the hold-down and release mechanisms (HDRMs) for the Iridium Satellite Constellation. The project included design and qualification of the hardware, followed by an aggressive delivery schedule of weekly shipments over the course of 22 months. This delivery schedule matched Iridium's planned production rate of 1 satellite per week for the 80 spacecraft to be manufactured.

In addition to the HDRM hardware, a device was needed to cage and release the gateway and cross-link antenna gimbals. An HOP pinpuller concept was selected as the most straightforward and cost-effective solution. Twelve (12) of the pinpullers were required per spacecraft, and with spares, over 1000 units were required for the constellation.

Starsys would be a supplier to the manufacturer of the antenna subsystems. The pinpullers would be shipped to the customer, installed in the antenna, tested, and delivered to the prime contractor for assembly into the spacecraft. All of the development work would be done with our customer. We did not work directly with the end-user of the spacecraft.

Commercial Design Approach

Design for a high-volume commercial application was a significant shift for Starsys. The target price for the pinpuller was roughly \$600 per unit, with half the costs estimated to come from parts, and half from labor. At the time, typical paraffin actuators were built in lot sizes of 5, at almost 10 times this target cost. The sheer volume of hardware to be delivered week after week required that Starsys take a very different approach to the design, assembly, and testing of the pinpuller.

¹ Starsys Research Corporation, Boulder, CO

Starsys would need to balance two very different design approaches. One was high-reliability space-flight component design, with which we were very familiar. The other was design for high-volume manufacturability, and "design to cost". Emphasis was placed on reducing costs, minimizing part count, and keeping the device simple to avoid production problems and maintain delivery schedule.

Results

In balancing these different approaches, choices were made in the design that had some unexpected consequences. One was in the area of on-orbit control of the actuator. The spacecraft design was already complete when the actuator design began, so the options for control were limited to a single timed power signal to operate the actuators. Assumptions were made during the design phase about the feasibility of this approach. The assumptions were not adequately checked out, and we were well into the production phase when it became clear that the proposed control scheme would not work. It required a significant effort and re-programming of software to arrive at a workable control method.

Another result of the aggressive design approach was an actuator that was less user-friendly, and more prone to damage at the hands of unskilled operators. Normally, after operation, a reset tool re-extends the pin to its proper start position. It was possible for the actuator pin to be pulled out too far (e.g., by hand) during ground reset. Once this happens, the rear seals are un-seated from their bore. The actuator will not pressurize, and the pin will not pull. Since the reset process is fairly straightforward, we believed proper training and process controls could prevent this.

Resetting the unit in the actual spacecraft production environment, however, was more difficult than we envisioned during the design phase. As a result, five units on the first spacecraft were unknowingly over-extended prior to flight, and did not actuate on-orbit. Fortunately, the signal could be re-routed and the disabled antenna did not compromise the system. The problem was corrected through improved procedures and re-training, and no other actuators were damaged.

After Iridium, an improved version of the pinpuller was developed for the Orbview program. The new design addressed each of the weaknesses of the Iridium design. For example, it contained an internal, redundant power-interrupt feature making it very easy to integrate and control. The success of the revised pinpuller has given perspective on what is truly meant by simple, robust, and cost-effective design. It has led us to re-examine the Iridium process and wonder if the design team had taken commercial spacecraft practices too far.

Paraffin Actuators and the Iridium Design

A paraffin actuator is a relatively simple device compared to many other spacecraft components. It utilizes the thermal expansion of paraffin to do work. Paraffin is contained inside a sealed chamber, which is typically heated by a Kapton-film resistance heater. Once the paraffin reaches its melting point, it expands approximately 15%, creating hydraulic pressure inside the device. This pressure is translated into linear motion of the output shaft. Pressure continues to increase as long as the heating is continued, so turning power off upon completion of the stroke is necessary to prevent damage due to excess heat and pressure. If power is not turned off, component parts will degrade, outgas, and ultimately, seal failure will occur. Some standard HOP designs are shown in Figures 1 and 2.

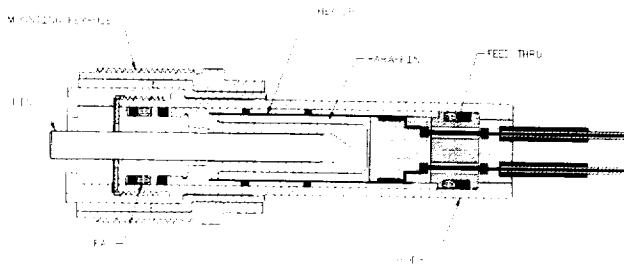


Figure 1. IH-5055-type HOP actuator

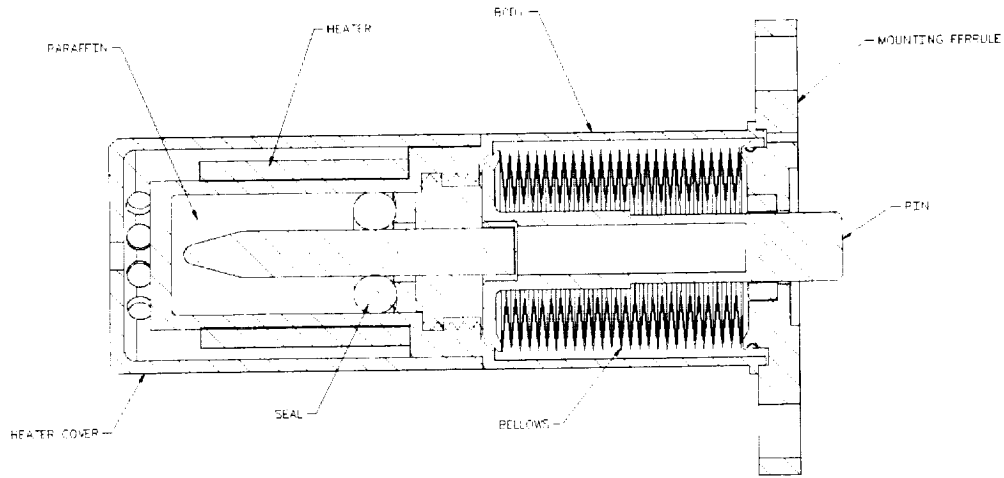


Figure 2. EH-3525 Hermetically Sealed HOP Actuator

A cross section of the Iridium pinpuller design is shown in Figure 3. The body, or pressure vessel, is titanium with a kapton heater applied to the surface. The titanium pin has Viton o-ring seals at each end. The larger diameter of the rear seals creates a net retraction force on the shaft when the paraffin chamber pressurizes. A Torton mounting flange provides the mechanical interface, and good thermal isolation so that a spacer is not necessary.

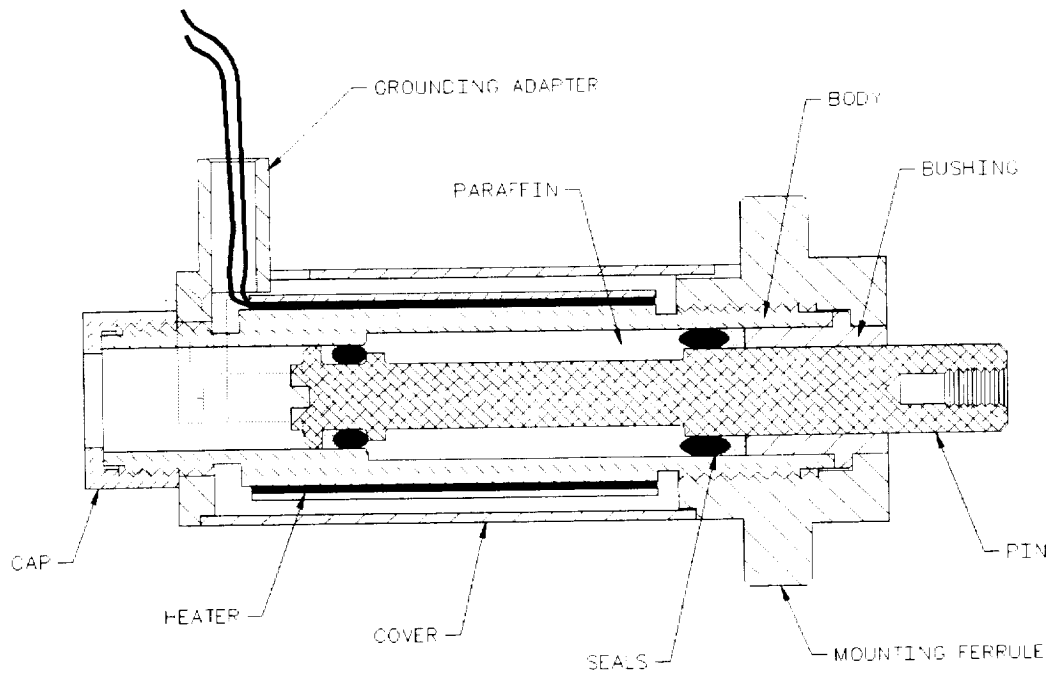


Figure 3. Iridium Pinpuller, extended position

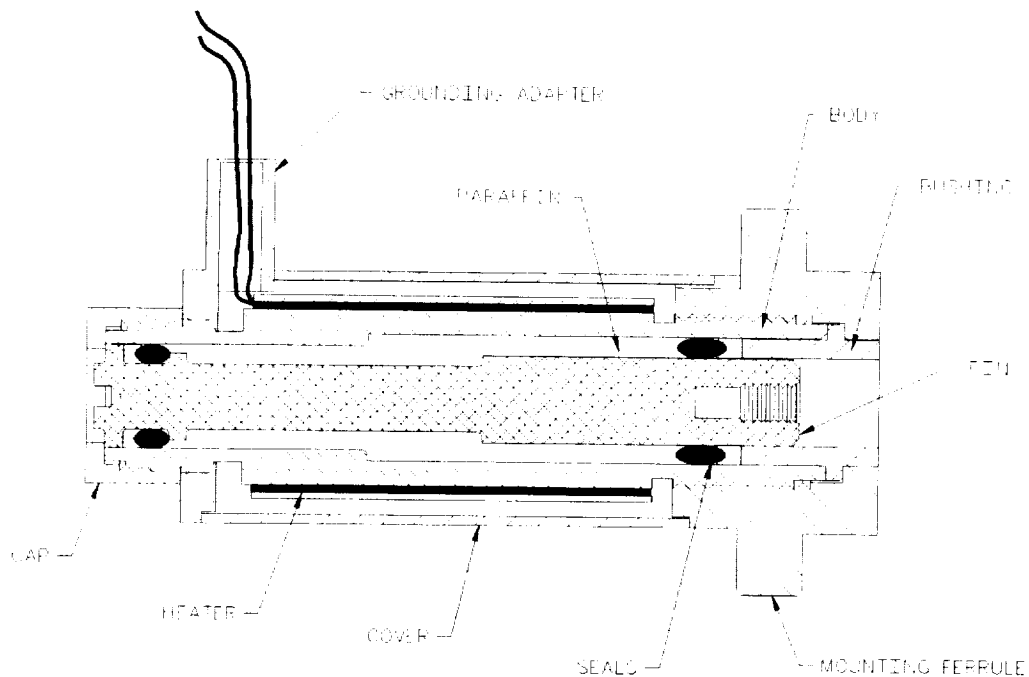


Figure 4. Iridium Pinpuller, retracted position

The electrical interface is simply a 2-wire twisted, shielded pair for power to the heater. The actuator is covered with a high-emissivity Flexible Optical Surface Reflector (FOSR) thermal control film to provide margin against self-actuation due to solar exposure.

Control Strategy: An Over-Constrained Design

Design Constraints

On orbit, only a single operation of the pinpuller was required to release the gimbals. The pinpuller needed to release a shear load of up to 445 N (100 lbf), over a temperature range of -65°C to $+70^{\circ}\text{C}$, given a variable input voltage of 22 VDC to 36 VDC. For ground testing, a reset tool provided by Starsys would be used to re-extend the pin for the next operation.

Options for controlling the actuator were very limited due to the existing design of the gimbals. The slip rings in the gimbals only allowed for a two-wire connection to each actuator for the heater. No wires were available for shutoff telemetry, such as a limit switch. After actuation, proper movement of the antenna stepper motors would indicate successful antenna deployment. However, this could not be utilized to control the pinpullers. The baseline design called for using a single timed pulse of power to operate the actuators under all conditions.

Actuation time is a function of how long it takes the device to reach operating temperature. Variations in start temperature and bus voltage strongly effect the time required for actuation. Ideally, power is supplied to a paraffin actuator only until deployment occurs, and then it is promptly discontinued. If power is not turned off, the actuator continues to heat, causing damage to the heater, and eventually leading to seal failure. Though the Iridium actuator was only required to operate once on orbit, paraffin release from the actuator could damage the spacecraft's horizon sensors. On the other hand, if power is not continued for long enough, the actuator may not operate under worst case conditions (low temperature and low voltage).

If temperature and voltage are known at the time of operation, then the control problem is greatly simplified. The pinpuller can be characterized in ground testing across the entire range of operating

conditions. On orbit, the conditions at the time of deployment can be read, and the appropriate power-on time determined by a software table look-up. However, temperature and voltage at the time of deployment would not be available. Temperature sensors were not possible since no additional wiring was available. Even if wiring were available, the actuators were on different sides of the spacecraft, which would see different operating environments. Several temperature sensors would have been required. And there was no plan to read bus voltage. The voltage at time of deployment could vary between 22 and 36 V, or 11 watts of input power to almost 30 watts! We did not know if a single timed power pulse could work across such a wide voltage and temperature range, yet there was little flexibility in these requirements.

An alternative concept was presented as a solution during an early design meeting. Starsys could design an internal power-disconnect, which would open the power circuit when the pin had pulled, providing inherent control. However, to keep overall program cost down, development work was discouraged. Emphasis was placed on utilizing proven, existing designs. To our customer, the risk, cost and schedule of this level of design work did not fit the program philosophy. Starsys agreed to design the actuator such that the single time-out approach would work.

To summarize, the design challenge of the time-out control strategy is as follows: select a single power-on time that guarantees full actuation can occur from the low-temperature, low-voltage condition, and then verify that the actuator can survive this same power duration with the high voltage condition from the high temperature. Failure of either one of these would jeopardize a major spacecraft function.

Strategy for Time-out Control

First, the heater was sized for operation under the worst case conditions. The specification required full pin retraction within 12 minutes in the coldest environment (-65°C) at the lowest voltage (22 VDC), with a partially failed heater operating at 75% of capacity. Using a model that balances heat input with conductive losses at actuation temperature, and adding appropriate margin, it was found that 8 watts was sufficient to meet the requirement. This dictated a nominal heater resistance of 44 ohms overall.

The heater design was also driven by the 2-wire limitation. Normally, 4 heater wires are desirable for two separate, redundant heater circuits. The design challenge was to build some degree of redundancy into the 2-wire circuit. This was achieved through the layout of the resistive elements within the Kapton-laminated heater. Four separate heater traces were placed between two "bus-bar" traces, all operating in parallel with an overall resistance of 44 ohms. In theory, a single element failure would still leave 3 other traces intact (or 75% of heater capacity), allowing full retraction under the worst-case conditions.

The heater is a critical component in the actuator, and methods for verifying proper heater performance had already been well developed. For example, 100% incoming inspection is performed, including an electrical test. In-process inspections exist for the application of the heater to the body. Electrical verification tests are performed regularly for the remainder of assembly and testing process. Given these procedures, and the robust heater design, the sacrifice of full heater circuit redundancy was traded for a simple two-wire power circuit.

With the heater sized properly for worst case operation, the issue of actuator survival was addressed. The actuator would need to survive for the duration of the power signal under hot, high voltage conditions. The operating pressure inside the actuator, under nominal 222-N (50 lbf) load, is approximately 20.2 MPa (3000 psi). To prevent extrusion failure of the Viton seals, internal pressures must be kept below 68.9 MPa (10,000 psi). Some paraffin actuators incorporate a shear feature to achieve this. This is a part, usually a flat disk, which fails in pure shear due to excess internal pressure, allowing expansion of the wax chamber volume. The expansion reduces the hydraulic pressure to below critical levels, thereby reducing the risk of seal failure or rupture of the body. A shear disk was not to be included in the pinpuller.

The pinpuller shaft was given almost 100% excess travel beyond the required stroke to create more internal volume for wax expansion. After the 0.635-cm (0.250-in) stroke required for release, the pin would continue to retract another 0.635 cm (0.250 in) to an internal hard stop. To reach critical pressures with the pin at hard stop would require that the wax be brought to temperatures above the survival range of the heater. The temperature required to expand the paraffin to seal extrusion pressures (68.9 MPa or 10,000

psi) was estimated to be between 230°C and 250°C. The laminating adhesive layer of FEP in the heater softens and melts at approximately 200°C. Given the close spacing of the inconel heater traces and the action of melting and flowing FEP adhesive, the heating elements were expected to contact, burn, and fail at critical temperatures. Our observations of heat-damaged heaters supported this. On-orbit, heater failure is a much more desirable mode than seal failure (assuming deployment has already occurred).

In summary, the design strategy to make the single time-out control scheme work was:

- 1) High power input will ensure actuation at extreme conditions
- 2) 100% pin over-travel will minimize risk of over-pressurization
- 3) Heater failure will stop heat input before seal failure can occur

Problems with the Control Strategy:

The critical assumption that over-travel and heater failure would prevent paraffin release was not true. During survival testing, in which power to the actuator is left on indefinitely, heating continued 100% of the time until seal failure occurred. Heater failure was expected to take place at actuator temperatures of 200°C to 230°C. The actual survival temperature of the actuators was found to be 260°C to 270°C, due to extrusion of the rear seals. The heater design was extremely robust, and not even partial element failure was noted for the duration of the program. Ironically, this resistance to failure undermined our design assumptions and the control strategy.

The problem was compounded by a tolerance stack error, which was discovered after the first 15 ship-sets had been integrated. The error resulted in a gap (about 0.127-0.178 mm [0.005 in -0.007 in]) in the area of the rear seal when the pin is in the fully retracted position. The presence of this gap meant the rear seal could extrude, and paraffin could escape at pressures below 68.9 MPa (10,000 psi). The problem could be corrected, but the solution required removing 1.27 mm (0.050 in) of the pin over-travel. This reduced the margins on seal survival due to extended power by roughly 10%. This led us to perform testing on how long actuators could survive with the gap discrepancy, and with the 1.27 mm (0.050 in) of reduced over-travel. It was during this testing that we learned the heaters were not a failure mode to rely on to prevent paraffin release.

The awareness that the control strategy would not work occurred late in the program, almost 25% through the satellite production phase. The spacecraft systems engineers had the software ready to provide a fixed-duration power signal to the pinpullers. It was not clear what level of re-design and/or retrofit would be necessary to solve this problem. We worked very closely with the lead engineer of the spacecraft company to find a workable solution.

Both Starsys and our customer had been aggressive about utilizing a simple, low-cost release device. In our efforts to meet the program's needs, we were overly optimistic in our assumptions about how to control the device. Finally, those assumptions were not fully investigated until late in the program.

Solution of the Control Problem

The problem was approached in two steps: The first was to narrow the expected operating temperature and voltage range. This was carried out by the spacecraft company. The second was for Starsys to conduct a battery of survival and actuation time tests to characterize the performance of the pinpullers.

The initial voltage range was 22 VDC to 34 VDC. Closer analysis by the electrical team showed that at the time of deployment, the voltage range could be narrowed to 26 to 33 VDC. This reduced the possible power supplied from a range spanning 15.3 watts to a range of 9.4 watts, or an almost 40% narrower power range. The use of voltage regulators was considered, but 12 individual regulators would have been required due to wiring configuration. This was cost prohibitive and not a desirable solution. Temperature range was reduced in similar fashion. Changing deployment sequence on the spacecraft, and operating the pinpullers earlier narrowed the temperature range. The expected low temperature was increased from -65°C to -40°C, and +65°C remained as the high temperature.

A series of tests was performed in a thermal-vacuum chamber to determine survival times (and verify operation times) throughout the narrowed temperature and voltage range. Survival time was defined as the time to seal extrusion and paraffin release, which was a discrete, observable event in the test chamber. Survival times for actuators with the seal-gap discrepancy were also determined, since the first 15 ship-sets were potentially effected. Once enough data points had been collected, the data was plotted as a series of curves showing response time as a function of power input. A survival curve, showing survival times from +65°C as a function of input power, was added. The resulting plot is shown in Fig.5.

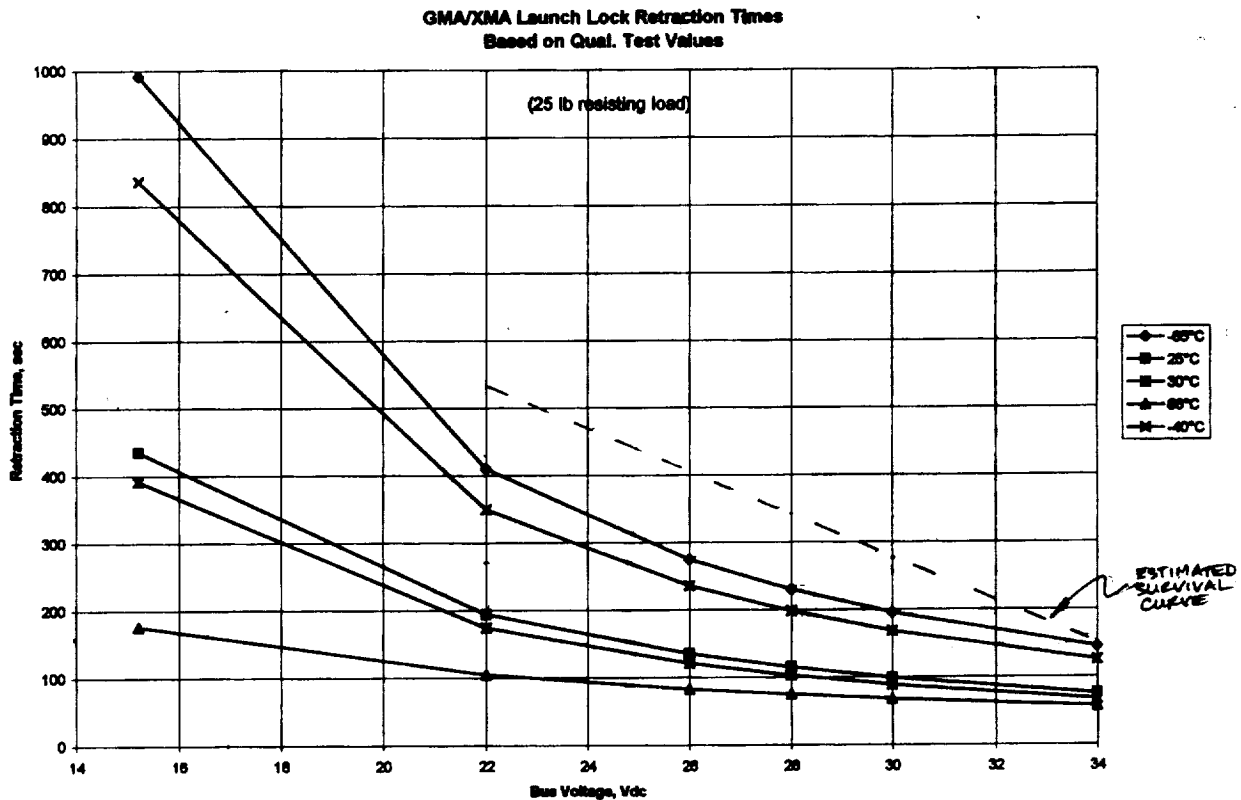


Figure 5. Response time curves (and estimated survivability line)

Even before the testing was complete it was clear that a single power-on time would not work over the wide range of operating conditions. The best solution to this was measuring bus voltage just prior to operation on-orbit, and having the system software select the power duration from a look-up table. It was apparent to Starsys that this was a considerable effort for the spacecraft company at this stage in the program. Nevertheless, a voltage feedback system and table look-up software was put in place on all spacecraft. In the unlikely event of incomplete deployment of one of the antenna, it would be possible to manually power individual pairs of actuators. However, this would have been very impractical for large numbers of actuators, and was considered only as a backup plan. The summary of the solutions adopted:

Summary of Solution to Actuator Control Problem

- 1) Voltage and temperature range narrowed by earlier deployment
- 2) Testing conducted to characterize actuator operation and survival
- 3) Bus voltage was fed back and used to select a power-on time (based on test results) via a table look-up in control software.
- 4) In case of incomplete deployment, manual powering of the actuators was possible.

This strategy was implemented with a 100% success rate on-orbit. With the exception of the five pinpullers damaged during ground operations (to be discussed in the next section) all cross-link and gateway antenna deployed as planned.

“Human Factors” in Ground Operations

An advantage to using HOP actuators is their ability to be used and reset multiple times for ground operations. The drive to reduce the part count and the complexity of those parts led to a design which was vulnerable to procedural errors by operators. As a result, 5 pinpullers on the first spacecraft were inadvertently damaged prior to flight, and were unable to deploy.

Design Choices

After operation, an HOP pinpuller must be reset. Reset consists of heating the unit to melt the paraffin, and then installing a specially designed reset tool, which screws into the front end of the retracted pin. The tool exerts a spring force on the shaft, which slowly re-extends the pin as the wax cools. Once the actuator is cooled to below the melting point of the paraffin, the tool can be removed, and the actuator is ready for the next operation.

The first prototype units of the pinpuller were designed with a step feature that would act as a stop against over-extending the pin. This step on the pin came to rest against the front seals as the actuator was reset. However, the step caused problems during the reset process. The actuator was required to reset with 68N (15 lbf) or less, and it took more force than this to push the pin through the solidifying paraffin. When the step did come to rest against the seals, it would force small bits of solid paraffin through the seals. In addition, there was the possibility that the stop feature might damage the front seals. The existing stop feature could not be used.

Any other design option for the stop feature meant adding parts, complexity in assembly, and cost. It would also add to the envelope, which was limited. However, without a stop feature for the extended position it would be possible to pull the pin out farther than the zero-position, which could un-seat the rear seals from the small (rear) bore. If left in that position and powered, the actuator will fail to pressurize, and liquid paraffin will flow around the rear seal and out of the actuator. Still, the feasibility of removing the stop feature altogether was considered.

There were design precedents for the lack of a front hard stop in the puller. Several models of paraffin actuator do not have a zero-stop and rely on the interface to limit pin motion. For example, the IH-5055 actuator rod is virtually unrestricted in its motion (in both directions) except by its interface. The issue was explored with our customer, and the decision we arrived at was to eliminate the front hard-stop feature. The zero-position of the pin would be established by the reset tool rather than a stop feature. To minimize the risk of over-extension, processes would be carefully controlled. Only properly trained technicians would use the qualified Starsys tool per the established procedures. Proper pin extension would also be verified following each reset to insure the pin had not been over-extended.

Results – Ground Operation Errors

The lack of a hard stop for the nominal shaft position made the actuator vulnerable to operator error. The confidence in process controls on the ground was unfounded for several reasons. First, though the reset process was easy at the antenna level, it was much more complicated at the spacecraft level. Physical access to the pinpullers was somewhat restricted. The antenna had to be powered in groups, and that meant resetting several actuators simultaneously. Moreover, the pinpullers were one small component out of many on the spacecraft, and probably received less attention than they did at the antenna level. These difficulties, combined with the variability of greater numbers of people working with the actuators at the integration facility, led to improper resetting of several actuators on the first spacecraft produced.

Starsys first learned of this through a telephone call received immediately after the launch of the first group of spacecraft. Five antenna on one of the spacecraft were not moving after all the pinpullers had all been operated. The pinpullers were operated a second time, with a longer power duration. Still, the stepper motors could not move the antenna. It was clear that the pins had not pulled, and that additional

powering of the devices would not help. We worked to support the investigation with both the antenna manufacturer and the spacecraft company.

Just a few weeks prior to the first launch, Starsys had been contacted about damaged pinpullers at both the antenna and spacecraft facilities. Each facility returned a unit to Starsys for evaluation, though each was already aware that the cause of the damage was improper operation. During testing, one unit was powered for well over 5 minutes when the maximum time for ground operation was set at 3 minutes. This actuator had obvious heat damage, extruded seal material, and had lost paraffin. Another unit had been manually over-extended during resetting. Apparently, the users had attempted to "help" the reset tool by pulling on it while the pin was extending. This defeated the built-in stop incorporated in the reset tool. Due to the compact design, extending the shaft only 1.27 mm (0.050 in) beyond its zero-point can unseat the rear seals. Once this happens, the actuator is compromised. If the operator pushes the shaft back in, there is a risk of tearing the seal on the body's interior corner. If the seal remains unseated, then at the next operation, the actuator will not fully pressurize, and paraffin will escape.

It quickly became clear that the reason the actuators did not deploy the antenna was that they had been reset improperly or otherwise damaged on the ground. Paraffin was found on the floor where the spacecraft was assembled as evidence of either over-extension or over-powering of the units. At this point, our involvement in the investigation was no longer necessary and we found it difficult to get further information from the spacecraft company. Sources indicated to us that training difficulties and workforce turnover were issues at the integration facility. Nevertheless, the problem was addressed by more thorough training of the operators. An inspection of the pin position was added following actuator reset, to verify proper extension. This solved the problem, and no other instances of improper reset occurred. The partially disabled spacecraft did not adversely effect the overall functioning of the satellite network. The communication signals were re-routed to other satellites to compensate.

Both the antenna contractor and the spacecraft manufacturer experienced difficulties in ground operations including excess power duration and improper resetting. Though the procedures were clear and well known, the magnitude of the project and the many people involved created many opportunities for error. Design decisions which simplified the device left too little margin for error in ground operations. The actuator was prone to "human factors", and though it showed better than "four-nines" reliability on paper, it was reduced to 5 failures in 1000 in actual use due to being damaged prior to flight.

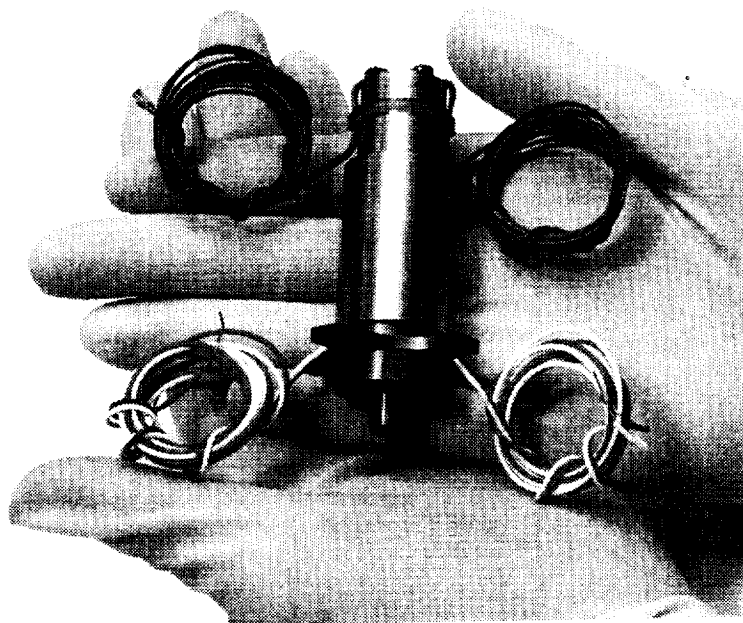


Figure 6. The Improved Design (Type SP-5025 pinpuller)

Improved Design of a Pinpuller

Design Improvements

The primary goal of the design improvement was to create a device which was not only easy to operate and reset on the ground, but also simple in its control requirements. Though the pinpuller was completely re-designed, its basic structure is very similar to the original design.

The key feature of the improved design is its ability to discontinue power after retraction is complete. This is achieved through the Circuit Interrupts (CIs), which is a high-reliability switching mechanism at the rear of the actuator. The contacts are held normally closed with a relatively high pre-load (13 to 89 N [3 to 20 lbf]). When the pin is fully retracted it reaches the contact, overcomes the pre-load, and opens the CI circuit. If the heater power is routed through this circuit, the power is "interrupted". The actuator will begin to cool, and the pin re-extends slightly due to the CI pre-load, closing the CI. Power will cycle on and off at a safe level in this manner until the external power supply is turned off. Two CIs are used in each actuator for full redundancy. The CI wires (2 pairs) are not internally connected to the heaters, so the end-user can choose the final wiring configuration. With two independent heater-circuits and two CI-circuits, there are a variety of wiring choices to support many different control philosophies. For example, the CIs can be wired in-series with the heaters, or they can be used separately for telemetry, or any combination of the two.

The CIs greatly simplify on-orbit control. If the heaters and CIs are wired in-series, the controller simply needs to supply a fixed-duration power signal that is at least as long as the worst case response time, plus margin. On the ground, operators need not be concerned about over-powering during the reset operation. Power can be applied until the CIs change state, and then the reset tool is applied. Power can be left on indefinitely without causing damage. A cross-section of the improved device is shown below.

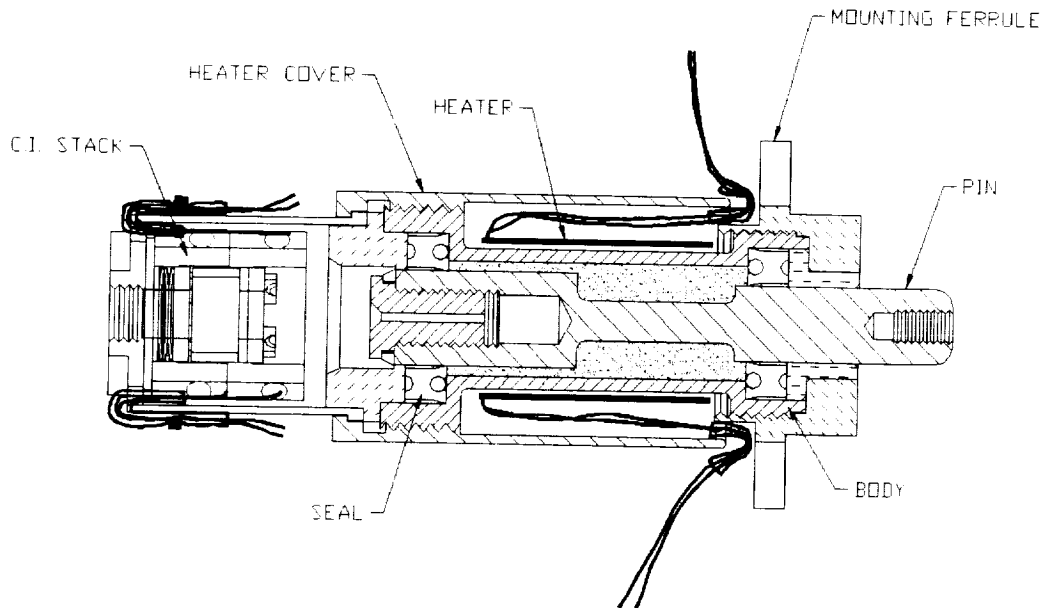


Figure 7. Cross-Section, Improved Design

The difficulties resetting the Iridium pinpuller were also addressed in the improved design. Over-extension of the pin was solved with the addition of a hard stop feature to limit extension and set the zero-position of the pin. The reset tool itself was redesigned to be easier to use, requiring less hand-strength from the user.

Changes were also made to improve the manufacturability of the device. For example, the Iridium-pinpuller had the mounting flange made from Torlon 4203L. Its high strength and good thermal insulation properties made it a good choice for the mounting interface. However, it is also hygroscopic and subject to

dimensional changes of up to 0.5% as water is absorbed over time. It also required a post-machining re-cure process that lasted 17 days. Titanium was used as the new mounting interface, with the addition of G10 fiberglass insulating washers to reduce conductive losses. The body of the pinpuller was also made easier to machine by eliminating the high-tolerance, high surface finish bores (25 micron or 10 μ -in) for the seals. Instead, the seals remain static in the bores, and the high surface finish is applied to the pin. This facilitates machining and inspection of the parts.

Cost Comparisons

In quantities of 1 to 4 units, the price of the revised pinpuller is about 30% higher than the old unit. However, the higher first cost is offset by the lower overall system costs due to the simplified control and operation. This can be seen in the market response to the improved design, and the fact that very few pinpullers are now sold without circuit interrupts.

In higher quantities, the unit cost difference is reduced. The Iridium unit was priced at roughly \$600. Starsys has costed a slightly higher volume of the improved pinpullers at roughly \$715 per unit, or a 19% difference. Assuming comparable design and development costs, the difference to the Iridium contract to use the improved design would have been about \$115,000. Starsys spent at least half that amount in additional testing to resolve the control issue. And many times this amount were most likely spent by the antenna supplier and spacecraft company. Though it is easy to analyze this in hindsight, the additional cost of the improved design would have been worthwhile.

Conclusions

Design drivers for commercial spacecraft can be very different than for custom spacecraft. The impetus to reduce cost is much greater, because in large volumes, small differences in component cost become large sums. The schedule pressure is greater, due to the business pressure to become profitable quickly in order to pay back investors. Large, multi-discipline design reviews are less common. Responsibility is spread over larger teams, and usually across several companies. These factors can have a strong impact on design choices and the overall success of the program.

Some element of the following items were present in each of the problems encountered on Iridium:

- Focus on meeting immediate price goals without fully considering downstream costs to implement.
- Early assumptions made to meet cost goals were not completely checked out during design process.
- Little communication between designer and final operator of equipment/spacecraft.
- Over-reliance on operator training and procedures to control risk of failure, rather than engineering those risks out of the system.
- Designers overly optimistic about ease of ground operation of equipment.

Summary of Conclusions

- Engineering controls are best way to manage the risk of failure. Design failure modes out of the equipment. Don't rely on processes, procedures, or training to manage failure modes.
- Direct contact with the end-user is preferable to communication through third parties, or instruction manuals. Given the magnitude of the Iridium project, specific on-site instruction in resetting the units would have been a good idea.
- There is no replacement for a well thought out Failure Modes, Effects, and Criticality Analysis (FMECA) of the final design, rather than a traditional reliability analysis. Ask the question "how could this device fail?"
- Ground operations must be considered in overall reliability, in addition to on-orbit operation.
- Consider "human factors". Manuals are not always read, and procedures are not always followed. Consider this in the FMECA.

- Expect more variability in production processes with higher volumes, multiple work shifts, etc. Commercial spacecraft get less high level attention and scrutiny than custom spacecraft.

The lessons learned on Iridium have had an effect on our approach to new designs. We consider issues such as ease of operation and reset more carefully. In short, we design hardware to do more so the user has to do less. More attention is given to control issues. We work with the customer on the details of the control system early in the design process. We make sure we have direct contact with the final operator of the spacecraft, and are available for support during integration and ground testing.

5-2/31

Design and Development of a Miniature Mechanisms Tool-kit for Micro Spacecraft

Cliff E. Willey^{*}, Brett Huettl^{**}, Stuart W. Hill^{*}

Abstract

With the continued push for smaller, faster, and cheaper spacecraft comes a new era in mechanism design. The desire to develop "Micro Satellites", along with advances in the processing and selection of materials, have created an abundance of opportunities to miniaturize mechanisms. Simple designs with direct applications of developing technologies are ideal for these miniature mechanisms. This paper will focus on the design and development of a miniature satellite "tool kit". The Johns Hopkins University Applied Physics Laboratory (APL) and Starsys Research developed six new miniature mechanisms under a NASA Advanced Technology Development Program. The mechanisms developed included a Micro and Mini Separation Nut, a Mini Rotary Actuator, a Mini Burn Wire Release, a Mini Linear Actuator, and a Mini Redundant Release Mechanism. This paper will discuss the concepts evaluated, designs chosen for fabrications, problems encountered during development, achieved performance characteristics, and recommendations for future development.

Introduction

Micro-satellites in the 10-100 kg range are being developed for scientific, commercial and military applications. For their size, these spacecraft will have very sophisticated payloads and missions. This is due to advances in miniaturization of electronics, RF systems, sensors, and instruments. The Johns Hopkins University Applied Physics Laboratory is developing many leading edge technologies for a wide variety of micro-sat applications. The APL micro-spacecraft concept (Figure 1) provides a modular-customizable bus that is 3-axis stabilized, has redundant IEEE 1394 data bus, on-board instrument processing, and makes use of developments in miniaturized electronics. NASA, military, and commercial micro-satellite programs are making similar advances with miniaturized payloads and electronics.

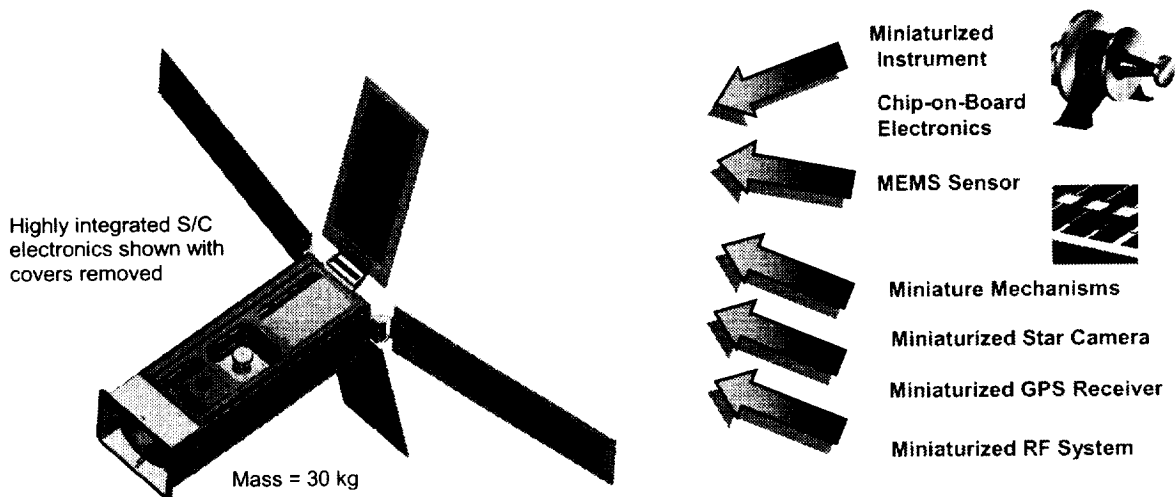


Figure 1. JHU/APL Concept MicroSat

^{*} Johns Hopkins University Applied Physics Laboratory, Laurel, MD
^{**} Starsys Research Corporation, Boulder, CO

Significant miniature mechanism developments are needed for these up-and-coming micro-satellite programs. Miniaturization is needed for deployment of solar arrays, booms, and instrument devices. There are some off-the-shelf mechanisms that are small, but these still require an order of magnitude reduction in size to meet the needs for micro-satellites. The Advanced Technology Development Program at JHU/APL is currently funding research for development of miniature mechanisms and is collaborating with Starsys Research to provide off-the-shelf selections of these devices. This has led to the creation of the Miniature Mechanisms Tool Kit. The tool kit contains 6 new mechanisms (Table 1) for use on instruments, solar arrays, and other deployable or mechanism driven device. All of these mechanisms can be easily scaled for a variety of output requirements and show promise for additional miniaturization.

Table 1. Mechanism Descriptions

Mechanism Type	Actuation Device	Company	Mass (gm)	Size (mm)	Power	Load Capability	Lifetime	Release Time
Micro Sep-Nut	Shaped SMA	Starsys	5	7.6X5.1X12.7	<2 watts	22 N	> 100 Actuations	~30 sec
Mini Sep-Nut	Shaped SMA	Starsys	20	15.2X15.2X25.4	2-5 watts	90 N	> 100 Actuations	30-60 sec
Rotary Latch	SMA Torsion Spring	Starsys	5	12.7X12.7X12.7	2-5 watts	0.042 N-m	> 100 Actuations	< 15 sec
Burn Wire Release	Fuse Wire	JHU/APL	0.07	10.2X7.0X3.9	1-2 amps X volts	45 N	1 Actuation	< 5 msec
Mini Linear Actuator	SMA Wire	JHU/APL	0.5	5.6X5.6X16	0.25 amps 8 volts	40 N	> 1000 Actuations	< 10 msec
Mini Redundant Release	Shaped SMA	JHU/APL	<3.8	10.2X10.2X23	2-4 watts	6 N	> 100 Actuations	30-60 sec

This project addressed the design of several types of mechanisms including separation nuts, release devices, linear actuators, and rotary actuators with a range of load capability. Performance requirements for these mechanisms are not well established due to the infancy of the micro-satellite designs. Therefore, assumptions were made for requirements to handle loads of 12-45 N, make the size small as possible, use low power, provide low shock, and make the mechanisms easily resettable. Shape Memory Alloy (SMA) was chosen to drive most of the mechanisms due to its capability of providing high forces in a very small package. SMA's are also very quick responding when electrically driven directly through the material. A burn wire mechanism was also developed by JHU/APL due its capability to be highly miniaturized yet provide good strength capability and reliable operation. The following sections will give a detail explanation of the six mechanisms developed.

Mini Separation Nut

Design Approach

The Mini Separation Nut was designed by Starsys to be similar in operation to conventional nut release devices and release a small screw. The design uses a segmented nut constrained by a collar. With the collar in place, the segments are held in the shape of a nut, allowing a mating screw to be threaded and tightened in place. The collar is maintained in position by a compression spring that prevents the collar from moving due to vibration loads. The collar is driven in opposition to the spring by a SMA element. To release the screw and nut, power is supplied to a heater or directly to the SMA element. As it is heated through its transformation temperature, the element recovers previously induced strain, and drives the collar to allow the segmented nut to separate, releasing the screw. When power is discontinued, the mechanism can be manually reset. The screw can then be re-inserted into the nut and the sequence repeated.

The SMA element consists of 3 SMA springs that are used to axially move a collar that restrains the nut segments (see Figure 2). The three SMA springs (2) are nested in a cylindrical housing (1). On top of these rests the Spring Washer (4) and collar (5). In the latched position, a compression spring (7)

maintains the collar in the proper position to restrain the three Nut Segments (6). The Segment Retainer Screw (3) is further used to constrain the position of the Nut Segments.

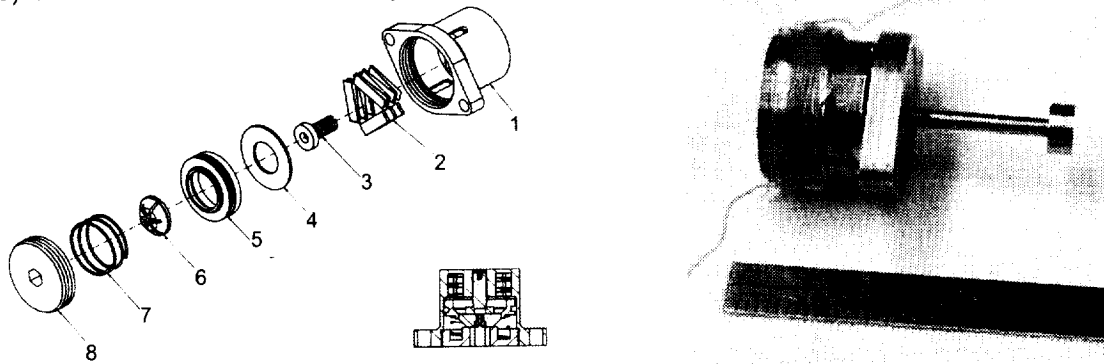


Figure 2. Mini Separation Nut Assembly

When power is applied to heat the mechanism, the SMA springs are warmed and extend. This extension pushes the Spring Washer and collar forward, which allows the Nut Segments to separate, releasing the screw (not shown). After power is discontinued and the SMA springs have been allowed to cool, the collar must be manually reset before the screw is installed. For heating the Mini Sep-Nut, a resistance wire was attached around the body.

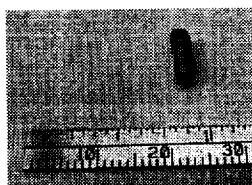
Characterization Testing and Problems Encountered

Complete characterization testing was not performed on this mechanism. After fabrication, assembly, and checkout, it was determined that the design could be improved to achieve a significant reduction in size and mass. This led to the development of the Micro Separation Nut outlined below.

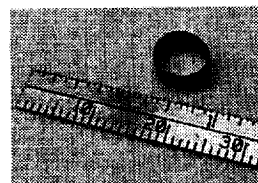
Micro Separation Nut

Design Approach

During the initial design process, four types of materials were examined to provide mechanism actuation; paraffin, Ostalloy, SMA wire, and SMA springs. The SMA spring was chosen as the most favorable approach due to the high stroke that could be achieved, the fairly quick response time, and the variety of available shapes. An SMA strip was formed into a band shape and depressed elliptically to grip the screw in the device (Figure 3). As the mechanism is heated, the spring expands to its original band shape and releases the screw. This spring concept has good stroke and output force to handle a variety of loading conditions on the screw and is extremely compact.



Compressed for locking



A After heating and release

Figure 3. Micro Separation Nut SMA Band Spring

Operation of the mechanism is very simple in order to be miniaturized (Figure 4). It is reset by inserting the screw (4) through the Housing (1) and past the inner diameter of the SMA spring (3). The Cap (2) holds the SMA spring properly in the Housing. The SMA spring is then manually compressed from two sides until it is secure around the screw. The mechanism may now be preloaded and is ready to be released. The Micro Sep-Nut is released simply by applying heat to the housing. As the SMA spring is heated, it returns to its circular shape, releasing the screw.

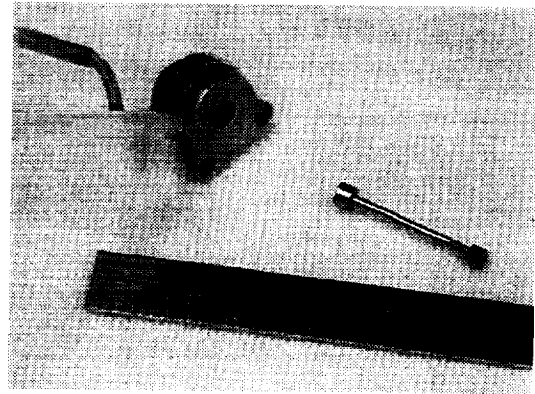
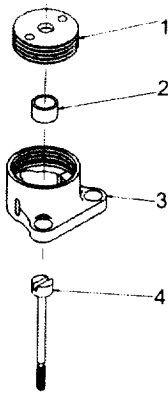


Figure 4. Micro Separation Nut Assembly

The SMA springs were fabricated from 0.15-mm thick by 2.2-mm wide ribbon formed into a circular shape (with two complete turns). Since the SMA springs are not powered directly, all the materials in the mechanism are metallic, primarily stainless steels, to better conduct the heat to the springs. Most of the components have been heat treated to increase the hardness, due to the small size.

Characterization Testing

Initial testing determined the voltage required to heat the SMA to its transition temperature. Table 2 shows the maximum temperature reached with a range of given input voltages.

Table 2. Micro Separation Nut Max Temperature

Input Voltage (VDC)	Current (amps)	Power (Watts)	Maximum Temp (°C)
0.5	0.06	0.03	29.1
1	0.11	0.11	34.7
1.5	0.16	0.24	52.7
2	0.22	0.44	68.2
2.5	0.26	0.65	88.0

After the prototype unit was fabricated, load tests were performed to determine the affect on the release time and temperature. The main goal was to determine the maximum load that could be restrained and released consistently. Thermal testing was also performed. It was taken to -30°C and up to +40°C and released with a nominal load of 22 N. There were some inconsistencies in the load at low temperature. It is not clear the cause of these variations. Table 3 summarizes the results of the thermal testing.

Table 3. Thermal Testing, Micro Separation Nut

Test Temp (°C)	Ambient Load (N)	Release Load (N)	Release Time (sec)	Release Temp (°C)
-30	22	18	65	64.4
41	22	27	16.8	72.6
39	22	31	16.1	62.8

Problems Encountered

Finding a heater for this mechanism was difficult. The small surface area available on the Micro Sep-Nut makes it hard to attach a standard foil trace-heating element. Traces were used from a larger foil heater and were soldered together and attached to the body with a small band of shrink tube. A diode was used as another heating approach. As power was applied to the diode it eventually providing enough heat to operate the SMA band and release the screw. Although it worked, the diode size nearly doubled the height and mass of the Micro Sep-Nut. Toward the end of the program, two sample custom heaters were delivered. The heaters were Kapton laminate with foil traces connected to lead wires. Unfortunately they were made with a fairly large lead wire (26 AWG). The lead wire size made the heater stiff and difficult to bend around the diameter of the housing. Both sample heaters ended up being damage during to installation.

Recommendations for Future Development

As discussed, the methods used for heating the mechanisms could use improvement. A vendor has been found to make a heater that would fit onto the Micro Sep-Nut and should easily be able to develop a heater for the Mini Sep-Nut. For future heaters, the smallest possible gauge lead wire (30 or 32 AWG) should be used for both mechanisms. Also, the manufacturer should preset the bend size to match the body diameter, by hot forming the heater around a mandrel.

Better characterization of the SMA springs is needed. The focus of the program and most effort (both time and budget) was spent on design, assembly, and overall characterization. The spring vendor was relied on to meet the design criteria specified. Since the SMA springs were made on a best effort basis, the vendor performed no verification.

Mini Rotary Actuator

Design Approach

A mini rotary actuator was designed and developed by Starsys Research that provides .014-.042 N-m of torque in two directions over a 120° rotational range. The rotary actuator could be used to open and close an instrument cover that weighs about ½ gram. It incorporates a detent latch that would be capable of maintaining the cover in either the open or cover closed position without the use of power. The holding torque for either of the two positions was to be equal to or slightly greater than the output torque of the rotary actuator.

Most of the design options considered for the actuator required linear motion be changed to rotary motion to obtain the required output. Three choices were examined for the actuator to operate the mechanism; a small paraffin actuator, SMA wire, and SMA springs. After some conceptual design work on the different actuators, the SMA spring was chosen as the most favorable approach. This was due to the high stroke that could be achieved, the fairly quick response time, and the variety of available sizes and outputs.

Two types of SMA spring shapes were evaluated in the final mechanism design. First, wave springs were formed from SMA strips to provide a good range of motion (Figure 5). Using opposing springs, the mechanism could drive a rack and pinion gear arrangement to convert linear motion to rotation. This design was deemed too large for the scale of mechanisms being developed and the prototype was not built.

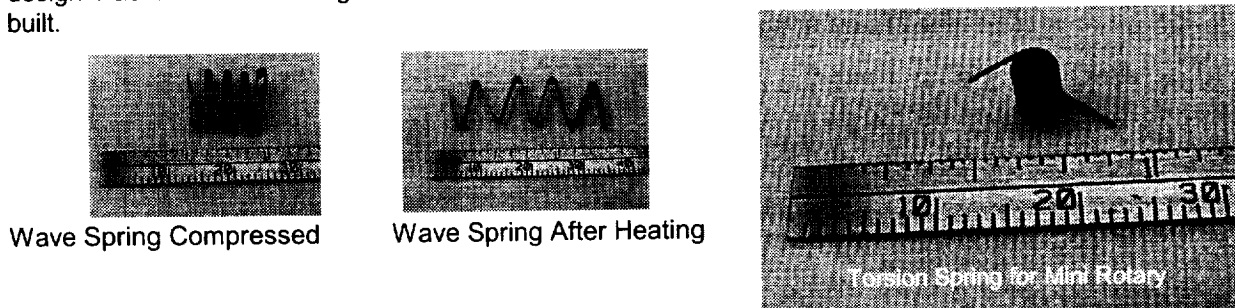


Figure 5. SMA Spring Designs

The final spring design chosen for the rotary actuator was a torsion spring formed from SMA wire (Figure 5). When installed, the torsion spring is wound past its nominal position around a mandrel. As heat is applied, the spring returns to its nominal position, providing the output torque. An oppositely wound spring on the mandrel provides an opposite torque so the mechanism can be operated in both directions. The mechanism assembly is shown in Figure 6.

For operation, one power lead is applied to the drive disk (providing a single common for either torsion spring). The other lead is attached to one of the exposed ends of the torsion springs (depending on the direction of desired output). The drive disk is keyed to the output shaft to transfer the rotation from the torsion springs. The output shaft also contains a stop that interfaces with one of the covers. This stop limits the rotation of the output shaft in either direction.

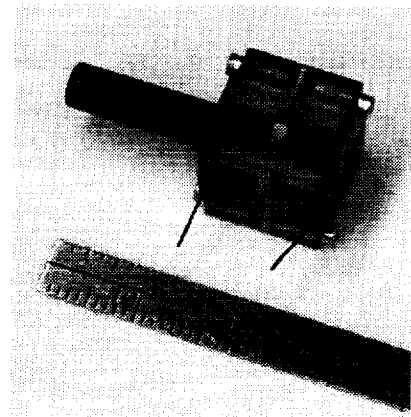
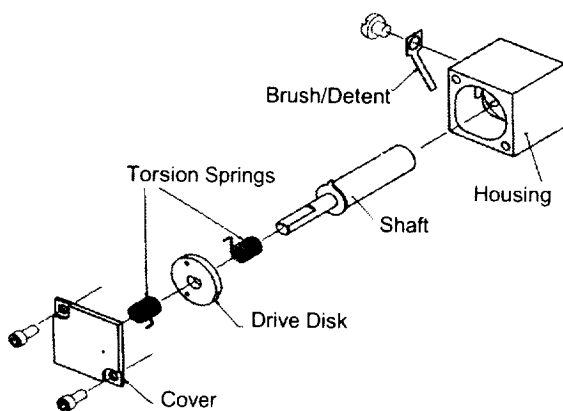


Figure 6. Mini Rotary Actuator

Characterization Testing

Because of the small size of the mechanism, it was difficult to measure some of the performance characteristics. We were unable to obtain an accurate measurement of the internal friction. Also, testing was limited since most of the effort was focused on developing the various designs and developing the torsion spring design into a functional prototype. No thermal testing or life cycling was performed on the mechanism. Operational testing showed the mechanism to be sensitive to power-on time. If a constant current was applied to the SMA spring, there was a risk of damaging the SMA spring by heating it to a temperature where the spring material is re-annealed. The best firing sequence for this mechanism would be several short (1-second maximum) pulses until telemetry signals the cover is to the open or closed position.

Torque measurements were made with a calibrated torque gauge attached to the output shaft of the mechanism. As the mechanism was powered, the output torque of 0.042 N-m was measured. This turned out to not be a very accurate measurement. The torque output of just the torsion springs themselves would have been more useful. However, no fixturing was developed to test the springs accurately.

Problems Encountered

The most difficult requirement of the design was that it was necessary for the mechanism to operate in both directions. This meant the mechanism had to be capable of opening and closing the cover. A simple unidirectional drive mechanism would have been much simpler, yet not nearly as useful. The main problem that the dual motion presented is that the output spring is always working to reset the opposite direction spring. This greatly reduces the available output torque, since approximately half the output torque is required to reset the other spring.

Another problem encountered during the design was how to incorporate a detent (required to maintain the rotary latch in either of the end positions). The initial approach used with the torsion spring design was a leaf spring of metal that contacted a flat on the drive disk in either the open or closed position. The leaf spring also provided the common contact point for the electrical circuit, since one end of both torsion springs was in contact with the drive disk at all times. This approach resulted in too much drag on the drive disk, decreasing the amount of output torque available. The leaf spring also provided little actual holding torque for the mechanism in either of the end positions.

Recommendations for Future Development

The ultimate success of this design will rely on further refinement of the SMA torsion spring. The torque of the spring is considerably less than needed for the desired output torque of the mechanism. Increasing the wire diameter will eventually result in an increased output torque, but it will at some point lead to a larger overall mechanism.

The detent approach initially used in the design needs improvement. Another approach to consider is to use another SMA device to latch and unlatch the mechanism in either end position. Ideally this would be connected in series with the torsion spring so that when power is applied, it both releases the latching device and operates the torsion spring. However, the practical implementation of this could be difficult. It may be necessary to add a second circuit to operate the latching component if a SMA device is used. This too could add complexity in being able to properly time the events.

Crimp contacts need to be added to the ends of the SMA springs for electrical connection. The prototype was connected manually and this was not practical for actual flight use. It was found the SMA wire does not easily accept solder. For the common contact the drive disk, it needs a method to reduce drag from the wire contact. One solution may be to add a metal shaft through the output shaft to contact the drive disk and then crimp or solder a contact onto the end of this. The end would then be allowed to rotate freely as the mechanism rotates.

Miniature Burn Wire Release

This tiny release mechanism was developed at APL for a miniature instrument cover or similar device needing an extremely compact, low mass, and low power actuation device. It uses a burn wire to directly carry the tensile load of a cover or screw that is attached to its retainer. Current applied to the wire will break or fuse the wire at the location of the retainer to cause release of the hardware attached to it. This is unique from other types of satellite burn wire releases. This mechanism uses the wire to directly carry the tensile load; therefore it is a highly simplified design that can be greatly miniaturized. It is also an easy design to scale up or down according to the requirements of the device it is attached to.

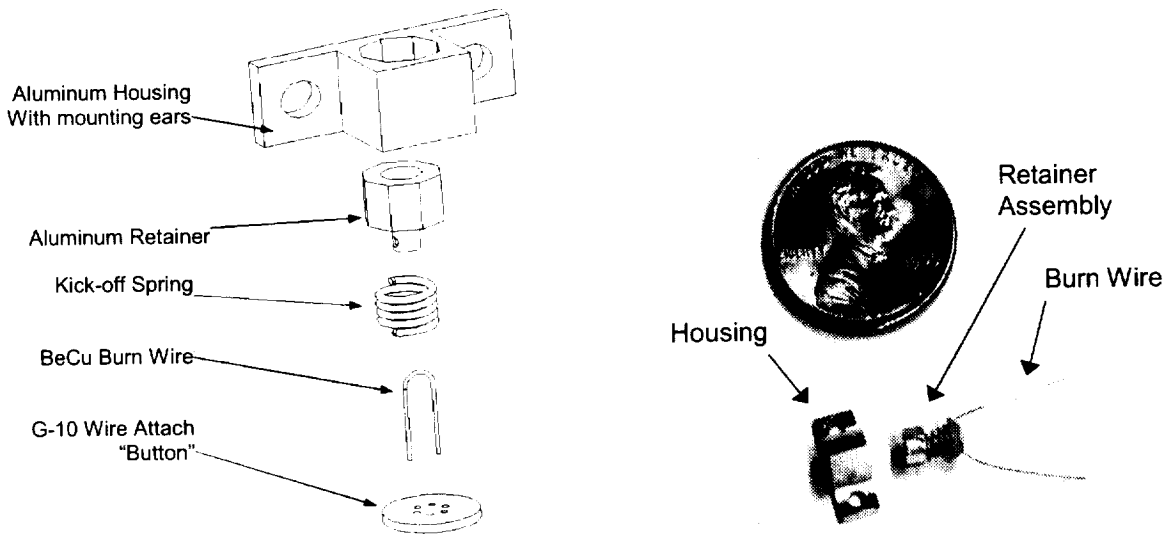


Figure 7. Mini Burn Wire Release Assembly

Design Approach

It was determined early in the design process that to highly miniaturize this mechanism, it had to contain the fewest parts possible. The burn wire release mechanism (shown in Figure 7) has only 5 components with only one of those that are released with the cover. These components are also multifunctional. The burn wire is used to hold the mechanism together, carry the restraint load, make electrical connection, and initiate the release action. Wire size was based on restraining a 100-gram cover. The rest of the mechanism was designed to package as compactly as possible and provide thread for a small screw. A kick-off compression spring was incorporated to overcome friction or other small forces that might hang-up the mechanism. Beryllium copper was chosen for the wire material based on its excellent mechanical properties as well as its high resistivity. Pure copper wire of the same diameter takes a much higher current to burn. Stainless steel wire has similar properties as BeCu and could work as well.

The mechanism is assembled by looping the wire through a retainer and bonding it to the isolation button. Between the button and the retainer is a kickoff spring, which pre-loads the burn wire and maintains the position of the retainer within the housing. To operate the mechanism, current is applied to the wire and resistance heats the wire in a predictable manner like a circuit fuse. A short section of the wire is etched to a slightly smaller diameter and the heating concentrates at this point. At high temperatures, the wire loses its mechanical strength and breaks in the desired location. Additionally, the kick-off spring creates a stress concentration in the area of the etching, which causes a higher resistance and greater control of the wire breakage. Reaction time of the mechanism is very quick and it produces no shock. The kick-off compression spring assists deployment by quickly separating the two halves of the mechanisms. It is a single cycle mechanism and needs replacement after usage. The housing can be made to plug-and-play, similar to a fuse, and allow quick changes between uses.

Characterization Testing

Testing of this mechanism was conducted to characterize and optimize the performance. It was broken down into four distinct sets of testing: etching, mechanical strength, electrical, and operational. Etching tests were first conducted on the burn wire in order to determine an ideal etching process and to verify that the process produced consistent wire mechanical properties. Wire diameters chosen were 0.20-mm and 0.30-mm wire that was to be etched down to 0.15 mm and 0.20 mm diameters respectively in a 2.5 mm localized area of the wire. The first etching solution used was an ENDPLATE AD-485 that consisted of 11 kg AD-485 and 1500 mL sulfuric acid in 76 L of water. This was a very aggressive solution that took 12 minutes to achieve the desired etch. However, the wires came out of this process very brittle and snapped easily when lightly handled. It was concluded that this solution could have caused hydrogen embrittlement in the etched wire drastically reducing its mechanical properties. A less aggressive etching was considered using a Nitric acid solution at low concentrations. Hand calculations suggested that etching would take approximately 36 hours to complete and quick test proved to take even longer. A compromise was achieved using an AD-485 solution containing 2.3 KG AD-485 and 757 mL sulfuric acid in 76 L of water. This AD485 mix provided good corrosion rates of about 2 hours without affecting the mechanical properties of the wire. A fixture was designed to suspend multiple wire samples into the etching solution for batch processing and to control the etching to a precise section of wire. A sample etched wire is shown in Figure 8.



Figure 8. BeCu Wire Samples

Mechanical strength testing of the etched wires was conducted after the etching process to gauge process consistency and Ultimate Tensile Strength. These tests were conducted on over 50 BeCu wire samples of varying etched diameters. The tested wire was threaded through an aluminum retainer, identical to the one used in the mechanism, and then loaded into a pneumatic tensile testing machine. Baseline strength tests were conducted on unetched samples of the BeCu wire to compare against the strength results of the etched samples.

The load to failure of the unetched 0.20 mm samples in testing was found to be approximately 37.8 N and the load to failure in the 0.30 mm unetched samples was approximately 71.2 N. Results from the mechanical testing of these etched samples displayed a directly related, linear relationship between the etched diameter of the wire and the load to failure of that sample. As etched diameters decreased, the load to failure of the sample decreased on a linear progression from the other tested samples of etched

wire. From this mechanical testing, it was concluded that the etching process with the AD-485 solution did not adversely affect the mechanical properties of the wire, and these etched wires would be able to consistently support the load requirements for the Burn Wire Mechanism.

Electrical testing of the samples was performed to determine the electrical characteristic that would be required to efficiently break the burn wire at the etched portion of the sample. Similar to the mechanical testing, the aluminum retainer identical to the one used in the mechanism was used in the electrical tests with the burn wire sample threaded through it. A preload of approximately 9 N was applied to the aluminum retainer. Initial testing of both the 0.20-mm and 0.30-mm wire began at 28.8 V and 7.5 A, which is a standard setting on most satellites. Both types of wire successfully broke at the etching. Some damage to the aluminum retainer was observed due to the large voltage running through the burn wire before breaking. Also, the wire developed a black carbon like deposit on it. Minimum power requirements were determined next and are shown in Table 4. A range of amps and voltage can be accommodated with this mechanism and the wire diameter and etch diameter can be changed to accommodate a lower setting if needed.

Table 4. Burn Wire Electrical Tests

Wire Diameter	Etch Diameter	Low Power Setting	Optimum Power Setting	High Power Limit
0.3 mm		7.5 amps@ 7.5 volts	7.5 amps@ 7.5 volts	28.8 amps@ 7.5 volts
0.3 mm		7.5 amps@ 7.5 volts	7.5 amps@ 7.5 volts	28.8 amps@ 7.5 volts
0.2 mm	0.18 mm	6 amps@ 8 volts	10 amps@ 15 volts	28.8 amps@ 7.5 volts
0.2 mm	0.15 mm	5 amps@ 5 volts	7.5 amps@ 7.5 volts	28.8 amps@ 7.5 volts

Finally, after the initial three sets of tests, actual tests of the mechanism in a simulated operational setup were conducted. All of the information about the performance of the burn wire from the previous three sets of tests was incorporated into the mechanism. The setup for operational testing called for the assembly of the actual mechanism itself and installing it into a mock instrument cover.

Applied current to the mechanism caused the burn wire to break as predicted at the etched area of the wire and the instrument cover easily deployed. This process was completed over 20 times with the 0.20-mm wire etched to 0.15 mm. As for the operational tests with the 0.30-mm samples, many times the current required to break the wire and deploy the cover caused the burn wire to weld itself into the aluminum retainer and restrict the cover from opening. This performance of the 0.30-mm wire proved again that this configuration was not the optimal way to assemble the Burn Wire mechanism. One unexpected problem with the Burn Wire mechanism that was encountered in both the 0.20-mm and 0.30-mm configurations was the occurrence of electrical arcs from the wire itself to portions of the instrument cover, attachment bracket, or even the mechanism itself. This was a noticeable problem in the operation of the mechanism, but one that can be resolved with changes in material selection of components.

Overall, the Burn Wire mechanism performed extremely well during operational testing. As with all new technologies, problems were encountered; however, these problems are seen as ones that require minor design changes rather than overall changes that could affect other aspects of the mechanism that have already been tested.

Recommendations for Future Development

Using non-conducting materials in the mechanism would minimize shorting damage. Shorting of the wire over to an instrument is an unacceptable problem for this design, especially when integrated with sensitive instruments several shorts occurred during tests. Components that were damaged and any others threatened by possible shorting or arcing could be made from a ceramic to give it the strength and electric isolation needed to prevent such a problem. The housing, which is a critical component of the

design, could also be made from Torlon or other thermoplastic. This would provide a low friction sleeve to hold the retainer.

The housing can be redesigned to make this mechanism a plug-in item to make testing easier. All assemblies were hand installed into the test housings and each electric lead connected manually. A package similar to a bus fuse could be designed to ease handling and installation of the mechanism. Handling of miniature screws should be avoided because of how fragile they are and how easy it is to lose them within an instrument, which was demonstrated time and again throughout testing.

Further miniaturization is possible with this mechanism. In order to hand machine and hand assemble the prototype, standard fit and tolerances were used. Alternative fabrication process should be considered to take the mass and volume another step towards being a "micro" sized mechanism. The prototype burn wire mechanism has been shown to have excellent reliability and the possibility for further miniaturization. It is simple in design and the burn wire tests have shown very consistent results. It currently meets the criteria for miniature instrument covers, but has possibility for use in numerous applications on a micro-satellite program. The mini burn wire release may develop into a key mechanism device for the APL MicroSat program.

Mini Linear Actuator

Linear actuators are prevalent in satellite programs as triggers or switches for mechanical devices. There is a definite need for a miniaturized version of this type of mechanism for future micro satellites. This mini linear actuator, developed at APL, is designed to provide a quick acting, low shock linear motion. This mechanism has progressed in development from first prototype into a more optimized prototype. The second prototype was designed and constructed after a small set of cursory tests was conducted on the initial prototype. From the lessons learned, a large decrease in size and mass was obtained without performance loss.

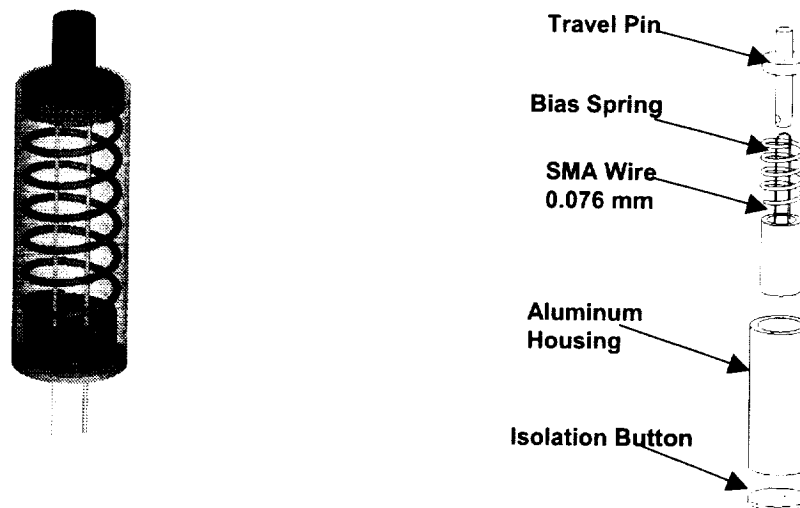


Figure 9. Mini Linear Actuator

Design Approach

The motion (or strain) of typical SMA materials is limited to 8% of the amount of material. A nominal design for this mechanism would limit strain to 2% to ensure adequate fatigue margin. Therefore, this restriction, as well as the amount of wire contained within the mechanism itself, limits the stroke this mechanism will be able to produce. For example, a wire length of 20 mm (0.8 inch), the stroke would be 0.4 mm (0.014 inch). In this design, Nickel-Titanium wire is heated by running current through the wire. The current heats the wire directly via resistance in the wire. Response time is very quick, (~1/10 sec), and the device is not too sensitive to its external thermal environment (in air). Through a strain recovery

process in the material, the wire contracts when heated and returns when cooled using the compression bias spring. It is a self-latching device that is fully testable. The assembled concept is shown in Figure 9.

Both prototype mechanisms utilize SMA wire for actuating this mechanism. It works as a high force, low shock pin puller that can trigger a number of latch devices on instruments shutters or covers. The mini linear actuator is self-resettable using a bias return spring (Figure 9) and can operate in-flight for numerous actuations without any external assistance or resets. With design improvements, the second unit had an 85% reduction in mass and volume and improved the performance of the pin actuation.

Characterization Testing

Operational test were performed on both units using a simple electrical circuit directly connected to the SMA wire. This electrical circuit was able to repetitively cycle the mechanism through its entire range of motion through the use of a capacitor. The circuit delivered 0.25 A at 8.5 V with the capacitor charging and discharging every two to three seconds. Motion of the travel pin created by the contracting SMA wire was measured through the use of a Linear Voltage Displacement Transducer (LVDT) in direct contact with the travel pin of the mechanism. When the travel pin is displaced by the SMA contractions, this causes the LVDT to displace and record the motion. Pin displacement for the first test unit was approximately 0.30-0.33 mm, which is also predicted through calculation. The second test unit incorporated a longer SMA wire (in a smaller package design) and increased displacement to 0.53 mm. Figure 10 shows the results from the second mechanism tests. Note the consistent and repeatable motion displayed by the mechanism.

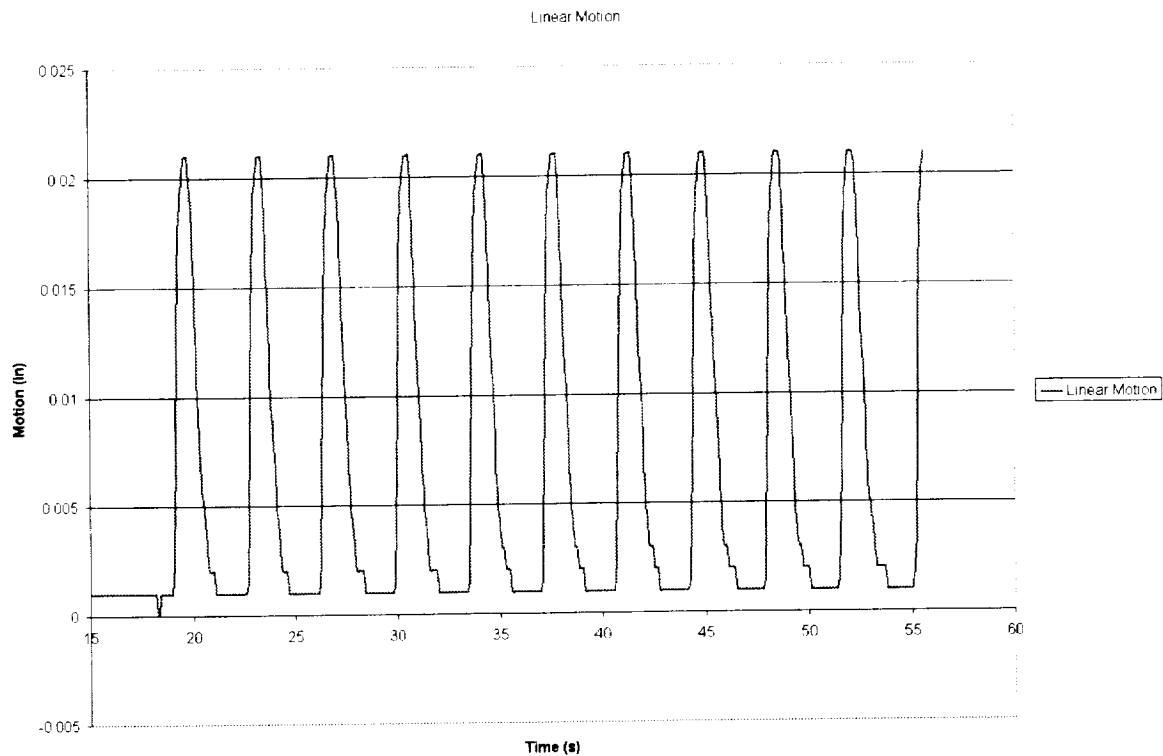


Figure 10. Mini Linear Actuator Operational Tests Results (Second test unit)

Lifetime testing was conducted on the second unit following the characterization testing using the same setup and equipment. This test revealed that the mechanism performed nominally for over 1000 cycles followed by a gradual decay of performance until failure at 12,000 cycles (after 10 hours of operation). This was performed in-air under ambient conditions and is to be followed by thermal-vacuum testing that is yet to be conducted.

Recommendations for Future Development

One of the best features of this device is its capability to be easily adapted for heavier or longer wire in order to provide additional performance capability. Larger displacements of the travel pin can be achieved by adding length to the wire and mechanism. Larger pin retraction force and electrical redundancy can be achieved through the use of several SMA wires instead of a single wire as in this design. Wire gauge, length, and arrangement of the SMA element that drives this mechanism are areas of further interest for characterization tests.

Overall, this mechanism is an extremely light, small, and reliable mechanism that can be used in many applications that require the use of a simple mechanical linear actuator. Testing of the mechanism first validated the concept and then demonstrated the improved performance acquired by a few modifications in the design. Through the use of SMA technology, this mechanism has great potential that will enable it to be a valuable component of the Micro-Mechanism toolkit.

Mini Redundant Release Mechanism

This miniature release is designed to provide electrical and mechanical redundancy. Most mechanisms strive for redundancy in the electrical connections but have single points of failure in the mechanical operation. This mechanism provides multiple redundancies with its ability to operate (release a plunger) with two of the three SMA elements operating. The mini redundant release is in a very early stage of development, and one test unit has been built. Characterization and testing of the mechanism is just getting started and shows a lot of promise.

Design Approach

This prototype mechanism contains shaped SMA strips that lock a restraint shaft for an instrument cover, solar array, or other system needing a release device. SMA strips grip the end of the shaft while in a cold state. When powered and brought to a higher temperature, the SMA strips change shape to "open the lock". Figure 11 shows an exploded assembly view of the mechanism. Full mechanical redundancy is achieved because the device still operates if one of the strips fails to open. A resistor heater on the housing provides the temperature control. This design can be converted to direct current heating to increase the response time. Direct current heating will also provide further electrical redundancy. Simple construction lends to miniaturization. This mechanism can be miniaturized much further depending on the holding force needed. The assembled concept is shown in Figure 11.

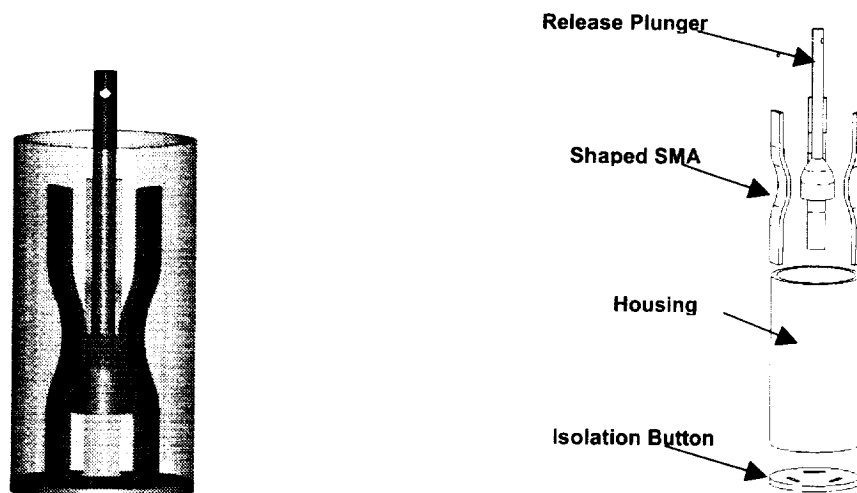


Figure 11. Mini Redundant Release Device

Recommendations for Future Development

Initial fabrication and testing on the prototype mechanism showed the need for proper tooling to manufacture and shape the SMA material in a consistent manner. The first prototype used hand shaped

SMA material that successfully operates the mechanism, but pullout force fluctuates depending on how well the SMA shaping is performed. Tolerances need to be held tighter within the assembly.

A higher level of redundancy can be achieved with heater elements directly attached on each strip. Also, there will be faster response times for initiation of the release if heaters drive the SMA rather than the entire housing and assembly. APL has applied heaters to similar types of material.

Leaf springs may be incorporated into the design to provide a reset capability and also to provide a means for having consistent reset. A range of strip sizes and various ways of restraint on the plunger will be investigated. This could lead to a more optimum approach, higher restraint capability, and greater miniaturization.

Lessons Learned

Designing and developing mechanisms at this scale requires a different approach than what most mechanism designers are accustomed to. There are a number of considerations that must be addressed in order to ensure correct, optimal performance of these mechanisms. These issues also encompass not only operational considerations, but also issues that indirectly affect a mechanism's performance if not adequately addressed, such as fabrication and assembly.

Tolerances and Working with Small Parts

Working with parts this scale intrinsically leads to tolerance issues. A small dimensional discrepancy on a part can lead to a significant change in mechanism performance. On the Mini Sep-Nut, the initial parts were machined with too great of tolerance, preventing the nut segments from forming a tight nut to thread the screw into. In a second iteration, the collar was machined-to-fit to achieve a close fit with the housing and nut segments, providing a tight interface for the screw threads. It is important to remember when designing small components that some of the parts may need secondary machining to achieve the desired assembled fit. The mechanisms in this tool kit were designed so that the dimensional variations lead to a minimal impact on the mechanism's overall performance.

The size of the components created some difficulties in fabrication. As discussed, tight tolerances required on small dimensions made the parts more expensive. The most difficult parts to machine were the screw and nut for the Micro Sep-Nut. The screw had a 0.80-127 thread with a 0.76-mm shaft. The screw size and thread made the component very fragile. During the cutting of the threads, the shaft deformed. It would have been beneficial to utilize a specialized vendor with a Swiss milling machine and experience in fabricating miniature components.

Miniaturized components are very difficult to handle with manual machining and hand assembly processes. Automated or tooled processes are needed to hold tighter tolerances, improve consistency, and simplify the assembly of the actual mechanism. Additional attention could be required due to possible changes in material selection, which might also introduce new challenges in the fabrication of components and assembly of the mechanism.

Shape Memory Alloy

The use of Shape Memory Alloy (SMA) creates a number of considerations that must be examined as part of the design process. Additional work with SMA will allow for additional understanding of this unique material and configurations that optimize its performance.

It is critical to carefully characterize the performance of the SMA element prior to incorporating it into the design. By doing so, this will help the designer understand the behavior of the SMA. Many of the custom shapes or forms are somewhat inconsistent in their behavior, and it is important to understand these effects and how they will impact the overall mechanism design.

The control strategies for applying power directly to the SMA must be carefully considered and applied. It is easy to damage the SMA element if power is applied for too long. If the SMA element is heated for too long, it can take a new set.

Conclusions

The key factor for shrinking mechanism size is to reduce complexity. The mini separation nut design was taken from a conventional separation system and was simply scaled down. It was judged to be not quite miniaturized for the micro satellite uses that was envisioned. By radically redesigning the mini separation nut, the micro separation nut was able to get the performance needed with 3 components instead of 8 and was 75% lighter and smaller and lighter than the mini separation nut. Another example is the burn wire mechanism, which is the smallest and lightest in the tool kit due its simplified and streamlined design. Its this kind of streamlining that is needed to address the micro satellite needs.

Some of these mechanisms give up redundancy for simplicity. This may be a risk that constellations of small and inexpensive micro satellite constellations will be willing to take. If redundancy is required, there are options in this tool kit that provide it. Micro mechanisms are going to need to break from traditional mechanism design to meet the need of future micro satellites.

The problems encountered in this project were not completely addressed and fully tested. Continuation of this project is expected to look in more detail at manufacturability, assembly, characterization of SMA's and, and power and mass optimization for these mechanisms. From the brief testing performed, there appears to be attainable solutions to all the problems encountered. Future work should yield mechanisms that are qualified for flight. These will be some of the smallest and lightest mechanical components available that provide precise and consistent performance for micro satellite as well as traditional satellite programs.

References

- Helvajian, Henry. "Microengineering Aerospace Systems." *The Aerospace Press, American Institute of Aeronautics and Astronautics*, 1999.
- Madou, Mark. "Fundamentals of Microfabrication." *CRC Press*, 1997
- Waram, Tom. "Actuator Design Using Shape Memory Alloys." *Second Edition*, 1993

REPORT DOCUMENTATION PAGE

Form Approved
OMB No. 0704-0188

Public reporting burden for this collection of information is estimated to average 1 hour per response, including the time for reviewing instructions, searching existing data sources, gathering and maintaining the data needed, and completing and reviewing the collection of information. Send comments regarding this burden estimate or any other aspect of this collection of information, including suggestions for reducing this burden, to Washington Headquarters Services, Directorate for Information Operations and Reports, 1215 Jefferson Davis Highway, Suite 1204, Arlington, VA 22202-4302, and to the Office of Management and Budget, Paperwork Reduction Project (0704-0188), Washington, DC 20503.

1. AGENCY USE ONLY (Leave blank)	2. REPORT DATE May 2001	3. REPORT TYPE AND DATES COVERED Conference Publication	
4. TITLE AND SUBTITLE Proceedings of the 35th Aerospace Mechanisms Symposium		5. FUNDING NUMBERS 712-30	
6. AUTHOR(S) Edward A. Boesiger, Compiler		8. PERFORMING ORGANIZATION REPORT NUMBER A-00V0037	
7. PERFORMING ORGANIZATION NAME(S) AND ADDRESS(ES) Ames Research Center Moffett Field, CA 94035-1000			
9. SPONSORING/MONITORING AGENCY NAME(S) AND ADDRESS(ES) National Aeronautics and Space Administration Washington, DC 20546-0001		10. SPONSORING/MONITORING AGENCY REPORT NUMBER NASA/CP-2001-209626	
11. SUPPLEMENTARY NOTES Sponsor: Mechanisms Education Association Point of Contact: Ronald E. Mancini, Deputy Chief, Systems Engineering Division, Ames Research Center, MS 213-1, Moffett Field, CA 94035-1000			
12a. DISTRIBUTION/AVAILABILITY STATEMENT Unclassified — Unlimited Subject Category 15 Distribution: Standard Availability: NASA CASI (301) 621-0390		12b. DISTRIBUTION CODE	
13. ABSTRACT (Maximum 200 words) The proceedings of the 35th Aerospace Mechanisms Symposium are reported. Ames Research Center hosted the conference, which was held at the Four Points Sheraton, Sunnyvale, California, on May 9-11, 2001. The symposium was sponsored by the Mechanisms Education Association. Technology areas covered included bearings and tribology; pointing, solar array, and deployment mechanisms; and other mechanisms for spacecraft and large space structures.			
14. SUBJECT TERMS Spacecraft components, solar array deployment, bearings, tribology, covers, latches, dampers, retraction mechanisms.		15. NUMBER OF PAGES 312	
17. SECURITY CLASSIFICATION OF REPORT Unclassified		16. PRICE CODE A14	
		20. LIMITATION OF ABSTRACT	
18. SECURITY CLASSIFICATION OF THIS PAGE Unclassified		19. SECURITY CLASSIFICATION OF ABSTRACT	



